Steel Fibre Reinforced Self-Compacting Concrete

(from Micro-Mechanics to Composite Behaviour)

Dissertation submitted by

Vítor Manuel do Couto Fernandes da Cunha

to University of Minho for obtaining the Degree of

Doctor in Civil Engineering

Supervisor:

Prof. Doutor Joaquim António Oliveira Barros

Co-supervisor:

Prof. Doutor José Manuel Sena Cruz

ISBN: 978-972-8692-44-5
Printed in Portugal

Preface

This thesis is handled in as a partially fulfilment of the requirements to obtain the *Philosophiæ Doctor* degree in the scientific domain of Civil Engineering and Mining, namely, the Structural area of knowledge. The academic proofs were carried out at the School of Engineering, University of Minho.

The author gratefully acknowledges all the support of his main supervisor, Assoc. Prof. Joaquim Barros, from University of Minho, as well the co-supervisor Prof. José Sena, also from University of Minho, not only for their obligingness and friendly support, but also for their profuse wisdom and knowledge.

To them, my sincerely thanks. It was a pleasure working with you!

The author also wishes to acknowledge the scholarship SFRH/BD/18002/2004 provided by the Portuguese Foundation for Science and Technology, FCT.

The experimental work would not have been realised so straightforwardly without the enthusiastic dedication of the laboratory technicians, particularly, Sr. José Matos and Marco Jorge. I am grateful for their help during the execution of the experimental tests, and for helping to solve the arisen technical problems. I also would like to acknowledge the help of Delfina Gonçalves, from Civitest company, on the experimental program. Of course, I want to thank all my colleagues in the Civil Engineering Department, specially, the ones from the Structural Group.

To all the secretarial staff, my deeply thanks, not only for the completely unselfish help on the bureaucratic issues, but also for their joyful fellowship.

An exquisite thanks to my alter-ego "Zé Gusto", also known as "Tira", who turned this period very funny and enjoyable, enlightening me throughout this work without getting senile and completely lunatic. Or not!

I owe special thanks to all my numerous friends for their sincere friendship. I will try not to forget anyone. Otherwise, my apologies in advance. So, thank you: Andreia, Alberto "Bertinho", Aline, Alexandre Antunes "Boss", Ana Cristina, Ana Isabel, Artur "Quinta", Álvaro "Barocas", Barbara "Barbie", Bruno, Carla Pina, Carlinha, Carlos, Carlos Daniel, Carlos Ma-

galhães, Catarina, Claudia, Diana, Eduardo “Paraíba”, Evandro “Ivan”, Francisco “Chicote”, Frank “Morelli”, Guida, Joana “Quinhas”, Joana Resende, Jocilene, Jorge “Lambes”, Leo Bridi, Ligia, Luís Abreu, Luís Neves, Ferraz “Chara”, Manuela “Nelinha”, Mariana, Marta, Mário, Martinho “Leão”, Miguel “Jardel”, Nuno “Curto”, Nuno “Piri”, Nuno Rebelo, Pedro Lança, Ramoa “Mingos”, Russel, Rute, Regina, Rita, Rosa, Sena “Neca”, Susana “Sussu”, Susana Simões, Teresa, Teresa “Té”, Tiago “Tita”, Tiago Figueira “Brinco”, Tiago Miranda, Tomé, Zé “Turiz”, Zé Campos e Matos, Zé Pedro “Palmeira” and Zé Pina.

Finally, I would say that this work is a result from the unconditional and indulgent support and love of my family, particularly, my parents, sister and grandparents. Thanks for your patience. I also would like to perpetuate the memory of my uncle who suddenly left us.

Abstract

The use of steel fibre reinforced self-compacting concrete, SFRSCC, probably, will swiftly increase in the next years, since this composite material introduces several advantages on the concrete technology. In fact, the partial or total replacement of the conventional bar reinforcement by discrete fibres optimizes the construction process. The assembly of the reinforcement bars in the construction of concrete structures has a significant economic impact on the final cost of this type of constructions, due to the man-labour time consuming that it requires. In the modern societies, the cost of the man-labour is significant, so diminishing the man-labour will decrease the overall cost of the construction. In the fresh state, SFRSCC homogeneously spreads due to its own weight, without any additional compaction energy. Driven by its own weight, the concrete has to fill a mould completely without leaving entrapped air, even in the presence of dense steel bar reinforcement.

Due to these reasons, SFRSCC is a very promising construction material with a high potential of application, mainly in the cases where fibres can replace the conventional reinforcement. At the present time, however, the SFRSCC technology is not yet fully developed and controlled, and, much less, the mechanical behaviour of the SFRSCC material.

The present work aims to increase the knowledge in these areas. Therefore, experimental, analytical and numerical research was carried out. The main purpose was to achieve, as much as possible, a consistent comprehension of the behaviour of this composite material, and to collect data for the calibration of the analytical formulations and FEM-based numerical models developed in scope of this research program.

The experimental research covers aspects from distinct scale levels. At a micro-level, the micro-mechanics aspects of fibre reinforcement are analysed, while at a meso-level, the fibre distribution structure into the hardened concrete is key aspect investigated. The research carried out at a micro/meso level enables to have a deeper understanding of the multiple reinforcement mechanisms and factors that influence the overall composite behaviour at a macro-level. Finally, at a macro-level, the composite mechanical behaviour, namely, the compressive, flexural and uniaxial tensile behaviour is assessed. The gathered experimental information at the distinct studied scale levels enables to acquire a deeper knowledge of the multiple reinforcement mechanisms involved. Finally, an integrated numerical approach was developed, which based on the fibres' micro-mechanical properties, is able of predicting the mechanical properties of fibre reinforced composites.

Resumo

A utilização de betão auto-compactável reforçado com fibras de aço, BACRFA, provavelmente, aumentará significativamente no decurso dos próximos tempos, visto que este material compósito introduz vários melhoramentos ao nível dos processos tecnológicos do betão. Na verdade, a substituição total ou parcial das armaduras convencionais, usadas no betão armado corrente, por fibras discretas de aço, contribui para o aumento da competitividade do processo construtivo. Para além dos benefícios tecnológicos, advém vantagens económicas devidas à redução na duração do tempo de construção, nomeadamente, na montagem de armaduras convencionais. Nas sociedades modernas, em que a competitividade na indústria da construção se apresenta cada vez mais intensa, e o preço da mão-de-obra tem aumentado constantemente, este material apresenta-se cada vez mais como uma solução competitiva. Contudo, presentemente, a tecnologia do BACRFA não está ainda totalmente potenciada, e as suas propriedades mecânicas ainda não são totalmente conhecidas.

O presente trabalho pretende contribuir para o aumento do conhecimento nestas áreas. Para tal foi desenvolvida investigação experimental, analítica e numérica. O principal propósito deste trabalho consistiu, tanto quanto possível, num exaustivo e consistente estudo das propriedades mecânicas deste material compósito, e na obtenção de dados para a calibração de modelos analíticos e modelos numéricos, estes últimos suportados na formulação do método dos elementos finitos.

A investigação experimental engloba o estudo do comportamento a diferentes escalas. A um nível micro, os principais mecanismos de reforço das fibras foram estudados e analisados. À meso escala foi dada especial atenção à distribuição das fibras numa matriz endurecida de BACRFA. A investigação do material a uma escala micro/meso permite o melhor conhecimento dos múltiplos mecanismos de reforço que influenciam o comportamento global do material compósito a um nível macro. Finalmente, a um nível macro, o comportamento do material compósito foi aferido para diversos tipos de carregamentos, respectivamente, tracção e compressão uniaxial assim como flexão.

A informação recolhida a diferentes escalas permitiu um melhor e profuso conhecimento dos múltiplos mecanismos de reforço envolvidos no BACRFA. Consequentemente, possibilitou a criação de uma estratégia numérica integrada que, de um ponto de vista racional e sustentável, facilita a previsão das propriedades mecânicas dos BACRFA baseada nas propriedades micromecânicas das fibras.

Notation and symbols

Abbreviations

1D, 2D, 3D	One, two and three-dimensions
3PBT	Three-point bending tests
ACI	American Concrete Institute
ASTM	American Society for Testing and Materials
CMOD	Crack mouth opening displacement
CoV	Coefficient of variation
CFRC	Conventional vibrated fibre reinforced concrete
EC 2	Eurocode 2
ECC	Engineered cement composite
EN	European Norm
FEM	Finite element method
FPZ	Fracture process zone
FRC	Fibre reinforced concrete
FRP	Fibre reinforced polymers
HPFRCC	High-Performance Fibre-Reinforced Cementitious Composite
JSCE	Japan Society of Civil Engineers
LNEC	Portuguese National Laboratory of Civil Engineering
LVDT	Linear voltage displacement transducer
IA	Inverse analysis
IP	Integration point
ITZ	Interface transition zone
IURD	Isotropic uniform random distribution
PID	Proportional-integral-derivative
RILEM	International Union of Laboratories and Experts in Construction Materials
RKN	Runge-Kutta-Nyström
SCC	Self-compacting concrete
SFRC	Steel fibre reinforced concrete
SFRSCC	Steel fibre reinforced self-compacting concrete
UTS	Ultimate tensile strength
UTT	Uniaxial tension test
WST	Wedge splitting test

Latin		
i.e.	*id est*	that is
et al.	*et ali*	and the others
e.g.	*exempli gratia*	for example
etc.	*et cetera*	and so on
vs.	*versus*	versus

Part I – Micro-Mechanical Behaviour of SFRSCC

Greek letters		
ε_f	Fibre strain	–
ε_c	Concrete strain	–
η	Factor that simulates the steepness pullout curve descending branch	–
κ_{b1}	Bond modulus of the real fibre	N/mm^3
κ_{b2}	Bond modulus of the fictitious fibre	N/mm^3
κ_e	Secant spring coefficient	N/mm
μ	Friction coefficient	–
ν_m	Poisson coefficient of the matrix	–
ν_f	Poisson coefficient of the fibre	–
θ	Fibre inclination angle	$^\circ$
σ	Normal stress	N/mm^2
σ_f	Normal stress in the fibre	N/mm^2
σ_{max}	Maximum pullout stress	N/mm^2
$\sigma_{b,max}$	Maximum tensile stress due to bending	N/mm^2
σ_{fu}	Fibre rupture stress	N/mm^2
σ_n^{ext}	Normal stress due to external loading	N/mm^2
σ_n^{shr}	Normal stress due to shrinkage	N/mm^2
σ_y	Yielding stress of the fibre	N/mm^2
τ	Bond stress	N/mm^2
$\overline{\tau}$	Average bond stress	N/mm^2
τ_{crit}	Critical shear bond resistance	N/mm^2
$\tau_f(s)$	Frictional stress for the fibre slip δ	N/mm^2
$\overline{\tau}_f$	Constant friction bond	N/mm^2
$\tau_0^{'}$	Frictional bond stress	N/mm^2

Continued on next page

Continued from previous page

ω	Fibre volume deformed under shear	mm^3
ξ	Damage coefficient of the shear stress deterioration	–
Γ	Bond energy of the interface zone	N/mm

Roman letters

a	Fibre debonded length	mm
d_f	Fibre diameter	mm
r_f	Fibre radius	mm
s	Slip	mm
s_0	Pullout slip correspondent to the maximum bond stress	mm
s_{crit}	Fibre slip corresponding the critical force	mm
s_{d0}	Fibre end slip at the full debonding stage	mm
$s_d(x)$	Component of slip that produces fibre deformation	mm
s_f	Fibre free-end slip	mm
s_l	Fibre loaded-end slip	mm
$\overline{s}_l^i$	Experimental loaded-end slip measured in the *i-th* scan	mm
s_k	Displacement difference between real and fictitious fibres	mm
s_{peak}	Pullout slip correspondent to maximum pullout load	mm
$t(x)$	Shear force per length unit at distance x from the fibre end	N/mm
t_f	Frictional shear force per unit length	N/mm
u_f	Displacement of the fibre in the axial direction	mm
u_m	Displacement of the matrix	mm
w	Crack opening displacement	mm
w/b	Water/binder ratio	-
A_f	Fibre's cross sectional area	mm^2
A_{f2}	Fictitious fibre cross sectional area	mm^2
A_m	Cross section area of the matrix	mm^2
E_f	Fibre´s Young modulus	N/mm^2
E_{f2}	Fictitious fibre's Young modulus	N/mm^2
E_m	Young modulus of the matrix	N/mm^2
L_{bent}	Length of the fibre bent zone	mm
L_b	Fibre embedded length	mm
L_{b2}	Fictitious fibre embedded length	mm
$L_{b,crit}$	Critical embedment length	mm
N	Pullout load	N
N_b	Pullout load developed on the bond zone	N

Continued on next page

Continued from previous page

N_{crit}	Critical pullout load	N
N_d	Pullout load developed on the debond zone	N
$\overline{N}_l^i$	Experimental loaded end force measured in the i-th scan	N
N_{sp}	Axial force in the fibre due to the hook	N
N_x	Component of the pullout load on the fibre axis	N
N_y	Component of the pullout load perpendicular to the fiber axis	N
S	Interfacial stresses along the fibre	$\mathrm{N/mm^2}$
V_f	Fibre volume over the embedded length	$\mathrm{mm^3}$
V_{fb}	Fibres volume fraction	–
W_{bent}	Plastic deformation energy under bending	$\mathrm{N \cdot mm}$
W_{shear}	Plastic deformation energy under shear	$\mathrm{N \cdot mm}$
P_f	Fibre cross section perimeter	mm

Part II – Mechanical Behaviour of SFRSCC (from meso to macro-scale)

Chapter 6 – Fibre Structure in the Composite Matrix

Greek letters		
φ	Fibre's in-plane angle	º
γ	Effective reduction of the fibre content	–
η	Fibre orientation factor	–
η_{2D}, η_{3D}	Fibre orientation factors for 2D and 3D systems	–
$\bar{\eta}_{b3}$	Stress transfer efficiency parameter in boundary layer	–
η_{exp}	Orientation factor determined by fibre counting at cross section	–
η_{img}	Orientation factor determined by image analysis procedure	–
λ	Fibre aspect ratio	–
θ	Fibre's out-plane angle	º
σ_m	Matrix tensile strength	$\mathrm{N/mm^2}$
$\sigma_{\|\|}$	Stress component parallel to the orientation plane of the 2D portion	$\mathrm{N/mm^2}$
$\sigma_\perp$	Stress component perpendicular to the orientation plane of the 2D portion	$\mathrm{N/mm^2}$
τ	Interface bond strength	$\mathrm{N/mm^2}$
ω	Degree of orientation of the fibre structure	–
ξ_{seg}	Fibre segregation degree	–

Continued on next page

Continued from previous page

Roman letters		
a	Ellipse major semi-axis	mm
b	Ellipse minor semi-axis	mm
d	Fibre diameter	mm
h	Cross section's height	mm
l_f	Fibre length	mm
t	Thickness of a concrete's slice	mm
x_c, y_c	Fibre gravity centre coordinates	mm
$\bar{y}$	Average of the fibre's vertical coordinate of a cross section	mm
A_f	Fibre's cross sectional	mm^2
L_V	Total fibre length in a unit volume of concrete	mm/mm^3
$N_f^{\|\|}$	Effective fibre content of a section parallel to the direction of the vibrating force (in SFRSCC parallel to crack surface)	$1/mm^2$
$N_{f,crk}^{\|\|}$	Fibre content at the specimen's crack surface	$1/mm^2$
$\check{N}_f^{\|\|}$	Minimum fibre content of a section parallel to the direction of the vibrating force (in SFRSCC parallel to crack surface)	$1/mm^2$
$N_f^{\perp}$	Effective fibre content of a section perpendicular to the direction of the vibrating force (in SFRSCC parallel to crack surface)	$1/mm^2$
$\check{N}_f^{\perp}$	Minimum fibre content of a section perpendicular to the direction of the vibrating force	$1/mm^2$
N_f^{3D}	Expected nominal fibre content assuming 3D distribution	$1/mm^2$
V_f	Nominal fibre content	$\%/mm^3$

Chapter 7 – Compressive behaviour (age influence and modelling)

Greek letters		
α	Parameter of the $\sigma_c - \varepsilon_c$ relationship	–
$\alpha(t)$	Variation of parameter α with age t	–
$\alpha(f_{cm}(t))$	Variation of parameter α with the compressive strength	–
ε_a, ε_b	Strain for the σ_a, σ_b levels in the elasticity modulus determination test	–
$\varepsilon_{a,n}$, $\varepsilon_{b,n}$	Strain correspondent to the stress limits of the n^{th} cycle	–
ε_c	Compressive strain	–
ε_{c1}	Compressive strain at peak stress	–
$\varepsilon_{c1,28}$	Compressive strain at peak stress at an age of 28 days	–
$\varepsilon_{c1}(t)$	Compressive strain at peak stress at an age t	–

Continued on next page

Continued from previous page

$\varepsilon_{c,lim}$	Compressive strain that limits the applicability of the $\sigma_c - \varepsilon_c$ relationship's first branch	–
μ	Mean of the population	–
σ^2	Variance	–
σ_a, σ_b	Stress levels in the elasticity modulus determination test	N/mm^2
$\sigma_{a,n}$, $\sigma_{b,n}$	Average of the stress limits of n^{th} cycle	N/mm^2
σ_c	Compressive stress	N/mm^2
ξ	Constant of the $\sigma_c - \varepsilon_c$ relationship	–

Roman letters

a, b, c, d, e	Dimensionless parameters used in analytical expression for modelling the compressive behaviour mechanical properties	–
d_{dof}	Number of degrees of freedom	–
d_f	Fibre diameter	mm
f_{cm}	Average compressive strength	N/mm^2
$f_{cm,28}$	Average compressive strength at an age of 28 days	N/mm^2
$f_{cm}(t)$	Average compressive strength at an age t	N/mm^2
l_f	Fibre length	mm
n	Number of sample values	–
n^{eff}	Total number of experimental points used in the fitting procedure	–
p	Total number of adjustable parameters used in fitting procedure	–
w_{ij}	Pondered weights ascribed to each experimental point	–
$\bar{x}$	Mean of a sample	–
y_{ji}	Measured values of the dependent variables	–
$z_{\alpha/2}$	Upper $\alpha/2$ percentage point of the t-Student distribution	–
$E_{c,n}$	Elasticity modulus correspondent to the n^{th} test's cycle	N/mm^2
E_{ci}	Elasticity modulus	N/mm^2
$E_{ci,28}$	Elasticity modulus at an age of 28 days	N/mm^2
$E_{ci}(t)$	Elasticity modulus at an age t	N/mm^2
G_c	Volumetric energy dissipated under compression	N/mm^2
$G_c(t)$	Volumetric energy dissipated under compression at an age t	N/mm^2
T_{50}	Concrete's flow time to reach a spread diameter of 50 cm	s
V_f	Fibre volume content	$\%/mm^3$

Chapter 8 – Post-Cracking Behaviour (experimental and numerical analysis)

Greek letters		
δ_2, δ_3	Deflection limits for determining the $D^f_{BZ,2}$ $D^f_{BZ,3}$ energy absorption capacities, respectively	mm
δ_{avg}	Average displacement in the uniaxial tensile test	mm
δ_L	Deflection at the limit of proportionality	mm
$\delta_{R,i}$	Deflection levels for computing the flexural residual strengths	mm
η_θ	Fibre effectiveness factor	–
$\eta_{\theta,3PBT}$	Fibre effectiveness factor obtained from the the three-point bending test's specimens	–
$\eta_{\theta,UTT}$	Fibre effectiveness factor obtained from the the uniaxial tensile test's specimens	–
$\eta_{\theta,SPLT}$	Fibre effectiveness factor obtained from the the splitting-tension test's specimens	–
ν_c	Poisson's ratio of concrete	–
ρ	Concrete's density	N/mm^3
σ	Tensile stress	N/mm^2
$\sigma_{0.3mm}$	Tensile stress for a crack opening width of 0.3 mm	N/mm^2
σ_{1mm}	Tensile stress for a crack opening width of 1 mm	N/mm^2
σ_{2mm}	Tensile stress for a crack opening width of 2 mm	N/mm^2
σ_{nom}	Nominal tensile strength	N/mm^2
σ_{peak}	Maximum tensile stress	N/mm^2
$\bar{\sigma}_w(w)$	Average stress - crack opening curve	N/mm^2
$\sigma_{w,k}(w)$	Characteristic stress - crack opening curve	N/mm^2
Roman letters		
b	Width of the RILEM's specimen	mm
d	Height of the splitting-tension test specimen	mm
e^i	Error for the i^{th} $\sigma - w$ relationship's parameters set	–
$f_{ct,L}$	Stress at the limit of proportionality	N/mm^2
f_{eq}	Equivalent flexural tensile strength	N/mm^2
$f_{R,i}$	Residual flexural tensile strength	N/mm^2
h_{sp}	Net cross sectional area of the RILEM's specimen	mm
k	Confidence level	%

Continued on next page

Continued from previous page

t	Thickness of the splitting tension test specimen	mm
w	Crack opening width	mm
w_u	Ultimate crack opening width	mm
A_{exp}	Area of the experimental flexural load - deflection curve	$\mathrm{N}\cdot\mathrm{mm}$
A_c	Net cross sectional area of the RILEM's beam	mm^2
A_f	Cross sectional area of the fibres	mm^2
A_{num}	Area of the numerical flexural load - deflection curve obtained by IA	$\mathrm{N}\cdot\mathrm{mm}$
D^c_{BZ}	Energy absorption capacity due to the plain concrete contribution	$\mathrm{N}\cdot\mathrm{mm}$
D^f_{BZ}	Energy absorption capacity due to the fibre contribution	$\mathrm{N}\cdot\mathrm{mm}$
F_L	Load at the limit of proportionality	N
F_T	Tenacity index (JSCE – SF4 1984)	$\mathrm{N}\cdot\mathrm{mm}$
G_f	Fracture energy	N/mm
G_{F1mm}	Energy dissipated up to a crack opening of 1 mm	N/mm
G_{F2mm}	Energy dissipated up to a crack opening of 2 mm	N/mm
$\bar{G}_{F2mm}$	Average value of the energy dissipated up to a crack opening of 2 mm	N/mm
$G_{F2mm,k}$	Characteristic value of the energy dissipated up to a crack opening of 2 mm	N/mm
I_N	Tenacity indexes (ASTM C1018-89 1991)	$\mathrm{N}\cdot\mathrm{mm}$
L	Span's length of the RILEM's beam	mm
$L_{b,proj}$	Average projected embedded fibre length	mm
L_f	Fibre length	mm
N_f	Total number of fibres at the fracture surface	–
N_f^{eff}	Number of effective fibres at the fracture surface	–
P	Load value from the splitting tension test	N

Chapter 9 – Finite Element Model with Short Discrete Embedded Fibres for FRC

Greek letters		
α	Fibre inclination towards the pullout load direction	º
β	Shape parameter of the Weibull distribution, and also shear retention factor	–
δ	Scale parameter of the Weibull distribution	–
$\varepsilon^{cr}_{n,ult}$	Ultimate crack normal strain	–
$\gamma^{cr}_{t1,n}$	Ultimate crack shear strain corresponding to $\hat{t}_1$ sliding directions	–
$\gamma^{cr}_{t2,n}$	Ultimate crack shear strain corresponding to $\hat{t}_2$ sliding direction	–
λ	Shape parameter of the Weibull distribution	–

Continued on next page

Continued from previous page

ν_c	Poisson's ratio of concrete	–
ϖ	Scale parameter of the Weibull distribution	–
θ	Angle between fibre and crack's normal vector	º
τ_p^{cr}	Crack shear strength	N/mm^2
$\Delta\underline{\varepsilon}$	Incremental strain vector	–
$\Delta\underline{\varepsilon}^{co}$	Incremental strain vector with the uncracked concrete contribution	–
$\Delta\underline{\varepsilon}^{cr}$	Incremental crack strain vector in the global coordinate system	–
$\Delta\underline{\varepsilon}_l^{cr}$	Incremental crack strain vector in the local coordinate system	–
$\Delta\varepsilon_n^{cr}$	Incremental normal crack strain	–
$\Delta\gamma_{t1}^{cr}$	Incremental crack shear strain according direction $\hat{t}_1$	–
$\Delta\gamma_{t2}^{cr}$	Incremental crack shear strain according direction $\hat{t}_2$	–
$\Delta\underline{\sigma}$	Incremental stress vector	N/mm^2
$\Delta\underline{\sigma}_l^{cr}$	Incremental crack stress vector in the local coordinate system	N/mm^2

Roman letters

$\underline{a}^f$	Matrix with the direction cosines	–
b_{rct}	Width of prismatic specimen	mm
f_{ct}	Concrete's tensile strength	N/mm^2
$f_{\mathrm{X}}(\ldots)$	Relative frequency of pseudo-Weibull distribution	–
h_{cyl}	Height of cylindric specimen	mm
h_{rct}	Height of prismatic specimen	mm
k	Constant parameter from the Cornelisson tensile law	–
l_b	Crack band width	mm
l_f	Fibre length	mm
l_{rct}	Length of prismatic specimen	mm
m_f	Mass weight of a single fibre	g
$\hat{n}$	Normal direction to the crack plane	–
$\hat{t}_1$, $\hat{t}_2$	Orthogonal directions to $\hat{n}$	–
r_{cyl}	Radius of cylindric specimen	mm
A_f	Fibre cross sectional area	mm^2
$\bar{A}_f$	Reduced shear area for circular section	mm^2
$\underline{B}_c$	Strain - displacement matrix	1/mm
C_f	Fibre content	g/mm^3
$\underline{D}$	Tangent constitutive matrix	N/mm^2
$\underline{D}^{co}$	Elastic constitutive matrix of the uncracked concrete	N/mm^2
$\underline{D}^{cr}$	Crack's constitutive matrix	N/mm^2

Continued on next page

Continued from previous page

D_I^{cr}	Mode I stiffness modulus	N/mm^2
D_{II}^{cr}	Stiffness modulus of the shear fracture Mode II	N/mm^2
D_{III}^{cr}	Stiffness modulus of the shear fracture Mode III	N/mm^2
$\underline{D}^{crco}$	Elasto-cracked constitutive matrix	N/mm^2
E_c	Concrete's Young modulus	N/mm^2
$F_{\mathrm{X}}(\ldots)$	Cumulative frequency of pseudo-Weibull distribution	–
G_c	Elastic shear modulus	N/mm^2
G_f	Fracture energy of concrete in Mode I	N/mm
$G_{f,s}$	Shear fracture energy of concrete	N/mm
J	Jacobian	–
$\underline{K}^{rc}$	Stiffness matrix of solid element with fibre reinforcement	N/mm
$\underline{K}^{crco}$	Stiffness matrix of of the concrete contribution	N/mm
N_f^{Vol}	Number of fibres contained in specimen	–
$\underline{T}^{cr}$	Transformation matrix from local to global coordinate system	–
$\underline{T}^{f}$	Transformation matrix from fibre's local to global coordinate system	–
V_s	Specimen's volume	mm^3

Contents

List of Figures

List of Tables

Chapter 1

Introduction

1.1 Motivation

The widespread employment of concrete in structures has been among us for millenniums, probably, since the Egyptian civilization (Campbell and Folk 1991). However, it was during the Roman Empire that the arisen of this material enabled a revolution on the construction of structures, namely, on concrete vaulted structures. Consequently, back on those days, this allowed and pushed to revolutionarily new designs both in terms of structural complexity and dimension, e.g. Pantheon and Basilica of Maxentius (Lancaster 2005).

For the past two millenniums, the concrete technology has faced endless developments, particularly, from mid of the eighteenth century. Since it is out of the scope of this work and would be quite fastidious to enumerate them, a description of some of these advances can be found elsewhere (e.g. Mindess et al. 2003). Even though the endless breakthroughs, there are still some problems related to the utilisation of this material. More precisely, these "problems" can be regarded rather as disadvantages from cementicious materials, in comparison to other materials commonly used nowadays, e.g. steel. Concrete being a "quasi-fragile" material has almost no ductility, additionally, has a very low tensile strength. Therefore, the utilisation of rebars is mandatory, in order to bridge the cracks and to face up with the tensile forces which are often larger than the concrete's tensile strength. Moreover, the concrete structures' self-weight is quite considerable, if comparing with steel structures with the same bearing capacity, thus a great deal of concrete's material is just for supporting the dead-loads. This larger amount of material, and "redundant" for the final structural purpose of sustaining something, and not itself, besides the setbacks from a sustainability point of view, will enhance the man-labour time used for mounting both the rebars and the heavier choring systems. Finally, concrete is

not a maintenance-free material. During, the service life of concrete structures, they will be subjected to distinct grades of loading, which may produce distinct grades of structural damage, i.e. cracks, hence subsequently harmful substances can penetrate through cracks and cause the corrosion of reinforcement. This is also influenced by the porous nature of concrete.

With regard to copping with the abovementioned disadvantages, in the past recent years, have arisen several new cement based materials, such as: slurry infiltrated fibre concrete (Hackman et al. 1992, Naaman 1992, Hauser and Worner 1999), SIFCON, steel fibre reinforced self-compacting concrete (Groth 2000, Grünewald 2004, Schumacher 2006), SFRSCC, engineered cement composites (Li and Leung 1992, Li and Wu 1992, Leung 1996), ECC, high performance fibre reinforced concrete (Markovic 2006, Lappa 2007), HPFRC, between other materials and designations. From these enumerated alternatives, the utilization of SFRSCC poses a very feasible and rational solution to some problems of conventional concrete. This material does not intend to solve all the referred disadvantages of conventional concrete, but to greatly mitigate them. Recently, other materials as ECC and HPFRC exhibiting multiple cracking, have shown astonishing mechanical performances, however these have yet some drawbacks. In spite of their outstanding properties, until the present time, structural realizations in ECC and HPFRC are yet scarce, mainly, due to (Kabele 2000):

- limited experience with ECCs' structural behaviour;
- non-existence of design codes that would permit to take advantage from the material's pseudo strain-hardening behaviour;
- high fibre cost, which makes the composite several times more expensive than ordinary concrete.

To deal with the first itemized reason, several experimental works have been conducted in the past decade (e.g. Naaman 2003, Kanda and Li 2006, Markovic 2006, Lappa 2007). On the other hand, this material is quite onerous, mainly, due to the high fibre cost which arises from the fact that, these advanced materials have been initially designed/tailored with hi-tech industrial fibres, created originally for low-volume applications in aerospace and military industry (Kabele 2000). As the material technology evolutes, this issue can be settled down with the appearance and utilization of new low-cost fibres.

In what concerns the use of SFRSCC, this material introduces several advantages on the concrete technology. In fact, the partial or total replacement of conventional bar reinforcement by discrete fibres in certain concrete structures contribute to decrease their construction time and costs, and collaborates for the enhancement of their durability. The assembly of the reinforcement bars in the construction of concrete structures has a significant economical impact

on the final cost of this type of constructions, due to the man-labour time consuming that it requires. Nowadays, the cost of the man-labour is significant, hence diminishing the man-labour will decrease the overall construction's cost. In the fresh state, SFRSCC homogeneously spreads due to its own weight, without any additional compaction energy. To homogeneously fill a mould, SFRSCC has to fulfil high demands with regard to filling and passing ability, as well as segregation resistance. Driven by its own weight, the concrete has to fill a mould completely without leaving entrapped air. For these reasons, SFRSCC is a very promising construction material with high potential of application, mainly in the cases where fibres can totally replace the conventional reinforcement. At the present time, however, the SFRSCC technology is not yet fully developed and controlled, and, much less, the mechanical behaviour of the SFRSCC material.

This material, as briefly enlightened in the previous paragraph, has its origins and congregates the benefits from two independent types of concretes: self-compacting concrete, SCC, and conventional fibre reinforced concrete CFRC.

Self-compacting concrete was first developed in Japan, in 1988, aiming to improve the durability of concrete structures. The durability of concrete is intimately related to the level of compaction achieved while casting. Therefore, the development of a self-compacting concrete capable of being compacted purely by its own weight, i.e. without the need of any external vibration system, and into some extent independent from the man-labour's quality, started to seem a feasible alternative to be developed (Okamura and Ozawa 1996). The employment of self-compacting technology renders great benefits, mainly, when used to improve construction systems previously based on conventional concrete, which require compaction operations. Moreover, the vibration systems commonly used in compaction can easily cause segregation of concrete, thus jeopardizing its quality. The durability and reliability of a concrete structure is dependent on the compaction made by skilled workers, and if the aim is to achieve durable concrete structures independently from the man-labour's quality, vibration compaction systems should be discarded.

On the other hand, short and randomly distributed fibres are often used to reinforce cementitious materials, since they offer resistance to crack initiation and, mainly, to crack propagation. In CFRC materials of low fibre volume fraction the principal benefits of the fibres are effective after matrix cracking has occurred, since fibres crossing the crack guarantee a certain level of stress transfer between both faces of the crack, providing to the composite a residual strength, which magnitude depends on the fibre, matrix and fibre/matrix properties. The most benefited properties by the fibre addition to the concrete, in the concrete hardened state, are the impact strength, the toughness and the energy absorption capacity. A detailed description of the benefits provided by the fibre addition to concrete can be found elsewhere, (Balaguru and Shah 1992,

Casanova 1996, ACI 544.1R-96 1996). The fibre addition might also improve the fire resistance of cement-based materials (Kodur and Bisby 2005), as well as the shear resistance (Rosenbusch and Teutsch 2003).

Nevertheless the widespread use of SFRC on full load bearing structural applications is yet to some extent limited, if having in mind that the appearance of this material dates back to the early sixties. The high scatter of the SFRC material behaviour, in part due to non-uniform fibre dispersion, conduces to the mistrust in this material. In order to overcome these doubts it is of vital importance reducing the material behaviour scatter and, consequently, enabling the adoption of lower material safety factors (Shah and Ferrara 2008). Thus, it is necessary to effectively control the fibres dispersion within a structural element along its manufacturing and casting process. An improper casting of a structural element will lead to a higher non-uniformity in the fibres dispersion, which could result in reduced or even nil amount of fibres on certain spots of the structural element. These locations may jeopardize the structural performance either in terms of failure mechanisms and ultimate loads (Ferrara and Meda 2006, Shah and Ferrara 2008).

The use of self-compacting matrices takes advantage of the elimination of any kind of external vibration and rheological stability in the fresh state, which assures a more uniform distribution of fibres within the structural elements (Shah and Ferrara 2008). Self-compacting concrete is effective in guaranteeing a more uniform dispersion of fibres within the specimen, as well in effectively orienting them along the casting direction. When comparing the fibre distribution in plates of self-compacting concrete and conventional vibrated ones, the fibre dispersion is almost twice as much scattered in the vibrated ones (Shah and Ferrara 2008). Throughout a suitable balance of the fresh state concrete properties, mainly the fluid viscosity, fibres can be effectively oriented along the direction of the flow (Ferrara et al. 2007, Stähli et al. 2008). Therefore, it is desirable to design, together with the mix composition, also the casting procedure, so that the concrete flow direction along which fibres may be aligned, coincide with the direction of the principal tensile stresses within the structural element when in service, and consequently enhance the structural performance (Ferrara et al. 2008).

1.2 Scope of the research

The present work involves experimental, analytical and numerical research. The main purpose is to achieve, as much as possible, a consistent comprehension of the behaviour of this composite material, and to collect data for the calibration of the analytical formulations and FEM-based numerical models.

The development of advanced cement-based composites materials, in which SFRSCC is

comprised, is often based on empirical assumptions. Nevertheless, for a rational development of these materials, the volumetric content of fibres comprised into the material must be rationalized, avoiding the use of excessively large fibre contents. To fulfil this goal, micro-mechanics and fracture mechanics should take part in the design phase of these composite materials (e.g. Li and Leung 1992, Li and Wu 1992, Leung 1996). Even nowadays, fracture and failure processes in concrete materials and structures remain a challenging problem in Mechanics, since they play an important role in the development of those new/advanced materials for construction industry. Moreover, they enable to enhance the knowledge of the properties of structures, e.g. their durability and resistance. Through the past decades, Materials Science has been studied on different scales. Concrete is a multi-scale material (Van Mier 1997), thus it is possible to elaborate a multi-scale diagram for fibre reinforced concrete as depicted in Figure 1.1.

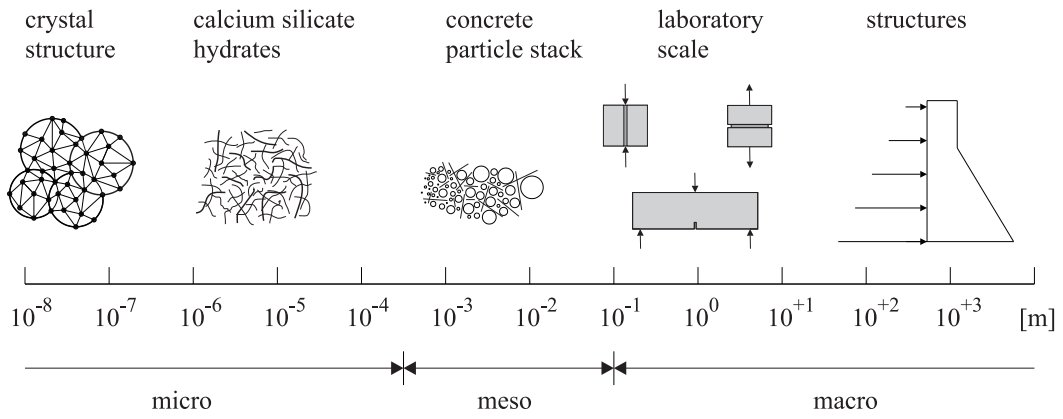

Figure 1.1: Distinct scales of observation, from atomic structure to large-scale building and engineering structures (after Van Mier 1997).

The experimental research covers aspects from distinct scale levels (see Table 1.1). At a micro-level, the micro-mechanical aspects, i.e. fibre reinforcement mechanisms involved on the fibre pullout, are investigated, while at a meso-level the fibre distribution structure into the hardened concrete is assessed. The research carried out at a micro/meso level enables to have a deeper understanding of the multiple reinforcement mechanisms and factors that influence the overall composite behaviour at a macro-level. Finally, at macro-level, the composite mechanical behaviour, namely the compressive, flexural and uniaxial tensile behaviour is studied. Since one of the most important applications of SFRSCC is the pre-casting industry, where demoulding the elements as soon as possible is an important economical requirement, the influence of the concrete age on the compressive behaviour of the SFRSCC was also investigated in order to contribute for a safe demoulding process at early ages. It should be noted that the

Table 1.1: Overview of the performed experimental tests.

		Test method	Dimensions	Mixtures	Aim
Part I - Micromechanics	Compression	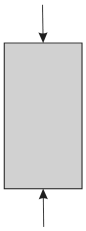	Cylinder: diameter of 150 mm, height of 300 mm	CFRC SFRSCC: 30 kg/m^3	Matrix quality control
	Pullout	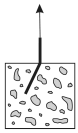	Cylinder: both diameter and height of 80 mm	CFRC SFRSCC: 30 kg/m^3	Assessment of the influence of: . embedded length . orientation angle . fibre type . matrix type
Part II -Mechanical behaviour	Compression	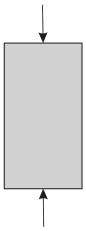	Cylinder: diameter of 150 mm, height of 300 mm	SFRSCC: 30 kg/m^3 45 kg/m^3	Matrix quality control Assessment of the influence of: . age . fibre content
	Splitting	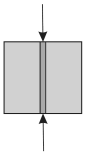	Cube: 150 mm edge	SFRSCC: 30 kg/m^3 45 kg/m^3	Assessment of the post-cracking parameters Influence of the fibre structure
	Tension	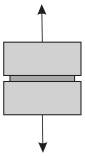	Cylinder: both diameter and height of 150 mm	SFRSCC: 30 kg/m^3 45 kg/m^3	Assessment of the post-cracking parameters Influence of the fibre structure: . orientation . density
	Bending	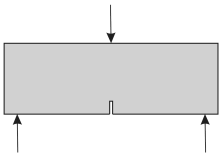	Prism: section 150x150 mm^2 length of 600 mm	SFRSCC: 30 kg/m^3 45 kg/m^3	Assessment of the post-cracking parameters by inverse analysis Influence of the fibre structure: . orientation . density . segregation

different investigated loading conditions have been limited to the short-term response, i.e. no creep and shrinkage were treated in the present work. The experimental investigation carried out at a macro-level, i.e the assessment of the composite mechanical properties, was comprised

in, and continued from, a research program/project for the development of lightweight sandwich SFRSCC panels for pre-casting industry. The requirements established for this SFRSCC were the following: average compressive strength at 24 hours greater than 20 MPa; equivalent flexural tensile strength greater than 2 MPa at this age; content of cement not exceeding 400 kg/m^3 (Pereira et al. 2004, 2005).

With the gathered experimental information at the distinct studied scale levels, analytical and numerical tools are developed. One of the objectives is to acquire a deeper knowledge of the multiple reinforcement mechanisms involved. Thus, an integrated numerical approach was developed, which based on the fibres' micro-mechanical properties is able of predicting the mechanical properties of fibre reinforced composites.

1.3 Outline of the Thesis

This thesis is organized into two major parts comprising ten chapters. In Part I, throughout Chapter 2 to Chapter 5, are addressed the micro-mechanical aspects of fibre reinforced composites, namely, CFRC and SFRSCC. On the other hand, Part II, comprising Chapters 6 to 9, deals with the mechanical behaviour of SFRSCC at meso/macro level. In both parts are comprised both experimental and analytical/numerical research.

1.3.1 Part I – Micro-mechanics

Chapter 2 provides a literature review on the micro-mechanical behaviour of fibre reinforced concrete. It is presented a deep insight view of the pullout behaviour of smooth and hooked end steel fibres, particularly, the main fibre reinforcement mechanisms that occur during fibre pullout. The micro-mechanical behaviour of other steel fibres types will also be briefly addressed, however, the analysis will be restricted to an overall micro-mechanical performance. Other relevant aspects to determine and understand the pullout load - slip relationship of a fibre will be focused.

Chapter 3 presents a preliminary study of the fibre geometry influence on the pullout behaviour of FRC. A pullout test set-up is presented, emphasis is given to the accurate acquirement of the pullout load *vs.* end-slip relationship. Three distinct types of hooked end steel fibres are used. The influence of the variation of the geometrical dimensions, due to the manufacturing processes, on the pullout behaviour is assessed.

In Chapter 4, the pullout behaviour of hooked end fibres on a steel fibre reinforced self-compacting concrete medium, SFRSCC, is investigated. The pullout tests were performed with hooked and smooth fibres. Additionally, the influence of the embedment length and fibre orientation on the pullout response was assessed.

In Chapter 5, a numerical method to obtain an analytical bond stress - slip relationship is developed. The experimental pullout responses presented in Chapter 4 are used to obtain the correspondent local bond - slip laws.

1.3.2 Part II – Composite behaviour

Chapter 6 deals with the fibre distribution structure, at a meso-level, in the hardened SFRSCC specimens. A very brief review is presented on the parameters that define the fibre distribution and factors that influence it. The fibre density, orientation factor, fibre efficiency factor and segregation factor are ascertained for the SFRSCC compositions.

In Chapter 7, the compressive behaviour of SFRSCC is investigated experimentally for five distinct ages, from the early hours (12 hours) up to the 28 days. This study was carried out for two fibre contents. The principal mechanical properties of the SFRSCC, such as: the compressive strength, the elasticity modulus, strain at peak stress, and the volumetric dissipated energy are determined. Moreover, are presented empirical/analytical expressions for predicting these mechanical parameters. Finally, an analytical equation is proposed for modelling the compressive stress - strain behaviour of SFRSCC, from the early hours up to the 28 days.

Chapter 8 deals with the SFRSCC post-cracking behaviour. The advantages/disadvantages of different test methods are presented and discussed, namely, uniaxial tensile test, three-point bending test and splitting tension test. The post-cracking parameters obtained from distinct tests are presented and analysed. The stress-crack opening relationship, in the three-point bending test, is obtained from the following approaches: (1) material testing, i.e. from the obtained load - deflection response; (2) inverse analysis, i.e. the stress - crack opening relationship is obtained in order to fit, as accurate as possible, the force - deflection registered in three-point notched beam tests; and (3) adjustment of the stress - crack opening relationship to have into account the fibre efficiency factor.

In Chapter 9, a numerical approach supported on the finite element method is presented for modelling the behaviour of SFRSCC. The developed approach considers SFRSCC as a two phase material: self-compacting concrete, SCC, and fibres. SCC is simulated by a multi-fixed smeared 3D crack model, while fibres are modelled as discrete embedded cables, whose internal forces are obtained from the pullout force - slip relationships recorded in pullout tests (Chapter 4). The embedded cables inserted into the finite element mesh are randomly generated by a developed algorithm. For that purpose, the fibre distribution parameters assessed in Chapter 6 are used. The model is appraised by simulating the mechanical behaviour of the SFRSCC compositions on the uniaxial tension tests and three-point bending tests (Chapter 8).

Finally, the major conclusions are presented in Chapter 10 together with suggestions for future research.

Part I

Micro-Mechanical Behaviour of SFRSCC

Chapter 2

Literature Overview of Fibre Pullout

2.1 Introduction

Short and randomly distributed fibres are often used to reinforce cementitious materials, since they offer resistance to crack initiation and, mainly, to crack propagation. In fibre reinforced cementitious composites, FRC, of low fibre volume fraction the principal benefits of the fibres are effective after matrix cracking has occurred, since fibres crossing the crack guarantee a certain level of stress transfer between both faces of the crack, providing to the composite a residual strength, which magnitude depends on the fibre, matrix and fibre/matrix properties. The mechanical performance of FRC is highly influenced by the fibre dispersion, since the effectiveness of fibres depend on how the fibres are oriented, their location and arrangement within the cement matrix. Considering the aforementioned and that fibre and matrix are bonded together through a weak interface, study of the interfacial behaviour is important for understanding the mechanical behaviour of such composites.

The effectiveness of a given fibre as a medium of stress transfer is often assessed using a single fibre pullout test, where fibre slip is monitored as a function of the applied load on the fibre (Naaman and Najm 1991, Banthia and Trottier 1994, Li and Chan 1994, Groth 2000). Several test and specimens configurations have been developed for measuring the fibre pullout load *vs.* slip response. These kind of tests can be performed with a single or multiple fibres. The case of a multiple fibre pullout test, where a certain number of fibres are loaded simultaneously instead of a single fibre, is difficult to perform. Moreover, the correlation between the results with a random distributed fibre composite is also complicated, due to these kind of tests being commonly performed with all fibres aligned (Bartos 1981). Ouyang et al. (1994) performed pullout tests on multiple fibres with different inclinations. However, the correlation with a

random distributed fibre composite is difficult, since the inclination of the fibres in each specimen was the same.

In spite of the belief sometimes held that no correlation exists between the behaviour of fibre in a single fibre pullout test and its behaviour in a real composite (Hughes and Fattuhi 1975, Maage 1977), the data derived from single pullout tests can give relevant contribution to optimise the properties of fibre reinforcement cement composites. The available research indicates that there is not an ideal test or model to fully predict the mechanical behaviour of steel fibre reinforced concrete, even for the basic case of uniaxial tension, since the relationships withdrawn from the uniaxial tension test can not be representative of all fibre types, cement matrices, fibre orientation and distribution in real structures. However, from the analysis of the fibre reinforcement mechanisms in a single pullout test, the key aspects of the overall behaviour of a composite material tested under uniaxial tension can be assessed.

The post-cracking behaviour of random discontinuous fibre reinforced brittle-matrix composites can be predicted by the use of a stress - crack opening displacement relationship, $\sigma - w$. Several authors developed micro-mechanical models for obtaining the $\sigma - w$ relationship, since for quasi-brittle materials, the stress - crack opening relationship that simulates the stress transfer between the faces of the crack has a significant impact on the behaviour of a structure after its cracking initiation. In case of FRC, the $\sigma - w$ relationship can be approximated by averaging the contributions of the individual fibres bridging the matrix crack plane, defining for this purpose probability-density functions of the centroidal distance of fibres from the matrix crack plane, and of the orientation angle (Li et al. 1991). Visalvanich and Naaman (1983) derived a semi-empirical model to simulate the tension - softening behaviour of a cement based material reinforced with discontinuous randomly distributed steel fibre. In this work they assumed a purely frictional fibre/matrix interface and the possibility of fibre fracture was not contemplated. Based on the assumptions of the latter model, Li (1992) developed an analytical model which take into account an additional frictional effect called snubbing effect (factor which considers the angle effect of non-aligned fibres on the pullout load). Maalej et al. (1995) extended the latter fibre pullout model by explicitly accounting for potential fibre tensile rupture.

The latter models, which are based on an averaging process of all the forces that are carried out by the fibres over a crack plane by modelling the main mechanisms on a single fibre pullout, can provide the general material composite behaviour with reasonable accuracy. However, they do not account for some aspects, such as, fibre bending rupture, and matrix spalling at the exit points of inclined fibres. Moreover, the possible interaction between neighbouring fibres, as well as, the modification of the matrix modulus and packing density by the addition of fibres are neglected in the abovementioned models.

Another difficulty on the prediction of the post-cracking behaviour of a composite in a real

structure is that the material behaviour in a test specimen may differ from the behaviour of a real structural element. It is well described in literature that various casting procedures, as well, structural shapes may result in predominant fibre orientation into parallel planes (Stroeven 1986a, RILEM TC 162-TDF 2002a), or in the case of steel fibre reinforced self-compacting concrete along the flow itself (in the fresh state) and the flow along the walls (Grünewald and Walraven 2003). The fibre orientation nearby the walls of a structural element will not be representative of the material, but of a structure (Stroeven 1986a). A predefined orientation of the steel fibres parallel to the tension direction in a test specimen may result in an overestimation the post-cracking mechanical properties of the steel fibre reinforced concrete, when compared with specimens of equal amount of fibres but with a random fibre orientation.

2.2 Pullout behaviour of steel fibres (micro-mechanical)

In this section, the pullout behaviour of smooth steel fibres and hooked end steel fibres will be discussed from a micro-mechanical point of view. The mechanical behaviour of other steel fibres types will be discussed more briefly in a posterior section, not from a physical point of view, but from the overall mechanical behaviour performance standpoint. The most relevant aspects to determine and understand the pullout load - slip relationship of a fibre will be focused. The interfacial transition zone, ITZ, is also here referred in a succinct and qualitative way, in order to help understand further micro-mechanical considerations.

2.2.1 Fibre/matrix interface

A fibre reinforced cement composite is composed by the mixture of aggregates, cement paste and fibre, bonded to each other at an interface, which is commonly called the interface transition zone, ITZ. The properties of this zone depend on many parameters, such as the nature of the binder, the presence of additions, and the water/cement ratio. The properties and bonding quality of the interface plays a primordial role on the behaviour of the composite material. In fibre reinforced cement composites, the ITZ behaviour has, even, a more relevant role on the mechanical behaviour of FRC than in plain concretes, since the fibre aspect ratio is considerably high, and, therefore, the contact surface area is larger than that of the aggregates.

The formation of ITZ can be explained by the wall-effect, since there is a non-efficient packing of the binder particles in the fresh state, which leads to a high amount of empty space that only will be partially filled with hydration products. The syneresis process (Chandra 2002) can also justify the morphology of the ITZ. During syneresis, the exudation of the cement gel produces the release of the water molecules from the gel structure. This leads that the particles

arrangement of the originally homogeneous mass, at the contact surfaces, will readjust into two separate parts, a water rich and a solid rich mass.

In spite of existing several explanations for the formation of the ITZ, the main outcome withdrawn of the ITZ formation is that all these phenomena at this zone result in a significantly higher porosity than in the bulk paste, and also in an increase amount of calcium-hydroxide (CH) crystals, Figure 2.1(a). For this reason the ITZ has substantially lower strength and stiffness when compared to the bulk cement paste (Diamond and Huang 2001). Test results of the microhardness of concrete around the steel fibre (Wei et al. 1986) indicate that the microhardness in the ITZ is lower than in the bulk cement matrix, Figure 2.1(b), and that the width of the interface zone is of about 75 μm. Bentur and Mindess (1990) determined with a SE Microscope that the width of the ITZ ranges from 20-50 μm, whereas Li and Stang (1997) points out values on the order of 40-70 μm thickness.

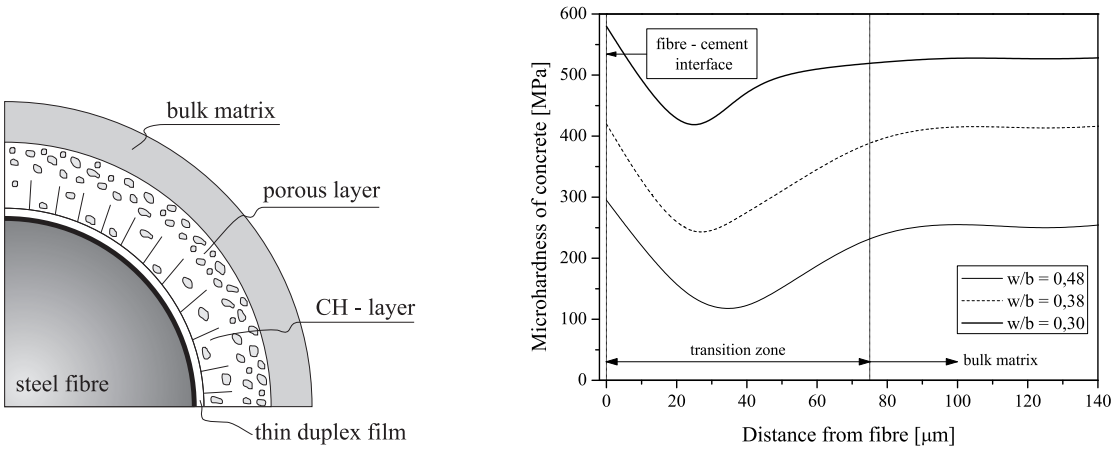

(a) (b)

Figure 2.1: Interface transition zone: (a) Transverse cross-section through a steel fibre (adapted from Bentur and Mindess 1990); (b) Results of microhardness tests around steel fibres (adapted from Wei et al. 1986).

Densification of the ITZ strengthen the transition zone and thus, enhance the fibre/paste interfacial bond strength. This can be accomplished with the reduction of water/cement and/or the use of micro-fillers, e.g. micro-silica. This can be observed in Figure 2.1(b), where the strength of the ITZ increases with the reduction of the water/binder ratio. However, not always densification of the transition zone results in bond strength improvement (Li and Stang 1997). There are other parameters which influence the hardness of the ITZ. In fact, with the increase of aggregate porosity, in general, bond strength increases, since the binder impregnates

more deeply the aggregate border, extending the adhesion zone more to the interior. On the other hand, the absence of porosity in steel fibres surface extends the adhesion zone to an outer zone from the fibre. The debonding of the surround interface between the fibre and the paste occurs at a weak zone, at a certain distance from the fibre surface (Wei et al. 1986, Bentur and Mindess 1990), and not in the actual contact paste/fibre surface, being a direct consequence of the differences between the ITZ structure and the rest of the cement paste, Figure 2.1(b).

2.2.2 Bonding

The micro-mechanical behaviour of fibre reinforced cementitious composites is somehow very complex, in part due to the presence and combined action of several mechanisms of bond. According to Naaman and Najm (1991) the principal bond mechanisms during the pullout of a fibre that contribute to the ductility of the composite material are: adhesion, friction, mechanical and fibre interlock.

The adhesion or chemical bond represents the resistance offered by interface transition zone between the fibre and concrete matrix that surrounds it, therefore this type of bond depends on the ITZ properties. The chemical bond is the first mechanism to be activated on the pullout. During this initial phase, the fibre and matrix deformations are fully compatible, in such a way that the bond of the fibre/matrix interface does not suffer any damage. As previously said, fibre matrix interface can upon depend on several parameters and also be improved by several ways. However, due to the brittle nature of adhesion, the bond improvement observed in a single pullout test does not translate in an equal improvement at the composite level (Naaman and Shah 1976). After full debond is attained, frictional stresses are generated due to the abrasion and compaction processes on the interfacial zone throughout the slipping of the fibre along its channel.

The mechanical bond can be obtained by fibre deformation processes. This leads to local interaction between fibre and matrix on the millimetre scale, and from a macroscopic point of view can be regarded as a roughening effect (Li and Stang 1997). All steel fibres at the present days have their bond improved through mechanical deformations (e.g. crimping, indenting, or adding at their ends hooks, paddles or buttons), since this technique has proven to be the most effective one in improving fibre/matrix bond (Banthia and Trottier 1994, Li and Stang 1997). While for a smooth fibre, the slip mainly depends on the break down of chemical adhesion and on friction, for deformed fibres (e.g. crimping, indenting or hooked end) it is generally accepted that the chemical bond can be neglected in favour of the mechanical bond between the fibre "deformations" and the surrounding concrete (Maage 1977). Finally, fibre to fibre interlock exists only in high volume fraction of fibre reinforcement, e.g. $\simeq 10\%$ of steel fibres in

SIFCON (Homrich and Naaman 1987), where the fibres are in contact with each other. For the current volume fraction of fibre reinforcement used in conventional fibre reinforced composites, fibre to fibre interlock should be not taken into account.

The type of bond was also categorised by Bartos (1981) and Gray (1984) in accordance with the nature of stress transfer and type of interface:

- **Shear bond**: Transfer of the parallel stresses to the longitudinal axis of the fibre. When mobilised, this type of bond assures the deformation compatibility between fibre and matrix. If the shear bond stress exceeds a limit value, it will be observed a relative displacement of the fibre towards the cementitious matrix. In this case, shear bond in a length where a relative displacement between the fibre and matrix occurs, corresponds to a friction phenomena.

- **Tension bond**: This stress component enables to resist forces perpendicular to the interface. This type of bond can be mobilised by phenomena due to mechanical stresses (e.g. Poisson coefficient), or due to physical phenomena (e.g. concrete shrinkage). This radial bond is usually ignored in models for a single fibre. Remark that, however, for a random fibre distribution over a cementitious matrix, the fibre interaction with each others can produce local confinements, which could better mobilise this kind of bond (Kelly and Sweben 1976).

On the other hand, the average fibre orientation and fibre spacing influence the efficiency of a group of fibres. The pullout resistance may decrease as the distance between fibre decreases, due to the higher probability of mutual influence of the fibres stress fields (Naaman and Shah 1976).

2.2.3 Critical embedment length

The failure mode of the fibre reinforced concrete is highly influenced by the stress transfer between the fibre and cementitious matrix. After matrix cracking, and for a smooth fibre without anchorage, it can be observed two failure modes: the fibre rupture and the fibre sliding.

The most elementary model consists on balancing the forces on a smooth fibre submitted to traction load. Assuming the hypothesis of an uniform distribution of the adherence, $\bar{\tau}$, over the fibre, it is possible to define a critical embedment length:

$$L_{f,crit} = \frac{\sigma_{fu} \cdot d_f}{4\bar{\tau}} \tag{2.1}$$

where σ_{fu} and d_f are, respectively, the fibre rupture stress and diameter. If the fibre embedment length is higher than the value of $L_{f,crit}$, the fibre will fail, if not, the fibre will slide.

This simplest model is the basis of the study of the fibre/matrix interface. The reinforcement mechanisms in this case depend on the mechanical properties of the material, the adherence phenomena between the fibre and the matrix, and the geometrical dimensions of the fibres. However, there are other parameters that influence the reinforcement mechanisms, such as: the fibre orientation respect to the load, the fibre geometry configuration (e.g. fibres with anchorages or corrugated) and the fibre/matrix interfacial bond stress that is not constant over the fibre embedded length.

2.2.4 Pullout mechanisms of aligned fibres

Smooth fibres

Generally, the overall mechanical behaviour of a smooth steel fibre can be described as the combination of two mechanisms: debonding of the surround interface and frictional slip of the fibre. Afterwards the embedment fibre length is fully debonded, the fibre pullout occurs under frictional resistance.

The pullout behaviour of an aligned fibre can be represented by a load - slip curve as shown in Figure 2.2. In the first phase of the pre-peak branch, the pullout load almost linearly increases with the slip. However, before the peak load (B) is attained, usually, a nonlinear phase in the pullout load-slip curve is observed. Therefore, in the pre-peak branch two distinct phases are usually observed. The first one, a linear ascending part (OA) which is associated with the elastic bond. The second part of the pre-peak branch (AB) starts with the micro-cracking of the ITZ, corresponding to the initiation of the debonding process. The non-linearity observed in this part is regarded as an indication of an interfacial crack propagation (Shah et al. 1995). The interfacial crack stably propagates up to the peak load, and is usually designated as the critical crack length.

After the maximum load is reached, the load decreases with the increase of slip, which corresponds to unstable interfacial crack growth on the post-peak behaviour, i.e. the interfacial crack grows even though the pullout load decreases, and full debonding will occur (C). Subsequently, the fibre pullout occurs under frictional slip (CD). In this part of the post-peak branch the load also decreases with the increase of slip, since the available frictional area decreases as well the roughness of the failure surface.

When a smooth fibre is submitted to a pullout load, as previously seen, the load transfer at the fibre/matrix interface is effectuated firstly by the adhesion bond stresses and after by the frictional stresses. However, during the debonding phase, if the pullout load attains the force

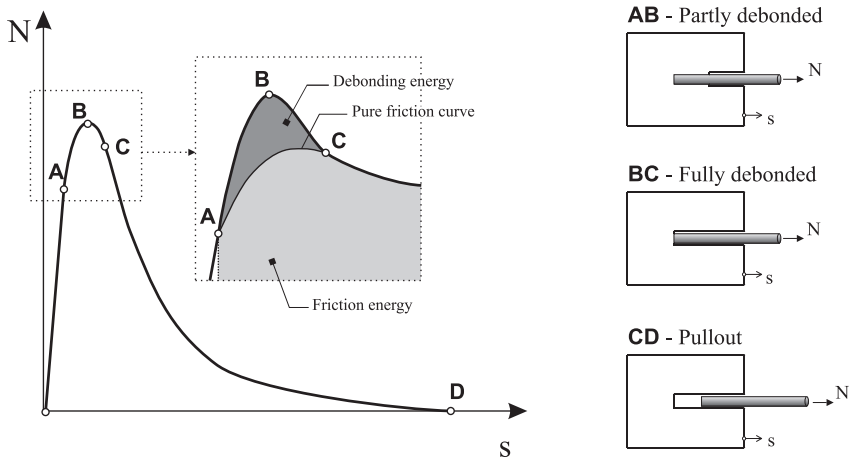

Figure 2.2: Pullout relationship between the load and the end-slip for a smooth fibre.

corresponding to the fibre tensile strength without being exceeded the bond strength, it will be observed the fibre rupture. Notice that this case is not intended from the reinforcement point of view, since the energy dissipated by this failure mode is limited, and is released abruptly without mobilizing the potential benefits of fibre reinforcement in terms of increasing the concrete toughness. In fact, if the tensile strength of the fibre is not attained, the fibre/matrix interface properties will progressively degrade generating a mechanism with higher dissipated energy.

Hooked end fibres

The pullout behaviour of hooked end steel fibres, in similitude to smooth fibres, consists also on debonding and frictional pullout. In what concerns to the debonding phase of this type of fibre, the process has generally the same character of the one reported for smooth fibres. However, in the frictional pullout, significant differences can be found between these two types of fibres. In the hooked end fibres frictional pullout is accompanied by a mechanical bond mechanism correspondent to the mechanical interlock and plastic deformation of the hook.

In Figure 2.3 is depicted the pullout curve for both smooth and hooked end fibres. The pre-peak behaviour of a hooked end fibre can be described by three branches associated to distinct phenomenon's. The ascending parts OA and AB are associated, respectively, to the adhesive bond and to the debonding process until full debonding occurs at point B. However, in opposite to the smooth fibres behaviour, after full debond is attained an additional load increase (BC) is observed due to the mechanical anchorage provided by the fibre hook. At the maximum pullout load (C) both curvatures 1 and 2 are deformed (see Figure 2.3), afterwards the mechanical anchorage starts to become progressively deformed, the pullout load starts to decrease (CD). While the fibre is not fully straightened (DE) another peak load is observed, which coincide with the fibre (curvature 2) passing the last corner of the fibre imprint made

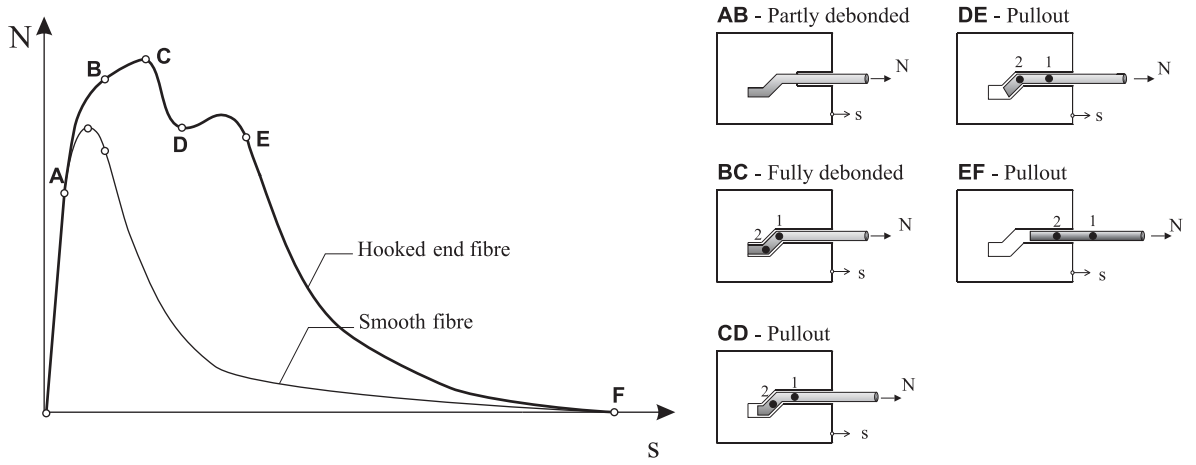

Figure 2.3: Pullout relationship between the load and the end-slip for hooked end fibre.

in the matrix. Finally, after the fibre is fully straightened, the pullout process occurs under frictional resistance (EF) as in smooth fibres. Remark that in hooked end fibres, usually the fibre hook is not fully straightened, which will increase the frictional stresses, resulting in a higher residual pullout load at the final stage of the pullout (see Figure 2.3).

2.2.5 Pullout mechanisms of inclined fibres

On the pullout of an inclined fibre with respect to the pullout load, as on the pullout of aligned fibres, debonding of fibre/matrix interface and sliding of the fibre on the debonded interface mechanisms are also observed. However, for inclined fibres other additional mechanisms usually occur: bending of fibres at the matrix crack surface and spalling of the matrix due to the fibre bending.

When a fibre is pulled out from a matrix at an inclined angle, θ, the pullout load, N, can be decomposed into two components, N_x and N_y (see Figure 2.4). From this two components of the pullout load only the component on the fibre axis, N_x, is dedicated to the debonding/pullout of the inclined fibre generating interfacial stresses along the fibre (S), and is currently termed as the pulley effect (Shah et al. 1995).

The pullout resistance of inclined fibres, for an angle smaller than 45°, usually is higher than the one of aligned fibres (Brandt 1985). This may be due to several mechanisms associated to the component N_y. As a consequence of the fibre inclination with respect to the pullout load, there are additional concentrated stresses where the fibre is bent. These concentrated stresses may cause local concrete spalling, since the concrete between the fibre and the crack plane is crushed or pushed off. For these reasons, in the pullout of inclined fibres, the matrix strength is extremely important, whereas a weak matrix is prone to spalling and local damage due to the additional concentrated stresses. However, local stiffness of the matrix can vary

significantly, and spalling of the matrix at crack surface fibre exit depends on whether or not there are aggregates or even fibre interlock at this zone (see Figure 2.4). In the case where the concrete spalling occurs the fibre can easily bend, and the stress carried by the fibre is reduced. The pullout resistance of inclined fibres may also depend on fibre bending (Morton and Groves 1974) or fibre yielding mechanisms (Brandt 1985), and on an additional frictional resistance on the fibre matrix interface due to local compression (Li et al. 1990).

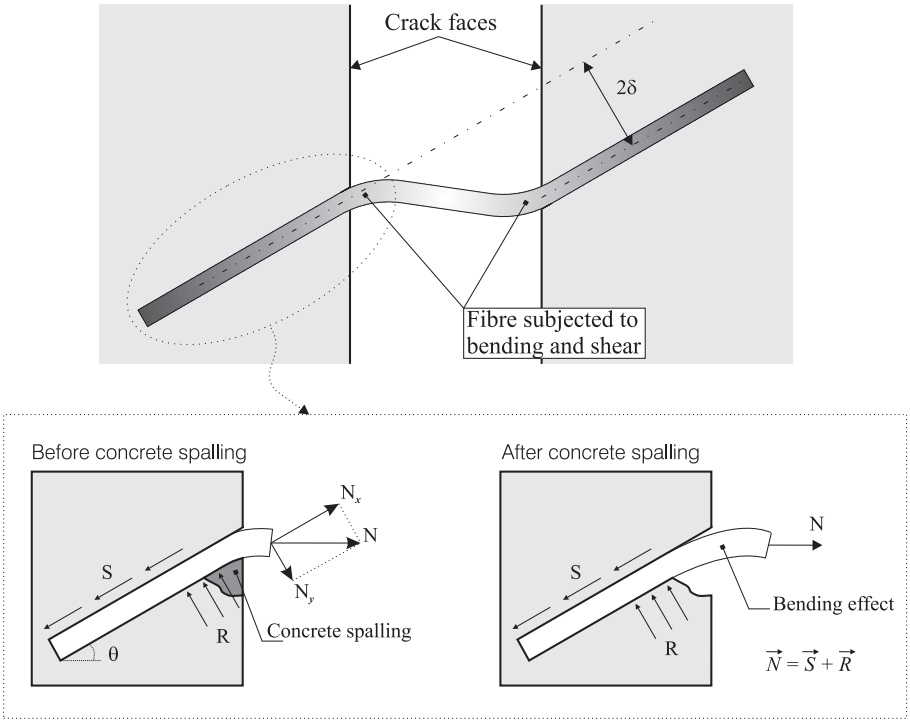

Figure 2.4: Bending and shearing of an inclined fibre across a crack and the components of a crack bridging force (based on Leung and Geng 1998).

The bending or yielding mechanism is present for small pullout loads, since the fibre will almost immediately be bent when the pullout load starts to be applied. On the other hand, frictional stress at the fibre/matrix interface will be generated only when the fibre starts to slip, and for this to occur the interface has firstly to debond. Since the slip value prior to peak load is relatively small, the effect of frictional stress on the pullout load of inclined fibres may not be significant before the peak load (Shah et al. 1995). Therefore, both the pulley effect and bending mechanism may be the principal factors to the increase of the peak pullout load for inclined fibres. Nevertheless, the influence of frictional stress becomes more important after the peak load, since slip is more significant.

2.2.6 Concept of energy dissipated on the fibre pullout

The phase correspondent to the elastic deformation of the fibre is observed for a small slip. Therefore, in the calculus of the energy dissipated on the pullout of the fibre, the component due to the fibre deformation can be neglected, and only the energy dissipated on the debond and frictional phenomena is considered, assuming that the fibre has rigid body movement. Hereinafter, frictional stress represents indistinguishably the shear stress occurred in the debond and frictional phases of the pullout process. Assuming that the debond/friction behaviour can be simulated by a $\tau_f(s)$ law, the work produced on the fibre pullout is given by:

$$W = \int_0^{l_f} \pi \cdot d_f \cdot \tau_f(s)(l_f - s) \cdot ds \tag{2.2}$$

where d_f, l_f and s are the fibre diameter, the fibre embedded length and fibre slip, respectively. Kelly (1970) proposed a constant value for the frictional stress law ($\tau_f(s) = \tau_{fc}$) obtaining the equation 2.3 for the work produced under pullout.

$$W = \pi \cdot d_f \cdot \tau_{fc} \frac{l_f^2}{2} \tag{2.3}$$

Assuming a polynomial law $h\,(s/l_f)$, where (s/l_f) is the normalized slip variable, the equation for determining the work produced is given by:

$$W = \alpha \cdot \pi \cdot d_f \cdot \tau_{fc} \cdot l_f^2 \tag{2.4}$$

where α is a constant value that depends on the integration of polynomial function $h(s/l_f)$. Equation 2.4 shows that the energy dissipated on the pullout of a smooth fibre from a matrix varies quadratically with the embedded length of the fibre.

Several authors (Helfet and Harris 1972, Hing and Groves 1972, Brandt 1985) have reported that for inclined fibres an additional amount of work is required to fully pullout a fibre. This additional energy absorption can be assigned to different mechanisms, such as: the plastic deformation under shearing (Helfet and Harris 1972), or to plastic deformation under bending (Hing and Groves 1972), both for the fibre. In a simplified way, the plastic deformation energy under shear, W_{shear}, can be considered proportional to the fibre volume deformed, to the ultimate shear resistance of the fibre, τ_{crit}, to the crack opening, w, and to the fibre orientation angle, θ (see Figure 2.4):

$$W_{shear} = \frac{\pi}{4} \cdot d_f^2 \cdot w \cdot \theta \cdot \tau_{crit} \tag{2.5}$$

However, the previous model presents some limitations. In fact, the deformation under shear can only occur if the matrix surrounding the fibre can support the stress increments derived from the imposed strain increments. As it was previously indicated, local spalling of the matrix can occur, which is followed by bending of the fibre. The energy dissipated calculated by equation 2.5 can be regarded as the upper limit value of the plastic energy that can be dissipated.

For the case that the dissipated energy is determined assuming a plastic deformation under fibre bending, it is necessary to define a criterion for the material behaviour. In case the fibre curvature is sufficiently small, the matrix damage is limited, moreover is realistic to assume the formation of a plastic hinge. Hing and Groves (1972) propose to determine the plastic deformation energy by considering that the fibre is in a first phase bent with an angle θ, and as the fibre deformation process starts this same angle must be updated:

$$W_{bend} = 2 \cdot \frac{\sigma_y \cdot d_f^3}{6} \cdot \theta \tag{2.6}$$

Unfortunately these authors run up against the problem of the determination of the angle θ and it is then impossible to determine the total dissipated energy.

More recently, assuming the fibre as an elastic material, and considering that the maximum tensile stress in the fibre section reaches the yield stress material under the pullout load, Ouyang et al. (1994) presented the following equation for determining the additional bending energy, which is based on the yield stress of the fibre:

$$W_{bend} = \frac{\sigma_{b,max}^2 \, \pi \, L_b \, r_f^2}{8 E_f} \tag{2.7}$$

where $\sigma_{b,max}$ is the maximum tensile stress due to bending (the stresses resulting from tension are subtracted), L_b is the length of the bent zone of the fibre and is assumed to be proportional to the pullout slip ($L_b = m \cdot u_f$), where $m = 20$ and u_f is the fibre's pullout slip evaluated based on the solution provided by Stang et al. (1990), and r_f is the fibre radius.

2.3 Experimental research on the pullout behaviour of fibre reinforced composites

The composite behaviour of steel fibre reinforced concrete, SFRC, is governed by the addition of the individual contribution of the single fibre interaction with the matrix. In spite of theoretically being possible to predict the bulk behaviour of SFRC from the single fibre pullout

performance, this task is considerably hard since there are several complex mechanisms involved in the overall composite behaviour. Single pullout tests have been carried out in the past 30 years to optimise the combination of both fibre type and concrete mix, and to understand the mechanisms of fibre reinforcement.

The pullout study of smooth fibres has reached its peak during the 80s. Analytical studies were carried out to justify the fibre benefits of fibre addition to cementitious matrices (Bartos 1981, Brandt 1985). Over the years, so-called improved shaped fibres have been brought onto the market by different producers with claimed better performances than smooth fibres (Naaman and Najm 1991, Chanvillard 1993). When the fibre has mechanical anchorages, they can be straightened during its pullout, therefore being necessary to take into account the energy dissipated in the fibre straightening process (Maage 1977, Chanvillard 1993). Recently the pullout study of a single fibre is resurging due to the development and increasingly application of new types of concretes, such as: self-compacting fibre reinforced concrete (Groth 2000) and high performance concretes with hybrid reinforcement (Markovic 2006, Lappa 2007). It is well recognised of the importance of fibre/matrix bond in the behaviour of fibre reinforced concrete. Moreover, in these new types of concretes is commonly used the inclusion of fine filler materials that modifies the properties of the interface transition zone, i.e the fibre/matrix bond, therefore its influence on the performance of the composite behaviour should be assessed.

There are several factors that affect the pullout behaviour of steel fibres. Throughout the last 30 years, pullout performance of steel fibres embedded in cementitious matrices has been assessed as a function of several variables. From these variables can be pointed out: the matrix quality (Wei et al. 1986, Naaman and Najm 1991, Banthia and Trottier 1994), fibre inclination (Morton and Groves 1974, Naaman and Shah 1976, Ouyang et al. 1994, Banthia and Trottier 1994), fibre embedment length (Chanvillard 1993, Li and Stang 1997, Robins et al. 2002), the rate of loading application (Gokoz and Naaman 1981, Banthia and Trottier 1991, Bindiganavile and Banthia 2001), temperature of the environment (Banthia and Trottier 1992).

In this section the analysis is restricted to the influence of the fibre type, fibre orientation, matrix quality and fibre embedment length on the pullout response of a single fibre.

2.3.1 Influence of fibre type

The short fibres used in concrete can be classified in different ways. First, according to the fibre material, which can be natural, both organic and mineral, or man made (e.g. steel, titanium, carbon, glass, etc.). Second, according to their physical/chemical properties, such as: density, surface roughness, non-reactivity with cement matrix, fire resistance, etc. Third according to their mechanical properties such as: tensile strength, elasticity modulus, elongation

to failure, surface adhesion properties, etc. Moreover, once a fibre has been selected, an infinite combination of geometric properties related to its cross sectional shape, length, diameter or equivalent diameter, and surface deformation can be selected.

There are several types of steel fibres available, which differ in size, shape and material properties. Due to different materials and manufacturing processes, the mechanical properties such as, tensile strength and grade of mechanical anchorage differ considerably from each fibre. These differences have a significant effect on the fibre pullout behaviour and, consequently, in the overall behaviour of FRC under loading. Some typical profiles of steel fibres commonly used in concrete technology are presented in Table 2.1

Table 2.1: Steel fibre profiles.

Longitudinal profile		Cross section
	Smooth	Round, flat or any shape
	Indented Etched Roughened	
	Flat-ended	Round or flat
	Buttons-ended	Round
	Hooked-ended	
	Crimped Corrugated	Round, flat or any shape
	Polygonal twisted	Polygonal (triangular or rectangular)

As it was described in a previous section, the behaviour of aligned smooth steel fibres during its debond is mainly governed by the adhesion and friction mechanisms, while for non-aligned smooth fibres with the pullout load direction other mechanisms must be taken into account, such as, the fibre internal work due to its shear and bending deformation, as well as the energy dissipated in the deformation of the matrix surrounding this fibre critical zone. Due to the weak bond between steel and cement matrix, the pullout energy of a smooth fibre is small. This problem may be solved by optimising the fibre anchorage properties (Chanvillard 1993), in order to develop better bond between the fibre and matrix. The fibre can be modified along its length by roughening or etching its surface, or by inducing other mechanical deformations.

Other way of improving the bond is to enhance the chemical and physical bonding of wire surfaces to the cement paste (Hannant 1987, ACI 544.1R-96 1996).

Among various attempts to improve the bond - slip characteristics of steel fibres bonded to cementitious matrices, the most effective is mechanical deforming (Banthia and Trottier 1994, Li and Stang 1997). Steel fibres have a significant advantage over other fibres in terms of the facility in which they can be deformed and indented to improve their anchorage to cementitious matrices. Mechanical deformations in the form of hook, cone or crimp placed at the end or along the fibre have proven to be very effective in improving pullout resistance and, consequently, on enhancing several mechanical properties of the composite (Soroushian and Bayasi 1991, Naaman and Najm 1991, Banthia and Trottier 1994, Rossi and Chanvillard 1996, Groth 2000).

More recently, Naaman (2003) developed a new kind of steel fibre of optimised geometry to increase the performance of steel fibre reinforced concretes. An originally, triangular or square fibre cross section assumes a polygonal cross section shape after twisting mechanical treatment (see Table 2.1). This fibre is made of high strength steel wire, approximately with a tensile strength of 2000 MPa.

In Figure 2.5 are depicted the typical pullout load - slip responses for some commonly used steel fibres (smooth, hooked end, crimped, buttons-end) and for the polygonal twisted fibre developed by Naaman (2003). Figure 2.5(a) shows clearly the benefits of the fibres mechanically deformed, when compared with a smooth fibre, on the peak pullout load and pullout energy. In what concerns to the polygonal twisted fibres, the key feature of these fibres is that when pulled-out from a cement matrix, its resistance increases with fibre slip. Increasing the lateral surface area of a fibre, for the same cross section, increases frictional and adhesive bond forces along the fibre that leads to an increase in pullout resistance and thus in fibre efficiency. On the other hand, during the fibre pullout, the fibre additional stiffness provided by the untwisting process will improve the ductility of the pullout load - slip response; since a slip hardening will occur.

In Figure 2.5(b) are compared the pullout responses of deformed fibres. The crimped fibre presents a higher pullout energy, since they have more curved parts than hooked end fibres, so that more energy is needed to deform them, in comparison with hooked end fibres (Chanvillard 1993, Groth 2000). The buttoned end fibre has a higher pullout resistance, in spite of the lower pullout energy due to its rupture at peak pullout force. Remark that the pullout responses of Figures 2.5(a) and 2.5(b) cannot be compared, since the fibre embedment length, L_b, and the matrix compressive strength, f_c, are distinct.

In the case of a deformed fibre, both fibre and matrix are severely stressed during pullout, therefore fibre fracture and matrix splitting occur more commonly than in smooth fibres. For this reason, material properties like elastic modulus, strength, strain capacity, etc., for both

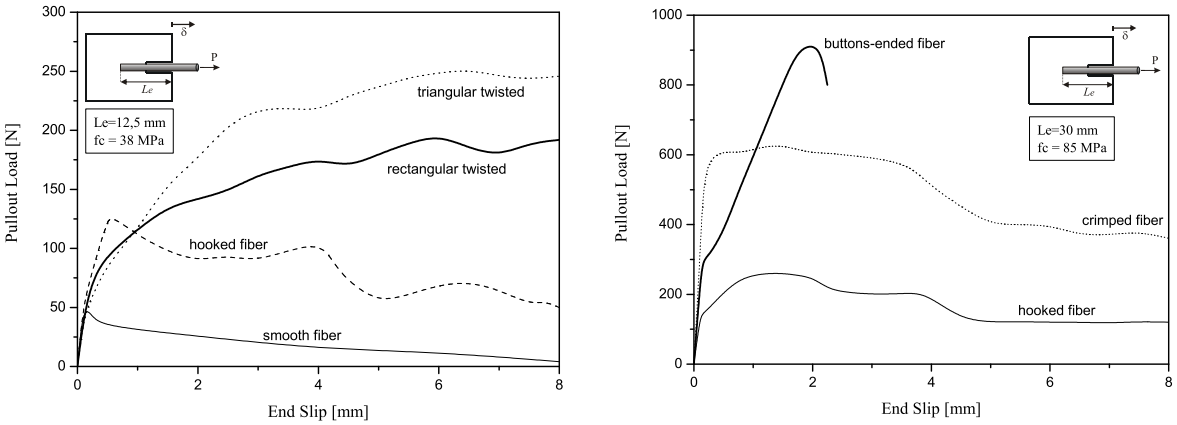

(a) (b)

Figure 2.5: Comparison of typical pullout response of different steel fibres: (a) adapted from Naaman (2003), (b) adapted from Banthia and Trottier (1994).

fibre and matrix, are more significant in the case of deformed fibres than for smooth fibres (Banthia and Trottier 1994).

2.3.2 Influence of fibre orientation

In fibre reinforced concrete, the fibres are rarely aligned in the same direction of the pullout load. This is a consequence of the production technology of dispersed reinforcement provided by discontinuous fibres in the bulk material.

In Figure 2.6(a) are depicted different relations between the fibre inclination angle and the normalised values of the maximum inclined pullout force, where $N_{inclined}$ is the pullout force for an angle inclination ranging from 0° and 60°, and $N_{aligned}$ is the pullout force of an aligned fibre with respect to the load. In general, the pullout resistance of inclined fibres is higher than of the aligned fibres, even for a significant inclination angle of 60°, the exception are the cases of Bartos and Duris (1994) and Leung and Geng (1998). However, it should be noticed that the values of the fibre slips correspondent to the maximum pullout load of an inclined fibre were much larger than of the aligned fibres. Since the fibre slip at maximum pullout load for an inclined fibre can range from 0.5 to 4 mm, the previous remarks do not say much of the fibre performance on a real structural element. Regarding durability, serviceability limit sates, an appropriate crack width for a structural element would lay between 0.1 to 0.4 mm (EN 1992-1-1 2004). However, these crack opening values should be taken into account carefully, since distinct allowable crack openings could be established for different fibre reinforced concrete applications, such as: small to moderate crack openings in slab on grade applications, or large crack openings in tunnel linings and in structures designed to dissipate energy when subjected to seismic loading. Taking into account the previous observation, in Figure 2.6(b) are represented

the relation between the fibre inclination angle and the pullout load registered at a constant fibre slip of 0.5 mm. For this fibre slip, i.e. crack opening (it is assumed that crack opening is similar to fibre slip), the pullout forces of inclined fibres are higher than for aligned fibres until an inclination angle of 15°, decreasing significantly for larger values of this angle. The exceptions were the cases of Bartos and Duris (1994) and Leung and Geng (1998), where pullout load of inclined fibres was always lower than of the aligned fibres.

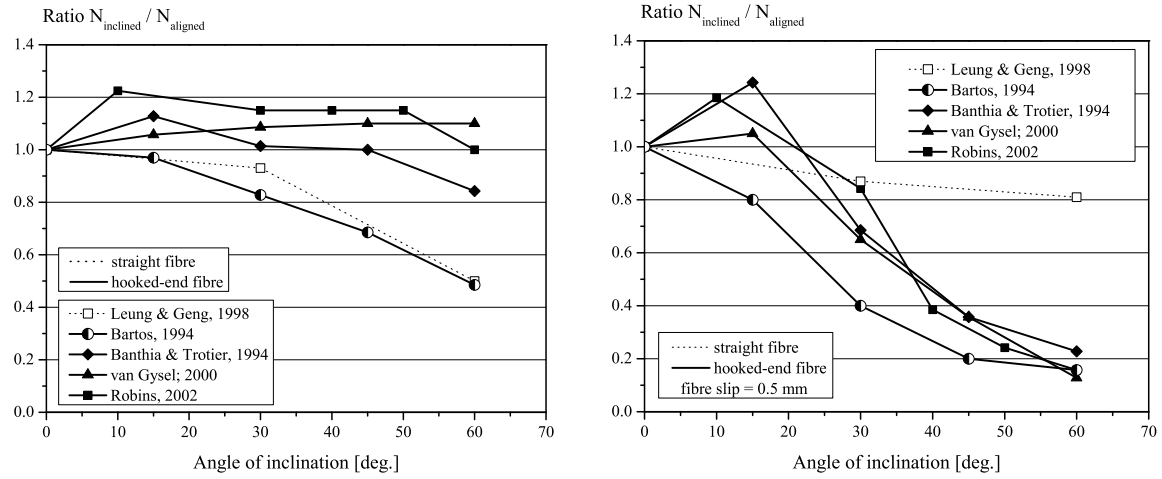

(a) (b)

Figure 2.6: Relationship between normalized pullout force of an inclined fibre and the angle of fibre inclination: (a) for fibre slips at which the maximum pullout was achieved, (b) at a constant fibre slip of 0.5 mm.

It should be noticed that the scatter of the results found between these authors (Banthia and Trottier 1994, Bartos and Duris 1994, Leung and Geng 1998, Gysel 1999, Robins et al. 2002) can be assigned to distinct parameters that also influence the pullout response and can not be regarded independently, such as: concrete matrix strength, fibre embedment length and fibre cross section dimensions, fibre strength, dimensions of the fibre mechanical anchorage, fibre surface characteristics, etc. For instance, as fibre inclination angle increases (for $\theta > 30^o$), the pullout response of a hooked end fibre becomes less influenced by the matrix strength and increasingly more influenced by the mechanical properties provided by the straighten of the fibre with respect with load direction. Another example is whenever the mechanical anchorage of the fibre is not fully mobilised, i.e if the embedment is less than the length of the fibre mechanical anchorage (not larger than 5 mm in the majority of the fibres). In this case the orientation of the fibre has a minor significance on the pullout behaviour (Robins et al. 2002).

In Figure 2.7 are depicted the pullout relationships of hooked end fibres with different incli-

nation angles. The fibre ultimate tensile strength, UTS, is also indicated in this figure, revealing that the peak loads remained far below the fibre UTS. However, fibres under inclination angles of 45° and 60° fractured below their ultimate tensile strength. This phenomenon was observed by several authors for hooked end fibres (Banthia and Trottier 1994, Gysel 1999, Robins et al. 2002) and corrugated fibres (Banthia and Trottier 1994, Chanvillard and Aïtcin 1996) for distinct fibre inclinations, and can be explained by the relatively high stress concentrations at the fibre bending point. According to Banthia and Trottier (1994), the additional shear stresses imposed on inclined fibres, at the point they exit the matrix, will favour the fibre intercrystal slippage within an atomic level point of view, causing a reduction on both the yield and ultimate strength of the material.

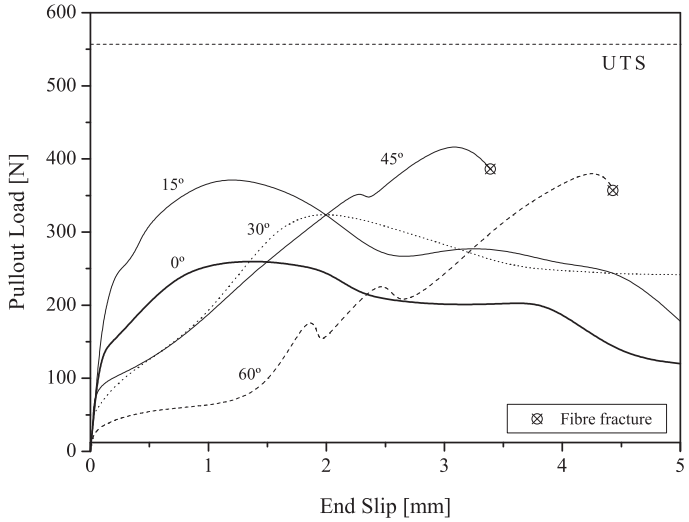

Figure 2.7: Pullout relationships for hooked end fibre from a high strength matrix (85 MPa) at various inclination angles (Banthia and Trottier 1994).

In conclusion, the peak load and toughness are, in general, maximized for inclination angles laying between 0° and 20°. Higher angles usually lead to a lower pullout load on the first phase of the pullout behaviour, which should not be neglected, since from the point of view of the fibre performance in the structure, this phase is an important one. However, depending on the fibre type, matrix strength, and other parameters, the maximum pullout load may increase with the fibre inclination up to an angle of about 45° (Naaman and Shah 1976, Banthia and Trottier 1994, Robins et al. 2002).

Theoretically, the toughness should increase with the inclination angle, since inclined fibres undergo plastic bending of successive sections of the fibres during pullout. Moreover, as bigger is the inclination angle, the higher is the normal force applied to the fibre at the bend, in-

creasing friction stresses at the debonded interface, which contribute also to increase the work requirements to fully pullout a fibre. In spite of that, for deviation angles higher than 20°, the toughness decreases significantly, which may be justified by the fact that for higher inclination angles the fibre generally fractures in an earlier stage.

2.3.3 Influence of embedment length

The pullout response is expected to be improved from the increase of the embedment length, since a larger fibre surface area is in contact with the cement matrix, safeguarding that both the fibre geometry and matrix quality are the same. This holds mainly true for smooth fibres (Li and Stang 1997). However, for some deformed fibres, e.g. hooked end steel fibres, the maximum pullout load may be higher for a smaller embedment length (Robins et al. 2002, Grünewald 2004). This may be justified by the fact that in a hooked end fibre the mechanical component of the bond, corresponding to the plastic deformation of the fibre hook, is more significant than the component due to the debonding of the fibre over a certain embedded length. This was experimentally assessed by Naaman and Najm (1991). Thus, the maximum pullout load of deformed fibres depends principally on the grade of the hook's mobilization. In addition, Robins et al. (2002) observed on the pullout behaviour of hooked end fibres that a fibre with an embedded length smaller than 5 mm, which usually is the length of the hook for a 30 and 60 mm fibre length, the mobilisation of the potential fibre pullout strength cannot fully occur. This results on a significant turn down of both the maximum pullout load and toughness. On the other hand, for fibres with mechanical deformations along the fibre length, the embedded length improves significantly both the maximum pullout load and toughness. This is due to the fact that as higher is the fibre embedded length, more number of mechanical deformations are mobilised. This was observed by Chanvillard (1993) for corrugated fibres and by Groth (2000) for indented steel fibre.

2.3.4 Influence of the matrix properties

The mechanical quality of the matrix, which can be evaluated from its compressive strength, depends upon several factors, such as: water/cement ratio or water/binder ratio, presence of fine filler materials, type and quality of the cement, maximum dimension and type of aggregates, etc. Since the fibre/matrix bond is influenced by the properties of interfacial transition zone, the matrix quality plays an important role on the fibre pullout behaviour.

Figure 2.1(b) shows that, the water/binder ratio (w/b) influences the density and micro-hardness of the fibre concrete interfacial transition zone (Wei et al. 1986), therefore influencing the pullout behaviour of fibres. Several authors have reported improvement of the maximum

pullout load with the decrease of the w/b ratio for both hooked end fibres (Banthia and Trottier 1994, Groth 2000) and crimped fibres (Banthia and Trottier 1994, Chanvillard and Aïtcin 1996). On the other hand, the toughness generally decreases with the decrease of w/b ratio, which can be justified by the brittleness increment of the fibre/matrix interface with the increase of the matrix strength (Banthia and Trottier 1994). Moreover, within a high strength matrix, deformed fibres have higher probability of fracture at an early stage of pullout, and consequently, the fibre pullout toughness decreases significantly.

Several matrix modifications have been examined as a possible way of improving the bond slip of fibres in a cementitious matrix. This includes the addition of fine filler materials, e.g. silica fume, fly ash, limestone filler, metakaolin or polymer additions. These additions are often used with several purposes, such as increasing the matrix strength, concrete durability or even its workability. The average grain size of these particles is considerably smaller than the ones of the cement, therefore the empty spaces between the cement particles and the fibre, in the interface zone, can be efficiently filled, leading to a higher packing density of the interface. Furthermore, some additions (e.g. silica fume, fly ash, metakaoline) exhibit a pozzolanic reaction. This reaction improves the strength and quality of the interfacial transition zone, ITZ, since during this reaction the calcium-hydroxide crystals are partly replaced by other stronger crystals, e.g. in the case of silica fume are replaced by the calcium-silicate crystals (Bentur and Mindess 1990). The addition of polymers is another technique to dense the ITZ, i.e. to get a higher packing density. The use of silica fume may also increase the concrete shrinkage 2-3 times when compared to a concrete without it. This will produce a higher clamping pressure on the fibre that could lead to an improvement of the debonding and frictional pullout resistance (Li and Stang 1997). Robins et al. (2002) observed that the addition of silica fume (10 % in vol.) improved both the maximum pullout force and toughness of hooked end fibres up to approximately 50 %. Guererro and Naaman (2000) also reported an improvement of the maximum pullout force in 50 % with the addition of fly ash (20 % in vol.).

The presence of short fibres, either steel or polypropylene, in the pullout medium can improve the maximum pullout load of hooked end steel fibres. In the first phase of the pullout, when micro-cracking starts to develop, short fibres bridge those micro-cracks mitigating their propagation, which will increase the energy, i.e. pullout force, needed to deform the curvatures of the hook (Markovic 2006), see Figure 2.2. In Figure 2.8 is depicted the improvement on the pullout behaviour of hooked end steel fibres (Dramix RC-80/60-BP) on concretes containing short steel fibres (Dramix OL 13/0.20, fibre length $l_f = 13$ mm and fibre diameter $d_f = 0.2$ mm). An increase of about 40 % was observed in the maximum pullout load with an addition of 2 vol. % of short steel fibres.

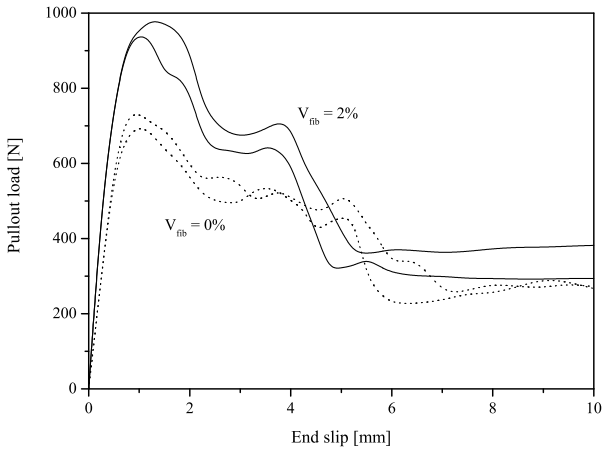

Figure 2.8: Influence of short fibres in the pullout medium on the pullout behaviour of hooked end steel fibres (Markovic 2006).

2.4 Models for predicting the pullout of fibres

One of the first pullout models was proposed by Lawrence (1972), which relates the shear stress distribution along the fibre to the elastic properties of the matrix and fibre. In addition, the solution was extended for the case of a partially debonded fibre, assuming constant frictional shear stress along the failed interface. Laws et al. (1972) applied the analytical model developed by Lawrence (1972) to the study of glass fibre reinforced cement composites failure.

Based on the Lawrence (1972) model, other models were developed to simulate the fibre pullout problem (Gopalaratnam and Shah 1987, Lim et al. 1987, Wang et al. 1988, Stang et al. 1990, Naaman et al. 1991b, Leung and Li 1992). These models are one-dimensional, with many common features. They include a shear-lag model for predicting the bond stress variation, over the fibre embedded length, due to the fibre slip, in full bond conditions, gradual debonding, and free frictional sliding. In their study, Wang et al. (1988) considered only frictional bond. Lim et al. (1987) and Naaman et al. (1991b) deduced the force distributions in the fibre and matrix. Leung and Li (1992) developed a two-way debonding theory, in which the debonding can progress from both fibre ends. In other models, it is assumed that the interfacial shear bond stresses are elastic in the beggining/at the first stage, but gradually debonding takes place at the interface and the stress transfer is shifted to a frictional one (Gopalaratnam and Shah 1987). To describe the debonding criterion, basically two different approaches can be used: a strength-based criterion (or stress-based) and a fracture-based criterion. In the stress-based models, it is assumed that debonding initiates when the interfacial shear stress exceeds the shear strength. For the fracture-based models, on the other hand, the debonding zone is treated as an interfacial crack. The conditions for the debonding propagation are considered, in terms of fracture parameters of the interface and an assumption that, to drive the debonded

zone forward, adequate energy must be supplied; see Stang et al. (1990) and Li and Stang (1997).

Nevertheless, the models for smooth fibres are of limited use for hooked end fibres, since the behaviour of hooked end fibres is dominated by the mechanical anchorage. In hooked end fibres the bond strength may be meaningless when compared to the parcel provided by the mechanical bond (Naaman and Najm 1991, Robins et al. 2002).

Alwan et al. (1999) developed an analytical model to predict the mechanical contribution of anchorage forces in hooked end steel fibres. This model is based on the concept of frictional pulley along with two plastic hinges. The mechanical bond provided by the hook is considered as a function of the work needed to straighten the fibre during pullout. To predict the full pullout response is needed a two-step process corresponding to the contribution of the two hinges, and then one hinge superposition of the frictional and mechanical components. To overcome this two step process Sujivorakul et al. (2000) developed an analytical model where both the frictional bond and mechanical anchorage components are combined in the solution. This model is an extension of the smooth fibre pullout model previously developed by Naaman et al. (1991b), where the adoption of a nonlinear spring component in the latter model intends to simulate the mechanical anchorage reinforcement mechanism.

Bentur and Mindess (1990) point out the importance of proper evaluation of the pullout behaviour, which should not be based on the determination of a limited number of numerical parameters (e.g. maximum pullout load, embedment length and fibre cross-sectional geometry), but rather it should include analysis of the entire curves obtained during such tests. The problems of correctly interpreting fibre pullout tests can partly explain the huge differences in the quoted values of the interfacial shear bond strength, which in the literature range from 0.5 up to 9 MPa, while the interfacial shear friction ranges from 0.5 to 5 MPa; see Beaumont and Aleska (1978), Bartos (1981), Bentur and Mindess (1990), Gopalaratnam and Shah (1987), Li and Stang (1997), Groth (2000) and Grünewald (2004). In general, the higher bond strength values were evaluated from the peak-load values.

2.4.1 Perfectly bonded/debonded smooth fibre model (Stang et al. 1990)

For the current steel fibre dimensions, the pullout problem is mostly governed by frictional pullout, where the fibre slip is of the millimetre magnitude. On the other hand, the slips that are due to the rupture of the chemical bond can often be neglected, inasmuch as the chemical bond only is mobilised over a very small slip (only a few micrometers). This has lead to the development of perfectly bonded/debonded models.

Amongst these models, the stress-based approach and the fracture mechanics approach are

the most referred, therefore they are discussed in the present work. Both approaches have the aim of checking if the fibre is still perfectly bonded, or has already been debonded. In the stress-based approach the fibre is debonded from the matrix once the shear stress reaches a critical value τ_{crit} in a certain point. On the other hand, in the fracture mechanics approach, an energy criterion for debonding is defined taking into account the chemical bond Γ of the interfacial transition zone, ITZ.

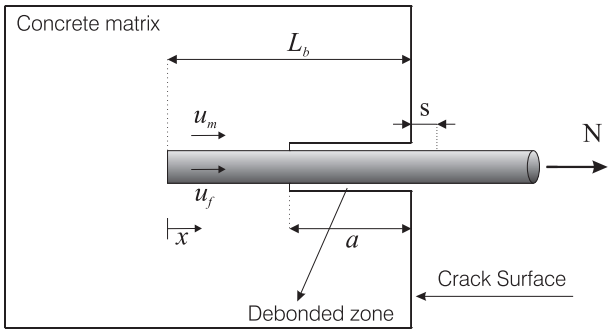

Figure 2.9: Pullout of a single fibre perfectly bonded/debonded.

Stress-based approach

Consider the plane model shown in Figure 2.9, where a single fibre is embedded in a matrix with an embedment length L_b. The fibre is assumed to have constant cross sectional area, A_f, and a constant Young's modulus, E_f. The displacement of the fibre in the axial direction, u_f, is assumed to be constant over fibre cross section, and can be calculated when a fibre has a debonded length a, applying equation 2.8. A detailed description of the constitutive relations, as well as the equilibrium equations can be found in Stang et al. (1990).

$$u_f(x) = \begin{cases} \dfrac{N - t_f \cdot a}{w \cdot E_f A_f} \cdot \dfrac{\cosh(w \cdot x)}{\sinh[w(L_b - a)]} & 0 \le x \le L_b - a \\ \dfrac{N - t_{fr} \cdot a}{w \cdot E_f A_f} \cdot \coth\left[w\left(L_b - a\right)\right] - \dfrac{N - t_f \cdot L_b}{E_f A_f}\left(L_b - a\right) & \\ \qquad - \dfrac{t_f}{2E_f A_f}\left(L_b - a\right)^2 + \dfrac{N - t_f \cdot L_b}{E_f A_f} \cdot x + \dfrac{t_f}{2E_f A_f} \cdot x^2 & L_b - a \le x \le L_b \end{cases} \tag{2.8}$$

where t_f, d_f and N are, respectively, the frictional shear force per unit length along the debonded interface, the fibre diameter and pullout force that is acting on the fibre; x is the

distance from the embedded fibre end to the point where displacement u_f is considered. In equation 2.8, w and k are defined by:

$$w = \sqrt{\frac{k}{E_f A_f}} \qquad [1/mm] \tag{2.9}$$

and

$$k = \frac{t(x)}{u_m(x)} \qquad [N/mm^2] \tag{2.10}$$

where $t(x)$ and $u_m(x)$ are the shear force per unit length at a distance x from the fibre end, and the displacement of the matrix at a distance x from the fibre end. Remark that, in the aforementioned equations, the length unit is given in [mm], whereas the force unit is in [N].

Equation 2.8 is the general equation of the perfectly bonded/debonded model for obtaining the fibre displacement at any fibre point. However, the total fibre displacement at the crack surface, s, is of special interest (see Figure 2.9). To obtain this displacement, it must be substituted $x = L$ in equation 2.8. Moreover, to solve this equation, the length of the debonded zone, a, must be defined. For this purpose a stress criterion is defined for debonding, based on the assumption that debonding only occurs when the shear stress at the fibre/matrix interface reaches a critical value. This criterion is expressed in terms of force per length, and assuming that debonding starts once the force per length, t, reaches the critical force per unit length around the fibre, t_{crit}, which is a constant value. It is also assumed that the fictional shear force, t_f, is expressed in terms of t_{crit}. For a certain debonded length a, the shear stress has a maximal value at the place where the debonded zone ends, therefore the condition for debonding can be written as:

$$N = t_f \cdot a + \frac{t_{crit}}{w} \tanh\left[w\left(L_b - a\right)\right] \tag{2.11}$$

This model can simulate the basic pullout behaviour of a aligned smooth fibre, since the load - displacement relationship during debonding, $N-s$, can be obtained numerically, by substituting $x = L_b$ in equation 2.8 and eliminating the length of debonded zone a from equations 2.8 and 2.11, i.e., $a = 0$.

Fracture mechanics approach

The fracture mechanics is based on an energy approach that considers that the propagation of the debonding zone requires a certain energy, which is characteristic for the bond between the

fibre and the matrix. In this model (Stang et al. 1990, Li and Stang 1997), it is assumed that debonding takes place when the energy release rate reaches a critical value, which is related to the fracture work of the interface Γ. Adopting a certain displacement continuity assumption as approximation for the shear lag strain energy, the work done by friction and a constitutive relation for the matrix shear lag, the stress in the fibre can be established in function of the total pullout displacement relative to the crack surface, s, (see equation 2.12).

$$\sigma_f = \frac{N}{A_f} = 2\sqrt{\left(\frac{t_f}{\pi \cdot d_f} s + \Gamma\right) \cdot \frac{2E_f\,(1+\eta)}{d_f}} \tag{2.12}$$

with,

$$\eta = \frac{E_f \cdot V_f}{E_m\,(1 - V_f)} \tag{2.13}$$

where σ_f $[N/mm^2]$ and Γ $[N/mm]$ are, respectively, the axial stress in the fibre at the place of the crack surface and the bond energy of the interface transition zone, ITZ, per unit bonded interface area; V_f and E_m $[N/mm^2]$ are the volume fraction of fibres and the Young modulus of the matrix.

Once debonding has just finished, the maximum pullout stress, σ_{max}, is attained. σ_{max} and the corresponding pullout displacement, s_{peak}, when debonding has just completed can be determined by:

$$\sigma_{max} = \frac{t_f \cdot L_b\,(1+\eta)}{A_f} + \sqrt{\frac{8\Gamma \cdot E_f\,(1+\eta)}{d_f}} \tag{2.14}$$

$$s_{peak} = \frac{t_f \cdot L_b^2\,(1+\eta)}{2E_f \cdot A_f} + \frac{L_b}{E_f}\sqrt{\frac{8\Gamma \cdot E_f\,(1+\eta)}{d_f}} \tag{2.15}$$

It should be noted that, equation 2.12 is only valid if the fibre has not yet fully debonded from the matrix. After the fibre has fully debonded, it starts to slip out. Li and Stang (1997) suggest equation 2.16 for determining the frictional shear stress in the fibre for this stage.

$$\tau = \tau_{crit} + \Delta\tau(s) = \tau_{crit} + a_1 \cdot s + a_2 \cdot s^2 \tag{2.16}$$

where τ_{crit} is the ultimate frictional stress for the interface between concrete and fibre before the

fibre starts to slip. The coefficients a_1 and a_2 are empirical constants to take into account the dependency of frictional shear force per unit length on the pullout length. The latter constants can be obtained from direct pullout tests of single fibres. In Li and Stang (1997) can also be found the values of the parameters of equation 2.16 for different fibres types and concrete mix compositions.

Moreover, there is evidence that τ_{crit} may be sensitive to lateral pressure, Leung and Geng (1995) found that τ_{crit} obeys a Coulomb type friction law with coefficient of friction μ:

$$\tau_{crit} = \tau_{crit}^{'} + \mu\sigma_n^{shr} + \mu\sigma_n^{ext} \tag{2.17}$$

where $\tau_{crit}^{'}$ is the friction of the contact surfaces without any residual normal stress due to shrinkage (σ_n^{shr}) or external normal stress (σ_n^{ext}).

2.4.2 Smooth fibre with an end anchorage model (Sujivorakul et al. 2000)

In Figure 2.10 is schematically represented the pullout model of a smooth fibre with an end anchorage embedded in a matrix. The fibre is decomposed in two parcels, the one corresponding to the smooth part of the fibre and the other corresponding to the anchorage itself. The first one corresponding to the smooth part is modeled by a fibre that has a cross sectional area A_{f1}, a elastic modulus E_{f1} and is embedded over a length L_b in a matrix with a cross section A_m and elastic modulus E_m. On the other hand, the mechanical anchorage is modeled by a spring which connects the fibre to a similar fictitious fibre along its axis (see Figure 2.10). The fictitious fibre is assumed to have a cross sectional area $A_{f2} = A_{f1}$, a elastic modulus $E_{f2} = E_m$ and length L_{b2}. The fictitious fibre is coupled to the spring to overlap some limitations that would occur if the model had only a nonlinear spring, since the introduction of a fictitious fibre allows to model the movement of the matrix at the embedded end of the fibre, which could not be simulated with the spring exclusively.

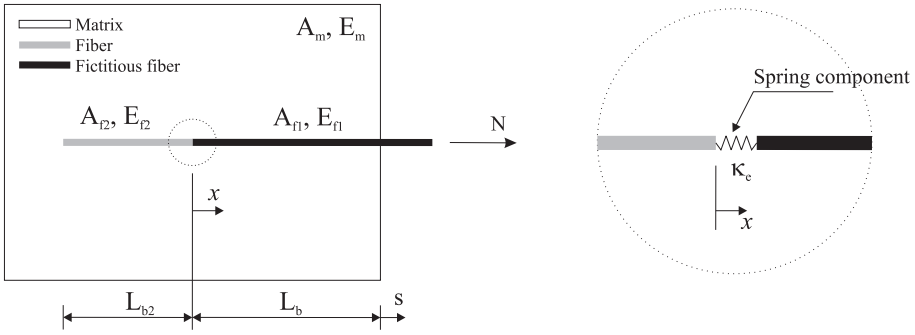

Figure 2.10: Representative pullout model for a smooth fibre with an end anchorage.

To account with the interfacial bond, a bond shear stress *vs.* slip relationship between the fibre and matrix is used. Sujivorakul et al. (2000) assumed a linear elastic relation until the bond strength, τ_{crit}, of the interface is attained. Afterwards τ_{crit} is reached at the interface, the shear stress drops to a constant frictional bond, τ_f. On the other hand, the bond shear stress *vs.* slip relation of the fictitious fibre is linear without debonding. In Figure 2.11 are depicted the adopted bond stress *vs.* slip relationships. The influence of the mechanical anchorage is modeled from the stiffness attributed to the spring, κ_e, see Figure 2.10, which expresses the relationship between the force and the displacements at the embedded end of the fibre.

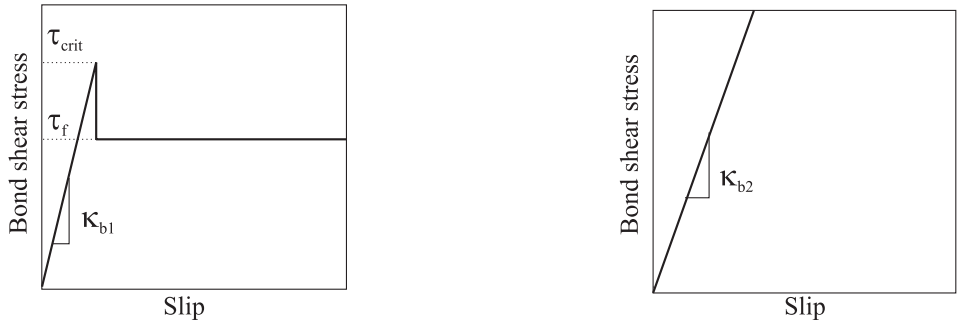

Figure 2.11: Assumed bond shear stress *vs.* slip relationships: (a) fibre, (b) fictitious fibre.

The derivation of the mathematical equations of the model are presented elsewhere (Sujivorakul et al. 2000). The complete pullout load *vs.* slip curve is divided in three distinct regions: pre-critical region, partial debonding region and pullout region. Moreover, for every region an iterative procedure is necessary to obtain the correct value of κ_e that satisfies the boundary conditions.

Pre-critical region

In this phase, the fibre will not start debonding until the bond shear stress (which is maximum at the crack tip, i.e. $x = L_b$) reaches the shear bond stress τ_{crit}. The critical load, N_{crit}, can be computed when the shear stress is equal to τ_{crit} at $x = L_b$ by:

$$N_{crit} = \frac{\tau_{crit}\psi}{\lambda_1 \left(Ae^{\lambda_1 L_b} - Be^{-\lambda_1 L_b}\right)} \tag{2.18}$$

with,

$$\left.\begin{aligned} \lambda_i &= \sqrt{K_i Q_i} \\ K_i &= \frac{\psi \kappa_{bi}}{A_m E_m} \\ Q_i &= 1 + \frac{A_m E_m}{A_{fi} E_{fi}} \end{aligned}\right\} \quad i = 1, 2 \tag{2.19}$$

where ψ, κ_{b1} and κ_{b2} are the fibre perimeter, the bond modulus of the real fibre and fictitious fibre, respectively. The constant κ_{b2} can be assumed from knowing the shear strength of the matrix, whereas κ_{b1} and the other parameters of the bond shear stress relationship can be determined from the inverse problem between the pullout test and the analytical solution on a smooth fibre (Naaman et al. 1991b). The unknown constants A and B are determined from the boundary conditions of the problem.

For a point correspondent to a load $N \leq N_{crit}$, the displacement at the crack tip s can be determined with equation 2.20. The critical point (N_{crit}, s_{crit}) has to be determined by an iterative procedure, a flowchart for determining this point and others contained in this region is given by Sujivorakul et al. (2000).

$$s = \left(\frac{N}{A_m E_m}\right)\left(\frac{Q_1}{\lambda_1}\right)\left[A\left(e^{\lambda_1 L_b} - 1\right) + B\left(1 - e^{-\lambda_1 L_b}\right)\right] \tag{2.20}$$

Partial debonded region

In this region, afterwards the N_{crit} is reached, the fibre will have two interfacial zones, a bonding zone and debonding zone with a length u. The length of the debonded zone will grow with the displacement at the crack tip s until $u = L_b$. Over the length of the debonded zone the interfacial shear stress is constant and equal to τ_f. The external force N is given by equation 2.21 and is the sum of the force developed on the bonded zone, N_b, and the force due to frictional resistance on the debonded zone N_d.

$$N = N_b + N_d = \frac{\tau_{crit}\,\psi}{\lambda_1\left(A\,e^{\lambda_1(L_b-u)} - B\,e^{-\lambda_1(L_b-u)}\right)} + \tau_f\,\psi\,u \tag{2.21}$$

In turn, while $u \leq L_b$, the displacement of the fibre at the crack tip δ can be computed by:

$$s = \frac{N\,(Q_1-1)\,u}{A_m\,E_m} - \frac{u^2\,\tau_f\,\psi}{2A_m\,E_m}\,(Q_1-2) - \frac{u\,L_b\,\tau_f\,\psi}{A_m\,E_m}\left(\frac{n}{A_m\,E_m}\right)\left(\frac{Q_1}{\lambda_1}\right) \left[A\left(e^{\lambda_1(L_b-u)}-1\right)+B\left(1-e^{-\lambda_1\,(L_b-u)}\right)\right] \tag{2.22}$$

Pullout region

When the debonded zone of the fibre reaches $u = L_b$, a dynamic mechanism of pullout will develop with rigid body displacement of the real fibre, which will be equal to the pullout slip, s. For this region, from the static equilibrium, the pullout load can be determined by:

$$N = \kappa_e s_k + \tau_f\,(s)\,\cdot\psi\,(L_b - s) \tag{2.23}$$

where s_k and $\tau_f(s)$ are the displacement at the embedded end and the frictional stress for the slip s, respectively. Since the fibre undergoes some elongation, the displacement at the embedded end s_k is smaller than the displacement at the fibre tip s. However, for the case of large displacements, the elastic elongation of the fibre is very small compared to the rigid body displacement, so that it can be assumed for large displacements that $s_k = s$. The displacement s_k can be determined by:

$$s_k = \frac{A_{f1}E_{f1}}{(A_{f1}E_{f1}+\kappa_e(L_b-s))}\cdot\left[s - \frac{\tau_f(s)\cdot\psi(L_b-s)^2}{2A_{f1}E_{f1}}\right] \tag{2.24}$$

In turn, the frictional stress for the slip s can be determined with the following equation:

$$\tau_f(s) = \tau_f\cdot\frac{\exp^{-(s-s_0)^\eta} - \xi\exp^{-(L_b)^\eta}}{1-\xi\exp^{-(L_b-s+s_0)}}\cdot\frac{1-\exp\left(\dfrac{-2\nu_f\cdot\mu(L_b-s+s_0)}{E_f r_f\left(\dfrac{1+\nu_m}{E_m}+\dfrac{1-\nu_f}{E_f}\right)}\right)}{1-\exp\left(\dfrac{-2\nu_f\cdot L_b}{E_f r_f\left(\dfrac{1+\nu_m}{E_m}+\dfrac{1-\nu_f}{E_f}\right)}\right)} \tag{2.25}$$

that was proposed by Naaman et al. (1991b), since for large slips the assumption of constant friction is not valid due to the deterioration of the τ_f when slip increases. In equation (2.25), s_0 is the end slip at the full debonding stage, which can be determined by substituting $u = L_b$ in equation 2.22. The parameter ξ is the damage coefficient related to the rate at which the

frictional shear stresses deteriorates, η is a factor that simulates the steepness of the descending branch of the pullout curve, and ν_m and ν_{f1} are the Poisson coefficients for the matrix and the real fibre, respectively.

2.5 Test configuration

The test configuration should simulate the fibre located in the composite under a realistic stress situation, avoiding unrealistic stress concentrations around the fibres. Moreover, a realistic variation of the fibre orientation, embedded length and an accurate measurement of the fibre pullout should be possible. Several tests assemblies have been used to carry out fibre pullout tests. Nevertheless, up to date, a standard method has not yet been acknowledged. It is well described in literature that test set-up and loading conditions can strongly affect the results. The tests results are particularly sensitive to the occurrence of stresses normal to the loading direction. These can be induced by the test set-up configuration, as well as by matrix shrinkage during its curing process. Therefore, the curing conditions and other preparation methods must be maintained constant in order to mitigate the scatter of the results between different tests.

Two major groups of pullout test configurations arise from experimental research carried out in the past. The pullout tests can be performed on both single-sided specimens, see Figures 2.12(a) to 2.12(c), and double-sided specimens, see Figures 2.12(d) and 2.12(e), using both a single fibre or an array of fibres. Single-sided test profiles have been carried out with the configuration as in Figure 2.12(a), by e.g. Grünewald (2004) and Markovic (2006). The test set-up as depicted in Figure 2.12(b) has been used by e.g. Naaman and Najm (1991) and Groth (2000), whereas the configuration represented in Figure 2.12(c) has been used by e.g. Li and Chan (1994). On the other hand, double-sided test specimens were also used by several authors to access the fibre pullout behaviour (Naaman and Shah 1976, Chanvillard 1993, Banthia and Trottier 1994, Ouyang et al. 1994, Robins et al. 2002).

In both cases of a single-sided and double-sided specimen configurations some back points can be pointed out, and several aspects should be paid in attention. For the single-sided specimen, the fibre length that gets out of the matrix block must have the necessary free length to be fixed at the test machine grip, in such a way that the slip between the fibre and the grip can be neglected. Moreover, in case that a steel ring at the upper side of the specimen is used as a support, see Figure 2.12(b), lateral confinement to the fibre due to compressive stresses transferred through surrounding concrete could exist depending on the sample and steel ring dimensions. This stress field can unrealistically improve the pullout behaviour of the fibre due to the lateral confinement applied to the fibre.

In respect to the double-sided specimen, care must be taken to ensure that pullout only

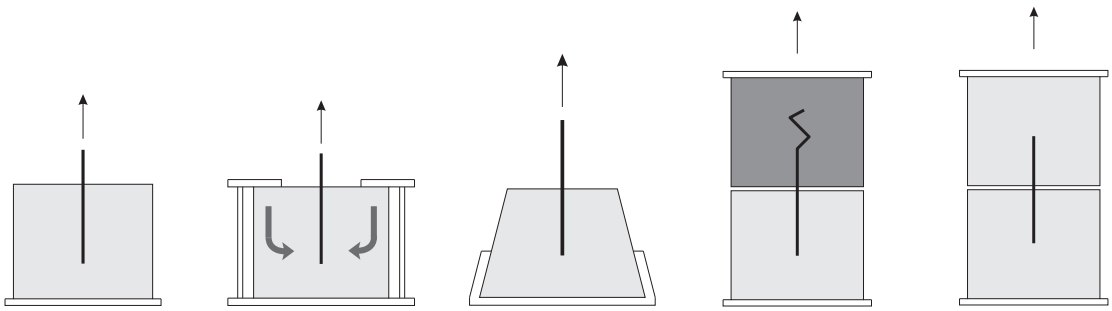

(a) (b) (c) (d) (e)

Figure 2.12: Examples of pullout test configurations: (a) to (c) single-sided specimen; (d) and (e) double-sided specimens

occurs at one of the specimen two halves. This can be achieved, by example, applying an additional mechanical anchorage on the fibre end at one of the specimens halves, see Figure 2.12(d), or with using a matrix strength at one of the halves considerably higher than at the other half, or even taking a higher embedment length on one of the specimens halves, see Figure 2.12(d). However, in spite of all of these measures, it is highly questioned if the pullout really occurs exclusively on one of the halves. On the other hand, if the fibre is placed perfectly centred in the specimen, the global behaviour would be symmetric, since equal slips would be observed in both specimen halves, Figure 2.12(e), although this being highly improbable to happen due to lack of sufficient accuracy to exactly place the fibre as well as on assuring symmetry for the material properties. In such case, it is highly probable that the pullout responses would depend on displacements that are mixed from each side during the initial part of the curve, resulting in a more difficult task to interpret the results.

In conclusion, from a conceptual point of view, these assemblies differ in the way of extracting the fibre from the matrix and of positioning the fibre at the time of manufacture. However, in all the cases the goal of these assemblies is to measure the force necessary to pullout or fracture the fibre.

Chapter 3

Influence of Hooked End Steel Fibres Characteristics on the Pullout Behaviour

3.1 Introduction

The composite behaviour of steel fibre reinforced concrete, SFRC, is governed by the addition of the individual contribution of the single fibre interaction with the matrix. In spite of theoretically being possible to predict the bulk behaviour of SFRC from the single fibre pullout performance, this task is considerably hard since there are several complex mechanisms involved in the overall composite behaviour. Single pullout tests have been carried out in the past 30 years to optimise the combination of both fibre type and concrete mix, and to understand the mechanisms of fibre reinforcement. The short fibres commonly used in concrete can be classified in different ways. First, according to the fibre material, which can be: natural, both organic and mineral, or man made (e.g. steel, titanium, carbon, glass, etc). Second, according to their physical/chemical properties, such as: density, surface roughness, non-reactivity with cement matrix, fire resistance, etc. Third, according to their mechanical properties such as: tensile strength, elasticity modulus, elongation to failure, surface adhesion properties, etc. Moreover, once a certain fibre has been selected, an infinite combination of geometric properties related to its cross sectional shape, length, diameter or equivalent diameter, and surface configuration can be selected. There are several types of steel fibres available, which differ in size, shape and material properties. Due to different materials and manufacturing processes, the mechanical properties such as, tensile strength and grade of mechanical anchorage differ considerably from each fibre. These differences have a significant effect on the fibre pullout

behaviour and, consequently, in the overall behaviour of SFRC under loading (Banthia and Trottier 1994, Naaman 2003).

In this chapter, it will be presented a study about the influence that the fibre characteristics have on the fibre pullout behaviour. It was opted to conduct this study with an intermediate strength class conventional concrete. This study has also the purpose of selecting the hooked end steel fibre to be used in the steel fibre reinforced self-compacting concrete investigated in the next chapters. Moreover, the pullout results obtained in the conventional concrete medium will be used to stress out the eventual differences between the pullout behaviour on a self-compacting and conventional concrete. The pullout tests were carried out with fibres at three different orientation angles, respectively, 0^o, 30^o and 60^o, whereas the adopted fibre embedded length was maintained equal to 15 mm.

An analysis of the fibre geometric properties, namely, diameter, length, weight, aspect ratio and anchorage geometric dimensions was carried out. The influence on the pullout behaviour of the abovementioned parameters was assessed.

3.2 Fibre geometry and mechanical properties control

In this section are presented the results of the fibre geometry analysis for the three types of fibres studied. In order to check out the fibre geometry conformity, for application in fibre reinforced concretes, it was followed the ASTM A820-90 (1990) standard. Even though all the three fibre types studied are commercialized for this kind of concretes, and therefore at the first sight complying with the required specifications, the previous referred standard was used more in the sense of providing a methodology in the fibre geometry assessment.

The three hooked ends steel fibres will be designated by type A, B and C, and were manufactured by distinct producers. According to the manufacturers, the announced fibre length for the three fibre types is 60 mm, the declared diameter for the fibre type A and C is 0.75 mm, whereas for the type B is 1 mm. Supported in a visual inspection of the fibres, i.e. qualitative analysis, it was possible to withdraw two brief conclusions. Firstly, the fibres type B and C presented their longitudinal axis slightly warped. This was more pronounced in the fibres from type C, which have a smaller diameter and, consequently, a lower flexural stiffness. This can also be regarded as a direct result from fibre commercialization method, specifically, its transportation and packaging. On the other hand, in the case of the fibre type A that fact does not occurs, since these fibres are commercialized glued in combs, which increases the flexural stiffness and, therefore, the fibre warping during its transportation and packaging procedures. Secondly, at the first sight the hook dimensions and shape of the fibre type B and C are somewhat irregular.

3.2.1 Dimensions and tolerances

The measurement of the distinct fibre geometry dimensions, previously enumerated, were carried out according to the recommendations of the ASTM A820-90 (1990) standard. For the geometric control were randomly selected 10 fibres from each type. The fibre length and diameter were measured with an electronic calliper that had a precision of ±0.01 mm, see Figure 3.1(a). While, the fibre weight was assessed with a digital scale of ±0.0001 g, as depicted in Figure 3.1(b). As established in the referred standard, deformed cold-drawn wire fibres, which is the present case of the studied fibres, are characterized by their diameter, d, or equivalent diameter, d_e, and length (out-to-out) after being mechanically deformed, l_n. The nominal aspect ratio, λ_n is defined as l_n/d or l_n/d_e. With regard to the fibre geometric conformity checking, resultant from its manufacturing, the ASTM A820-90 (1990) establishes that both diameter and length should not have a ±10% variation higher than that specified in the fibre technical data sheet, whereas the aspect ratio should not differ more than ±15% the one announced. Moreover, a minimum of 90% of the tested fibres must fulfil the tolerances previously referred.

(a) (b)

Figure 3.1: Measurement devices: (a) digital calliper and (b) digital scale.

3.2.2 Mass

In Table 3.1 are included, for each fibre type, the average weight value, M_{avg}, correspondent standard deviation, s_d, and coefficient of variation, Cov. From the obtained results it can be ascertained that fibres type A and C have similar weights, of approximately 0.20 g as expected, since both the fibre producers claim on their data sheets the same geometry dimensions. How-

ever, the CoV value is significantly smaller in the fibre TYPE A. On the other hand, the fibre TYPE B weight is approximately two times of the other fibres, with an average value about 0.42 g.

Table 3.1: Measured fibre average mass values.

FIBRE TYPE	M_{avg} [g]	s_d [g]	CoV [%]
A	0.2053	0.001	0.7
B	0.4249	0.007	1.6
C	0.2038	0.012	5.8

3.2.3 Length

The average nominal length, $l_{n,avg}$, of each fibre type, and the respective standard deviation and coefficient of variation values are given in Table 3.2. Additionally, it is also included the average percentage in which the measured fibre length differs from the length value announced by each manufacturer, designated as Tol_{avg}. The CoV values of the fibre length measured for all fibre types is quite low. Regarding the fibres TYPE A and C, the average measured length is smaller than the announced by the corresponding producers, in opposition to that evidenced in the fibre TYPE B. The difference between the measured length and the one proclaimed by the producers, for the totality of the tested fibres, was lower than the ±10% limit established in the ASTM A820-90 (1990).

Table 3.2: Measured fibre average length values.

FIBRE TYPE	$l_{n,avg}$ [mm]	s_d [mm]	CoV [%]	Tol_{avg} [%]
A	58.38	0.051	0.1	2.7
B	60.51	0.260	0.4	0.8
C	57.56	0.337	0.6	4.1

3.2.4 Diameter

In Table 3.3 are indicated the average values of the diameter, d, or equivalent diameter, d_{eq}, and the corresponding standard deviation and coefficient of variation. Additionally, it is given the average percentage difference, in modulus, between the measured and the announced fibre diameter, $|Tol_{avg}|$, since for the fibre TYPE C this difference is in some cases negative and in

others positive. It should also be pointed out that, after some measurements of diameter of the fibre type B, it was evidenced that some did not presented a circular cross section. The majority of the latter fibres present a rectangular cross section with rounded corners. The smallest edge of the cross section ranges between 0.90 and 0.98 mm, while the biggest edge sets between 1.05 and 1.15 mm. The latter fact could be ascribed to the deforming procedure of the fibre for obtaining the mechanical anchorage, i.e. the hooked ends. Therefore in the case of fibre type B, the diameter indicated in Table 3.3 corresponds to a equivalent diameter, which was computed by:

$$d_{eq} = \sqrt{\frac{4M}{\pi \cdot l_n \cdot \rho}} \tag{3.1}$$

where ρ is the volumetric mass value for the steel, and in the present work was adopted the value of 7850 kg/m^3, as suggested by the ASTM A820-90 (1990). The difference between the measured diameter and the one proclaimed by the producers, for the whole tested fibres, was lower than the ±10% limit establish in the latter standard.

Table 3.3: Measured fibre average diameter values.

Fibre type	d or d_{eq} [mm]	s_d [mm]	CoV [%]	$\lvert Tol_{avg} \rvert$ [%]
A	0.74	0.003	0.4	1.5
B	1.07	0.009	0.9	6.6
C	0.74	0.020	2.7	2.1

3.2.5 Aspect ratio

The average nominal aspect ratio, $\lambda_{n,avg}$, for each fibre type studied and correspondent standard deviation, coefficient of variation and the average percentage in which the computed nominal aspect ratio differs from the one announced by each manufacturer are given in Table 3.4.

Table 3.4: Fibre aspect ratio computed from the measured dimensions.

Fibre type	$\lambda_{n,avg}$ [-]	s_d [-]	CoV [%]	Tol_{avg} [%]
A	79.0	0.378	0.5	1.2
B	56.7	0.625	1.1	3.2
C	77.4	2.043	2.6	5.4

The difference between the measured diameter and the one proclaimed by the producers, for the whole tested fibres was lower than the ±15% limit establish in the ASTM A820-90 (1990) standard.

3.2.6 Anchorage

Throughout the fibre dimensions measurement, with a mere visual inspection it was ascertained that the fibre hooked end dimensions and shape in some cases shown a significant scatter. In order to assess this in qualitatively fashion, the fibres were electronically scanned and the measurement of the end hook was performed with the help of a computer aided design software (AutoCad 2010 from AutoDesk®). In Figure 3.2 are depicted the parameters that define the hook dimensions and shape. These parameters were measured throughout the fibre longitudinal axis.

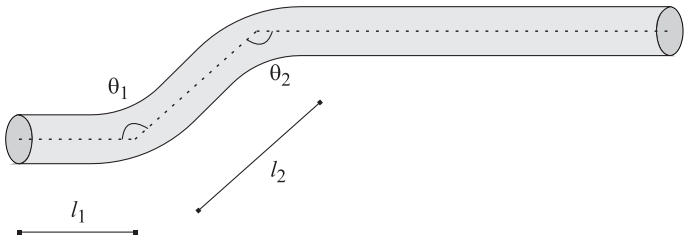

Figure 3.2: Scheme of the parameters that define the hook geometry.

In Table 3.5 are included the average values of those parameter, Avg, and the correspondent standard deviation and coefficient of variation. For each fibre type was used a 10 fibre set, in each fibre the dimensions of the two hooked ends were measured, resulting in 20 measurements for each parameter.

From the obtained results, it is possible to conclude that the fibres TYPE A and C have very similar hook lengths. The influence of the hook length on the fibre pullout response will be discussed further ahead. When comparing those two fibres, and concerning the bending angles of the hook (θ_1 and θ_2), the average values are slight higher in the fibre TYPE C. The coefficients of variation of the hook l_1 length were similar in the fibre TYPE A and C, whereas the parameters l_2, θ_1 and θ_2 for the fibre TYPE C presented higher coefficient of variation values. Regarding the fibre TYPE B, the hooked end length dimensions were significantly higher than in the other fibres. It should also be remarked the high coefficient of variation obtained for the parameter l_1 for this fibre. In conclusion, the fibre TYPE A has shown a considerable smaller variation of both their hook dimensions and shape.

Table 3.5: Measured values of the fibre anchorage dimensions.

Fibre type			*Avg* [-]	s_d [-]	CoV [%]
A	l_1	[mm]	2.2	0.20	8.9
	l_2		2.5	0.14	5.6
	θ_1	[°]	139	2.19	1.6
	θ_2		138	1.89	1.4
B	l_1	[mm]	3.3	0.83	24.9
	l_2		4.0	0.54	13.3
	θ_1	[°]	147	3.09	2.1
	θ_2		140	5.86	4.2
C	l_1	[mm]	2.2	0.19	8.6
	l_2		2.6	0.26	10.0
	θ_1	[°]	145	6.77	4.7
	θ_2		145	5.66	3.9

3.2.7 Tensile strength

The fibre tensile strength was assessed on a electromechanical Lloyd® LR30K machine with a capacity of 30 kN. The tests were carried out under closed-loop displacement control performed by the testing machine internal displacement transducer, with a displacement rate of 10 µm/s. A valid tensile test was only considered when the fibre fracture occurred out of the grips influence zone. Consequently, in order to fulfil the previously established criterion and obtaining 10 valid tests per fibre type, it were necessary to perform 12 tests for the fibre type A, 13 tests for the fibre type C and 14 tests for the fibre type B.

The average tensile strength, $f_{u,avg}$, characteristic tensile strength, $f_{u,k}$, correspondent standard deviation and coefficient of variation are given in Table 3.6. The characteristic tensile strength was computed with equation 3.2 for a 95% confidence interval corresponding to the lower-confidence limit, moreover it was assumed a t-student distribution:

$$f_{u,k} = f_{u,avg} - t_{\alpha/2,n-1} \cdot s_d/\sqrt{n} \tag{3.2}$$

where $f_{u,avg}$ and s_d are, respectively, the average tensile strength and standard deviation of a random sample with a normal distribution, being n the number of tested specimens. For the studied sample size, $t_{\alpha/2,n-1}$ yields the value of 2.262. Remark that all the studied samples have a normal distribution, since all of them passed the Shapiro-Wilk normality test (Montgomery and Runger 1994).

The tensile strength ascertained for the three fibre types was similar, nevertheless the fibre TYPE A shown a tensile strength, approximately, 10% higher than the other fibres. Remark also that the announced tensile strength values in the technical data sheets are lower than those obtained in the tensile tests.

Table 3.6: Average and characteristic values of the fibre tensile strength.

FIBRE TYPE	$f_{u,avg}$ [MPa]	s_d [MPa]	CoV [%]	$f_{u,k}$ [MPa]
A	1313	40.5	3.1	1284
B	1153	32.7	2.8	1130
C	1184	32.4	2.7	1161

3.2.8 Ductility

The fibre ductility was ascertained in a qualitative fashion as suggested by the ASTM A820-90 (1990) standard. The referred standard establishes a simple bending test for the fibres, in which the fibres shall withstand bending up to an angle of 90º without breaking. Remark that this test only provides an indication of the fibre ductility, and subsequently to the fibre rupture strength on handling and mixing operations. Hence, the ductility of a fibre reinforced composite can not be inferred from this test. Every single fibre passed the test, thus being in conformity with the ascribed in the standard, see Figure 3.3.

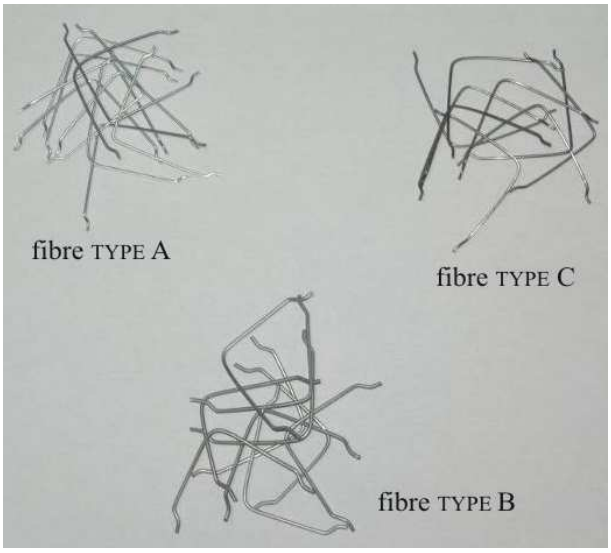

Figure 3.3: Ductility test as suggested by ASTM A820-90 (1990).

3.3 Fibre pullout tests

3.3.1 Concrete mixture and test specimens

The pullout tests on single steel fibres were performed using cylindrical concrete specimens. The diameter and height of each specimen was 80 mm. In order to produce the specimens, a special mould was designed, able to accommodate 81 fibres fixed at its bottom (see Figure 3.4). This device was used to cast 81 pullout specimens simultaneously, allowing a correct placement of the fibre and keeping the desired embedded length and orientation angle.

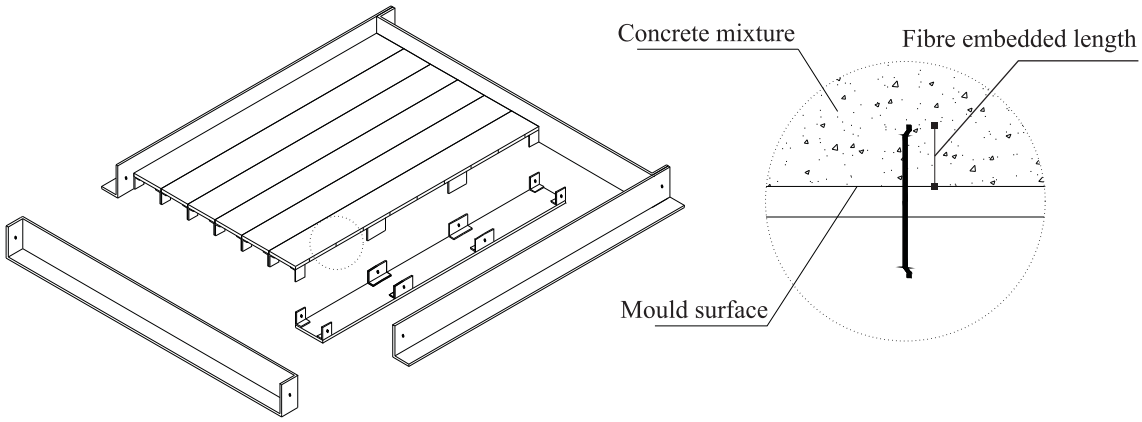

Figure 3.4: Device used to cast the pullout specimens.

For each fibre brand (type A, B and C) and orientation angle (0, 30 and 60°) were produced 5 specimens with hooked end fibres and 4 specimens with smooth fibres. An embedment length of 15 mm was adopted for all specimens. After casting, the concrete slab was cured at a temperature of 20°C and at a relative humidity of about 95%. After 7 days, the concrete was demoulded, and cylindrical specimens containing each one single fibre were drilled out from the slab (Figure 3.5).

(a) (b)

Figure 3.5: (a) Slab after drilling the specimens and (b) pullout specimen.

The fibre pullout tests were performed at approximately 35 days. The compressive strength of the concrete was assessed by performing compression tests with three cubic specimens of an edge length of 150 mm. The average value of the concrete compressive strength, at the testing age (35 days), was 59.8 MPa with a coefficient of variation of 2.6%. Regarding the EN 1992-1-1 (2004), the concrete strength class is the C40/50.

3.3.2 Experimental set-up

The pullout tests were performed on a electromechanical Lloyd® LR30K machine with a capacity of 30 kN. The built-in load cell of the test machine, for the expected experimental load values, was not enough accurate. In order to acquire more precise recordings of the load values, a HBM® S9 load cell with a capacity of 5 kN and accuracy class 0.05 was attached to the machine test frame.

The single-sided specimen is mounted in a steel frame, see Figure 3.6. This frame incorporates one steel plate attached to testing machine frame and a steel ring coupled to the first by three steel screws. The protruding end of the steel fibre is fastened to a standard Lloyd® grip which allows a secure hold of the fibre. However, due to the small fibre diameter, special attention was given in fastening the fibre, since deforming the fibre end could induce that the fibre would break at the grip.

For the measurement of the fibre pullout slip, three LVDTs (linear stroke +/- 5mm) were used. In order to exclude measuring deformations of the testing rig and fibre slip at the grip, the LVDTs were fixed at the upper steel ring and touching the bottom surface of an aluminium plate fixed to the fibre. The plate was fixed to the fibre with two fine screws and was used as a support for this LVDT configuration, detail in Figures 3.6(c) and 3.6(d). Since the three LVDTs were disposed around test specimen forming an angle of 120 degrees between consecutive LVDTs, the actual pullout slip of the fibre is the average of the three LVDTs readouts. The closed-loop displacement control was performed by the testing machine internal displacement transducer. This control procedure guaranties a stable response during the tests and ensures that a constant deformation rate is kept even for e.g. the case of catastrophic debonding during single fibre pullout, i.e. it turns possible to obtain the pullout post-peak behaviour. In all pullout tests, it was used the same displacement rate of 10 μm/s.

For the adopted test set-up, in which a steel ring at the upper side of the specimen is used as a support, see Figure 3.6(b), lateral confinement of the fibre by compressive stresses could exist depending on the sample dimensions. These stress concentrations can unrealistically improve the pullout behaviour of the fibre due to the lateral confinement. This was observed by Markovic (2006) for a cylindrical specimen with 65 mm diameter and 50 mm height. Taking

(a)

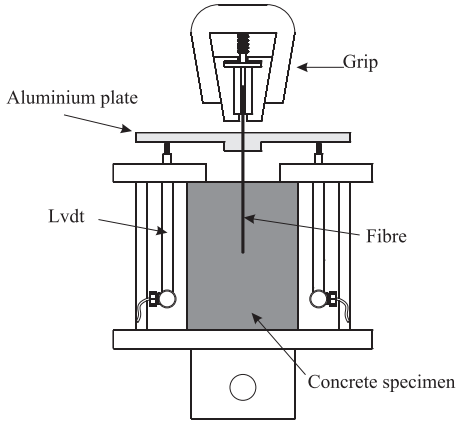

(b)

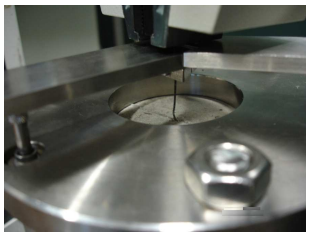

(c)

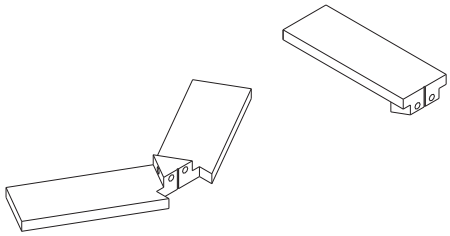

(d)

Figure 3.6: Configuration of the single fibre pullout test: (a), (b) general view, and (c), (d) detailed view of the aluminium plate fixed to the fibre.

into account this, a linear-elastic finite element simulation was used to select the steel ring hole and specimen dimensions in order to avoid the development of arch action by the compressive stresses. With the adopted solution, composed by a cylindrical specimen with 80 mm diameter and height, and a 60 mm diameter ring hole, no compressive stresses nearby the fibre were developed.

3.3.3 Failure modes

The typical failure modes observed on the pullout tests are schematically represented as the projection on the longitudinal plane of the cylinder from which the fibre was pulled out, and are depicted in Figure 3.7. The totality of both hooked and smooth aligned fibres were completely pulled out, see Figure 3.7(a). In the case of hooked fibres, after debonding of the fibre/matrix interface, the hook was fully straightened. This failure is designated as Fm1. A similar failure mode, Fm2, was observed for some inclined fibres, however, in opposite to aligned fibres, spalling of the matrix at the fibre bending point was observed, Figure 3.7(b). During the pullout of inclined fibres was also observed fibre rupture, being this failure mode designated by Fm3, see Figure 3.7(c). This failure mode was always preceded by matrix spalling. Another observed failure mode, Fm4, was by matrix spalling, which is depicted in Figure 3.7(d). In this case the

fibre is almost fully pulled out of the concrete specimen, however, when the embedded end of the fibre approaches the exit point of the concrete matrix, it detaches a portion of concrete near the fibre bending point. This failure mode only occurred for fibres with an orientation angle of 60°. Moreover, it was more common for the fibres with the highest diameter, i.e. the fibre TYPE B. The pullout specimens where the conditions of premature fibre or matrix failure were observed occurred exclusively for inclined fibres. Moreover, for a 30° orientation angle has occurred predominantly fibre pullout with matrix spalling. Regarding the hooked end fibres with a 60° orientation angle, only for the fibre TYPE C was observed fibre rupture for all the specimens of this series, whereas for the other two fibres types were observed both FM2 and FM4 failure modes.

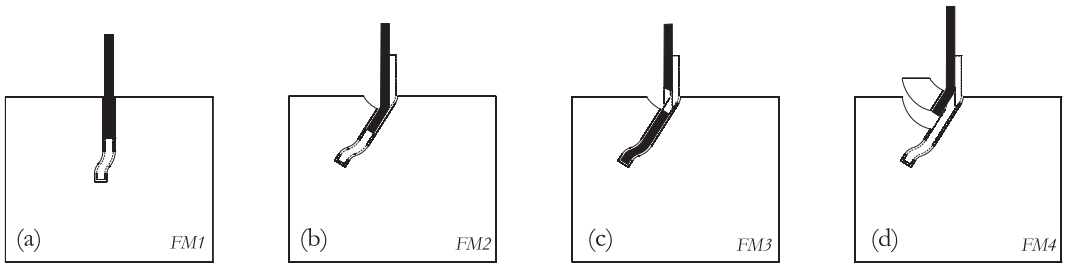

Figure 3.7: Typical failure modes observed during the pullout tests.

In Table 3.7 are indicated the failure modes observed for each series. When more than one failure mode occurred for a specific series, the number of specimens corresponding to each failure type was indicated between parenthesis.

Table 3.7: Failure modes observed during the pullout tests on conventional concrete.

FIBRE TYPE		Inclination 0°	30°	60°
Smooth	A	FM1	FM2	FM2
	B	FM1	FM2	FM4
	C	FM1	FM2	FM2(3); FM4(1)
Hooked	A	FM1	FM2	FM3(3); FM4(2)
	B	FM1	FM2(3); FM3(2)	FM3(2); FM4(3)
	C	FM1	FM3	FM3

The fibre rupture observed for hooked inclined fibres is a result of both a strong and compact concrete matrix, and a good fibre anchoring in it. Due to the higher tensile strength of the fibre TYPE A comparatively to the others, this kind of fibres failed only for higher orientation angles

(60^o), since as the orientation angle increases, the stress concentration present in the bent part of the fibre will also increase, consequently subjecting the fibre to a higher maximum tensile stress due to a mixed tensile - bending mode. A more detailed discussion of this phenomena will be given in Chapter 4. When comparing the fibres type B and C (with similar tensile strengths), one may be lead to think that the higher diameter of the fibre type B would avoid fibre rupture. However, the lengthier hook of the latter fibre provides a higher grade of the anchorage mechanism. Thus, fibre type B was subjected to higher pullout loads, and consequently, to a higher stress state.

3.3.4 Pullout load - slip curves

The average pullout load - slip experimental relationships for the tested series are depicted in Figure 3.8, whereas within Annex I, the pullout load - slip relationship for each single specimen tested is presented. Since the reading range of the displacement transducers was limited to a smaller value than the fibre embedment length (15 mm), the abovementioned experimental relationships are depicted up to a maximum slip of 8 mm. In spite of that, the tests were continued until the fibre was completely out of the concrete specimen. If premature failure did not occur the final fibre slip will be approximately the fibre's embedded length, i.e. 15 mm.

For both the type A and C hooked aligned fibres analysed, the average pullout load - slip curve shape was very similar, as expected, since as previously ascertained in the geometrical study of the fibres, both fibres have almost identical dimensions (see Tables 3.3 and 3.5). On the other hand, although the similitude of the average pullout - slip curve shape of the three types of fibres, the response of the fibre type B has shown a significantly higher pullout load and dissipated energy, as expected, since the contact surface of this fibre is larger due to the higher perimeter of its cross section. The larger dimensions of the hook of this last fibre has also contributed to its better performance. The pre-peak branch of these pullout load - slip curves is made up of a linear and nonlinear part. The first one is associated with the elastic bonding, whereas the nonlinear part starts with the micro-cracking of the interface, corresponding to the debonding process. The loss of stiffness associated to the pre-peak nonlinear branch is justified by the irrecoverable deformation component of the fibre and the surround paste at the zone of the hooked end, when this part of the fibre starts being straightened. After the peak load is attained, as the fibre mechanical anchorage becomes progressively mobilised with the increase of the slip, a gradual load decay is observed until the full straightening of the hook. Afterwards, fibre/paste friction is the commanding mechanism of the pullout behaviour. In this part of the post-peak branch, the load decreases with the increase of slip, since the available frictional area decreases, as well as the roughness of the failure surface.

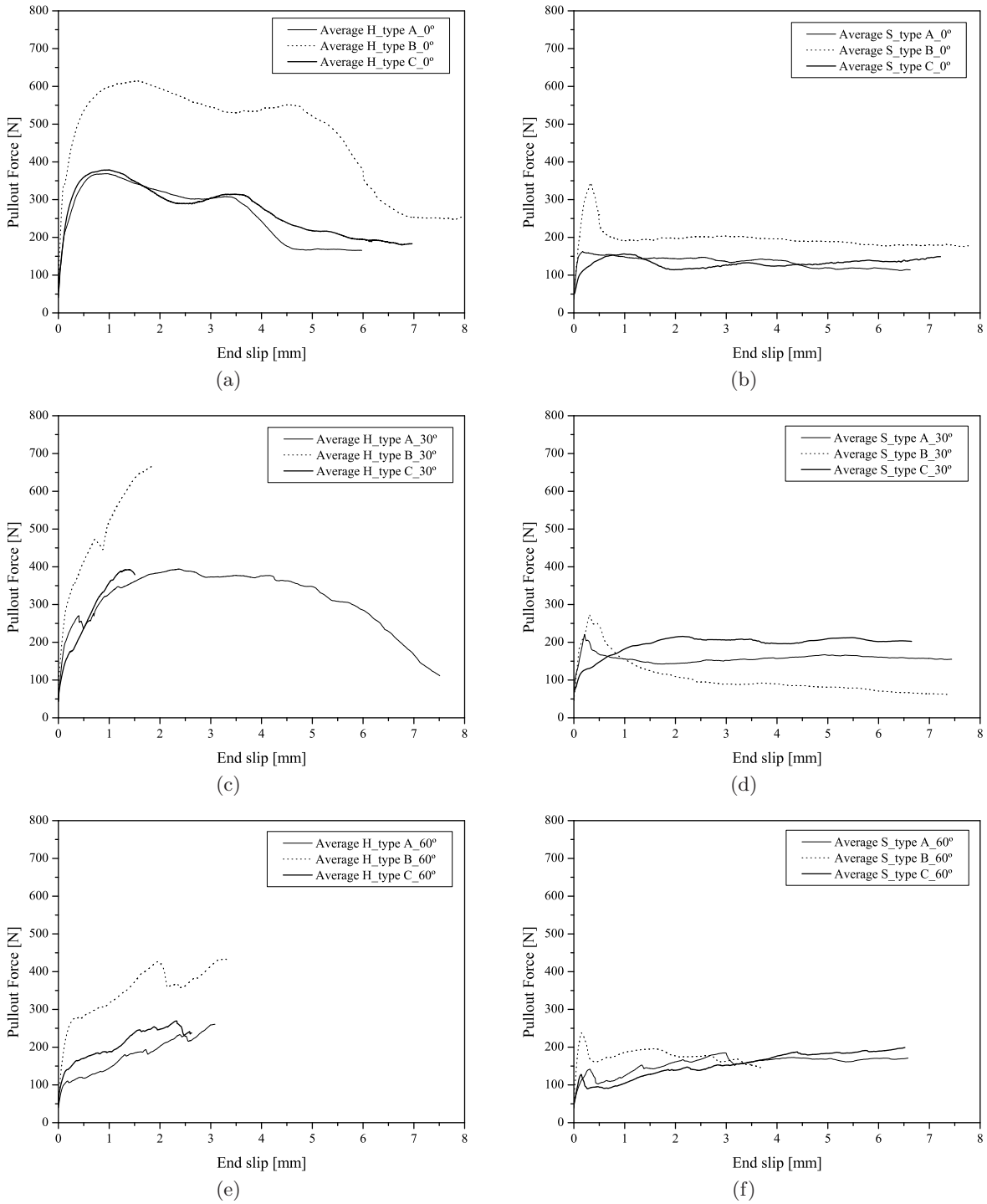

Figure 3.8: Average pullout - slip curves for a orientation angle: (a) hooked and (b) smooth with 0 degrees; (c) hooked and (d) smooth with 30 degrees, and (e) hooked (f) smooth with 60 degrees.

Discussion of the response of aligned series

As previously stated, the pullout - slip curves' shape for the three kinds of fibres are quite similar, however, there are some minor differences that are of interest to be discussed. Regarding the initial linear branch, the fibre type B has shown a stiffer behaviour when comparing to the other fibre types. Since in the elastic phase the pullout force is almost linearly dependent on the fibre specific embedded surface area, the higher is this area the larger will be the pullout force. Regarding the post-peak behaviour of the fibres type A and C, the pullout process occurs under frictional resistance at an approximately 4.5 mm slip, which corresponds to the straightened hook length of both fibres (see Table 3.5). After this slip is attained, it would be expectable that the residual pullout load for both fibre types should be almost the same, since both have the same diameter, it would be feasible to think that, consequently, they should have similar frictional resistance. However, the fibre type C presented a slightly higher residual pullout load on the frictional debonding stage. This may be related with the warping of the longitudinal axis observed in the fibre type C which may have contributed to enhance the frictional bond performance of this fibre, see Figure 3.8(a). On the other hand, as expected, in the fibre type B the pullout process occurs under frictional resistance for a higher slip, nearby the 7 mm, since for this fibres the hook length is considerably lengthier than for the other two types of fibres. It should also be noticed that for each fibre type, a high scatter was observed for the single specimen pullout response (see Annex I). If having in account the geometrical study previously performed, this was expected for both fibres type C and type B, since these fibres have high values of the coefficient of variation for their geometrical dimensions. However, this scatter was also observed in fibre type A, in spite of having revealed a considerably smaller variation on their geometrical dimensions when compared to the other two types of fibres. Moreover, the fibre type A has presented a higher scatter of their single specimens pullout responses comparatively to the type C fibres (see Annex I). Remarking that the pullout behaviour is strongly influenced by the geometrical properties of the fibre, such observation was not expected. This could be related to the concrete mixture used, having in mind that it was used a conventional concrete mixture with a low workability and that this concrete was not manufactured on a laboratory, i.e. with a restrict quality control, consequently, the high heterogeneity and voids of the mixture could favour the higher scatter and influencing the obtained results. Therefore, it can be pointed out that for both the fibres and matrix studied, the matrix heterogeneity plays a more important role on the pullout response scatter, than the observed variation of the fibre dimensions.

In what concerns to the smooth aligned fibres, fibre type B has shown a typical pullout behaviour for a smooth aligned fibre. In general, the pre-peak branch of the pullout - slip

curve of a smooth fibre, in similitude to the hooked fibres, is also made up of a linear and nonlinear part. However, for the smooth fibres the nonlinear part of the ascending branch is less pronounced than in hooked fibres, since it starts very close to the peak load. In smooth fibre type B , after the peak load is attained a sudden drop is observed, which corresponds to an abrupt increase of damage at the fibre/paste interface (unstable debond). Afterwards, fibre/paste friction is the commanding mechanism of the pullout behaviour. Comparing the average hooked and smooth curves for fibre type B , see Figures 3.8(a) and 3.8(b), it can be observed a significant higher peak pullout load and dissipated energy for the hooked series, as a result of the end hook mobilization. Moreover, in the hooked series the residual pullout load after full mobilization of the hooked end, i.e. for a slip higher than 7 mm, is slightly higher than for the smooth series, compare Figures 3.8(a) and 3.8(b). Having in mind that, when this stage is attained in the hooked fibres, the hooked end is fully straightened and the fibre is under frictional pullout as a smooth fibre after the peak load, one could be mislead to think that in this stage the residual pullout load should be the same. However, in hooked fibres the residual pullout load in frictional pullout stage is indeed higher than for the smooth fibres, since the hooked end hardly is fully straightened and will increase frictional stresses between the fibres and surrounding matrix.

On the other hand, for the smooth fibres type A and C, the pullout behaviour was quite different from the theoretical pullout behaviour of a smooth fibre, which was observed for the fibre type B, Figure 3.8(b). Besides the peak pullout load and dissipated energy differences between the fibre type B and the other two types of fibres, which would be expected regarding the distinct diameters, the main difference was in the shape of the pullout curve. In the pre-peak branch, fibre type C has shown a considerable nonlinear part, in resemblance to the hooked fibres behaviour. Moreover, for both fibres type A and C after the peak load it was not observed a sudden drop due to unstable debond.

Discussion of the response of inclined series

In the case of hooked fibres with a 30^{o} orientation angle, as previously seen, for the three fibres types, two failure modes have occurred, which was reflected into two distinct types of pullout - slip curves (see Annex I). All the fibres type A were fully pulled-out, whereas all the fibres type C failed by fibre rupture. On the other hand, for the fibre type B was observed both the abovementioned failure modes. In Figure 3.8(c), the average curve is represented up to the slip where the fibre rupture took place, therefore the curve averaging was performed only up to a slip correspondent to the peak load. The average experimental pullout curves of fibres type A and C exhibit similar peak pullout loads, however, the dissipated energy for

the fibre type A is considerably higher than for fibre type C. Hence the slight difference observed between the tensile strength of fibres type A and C (nearby 10 % higher in fibre type A) influences considerably the dissipated energy on the fibre pullout. Concerning the fibre type B, even though the average tensile strength of these fibres is similar to the fibre type C, there were some fibres of type B that were fully pulled-out (see Annex I). This was due to the higher diameter of the fibre type B, i.e. higher cross sectional area, which assured a higher bearing capacity to the fibre. However, it should be regarded that, even though the higher fibre diameter, there were some fibres that failed by fibre rupture. This could be related to the length of the hook of fibre type B, which is much higher than in the other fibres. As a consequence of the lengthier hook, a higher mobilization level of the hook mechanism is assured, since it is needed a higher pullout force to deform the hook, resulting in higher stresses concentration. Finally, it can be remarked that, a higher diameter is not an univocal condition for avoiding fibre rupture, as the hook dimensions should also be taken in account.

The pre-peak branch for the curves of hooked fibres with a 30^o angle is similar to the one observed for aligned hooked fibres, compare Figures 3.8(a) and 3.8(c). However, the nonlinear part is more pronounced than for aligned fibres, due to the cracking and spalling of the matrix at the fibre bending point, as a consequence of the additional stress concentration at this zone for inclined fibres. For some specimens, sudden load drops were observed before attaining the peak load (see Annex I), which was a consequence of matrix wedges that have spalled, after the completion of wedge each spalling off, a new more stable wedge will be formed, and the remaining fibre segment embedded in the matrix will then be pulled out. Whenever for a 30^o orientation angle the hooked fibre did not rupture, and therefore the fibre was fully pulled out, the post-peak behaviour could be assessed (see Annex I).

The post-peak curve of the hooked fibre type A with a 30^o orientation was slightly different to the one observed for the aligned series. In a first stage, for the inclined fibres, the load decay was smoother than for aligned fibres. Afterwards, an approximately slip of 4.5-5.0 mm (corresponding just about to the straightened hook length), a more pronounced load decay was observed, Figure 3.8(c). Whenever the post-peak pullout behaviour of the hooked fibre type B with a 30^o orientation could be assessed, i.e. did not exhibit a fibre rupture mode, it was observed a very high scatter (see Annex I), which may be related to both the matrix and hook dimensions heterogeneity observed for fibre type B.

On the other hand, smooth fibres with an orientation angle of 30^o revealed two distinct pre-peak behaviours. Regarding the series of fibres type A and B, the pre-peak behaviour was similar to the theoretical behaviour expected for aligned smooth fibres, Figure 3.8(d). Due to the bending mechanism associated to fibre orientation angle, it would be expected that a higher peak load would be attained than for aligned fibres. However, this was only observed

for the fibre type A. The lower peak pullout load of the fibre type B inclined fibres, may be concerned with an anomalous failure mode and, hence, obtaining biased results. Concerning the pre-peak behaviour of inclined fibre type C, and in similitude with aligned fibre type C, a significant nonlinear branch was observed, however with a higher peak pullout load, due to both the pulley effect and bending mechanism, see Figures 3.8(b) and 3.8(d).

With respect to the post-peak behaviour of smooth fibres with an orientation angle of 30°, the load decreases with the increase of slip. Comparatively to the aligned smooth fibres, the load decay is lesser abrupt, since the influence of the frictional resistance is more significant for inclined fibres. For the inclined fibres type A and C, after the peak, the residual pullout load is higher than the aligned series. On the other hand, fibre type B with a 30° orientation has a lower residual pullout load than the correspondent aligned fibres. Moreover, when comparing with fibres type A and C for the 30° orientation angle, the fibre type B also exhibited a lower residual pullout load after the peak, Figure 3.8(d), in spite of the higher embedded surface area due to a higher diameter.

A completely distinct behaviour was observed for the series with an orientation angle of 60°, Figures 3.8(e) and 3.8(f). As previously seen, the hooked series with the latter orientation angle failed by fibre rupture, with the exception of one specimen (see Annex I), whereas in the smooth series fibres were fully pulled out. As the orientation angle increases, the stresses concentration at the fibre exit point from the matrix increases, therefore the concrete matrix will be more prone to cracking and spalling. In terms of pre-peak behaviour, this will be decoded in a significant loss of stiffness. Comparing, respectively, Figures 3.8(c), 3.8(d), with Figures 3.8(e), 3.8(f), can be perceived that for the series with an 60° angle, cracking and spalling starts for a lower load level. Moreover, as a larger portion of concrete is pushed or pulled out, a larger fibre length can be more easily bent favouring the stiffness decrease up to the peak load.

3.3.5 Influence of the fibre's orientation angle

In Figure 3.9(a) is depicted the influence of the fibre's orientation angle on the peak pullout load. It was not observed a significant variation of the peak pullout load with the variation of the orientation angle. Nevertheless, in general, it was ascertained a slight increase of the peak pullout load from a 0° to a 30° orientation angle followed by a decrease for a 60° orientation angle. The only exception was the smooth series of the series of fibre type B and could be related to an eventual anomaly during testing.

For the peak pullout load of the hooked series with a 30° orientation angle, a 10% increment was observed for the fibre type A, whereas for both the other two fibres was observed a similar increment of 9%. On the other hand, regarding the smooth series, this increment for a 30° angle

was even higher. Thus, a 26% and 30% increment was computed for the fibres TYPE A and C, respectively. The differences on the peak pullout load variation from a 0° to a 30° fibres' orientation angle, between the smooth and hooked series are ascribed to the distinct pullout mechanisms mobilised for these series. For the hooked series, there is the contribution of the hooked end mechanical deformation to the overall pullout response, which is quite significant (as will be seen in the next section). Hence, the parcel due to the pulley effect (present in the inclined fibres) will be smaller, in percentage terms, for the hooked series than for the smooth series.

Concerning the series with an orientation angle of 60°, in general, and with the exception of the smooth series of the fibres TYPE B and C, it was observed a decrease on the peak pullout load ranging from 13 to 19%, from a 30° to 60° orientation angle. As the fibre orientation angle increases, the stress concentration at the fibre's exit point also increases. Since inclined fibres are subjected to a mixed tensile-bending loading state, this stress concentration will subject the fibre to a higher shear state, thus decreasing the pullout load due to premature rupture of the fibre. This aspect will be addressed in more detail in the next chapter.

The influence of the orientation angle on the slip at the peak pullout load is depicted in Figure 3.9(b). It is not observed a clear trend, this is in part due to the considerable high scatter for both the 0 and 30° orientation angle's series, in particular for the smooth fibres. However, in general, the slip at the peak pullout load was higher for the series with a 60° orientation angle. Moreover, the slip at peak load for this series revealed a smaller scatter than for the other ones. For the hooked series, in which the scatter was smaller, it is observed an increment of the slip at peak load with the orientation angle.

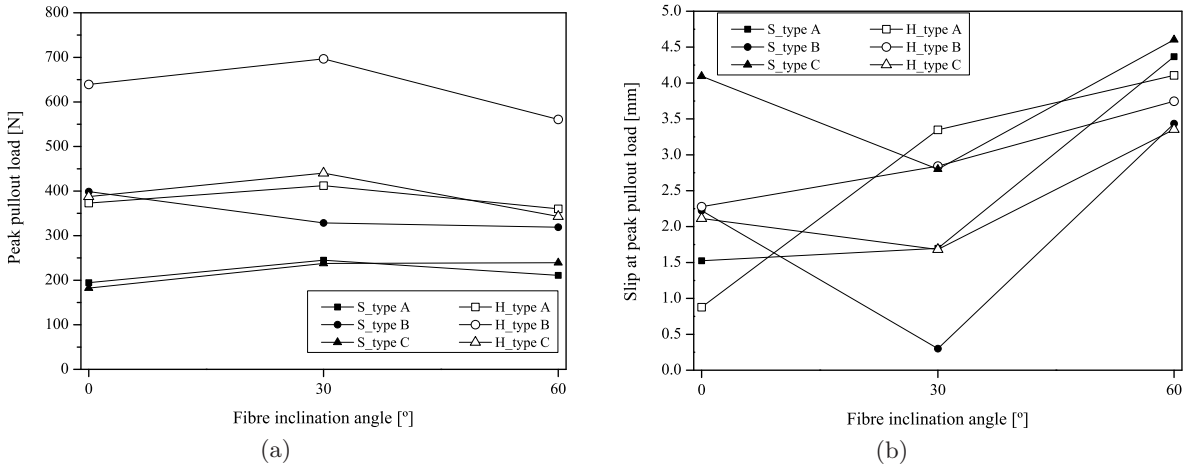

(a) (b)

Figure 3.9: Influence of the orientation on the: (a) peak pullout load, (b) slip at peak pullout load.

In Figures 3.10(a) and 3.10(b) is represented the variation of the pullout load at a slip

of 1 mm, N_{1mm}, and 3 mm, N_{3mm}, respectively, with the orientation angle. Regarding the smooth series, there was not a noteworthy observation, thus there is not a clear evidence that the fibre's orientation influences the pullout load for the latter slips. On the other hand, for the hooked series, it was ascertained a decrease on N_{1mm}, from a 0 to a 30º orientation angle, ranging between 6 to 13%. When increasing the orientation angle, i.e. from 30 to 60º, the decrease on N_{1mm} is considerably higher, and lays between 39 to 56%. Regading the variation of N_{3mm} with the orientation angle, also for the hooked series, in general there is a decrease on the latter pullout load when increasing the fibre's angle. Remark that, the exceptions of the fibres TYPE A and C series, with an orientation angle of 30º, can be justified by the observed failure modes. In fact, for this orientation, all the fibres from TYPE A were fully pulled out, whereas the totality of the fibres TYPE C failed by fibre rupture for a slip smaller than 3 mm, consequently, the average value of N_{3mm} is zero. On its turn the fibres TYPE B failed either by fibre pullout or fibre rupture.

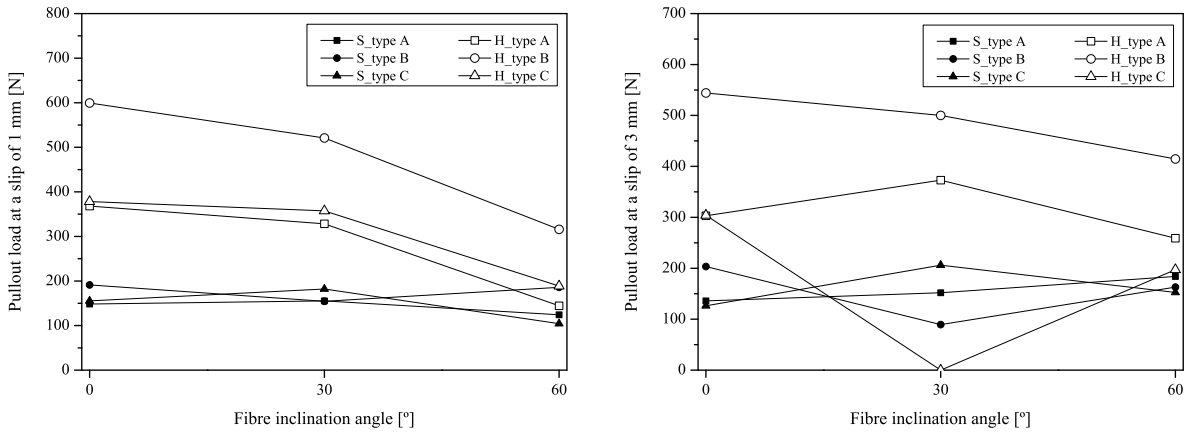

Figure 3.10: Influence of the orientation on the pullout load at a slip of: (a) 1 mm and (b) 3 mm.

In Figures 3.11(a) and 3.11(b) is depicted the influence of the fibre's orientation angle on the dissipated energy up to a slip of 1 mm, G_{1mm}, and 3 mm, G_{3mm}, respectively. In similitude to N_{1mm} and N_{3mm}, for the smooth series, there was not a noteworthy variation of G_{1mm} and G_{3mm} with the orientation angle. Regarding the variation of G_{1mm} from an orientation angle of 0º to 30º, for the hooked series, there is a decrease of nearby 20%. When increasing the angle, i.e. 60º, the observed decrease for G_{1mm} is even higher, nearby 31% for both TYPE C and TYPE B fibres and 53% for the fibres TYPE A.

In what concerns to the variation of G_{3mm} with the orientation angle for the hooked series, it can be withdraw similar conclusions to ones for the N_{3mm}. As it will be discussed in a posterior section, the value of G_{3mm} is intimately related to the N_{3mm} value. In general, G_{3mm}

decreases with the orientation angle. The only exception was the fibre type A with an angle of 30º. This slight increase was only observed for the latter series, due to the fact that this fibres were fully pulled out, in opposition to the other series in which fibre rupture occurred for slips smaller than 3 mm, thus decreasing the dissipated energy.

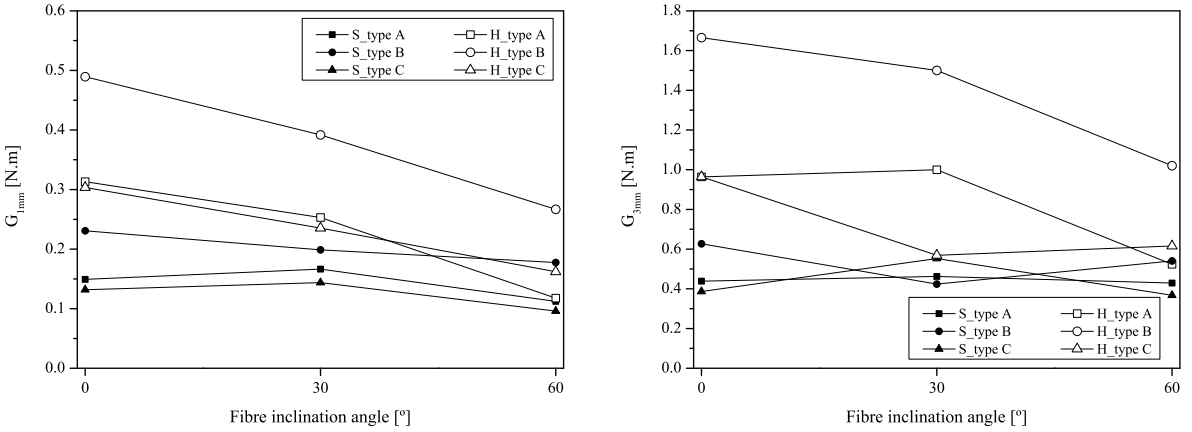

(a) (b)

Figure 3.11: Influence of the orientation on the energy absorption up to a slip of: (a) 1 mm and (b) 3 mm.

3.3.6 Influence of the fibre type

In Figure 3.12(a) is represented the influence of the fibre type on the peak pullout load. In general it was observed a higher peak pullout load for the hooked series, when comparing with the correspondent smooth series. This was expected, since afterwards the elastic bond stage is completed (common to the both fibre types), the hooked end starts to be mobilised. Thus a higher pullout load is needed for the plastification of the hooked end underwent during the fibre pullout from the matrix imprint channel. The increase on the peak pullout load for the hooked series, depending on the fibre's orientation angle, ranges between $[68-92\%]$, $[60-112\%]$ and $[43-113\%]$ for the fibres type A, B and C, respectively.

If analysing exclusively the smooth series, for the fibre type B, which has the highest diameter (≈ 1 mm), comparatively to the other two types of fibres with an announced diameter of 0.75 mm, the peak pullout load increased in between 38 to 105%, depending on the correspondent orientation angle, being the increase of the fibre diameter responsible for this trend. If a similar reasoning is assumed for the hooked series, the increase of the peak pullout load for the fibre type B ranges between 61 and 71%. Regarding the hooked series, besides the latter fibres' higher diameter, this fibre type has also a lengthier hooked end. Thus, it would

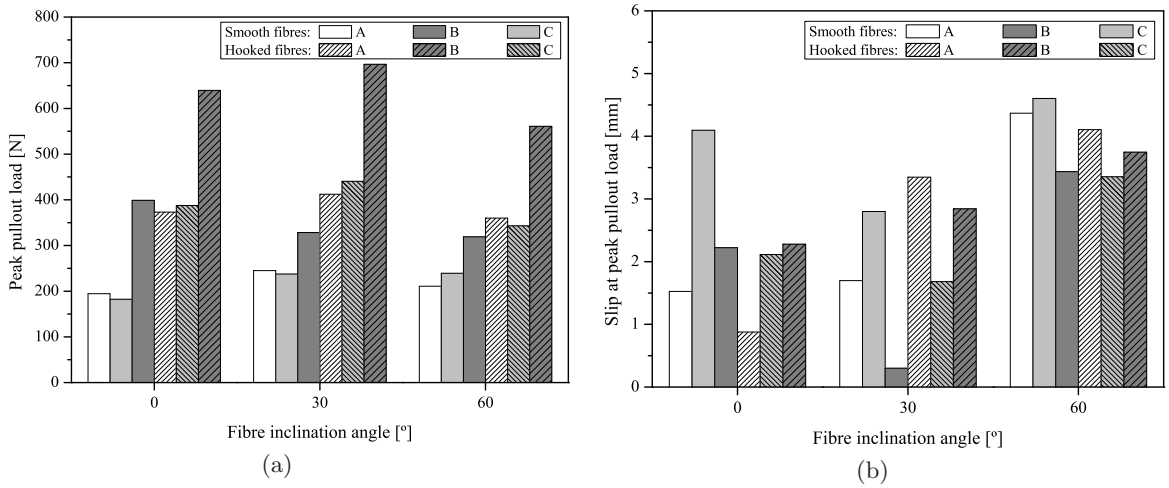

Figure 3.12: Influence of the fibre type on the: (a) peak pullout load, (b) slip at peak pullout load.

be expectable a higher increase on the peak pullout load when using the fibre TYPE B.

The fibre type did not influence clearly the slip at peak pullout load, see Figure 3.12(b). The absence of a clear trend for the slip at peak load maybe, in part, justified by the high scatter of the individual pullout responses (see Annex I). If having in mind the theoretical pullout response of both smooth and hooked fibres (as shown in Chapter 2), this lack of trend was also not expected.

In Figures 3.13(a) and 3.13(b) is represented the influence of the fibre type on the pullout load at a slip of 1 mm, N_{1mm}, and 3 mm, N_{3mm}, respectively. The pullout load N_{1mm} for the fibre TYPE B with hooked ends was approximately 54 to 63% higher than for the other hooked series with the lowest diameter. The pullout load N_{1mm} for the smooth fibre TYPE B was approximately 18 to 59% higher than the smooth fibres TYPE A and C series. When comparing hooked and smooth series from the same brand, the difference on N_{1mm} value between those fibres is quite high. The only exception was the series of fibre TYPE A with an orientation angle of 60º, in which the increase for the hooked fibres of the N_{1mm} value was only 6%. For the orientation angles of 0 and 30º, the hooked series shown an increase on N_{1mm} of [111-149%], [186-205%] and [132-143%] for the series of fibres TYPE A, B and C, respectively.

In what concerns the variation of N_{3mm} with the fibre type, it can be pointed out similar conclusions to the ones for the N_{1mm}. Since for the TYPE C fibres occurred fibre rupture for a slip within 1 and 3 mm, the previous remarks are not applicable to this series, since N_{3mm} is null.

In Figures 3.14(a) and 3.14(b) are depicted the influence of the fibre type on the variation of the energy dissipated up to a slip of 1 mm, G_{1mm}, and 3 mm, G_{3mm}, respectively. Regarding G_{1mm}, the conclusions that can be withdraw are very similar to those discussed for the N_{1mm},

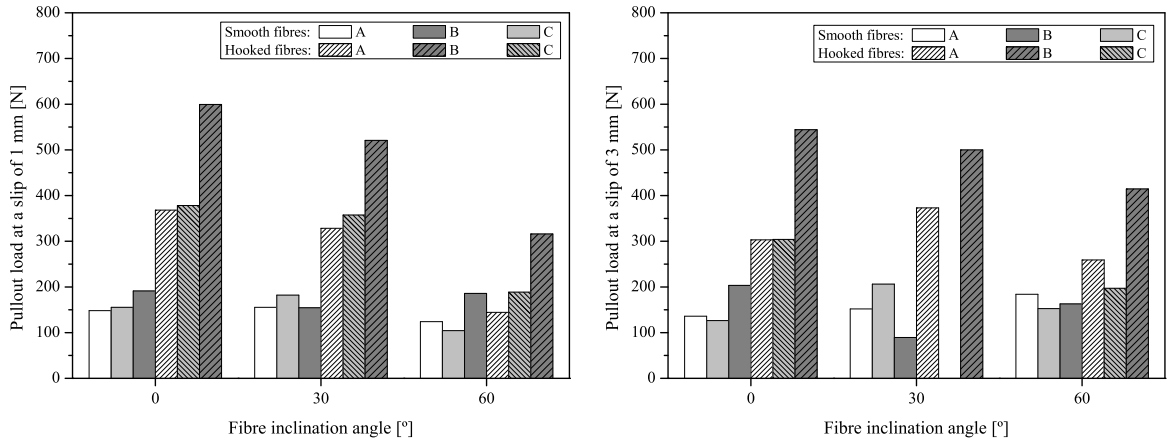

Figure 3.13: Influence of the fibre type on the pullout load at a slip of: (a) 1 mm and (b) 3 mm.

when comparing Figure 3.14(a) with Figure 3.13(a). As it will be seen in the next section, the relationship between these two parameters is quite high.

On the other hand, the influence of the fibre type on G_{3mm} is somehow distinct, depending on the orientation angle. For the slip at which this dissipated energy is computed, some specimens have failed prematurely (by e.g. fibre rupture or matrix spalling) turning a clear analysis more difficult. In a general fashion, the dissipated energy G_{3mm} increased for the fibre series with hooked ends and for the series with the highest diameter (i.e. fibre TYPE B series). For the hooked fibre TYPE B the increase on G_{3mm} ranged between 51 to 94% if comparing with the correspondent fibre TYPE A series. Since for the hooked TYPE C series was observed fibre rupture for the totality of the specimens with a 30º orientation, comparatively to the referred fibres, the increase of the G_{3mm} for the fibre TYPE B can go up to 163%.

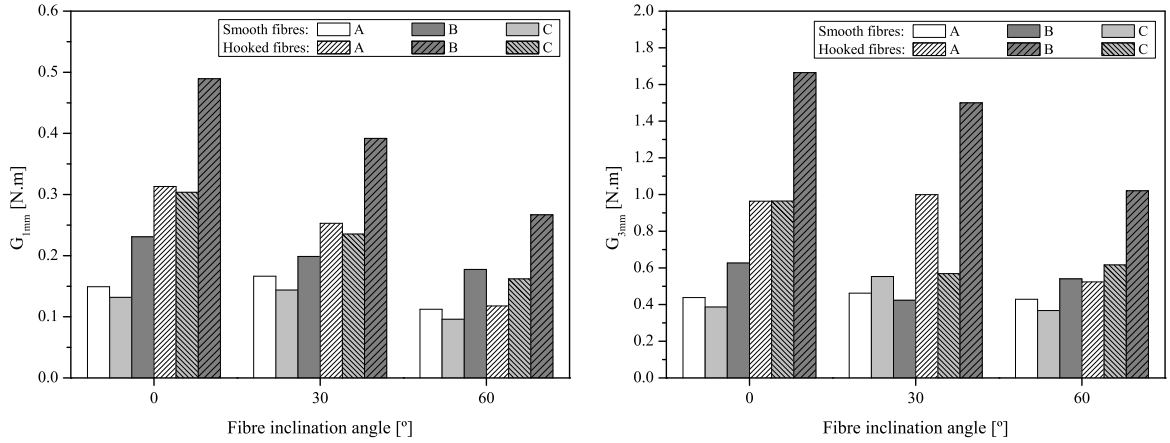

Figure 3.14: Influence of the fibre type on the dissipated energy up to a slip of: (a) 1 mm and (b) 3 mm.

3.3.7 Relationships between fibre's micro-mechanical parameters

In this section it will be presented and discussed several plots between distinct fibre's micro-mechanical parameters. It is not intended to find any type of empirical/semi-analytical relationships between those parameters, but to render a more clear insight on the interaction of the distinct parameters that in some extent partially characterize the pullout response.

In Figures 3.15(a) and 3.15(b) is comprised the relationship between the peak pullout load, N_{max}, and the pullout load N_{1mm} and N_{3mm}, respectively. For both relationships, it is visible a clear linear trend between N_{max} and both N_{1mm} and N_{3mm}, nevertheless the scatter for these relationships being quite high. In general N_{1mm} and N_{3mm} increase with N_{max}, the only exceptions were observed for N_{3mm} regarding the fibres that failed by fibre rupture.

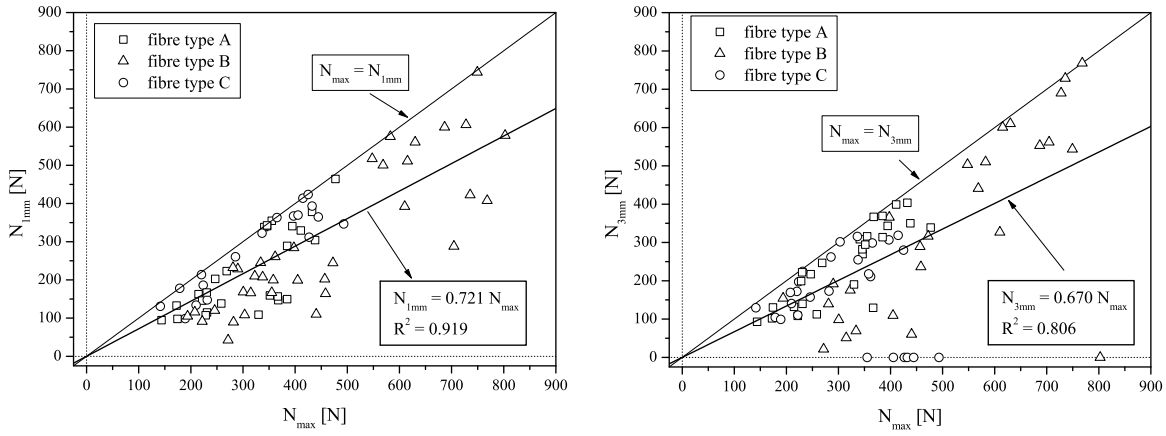

Figure 3.15: Relationship between peak pullout load and pullout load at a slip of: (a) 1 mm and (b) 3 mm.

In Figures 3.16(a) and 3.16(b) is depicted the relationship between the peak pullout load, N_{max}, and the dissipated energy up to a slip of 1 mm, G_{1mm}, and 3 mm, G_{3mm}, respectively. A clear linear trend is observed for both relationships, where a relatively small scatter can be pointed out for the relation between N_{max} and G_{1mm}.

If the dissipated energy up to a certain slip is correlated with the pullout load correspondent to the same slip, e.g. $N_{1mm} - G_{1mm}$, the scatter previously observed will be significantly reduced, compare Figures 3.16(c) and 3.16(d), with Figures 3.16(a) and 3.16(b), respectively. As an illustration, for the $N_{1mm} - G_{1mm}$ relationship, if a linear-fitting of the data is performed, a correlation factor $R^2 = 0.97$ is obtained, which emphasizes the good agreement between these two parameters. The lowest scatter observed for the $N_{1mm} - G_{1mm}$ relationship, comparatively to the one of $N_{3mm} - G_{3mm}$, can be justified by the pullout process being in its initial stage.

Notice that, as the slip increases the distinct pullout mechanisms will be further mobilized in different ways, and additionally distinct failure modes will be observed. Moreover, this will be enhanced by two aspects, namely: the concrete matrix heterogeneity; the abovementioned plots comprise data from distinct fibres types and orientation angles.

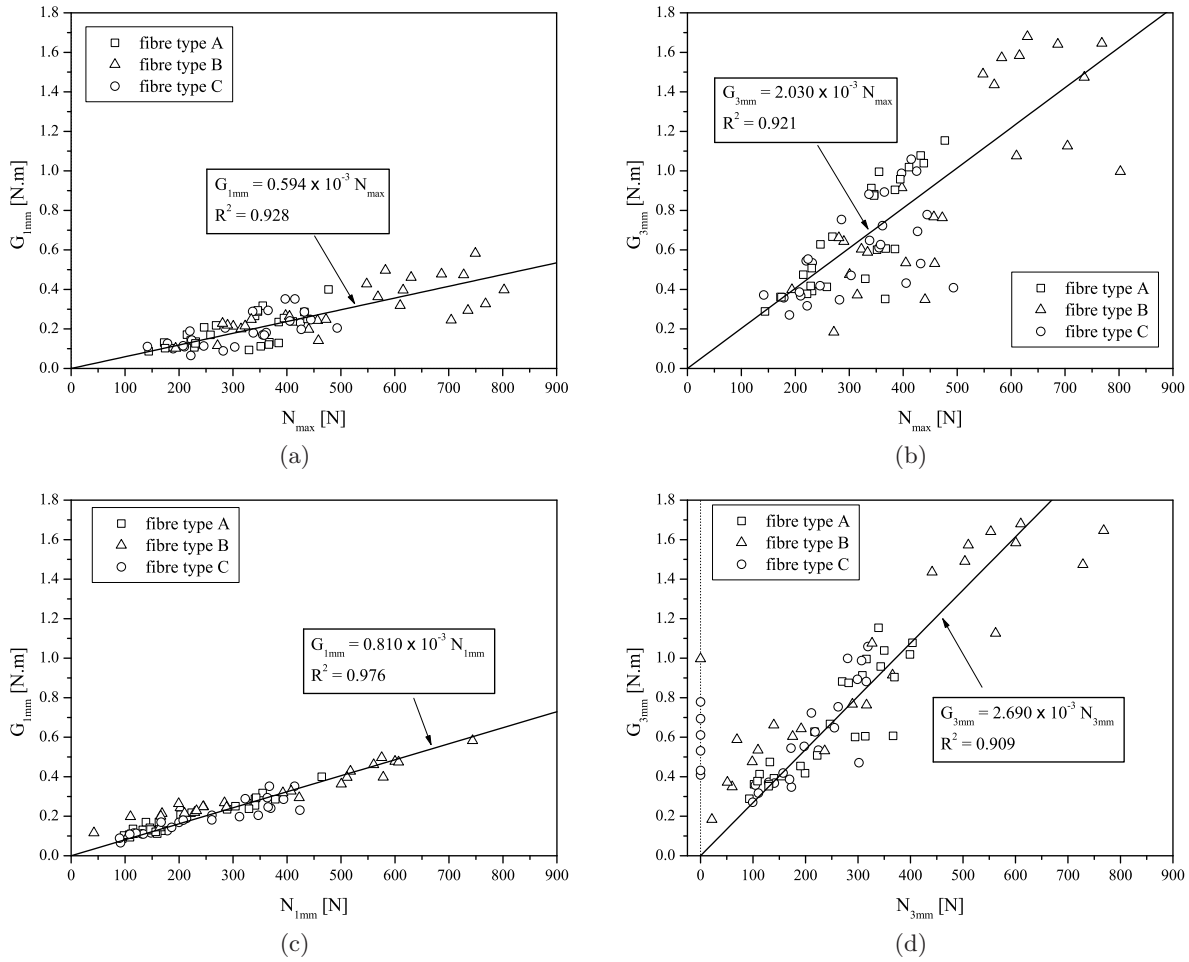

Figure 3.16: (a), (b) Relationship between N_{max} and the dissipated energy G_{1mm} and G_{3mm}, respectively; (c) Relationship between N_{1mm} and G_{1mm}, (d) Relationship between N_{3mm} and G_{3mm}.

3.4 Conclusions

In the present chapter was carried out a comparative analysis between three types of hooked end steel fibres, designated by fibres TYPE A, B and C. For this purpose the fibre geometry dimensions were checked out and the mechanical properties were assessed, namely, the fibre tensile strength and fibre/matrix bond strength. Additionally, it was also checked out if the fibres complied with the ASTM A820-90 (1990) requisites for their use in fibre reinforced concrete.

3.4.1 Fibre quality control and pullout performance

Regarding the obtained results, as it was expected, the fibre types studied were in conformity with the ASTM A820-90 (1990). In what concerns to performed geometry dimensions control, respectively, mass, diameter and length, the fibre TYPE A presented a significantly lower variation of the referred dimensions than the other two types of fibres. Moreover, due to the commercialization method of the fibres TYPE B and C, these showed up a slight warping along their longitudinal axis, being this more relevant for the fibre TYPE C, since the latter fibre has a smaller diameter and consequently, has a smaller flexural stiffness. On the other hand, the fibre TYPE A did not show this so called warping, probably, due to their commercialization method, since they are glued in bundles, they have a considerably higher flexural stiffness during its transportation and packaging.

The fibre tensile strength was similar for the three fibre types, nevertheless TYPE A of fibres presented a tensile strength, approximately, 10% higher than the other fibres.

Regarding the pullout performance, the fibres TYPE A and C, for a 0^o orientation angle, revealed similar performance, as it was expected, since they are both very similar from the geometrical point of view. However the pullout performance of fibre TYPE A showed up a considerable higher scatter, when comparing to the fibre TYPE C, which would not be expected if having in consideration the geometry control previously carried out. A possible and feasible explanation may be related to the fact that, the concrete used in this study was a conventional construction concrete with a low workability. Consequently, this will favour a higher void ratio and a higher matrix heterogeneity, which may have influenced slightly these results.

When comparing the pullout performance of those two types of fibres, for an orientation angle of 30^o, the dissipated energy for the fibre TYPE A is considerable higher than for the fibre TYPE C, in spite of the maximum pullout load being quite similar. This difference is ascribed to the distinct failure modes observed for each brand, i.e. fibre pullout for fibre TYPE A and fibre rupture for fibre TYPE C. Hence, the slight difference observed between the tensile strength of fibres TYPE A and C (nearby 10% higher in fibre TYPE A) influences considerably the dissipated energy during the pullout process.

The pullout response of the fibres with a higher diameter and hook length (fibre TYPE B) has shown, in general, a significantly higher pullout load and dissipated energy, when comparing with the other two brands of smaller diameter.

3.4.2 Adopted fibre brand for SFRSCC

The fibre to be used in steel fibre reinforced self-compacting concrete was selected based on the pullout performance of each fibre brand. The two types of fibres with similar geometry,

in general, they exhibited a very similar behaviour. However, the pullout response of the fibre type A was considerably better for an orientation angle of 30º. Thus, and apart economical aspects, intuitively this fibre is chosen in detriment of the fibre type C. This option is also supported in the fact that, the average fibre's orientation angle with regard to an active crack will be nearby the 30º. This will be addressed further ahead, on the discussion of the composite's fibre distribution.

On the other hand, opting from the fibres type A and B is not a so straightforward task, since these fibres have distinct geometry dimensions. Hence, if the same volumetric fibre content is used, the theoretical number of fibres expected to intersect an active crack will be distinct. Assuming a 3D isotropic uniform random distribution of the fibres, it can be computed the fibre density expected to intersect a certain plane. Adopting the latter 3D distribution and the correspondent fibres geometries, it is expected that for the fibre type A there will be approximately 78% more fibres intersecting a certain plane. In table 3.8 is presented the obtained increment, in percentage terms, on the studied micro-mechanical parameters, when using the fibre type B hooked fibres instead of the fibre type A. Here, it will not be detailed the adopted methodology, since it will be addressed and detailed in Chapter 6.

Table 3.8: Increment on the micro-mechanical parameters, when using the fibre type B.

Angle	N_{max}	N_{1mm}	N_{3mm}	G_{1mm}	G_{3mm}
0º	71%	63%	79%	57%	73%
30º	68%	58%	34%	55%	50%
60º	56%	119%	60%	124%	94%

From the analysis of the previous table, and thinking in averaging terms, in general, the increments observed on the micro-mechanical parameters properties for a single type B fibre are smaller than the increment on the fibre density for the fibre type A ($\approx$ 78%). Thus, probably, the overall mechanical behaviour of a composite reinforced with fibre type A will be better than other composite reinforced with fibre type B. For these reasons, the fibre type A was used in the composition of the steel fibre reinforced self-compacting concrete.

Please, have in mind that, in spite the composite overall mechanical behaviour can be regarded as the sum of the individual fibre micro-mechanical contribution; due to the panoply of the involved fibre reinforcement mechanisms, complexity and their interaction (group effect), the previous assumption may not be entirely accurate and will be less true as the fibre volumetric content increases.

Chapter 4

Pullout from a SFRSCC Medium Experimental Results

4.1 Scope of tested parameters

The main scope of this chapter is to access the fibre pullout bond - slip behaviour on a steel fibre reinforced self-compacting concrete medium, SFRSCC. In opposition to conventional concrete matrices, such as the one used in the previous chapter, these matrices are rather innovative, since for attaining self-compactibility they have to fulfil high demands with regard to filling and passing ability, as well as segregation resistance. In order to accomplish these requirements, it should be used high percentage of fine materials, low water/binder ratios, technological advanced admixtures, and considerable high amounts of cement and fine additions. In steel fibre reinforced cement composites, the interface between fibre and cement paste is the weak link of its micro-structure. Therefore, study of the interfacial behaviour is important for understanding the mechanical behaviour of such composites.

The pullout tests presented here may be divided into two main groups, according to the type of fibres used: hooked and smooth. The benefits of the fibres mechanically deformed (e.g. hooked end), when compared with a smooth fibre, on the peak pullout load and pullout energy are well documented. In spite of that, in the present work smooth fibres were tested, with the main purpose of isolating the adherence bond from the mechanical bond provided by the hook. This makes it possible the separate assessment of the influence of the various mechanisms of bond. Furthermore it allows to develop rational analytical models to describe bond in fibre reinforced cement-based composites, e.g. SFRSCC. Within these two main groups

it was assessed the influence on the pullout response of the fibre embedment length and fibre orientation. In all performed tests it was used a hooked end steel fibre of TYPE A with a length (l_f) of 60 mm, a 0.75 mm diameter (d_f), an aspect ratio (l_f/d_f) of 80 and a yield stress of 1100 MPa. In order to perform the smooth fibre tests, the hook of the fibres were cut with a pliers.

Code names were given to the tests series, which consist on alphanumeric characters separated by underscore. The first character indicates the fibre type (S - smooth; H - hooked), the second string indicates the embedded length in mm (for instance, lb10 represents a fibre with an embedded length of 10 mm) and finally the last numeral indicates the fibre inclination angle, in degrees, with the fibre pullout force orientation. The complete overview of all the fibre pullout tests performed, with reference to their type, aspect ratio, embedded length (l_b) and inclination angle, is given in Table 4.1.

Table 4.1: Overview of the performed pullout tests.

SERIES	Fibre type	l_b [mm]	Angle [°]	N. Specimens
S_lb10_0	Smooth	10	0	3
S_lb10_30			30	3
S_lb10_60			60	3
S_lb20_0		20	0	3
S_lb20_30			30	3
S_lb20_60			60	3
S_lb30_0		30	0	3
S_lb30_30			30	3
S_lb30_60			60	3
H_lb10_0	Hooked	10	0	6
H_lb10_30			30	6
H_lb10_60			60	6
H_lb20_0		20	0	6
H_lb20_30			30	6
H_lb20_60			60	6
H_lb30_0		30	0	6
H_lb30_30			30	6
H_lb30_60			60	6

4.2 Concrete mixture, test specimens and test set-up

The materials used in the composition of the steel fiber reinforced self-compacting concrete, SFRSCC, were: cement (C) CEM I 42.5R, limestone filler (LF), superplasticizer (SP) of third

generation based on polycarboxilates (Glenium 77SCC), water (W), three types of aggregates fine river sand (Fs), coarse river sand (Cs) and crushed granite 5-12 mm (Ca) and type A hooked end steel fibres.

The method used to define the composition of the SFRSCC and the mixing procedure is described in Chapter 7. Regarding the properties of the SFRSCC in the fresh state, it was observed a spread of the fresh concrete over 700 mm, when testing with the Abrahm's cone in an inverted position, i.e. the concrete flowing throughout the smaller orifice. Table 4.2 includes the composition that has best fitted self-compacting requirements for the adopted fibre content, (Cf). Remark that, in Table 4.2, Ws is the water necessary to saturate the aggregates and W/C is the water/cement ratio. The Ws parcel was not used to compute the W/C ratio, on the other hand to compute the latter ratio was considered the water parcel from the superplasticizer.

Table 4.2: Composition for 1 m^3 of SFRSCC.

Cf [kg]	Paste/Total volume [%]	Cement [kg]	Lf [kg]	Water [dm^3]	Ws [dm^3]	Sp [dm^3]	Fs [kg]	Cs [kg]	Ca [kg]	W/C [-]
30	0.34	359.4	312.2	96.9	64.7	6.9	108.2	709.4	665.2	0.29

The pullout specimen's dimensions and geometry used for SFRSCC were identical to the one used for the conventional concrete, view previous chapter. After casting, the concrete slab was cured at a temperature of 20°C and a relative humidity of about 95%. After 30 days, the concrete was demoulded, and cylindrical specimens containing each one single fibre were drilled out from the slab. The fibre pullout tests were performed at approximately 180 days according the procedure described in Chapter 3. The concrete's compressive strength was assessed by three cubic specimens with an edge length of 150 mm. The average value of the concrete compressive strength, at the testing age, was 83.4 MPa with a coefficient of variation of 0.9%. Moreover, six single fibres were tested under direct tension in order to assess the fibre tensile strength. The average value of the fibre tensile strength was 1141 MPa with a coefficient of variation of 2.0%. Notice that, this tensile strength was nearby 10% smaller than the one for the same fibre type used in the pullout study carried out for conventional SFRC, view Table 3.6.

4.3 Pullout test results

4.3.1 Failure modes

The failure modes observed during the fibre pullout tests from the self-compacting concrete were identical to the ones observed for conventional concrete, see section 3.3.3. However, there

is a noteworthy difference. Whenever matrix spalling has occurred, in both conventional and self-compacting concrete, the volume of the concrete parcel which is detached during spalling is smaller for self-compacting concrete. This is due to both the higher strength and stiffness of the self-compacting concrete.

The totality of both hooked and smooth aligned fibres were completely pulled out, see Figure 3.7(a). In the case of hooked fibres, after debonding of the fibre - matrix interface, the hooked was fully straightened. This failure is designated as FM1. The cross section striction at the end of the hook curvatures produced by the straightening of the hook is depicted in Figure 4.1. A similar failure mode, FM2, was observed for some inclined fibres, however in opposite to aligned fibres, spalling of the matrix at the fibre bending point was observed, Figure 3.7(b). Nevertheless, the most common failure mode observed during the pullout tests of inclined hooked fibres was fibre rupture, FM3, see Figure 3.7(c). Another observed failure mode, FM4 was by matrix spalling, which is depicted in Figure 3.7(d). In this case the fibre is almost fully pulled out of the concrete specimen, however, when the embedded end of the fibre approaches the exit point of the concrete matrix it detaches a portion of concrete near the fibre bending point. This failure mode was only observed for a few fibres with an inclination angle of 60° and an embedded length of 10 mm. The pullout specimens where the conditions of premature fibre or matrix failure were observed, occurred exclusively for inclined fibres. Moreover, fibre rupture was the predominant failure mode for a 30° inclination angle, whereas matrix failure was detected for an angle of 60° and lower embedded lengths. Similar finds were observed for hooked fibres pulled out from a high strength matrix by Banthia and Trottier (1994).

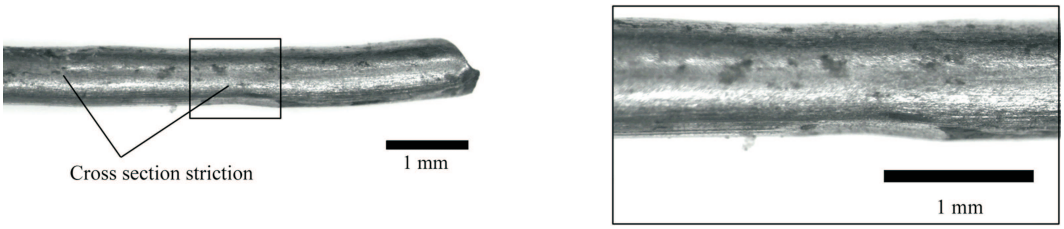

Figure 4.1: Cross section striction at the hooked end.

In Table 4.3 are indicated the failure modes observed for each series. When more than one failure mode occurred for a specific series, the number of specimens corresponding to each failure type was indicated between parenthesis. Due to technical problems, the series S_lb10_0 and S_lb10_30 could not be correctly tested, therefore they are not presented.

The fibre rupture observed for hooked inclined fibres is a result of both a strong and compact

concrete matrix, and a good fibre anchoring in it. The fibre rupture stresses observed for inclined fibres were smaller than the fibre tensile strength (1141 MPa). As already mentioned, this tensile strength was nearby 10% smaller than the one for the type A fibres used in the pullout study carried out for conventional concrete, nevertheless was slightly higher than the nominal tensile strength of 1100 MPa announced by the manufacturer. This may, quite surely, be responsible of fibre rupture being the primarily failure mode for hooked end fibres with an inclination angle of 30º in SFRSCC, in contrast to the observed for conventional concrete. However, have in mind that, the compressive strength and compactness of the self-compacting matrix is higher than for the studied conventional concrete. This could also have favoured the fibre rupture.

Table 4.3: Failure modes observed during the pullout tests on self-compacting concrete.

Smooth series	Failure mode	Hooked series	Failure mode
S_lb10_0	-	H_lb10_0	Fm1
S_lb10_30	-	H_lb10_30	Fm2(2); Fm3(4)
S_lb10_60	Fm4	H_lb10_60	Fm3(5); Fm4(1)
S_lb20_0	Fm1	H_lb20_0	Fm1
S_lb20_30	Fm2	H_lb20_30	Fm2(2); Fm3(4)
S_lb20_60	Fm2	H_lb20_60	Fm3
S_lb30_0	Fm1	H_lb30_0	Fm1
S_lb30_30	Fm2	H_lb30_30	Fm3
S_lb30_60	Fm2	H_lb30_60	Fm3

The average value of the fibre rupture stress for a 30º inclination angle was about 865 MPa, whereas for a 60º angle this value was 736 MPa. This can be explained by the fact that the fibre is submitted to a mixed tensile - bending mode. The fibre rupture for lower stresses than the direct tensile stress is a result of the stress concentrations present in the bent part of the fibre. The strength capacity under composed bending is governed by an interaction diagram between the normal tensile force and the flexure moment. As the bending moment increases, the tensile force corresponding to the ultimate capacity envelope of a section subjected to composed bending must decrease. Moreover, as the inclination angle increases, the bending moment will increase resulting therefore in a decrease of the tensile rupture stress. From an atomic level point of view, the additional shear stresses imposed on the fibres at the matrix exit, favour the intercrystal slippage within the crystal system in steel, hence lowering both the yield and ultimate strength of the material (Banthia and Trottier 1994).

4.3.2 Pullout load - slip curves

In Figure 4.2 are depicted the average pullout load - slip curves for the tested series. The pullout curve for each single specimen can be found in Annex II. Comparing the individual fibre pullout responses with those obtained from a conventional concrete medium, it is observed a significant smaller scatter on the micro-mechanical behaviour of fibres pulled-out from a self-compacting concrete (see Annexes I and II). This may be ascribed to both the lower heterogeneity and higher stiffness of the self-compacting concrete matrix.

In general, for both hooked and smooth aligned fibres analysed, the configuration of the pullout load - slip curve was similar, regardless the fibre embedded length but, as expected, the peak load and the dissipated energy increased with it, see Figures 4.2(a) and 4.2(b). The vertical offset distance between curves can be regarded as the fibre embedded length contribution to the bond increment or decrement. The pre-peak branch of these pullout - slip curves for both hooked and smooth fibres is made up of a linear and nonlinear part. The first one is associated with the elastic bonding, whereas the nonlinear part starts with the micro-cracking of the interface, corresponding to the debonding process. The non-linear part of the ascending branch is more pronounced in hooked fibres. The lost of stiffness associated to the pre-peak nonlinear branch could be due to the irrecoverable deformation component of the fibre and the surround paste at the zone of the end hook, when this part of the fibre starts being straightened. On the other hand, for smooth fibres the nonlinear part of the ascending branch has a relative small amplitude, since starts very close to the peak load. In smooth fibres, after the peak load is attained a sudden drop is observed, which corresponds to an abrupt increase of damage at the fibre/paste interface (unstable debond). Afterwards, fibre - paste friction is the commanding mechanism of the pullout behaviour. In this part of the post-peak branch, the load decreases with the increase of slip, since the available frictional area decreases, as well as the roughness of the failure surface. On the other hand, the post-peak load decay in hooked fibres was not so abrupt than in smooth fibres, since with the increase of the slip the fibre mechanical anchorage starts to become progressively mobilised. At an approximately 4.5 mm slip (corresponding approximately to the straightened hook length), the pullout process occurs under frictional resistance in similitude to smooth fibres.

In the case of hooked fibres with a 30º inclination angle, as previously seen, occurred two failure modes, which will reflect into two distinct types of pullout - slip curves (see Annex II). In Figure 4.2(c), the average curve is represented up to the slip where the fibre rupture took place, therefore the curve averaging was performed only up to a slip correspondent to the peak load. The pre-peak branch of these curves is similar to the one observed for aligned hooked fibres. However, the nonlinear part is more pronounced than for aligned fibres, due to the cracking

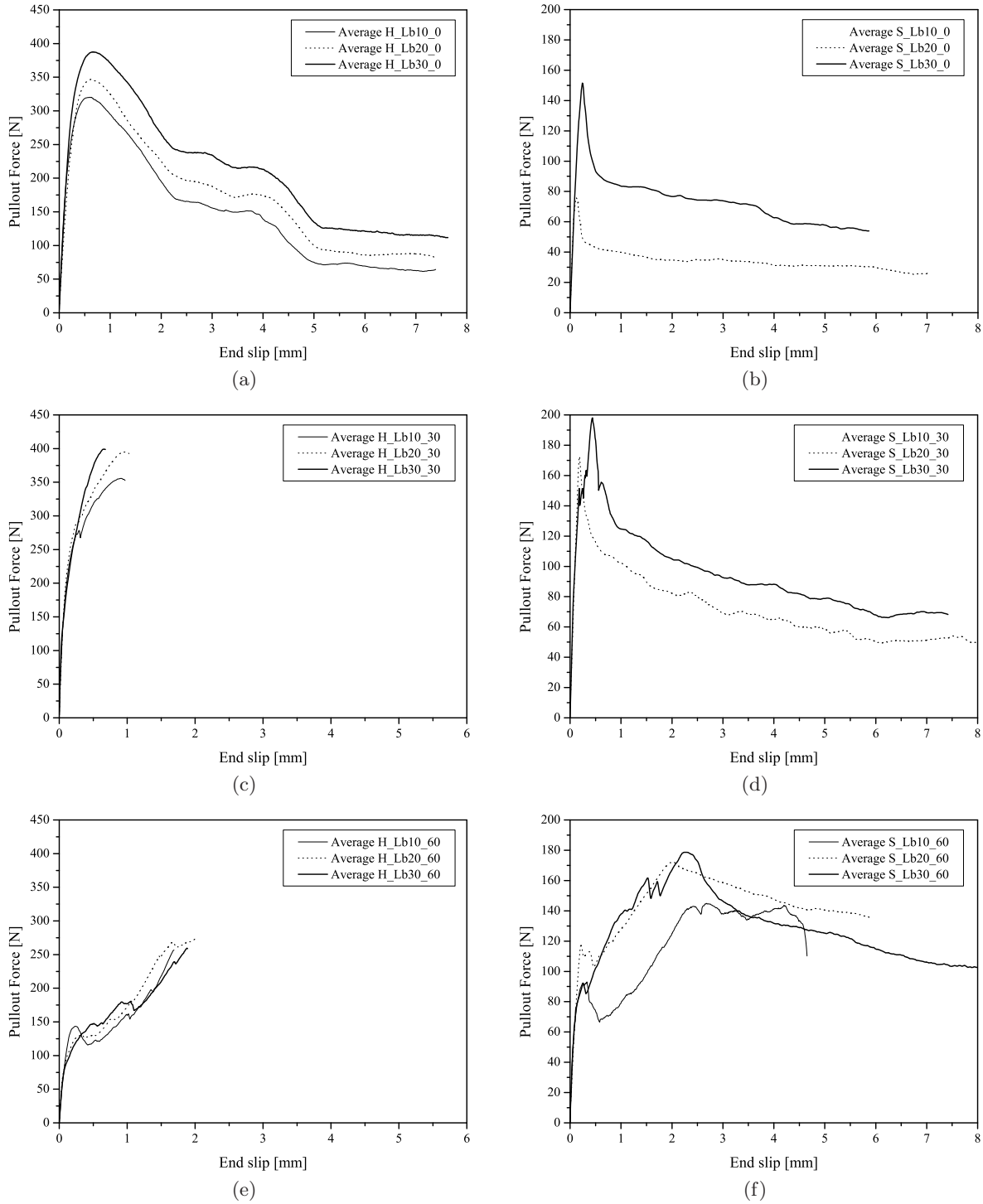

Figure 4.2: Average pullout load - slip curves for a fibre inclination angle: (a), (b) 0 degrees; (c), (d) 30 degrees, and (d),(f) 60 degrees.

and spalling of the matrix at the fibre bending point, as a consequence of the additional stress concentration at this zone for inclined fibres. For some specimens, sudden load drops were observed before attaining the peak load (see Annex II), which was a consequence of the spalling of the matrix wedges. After each completion of wedge spalling off, a new more stable wedge is formed, and the remaining fibre segment embedded in the matrix is then pulled out. Whenever for a 30^o inclination angle the hooked fibre did not break, and therefore the fibre was fully pulled out, the post-peak behaviour was assessed (see Annex II). The post-peak curve of the latter specimens was similar to the observed for aligned series, however, an increment of the residual force was perceived up to a slip of 4 mm. This was more easily noticeable for the hooked fibres with an 20 mm embedded length. Such difference is ascribed to the frictional resistance increase due to the force component perpendicular to the fibre axis. Afterwards, at slip of about 4.5 mm (corresponding approximately to the straightened hook length), a significant load decay was observed. For higher slips, only for the fibres with a 20 mm embedded length was seen an increase of the frictional resistance.

On the other hand, smooth fibres with an inclination angle of 30^o revealed two distinct pre-peak behaviours. Regarding the series with an embedded length of 20 mm, the pre-peak behaviour was identical to the one observed for the aligned smooth fibres, with the exception that a higher peak load was attained, as a consequence of the bending mechanism associated to fibre inclination angle. For a larger embedded length (30 mm), before reaching the peak load it is observed a decrease of the stiffness subordinated to several load decays corresponding to the cracking or spalling of the concrete matrix, see Figure 4.2(d). With respect to the post-peak behaviour, the load decreases with the increase of slip. Comparatively to the aligned smooth fibres, the load decay is lesser abrupt, since the influence of the frictional resistance is more significant for inclined fibres.

A completely distinct behaviour was observed for the series with an inclination angle of 60^o, view Figures 4.2(e) and 4.2(f). As previously seen, the hooked series with the latter inclination angle failed by fibre rupture, with the exception of one specimen (see Annex II), whereas the smooth series fibres were fully pulled out. As the inclination angle increases, the stresses concentration at the fibre exit point from the matrix increases, therefore the concrete matrix will be more prone to cracking and spalling. In terms of pre-peak behaviour, this is decoded in a significant loss of stiffness. Comparing Figures 4.2(c), 4.2(d) and Figures 4.2(e), 4.2(f), respectively, it can be perceived that for the series with an 60^o angle, cracking and spalling starts for a lower load level. Moreover, as a larger portion of concrete is pushed or pulled out, a larger fibre length can be more easily bent favouring the stiffness decrease up to the peak load. Regarding the post-peak in smooth fibres a gradual load decay was observed, in opposite to smooth fibres aligned and with a 30^o angle, since for a 60^o inclination angle the

frictional resistance due to the force component perpendicular to the fibre axis is much higher. Another interesting point was that the post-peak load decay for a 60º inclination angle was more significant for higher embedded lengths. For the S_lb10_60 series a plateau is observed after the peak load is attained, which abruptly finishes with the matrix spalling, without the fibre being completely pulled out.

4.3.3 Influence of the embedded length

The influence of the embedded length, L_b, on the maximum pullout load, N_{max}, is represented in Figure 4.3(a). In general, the N_{max} increased linearly with the embedded length for both hooked and smooth fibres. The series H_lb_60 was the only exception, since it was observed a decrease on the N_{max} for a 20 mm embedment length. In the case of aligned fibres the influence of L_b was more significant on the smooth fibres, since an increase of more than 100% on N_{max} occurred, increasing L_b from 20 to 30 mm, while relatively small increments were registered for the hooked end fibres. In fact, for hooked fibres the increment of L_b from 10 to 30 mm provided an increase in the N_{max} of about 20%. These results demonstrate that the pullout response of hooked fibres at given embedment length is predominantly influenced by the mobilisation and straightening of the hook, which is in accordance with published findings (Naaman and Najm 1991, Robins et al. 2002). For inclined smooth fibres, in resemblance to the aligned hooked fibres, the N_{max} increase with L_b was also relatively small, 17% and 23% for an inclination angle of 30º and 60º, respectively. These results can also point out that, in inclined fibres, the frictional resistance due to the force component normal to the fibre axis (originated by the inclination angle) plays a more important role on the peak pullout load than the embedded length. Therefore, for the hooked series, the increase of N_{max} with L_b will be smaller than for smooth fibres. Moreover, this increment will decrease with the inclination angle (20%, 15% and 7%, respectively for the hooked series with a 0º, 30º and 60º).

Additionally, comparing the curves of the hooked and smooth series in Figure 4.3(a), without regarding to specific details, can be clearly perceived two distinct facts. Firstly, in a general manner the variation of the maximum pullout load with the embedded length can be approximated by a straight line, in which the slope reflects the variation of the pullout load per fibre embedment length. Secondly, a vertical offset between the curves corresponding to the smooth and hooked series can also be identified. This offset distance between those curves represents the contribution of the mechanical anchorage to the N_{max}. Moreover, this contribution was not significantly influenced by the embedment length.

The influence of the embedded length on the slip at the peak load, s_{peak}, is depicted in Figure 4.3(b). For both smooth and hooked aligned fibres a slight increase of s_{peak} with L_b was

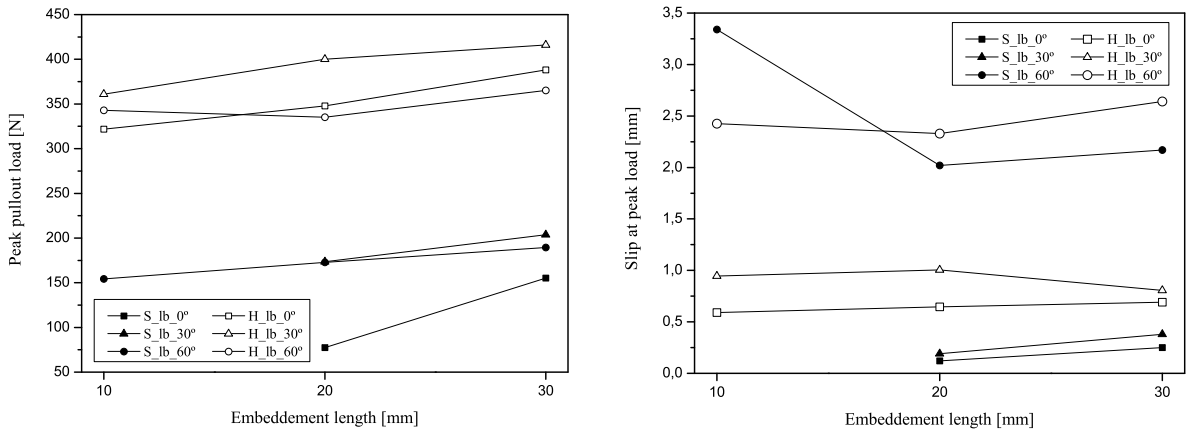

(a) (b)

Figure 4.3: Influence of bond length on the (a) peak pullout load and (b) slip at peak load.

observed, whereas for inclined fibres was not found any clear relevance of the embedded length influence on the s_{peak}.

The allowable crack opening in fibre reinforced structural elements depends on a specific application. Therefore it is of special interest to assess the mechanical pullout properties, e.g. the maximum pullout load and toughness, for a determined crack opening (i.e. slip). The pullout toughness was computed by integrating the load - slip curve up to slips of 1 and 3 mm, which were respectively designated by G_{1mm} and G_{3mm}. In Figures 4.4(a) and 4.4(b) is depicted, respectively, the embedment length influence on G_{1mm} and G_{3mm}. The average values of these parameters, as well as the correspondent variation coefficients are indicated in Annex II. In general, as the fibre embedded length increases, the toughness for a given slip also increases. However, series H_lb_30 was an exception to the latter assertion, since G_{1mm} and G_{3mm} fall off for an embedded length of 30 mm. The reason of this occurrence is due to distinct types of pullout failure observed for each series (see Table 4.3). For the H_lb30_30 specimens, fibre rupture has always occurred, whereas for the other embedded lengths of the series H_lb_30 there were specimens from which the fibre was completely pulled out. Moreover, the toughness of the latter specimens is considerably larger than the toughness of the ones where fibre rupture occurred (see individual pullout curves in Annex II). As a result, the average toughness value for series H_lb30_30 is smaller than for the other embedded lengths with the same inclination angle. Besides, the fact that G_{3mm} of the H_lb30_30 series has been smaller than the smooth fibre series with the same inclination angle and embedded length, may also cause bewilderment. Anyhow, once again this was due to the fibre failure modes observed for each series. Since, for the S_lb30_30 all the specimens failed by pullout in opposite to the correspondent hooked series that failed by fibre rupture for an approximate slip of 1 mm. Therefore, the overall toughness is markedly influenced by the type of failure, since fibre fracture will significantly reduce the

toughness when comparing to fibres that underwent a complete pullout.

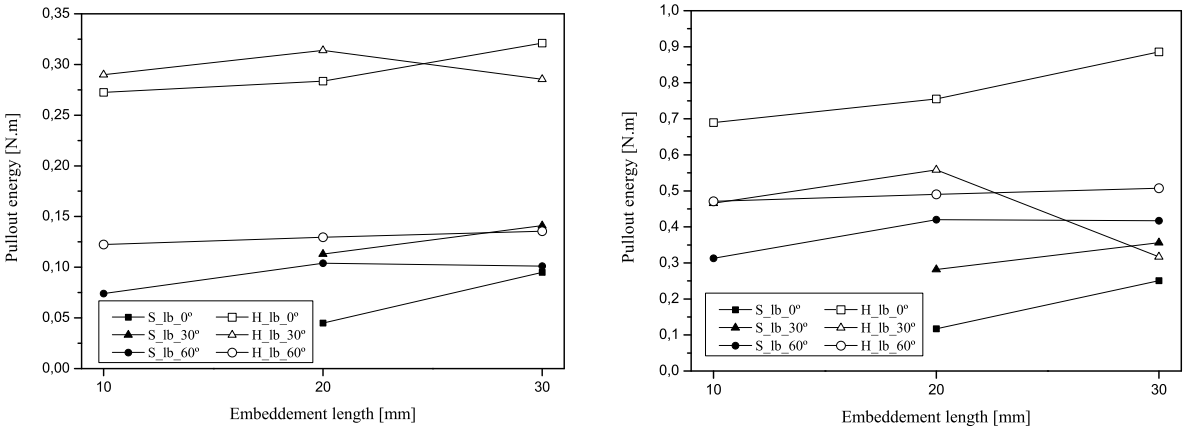

Figure 4.4: Influence of bond length on pullout energy dissipated up to a slip of:(a) 1 mm (b) 3 mm.

For the aligned series, since always took place the complete fibre pullout, the increase of both G_{1mm} and G_{3mm} with the increase of the embedded length was more significant than for inclined fibres. Regrading the H_lb_0 series, G_{1mm} and G_{3mm} increased with L_b 18 and 28%, respectively. Inasmuch the smooth fibres this increase was even more considerable, since both G_{1mm} and G_{3mm} increased with L_b more than 100%. Once more, previous demonstrates that the pullout response of hooked fibres at given embedment length is predominantly influenced by the mobilisation and straightening of the hook.

4.3.4 Influence of the fibre orientation angle

In Figure 4.5(a) is depicted the influence of the inclination angle on the maximum pullout load, N_{max}. In general, the N_{max} increases up to a inclination angle of 30º and then decreases for 60º angle. For both hooked and smooth fibres the highest maximum pullout load was observed for an inclination angle of 30º. However, the increase of the maximum pullout load with the inclination angle was more significant on the smooth fibre series. For the latter, the series with a 30º inclination angle have a N_{max} 30 to 125% higher than the aligned smooth fibre series. On the other hand, for the hooked fibre series with a 30º inclination angle, the N_{max} is just 7 to 15% higher than aligned hooked fibre series. In spite of the increase of the frictional pullout component with the inclination angle, increasing the angle from 30º to 60º will provide a slight decrease on the N_{max}. Remember that for the inclined hooked series the pullout occurred generally by fibre rupture. Moreover, the average fibre rupture load was smaller for the series with a 60º inclination angle than for 30º, as previously explained.

The slip at peak load, s_{peak}, increased with the inclination angle for both hooked and smooth fibres. The trend of the s_{peak} evolution with the inclination angle was very similar for all the series, see Figure 4.5(b). First, a slight increase on the s_{peak} for a 30º angle was observed, afterwards the s_{peak} increased considerably. In fact, for the smooth series with 60º inclination angle, the s_{peak} was approximately 5 to 9 times higher than for a 30º angle, whereas for the hooked series it was 1.3 to 2.3 times higher. The significant higher values of s_{peak} for a 60º angle can be ascribed to other additional mechanisms that usually occur on inclined fibres in opposite to aligned fibres. As the fibre inclination angle increases, the stresses concentrated at the fibre bending point also increase. This leads to a more significant portion of concrete that is crushed or pushed off at the crack plane. As the volume of concrete that spalls is higher, a larger fibre's protruding length (i.e. extending out beyond the concrete matrix) is deformed without any constraints (see Figure 2.4), which will add to the measured slip a supplementary displacement correspondent to the deformation of the protruding part of the fibre. So, for large inclination angles, such as 60º, the slip includes a significant parcel which is due to fibre deformation.

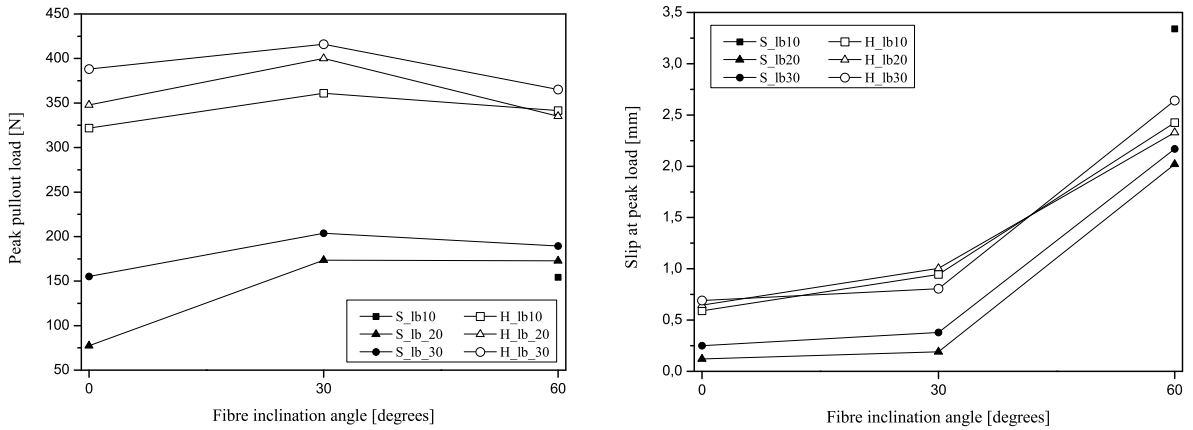

(a) (b)

Figure 4.5: Influence of inclination angle on the: (a) peak pullout load and (b) slip at peak load.

The capacity level of a fibre can be given as the ratio of the maximum tensile stress observed in the fibre during pullout (σ_{max}) and the tensile strength of the fibre steel (σ_y). The analysis of this ratio allows to assess the optimisation level of the fibre utilised in conception of the present self-compacting concrete, i.e. if the fibre type and aspect ratio are adequate to the matrix strength. As perceived in a previous section, the rupture stress for inclined fibres was smaller than the one obtained experimentally in the direct tension tests, since in the former case a tensile stress due to bending limits the tensile stress component due to axial load (see Figure 4.6). As the inclination angle increases, the bending moment will increase and the axial force must decrease in order to attend the ultimate capacity diagram of the cross section under

composed bending. Therefore, for the computation of the σ_{max}/σ_y for the inclined series, the tensile strength obtained in direct tension tests was not used. In order to accomplish a better interpretation of the results, for the inclined series, the tensile strength was computed as the ratio between the average rupture load observed in the pullout tests and the fibre cross section area ($\sigma_{max} = N_{max}/A_f$). The influence of the inclination angle on the ratio σ_{max}/σ_y is depicted in Figure 4.7.

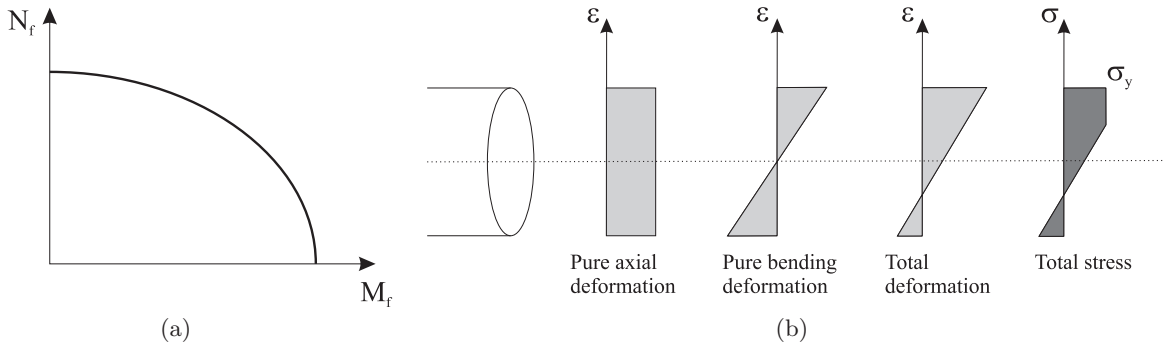

Figure 4.6: Composed bending: (a) interaction diagram between bending moment and axial force (b) strain and stress distribution on the fibre cross section.

The peak pullout force of a fibre, or its corresponding tensile stress, should not be determined exclusively at the maximum stage, i.e. at the correspondent slip at peak load, since this does not say much about the performance of fibres in real structures. In fact they should be determined at normative values of the fibre slip, i.e. of the crack width. As it was previously seen, the maximum pullout load can be observed for distinct slips, see Figure 4.5(b), ranging 0.2 to 3.3 mm depending on the type of fibre, embedment length or inclination angle. The allowable crack openings (fibre slip) in real structural elements depends on the durability. These values can lay out between 0.1-0.4 mm regarding durability (EN 1992-1-1 2004). In Figure 4.8 is depicted the ratio between the tensile stresses of aligned and inclined fibres, at fibres slips (which is related to crack widths) of 0.1, 0.25, 0.5 and 1 mm, for both hooked and smooth fibres.

Figure 4.8(a) shows that hooked fibres inclined at 60º possess the lowest efficiency for all fibre slips (i.e. at all crack widths). Hooked fibres inclined at 60° are 1.5 to 2.6 times lesser effective when compared to fibres aligned with the tensile load. Regarding the fibres with a 30º inclination, a positive effect is mainly observed at very small fibre slips (0.1 mm). For the latter inclination, no significant differences were observed for larger slips, when compared to aligned fibres. In opposite to this observation, results of several researchers, shows that for a 30º angle

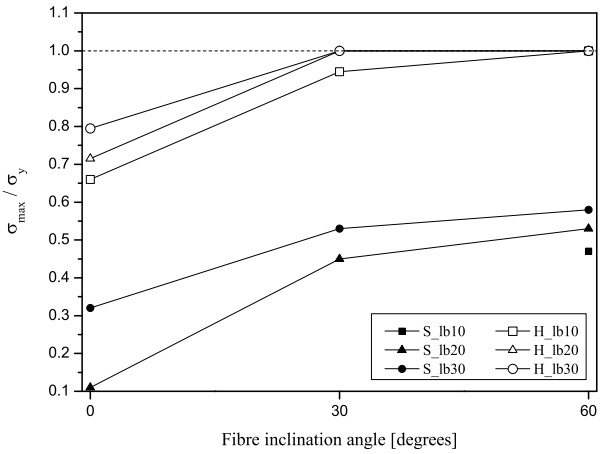

Figure 4.7: Ratio between the highest achieved tensile stress, σ_{max}, and the fibre tensile strength, σ_y.

the efficiency of hooked fibres is significantly smaller than for aligned fibres. The tensile stress in a 30º inclined fibre can be up to 2.5 times smaller than for aligned fibres (see Figure 2.6). The discrepancy between the obtained results and those depicted in Figure 2.6 can be due to the differences between the self-compacting and conventional concrete matrices. The high strength matrix of the self-compacting concrete used is in general considerably more compact, i.e has fewer voids, than a conventional matrix. Remark that, as a consequence of the fibre inclination, there are additional concentrated stresses nearby the concrete surface fibre exit. Therefore, a weaker matrix or less compact (e.g. conventional concrete) is more prone to spalling and local damage. As concrete spalling occurs the fibre can easily bend, and the stress carried by the fibre is reduced. On the other hand, on fibres with a 30º inclination angle pulled-out from high performance reinforced concrete (with "micro" fibres to increase the splitting tensile strength of the matrix) was also observed a positive effect (Markovic 2006). Consequently, in opposite to conventional matrices, high compacity matrices (e.g. self-compacting concrete or high performance cement composites) can improve the effectiveness of inclined fibres for 30º angles.

Inasmuch as for smooth fibres, the efficiency for both inclinations studied was higher, comparatively to hooked fibres, see Figure 4.8(b). For a 30º inclination angle depending on the fibre slip the efficiency of the inclined fibre can reach up to 2.2 times of an aligned smooth fibre. This increase is more significant in smooth fibres, since this kind of fibres did not fail by fibre rupture, in opposite to the hooked fibres. On the other hand, for fibres with a 60º inclination angle the efficiency increased only for higher slips, i.e. 0.5 and 1 mm, whereas for the other fibres slips the fibre efficiency was almost the same as for aligned fibres. The absence of a mechanical anchorage in the smooth fibres will lead to smaller pullout forces, consequently, the concentrated stresses nearby the concrete surface fibre exit due to fibre angle will be smaller.

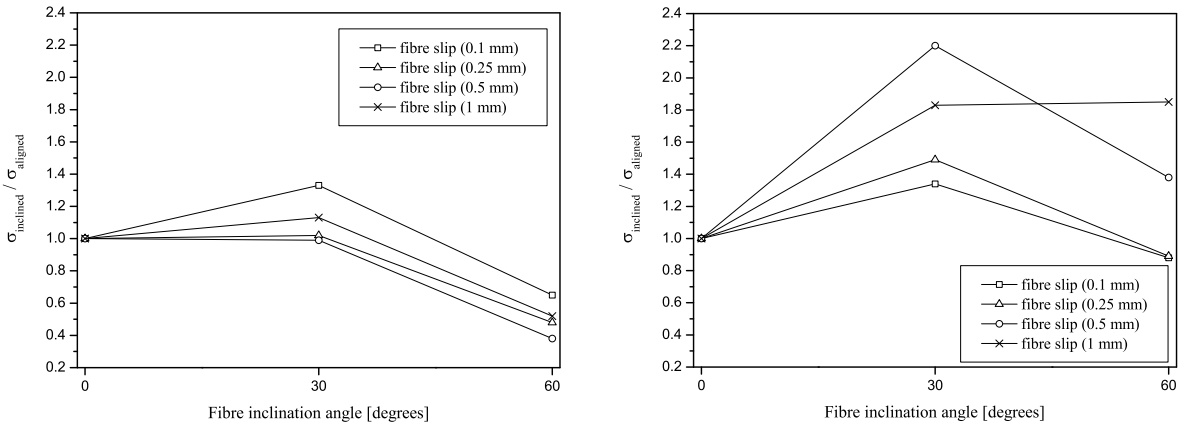

Figure 4.8: Ratio between the tensile stresses in aligned and inclined fibres (0°, 30° and 60°), at different fibre slips for: (a) hooked and (b) smooth fibres.

Considering the abovementioned, when pulling out smooth fibres, the fraction of concrete matrix damaged will be smaller. Therefore, the efficiency of a smooth fibre at an inclination angle of 60° is not so compromised as for the hooked fibres.

In Figures 4.9(a) and 4.9(b) is depicted, respectively, the influence of the inclination angle on the toughness up to a slip of 1 mm, G_{1mm}, and 3 mm, G_{3mm}. In general, an increase of G_{1mm} was observed up to an inclination angle of 30° followed by a decrease for a 60° angle. With regard to the hooked series a significant reduction (118 - 155%) of G_{1mm} for a 60° inclination angle was observed. As the inclination angle increases, the frictional resistance also increases supplying an additional parcel to the overall energy necessary to pullout the fibre. In spite of that, when pulling out at an angle, the fibre will appoint the matrix nearby the fibre bending point under additional stress. As the angle increases more, splitting of the matrix becomes more considerable and arises for lower load levels. Additionally, for the last mentioned series, as the matrix becomes more spalled for smaller slips, the loss of stiffness due to the fibre bending starts also for a lower load level, repercussing on a lower toughness (see Figure 4.2). On the other hand, for the series of smooth fibres with a 60° inclination angle, though the decreasing of toughness, a significantly smaller decrease was observed than the one for the latter hooked series.

Looking upon the influence of the inclination angle on the G_{3mm}, two distinct trends could be perceived for each the smooth and hooked fibres. Concerning the smooth series an increase of G_{3mm} was observed with the increase of the inclination angle, while for the hooked series it was observed the opposite. The prior finding has a feasible explanation. In the case of inclined smooth fibres, as previously said, the principal mechanism that contributes to the toughness increase is the additional frictional resistance provided by the inclination angle. This

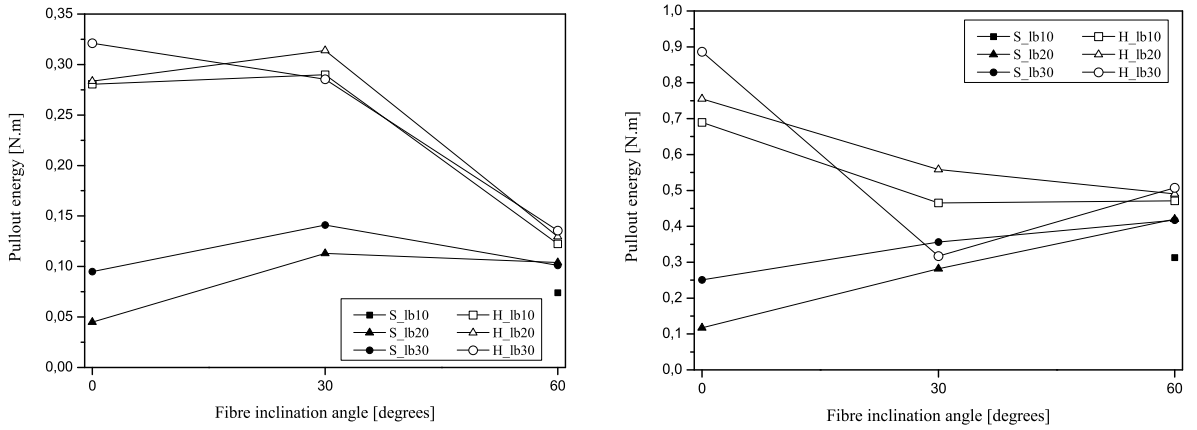

Figure 4.9: Influence of the inclination angle on pullout energy dissipated up to a slip of: (a) 1 mm (b) 3 mm.

was only reflected for G_{3mm}, and not for G_{1mm}, since the frictional resistance will become more important for higher slips, which is in accordance with other authors findings (Shah et al. 1995). In opposite, regarding the inclined hooked series, as also previously said, the influence on the pullout mechanisms of the additional frictional resistance is less significant than the mobilisation of the hook. This fact, associated to the fibre rupture observed in these series at a slip smaller than 3 mm, contributed to the decrease of toughness. The toughness of the series H_lb30_30 was smaller than expected, in comparison to the other series with a 30^o angle, since fibre rupture occurred for the totality of the series specimens.

4.3.5 Influence of the matrix type

In Figure 4.10 are comprised both smooth and hooked fibres' pullout responses obtained from a conventional vibrated fibre reinforced concrete, CFRC, and from a SFRSCC. The pullout curves for a CFRC presented in the referred figure were the ones obtained and discussed in the previous chapter corresponding to the fibre TYPE A. Since these responses were obtained for a fixed embedded length of 15 mm, and because the SFRSCC responses were assessed for other embedded lengths, the experimental envelope and average pullout curve for the SFRSCC specimens relate to both the series with 10 and 20 mm. Notice that, for the smooth series this comparison was not possible due to technical problems with the series of 10 mm fibre embedment length, therefore the series with 20 and 30 mm were used for comparison purpose.

The scatter obtained for the fibre pullout responses from CFRC was considerably higher than for SFRSCC, in particular for the smooth series. In addition, if having in mind that the envelope presented for SFRSCC responses regards two series with distinct embedded lengths, one may say that these differences in the responses' scatter are even more substantial. As

previously referred, the differences between the CFRC and SFRSCC responses' scatter, may be ascribed primarily to the matrix heterogeneity of the conventional vibrated concrete. However there are other factors that may enhanced this. Even though the casting of the slab containing the CFRC specimens was carried out with care, the low workability and higher dimension of the maximum aggregate in CFRC composition (25 mm, in opposition to 15 mm for SFRSCC) may caused that some fibres have warped. The fibre warping could have enhanced both the response's scatter and the pullout behaviour for this series.

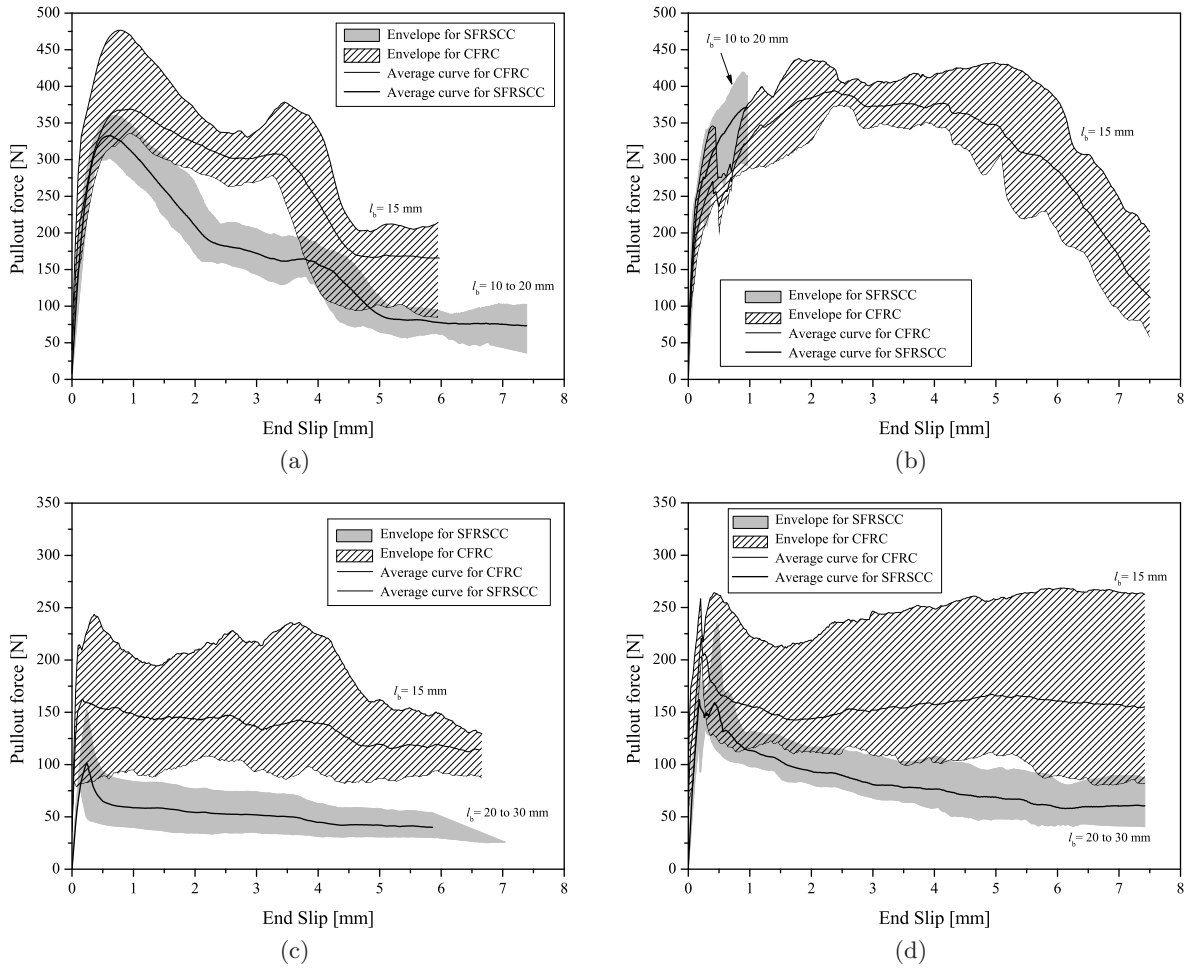

Figure 4.10: Fibres TYPE A pullout response for CFRC and SFRSCC: (a), (b) hooked fibres with a 0 and 30º inclination, respectively; (c), (d) smooth fibres with a 0 and 30º inclination, respectively.

Regarding the hooked series, Figures 4.10(a) and 4.10(b), the principal differences between the pullout responses between SFRSCC and CFRC are during the post-peak stage. In what concerns to the pre-peak behaviour, the CFRC aligned hooked fibres presented an average maximum pullout load nearby 10% higher than of the correspondent SFRSCC fibres. On

the other hand, for an inclination angle of 30º, the average pullout load up to a 1 mm slip was higher for the SFRSCC specimens, i.e. up to the slip correspondent to fibre rupture of these specimens. For this inclination angle (30º), there were no significant differences on the maximum pullout load. However, the pullout load at a slip of 1 mm was approximately 15% higher for the SFRSCC specimens. This was due to both the higher strength and compactness of the self-compacting matrix, as the pullout response up to fibre rupture was more stiffer. Since the CFRC matrix had a smaller strength, the matrix spalled more often and for a lower pullout load (compare individual pullout responses from Annexes I and II).

The post-peak response of the aligned hooked fibres pulled-out from CFRC specimens was better than the one from SFRSCC. If a brief analysis is carried out, just by viewing the responses of smooth fibres from those matrix types, Figure 4.10(c), it can be noticed that after the peak load is attained, i.e. in smooth fibres corresponds to the end of the elastic/chemical debonding stage, the pullout load is considerably higher for CFRC. This is even of more preponderance, if having in mind that, the SFRSCC smooth series are for higher embedment lengths than for the CFRC smooth series. Therefore, the frictional pullout strength is considerably higher for CFRC. Even though the pullout results from the CFRC could be overestimated, as previously referred (see section 3.3.4), it is feasible to ascribe this to differences on the composition of those matrices. These aspects will be further detailed in section 4.4 and more easily perceived, since it will be presented the isolated contribution of each reinforcement mechanism.

The post-peak pullout of hooked fibres from a self-compacting matrix could not be assessed, since for this matrix the predominant failure mode was fibre rupture, in opposition to the observed for CFRC. The average dissipated energy up to a 3 mm slip was approximately 100 % higher for fibres pulled out from a CFRC, obviously, this difference will be increased as the energy is computed for higher slips. On the other hand, the energy dissipated up to 1 mm was nearby 20% higher for the fibres pulled out from a SFRSCC. The differences between fibres pulled-out with a 30º angle from CFRC and SFRSCC, in the post-peak stage, are not just ascribed to differences between those matrices. Since the tensile strength from the fibres used in SFRSCC pullout tests was unexpectedly lower than the ones used for CFRC. Remember again that those fibres were from both the same brand and type, however were from distinct shipments.

4.3.6 Relationships between fibre's micro-mechanical parameters

In this section it will be presented and discussed several relationships between distinct fibre's micro-mechanical parameters. Once again is emphasized that it is not intended to find any type of empirical/semi-analytical relationships between those parameters, but only to render

a more clear insight on the interaction of the distinct parameters. In addition, the data for the conventional vibrated fibre reinforced concrete, CFRC, presented in section 3.3.7 is also comprised.

In Figures 4.11(a) and 4.11(b) is depicted the relationship between the peak pullout load, N_{max}, and the pullout load N_{1mm} and N_{3mm}, respectively. Regarding the SFRSCC, for both relationships, it is visible a linear trend between N_{max} and both N_{1mm} and N_{3mm}, nevertheless the scatter for these relationships is quite high. In similitude to what was observed in the CFRC, in general N_{1mm} and N_{3mm} increase with N_{max}, the only exceptions were related with the fibres that ruptured prematurely.

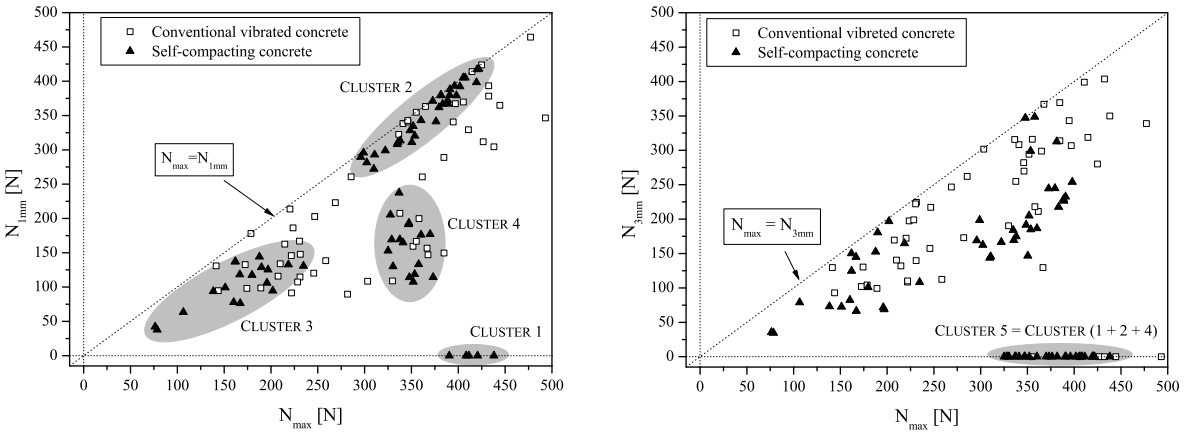

(a) (b)

Figure 4.11: Relationship between peak pullout load and pullout load at a slip of: (a) 1 mm and (b) 3 mm.

Nevertheless, within the scatter of the SFRSCC relationships can be clearly ascertained some clusters. Notice that, that the scatter on SFRSCC is predominantly resultant from distinct pull-out responses for each series studied, since within each series the scatter response was relatively low. In opposition, for CFRC, the pullout response within the same series was considerably higher, thus it was not possible to identify, so clearly, clusters from pullout responses regarding distinct series. Within Figure 4.11(a) were identified four distinct data subsets: CLUSTER 1 includes the hooked fibres with an embedded length of 30 mm and with an inclination of 30º; CLUSTER 2 comprises the aligned hooked fibres, and the hooked fibres with an inclination of 30º, namely, with a 10 and 20 mm embedded length; CLUSTER 3 regards to all the smooth fibres; whereas CLUSTER 4 includes the hooked fibres with an inclination of 60º. For the relationship $N_{max} - N_{3mm}$, it was identified one data subset in which the fibres have ruptured for a slip smaller than 3 mm. This was designated as CLUSTER 5, and in general, this group

includes the data from CLUSTER 1 and 4, and in addition the fibres with an inclination of 30º from CLUSTER 2.

In Figures 4.12(a) and 4.12(b) is depicted the relationship between the peak pullout load, N_{max}, and the dissipated energy up to a slip of 1 mm, G_{1mm}, and 3 mm, G_{3mm}, respectively. A linear trend is observed for both relationships. The scatter for the relation between N_{max} and G_{1mm} is considerably smaller, in spite of not being so visible due to the scale of the plot. For this relationship it was identified a new subset, CLUSTER 6, which is nonetheless than the data from CLUSTER 2 and CLUSTER 1. Since the fibres from CLUSTER 1 ruptured before a slip of 1 mm, in general, the G_{1mm} value for these specimens was smaller than for the ones from CLUSTER 2.

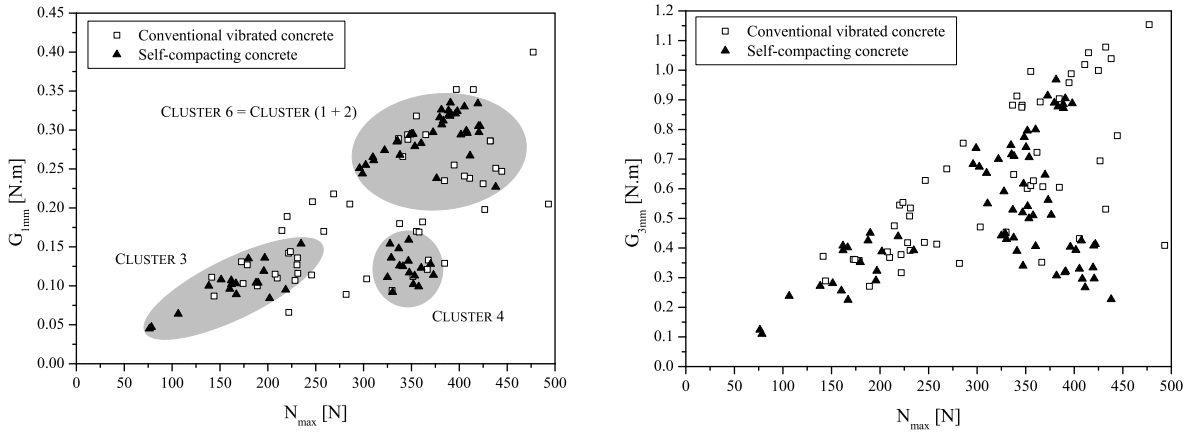

(a) (b)

Figure 4.12: Relationship between N_{max} and the dissipated energy: (a) G_{1mm} and (b) G_{3mm}, respectively.

The worse correlation, in a qualitative fashion, between N_{max} and both N_{3mm} and G_{3mm} was expected, since these entities usually are assessed at different stages of fibre pullout, depending on the tested series, i.e. fibre's embedded length and inclination. Thus, if the dissipated energy up to a certain slip is correlated with the pullout load correspondent to the same slip, e.g. $N_{1mm} - G_{1mm}$, the scatter previously observed will be significantly reduced, compare Figures 4.13(a) and 4.13(b), with Figures 4.12(a) and 4.12(b), respectively. The reduction of the scatter on the $N_{1mm} - G_{1mm}$ relationship, is in part ascribed to the translation of CLUSTER 4 towards CLUSTER 3, see Figure 4.13(a). Remember that CLUSTER 4 comprises the hooked series with an inclination of 60º, which ruptured for relatively high pullout load, but had a relatively low stiffness in the initial phase of the pullout, since the matrix has spalled for a lower load, due to the higher stresses concentration at the fibre exit point. In what concerns

the $N_{3mm} - G_{3mm}$ relationship, it were identified 3 clusters. Remark, that Cluster 5 includes the data from Cluster 1 and 4, and in addition the fibres with an inclination of 30° from Cluster 2. In Figure 4.13(b), the subset identified as Cluster 2 only comprises the aligned hooked series.

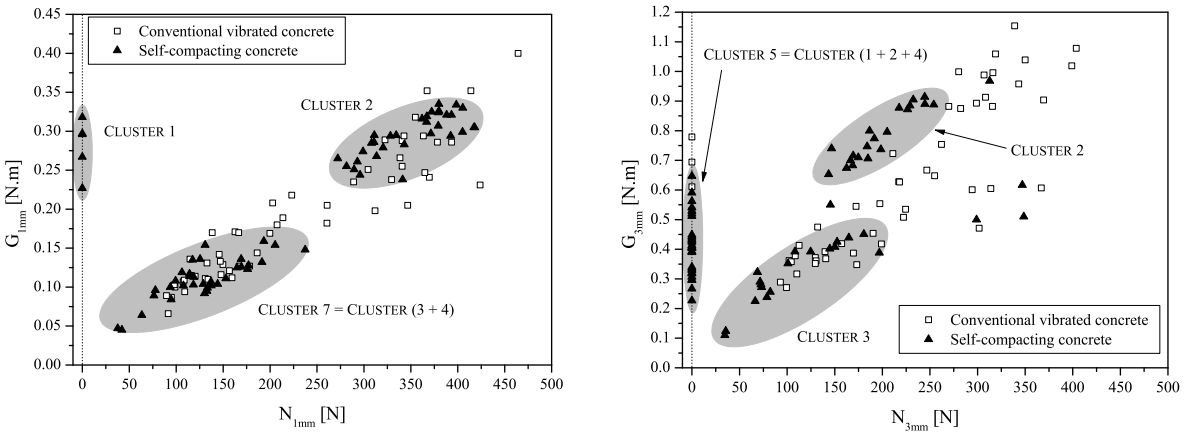

(a) (b)

Figure 4.13: (a) Relationship between N_{1mm} and G_{1mm}, (b) Relationship between N_{3mm} and G_{3mm}.

4.4 Mechanical contribution of the hooked end

In Figure 4.14(a) is depicted the contribution of the hook mechanism on the overall pullout behaviour of aligned fibres. The mechanical component of bond, curve 3 in Figure 4.14(a), was obtained by subtracting the average curve of the hooked series, curve 1 in Figure 4.14(a), to the correspondent average curve of the smooth series, curve 2 in Figure 4.14(a). Comparing curves 3 obtained for both the 20 mm and 30 mm embedment lengths, respectively, in Figures 4.14(a) and 4.14(b), it can be observed that these curves are extremely similar. This also reveals that if the full mobilisation of the hook is attained, the mechanical component of the hook is not influenced by the embedment length. This will not be true if the embedment length is smaller than the length of the hooked end (Robins et al. 2002), which is not the case of the present work.

In order to assess, in a quantitative way, the contribution of the hook straightening and deformation on the overall pullout behaviour of aligned hooked fibres, it was used the curve 3 depicted in Figure 4.14 to compute the maximum pullout load and toughness ratios between the later curve and the correspondent average curve of the hooked series (curve 1). For the maximum pullout load, the contribution of the hook mechanism was of 88% and 77%, respectively

for a 20 and 30 mm embedded length. Regarding both G_{1mm} and G_{3mm} the endowment of the hook was about 84% and 71% for an embedded length of 20 and 30 mm, respectively. Obviously, in the case of aligned hooked fibres the influence of the hook on the pullout behaviour decreases when the embedded length increases, since the debonding process proceeds throughout a larger distance on the case of the series with 30 mm, and, additionally, the mechanical component was not influenced by the embedded length.

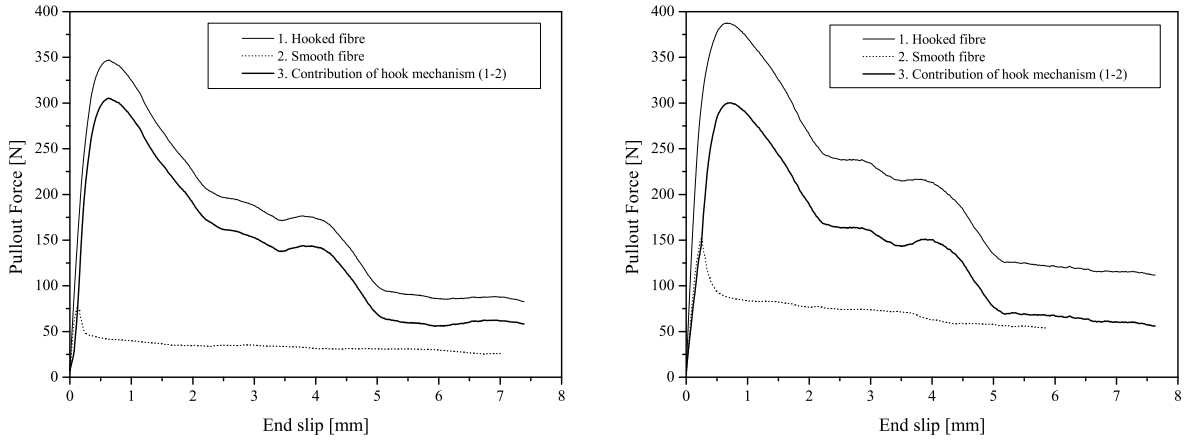

Figure 4.14: Contribution of the end hook to the overall pullout behaviour in aligned hooked end fibres with an embedded length of: (a) 20 mm and (b) 30 mm.

On the other hand, for inclined fibres, the assessment of the contribution of the hook is not so easy, since for inclined hooked fibres several other mechanisms arise in comparison with aligned fibres. Those mechanisms are respectively: the additional frictional resistance due to the force component normal to the fibre axis, the deformation, bending and plastification on the bending point of the fibre, and finally, spalling of the concrete matrix nearby the fibre exit point of the concrete. Moreover, these mechanisms during the pullout process interact with each others. In Figures 4.15 and 4.16 is depicted, respectively, the contribution of the end hook mechanism on the overall pullout behaviour of fibres with a 30° and 60° inclination angle. The contribution of the hook mechanism for inclined fibres was assessed in a similar way to the aligned fibres. Comparing this contribution for aligned and inclined fibre (see Figures 4.14, 4.15 and 4.16), can clearly be observed that as the inclination angle increases, the contribution of the hook mechanism decreases. In fact, for inclined fibres with a 30° angle, the hook influence on the maximum pullout behaviour was about 54%, whereas for a 60° inclination angle was of 48%. Regarding the G_{1mm}, the hook contribution was about 58% for a 30° angle and 20% for the 60° angle.

The previous assertions for the inclined series (30º and 60º) must be regarded with care, since in the present work fibre rupture occurred. Therefore, these assumptions can only be applied to the slip corresponding to fibre rupture. Moreover, for fibres with a considerable inclination angle, such as 60º, there is significant parcel of the slip that is due to the bending deformation of the fibre. Figures 4.15(b) and 4.16(b) point out that the end hook only starts to be mobilized for large slips (over 1 mm).

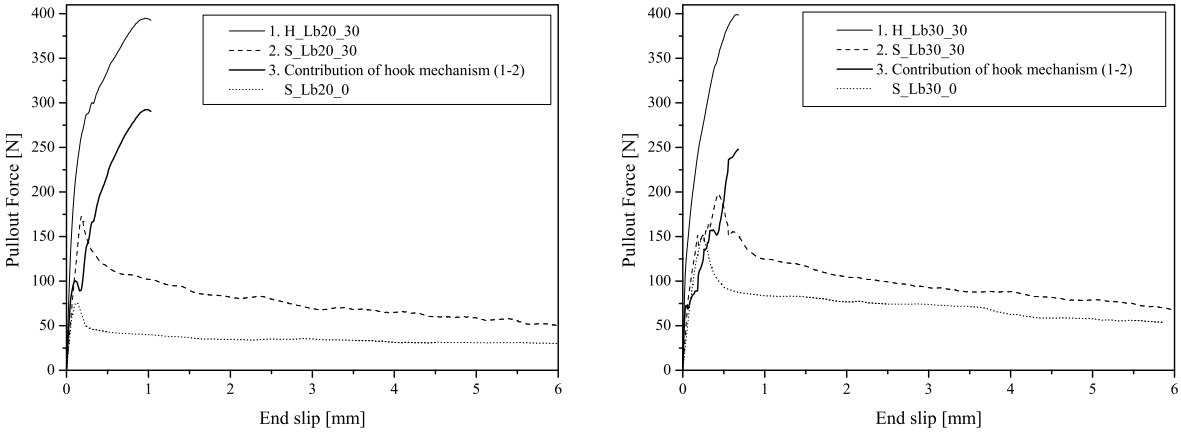

(a) (b)

Figure 4.15: Contribution of the end hook to the overall pullout behaviour in hooked end fibres with a 30º inclination angle: (a) 20 mm and (b) 30 mm.

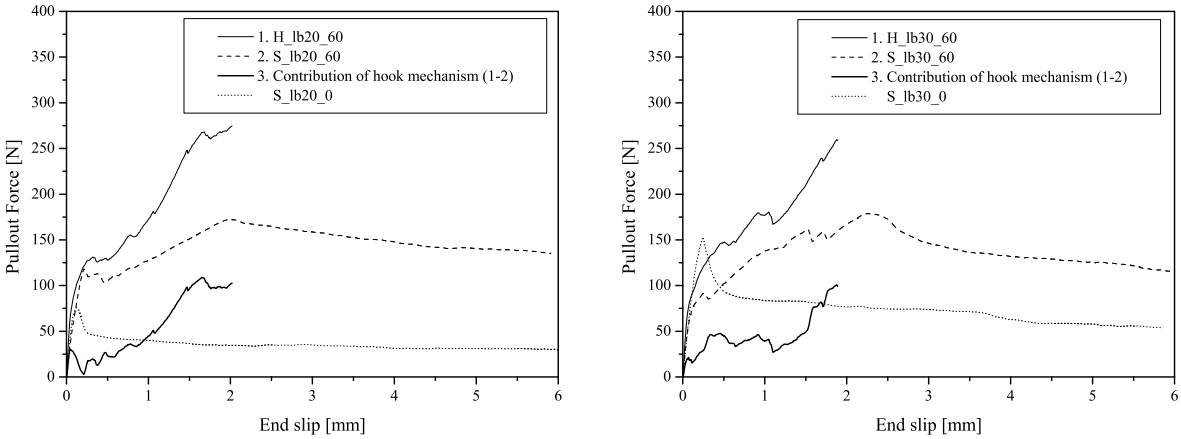

(a) (b)

Figure 4.16: Contribution of the hook to the overall pullout behaviour in fibres with a 60º inclination angle: (a) 20 mm and (b) 30 mm.

In order to enlighten the validity of these arguments, the mechanical contribution of the

end hook was acquired for a single specimen from the series with an inclination angle of 30° and 60° which has been fully pulled out (see Figure 4.17). The mechanical contribution curve withdrawn from the H_lb20_30 specimen is very similar to the one obtained for the aligned series (see Figure 4.14). Regarding the curve of the mechanical contribution related to the H_lb10_60 specimen, can be withdrawn that the contribution of the hook to the maximum pullout load was of 60%, whereas the input to G_{3mm} was 45%. This also points out that even in the case that fibre rupture does not occur, for a high inclination angle (60°) the contribution of the end hook to the overall pullout behaviour is not so significant as in aligned fibres.

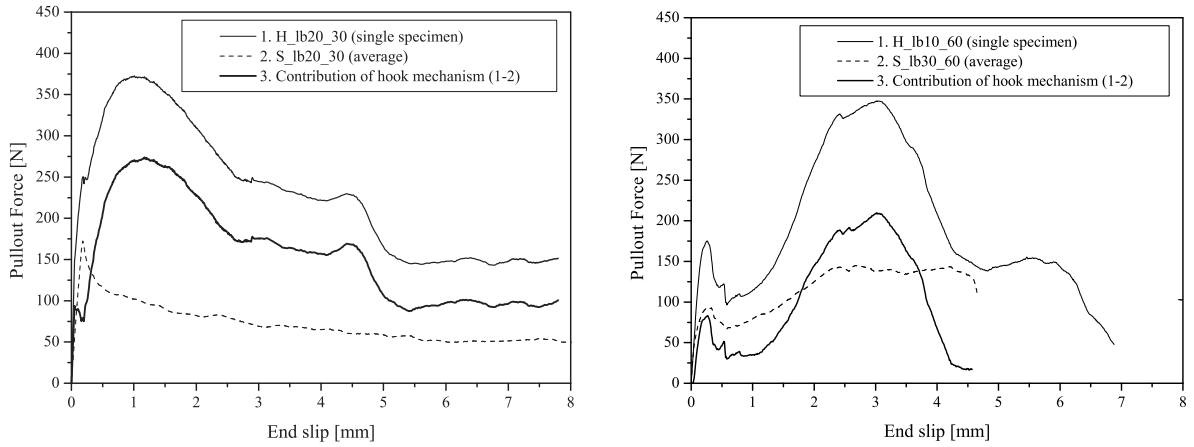

Figure 4.17: Contribution of the hooked end to the overall pullout behaviour for the single specimen from series: (a) H_lb20_30 and (b) H_lb10_60.

4.4.1 Self-compacting concrete vs. conventional vibrated concrete

In Figure 4.18 is depicted the contribution of the hook mechanism on the overall pullout behaviour of aligned fibres extracted from a conventional vibrated concrete, CFRC. The mechanical component of bond (curve 3) was determined in the same way as previously described for the SFRSCC specimens. When comparing the hook's mechanical contribution in CFRC specimens with the correspondent in SFRSCC specimens (see Figure 4.14), it is ascertained that for CFRC the abovementioned mechanism has a relatively smaller contribution to the overall pullout response. In fact, at and after the pullout peak-load, the hook contribution in a CFRC medium is nearby 60%, whereas for a SFRSCC medium and regarding the series with a 20 mm embedded length was roughly 80%.

This difference within the hook's contribution in a CFRC and SFRSCC is related to the distinct strength and compactness between those matrices. In Figures 4.19(a) and 4.19(b) is

depicted the fibre imprint channel in a CFRC and SFRSCC matrix, respectively, for an aligned hooked fibre. For a SFRSCC matrix the imprint of hook is more clear, moreover the angles that define the imprint in the matrix are closer to the angles that defined the fibre's hook shape previously from having been pulled-out. Therefore, due to the high stiffness of the SFRSCC, a higher grade of hook's plastification has to be attained in order that the fibre is fully pulled-out.

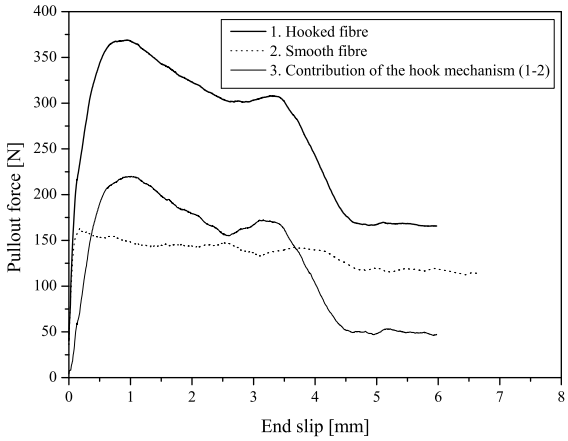

Figure 4.18: Contribution of the end hook to the overall pullout behaviour in aligned fibres with an embedded length of: (a) 20 mm and (b) 30 mm.

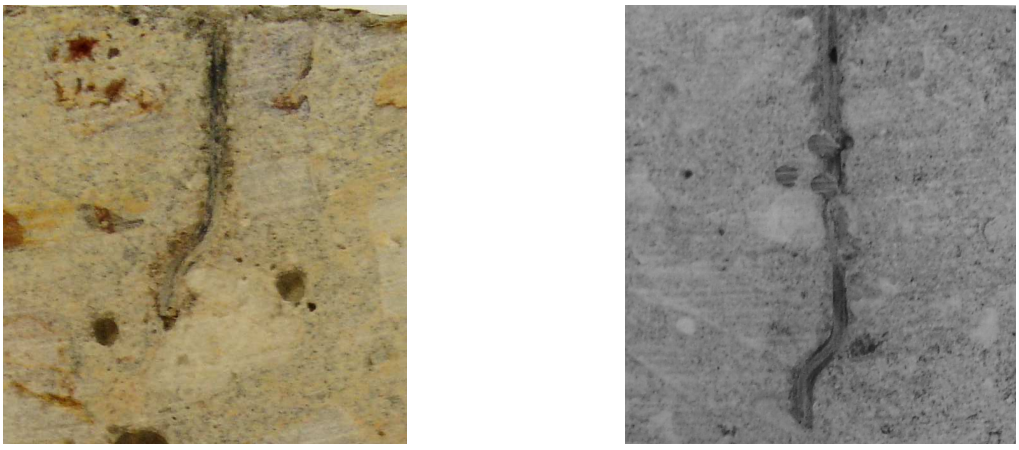

(a) (b)

Figure 4.19: Fibre type A imprint channel in a: (a) CFRC and (b) SFRSCC.

On the other hand, the curvature of the hook's imprint in the CFRC matrix is considerably smoother than the sharp angles observed for the SFRSCC matrix. Since the CFRC matrix was less stiffer than the SFRSCC, it was more prone to micro-cracking during the plastification of the hooked end, so that the fibre could be fully pulled-out. This lead to two interesting

aspects. The first, a lower grade of the hook's mechanical contribution, as already discussed and visualized in terms of pullout load - slip response, compare Figures 4.18 and 4.14. The other relevant aspect is that afterwards the hook has passed through both imprint curvatures, the frictional resistance will be higher than in SFRSCC, since the hooked end in a CFRC is not so straightened as in a SFRSCC. This increase on the frictional resistance of the hooked fibres is not only ascribed to the hook's deformation grade. Remark, that for smooth fibres, the frictional pullout resistance in CFRC is considerably higher than in SFRSCC, see Figures 4.10(c) and 4.10(d). The lower fictional pullout strength in SFRSCC, may be related with the inclusion of large amounts of limestone filler, in order to attain self-compactability requirements. The limestone filler, which are very small spherical particles may have favoured the fibre slippage throughout the fibre's channel. The sizes of limestone filler are significantly inferior to cement grains with an approximate mean particle size of 5 μm (Pereira 2006).

4.5 Conclusions

The experimental results of hooked end steel fibres pullout tests on a SFRSCC medium were presented and discussed in this chapter. The influence of the fibre orientation, the fibre embedment length, as well as the matrix type on the fibre pullout behaviour was studied. Additionally, the role of the hook, on the overall pullout behaviour, is attained by isolating the contribution of the frictional bond component.

In general, two main pullout failure modes were observed during the pullout tests. The complete fibre pullout was observed for aligned hooked fibres and smooth (either aligned or inclined), whereas for inclined hooked fibres the principal failure mode observed was fibre rupture. The latter failure mode observed for hooked inclined fibres was a result of both a strong and compact concrete matrix.

Generally, the maximum pullout load increased linearly with the embedded length for both hooked and smooth fibres. However, this increase was more significant on the smooth fibres, since the pullout response of hooked fibres at a given embedment length is predominantly influenced by the mobilisation and straightening of the hook. Regarding the effect of the orientation angle, the maximum pullout load increased up to a inclination angle of 30^{o} and then decreased for a 60^{o} inclination angle. For both hooked and smooth fibres the highest maximum pullout load was observed for an inclination angle of 30^{o}. However, the increase of the maximum pullout load with the inclination angle was more significant on the smooth fibre series.

For both smooth and hooked aligned fibres a slight increase of the slip at peak load with the embedded length was observed, whereas for inclined fibres was not found any clear relevance

of the embedded length influence on the slip at peak load. On the other hand, regarding the influence of the orientation angle, a slight increase on the slip at peak load was observed for a 30º angle, whereas for a 60º angle, the slip at peak stress increased considerably. The significant increase of the slip at peak load for a 60º angle can be ascribed to other additional mechanisms that usually occur on the pullout of inclined fibres, in opposite to aligned fibres. In fact the measured slip includes a parcel that corresponds to the fibre deformation and matrix spalling.

The pullout toughness was computed by integrating the load-slip curve up to slips of 1 and 3 mm, respectively, G_{1mm} and G_{3mm}. In general, as the fibre embedded length increased the toughness to a given slip also increased. Moreover, for the aligned fibres, since always took place the complete fibre pullout (in opposite to inclined fibres in which, frequently, occurred fibre rupture), the increase of G_{1mm} and G_{3mm} with the embedded length was more significant than for inclined fibres. Looking upon the influence of the inclination angle on the toughness, in general, an increase of G_{1mm} was observed up to an inclination angle of 30º, followed by a decrease for a 60º angle. On the other hand, for the G_{3mm} two distinct trends were perceived for each the smooth and hooked series. Concerning the smooth series, an increase of G_{3mm} was observed with the orientation angle, while for the hooked series the opposite was observed. The overall toughness was markedly influenced by the type of failure, since fibre fracture significantly reduced the toughness when comparing to fibres that underwent a complete pullout.

Regarding the influence of the matrix type, the inclusion of large amounts of limestone filler in the SFRSCC, in order to attain self-compactability requirements, has an important influence in the fibre/matrix interface properties, namely, bond strength and mobilization of the mechanical anchorage. The principal differences between the pullout responses from SFRSCC and CFRC are during the post-peak stage. These differences arise from distinct grades of the hooked end mobilization and the frictional resistance. The higher strength and compactness of the SFRSCC matrix enables a better mobilization of the hook, however, both the smoothness of the matrix and limestone filler provide smaller resistance to the fibre pullout, mainly in the post-peak fibre pullout phase. The post-peak response of the aligned hooked fibres pulled-out from CFRC specimens had an higher residual pullout strength and toughness than the for SFRSCC. However for the series with an inclination of 30º, it was not possible to withdraw conclusive remarks due to the unexpected distinct tensile strengths of the fibres used in each either CFRC and SFRSCC compositions.

Chapter 5

Analytical Modelling of the SFRSCC Pullout Results

5.1 Introduction

Analytical models for pullout problems are only capable to determine a load - slip relationship $N(s)$ of a pullout test on basis of a given bond law, $\tau(s)$, i.e. the direct problem, where with $\tau(s)$ is obtained $N(s)$. The straightforward analytical determination of the bond stress *vs.* slip relationship for a given pullout curve, i.e. the inverse problem, where $\tau(s)$ is obtained from $N(s)$, is extremely difficult due to considerable complexities from mathematical point-of-view (Banholzer et al. 2005). Actually, to overcome this concern, the inverse problem must be approached as a direct problem complemented with a numerical fitting tool.

In the present section, the developed numerical method for obtaining an analytical bond stress - slip relationship will be described. The mathematical representation of the pullout problem is often expressed by a second order differential equation expressed in terms of forces (Naaman et al. 1991b, Sujivorakul et al. 2000, Banholzer et al. 2005). However, since in the present model the displacements of the concrete points at the interface between concrete and fibre were neglected, the differential equation was derived in terms of slip, after Russo et al. (1990), Focacci et al. (2000) and Sena-Cruz (2005). This model was used for both smooth and hooked fibres. However, for hooked fibres, in order to account for the mechanical anchorage resistance at the embedded end, an additional spring component at the embedded end of the fibre was included, Figure 5.1. The pullout problem of hooked fibres is markedly a three dimensional problem. Nevertheless it was approached as two dimensional problem, since otherwise it would be more

difficult to plant an analytical model. Moreover, it seemed feasible to model the interfacial bond of the hooked fibre as a two dimensional axisymmetric problem, since the hook length is relatively smaller than the fibre length, and then introduce the anchorage component by a spring.

5.2 Theoretical relationships

5.2.1 Local bond - slip

The equilibrium of the free body of an infinitesimal length dx of a fibre bonded to a concrete matrix can be given by (see Figure 5.1(c)):

$$\sigma_f \cdot A_f + \tau \cdot P_f \cdot dx = (\sigma_f + d\sigma_f) \cdot A_f \tag{5.1}$$

where $\tau = \tau\left(s\left(x\right)\right)$ is the local bond shear stress acting on the contact surface between fibre and concrete, and s is the slip, i.e. the relative displacement between the fibre and the concrete. In equation 5.1, σ_f, A_f and P_f are the normal stress, cross section area and perimeter of the fibre, respectively.

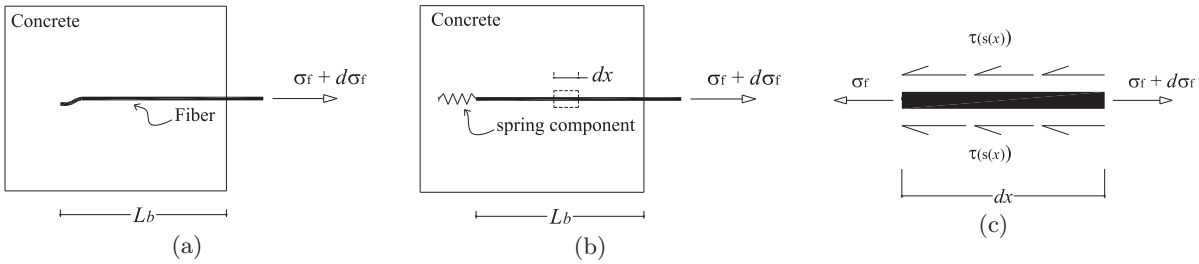

Figure 5.1: Axisymetric pullout model: (a) general problem, (b) simplified model (c) equilibrium of an infinitesimal fibre free-body.

Assuming that the fibre has a linear elastic constitutive law in the longitudinal direction ($d\sigma_f = E_f \; d\varepsilon_f$), equation 5.1 can be rewritten into:

$$\tau = \frac{E_f A_f}{P_f} \cdot \frac{d\varepsilon_f}{dx} \tag{5.2}$$

where E_f and ε_f are, respectively, the Young modulus and the strain of the fibre.

The strain components in a representative bulk of the fibre/concrete interface are indicated in Figure 5.2. The slip variation over an infinitesimal length, ds/dx, is given by:

$$\frac{ds}{dx} = \varepsilon_f - \varepsilon_c \tag{5.3}$$

where ε_c is the concrete strain. However, the contribution of the concrete deformability in the slip assessment may be neglected, since for the diameter of the steel fibres used in the current applications of SFRC, the deformation of the fibre is much higher than the deformation of the surrounding matrix. Several authors have neglected this component on the evaluation of the bond - slip relationship of reinforcing bars (Russo et al. 1990) or of FRP reinforcement (Focacci et al. 2000, Sena-Cruz 2005). In spite of this belief, in order to validate this assumption for small fibres, it was used an analytical model which took into account the deformation of the matrix surrounding the fibre (Sujivorakul et al. 2000) in the assessment of the pullout load - slip relationship. A sensitivity analysis was carried out using the latter model to evaluate the influence of the matrix deformation on the pullout response. For the current fibres lengths and matrix stiffness, the ε_c did not influence the slip value determination, since $\varepsilon_c << \varepsilon_f$.

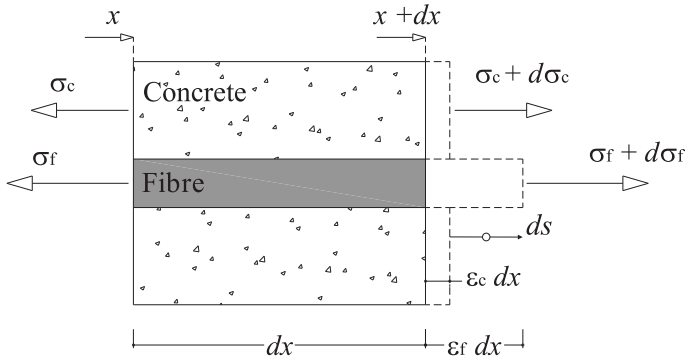

Figure 5.2: Stresses and strains on the fibre bond region.

Considering the abovementioned, neglecting the concrete deformability in the slip determination ($\varepsilon_c = 0$), incorporating the equation 5.3 into 5.2, the second order differential equation that governs the local bond phenomena of the fibre/matrix interface is given by:

$$\frac{d^2s}{dx^2} = \frac{P_f}{E_f\ A_f} \cdot \tau \tag{5.4}$$

5.2.2 Pullout load - slip relationship

The pullout load and slip relationship can be determined using either an energy approach (Focacci et al. 2000) or an equilibrium approach (Russo et al. 1990, Naaman et al. 1991b). In the present work will be adopted the energy approach.

Considering a steel fibre embedded into a concrete matrix over a bond length $\tilde{L}_b = L_b$, where N is the generic applied pullout force, and s_f and s_l are, respectively, the free and loaded end slips, with respect to the longitudinal axis of the fibre, x, starting at the free end (see Figure 5.3). When the fibre is slipping due to an applied pullout load, $\overline{N}$, the following functions can be evaluated along the fibre bond length: slip along the fibre, $s(x)$; bond shear stress along the embedded length, $\tau(x)$; fibre strain, ε_f; and the axial force, $N(x)$.

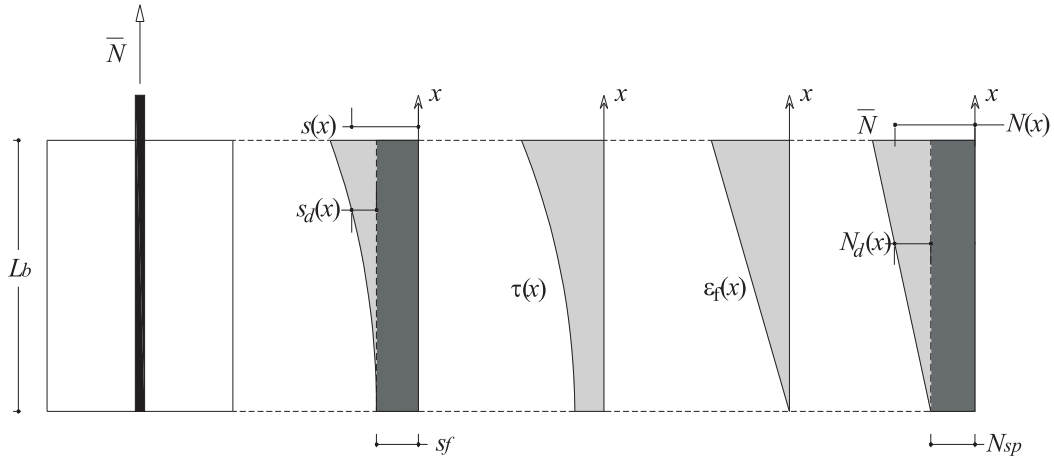

Figure 5.3: Entities evolved in the developed method.

In Figure 5.3 the slip diagram along the fibre, $s(x)$, can be regarded as the sum of two components. A constant component s_f that produces a rigid body displacement of the fibre, whereas the $s_d(x)$ component results from the deformation of the fibre. Moreover, for any point x of the fibre embedded length, just the $s_d(x)$ component will result in a fibre length change, and, therefore, contributing to the fibre deformation energy. Likewise, the axial force along the fibre, $N(x)$, can be decomposed into two components. A constant component N_{sp} due to the spring load (only in the case of hooked fibres) and the $N_d(x)$ component. Only the latter contributes to the fibre deformation energy, since in the adopted model it was assumed that N_{sp} will not produce a fibre length change. Therefore, the fibre deformation at a point x would be $\varepsilon_f(x) = N_d(x)/(E_f A_f)$. Considering a generic fibre cross section, constrained by $0 \leq \overline{x} \leq \tilde{L}_b$, and that the fibre lateral surface over embedded length is $\Omega = P_f \cdot \overline{x}$, the work performed by external forces acting on the range $0 \leq \overline{x} \leq \tilde{L}_b$ is:

$$W_{ext} = \int_{\Omega} \left(\int_{s_f}^{s(x)} \tau\,(s)\, ds \right) d\Omega = P_f \int_0^{\overline{x}} \left(\int_{s_f}^{s(x)} \tau\,(s)\, ds \right) dx \tag{5.5}$$

On the other hand, remarking that $V_f = A_f \cdot \overline{x}$ is the fibre volume over the embedded

length, the elastic energy of the fibre is:

$$W_{int} = \int_{V_f} \left(\int_0^{\varepsilon(x)} \sigma_f(\varepsilon_f)\, d\varepsilon \right) dV_f = A_f \int_0^{\overline{x}} \left(\int_0^{\varepsilon(x)} E_f \varepsilon_f d\varepsilon \right) dx$$
$$= \frac{A_f}{2E_f} \int_0^{\overline{x}} \sigma_f^2(x)\, dx \tag{5.6}$$

From equations 5.5 and 5.6 is obtained:

$$\int_0^{\overline{x}} \left(P_f \int_{s_f}^{s(x)} \tau(s)\, ds - \frac{A_f}{2E_f} \sigma_f^2(x) \right) dx = 0 \tag{5.7}$$

Since equation 5.7 must be satisfied for each value of $0 \leq \overline{x} \leq L_b$, this equation may be rewritten as:

$$P_f \int_{s_f}^{s(x)} \tau(s)\, ds - \frac{A_f}{2E_f} \sigma_f^2(x) = 0 \tag{5.8}$$

At $x = L_b$ equation 5.8 becomes:

$$P_f \int_{s_f}^{s\left(x=\tilde{L}_b\right)} \tau(s)\, ds - \frac{N_d^2}{2E_f A_f} = 0 \tag{5.9}$$

$$N_d = \sqrt{2E_f \cdot A_f \cdot P_f \int_{s_f}^{s\left(x=\tilde{L}_b\right)} \tau(s)\, ds} \tag{5.10}$$

Equation 5.10 allows to determine the generic applied pullout force for a smooth fibre, or in the case of a hooked fibre, the pullout load component at the fibre free end due to the interfacial bond of the fibre. Remarking that in the case of hooked fibres, the generic applied load is $\overline{N} = N_d + N_{sp}$ (see Figure 5.3), for the latter fibres the generic applied load is given by:

$$\overline{N} = \sqrt{2E_f \cdot A_f \cdot P_f \int_{s_f}^{s\left(x=\tilde{L}_b\right)} \tau(s)\, ds} + N_{sp} \tag{5.11}$$

5.3 Determination of the local bond stress - slip relationship

The local bond stress - slip relationship, $\tau - s$, was determined throughout the previous described theoretical relationships. The adopted method is supported on the work developed by Focacci et al. (2000) and Sena-Cruz (2005). In order to improve the performance of the method and to adapt it to the specificities of the present study, some modifications were implemented. In this section the implemented algorithm is described in detail.

5.3.1 Analytical bond stress - slip relationship

The obtained experimental pullout load - slip curves (see Figure 4.2) revealed a distinct pullout behaviour for the different fibre inclination angles studied, as previously described in Chapter 4. Therefore, in the present work, a distinct local bond law is proposed to define the stress-slip relationships for each inclination angle.

For the series with an inclination angle of 0º and 30º equations 5.12 and 5.13 were used, respectively.

$$\tau(s) = \begin{cases} \tau_m \left(\dfrac{s}{s_m}\right)^{\alpha} & \text{IF } s \leq s_m \\ \tau_m \dfrac{1}{1 + \left(\dfrac{s - s_m}{s_1}\right)^{\alpha''}} & \text{IF } s > s_m \end{cases} \tag{5.12}$$

$$\tau(s) = \begin{cases} \tau_m \left(\dfrac{s}{s_m}\right)^{\alpha} & \text{IF } s \leq s_m \\ \tau_m \left(\dfrac{s}{s_m}\right)^{-\alpha'} & \text{IF } s > s_m \end{cases} \tag{5.13}$$

where τ_m and s_m are, respectively, the bond strength and its corresponding slip. Parameter α defines the shape of the pre-peak branch, whereas α', α'' and s_1 describe the configuration of the post-peak branch of the curve. These relationships were selected due to its easiness and aptitude to accurately model the local bond stress-slip behaviour, as previously ascertained by several researchers (Eligehausen et al. 1983, Stang and Aarre 1992, Lorenzis et al. 2002, Sena-Cruz 2005).

On the other hand, for the series with a 60º inclination angle, the pullout load - slip curve could not be correctly simulated with the abovementioned laws. Consequently, for this inclina-

tion was adopted the quadri-linear law with the following generic form:

$$\tau(s) = \frac{\tau_i - \tau_{i-1}}{s_i - s_{i-1}} \cdot s + \tau_{i-1}, \quad s_{i-1} < s \leq s_i \tag{5.14}$$

where $i = 1, ..., 4$; τ_i and s_i are, respectively, the bond stress and its correspondent slip at point i, and τ_0 and s_0 are both zero and define the origin point of the bond stress - slip relationship.

5.3.2 Analytical relationship for the mechanical anchorage

The contribution of the end hook mechanism on the overall pullout behaviour was obtained separately for the series with a 0º, 30º and 60º inclination angle. The adopted procedure was described in section 4.4. In Figure 5.4 is depicted the analytical simulation of the hook mechanical contribution for the distinct inclination angles studied.

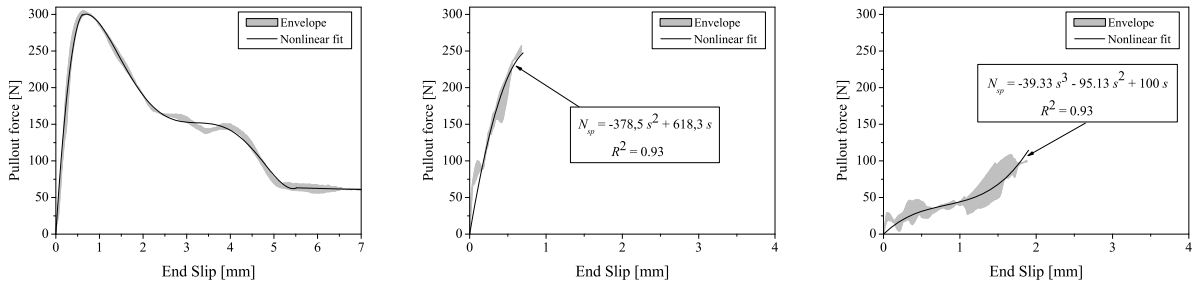

(a) (b) (c)

Figure 5.4: Analytical simulation of the hook mechanical contribution for the series with an inclination angle of: (a) 0º, (b) 30º and (c) 60º

The analytical expressions for the series with a 30º and 60º inclination angle are given in Figure 5.4, whereas for the aligned series the analytical expression is given by equation 5.15. Remark that for the inclined series the contribution of the hook was only assessed for an initial stage, since, in general, fibre rupture occurred during the fibre pullout on these series.

$$N_{sp} = \begin{cases} 918.98 \cdot s - 717.1 \cdot s^2 & \text{IF} \quad s \leq 0.6 \\ 2.2423 \cdot s^5 - 35.326 \cdot s^4 + 201.61 \cdot s^3 & \\ \quad -497.84 \cdot s^2 + 444.79 \cdot s + 171.96 & \text{IF} \quad 0.6 < s \leq 5.5 \\ -1.57 \cdot s + 70.0 & \text{IF} \quad s > 5.5 \end{cases} \tag{5.15}$$

5.3.3 Description of the method

Regarding the entities described in Figure 5.3, the boundary conditions at the free and loaded ends for smooth fibres and hooked fibres can be stated by equation 5.16 and equation 5.17, respectively. In the present method, both numerical and experimental entities are simultaneously used, hence the experimental ones were distinguished by an overline, i.e. $\overline{N}^i$ stands for the pullout force experimentally measured in the i-th scan read-out. Additionally, remark that for a smooth fibre $N_d(\tilde{L_b}) = \overline{N}$. On the other hand, for a hooked fibre, $\overline{N} = N_d(\tilde{L_b}) + N_{sp}$.

$$x = 0 \rightarrow \begin{cases} s(0) = s_f \\ N(0) = 0 \\ \varepsilon_f(0) = 0 \end{cases} \qquad x = \tilde{L}_b \rightarrow \begin{cases} s(\tilde{L}_b) = s_l \\ N(\tilde{L}_b) = \overline{N} \\ \varepsilon_f(\tilde{L}_b) = N_d(\tilde{L}_b)/(E_f A_f) \end{cases} \tag{5.16}$$

$$x = 0 \rightarrow \begin{cases} s(0) = s_f \\ N(0) = N_{sp} \\ \varepsilon_f(0) = 0 \end{cases} \qquad x = \tilde{L}_b \rightarrow \begin{cases} s(\tilde{L}_b) = s_l \\ N(\tilde{L}_b) = \overline{N} \\ \varepsilon_f(\tilde{L}_b) = N_d(\tilde{L}_b)/(E_f A_f) \end{cases} \tag{5.17}$$

where s_f and s_l are, respectively, the slips at the free and loaded ends, and A_f and E_f are the cross section area and elasticity modulus of the fibre.

The fibre pullout tests provide, in terms of pullout load, $\overline{N}$, and loaded end slip, $\overline{s}_l$, several scan read-outs, being $\overline{s}_l^i$ and $\overline{N}^i$ the values of the i-th scan read-out. Regarding these experimental results, the set of unknown parameters of a given local bond relationship (equations 5.12, 5.13 and 5.14) is obtained by fitting the differential equation 5.4 as accurately as possible. A computational code was developed and implemented, supported on the algorithm described in Figure 5.5. The second order differential equation 5.4 included in the algorithm is solved by the Runge-Kutta-Nyström (RKN) method (Kreyszig 1993), which is detailed in Annex III. The algorithm is built up from the following main steps:

1. the $\tau - s$ relationship is defined attributing values to the unknown parameters. The error, e, defined as the area between the experimental and analytical curves, is initialized;

2. the loaded end slip is calculated at the onset of the free end slip, $\tilde{s}_l$, (see Module A in Figure 5.6);

3. for the experimental i-th scan reading, the loaded end slip, $\overline{s}_l^i$, and the pullout force, $\overline{N}$ are read;

4. taking the loaded end slip, $\overline{s}_l^i$, and using equation 5.4, the pullout force at the loaded end, $N^i(s_l^i)$, is evaluated. In this case the following two loaded end slip conditions must be considered:

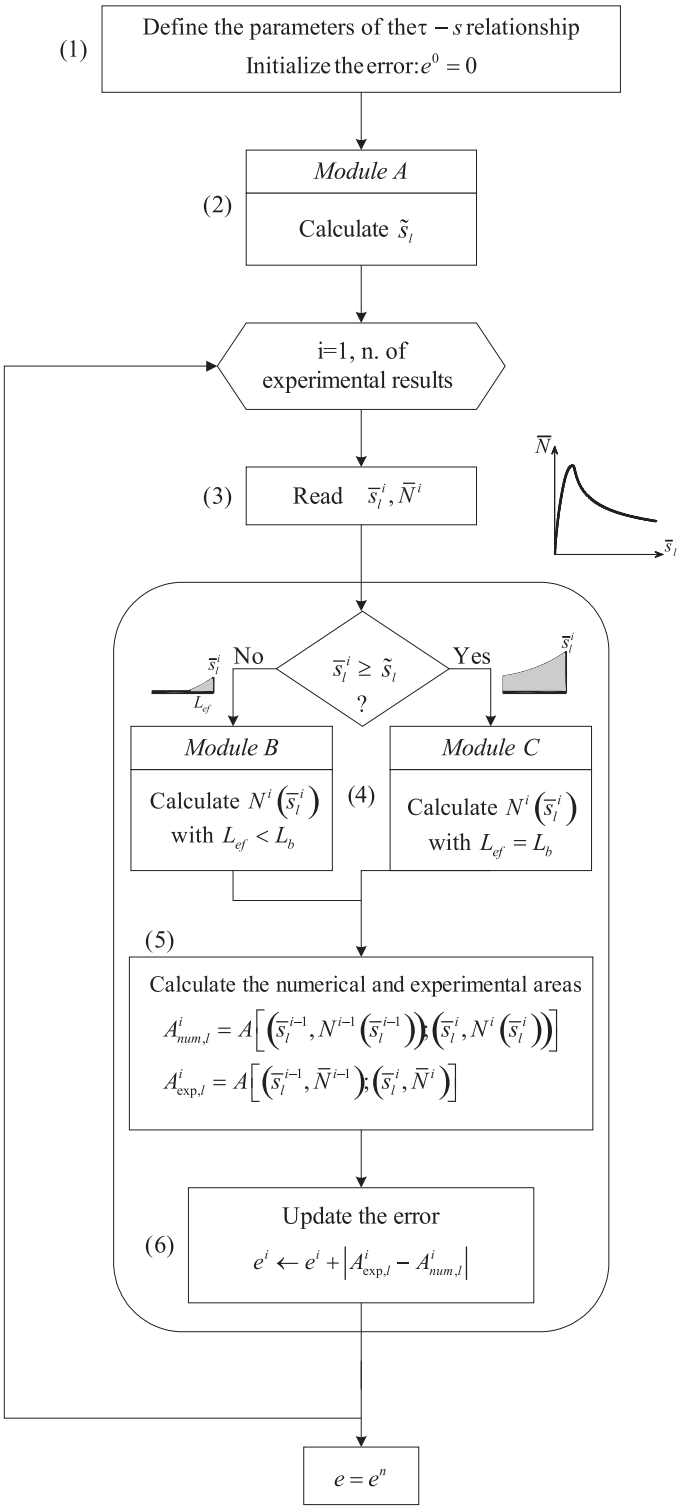

Figure 5.5: Algorithm implemented to obtain the local bond-stress slip relationship.

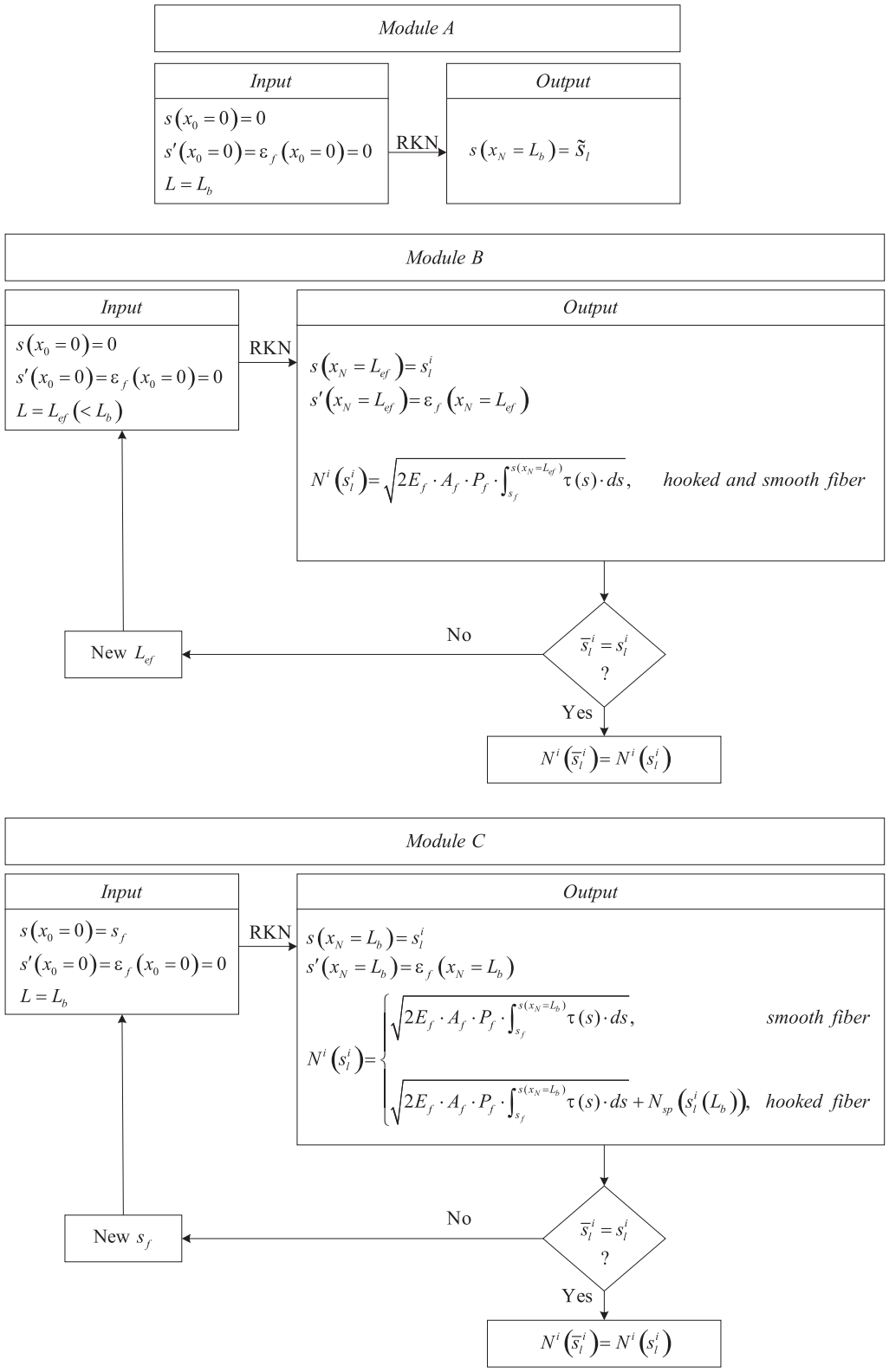

Figure 5.6: Modules A, B and C of the algorithm shown in Figure 5.5.

i) if $\overline{s}_l^i < \tilde{s}_l$, the determination of $N^i(s_l^i)$ must take into account that the effective bond length is smaller than the fibre embedded length (see Module B on Figure 5.6). For the case of hooked fibres, the mechanical anchorage contribution is not considered, since the fibre is not yet fully debonded;

ii) if $\overline{s}_l^i \geq \tilde{s}_l$, the evaluation of $N^i(s_l^i)$ is based on Module C (see Figure 5.6). In the latter module, the contribution of the hook end, $N_{sp}(s_l^i(L_b))$, is assessed by the equations presented in section 5.3.2;

5. the error associated with $N^i(s_l^i)$ is calculated. This error is the area between the experimental ($A^i_{exp,f}$) and numerical ($A^i_{num,f}$) curves. The points $(\overline{s}_l^{i-1}, N^{i-1}(\overline{s}_l^{i-1}))$ and $(\overline{s}_l^i, N^i(\overline{s}_l^i))$ are used to define the numerical curve, whereas the experimental curve is represented by the points $(\overline{s}_l^{i-1}, \overline{N}^{i-1})$ and $(\overline{s}_l^i, \overline{N}^i)$;

6. the error is updated.

In Modules B and C the Newton Raphson method is used. Whenever the Newton Raphson method fails, the bisection method is used as an alternative.

The algorithm previously detailed was used for both aligned and inclined fibres. In order to use it for inclined fibres several issues must be clarified. As previously said, the pullout behaviour of inclined fibres is a very complex problem, since several mechanisms interact with each others during pullout. The establishment of an analytical model that takes in consideration those mechanisms is much more difficult. Therefore, to simulate inclined fibres the following aspects were neglected: bending and plastification of the fibre, spalling of the concrete matrix at the fibre exit point, and finally, the change on the embedded length due to matrix spalling. Moreover, for ascertaining the local bond stress - slip law of inclined fibres only the pullout load component on the fibre axis was used, since it is the only component dedicated to generate interfacial stresses along the fibre. In practical terms, the pullout load component on the fibre axis is $\overline{N}^i \cdot \cos\alpha$.

The determination of the unknown parameters defining the bond stress - relationship, $\tau - s$, was performed by a back-analysis, i.e. determining the $\tau - s$ relationship in such a way that the difference between the numerical and experimental load - slip curves corresponds to minimum error, e. Additionally, two restriction conditions were added in order to assure similar values between the numerical and experimental peak pullout load and its corresponding slip (with a tolerance smaller than 2%). The back-analysis was performed by the exhaustive search method (brute force method), based on several parameters sets ascertained by a predefined range and step for each parameter of the corresponding set.

5.4 Parameters for the local bond stress - slip relationship

The values of the parameters of the defined local bond stress-slip relationships (see equations 5.12, 5.13 and 5.14) were determined using the numerical strategy described in section 5.3.3. The local bond stress - slip relationship for each series was calibrated from the average experimental pullout load - slip curve. In the model was adopted a Young modulus, E_f, of 200 GPa, a cross sectional area, A_f, of 0.562 mm^2 and a cross section perimeter, P_f, of 2.356 mm.

In Figures 5.7, 5.8 and 5.9 are depicted both the numerical pullout load - slip relationship and the experimental envelope for each tested series. On the other hand, the values of the parameters defining the local bond relationships obtained by back analysis are included in Table 5.1 (0^o series), Table 5.2 (30^o series) and Table 5.3 (60^o series). Moreover, in the abovementioned tables is also included the corresponding normalised error, $\overline{e}$, which was defined as the ratio between e and the area under the experimental curve.

The numerical curves fitted the experimental data extremely accurate even for high slips, as the normalised error in each series is quite low. In Tables 5.1, 5.2 and 5.3 are also indicated the average values and corresponding coefficients of variation of the local bond law parameters. In spite of the accurateness of the numerical simulation, the coefficients of variation of the bond law parameters were extremely high. This fact can be related to the method used in back - analysis (exhaustive search), since the parameters search is based on a previously defined range and step, i.e. the parameter variables are discrete. Moreover it was only used one objective function, i.e. difference between the area under the experimental and numerical curves to determine the best fit for each series. A possible way to solve this problem could be the utilisation of a multi-objective function.

Regarding the abovementioned, the interpretation of the obtained results can not be conclusive. However, in spite of the high coefficients of variation, some trends can be observed. For the series with a 30^o and 60^o inclination angle, the bond strength, τ_m (30^o) and τ_1 (60^o), decreased with the increase of the bond length. Moreover, the bond strength average value increased for the series with a 30^o angle (i.e. from 0^o to 30^o), and afterwards decreased abruptly (i.e. from 30^o to 60^o). The smaller bond strength value for the series with a 60^o inclination angle was expected, since for this series cracking of the matrix, and consequently degradation of the local bond strength, started for a lower load level. The higher value of the bond strength for the series with a 30^o angle can be explained by the fact that the frictional resistance increases with the inclination angle. Additionally remark that the post-peak branch of the local bond law is defined in function of the bond strength (see equation 5.13). On the other hand, the increase of the frictional resistance was even more pronounced for the 60^o series, however, with

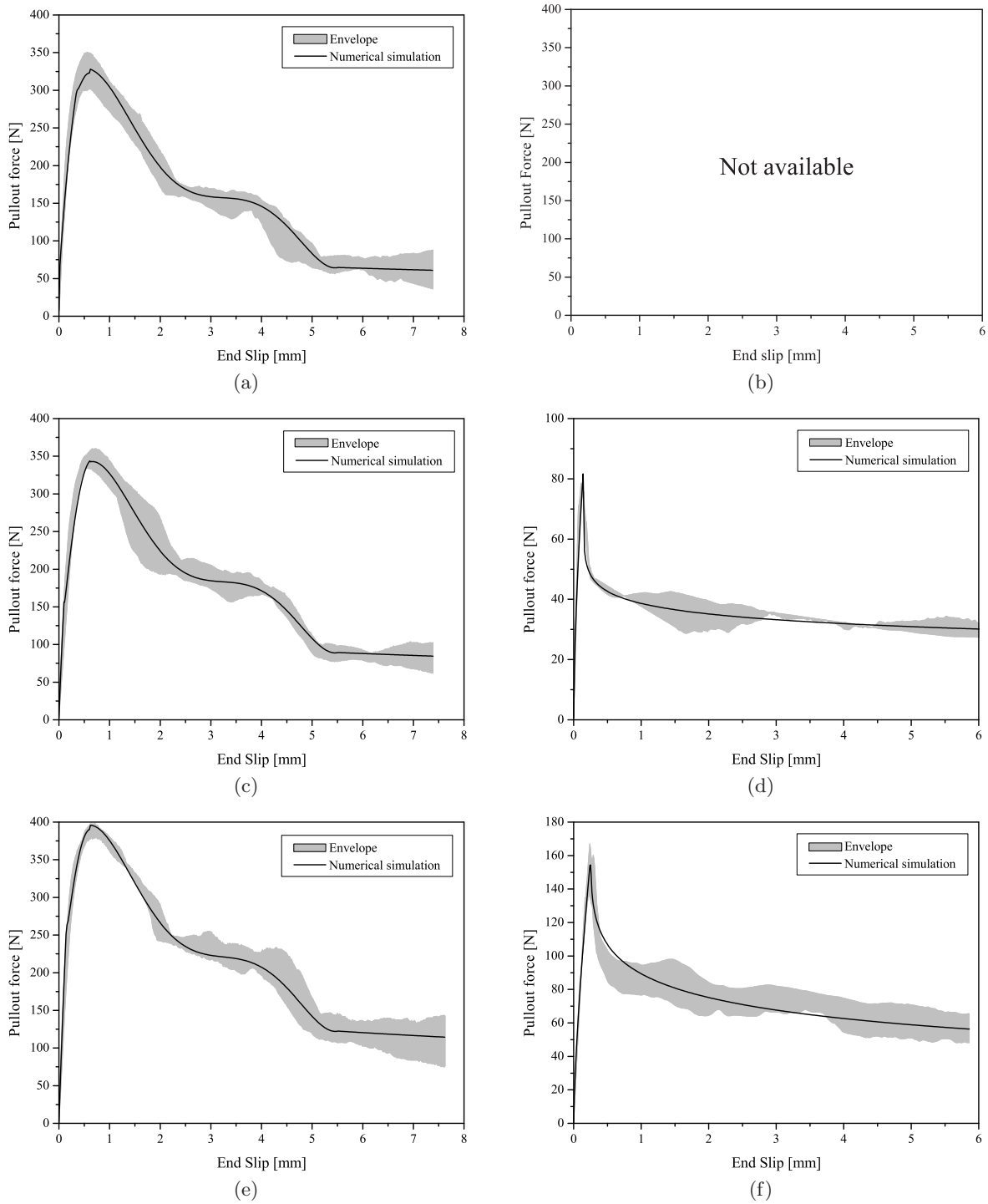

Figure 5.7: Pullout load - slip numerical simulation for a 0º fibre inclination angle: (a), (c) and (e) hooked end fibre with an embedded length of 10, 20 and 30 mm, respectively. (b), (d) and (f) smooth fibres with an embedded length of 10, 20 and 30 mm, respectively.

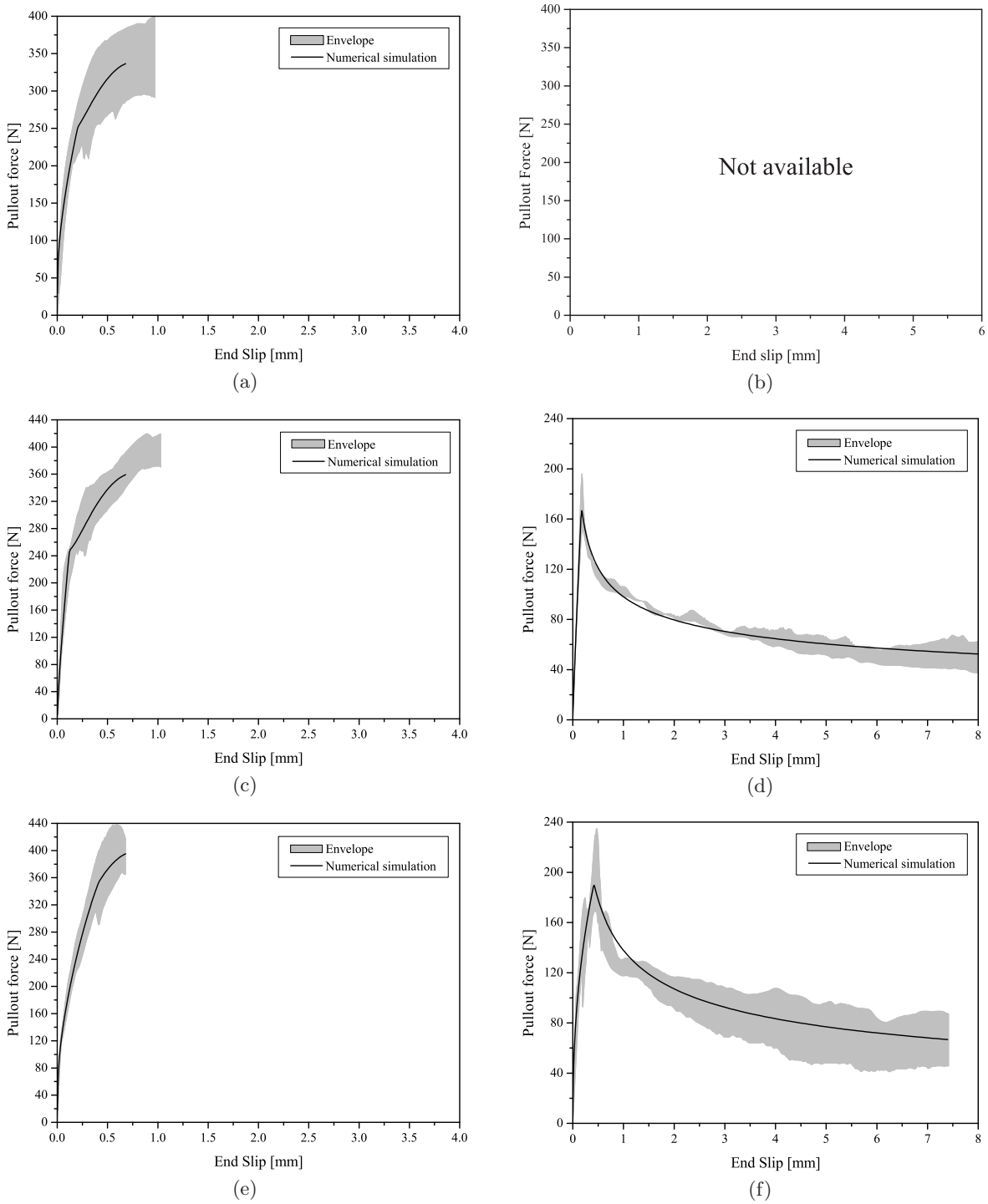

Figure 5.8: Pullout load - slip numerical simulation for a 30º fibre inclination angle: (a), (c) and (e) hooked end fibre with an embedded length of 10, 20 and 30 mm, respectively. (b), (d) and (f) smooth fibres with an embedded length of 10, 20 and 30 mm, respectively.

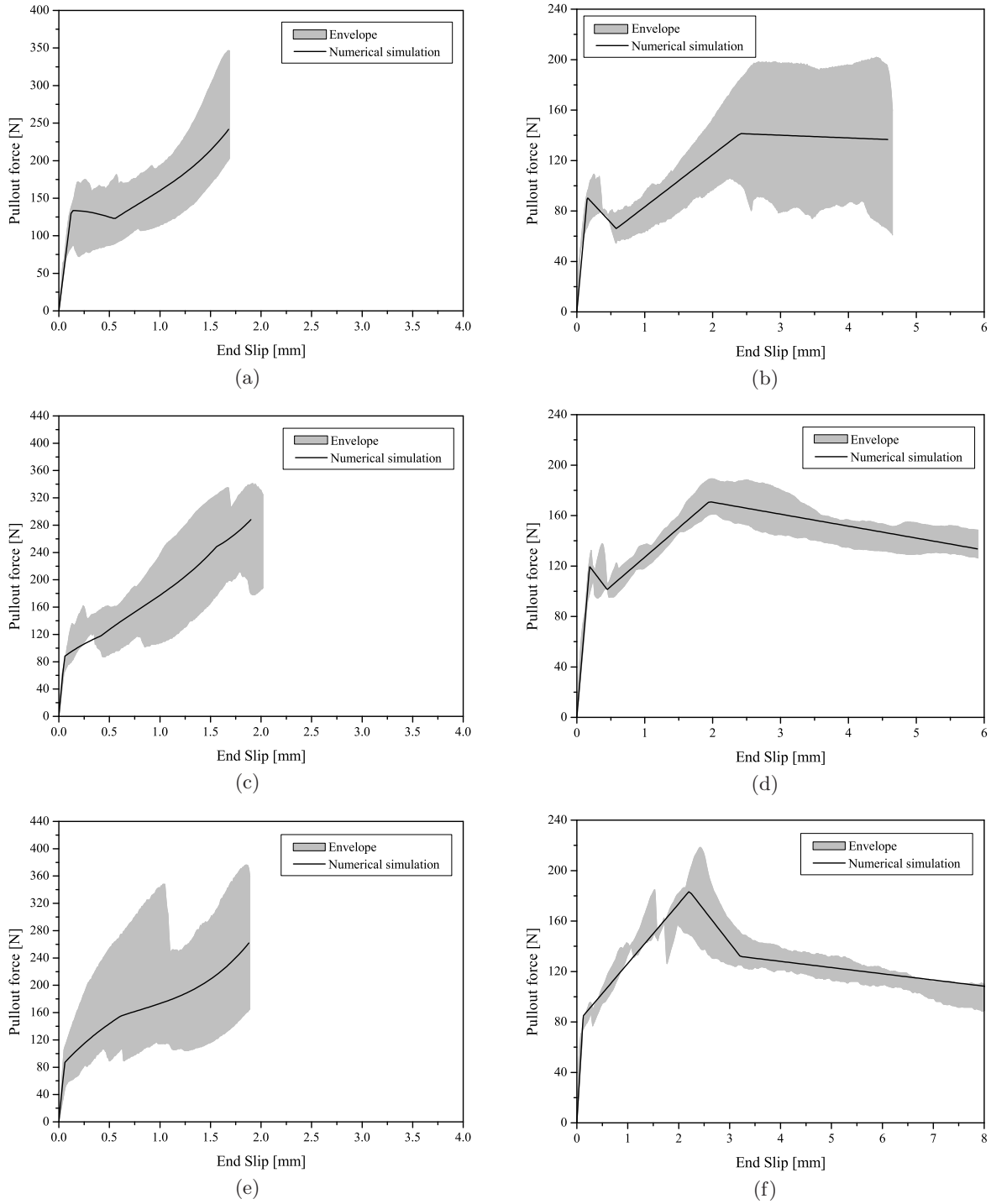

Figure 5.9: Pullout load - slip numerical simulation for a 60° fibre inclination angle: (a), (c) and (e) hooked end fibre with an embedded length of 10, 20 and 30 mm, respectively. (b), (d) and (f) smooth fibres with an embedded length of 10, 20 and 30 mm, respectively.

a lower bond strength. For these reasons the bond laws used for the series 0° and 30° are not suitable for the series 60°. Additionally, the multi-linear bond law used to model the series 60° allowed that the post-peak branch of this law could be defined independently of the bond strength parameter. Therefore, parameter τ_3 of the multi-linear bond stress - slip law can not be regarded as the bond strength, although being considerable higher than τ_1 (see Table 5.3).

Table 5.1: Parameters for the local bond stress - slip relationship obtained by back analysis for the aligned series.

SERIES	s_m [mm]	τ_m [MPa]	α [-]	α'' [-]	s_1 [mm]	$\overline{e}$ [%]
S_lb20_0	0.14	1.77	0.60	0.22	0.44	3.2
S_lb30_0	0.24	2.27	0.69	0.42	1.30	5.0
H_lb10_0	0.25	1.61	0.22	0.88	0.53	4.3
H_lb20_0	0.23	1.80	0.84	0.45	1.10	2.2
H_lb30_0	0.14	2.10	0.89	0.42	2.21	1.9
Average	0.20 (24%)	1.91 (11%)	0.65 (37%)	0.48 (45%)	1.11 (57%)	-

Values in round brackets are the coefficients of variation of the corresponding series.

Table 5.2: Parameters for the local bond stress - slip relationship obtained by back analysis for the series with an inclination angle of 30°.

SERIES	s_m [mm]	τ_m [MPa]	α [-]	α' [-]	$\overline{e}$ [%]
S_lb20_30	0.16	3.12	0.90	0.30	4.1
S_lb30_30	0.40	2.34	0.42	0.36	3.4
H_lb10_30	0.28	4.31	0.13	0.34	2.2
H_lb20_30	0.11	3.29	0.70	0.25	1.4
H_lb30_30	0.40	1.99	0.21	0.16	1.3
Average	0.27 (50%)	3.01 (30%)	0.47 (69%)	0.28 (28%)	-

Values in round brackets are the coefficients of variation of the corresponding series.

Table 5.3: Parameters for the local bond stress - slip relationship obtained by back analysis for the series with an inclination angle of 60°.

Series	s_1 [mm]	τ_1 [MPa]	s_2 [mm]	τ_2 [MPa]	s_3 [mm]	τ_3 [MPa]	s_4 [mm]	τ_4 [MPa]	$\overline{e}$ [%]
S_lb10_60	0.15	1.92	0.58	1.40	2.40	3.07	4.58	5.80	3.1
S_lb20_60	0.18	1.27	0.44	1.08	1.94	3.63	20	0	1.6
S_lb30_60	0.12	0.91	2.17	1.95	3.19	1.82	30	0	3.8
H_lb10_60	0.12	2.62	0.54	1.90	1.72	1.39	10	0	3.2
H_lb20_60	0.05	0.88	0.41	0.95	1.55	3.33	20	0	4.1
H_lb30_60	0.06	0.58	0.62	0.84	2.22	1.85	30	0	2.8
Average	0.11 (44%)	1.36 (56%)	0.79 (85%)	1.35 (36%)	2.17 (27%)	2.51 (37%)	19.1 (54%)	-	-

Values in round brackets are the coefficients of variation of the corresponding series.

5.5 Conclusions

To predict the experimental pullout load - slip relationships, an analytical model was developed. For this purpose a computational code was implemented with the developed analytical model. The local bond stress - slip law parameters were obtained by a back-analysis performed by the exhaustive search method. In the following paragraphs the main conclusions withdrawn in the present study will be presented.

The analytical model presented was able to simulate with extreme accuracy the experimental pullout load - slip curves, even for high slips for both hooked and smooth fibres (aligned or inclined). In the simulation of inclined fibres, the present model neglected the following aspects: bending and plastification of the fibre, spalling of the concrete matrix at the fibre exit point and, finally, the change on the embedded length due to matrix spalling. In spite of the accurateness of the numerical simulations, the coefficients of variation of the bond law parameters were extremely high. This fact can be related to the method used in back-analysis (exhaustive search), since the parameters search is based on a previously defined range and step, i.e. the parameter variables are discrete. Moreover, it was used only one objective function, i.e. difference between the area under the experimental and numerical curves, to determine the best fit for each series. A possible way to solve this problem could be the utilisation of a multi-objective function, hence additional study should be performed in order to ascertain the local bond law parameters with a lower coefficient of variation.

In spite of the high coefficients of variation for the local bond law parameters, some trends could be observed. For the inclined series, the bond strength decreased with the increase of the

embedded length increment. Regarding the influence of the inclination angle, the bond strength average value increased for the fibres at 30° (i.e. from 0° to 30°), and afterwards decreased abruptly (i.e. from 30° to 60°). The smaller bond strength value for the series with a 60° inclination angle was expected, since for this series cracking of the matrix and, consequently, degradation of the local bond strength started for a lower load level. A higher value of the bond strength parameter was obtained for the series with a 30° angle due to two main reasons: the higher frictional resistance observed for the inclined series, and to the fact that the post-peak stress of the local bond law used, for the series with a 30° inclination angle, was defined in such a way that it is dependent from the obtained numerical bond strength. The increase of the frictional resistance was even more pronounced for the 60° series, however, with a lower bond strength, since the bond law used for the 60° series allowed that the post-peak branch of this law could be defined independently from the bond strength parameter.

Part II

Mechanical Behaviour of SFRSCC (from meso to macro-scale)

Chapter 6

Fibre Structure in the Composite Matrix

6.1 Introduction

In fibre reinforced composites, FRC, relations of a law-of-mixture type are often used to describe the mechanical behaviour of the composite, assuming for this purpose that the fibres are distributed uniformly at random nature through the matrix. Therefore, in order to take into account a disorder nature of fibre distribution in general applications of FRC, it is used a coefficient which considers the fibre efficiency reduction (Stroeven 1986b). Moreover, usually this coefficient is obtained by regression, which best fits the experimental data (Swamy et al. 1974).

In spite of fibre distribution within a cementicious matrix being commonly assumed as "random", i.e. isotropic uniformly random distribution – IURD, nowadays it is widely accepted that are factors which promote the re-orientation of such fibres (Stroeven 2008). Amongst these factors, it can be pointed out the geometry of the fibre, casting procedure, geometry of the mould, compaction energy and rheology properties of concrete. The factors, which influence the fibre efficiency, can be divided into two main groups. The first group comprises the factors that lead to an increase of the fibre efficiency by the improvement of the bond properties of a single fibre, and were largely discussed in Chapter 2. The other group is related to the fibre structure. Among these factors it can be quoted the fibre distribution inhomogeneity along an element, segregation of fibres over the depth of an element, boundary effect and effectiveness of fibre orientation. All of them may either increase (in the case of a preferential alignment towards the direction of the principal tensile stresses) or reduce the residual strength of a FRC in comparison to the residual strength of a hypothetically FRC in which the fibres are uniformly

random distributed.

According to Stroeven and Shah (1978), the real fibre dispersion and orientation, in the more general case, can be expressed by a combination of three, two and one-dimensional fibre orientation arrangements, i.e. 1D, 2D and 3D systems. Nevertheless, according to Stroeven (1986b) it has been proven to be sufficiently accurate to assume the actual fibre distribution is governed by a mixture of two and three-dimensional fibre orientation arrangements. This holds true, if fibre orientation is not significantly deviated from the state of rotational symmetry, otherwise it would be necessary to add a 1D fibre orientation arrangement as well (Stroeven 1986b). In low-volume fibre reinforced concretes, the fibre reinforcement contribution in the un-cracked stage is quite reduced. Therefore, the prime contribution of the fibre reinforcement arises after the crack localization. Remark that not all local fibre reinforcement will be activated in the stress transfer over cracks, in fact only a small parcel of the fibres in bulk will take part in the crack opening control. These fibres are the so-called effective or active portion of fibres (Stroeven 2008). Moreover, the number of fibres intersecting the active crack will be correlated with the average spacing of fibres within the matrix (Soroushian and Lee 1990).

The post-cracking behaviour of fibre reinforced composites assessed from different types of test specimens does not necessarily provides the correct post-cracking relation to be used in structural design. There are several reasons that justify this statement. One of the most preponderant factors for possible errors is the deviation in preferred orientation between the fibre reinforcement in a test specimen and in a structural element. Moreover, the effectiveness of fibre reinforcement strongly depends on the fibre orientation towards the orthogonal direction(s) of the principal tensile stress(es) (Kooiman 2000). Therefore, the post-cracking material behaviour obtained from the test results has to be translated into the expected material behaviour in a structural element.

The widespread use of steel fibre reinforced concrete, SFRC, on full load bearing structural applications is yet to some extent limited, if having in mind that the appearance of this material dates back to the early sixties. The high scatter of the SFRC material behaviour, in part due to non-uniform fibre dispersion, contributes to the mistrust in this material. To contribute for a higher self-confidence in the use of FRC is of vital importance reducing the material behaviour scatter and, consequently, enabling the adoption of lower material safety factors (Shah and Ferrara 2008). Thus, it is necessary to effectively control the fibres dispersion within a structural element along its manufacturing and casting process. An improper casting of a structural element leads to a higher non-uniformity in the fibres dispersion, which results in reduced or even nil amount of fibres on certain spots of the structural element. These locations may jeopardize the structural performance either in terms of failure mechanisms and ultimate loads (Ferrara and Meda 2006, Shah and Ferrara 2008).

The use of self-compacting matrices takes advantage of the elimination of any kind of external vibration, resulting on improvements in terms of rheological stability in the fresh state which leads during casting to a more uniform distribution of fibres within the structural elements (Shah and Ferrara 2008). Self-compacting concrete is effective in guaranteeing a more uniform dispersion of fibres within the specimen, as well in effectively orienting them along the casting direction. When comparing the fibre distribution in plates of self-compacting concrete and conventional vibrated ones, the fibre dispersion is almost twice as much scattered in the vibrated ones (Shah and Ferrara 2008). Throughout a suitable balance of the fresh state concrete properties, mainly the fluid viscosity, fibres can be effectively oriented along the direction of the flow (Ferrara et al. 2007, Stähli et al. 2008). Therefore, it is desirable to design together with the mix composition also the casting procedure, so that the concrete flow direction along which fibres may be aligned, coincide with the direction of the principal tensile stresses within the structural element when in service and, consequently, enhance the structural performance (Ferrara et al. 2008).

This chapter provides a brief overview of the main factors which influence the fibre density and orientation in a concrete medium. Additionally, it is presented an insight view of distinct methodologies for ascertaining the fibre distribution in a cement matrix. The main parameters which characterize the fibre distribution within the studied self-compacting matrix will be assessed and discussed. These parameters enable a better comprehension of the differences between the post-cracking behaviour obtained from three-point bending tests and uniaxial tests, which will be posteriorly presented in Chapter 8. In addition, the fibre orientation factors experimentally ascertained will be also used in the numerical generation of virtual fibre meshes, to be used under the scope of the finite element method model developed and presented in Chapter 9.

6.2 Factors influencing the fibre structure

The main factors that can influence the morphological characteristics of the fibre distribution and favour the fibre alignment in a structural element are: boundary of formwork, specimen size, casting direction (gravity), type of compaction, mixture composition and rheological properties, and presence of reinforcing bars or other kind of obstacles. The fibre orientation in conventional steel fibre reinforced concrete, CFRC, has been investigated, by several researchers, e.g. Stroeven (1978, 1979), Babut (1986), Soroushian and Lee (1990), Toutanji and Bayasi (1998), Dupont (2003), Gettu et al. (2005). Within concrete matrices with high-flowability in the fresh state, such as self-compacting concrete, SCC, the flow direction strongly affects the fibre orientation. Obviously, in SCC the re-orientation of fibres due to vibration can be excluded, since for

this material it is not employed any kind of compaction's external energy. More recently, several authors have investigated the fibre orientation in self-compacting matrices, e.g. Grünewald (2004), Schumacher (2006), Markovic (2006), Lappa (2007), Torrijos et al. (2008), Vandewalle et al. (2008), Stähli et al. (2008).

The casting procedure and characteristics of the mould affect the fibre distribution. Moreover, the wall effect clearly depends on the ratios between the dimensions of the mould and length of fibres (Soroushian and Lee 1990, Torrijos et al. 2008). According to Torrijos et al. (2008) in beams cast vertically (like a column), a more homogeneous fibre orientation was found. However, the fibre reinforcement was notably less efficient from the mechanical point of view, since a relatively low content of fibres is oriented in the direction of the principal tensile stresses (Torrijos et al. 2008), see Figure 6.1. On the other hand, the orientation of fibres along the formwork boundaries, the so-called wall effect, is as more predominant as smaller are the specimens dimensions. Nevertheless, the volume at a FRC element affected by the wall effect also depends of the fibre length, since the fibre orientation is affected by the formwork boundaries up to a distance of one time the fibre length (Stroeven and Hu 2006). Hence, hypothetically speaking, if the fibre length and specimen dimensions ratio is maintained, the wall effect when decreasing the specimen dimensions (and consequently the fibre length) would have in percentage the same impact on the fibre orientation.

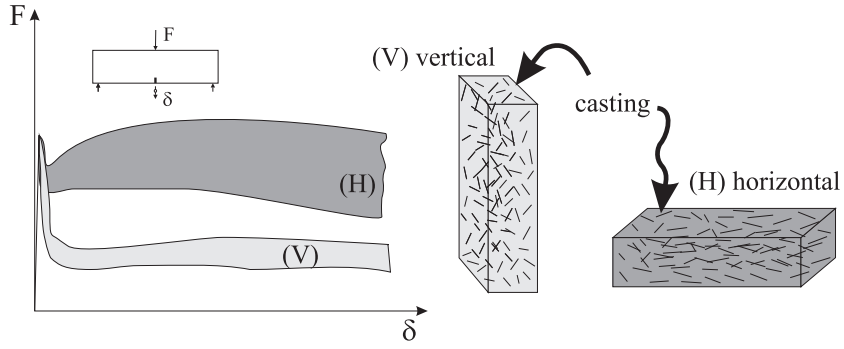

Figure 6.1: Influence of the casting procedure on the SFRSCC flexural behaviour.

In CFRC, fibre orientation, and consequently fibre density (the number of fibres per unit area crossing a certain section), are not only influenced by the boundaries that restrict the random orientation of fibres, but also by the compaction by vibration, which tends to re-orient the fibres in horizontal planes (Soroushian and Lee 1990). According to Gettu et al. (2005), internal vibration does not has a significant effect on the fibre orientation, since it appeared to preserve the fibre's isotropy. On the other hand, table vibration induces a preferential horizontal alignment of fibres. For over-vibrated specimens, in particular 90 seconds, a clear preferential

fibre orientation together with segregation were observed. Nevertheless, the abovementioned should be looked upon with care, since from other research (Babut 1986), the increase of the vibration time induced a fibre re-orientation, from a preferential horizontal orientation of the fibres (without vibration) to a more isotropic fibre orientation (vibration time of 180 seconds). The results from bibliography are somehow distinct, and cannot be regarded as an axiomatic true, since there are several parameters which are intercorrelated with the vibration time and thus affecting the fibre orientation in distinct ways.

Technological parameters, compaction and placing procedures influence not only the fibre orientation, but also other morphological characteristics of the fibre distribution (Stroeven 1979, Babut 1986). Other technological parameters such as fibre content, vibration frequency, workability (as influenced by the addition of superplasticizer) also influence the fibre distribution. Therefore all the aforementioned factors that affect the fibre morphology, directly influence the mechanical properties of a FRC. The boundary and segregation effects increase with the fibre volumetric percentage. However, remark that the segregation effect cannot be captured in sections perpendicular to the gravity axis (Stroeven 1979, Babut 1986). In research carried out by Babut (1986), the variation of the degree of segregation was low. In spite of that, a slight decrease of the segregation coefficient could be observed with an increase of fibre content (parallel to gravity axis), since the fibres are blocked by themselves and the aggregates skeleton. In what concerns to the influence of vibration time in the segregation degree, i.e. the fibre distribution over the cross sectional height of the specimens. Several authors (Stroeven 1979, 1986b, Babut 1986, Barros and Antunes 2003, Gettu et al. 2005, Ozyurt et al. 2007) have found similar findings, i.e. the increase of the vibration time increase the fibre segregation. Stroeven (1986b) observed that without compaction a rather uniform fibre distribution was observed along the height of the cross sections of conventional FRC. The type of fibre (hooked versus straight) does not have a significant influence on the fibre density and therefore on the segregation degree (Soroushian and Lee 1990).

In what concerns self-compacting concrete, several researchers (Grünewald 2004, Schumacher 2006, Lappa 2007, Stähli et al. 2008, Vandewalle et al. 2008, Ferrara et al. 2008) have observed in prismatic specimens a fibre alignment effect due to the concrete flow, since the fibres were mainly aligned perpendicular to the cross section of the prismatic specimen (fracture surface). Grünewald (2004) and Markovic (2006) have also observed an increase on the orientation factor with the fibre length increase. Beside the aforementioned fibre alignment, Lappa (2007) observed an alignment of fibres along a circular flow in the mould as the concrete was flowing from the the top to bottom of the mould. Moreover, according to Vandewalle et al. (2008), Stähli et al. (2008), after a certain flow distance the fibre alignment does not changes any more, similar findings were observed by Schumacher (2006). In the study carried out by

the latter author, the fibre segregation over the specimen's height due to the gravity influence was not significant. Indeed, more fibres were found in the specimen's top half, however, this tendency was not pronounced and was within the scatter observed for those cross-sections.

On the other hand, Stähli et al. (2008) assessed in a qualitative fashion the fibre segregation due to gravity, concluding that the fibre segregation leads to a much higher bending strength than expected due to fibre alignment only. Supposedly, the fibre alignment in self-compacting concrete along the flow may be ascribed to both the wall-effect and the velocity profile in concrete developed most likely due to frictional restraint along the walls of the mould (Stähli et al. 2008). In Figure 6.2 is schematically represented a possible explanation for the fibre alignment due to a non-linear velocity profile of the concrete's flow in the fresh state. The fibre alignment in prismatic specimens leads to higher post-cracking strength, when compared to conventional vibrated fibre reinforced concrete (Grünewald 2004, Vandewalle et al. 2008, Torrijos et al. 2008, Stähli et al. 2008, Ferrara et al. 2008).

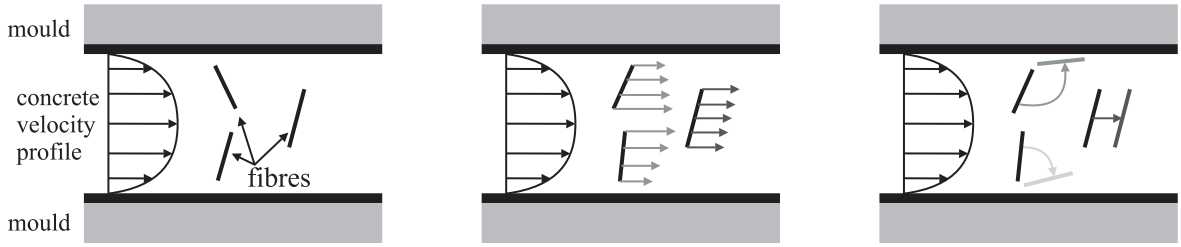

Figure 6.2: Explanation for the fibre alignment due to a non-linear velocity profile of the concrete's flow (Stähli et al. 2008).

6.3 Parameters of the fibre structure

In this section will be presented some analytical expressions found in literature (Krenchel 1975, Kasperkiewicz et al. 1978, Stroeven 1978, 1979, Kamerwara Rao 1979, Stroeven 1986b, Babut 1986, Soroushian and Lee 1990, Stroeven and Hu 2006) that can be used to characterize the fibre distribution within a cementicious matrix. They are generally based on the dimensions and volume of fibres used, and can be employed to predict the uniformity and isotropy of the fibre distribution as a function of the compaction and casting procedures.

6.3.1 Effective number of fibres

The expected number of fibres that intersects a plane, N_f^{3D}, (herein after will be designated by effective number of fibres) can be defined by (Babut 1986):

$$N_f^{3D} = \frac{2 \cdot V_f}{\pi \cdot d^2} \cdot 100/100 \text{ mm}^2 \tag{6.1}$$

where d and V_f are, respectively, the fibre diameter [mm] and the fibre content [per cent by volume]. This analytical expression is nonetheless than a simplification of equation 6.2 (Krenchel 1975, Soroushian and Lee 1990) assuming a three-dimensional isotropic uniform random distribution:

$$N_f = \eta \cdot \frac{V_f}{A_f} \tag{6.2}$$

where η and A_f [mm^2] are, respectively, a dimensionless orientation factor and the cross sectional area of a single fibre. The orientation factor η will assume the value of 0.5 for a three-dimensional isotropic distribution. Further ahead, it will be presented the derivation of η for the three, two and one-dimensional situations.

6.3.2 Minimum fibre content

The minimum fibre content intersecting an active crack plane, with regard to the mechanical properties of the FRC, may have a similar meaning to that of the minimum strength (e.g. tensile) of plain concrete (Babut 1986). The lowest value of effective fibre content of a section parallel to the direction of the vibrating force or to gravity force, $N_f^{||}$, can be selected to define the possible minimum number of fibres per unit area, $\check{N}_f^{||}$. The relative difference between the minimum effective number of fibres and the expected value of N_f^{3D} can be regarded as a reduction of the effective number of fibres (Babut 1986):

$$\gamma = \frac{N_f^{3D} - \check{N}_f^{||}}{N_f^{3D}} \tag{6.3}$$

6.3.3 Degree of orientation of the fibre structure

The degree of orientation of the fibre structure can be regarded as a preferential fibre orientation towards a certain direction. For partially planar-oriented fibre structures (laminar elements), which can be assumed as generated by the addition of two sub-sets, namely between a random fibre distribution (three dimensional structure), and another comprising fibres randomly distributed in planes (two dimensional structure); the degree of orientation can be determined by (Stroeven 1978, 1979):

$$\omega = (2\,t\,/\,l_f + 1) \cdot \frac{N_f^{||} - N_f^{\perp}}{N_f^{||} + (4/\pi - 1) \cdot N_f^{\perp}} \tag{6.4}$$

where, $N_f^{||}$ and $N_f^{\perp}$ are, respectively, the number of fibres per unit cross-sectional area in a slice of concrete, of thickness t, projected on a plane parallel and perpendicular to the filling direction, whereas l_f is the fibre length. When the degree of orientation is null, $\omega = 0$, signifies perfect isotropy. On the other hand, if $\omega = 1$ means that all the fibres are oriented in a plane perpendicular to the filling direction (see Figure 6.3).

Remark that the degree of orientation computed by equation 6.4 is based upon on stereological technique of feature counting of projections. If only the number of fibres crossing in a specific plane is available, equation 6.4 can be simplified for the limiting case of a thin slice ($t \to 0$):

$$\omega = \frac{N_f^{||} - N_f^{\perp}}{N_f^{||} + (4/\pi - 1) \cdot N_f^{\perp}} \tag{6.5}$$

Equations 6.4 and 6.5, which can be used to determine the degree of segregation, as previously referred, are valid for partially planar-oriented fibre structures. In the case of a significant deviation from the state of rotational symmetry, it is necessary to add a 1D fibre distribution arrangement as well (Stroeven 1986b). Thus, beside the degree of planar orientation there would also be a degree of linear orientation (Stroeven and Hu 2006).

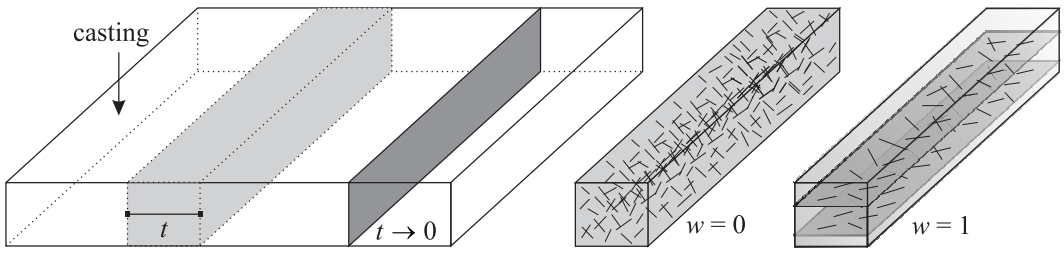

Figure 6.3: Degree of orientation of the fibre structure in laminar elements.

6.3.4 Segregation of fibres

Babut (1986) proposed a coefficient for inferring the fibre segregation degree, which can be defined by:

$$\xi_{seg} = \frac{1}{h \cdot N_f} \cdot \sum_{i=1}^{N_f} \bar{y}_i \tag{6.6}$$

where $\bar{y}$ and h are, respectively, the coordinate of the centre of gravity of the fibre reinforcement and the height of the analysed cross-section parallel to the vibration direction (Figure 6.4). In the case of ideal fibre distribution, without segregation, the value of ξ_{seg} is 0.5. If ξ_{seg} tends to 1, the fibres are disposed towards the bottom part of the cross section, whereas if ξ_{seg} tends to 0 the opposite occurs.

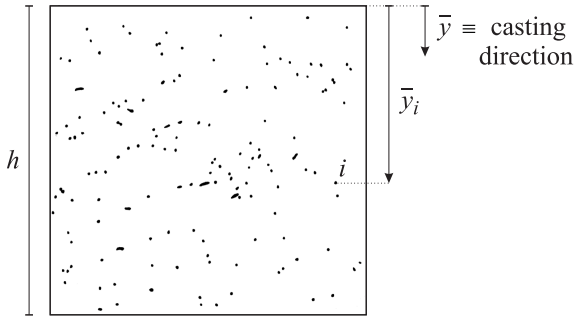

Figure 6.4: Procedure for inferring the fibre segregation degree.

6.4 Fibre orientation, efficiency and effectiveness

According to Kamerwara Rao (1979), the term fibre efficiency is used to indicate the performance of an individual fibre with a certain orientation relative to the tensile stress direction. On the other hand, the term effectiveness is used for the average value of the efficiency, obtained by considering all possible orientations of the fibre.

In Part I of this thesis was studied the efficiency of an individual steel fibre, by means of its pullout behaviour. Additionally it was shown that the fibre efficiency is strongly influenced by the fibre inclination angle towards the pullout load, i.e. relatively to the tensile stress.

6.4.1 Fibre orientation factors

One-dimensional case

For the one-dimensional case, the fibre orientation is inevitably aligned with the direction of the applied load. Theoretically, the fibre effectiveness is 1. Several authors (Kooiman 2000, Lappa 2007) suggest that the latter value would be the optimal one, since the fibre efficiency

is always optimal due to preferable fibre orientation regarding the fracture plane. However, in the author opinion this could be incorrect. As previously seen in the chapters regarding the micromechanical behaviour of a single fibre, the fibre efficiency is usually maximum for an orientation angle regarding the pullout load between 0 to 30 degrees. Other researchers found similar findings by conducting pullout tests for fibre inclination angles within 0 and 30°, namely, Banthia and Trottier (1994) for a 15° angle, and Robins et al. (2002) for a 10° angle. Consequently, the optimal effectiveness factor could not be 1, but a slightly lower value.

Two-dimensional case

In a two-dimensional system, it is assumed that the fibres are randomly oriented in a plane. In Figure 6.5(a) is depicted the 2D case where the fibre orientation angle θ between the embedded fibre length and the crack line (x-axis) can vary between 0 and π. According to Kamerwara Rao (1979) the average efficiency or effectiveness of multiple fibres, η_{2D}, can be determined from projecting the mean fibre length towards the direction of the tensile stress (y-axis). Moreover, it is assumed that all fibres comprised in the plane, represented by "crack line" in Figure 6.5(a), are subjected to a parallel translation until their gravity centre coincide at the intersection of the x and y-axis. Thus the mean effectiveness in a planar random system can be expressed by an orientation efficiency factor computed as follow:

$$\eta_{2D} = \int_0^{\pi} \frac{\sin\theta \cdot d\theta}{\pi} = \frac{2}{\pi} \tag{6.7}$$

Three-dimensional case

For the general case, where fibres can have any orientation in a three-dimensional system, the unit sphere model depicted in Figure 6.5(b) reflects the actual isotropic uniform random fibre dispersion in the specimen. Stroeven and Shah (1978) determined the spatial-random effectiveness adopting the geometric probability theory. Similarly to the 2D case, the fibres are imaginary translated from their original positions, while maintaining their orientations, and joined with one end in the sphere with a diameter equal to the fibre length. Assuming the xy plane as the crack plane and the z-axis as the tensile stress direction, the fibre effectiveness or three-dimensional orientation factor is given by (Stroeven and Hu 2006):

$$\eta_{3D} = \frac{\displaystyle\int_0^{\pi/2} \cos\theta \cdot \sin\theta \cdot d\theta}{\displaystyle\int_0^{\pi/2} \sin\theta \cdot d\theta} = \frac{1}{2} \tag{6.8}$$

where, the trigonometric term *cosine* represents the relative probability of fibre intersecting with crack, whereas the *sine* term is the relative spatial frequency as depicted in Figure 6.5(b). In space the fibre orientation is defined by two angles, however, the second angle (the one not related with the tensile stress direction) will lead to the same integration in the nominator and denominator, consequently, there is no effect on the orientation factor (Stroeven and Hu 2006).

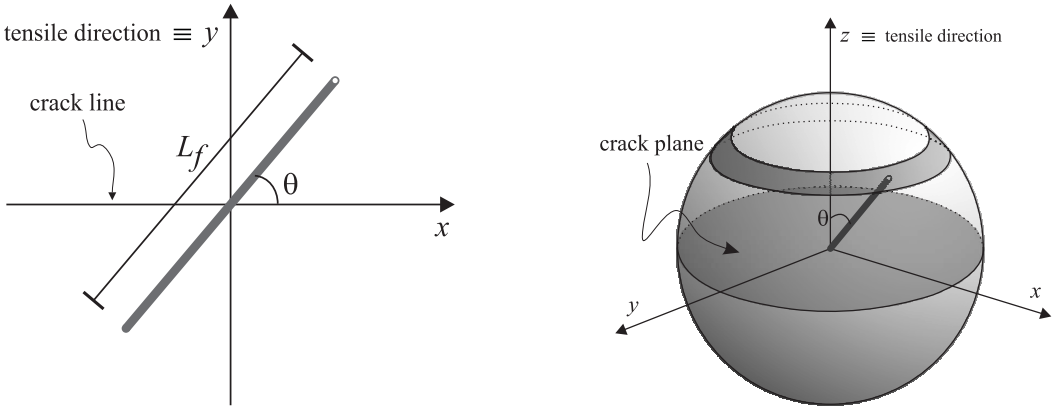

(a) (b)

Figure 6.5: Spatial averaging of fibre contribution to stress transfer over the leading crack: (a) two-dimensional case and (b) three-dimensional case visualizes by the unit sphere model.

6.4.2 Influence of the geometrical boundaries on fibre orientation

Several researchers have presented theoretical models to take into account the boundary restrictions imposed by a mould of a structural element in the fibre effectiveness of random short fibre reinforcement (Kamerwara Rao 1979, Soroushian and Lee 1990, Kooiman 2000, Dupont 2003, Stroeven and Hu 2006). In spite of their differences and complexity, commonly to all of them, an average fibre efficiency factor, η, can theoretically be computed considering both the dimensions of the structural element and fibre, and the wall effects.

The fibre orientation is strongly influenced nearby boundaries, especially when the fibre length is relatively large compared to the structural element or specimen dimensions. According to an analysis performed by Soroushian and Lee (1990) and Kooiman (2000), the effect of constrained orientation of fibres is mainly more predominant when the element dimensions are smaller than five times the fibre length. When the dimensions of the elements are considerably larger than the fibre length, the effect of constraint is reduced, consequently, the fibres' orientation approaches those of freely random orientated, i.e. without constraints from the boundaries.

Table 6.1 presents some examples of average orientation factors (η), computed from the theorethical models developed by Soroushian and Lee (1990), Kooiman (2000) and Dupont (2003), considering distinct fibre lengths and number of boundary surfaces. The orientation factor values computed from the distinct methodologies differed. Nevertheless, the differences between values obtained by Soroushian and Lee (1990) and Dupont (2003) are not considerable. The methodology presented by Soroushian and Lee (1990) has flaws if analysed within the scope of the geometrical statistics, geometrical probability theory or integral geometry field (Stroeven 1994, Stroeven and Hu 2006, Stroeven and Guo 2008). On the other hand, in the mathematical model proposed by Dupont (2003), the orientation factor is determined by averaging the orientation factor computed for three distinguished zones in a rectangular cross section. The adopted orientation factors for the bulk, with one boundary (zone 1) and two boundary conditions (zone 2) are, respectively, 0.5, 0.6 and 0.84 (see Figure 6.6). Dupont (2003) evaluated his model performance by comparing the calculated number of fibres with the number of fibres crossing a section assessed experimentally on 107 distinct specimens, involving different fibre types. The model provided good predictions of the number of fibres crossing a section.

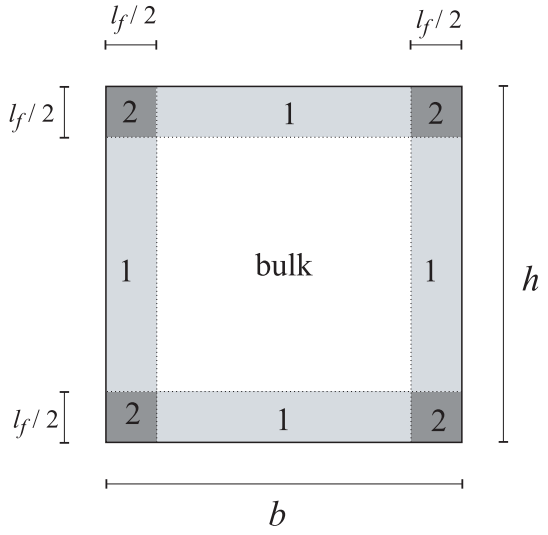

Figure 6.6: Distinct boundary conditions at a beam's cross section (after Dupont 2003).

More recently, Stroeven and Hu (2006) presented a three-dimensional model for fibre anisotropy supported on the geometrical probability theory, which take into account not only the boundary effect on the fibre orientation, but also the decline of the number of fibres toward the boundary surface. With this model, the authors predicted a decrease (nearby 10%) on the fibres' stress transfer capability at the boundary zones in comparison to the bulk performance according the same direction.

Table 6.1: Average orientation numbers available in literature, when considering boundaries.

Reference	Boundary surface	Specimen dimensions b [mm]	Specimen dimensions h [mm]	l_f [mm]	η [-]
Soroushian and Lee (1990)	2	150	150	60	≈ 0.48
	4				≈ 0.57
Kooiman (2000)	2	150	150	60	0.70
				30	0.66
Dupont (2003)	4	150	150	60	0.60
				30	0.55

6.4.3 Anisometry and anisotropy

As previously discussed, several factors related to the production of fibre reinforced composites, FRC, affect the distribution characteristics of the fibres within a cementicious matrix. Thus it is feasible to assume anisotropic mechanical behaviour for the FRC due to the anisometry in the fibre reinforcement (Stroeven 1979, 1986b, Stroeven and Hu 2006). The actual fibre distribution can be assumed as a mixture of three, two and one-dimensional fibre orientation arrangements, respectively, 3D, 2D and 1D. All the fibres geometrical centres are assumed dispersed randomly. However, fibres from the 1D portion are oriented parallel to the so-called orientation axis, while fibres from the 2D portion are oriented uniformly random parallel to the so-called orientation plane (Stroeven and Hu 2006).

For partially planar-oriented fibre structures, Stroeven (1978, 1979) demonstrated, based on the geometric probability theory, that the number of fibres per unit cross-sectional area in a slice of concrete, of thickness t, projected on a plane parallel to the filling direction can be computed as (see Figure 6.3):

$$N_f^{||} = L_V \left[(t/l_f + 0.5) + (2/\pi - 0.5) \cdot \omega\right] \tag{6.9}$$

where L_V is the total fibre length in a unit volume of concrete ($= 4V_f/\pi d^2$), l_f is the length of each single fibre and ω is the degree of orientation defined in section 6.3.3. In equation 6.9, V_f is the fibre content in volume and d is the fibre diameter. On the other hand, for the case of a plane perpendicular to the filling direction, the number of fibres projected on it is given by (Stroeven 1978, 1979):

$$N_f^{\perp} = L_V \left[(t/l_f + 0.5) - 0.5 \cdot \omega\right] \tag{6.10}$$

When only the data of the number of fibres crossing a specific plane is available, equations 6.9

and 6.10 can be simplified for the limiting case of a thin slice ($t \to 0$):

$$N_f^{||} = L_V \left[0.5 + (2/\pi - 0.5) \cdot \omega\right] \tag{6.11}$$

$$N_f^{\perp} = 0.5\, L_V \,(1 - \omega) \tag{6.12}$$

Hence, this anisometry of the fibre distribution is directly reflected in a anisotropic behaviour of the fibre reinforced composite. Stroeven (1986b) derived the following constitutive relationships for estimating the composite strength:

$$\sigma_{||} = \sigma_m \,(1 - V_f) + \frac{1}{6}\,\lambda\,\tau V_f \cdot (1 + 0.5\,c\,V_f) \tag{6.13}$$

$$\sigma_{\perp} = \sigma_m \,(1 - V_f) + \frac{1}{6}\,\lambda\,\tau V_f \cdot (1 - c\,V_f) \tag{6.14}$$

where λ and τ are, respectively, the fibre aspect ratio and interface bond strength, whereas c is a constant (computed from $\omega = cV_f$) in which ω is the degree of orientation. σ_m and V_f are, respectively, the mortar strength, the fraction of the cross-sectional area transmitting tensile strengths and the fibre volume fraction. On the other hand, in the case of a random uniform fibre dispersion can be found:

$$\sigma_{||} = f_{\perp} = \sigma_m \,(1 - V_f) + \frac{1}{6}\,\lambda\,\tau V_f \tag{6.15}$$

According to Stroeven (1986b), the strengths computed from equations 6.13 and 6.14, and using the values of ω determined by stereological computations from the image analysis procedure, are in agreement with experimental test results performed in different orthogonal directions. Analysing the latter equations, can be drawn out that the rearrangement of fibres in a specimen can either enhance fibre reinforcement effectiveness up to $V_f(1 + 0.5\,c\,V_f)$ in a favourable cross-section (see equation 6.13), or reduce the fibre reinforcement effectiveness to $V_f(1 - c\,V_f)$ (see equation 6.14).

More recently, Stroeven and Hu (2006) presented a complete three-dimensional solution to boundary cases in fibre reinforced composites, where the strength relationships in bulk and in boundary zones (i.e. having into account the wall-effect) are derived for prismatic specimens of fibre reinforced concrete. Assuming that, in most practical cases, fibre reinforcements develops a partially planar structure in bulk, the stress components parallel to the orientation plane of the 2D portion can be computed by:

$$\sigma_{||} = \sigma_m \, (1 - V_f) + \frac{1}{3} \lambda \tau V_f \, \bar{\eta}_{b3} \cdot (1 + 0.5\,\omega) \tag{6.16}$$

where $\bar{\eta}_{b3}$ is a stress transfer efficiency parameter in the boundary layer, which for prismatic elements with surfaces parallel to orientation plane of the 2D portion yields 0.203. The derivation of this parameter can be found elsewhere (Stroeven and Hu 2006). On the other hand, the stress components perpendicular to the orientation plane can be determined in a similar fashion by:

$$\sigma_{\perp} = \sigma_m \, (1 - V_f) + \frac{1}{3} \lambda \tau V_f \, \bar{\eta}_{b3} \cdot (1 - \omega) \tag{6.17}$$

6.5 Methods for analysing the structure of FRC

There are several methodologies for assessing the fibre structure within a concrete matrix (Soroushian and Lee 1990, Stroeven 1986b, Franchois et al. 2004, Ozyurt et al. 2006b, Barros et al. 2005, Ferrara and Meda 2006, Farhat et al. 2007, Vandewalle et al. 2008). These methods differ considerably on their complexity and on the type, amount and accuracy of the fibre structure's information that can be withdraw.

Among more expedite methods are the wash-out tests, which consist of after the mixing concrete procedure and respective mould filled, the concrete content in the mould is then poured over a sieve while the concrete is still in the fresh state. After washing out the coarse aggregates and fibres that remain in the sieve, steel fibres can be separated from the aggregates with a magnet. Finally just by counting and weighting them, the fibre concentration in the mixture can be evaluated (Vandewalle et al. 2008). However, this simple procedure has a main drawback since it cannot provide information about the fibre orientation in a specimen, but only about the fibre concentration. A similar method can be also used for assessing the fibre concentration in hardened cored specimens. The specimen can be crushed until the fibres are fully desegregated from the paste and aggregates, afterwards with a magnet the fibre parcel is separated and then weighted (Ferrara and Meda 2006).

Another method supported on fibre counting, which has widely been used by researchers, e.g. Soroushian and Lee (1990), Kooiman (2000), Dupont (2003), Barros et al. (2005) and Markovic (2006), can be the manual counting of fibres present in the fracture surface of a tested specimen. For low fibre content, this procedure presents simple and fast way of assessing the number of fibres that intersect an active crack plane. Comparatively to the wash-out methods, it presents information about the fibre density variation over a hardened concrete's section. However, this method has two main disadvantages. The first, is that it can not provide the orientation of the

fibres; the other is that in the case of fibre rupture, during the pullout process, there could be double counting of the fibres that have fractured. Moreover, regarding the mixtures with high fibre contents, this method would be extremely time consuming and strenuous, and in addition it would be difficult to ensure the accurate counting of fibres.

Other common methods that recently have been widely employed are supported on counting fibres on images of specimen sections and not on the specimen fracture surfaces. With this procedure, and in opposite to fibre counting on the fracture surface, it can be avoided the case of double counting fibres that eventually have fractured. In this method, the images could be from x-ray (Stroeven and Shah 1978, Kasperkiewicz et al. 1978) or simple photographs of the cross sections (Grünewald 2004, Markovic 2006, Lappa 2007, Hegger et al. 2008). The latter images can be counted manually (Grünewald 2004) or automatically with the help of an appropriate digital image analyser software (Markovic 2006, Lappa 2007, Hegger et al. 2008). Since the aggregates and paste have distinct reflective properties from the steel fibres, as the first ones absorb the light, and on contrary steel fibres reflect it, steel fibres can easily be distinguishable on a image with a proper threshold colour parameter.

Another type of methods are based on the measurement of distinct electrical properties (such as resistivity, capacity, etc.) of fibre reinforced composites (Franchois et al. 2004, Woo et al. 2005, Ozyurt et al. 2006b). These methods, when comparing to image analysis methods, are quite more straightforward and less time consuming. Ozyurt et al. (2006a) compared the electrical properties, namely, the matrix-normalized conductivity parameter with the orientation factor obtained from the image analysis procedure (counting fibres at cross sections) and found a linear relationship between them with a reasonable agreement. Moreover, this method showed its sensitivity to other sources of non-uniform fibre dispersion, such as clamping, segregation, among others.

Recently a novel technique such as computerized tomography (Farhat et al. 2007) was also used for inferring the fibre concentration, however, the latter only allows to have a global idea of the steel fibre concentration in a mixture.

6.5.1 Determination of the orientation factor by image analysis

Whenever a specimen is cut, the fibres intersected in the cross section, in the general case, will be visible as an ellipse. However, whenever the fibre longitudinal axis is perpendicular to the cross section, it will be visible a full circle. In the general case of an ellipse, the minor semi-axis of the ellipse, b, corresponds to the fibre diameter, whereas the major semi-axis, a, is the visible fibre length at that plane. This holds true if the fibres have a perfectly circular cross-section, which may be not entirely true even for supposedly circular fibres and depends

on their manufacturing process.

According to Eberhardt and Clarke (2001), the fibre orientation can be characterized by two angles: the in-plane angle φ and the out-plane angle θ (see Figure 6.7). The out-plane θ corresponds to the fibre alignment with regard to the loading direction. On the other hand, the in-plane angle φ regards to the orientation of the ellipse major semi-axis, a, with respect to an arbitrary in-plane direction. The out-plane angle θ can be determined by the ellipse semi-axis length of the fibre at the cross section by:

$$\theta = \arccos(b/a) \tag{6.18}$$

Remark that when analysing the fibre orientation angles from a single cross section, there will be ambiguity in the determination of the fibre orientation, since (θ, φ) and $(\theta, \varphi + \pi)$ orientations are indistinguishable (Eberhardt and Clarke 2001). Therefore, to fully ascertain the fibre orientation there will be the need of three perpendicular planes. However, with regard to the fibre crack bridging ability in the beams of this study, the response of fibres orientated with (θ, φ) and $(\theta, \varphi + \pi)$ would be equal. Hence it will sufficient to only regard one cross-section for each beam and the fibres out-plane angles in order to derive information on the fibre orientations.

The orientation factor can be determined with the ascertained out-plane angle via image analysis of the cross section from equation 6.19.

$$\eta_{img} = \frac{1}{N_f} \cdot \sum_{i=1}^{N_f} \cos\theta_i \tag{6.19}$$

where N_f is the total number of fibres counted at the cross section and θ is the out-plane angle, i.e. angle between the fibre longitudinal axis and the loading direction. N_f, can be obtained by just adding up all the visible ellipses and circles.

On the other hand, the dimensionless orientation factor, η, which gives an indication on the average orientation within a cross section can also be determined by counting the number of fibres present in a certain cross section, N_f [1/mm^2], and adopting the fibre volumetric fraction used in the mixture. According to Krenchel (1975) and Soroushian and Lee (1990) the factor η_{exp} can be obtained from:

$$\eta_{exp} = N_f \cdot \frac{A_f}{V_f} \tag{6.20}$$

where V_f [Vol.-%] and A_f [mm^2] are, respectively, the volumetric fraction of fibres and the cross sectional area of a single fibre.

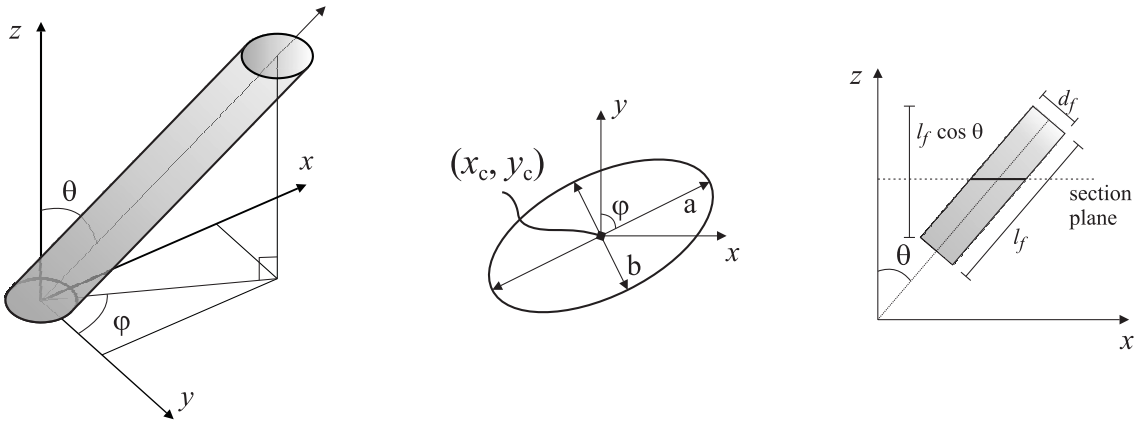

Figure 6.7: Left: Fibre in a 3D space, definition of the in-plane angle ϕ and out-of-plane angle φ; Midle: definition of an ellipse and the in-plane angle; Right: the probability that a fibre is cut by a section plane is proportional to its orientation angle θ (adapted from Eberhardt and Clarke 2001).

6.6 Assessment of the SFRSCC structure

In this section, it will be presented and discussed the results regarding the fibre distribution, namely, the fibre density, orientation and segregation in the self-compacting matrix studied. For this purpose, these parameters were computed from the geometric data that define the ellipses and gravity centre corresponding to the intersected fibres. The fibre structure assessment was supported on the image analysis of saw cut concrete surfaces. Moreover, the number of fibres present at the crack planes of the specimens tested, for assessing the steel fibre reinforced self-compacting concrete's post-cracking behaviour (in Chapter 8), will be also presented.

6.6.1 Procedure for assessing the structure of SFRSCC

As previously stated, there are several methods for determining the fibre distribution and orientation in steel fibre reinforced composites, in which the most promising are image-analysis, magnetic induction method, tomography and measurement of the concrete's electrical properties. In the present work the image analysis was chosen due its simplicity and relatively low cost of the necessary equipment.

Method of analysis

The adopted procedure for fibre detection comprised four main steps. Firstly, a concrete surface must be cut from the concrete specimens and, for better results, should be ground, since the polishment of the steel fibres enhances their reflective properties. Afterwards, an image of the surface is taken with a digital photograph camera. The third step incorporates three tasks:

Pre-Processing by using a rectification mask – in the present study the colour channels were eliminated, thus a grey-scale photograph is obtained; the Segmentation (by using thresholds); and the Classification in which the detection and calculation of the circles and ellipses corresponding to the fibres cross sections are performed. Finally, the Post-Processing step where the obtained results from the analysis software are evaluated.

The images used in the section analysis were taken with a high resolution digital camera (Canon EOS 450D^{TM}, with 12 Mpix). To avoid shadows and enable a correct illumination of the concrete surface, the camera was slightly inclined. Therefore, before the Classification process there was the need to rectify the image due to the inclination and also of the lens distortion. For this correction marks were executed (at defined distances) on the concrete surface, the calibration was then automatically performed by the used image analyser software. In Figure 6.8 are depicted an image sample obtained on the Pre-Processing, Segmentation and Classification procedures, respectively.

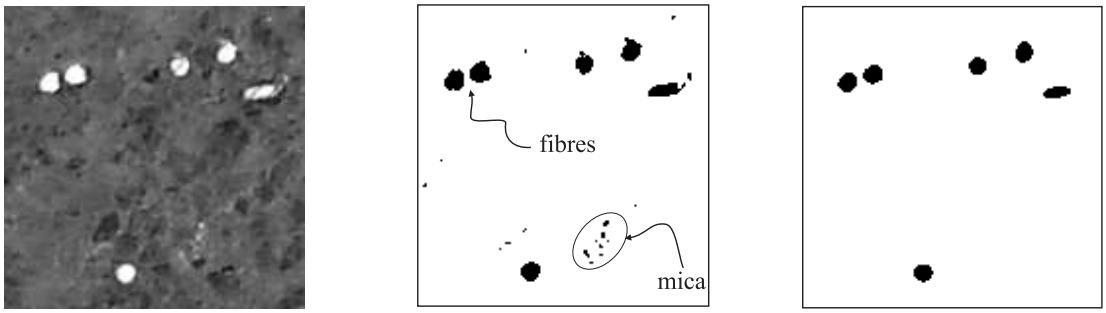

(a) (b) (c)

Figure 6.8: Image analysis procedure of the concrete's surface: (a) Pre-Processing, i.e. applied mask, (b) Segmentation procedure, and (c) Classification procedure.

In the Pre-Processing, since the photos of the specimens were coloured, a mask was applied to transform the photo into a grey scale format. In spite of the used image analyser program (GSA Image-Analyser^{TM}) enables the execution of the Classification procedure in coloured image, this would not lead to good results on the fibre identification. Afterwards, the segmentation of the fibre and non-fibre areas was achieved using a threshold function. The threshold is nonetheless than a grey scale limit. In the present work a static value for each of the analysed surfaces' photos was manually set up. Remark, however that there much more fancier procedures, such as automatic calculation methods of the grey scale limits (Hegger et al. 2008).

Even though the segmentation of fibre and non-fibre areas has been performed, there were some areas due to localized bright points that have been included as fibre areas, see Fig-

ure 6.8(b). Since in the present composition as a coarse aggregate was selected crushed granite, the mica comprised on its constitution had similar reflective properties to the fibres. This was eliminated during the Classification procedure. After the detection of the clusters marked as fibre areas, the boundary and interior areas are known. Hence, a selection restrain equal to the circular fibre cross section area ($\approx 0.442\ \text{mm}^2$) was applied, i.e. all the selected regions with a smaller area than the fibre are eliminated, compare Figures 6.8(b) and 6.8(c). Whenever an identified cluster consisted of more than one fibre, due to either a lower image or cut quality, or even in some cases two fibres touching themselves, the referred cluster must be divided into the correspondent fibres. Thus avoiding obtaining biased results of either the number of fibres at the concretes' surface and orientation (by means of the parameters that define the ellipse). In the present work this was achieved manually. After the Classification procedure was performed, a visual inspection of the obtained image and compared with the initial photo, the joined fibres were then separated with a tool comprised in the image analyser software. For the fibre volume ratios studied in the current work, this task is feasible to be performed manually, since in each analysed image there where a few cases like the above mentioned. However, as the fibre volume ratio increases, this task becomes more harder and time consuming, thus should be used automatic separation procedures. Hegger et al. (2008) implemented three distinct mathematical approaches for the fibre separation, and applied it on the fibre orientation's study of reinforced composites with a high fibre content.

Finally in the Post-Processing, the number of detected ellipses corresponds to the number of fibres at the concrete surface. Moreover the parameters that characterize the fibres such as, global coordinates, minimum and maximum radius and area are analytically computed.

Sampling of SFRSCC specimens

The analysis of the fibre structure was carried out either on prismatic specimens ($150 \times 150 \times 600\ \text{mm}^3$) used for the three point bending tests, and on cylinders (300 mm of height and 150 mm of diameter) used in the uniaxial tension tests (the experimental results of the latter tests will be comprised in Chapter 8). In the prismatic specimens, the cross sections' analysis was carried out after the mechanical tests have been performed. Two series with distinct fibre contents were studied, respectively, with $30\ \text{kg/m}^3$ and $45\ \text{kg/m}^3$. Hereinafter, they will be designated as Cf30 and Cf45, respectively. Each series comprised five prismatic and cylindrical specimens.

In Figure 6.9 are depicted the localizations of the cross sections analysed in the fibre structure assessment. In each prismatic specimen were analysed four cross sections parallel to the beam notch's plane and other perpendicular to the referred plane. Regarding the cross sections

parallel to the notch plane, i.e. to the crack surfaces, were chosen two sections nearer to the crack plane and the other two nearer to the corners. Since the cross section analysis was carried out after performing the bending tests, the sections nearest to the crack plane must be at least separated by half of the fibres' length, in order to rule out that fibres at the cross section have been pulled out during the three-point bending tests and, consequently, leading to distort results. On the other hand, the remain sections were also distanced from the corners more than half of the fibres' length, thus only comprising the same mould's boundary conditions as the planes nearer to the crack plane. Regarding the cylindric specimens, only one cross section was studied by the image analysis procedure. The latter was parallel to the notches preformed for inducing the crack plane on the uniaxial tension tests, thus perpendicular to the gravity direction during casting.

Finally, as previously mentioned, a restrain equal to the circular fibre cross section area ($\approx 0.442\,\text{mm}^2$) was considered for the fibre identification at a certain plane. This restraint excludes, from the count up, the cases when the fibre is just touching the studied plane, i.e when the smallest fibre embedded length is very reduced. However, the image analysis method does not allow to assess the number of effective fibres. Notice that a hooked fibre with an embedded length smaller than the hook length it will not be effective (Robins et al. 2002) and, nevertheless, could fulfil the adopted fibre cross section area restraint. For instance, a perpendicular fibre to the studied plane could have a cross sectional area of $0.442\,\text{mm}^2$ and an embedded length smaller than 5 mm, thus, for the fibre geometry adopted in this work, it would not be effective even though it would be count.

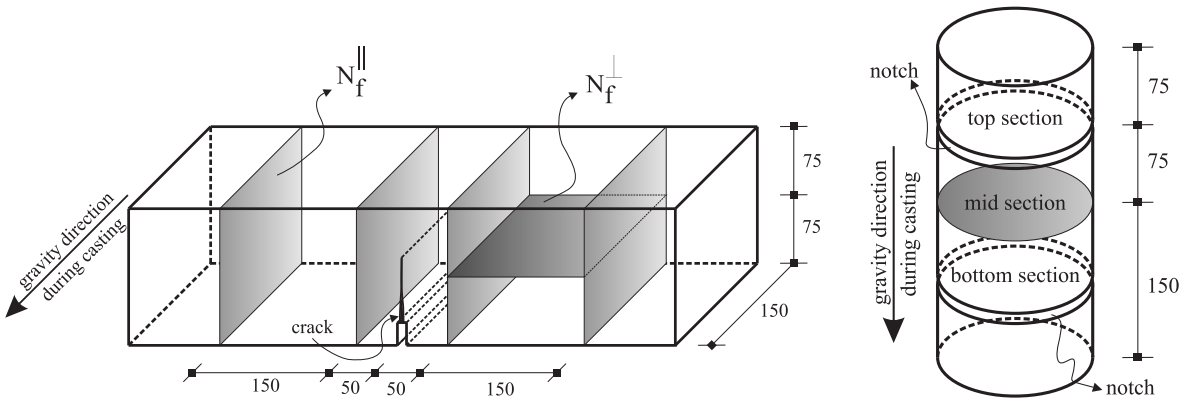

(a) (b)

Figure 6.9: Localization of the cross sections considered in the fibre distribution assessment: (a) prismatic specimens and (b) cylindric specimens (units in mm).

6.6.2 Experimental results on the prismatic specimens

Fibre density

In Table 6.2 are comprised the fibre density of the analysed prismatic specimens' cross sections. $N_f^{||}$ is the fibre density obtained from the cross sections parallel to the crack surface of the three point bending test specimens (see Figure 6.9), $N_{f,crk}^{||}$ is the fibre density at the crack surface analysed in a net cross section of 150×125 mm^2 and $N_f^{\perp}$ is the fibre density in a perpendicular plane to the crack surface (see Figure 6.9). The fibre densities $N_{f,crk}^{||}$ and $N_f^{\perp}$ were both determined from only one cross section per specimen, whereas $N_f^{||}$ was determined from four cross sections per specimen. Finally, $\check{N}_f^{||}$ and $\check{N}_f^{\perp}$ are defined as the minimum fibre densities observed in a specimen for the parallel and perpendicular directions, respectively,. Additionally, the theoretical fibre density for each series assuming a three-dimensional isotropic uniform random fibre distribution, N_f^{3D}, is also comprised. The latter parameter was computed using equation 6.2 and adopting $\eta = 0.5$ corresponding to the orientation factor for the theoretical 3D isotropic uniform random distribution.

Table 6.2: Fibre density on the prismatic specimens.

SPECIMEN		(nom.)	Parallel direction				Perpendicular direction		Min. num. fibres	
		N_f^{3D}	$N_f^{||}$	CoV	$N_{f,crk}^{||}$	CoV	$N_f^{\perp}$	CoV	$\check{N}_f^{||}$	$\check{N}_f^{\perp}$
		fibres/cm^2		%	fibres/cm^2	%	fibres/cm^2	%	fibres/cm^2	
Cf30	1	0.435	0.776	5.6	0.757	–	0.391	–	0.716	0.356
	2		0.655	12.8	0.555		0.356		0.533	
	3		0.734	7.5	0.501		0.542		0.501	
	4		0.644	4.2	0.656		0.596		0.612	
	5		0.804	6.6	0.635		0.627		0.627	
	Avg.	–	0.723	11.4	0.621	16.4	0.502	24.3	0.598	–
Cf45	1	0.653	0.995	6.9	0.896	–	0.761	–	0.896	0.587
	2		0.968	10.7	0.837		0.745		0.837	
	3		0.942	4.2	0.955		0.667		0.895	
	4		0.916	4.8	1.003		0.768		0.884	
	5		0.996	6.5	0.864		0.587		0.864	
	Avg.	–	0.963	7.1	0.911	7.4	0.706	11.0	0.875	–

Both the average and minimum fibre density according to the parallel and perpendicular directions to the crack surfaces increased with the volumetric fibre content, as expected. The theoretical increment of 50% on the fibre density (for $\eta = 0.5$), between Cf30 and Cf45 series, produced an increase in fibre density according the parallel direction of nearby 33%, whereas

in the perpendicular direction, an increment of 39% was observed. As an example, Figure 6.10 shows photos from cross sections with the fibres reflecting the light, and also the fibres obtained from the classification procedure for a certain specimen's cross section with 30 and 45 kg/m^3 of fibres.

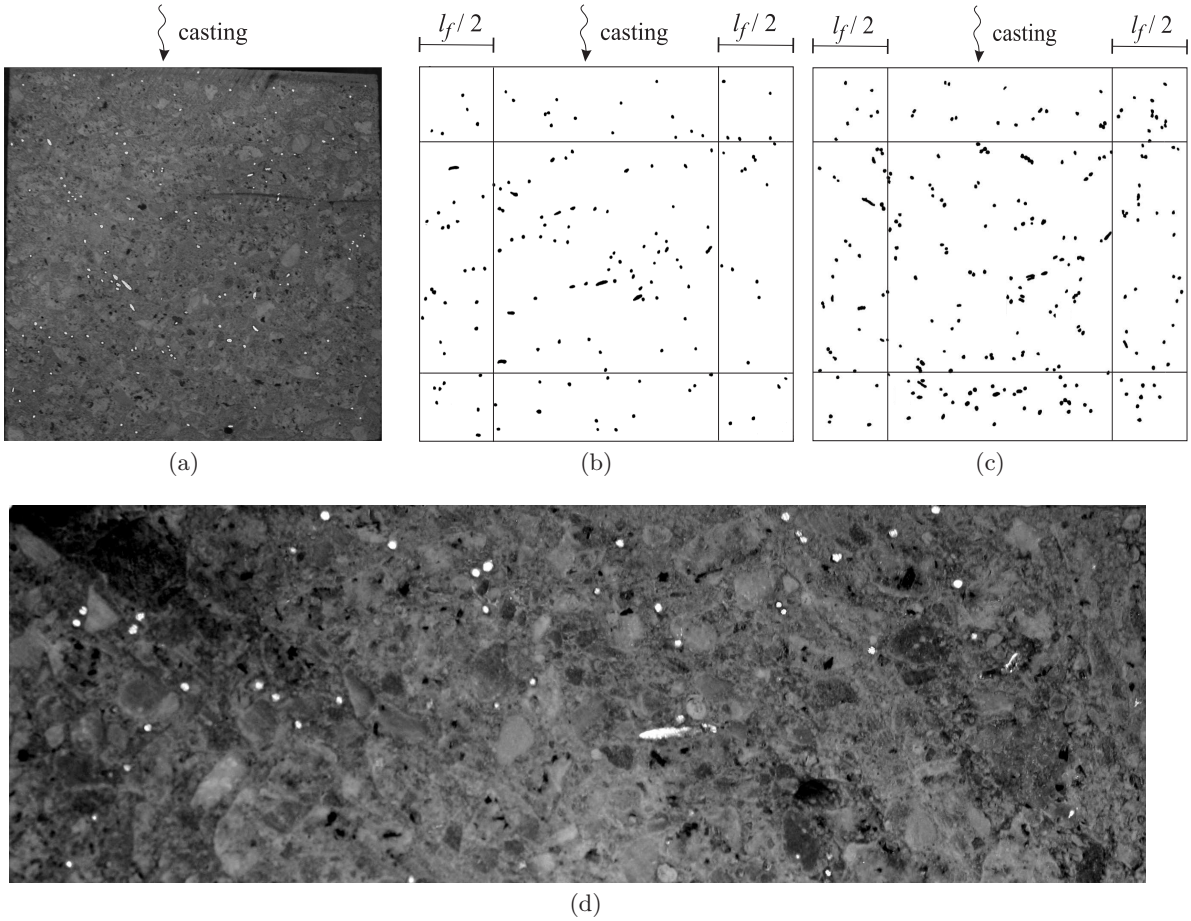

Figure 6.10: Examples of fibre distributions in a concrete surface: (a) photo of a Cf30 series specimen's cross section (parallel), (b) and (c) identification of the fibres in a parallel plane of a specimen of the Cf30 and Cf45 series; (d) zoom perspective from Cf30 series.

For both Cf30 and Cf45 series, the fibre density of the hardened SFRSCC specimens according to the parallel direction was significantly higher than the theoretical value assuming a 3D isotropic uniform random distribution. In fact, the $N_f^{||}$ was 66% and 47% higher than N_f^{3D}, respectively, for the Cf30 and Cf45 series. This increase can be regarded as an effective increase on the fibre density intersecting an active crack and can be ascribed to two intercorrelated reasons. The high flowability of the concrete in the fresh state, which favours the fibre alignment according the flow direction, namely along the lengthier dimension, i.e. beam's longitudinal

dimension. Moreover, there is also the wall-effect, in which the fibres within a distance from the mould surface smaller than half the fibre length, also tend to be preferentially aligned along to the surfaces. Approximately just 34% of the total prismatic volume ($150 \times 150 \times 600$ mm^3) will not be influenced by the wall-effect. Consequently, as the fibre orientation factor increases due to the fibre alignment, the probability of the fibre to intersect a plane perpendicular to the wall plane increases resulting a higher fibre density along the direction orthogonal to this plane.

The theoretical number of fibres N_f^{3D}does not have into account the cross sectional boundary conditions. A theoretical value of the expected number of fibres having in consideration the wall-effect can be computed with the mathematical model developed by Dupont (2003). For the purpose, this model yields an average orientation factor of 0.6 for the current specimen and fibre dimensions (see Table 6.1). Inserting this orientation value into equation 6.2 will render an expected fibre density of 0.522 and 0.783, respectively, for the Cf30 and Cf45 series. Therefore, if now $N_f^{||}$ is compared with the referred expected fibre densities considering the wall-effect, an effective increase of 39% and 23%, respectively, for the Cf30 and Cf45 series, can be observed. These effective increases can be just ascribed to the high flowability effect of the self-compacting concrete.

In Table 6.3 are included values withdraw from literature for the fibre density observed on prismatic specimens. Moreover, when applicable it was computed the effective increase of the fibre density in similitude to the performed for the studied compositions. For each cited reference is specified the fibre content, fibre's aspect ratio, fibre length and type of concrete. The SFRC is defined as traditionally vibrated steel fibre reinforced concrete, SFRSCC as steel fibre reinforced self-compacting concrete and HPHFC as high performance hybrid fibre concrete, i.e. there are used high fibre contents with distinct sizes.

The effective increase of the fibre density obtained from the literature for the self-compacting matrices range between 31 and 75% and are in consonance with the obtained results for the studied composition. On the other hand, concerning the results from literature for SFRC (Babut 1986, Barr et al. 2003), the effective increase on fibre density lays between 4 and 24%, which is smaller than the one observed for SFRSCC (Vandewalle et al. 2008, Torrijos et al. 2008). This differences are quite feasible, since for SFRC the only factor that will influence the effective increase on fibre density will be the wall effect, whereas for SFRSCC there will be also the effect of concrete's high flowability. In what concerns to HPHFC (Markovic 2006), the effective increase on the fibre density for the lengthier fibres, 60 mm, is within the observed values for the SFRSCC. Remark that the later type of concrete has also self-compatibility requirements. On the other hand, for the shorter fibres, with 13 mm length, the effective increase on the fibre density was just observed for the series with 36 kg/m^3 of fibres. Moreover, this increase is considerable smaller than the one observed for the fibres with 60 mm. This may be justified

Table 6.3: Fibre density obtained by other researchers on prismatic specimens.

Reference	fibre content [kg/m^3]	type of concrete	aspect ratio / length	N_f^{3D} [fibres/cm^2]	$N_f^{\|\|}$ [fibres/cm^2]	effective increase [%]
Babut (1986)	39	SFRC	66/25	2.00	2.38	19
	78			4.00	4.53	13
	117			6.00	6.26	4
Barr et al. (2003)	25		65/60	0.239	0.251	5
	50		80/60	0.725	0.843	14
	75		65/60	0.718	0.890	24
Markovic (2006)	36	HPHFC	65/13	7.958	8.550	7
	78		80/60	1.132	1.536	36
	144		65/13	31.83	29.98	-
Vandewalle et al. (2008)	30	SFRSCC	65/25	1.60	2.10	31
			65/60	0.28	0.49	75
Torrijos et al. (2008)	35		50/50	0.286	0.430	50

by two aspects. Firstly, due to the smaller fibre length, the parcel of the cross sectional area which is under the wall-effect will be considerable smaller.

Returning to the analysis of the values included in Table 6.2 and regarding the fibre density along the perpendicular direction, it were observed smaller average values and much closer to the N_f^{3D} values than for the parallel direction. The $N_f^{\perp}$ was approximately 15% and 8% higher than N_f^{3D}, respectively, for the Cf30 and Cf45 series. In fact, the minimum fibre density along the perpendicular direction, $\check{N}_f^{\perp}$, was smaller than the N_f^{3D} for both series. On the other hand, $\check{N}_f^{||}$ value was also nearer to the N_f^{3D} theoretical value, and in all sections the $\check{N}_f^{||}$ value was higher than N_f^{3D}. The obtained values of the coefficient of variation, CoV, for the computed fibre densities was higher in the Cf30 series. Nevertheless, the variation of the results in both series is relatively low, which indicates a good fibre distribution within the specimen volume, particularly in the Cf45 series.

In Figures 6.11(a) and 6.11(b) are depicted the fibre density in the cross sections designated as parallel, along the specimen's length, respectively, for the Cf30 and Cf45 series.

In general, it was not observed a significant variation of the fibre density along the prismatic beams' longitudinal length. However, at half the beam's longitudinal length a decrease on the fibre density was observed for both series. Remark, that fibre density at this location was assessed by manual counting of the fibres at the crack surface of the tested specimens (a fibre was considered effective either if it had its hook deformed or if it had rupture). In addition, these sections had a smaller cross sectional area due to the beam's notch, which was executed in a zone where it is present the wall-effect, i.e. probably with a higher fibre density. At a first sight, one can ascribe this reduction of the fibre density to fibre segregation during casting towards

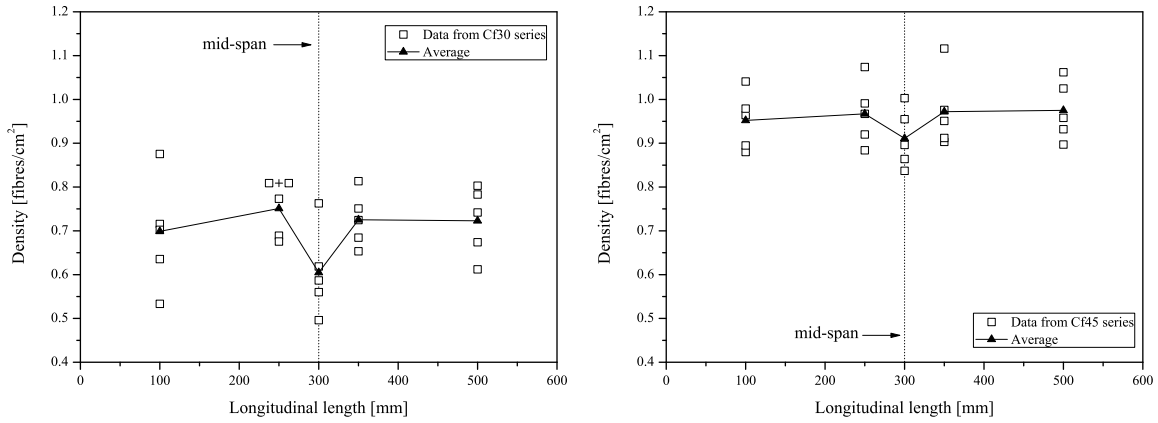

(a) (b)

Figure 6.11: Fibre density in the parallel direction along the specimen's length

the notched zone. However, this does not happens since the notch is made perpendicular to the casting direction. Another factor that could hypothetically enhanced this was that when breaking the specimen in two halves, in order to make it possible counting the number of fibres at the fracture surface, in the top of the specimen where the load is applied the concrete is crushed and disaggregated leading to a smaller number of fibres that still remain in the crack surfaces. This could have happened to some specimens, thus leading also to the higher CoV of the fibre density at this section.

Fibre orientation

The fibre orientation factors for each analysed section were computed by two distinct approaches. In the first approach, the orientation factor η_{img} is determined from equation 6.19 based upon the image analysing procedure of the elliptical axis of the intersected fibres, as described in section 6.5.1. The other approach consisted in computing the average orientation factor, η_{exp}, from equation 6.20, based on the counted number of fibres presented in Table 6.2. The latter can also be regarded as a fibre effectiveness factor, as designated by several authors. The results obtained from both approaches are included in Table 6.4.

The average orientation factor computed from the image analysis approach, in general, is higher than the correspondent η_{exp}, with the exception of the Cf30 series along the parallel direction. Both η_{img} and η_{exp} values along the parallel direction are relatively higher, nearby 15 to 30%, than the theoretical value of the orientation factor for a 2D isotropic random distribution, i.e. $2/\pi \approx 0.637$. Thus there is a clear preferential orientation of the fibres along the prismatic specimen's longitudinal axis, as the orientation factors observed experimentally lay within the theoretical values for a 2D (≈ 0.637) and 1D (1.0) uniform isotropic distribution.

Table 6.4: Fibre orientation factors on the prismatic specimens.

Specimen		Parallel direction				Perpendicular direction			
		η_{exp}	CoV	η_{img}	CoV	η_{exp}	CoV	η_{img}	CoV
		–	%	–	%	–	%	–	%
Cf30	1	0.891	5.6	0.779	1.6	0.449		0.643	
	2	0.753	12.8	0.754	2.6	0.409		0.671	
	3	0.844	7.5	0.775	1.7	0.623	–	0.734	–
	4	0.740	9.6	0.770	4.3	0.685		0.717	
	5	0.924	14.7	0.761	2.9	0.721		0.623	
	Avg.	0.830	11.3	0.768	2.7	0.577	24.3	0.698	5.6
Cf45	1	0.762	6.9	0.765	3.4	0.583		0.713	
	2	0.741	10.7	0.767	3.1	0.570		0.747	
	3	0.721	4.2	0.750	2.2	0.511	–	0.694	–
	4	0.701	4.8	0.737	3.3	0.588		0.682	
	5	0.763	6.5	0.752	4.2	0.449		0.658	
	Avg.	0.737	7.1	0.754	3.1	0.540	11.0	0.699	3.5

The average orientation factor η_{exp} decreased with the fibre content increase. This can be ascribed to the differences between the self-compatibility properties of the Cf30 and Cf45 series. In particular, the slightly higher flowability of the Cf30 mixture, since the increase on the fibre content led to a decrease of the total spread observed in the slump flow test. Moreover, it was also observed a decrease on the average value of η_{exp} from the parallel to the perpendicular sections. In opposite to the parallel sections, the η_{exp} for the perpendicular sections is relatively smaller and is quite close to the theoretical orientation factor for a 3D isotropic uniform distribution (0.5). On the other hand, the values of the average η_{img} computed for the Cf30 and Cf45 series did not differ much and are slightly higher than the theoretical orientation factor for a 2D isotropic uniform distribution (≈ 0.637).

The observed scatter on the fibre orientation factor was higher for the Cf30 series, and in particular for the perpendicular planes.

In Figure 6.12 is represented the relationship between the fibre density and the orientation factor computed from the cross section image analysis, η_{img}. There is no significant difference in this relation between the Cf30 and Cf45 series apart the natural offset in the fibre density in the Cf30 and Cf45 series. As previously observed in Table 6.4, the average values of η_{img} for both Cf30 and Cf45 series are very similar, being slightly lower for the Cf45 series. If the results' analysis is carried out just within each single series, one can state that there is slightly increase of the orientation factor with the fibre density. However, if the results of the two series are analysed together, then the fibre density does not affects so much the orientation factor, since the properties of the matrix in the fresh state play a more important role in the fibre

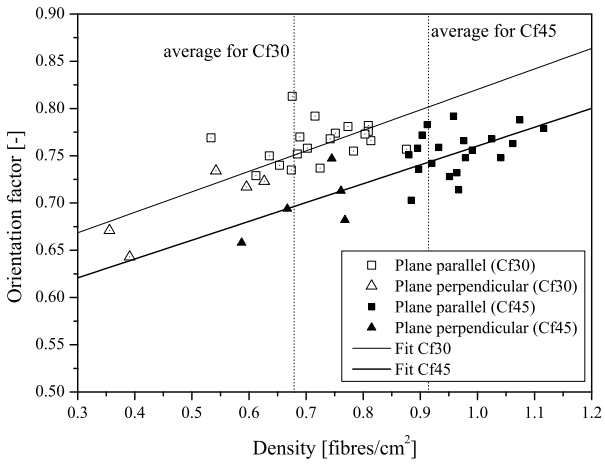

Figure 6.12: Relationship between the fibre density and orientation factor.

alignment. Nevertheless, it is clearly observed an increase of the orientation factor with the fibre density from the perpendicular to the parallel planes.

Influence of gravity on the fibre segregation

In Table 6.5 are included the segregation coefficients, ξ_{seg}, computed by equation 6.6, for the prismatic specimens regarding the gravity direction. This parameter was assessed in the cross sectional planes designated as parallel, see Figure 6.9(a), in order to give an idea of the segregation degree due to the gravity action. Since in self-compacting concrete is not applied external vibration, the segregation observed in the specimens is exclusively due to the gravity influence on the concrete's flow during the casting procedure. Remember, that ξ_{seg} is nonetheless than the ratio between the average fibre depth and the total depth of the cross section, thus if no segregation is observed $\xi_{seg} = 0.5$, on the other hand as the ξ_{seg} value is nearer to 0 or 1, the fibres tend to be segregated, respectively, to the top or bottom of the cross section.

The obtained average values of ξ_{seg} for the studied cross sectional planes were slightly higher than 0.5, approximately 7 to 10% higher. Thus, for the studied self-compacting concrete composition, and in particular for the rheological properties in the fresh state of this SFRSCC, was observed a slight fibre segregation towards the bottom of the prismatic specimen due to the gravity action. The differences between the Cf30 and Cf45 series were marginal. Nevertheless, for the Cf30 series, the average segregation coefficient was slightly higher than for the Cf45 series, and can be ascribed to the higher flowability of the Cf30 series as a consequence of the lower fibre content.

The scatter observed for both series was also relatively reduced, and the maximum value

Table 6.5: Fibre segregation on the prismatic specimens.

Specimen		Parallel direction		Perpendicular direction		Min./Max. ξ_{seg}	
		ξ_{seg}	CoV	ξ_{seg}	CoV	max.	min.
		–	%	–	%	–	–
Cf30	1	0.541	2.7	0.538	–	0.558	0.524
	2	0.543	2.4	0.527		0.550	0.524
	3	0.582	3.5	0.614		0.614	0.527
	4	0.547	3.3	0.554		0.554	0.571
	5	0.518	3.9	0.557		0.557	0.516
	Avg.	0.546	4.5	0.551	4.0	–	–
Cf45	1	0.532	1.4	0.518	–	0.548	0.517
	2	0.541	2.5	0.571		0.569	0.513
	3	0.544	1.9	0.531		0.561	0.522
	4	0.522	2.4	0.524		0.527	0.502
	5	0.556	1.7	0.538		0.563	0.534
	Avg.	0.539	2.2	0.536	2.1	–	–

of ξ_{seg} observed in a cross section was 0.614 which represents a degree of fibre segregation of 22.8%. In general, the ξ_{seg} values for the studied self-compacting concrete composition are slightly lower when comparing with values from literature, for conventional fibre reinforced concrete. Therefore, the fibre segregation in the studied self-compacting concrete is slightly lower than in conventional concrete. This held true if the conventional fibre reinforced concrete is vibrated, as commonly it is. For conventional fibre reinforced concrete, Babut (1986) obtained a $\xi_{seg} = 0.5$ for specimens without external vibration. In Table 6.5 are comprised segregation factors obtained from the literature for several fibre contents, fibre aspect ratio and vibration times. Remark, that the results from Barros et al. (2002) and Barr et al. (2003) were determined from the manual fibre counting at the crack surface, whereas results from Babut (1986) were obtained from the image analysis of cut cross sections.

6.6.3 Experimental results on the cylindric specimens

Fibre density

In Table 6.7 are included the fibre density of the analysed cylindric specimens' cross sections. The fibre density was assessed at three sections perpendicular to the specimen's longitudinal axis, at three distinct heights, namely, 75, 150 and 225 mm, respectively, designated of bottom, mid and top sections, as depicted in Figure 6.9(b).

For the Cf30 series, the fibre density was considerably higher at the specimen's mid section, nearby 53% when compared to the average value of the other two sections (bottom/top),

Table 6.6: Fibre segregation on prismatic specimens of conventional fibre reinforced concrete.

REFERENCE	fibre content [kg/m^3]	aspect ratio	vibration time [sec.]	ξ_{seg}
Babut (1986)	39	66/25	120	0.560
	78			0.570
	117			0.540
Barros et al. (2002)	10	80/60	40	0.540
	20			0.582
	30			0.596
Barr et al. (2003)	25	65/60	–*	0.605
	50	80/60		0.530
	75	65/60		0.543

* the vibration time is not specified.

whereas for the Cf45 series the fibre increase observed at the mid section was just about 24% when comparing with the average value of the other two sections. Regard that area of the mid section corresponds to a diameter of 150 mm and is larger than at the bottom and top sections (diameter of 120 mm), since for these last two sections the fibre density was assessed at the fracture surfaces, i.e. at the notched sections of the tensile specimens. This suggests that there is a higher amount of fibres nearby the cylindric mould walls, moreover as fibres are located closer the mould walls, there will be a wall effect which will favour the fibre alignment towards the longitudinal axis of the cylindric specimen, and consequently, perpendicular to the studied cross sections, increasing the fibre probability of intersection with the studied planes.

Concerning the Cf30 series, the measured average fibre density along the specimen's height was considerably smaller, nearby 57%, than the expected theoretical fibre density, $N_f^{3D} = 0.435$, assuming a 3D isotropic uniform random distribution. As previously seen, this theoretical value is related with the fibre inclination factor and fibre content (see equation 6.2), in addition it does not have into account the boundaries of the specimen, which promotes the preferential fibre orientation according a parallel direction to those boundary surfaces. Due to the geometric dimensions of the used cylinders, it was not expected such a significant difference, since a great volume of concrete is within the influence zone of the specimen's boundaries. Thus, the fibre density reduction observed, may be ascribe either to an improper filling of the mould or a bad fibre dispersion within the planetary mixture. On the other hand, for the Cf45 series, the measured fibre density and the correspondent theoretical one $N_f^{3D} = 0.649$ are quite similar. In fact, only for the bottom section was observed a difference worthy of register, with a measured fibre density 14% smaller than the theorectical one assuming a 3D uniform isotropic random distribution.

In Figure 6.13 is depicted the fibre density variation along the cylindric specimen's height.

Table 6.7: Fibre density on the cylindric specimens.

Specimen		(nom.)	Num. of fibres in the planes:			Min. num. fibres
		N_f^{3D}	Bottom	Mid	Top	$\check{N}_f^{\|\|}$ *
		fibres/cm^2				fibres/cm^2
Cf30	1	0.435	0.256	0.289	0.132	0.115
	2		0.283	0.317	0.283	
	3		0.327	0.373	0.230	
	4		0.177	0.340	0.265	
	5		0.115	0.458	0.309	
	Avg.		0.232	0.355	0.244	–
	CoV		36.7%	18.4%	28.2%	
Cf45	1	0.653	0.575	0.702	0.734	0.486
	2		0.486	0.605	0.716	
	3		0.522	0.775	0.566	
	4		0.672	0.662	0.645	
	5		0.548	0.741	0.548	
	Avg.		0.561	0.697	0.642	–
	CoV		9.5%	12.6%	13.1%	

* Parallel to the notched planes

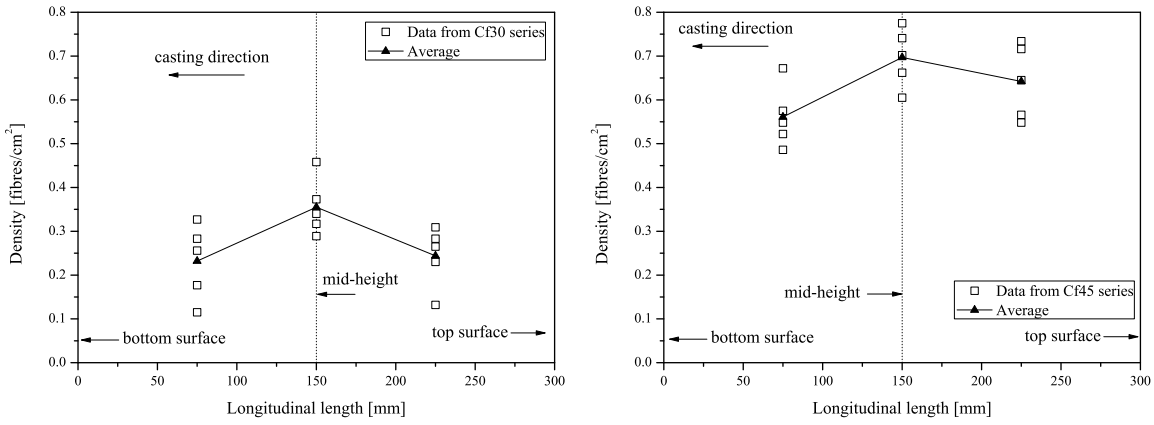

(a) (b)

Figure 6.13: Fibre density along the cylindric specimen's length for: (a) Cf30 and (b) Cf45 series.

Although it was observed a higher average fibre density at the mid section, due to the already explained reasons, in general no significant differences were observed between the bottom and top sections for the Cf30. On the other hand, regarding the Cf45 series, the fibre density observed for the top section was higher than at the bottom section, approximately 14%. Nevertheless, these small difference may suggest that in the cylindric specimens the fibre segregation due to both the high concrete flowability and gravity action is smaller than the one observed

for the prismatic specimens. In the author opinion, this may be related to the smaller mould dimensions and geometry of the cylinder, since the smaller mould's opening in which the fresh concrete is poured will not enable the concrete to freely flow in a specific direction.

Fibre orientation

In Table 6.8 are included the fibre orientation factors computed from two distinct approaches, as performed for the prismatic specimens, η_{img} from the image analysis procedure, and η_{exp} from equation 6.20, based on the counted number of fibres presented in Table 6.7.

Table 6.8: Fibre orientation factors on the cylindric specimens.

SPECIMEN		Bottom	Mid height		Top
		η_{exp}	η_{img}	η_{exp}	η_{exp}
Cf30	1	0.294	0.607	0.332	0.152
	2	0.325	0.542	0.364	0.325
	3	0.376	0.585	0.429	0.264
	4	0.203	0.553	0.391	0.305
	5	0.132	0.622	0.526	0.355
	Avg.	0.266	0.586	0.408	0.280
	CoV	36.7%	7.1%	18.4%	28.2%
Cf45	1	0.440	0.560	0.538	0.562
	2	0.325	0.593	0.464	0.421
	3	0.400	0.665	0.594	0.434
	4	0.515	0.612	0.507	0.549
	5	0.420	0.671	0.568	0.495
	Avg.	0.421	0.620	0.534	0.492
	CoV	16.3%	7.6 %	9.5%	13.1%

The average orientation factor computed from the image analysis approach, η_{img}, is considerably higher than the correspondent η_{exp}, this is only applicable to the mid section. As previously stated, η_{exp} is determined based upon the number of fibres counted at the cross section. Moreover, the fibre density at the bottom and top section, corresponding to the notched cross section of the tensile specimens of the Cf30 series, was unexpectedly lower than the theoretical fibre density assuming a 3D isotropic uniform distribution, thus leading to these low values that may be biased. The only exception was the mid section for the Cf45 series with a value of 0.534, i.e. 6.8% higher than the theoretical orientation factor for a 3D distribution $\eta_{3D} = 0.5$.

In what concerns to the orientation factor computed from the image analysis approach, the obtained values seem more realistic, and they were approximately 17 and 24 % higher than

the theorectical value for a 3D distribution, respectively, for the Cf30 and Cf45 series. For the smaller dimensions of the cylindric specimen (in comparison to the prismatic specimens) and casting direction, the fibre alignment along the fresh concrete flow is not so preponderant as in the prismatic specimens, thus it is quite feasible that the orientation factor is closer to 0.5 (3D distribution). However, having also in mind that the fibre's orientation within 36% of the cylinder cross sectional area will be influenced by the mould surface (wall-effect), for this reason is also feasible that the fibre orientation factor would be higher than 0.5. The obtained η_{img} average values suggest that the fibre structure is slightly aligned with the cylinder longitudinal axis, as they lay between the theoretical orientation factor for a 3D and 2D isotropic distributions with a value of, respectively, 0.5 and $2/\pi \approx 0.637$.

6.7 Conclusions

In this chapter was conducted an analysis of the fibre distribution within a self-compacting concrete matrix. With this purpose, it were ascertained some parameters that give an idea of the fibre structure, such as: fibre density, orientation and segregation. The obtained experimental results were compared with results from literature for conventional fibre reinforced concrete and other concretes with self-compacting ability. The fibre structure analysis was performed in cylindrical and prismatical specimens, by means of fibre counting at the fracture surfaces of the specimens used for assessing the mechanical properties of the SFRSCC, as well as using an image analysis procedure on sawn sections from the specimens.

Regarding the prismatic specimens, the fibre density and orientation factor were assessed in two orthogonal planes' directions. One parallel ($||$) to both the crack surfaces of the tested specimens and the concrete's flow direction, and another perpendicular ($\perp$). The fibre density measured for SFRSCC at the parallel planes, $N_f^{||}$, was considerably higher than the expected theoretical fibre density assuming a 3D isotropic uniform random distribution, N_f^{3D}. In fact, $N_f^{||}$ was between 47% and 66% higher than N_f^{3D}. This effective increase on the fibre density can be ascribed to both the wall-effect and high flowability of the concrete in the fresh state. This effective increase on the fibre density for SFRSCC was considerably higher than for conventional SFRC. This was to some extent expected, if having in mind that an eventual effective increase for conventional SFRC can only be justified by the wall-effect or a deficient fibre dispersion, i.e. fibre bundles at the measured sections. In what concerns to the fibre orientation factor, similar findings can be pointed out. In fact, the difference between the measured fibre density and the correspondent expected one of SFRSCC is due to an increase of the average orientation factor consequence of a fibre alignment along the concrete's flow direction. The degree of fibre segregation due to gravity effect on the SFRSCC was slightly smaller than the fibre segregation

of conventional SFRC (values withdraw from literature).

For the cylindric specimens, both the fibre density and orientation factor are much closer to the expected theoretical values assuming a 3D isotropic random distribution, when comparing with the results obtained from the prismatic specimens. However, in general, the experimental fibre density was smaller than the theoretical one for a 3D random distribution. Considering that the expected fibre density does not have into account the boundaries of the specimen, it is feasible to assume that a improper filling of the mould or a deficient dispersion within the planetary mixture has occurred. The ascertained degree of fibre segregation for the cylindric specimens due the gravity effect did not show any conclusions worthy of register.

At last, epitomizing, the fibre structure parameters assessed for the prismatic and cylindric specimens shown that there are considerable differences on their fibre structure. The differences on the fibre effectiveness found for each type of specimen, due to distinct geometries of the mould and casting procedures, will lead to distinct mechanical performance of the composite. The knowledge of how the fibre orientates within certain test specimens (e.g. cylindric - uniaxial tension tests; prismatic - three-point bending tests) enables a better understanding of the post-cracking behaviour derived from each experimental test.

Chapter 7

Compressive Behaviour of the SFRSCC (age influence and modelling)

7.1 Introduction

The existing material models are not able of simulating, with sufficient accuracy, the compressive behaviour of steel fibre reinforced self-compacting concrete, SFRSCC. The development of both the compressive strength and elasticity modulus are probably ones of the most intensely studied parameters of concrete. Mainly, this is due to the fact, that these parameters are ones of the most important and used in structural analysis. The development of the compressive strength and the elasticity modulus with age are dependent of several aspects, such as: water/cement ratio, type of cement, additives, puzzolans or other additions and curing conditions, namely, temperature and moisture. The mechanical properties of young concrete limit the construction speed and quality. Thus, a better understanding of these mechanical properties of concrete at early ages is essential for engineers to make their decisions during the construction phase. For steel fibre reinforced composites, the knowledge of the stress - strain behaviour under compression plays even a more important role than for plain concrete. Since, to take advantage of this composite higher toughness, the stress - strain curve is necessary for a correct evaluation of the structures's ductility.

A good knowledge of the stress - strain relationship at early ages plays also an important role in the determination of time for the removal of shoring and in the calculation of thermal stresses due to the hydration heat of cement and shrinkage stresses that occur during the hardening. A comprehensive understanding of the concrete members' behaviour, at an early age, is necessary

not only for the design and construction of the concrete structures, but also for the evaluation of durability and service life. Moreover, in the precasting industry, demoulding the elements as soon as possible is an important requirement. To assure safe demoulding process, the influence of the concrete age on the compressive behaviour of the SFRSCC should be known.

Concrete can be regarded as a multi-scale material consisting of aggregates embedded in a binder matrix. The properties of this material, depend on both the properties of its constituents and of the interface between these constituents. The presence of the weak interfaces zones allows the crack initiation and successive stable crack propagation before the peak load is attained. The nucleation, growth, interaction and coalescence of micro-cracking leads to the macroscopic failure of concrete, since in the post-peak behaviour, after the crack localization, it is induced an unstable crack propagation, i.e. decrease of the stress with the crack increase (Shah et al. 1995, Van Mier 1997). Thus, according to Van Mier (1997), the use of strain as state variable in constitutive laws for concrete is not accurate. Hence, fracture mechanics should be used to describe the failure of concrete, since the localized damage band can be physically simulated by a crack. Stress and strain variables used to define constitutive laws are, from an axiomatic point of view, only valid at a macro-level of analysis and, consequently, unsuitable to describe localized phenomena, like tensile and shear failure modes.

The full compressive stress - strain relationship, $\sigma_c - \varepsilon_c$, can be regarded as a structural response dependent on the adopted test set-up and specimen, rather than a pure material behaviour in a representative volume element. Since, there are structural changes at a scale of the same specimens' size magnitude, due to the macro-cracks growing process. In spite of that, representing the compressive material behaviour in terms of a $\sigma_c - \varepsilon_c$ relationship is quite useful in terms of structural design. Most model equations used presently have been developed for old-age concrete and for plain (Wang et al. 1978, Carreira and Chu 1985, CEB-FIP 1993) and current fibre reinforced concrete (Fanella and Naaman 1985, Ezeldin and Balaguru 1992, L. S. Hsu and C. T. Hsu 1994, Barros 1995, Nataraja et al. 1999). More recently, Yi et al. (2003) studied the effect of different concrete's strength classes and ages on the stress - strain relationship of current fibre reinforced concrete. The latter author, also proposes a model equation supported on the previous work of Carreira and Chu (1985). In the context of SFRSCC, and within the author knowledge, there are not appropriate stress - strain equations to model the early age concrete behaviour under compression.

In this chapter, the compressive softening behaviour of SFRSCC was investigated, within a structural point of view. Stress - strain laws are proposed to model the behaviour of the SFRSCC since the early ages. Additionally empirical expressions to predict the principal mechanical properties are presented.

7.2 Experimental program

7.2.1 Research parameters

The present experimental program was defined to evaluate the influence of the fibre content and concrete age on the uniaxial compressive behaviour of steel fibre reinforced self-compacting concrete, SFRSCC. For this purpose, two series with distinct fibre contents were prepared. The first one with 30 kg/m^3 is denominated by Cf30 and, the other, with 45 kg/m^3 designated by Cf45. Each of these series was composed by sub-series that were tested at distinct ages, respectively, 12 and 24 hours, 3, 7 and 28 days.

The stress-strain relationship was obtained as the direct result of the compression tests. Additionally, the principal mechanical properties of the SFRSCC, such as: the compressive strength, f_{cm}, the elasticity modulus, E_{ci}, strain at peak stress, ε_{c1} and the volumetric energy dissipated, G_c were also determined.

7.2.2 Concrete mixture

Conception method

The materials used in the composition of the SFRSCC, were: cement CEM I 42.5R, C, limestone filler, Lf, superplasticizer of third generation based on polycarboxilates (Glenium 77SCC), Sp, water, W; three types of aggregates (fine river sand, Fs, coarse river sand, Cs, and crushed granite 5-12 mm, Ca) and type A hooked end steel fibres. The adopted fibre had a length l_f=60 mm, a diameter d_f=0.75 mm, an aspect ratio l_f/d_f=80 and a yield stress of 1100 MPa.

In previous works (Pereira et al. 2004, 2005), a series of tests were carried out to achieve the optimum composition. The method used for defining the composition of the SFRSCC was based upon the three following steps:

1. the proportions of the constituent materials of the binder paste were defined;
2. the proportions of each aggregate on the final solid skeleton were determined;
3. binder paste and solid skeleton were mixed in different proportions until self-compacting requirements in terms of spread ability, correct flow velocity, filling ability, blockage and segregation resistance were assured.

In the first step, a series of tests were performed to achieve the optimum composition of the binder paste. To define the optimum percentage of Lf addition in the final composition, several mixes of Lf, cement and water were executed. The proportions of each component were defined in terms of volume, the water content was 66% of cement volume, and the percentage

of LF has varied between 0% and 125% of the cement volume. To promote the dispersion and deflocculation of the fine particles in suspension, a small constant quantity of superplasticizer was also added to each mix. The relative spread in the "Flow table" and the "Marsh cone" flow's time of each mix were measured. In order to have some guidance in the paste design phase, the compressive strength of each mix was also evaluated on 5 cm edge cubic specimens at an age of 7 days. A percentage of LF similar to the cement percentage has resulted in a good compromise between strength and flowability requirements. Moreover, this has also allowed to maintain the amount of cement on the final concrete mix only slightly above 350 kg/m^3 for the Cf30 series.

In the second step, the most appropriate proportions of the three types of aggregates were obtained executing mixes of distinct quantities of each type of aggregate, and weighting 5 dm^3 volume for each mix. The optimum aggregate mix was assumed to be the heaviest one, since it should correspond to the most compact. An estimated portion of fibres equivalent to 30 kg of fibres per m^3 of concrete was included in every mixture. Initially, only two of the three aggregates' types were mixed. After finding the optimum relation between those two, the third aggregate was added in distinct volumetric percentages, keeping constant the relation between the two first aggregates. These results indicated that the optimum solid skeleton was composed, in volume, by 49.5% of coarse sand, 40.5% of crushed stone and 10% of fine sand for the Cf30 series.

Relatively to the Cf45 series, since a higher content of fibres is used, the solid skeleton composition (aggregates) should be redesigned to avoid an increase of void content in the solid skeleton structure. The solid skeleton composition was evaluated according to the procedure previously described. The final composition of the solid skeleton for Cf45 series was (in percentage of volume): 46.75% of coarse sand, 38.25% of crushed aggregate and 15% of fine sand. Note that, the percentage of fine sand increased, while the relative percentage of coarse sand and crushed aggregate decreased. To obtain the percentage of the binder paste in the total volume of concrete, some mixes of concrete were conceived, varying the paste percentage. To attain the self-compacting requirements for the series with a fibre content of 45 kg/m^3, when compared to the Cf30 series, it was necessary to increase the ratio of paste/total volume, as well as the volume of the superplasticizer. The self compacting parameters were measured for each trial, performing the L-Box and the Slump Flow tests. In this phase the V-Funnel test was not used. In fact, this test is not feasible since the fibre has a length too high for the reduced overture of this test's apparatus.

Table 7.1 includes the composition that has best fitted self-compacting requirements, for the adopted fibre contents, CF, 30 and 45 kg/m^3. Remark that, in Table 7.1, WS is the water necessary to saturate the aggregates and W/C is the ratio water/cement. The parcel WS was

not used to compute the ratio W/C.

Table 7.1: Compositions for 1 m^3 of SFRSCC.

Cf [kg]	Paste/Total volume [%]	Cement [kg]	Lf [kg]	Water [dm^3]	Ws [dm^3]	Sp [dm^3]	Fs [kg]	Cs [kg]	Ca [kg]	W/C [-]
30	0.34	359.4	312.2	96.9	64.7	6.9	108.2	709.4	665.2	0.29
45	0.38	401.7	344.3	108.4	60.8	7.6	101.7	666.4	624.8	0.29

Mixing

A planetary mixer of vertical axis, with 360 l capacity, was used to manufacture the SFRSCC. In each series, approximately 250 l were produced. For every mixture, fine and coarse river sand, crushed granite, water, cement, limestone filler and the steel fibres were weighed separately. The accuracy of the scale device for the aggregates and binder was about 10 g, whereas for the other items the scale device's accuracy was about 1 g.

The aggregates were put into the mixer in a predetermined order regarding their dimensions, i.e. from the highest to the lowest aggregate dimension. First the crushed granite was added, then the coarse river sand and the fine river sand, and finally were mixed during one minute. Meanwhile, the aggregate saturation degree was determined. After this, it was added the necessary water quantity to saturate the aggregates (Ws), and the mixing continued again during one minute. Then, by this order, the limestone filler and cement were added, and another minute of mixing was taken. Afterwards, the water necessary to hydrate the cement was added with the mixing machine running. Finally, the superplasticizer and the steel fibres were added. The concrete was mixed during about 300 seconds, until it started to exhibit good homogeneity.

After mixing the concrete and before casting, the following properties were measured: flow spread and flow rate.

Properties of the fresh concrete

Figure 7.1 depicts the final state of a performed slump flow test for a self-compacting concrete with 45 kg/m^3 of fibres. No sign of segregation was detected. A total spread of over 700 mm was measured for both series, and the mixture showed good homogeneity and cohesion, even when flowing through the small orifice of the Abrams cone. Notice that when testing, the Abrams cone was always used in the inverted position.

Another parameter measured was the time to reach a spread diameter of 500 mm, T_{50}. For

the Cf30 series, T_{50} was 4.5 seconds, whereas for the Cf45 series a time of 5.2 seconds was measured.

Figure 7.1: Self-compacting concrete spread obtained on the slump flow test for a self-compacting concrete with 45 kg/m^3 of fibres.

7.2.3 Test specimens

The recommendation of RILEM TC 148-SSC (2000), for strain - softening tests under uniaxial compression, requires at least three test specimens per experiment. In the present work, six specimens were used for each series. This number of specimens was chosen to take into account the scatter, in order to obtain more realistic average and characteristic results.

Dimensions

Several authors recommend a minimum test specimen size according to the maximum dimension of the aggregate, or in the present case, the fibre length, since fibre is assumed as an aggregate. Kooiman (2000) and RILEM TC 148-SSC (2000) suggested that the minimum dimension of the test specimen should be at least five times the largest aggregate. On the other hand, the ACI Committee 544 (1988) recommend that the smallest specimen dimension should be three times larger than the fibre length and/or the maximum aggregate size. In the present work, fibres with a length of 60 mm were used, which suggests that the minimum test specimen size should be 180 mm or 300 mm according to the previous recommendations.

To have a representative zone that is not influenced by the confinement effect introduced by the steel load platens of the compression machine into the concrete (Mier 1984, Van Mier 1997), the specimen should have a length larger than twice the characteristic dimension of its

cross section (RILEM TC 148-SSC 2000, Camões 2002).

If a cylinder specimen is adopted, the previous recommendations point out the use of a specimen with a diameter of 180 mm and a length of 360 mm, or a specimen of 300 mm diameter and 600 mm length. If this last specimen was adopted, the number of specimens for each batch would have to be smaller than the desired number, due to the volume capacity of the mixer. Since the addition of fibres to a concrete matrix scatter increases the dispersion of the main relevant concrete properties, the minimum number of specimens, previously indicated, should be a priority requisite on the decision of selecting the specimen dimensions. In addition, since the dimensions of the smallest possible specimen are not too different of the cylindrical moulds available in the laboratory, 150 mm diameter and 300 mm height cylindrical specimens were adopted for the assessment of the compressive behaviour of the designed SFRSCC.

Production

The test results are affected by the way that the specimens are obtained and tested (Van Mier 1997). In fact, the relative direction between the concrete casting and the test loading, and the method for obtaining the specimens (sawing or casting) are some of the conditions that affect the stress - strain relationship recorded in the tests. This can be aggravated in fibre reinforced concrete specimens, since the shape and dimensions of mould, the casting method and the type of compaction affects the fibre orientation and fibre distribution within concrete and, consequently, different responses could be obtained.

According to the RILEM TC 148-SSC (2000) recommendation, to determine the strain - softening behaviour of plain concrete under uniaxial compression, there are two possibilities to manufacture the test specimens: casting them directly in the size required for the tests, or sawing them from larger blocks. The first alternative is preferred in the present work. This recommendation also suggests that cylinders must be cast vertically and the specimen top surface must be ground in order to assure that the specimen extremities are parallel and orthogonal to the specimens axis.

Within the scope of the present work, due to the smaller resistance of the test specimens for recent ages (12 and 24 hours), a cap of a self-levelling high resistance mortar was applied on the surface of specimen extremities in detriment of the surface grind procedure. In the test specimens with an age of 3, 7 and 28 days, the parallelism of the specimen end surfaces was assured by the grind procedure.

Obviously, the totality of specimens were cast without any external compaction energy.

Curing and demoulding

After the specimens having been cast, they were covered with a wet cloth to avoid moisture losses and were left in the laboratory until the day of the tests. During this period, the cloth was maintained soaked. This procedure was adopted by the fact that, due to the large quantity of specimens, they could not be all put in the fog room at 99% RH and 20°C as recommended by RILEM TC 148-SSC (2000). However, since the specimens were all the time covered by a wet cloth, the relative humidity value should be nearby the value recommended by RILEM TC 148-SSC (2000). The average temperature in the laboratory, during the experimental program, for the series with a fibre content of 30 kg/m^3 was approximately 10ºC; while for the series with 45 kg/m^3 of fibres was 20ºC. The temperature for the Cf30 series was slightly distinct than the one recommended by RILEM TC 148-SSC (2000). The specimens were demoulded on the testing day.

7.2.4 Test set-up

The uniaxial compressive tests performed for obtaining the elasticity modulus and the stress - strain relationship, were carried out in a servo-controlled equipment of 3000 kN maximum load carrying capacity.

Elasticity modulus

The determination of the elasticity modulus was performed according to the LNEC E397 (1993) Portuguese standard. Other standards, such as RILEM TC 14-CPC (1975) and ASTM C469 (1994) recommend similar procedures to those proposed by the adopted standard. According to this specification, the test should be carried out under force control over a certain number of cycles. The test ends when the strain difference, between two consecutive loading cycles, does not exceed 1×10^{-5}. In the initial phase of the test, a stress of 0.5 MPa (σ_b) is applied, and the corresponding strain is measured, ε_b. The stress is then increased at a velocity of 0.2 MPa/s until a stress level $\sigma_a = f_c/3$ is attained, where f_c is the compressive strength, previously obtained in a direct compression test. The stress σ_a is maintained during 90 seconds, and in the last 30 seconds of this period, the strains are recorded ε_a. After this period, the load is decreased at a stress ratio of 0.2 MPa/s until a stress level σ_b. This stress level is maintained during another period of 90 seconds, and in this period the strains are recorded only on last 30 seconds. The elasticity modulus is the average of the $E_{c,n}$ values obtained in each cycle:

$$E_{c,n} = \frac{\Delta\sigma_n}{\Delta\varepsilon_n} = \frac{\sigma_{a,n} - \sigma_{b,n}}{\varepsilon_{a,n} - \varepsilon_{b,n}} \tag{7.1}$$

where $\sigma_{a,n}$ and $\sigma_{b,n}$ are the average of the two stress limits of the n^{th} cycle, $\varepsilon_{a,n}$ and $\varepsilon_{b,n}$ are the correspondent strains. The axial displacement measurement was accomplished using three linear voltage displacement transducers, LVDTs, placed in such a way as depicted in Figure 7.2. The distance between the two rings should be greater than the length of the specimen edge or diameter with a minimum value of 100 mm. During testing, the distance between the two rings was 100 mm. Moreover, the ring device was positioned at mid height of the specimen.

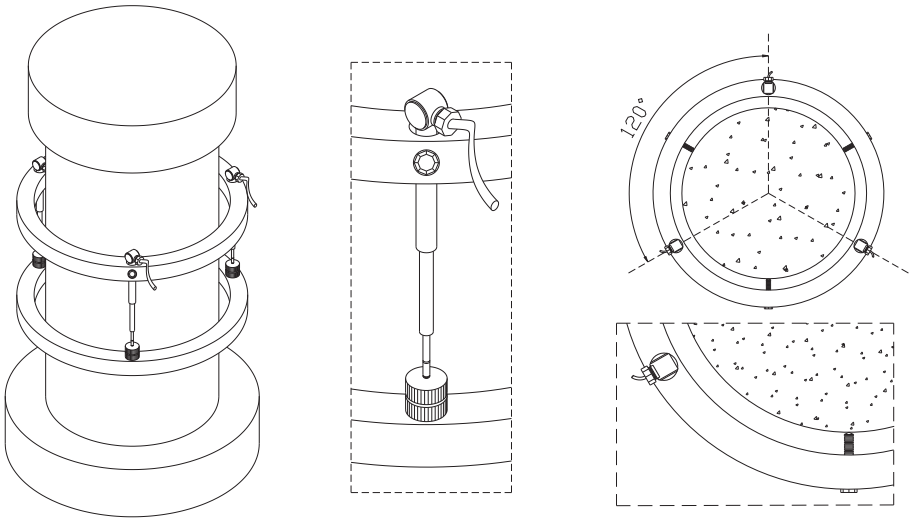

Figure 7.2: Set-up of the compressive test to obtain the elasticity modulus.

Stress - strain curve

To obtain the entire stress - strain curve, $\sigma_c - \varepsilon_c$, it is demanded that the tests overpass the peak stress and should be only ended when the residual stress in the post peak (softening phase) is a small percentage of the peak stress. To assure stable tests, in the softening phase, the testing equipment should have enough stiffness and sophisticated PID control should also be available. The used testing rig has these features, additionally the tests were carried out in displacement control.

During the test execution, the strains were obtained from the relative displacement of the loading platens. For this purpose, three LVDTs were disposed around the test sample forming an angle of 120 degrees between consecutive displacement transducers. Figure 7.3 shows the adopted test scheme. This test set up avoids that, the deformation of the test equipment is added to the displacements read by the LVDTs. This arrangement of the transducers also allows that the specimen deformation in the longitudinal axis, can be computed simply by the average readouts of the three transducers. There is no need to attend to the rotation of the

upper loading platen, since the computed average deformation is located at the longitudinal axis of the cylindrical specimen. The strain was then calculated from the average displacement readings divided by the height of the specimen.

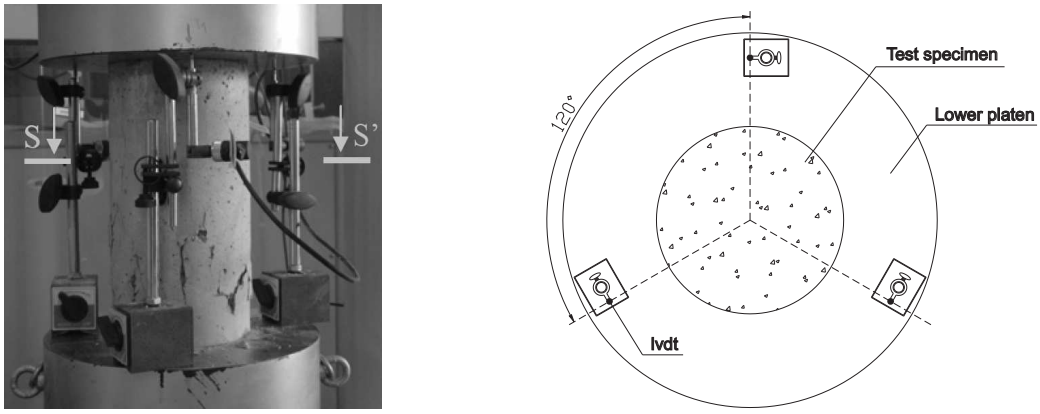

(a) (b)

Figure 7.3: Set-up of the compression test to obtain the stress - strain curve: a) general view, b) section s-s'.

According to RILEM TC 148-SSC (2000), the uniaxial compressive test for plain concrete specimens should be carried out with a displacement ratio of 1 μm/s $\pm$ 0.1 μm/s. However, for steel fibre reinforced concrete, SFRC, the tests can be performed with higher displacements ratios, since this material is considerable less britle than plain concrete. The Japanese recommendation JSCE – SF4 (1984) suggests displacements ratios between the 10 μm/s and 30 μm/s, for the uniaxial compressive tests on SFRC specimens. According to Barros (1995) the stability of the compressive test on SFRC specimens is guaranteed for those displacement ratios. In the present work, the compressive test was carried out using two distinct displacement ratios, a displacement ratio of 10 μm/s was used up to a deformation of 5 mm, while the remaining test phase was controlled at a displacement ratio of 30 μm/s. The test ended at an approximate deformation of 20 mm.

7.3 Failure modes

The typical failure modes observed in the specimens tested under uniaxial compression are schematically represented as the projection to the longitudinal symmetry plane of the cylinder, and are depicted in Figure 7.4. In the tested specimens two main failure modes, FM1 and FM2 were visualized. The third failure mode observed, FM3, was very similar to FM1; however a

larger volume of concrete at the specimen bottom zone was maintained with marginal damage on the specimens, in comparison to the specimens with a FM1 failure mode. An eventual fibre concentration in the specimen bottom part could justify this failure mode.

The FM1 failure mode is characterized by the formation of two cones on the extremities of the cylinder, whereas in the central zone there was the formation of compressive struts separated by vertical cracks. The central part of the cylinder and the cones were not detached due to fibres bridging the cracks, which assured the stress transfer between the rupture surfaces.

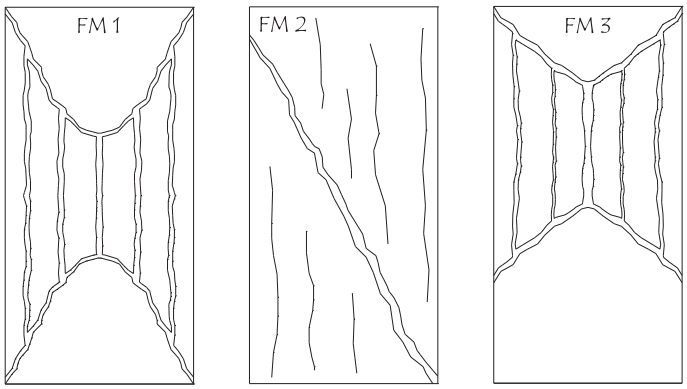

Figure 7.4: Scheme of the failure modes observed in the uniaxial compressive tests.

In the specimens failed in FM2 mode, after the formation of the vertical cracks, which were visible just before the peak load, a shear failure crack was formed in the beginning of the softening phase. The opening and the sliding of this shear failure crack have augmented up to the end of the test. In general, this failure mode leads to stress - strain responses of high volumetric energy, mainly in the softening phase. This can be justified by the fracture mode I energy dissipated in the opening process of the cracks positioned in the vertical (or quasi-vertical) direction (G_{fI}), and the fracture mode I and II energies dissipated in the opening (G_{fI}) and sliding (G_{fII}) of the surfaces of the shear failure crack, see Figure 7.5(a). Since the fibres bridging this shear crack offer resistance to crack opening, the energy dissipated for sliding the faces of this crack increases (higher effect of aggregate interlock).

Finally, the FM3 failure mode developed a smaller cone on the top part of the specimen, whereas the bottom part had little damage. As already mentioned, the higher fibre concentration in the specimen bottom part can justify the reduced damage verified in the almost bottom half part of the specimen. The confinement provided by this zone has forced the vertical compressive struts to propagate into the zone where a cone of confined concrete is formed due to the friction between the top steel platen of the equipment and the top specimen extremity. In result, the height of this cone become smaller. An eventual lower content of fibres in the

top part of the specimen could also have contributed for the decrease of the dimension of this concrete cone.

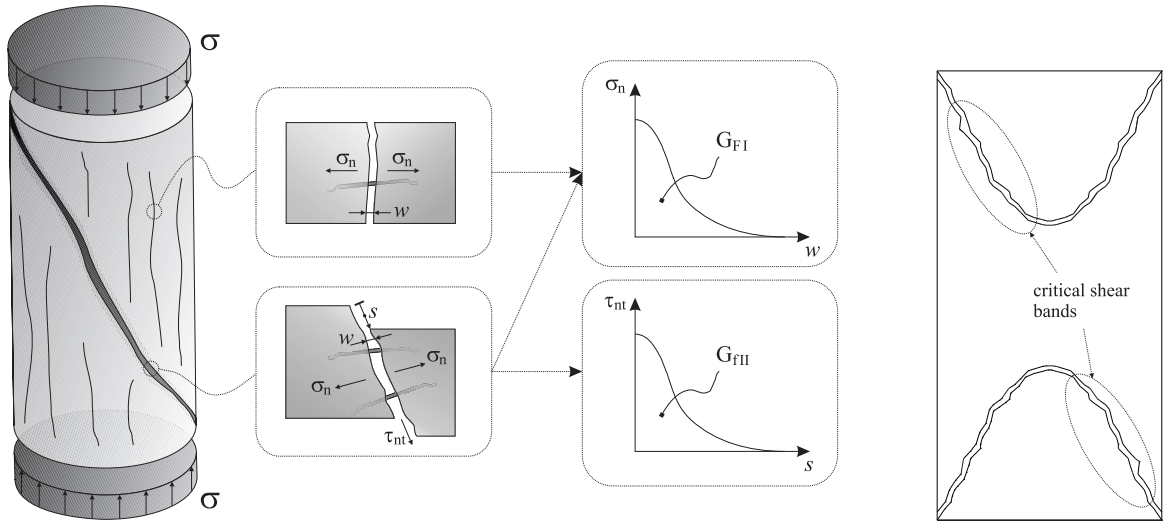

(a) (b)

Figure 7.5: (a) Fibre reinforcement mechanisms in failure mode FM2, (b) Critical shear bands in FM1 and FM3.

Table 7.2 indicates the failure modes observed in each series, whenever more than one failure mode is observed per series, the number of specimens which failed according either mode is included in parenthesis. The confinement provided by the machine steel platens and the existence of fibre reinforcement leads to two zones, at the specimens extremities, of higher resistance to the crack propagation into these zones. In plain concrete of moderate and low strength concrete, each one of these zones, generally, degenerates into conical geometry. However, in high strength fibre reinforced concrete, the fibre pullout resistance is much higher than the resistance offer by the fibres to the crack sliding. In result, when these highly confined concrete zones are displaced due to the applied load, the principal stresses in the contour of these zones are inclined forming inclined micro-cracks that degenerate into a shear failure crack band, see Figure 7.5(b). This justifies why only FM2 failure mode have occurred in the higher strength concrete series (3, 7 and 28 days), while FM1 and FM3 failure modes were visible in the remaining series with lower strength.

The specimens of the series with 3, 7 and 28 days, which in these series presented a lower toughness under compression, had a visible smaller number of fibres crossing the rupture surface. Figure 7.6 shows two specimens with a rupture mode by shear (FM2) containing distinct fibres densities crossing the rupture surface. A closer analysis to the fibres on the rupture surface

Table 7.2: Failure modes observed within the compressive tests.

Age	Series	
	Cf30	Cf45
12 hours	Fm2(1), Fm3(4)	Fm2(1), Fm3(5)
24 hours	Fm1(5), Fm2(1)	Fm2(1), Fm3(5)
3 days	Fm2	Fm2
7 days	Fm2	Fm2
28 days	Fm2	Fm2

showed that in general they did not fail. In some cases the hooked end of the fibres was stretched, which means that the pullout resistance of these fibres were effectively activated. However, in another cases the fibres were bent without the end hook being mobilized. This could be ascribed to the spalling of a concrete volume around the fibre's hooked end within the shear band.

(a) (b)

Figure 7.6: Shear rupture surface: (a) with fibres and (b) without fibres (image edited).

7.4 Stress - strain relationships

The stress - strain curves, $\sigma_c - \varepsilon_c$, for the Cf30 and Cf45 series are represented in Figures 7.7 and 7.8, respectively.

A larger nonlinear branch can be observed in the pre-peak behaviour of the younger specimens, namely, 12 and 24 hours. In fact, a pronounced nonlinear behaviour is observed in the pre-peak phase due to the aggregates – paste weak bond at this age. The porous structure of the interface is gradually converted into discontinuous micro-cracks and, finally, into continuous

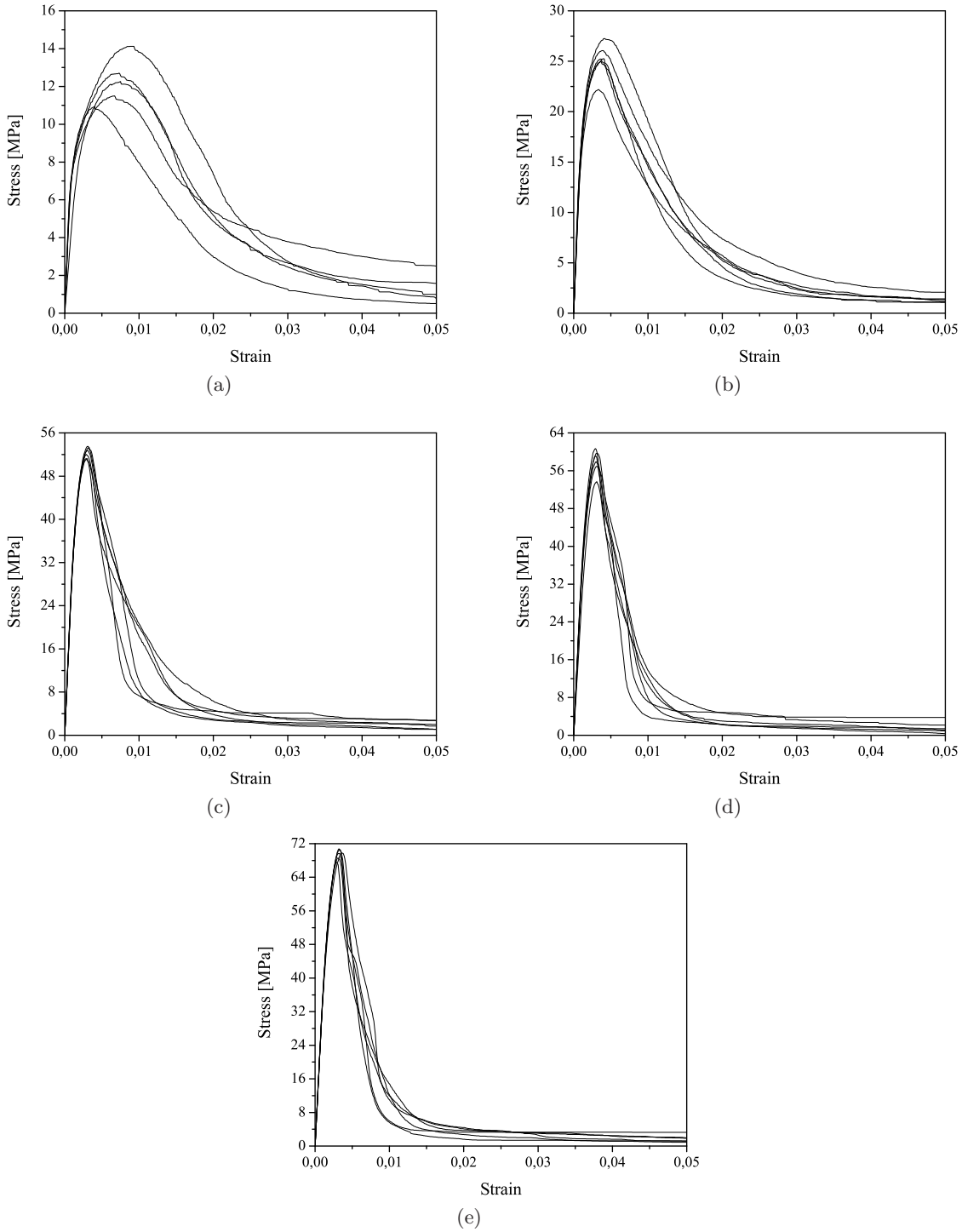

Figure 7.7: Experimental stress - strain relationships for the series Cf30: (a) 12 hours, (b) 24 hours, (c) 3 days, (d) 7 days and (e) 28 days.

cracks during the strain increment applied to the specimens. Since the stiffness of the paste is relatively low at these stages, this evolutive damage procedure is much more stable than in

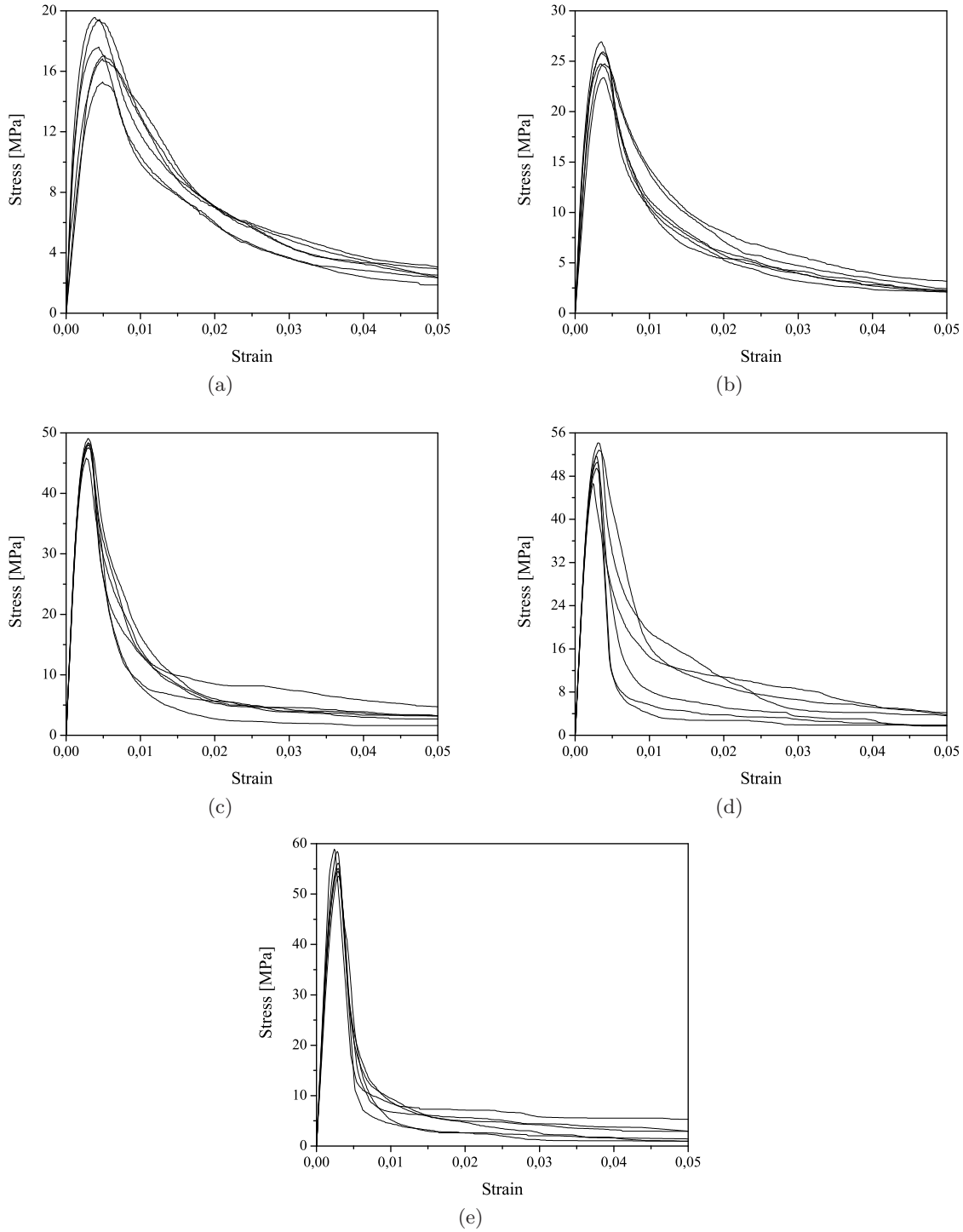

Figure 7.8: Experimental stress - strain relationships for the series Cf45: (a) 12 hours, (b) 24 hours, (c) 3 days, (d) 7 days and (e) 28 days.

older specimens. Consequently, a smother residual strength decay has occurred in the softening phase of the 12 hours specimens. At this age, eventually, the energy dissipated by the pullout

of the fibres after crack initiation is only a small part of the energy at older ages, since the bond strength and the stiffness of the fibre/concrete interface is still relatively low at this age. Moreover, throughout the concrete ageing, the interface and the paste become more stiff, resulting in a $\sigma_c - \varepsilon_c$ linear relationship of higher amplitude in the pre-peak phase. This stiffening and strengthening gaining process leads to more brittle responses in the post-peak phase.

Since fibres crossing the cracks did not break, the concrete energy absorption capacity would have increased with the content of fibres added to the mixture. However, this was not evidenced in the present research, which can be justified by the decrease of the compressive strength from Cf30 to Cf45 series, that caused a decrease in the fibre/concrete bond strength and, consequently, a decrease in the energy dissipated in the fibre pullout process. The decrease of the compressive strength from Cf30 to Cf45 series might be justified by the higher w/c ratio and LF percentage, as well as the lower content of coarse aggregate and coarse sand. As previously mentioned, these changes in the concrete composition were conducted in order to fulfil self-compactibility requirements.

The average $\sigma_c - \varepsilon_c$ curves are depicted in Figure 7.9. The average compressive strength for the older specimens 3, 7 and 28 days was higher on the Cf30 series. For these series, the softening branch was less abrupt than for the Cf45 series. On the other hand, the residual stress for large deformations was slightly higher in the Cf45 series.

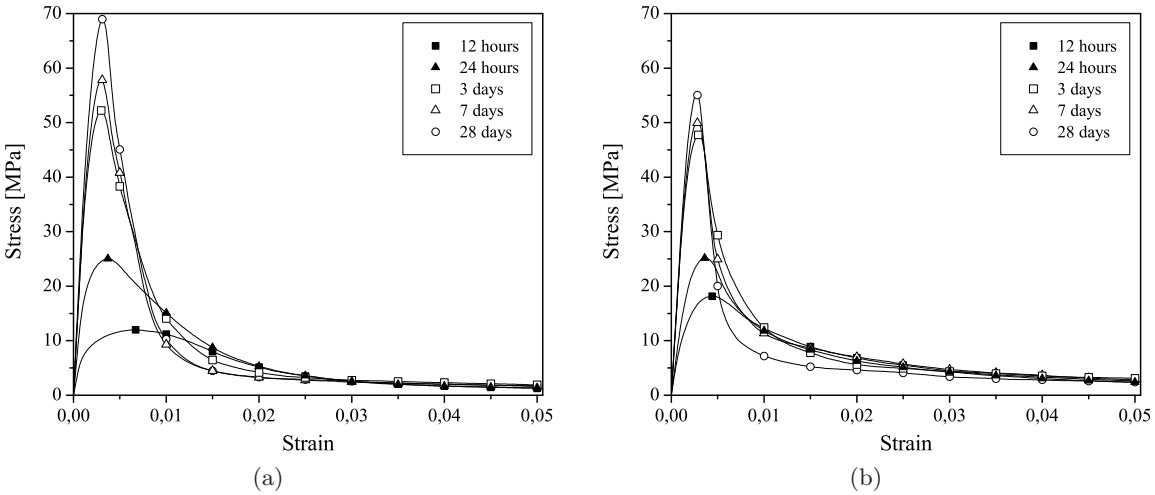

Figure 7.9: Average stress - strain relationships for the series: (a) Cf30 and (b) Cf45.

This increase on the residual strength for the Cf45 series, i.e. with higher fibre content, was expected since there is a higher probability of fibres bridging active cracks, and therefore enhancing the post-cracking behaviour as direct consequence of the fibre density increment.

However, the differences observed in the residual strength between the two series were rather small, in particular for the older series. A plausible explanation for this, may be appointed to the observed failure mode. For these designated older series, namely, 3, 7 and 28 days, the failure mode observed was by a shear crack band, see Figure 7.6(a). In the referred failure mode, the fibre reinforcement mechanisms mobilized, after the localization of the shear band, are due to a mixed fracture mode composed by crack opening and sliding. Since the crack sliding mode probably will be more influential than the crack opening mode. Having in mind that the fibre's shear resistance will be considerably smaller than the fibres pullout resistance, an increase on the fibre content will proportionate a small increase on the residual strength. This justification, may also be corroborated with the uniaxial tensile test results presented in Chapter 8, in which the same fibre content increase produced a significant enhancement of the post-cracking behaviour. Remark, that in the tensile test develops a pure crack opening mode in which the fibres are pulled out, in opposition to the mixed mode observed in the compressive tests.

Since the compressive strength for each series has varied considerably, the normalized stress - strain diagram, $\sigma_c/f_{cm} - \varepsilon$, can better evidence the influence of the fibres on the post-peak behaviour, for the different series. These diagrams for the tested series are represented in Figure 7.10. From the analysis of these diagrams it is clearly perceptible, that the younger series, respectively, 12 and 24 hours, have a more ductile behaviour when compared to the older ones.

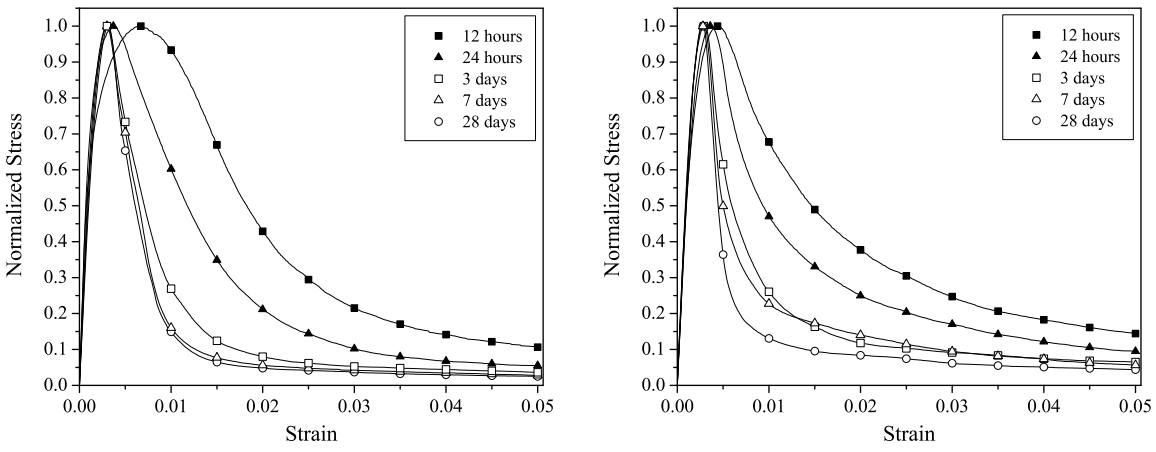

(a) (b)

Figure 7.10: Normalized stress - strain relationships for the series: (a) Cf30 and (b) Cf45.

7.5 Age influence on the mechanical properties

7.5.1 Compressive strength

Table 7.3 includes the average values of the compressive strength, f_{cm}, and the correspondent coefficients of variation, CoV. As expected, for both series, the f_{cm} increases with age. At 28 days, the Cf30 series had a higher compressive strength than the Cf45 series. The higher content of the binder paste on the series Cf45 should have lead to similar resistances. This may be explained due to the influence of the limestone filler and the curing temperature on the hydratation process of the Portland cement. Before advancing with a possible explanation for these results it is important to clarify the following remark: to produce self-compacting concrete it is advised to incorporate high concentrations of fine particles, e.g. limestone filler, in order to attain a high flowability and a high segregation resistance concrete (Okamura 1997).

Table 7.3: Average values of the SFRSCC compressive strength, f_{cm} [MPa].

SERIES		AGE				
		12 h	24 h	3 d	7 d	28 d
Cf30	Avg.	12.3	24.7	52.3	58.1	69.7
	CoV	9.95%	8.38%	1.90%	4.32%	1.73%
	$\left(\frac{f_{cm,t}}{f_{cm,28}}\right)$	0.176	0.354	0.750	0.833	1.000
Cf45	Avg.	17.6	25.3	47.9	51.0	56.2
	CoV	1.63%	1.24%	1.10%	2.61%	2.15%
	$\left(\frac{f_{cm,t}}{f_{cm,28}}\right)$	0.313	0.450	0.852	0.907	1.000

The strength growing with age is significantly influenced by the curing temperature (Kjellsen and Detwiler 1992, Schindler 2004). The higher compressive strengths for the Cf45 series at the younger ages may be due to the higher curing temperature and also to the higher content of filler. Although the filler material has often been considered to be inert, recent experimental research (Poppe and Schutter 2005) showed that limestone filler influences the hydration process. The very small particles of filler favour the rapid growth hydration, the hydrated crystals build more easily the connection between particles, and the crystalline micro-structure is established more rapidly, resulting on higher compressive strengths at early ages. For the 3, 7 and 28 days, the compressive strength was higher in the Cf30 series, due to the strength cross-over effect observed for a lower curing temperature, e.g. as smaller the curing temperature, the higher the compressive strength at old ages and vice-versa (Kjellsen and Detwiler 1992). This effect may also been outsized by the higher limestone filler content for the Cf45 series. More research should be done to understand the influence on the compressive strength of the changes

introduced in the solid skeleton from Cf30 to Cf45 series.

The influence of age on the concrete compressive strength is depicted in Figure 7.11. The growing process of the f_{cm} has two distinct phases: a high increase up to 3 days and a smooth increase after this age. After 3 days, the f_{cm} increase ratio was even less pronounced for the series Cf45. At the age of 3 days, the compressive strength is nearby 75 and 85% of the f_{cm} observed for 28 days for the Cf30 and Cf45 series, respectively. These ratios between the compressive strength at 3 and 28 days, for the studied self-compacting concrete, are slightly higher than values found in literature (Kjellsen and Detwiler 1992, D'Aloia 1997, Kim et al. 2000, Yi et al. 2003). Within the previous references, the observed ratios between the compressive strength at 3 and 28 days ranged between 45 to 70%. The widespread of the aforementioned ratio obtained in literature can be ascribed to several factors, e.g. to the distinct water/cement ratios used on those studies, which varied between 0.30 and 0.54, and consequently resulting in concretes with different class resistances.

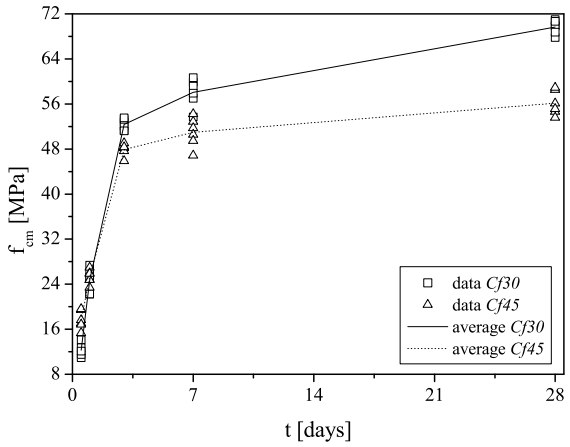

Figure 7.11: Influence of the age on the SFRSCC compressive strength, f_{cm}.

7.5.2 Elasticity modulus

The average values of the elasticity modulus, E_{ci}, and the correspondent coefficients of variation, CoV, are indicated in Table 7.4. These values were determined in accordance to the procedure detailed in section 7.2.4.

The E_{ci} increased with age for both series. The influence of the concrete age on the E_{ci} is depicted in Figure 7.12, from which it can be withdraw that E_{ci} has a similar variation with age as f_{cm}. However, for Cf30, the f_{cm} value increased between 7 and 28 days, while the E_{ci} of this series had a marginal increment in this period. The E_{ci} of the Cf45 series, after day three,

Table 7.4: Average values of the SFRSCC elasticity modulus, E_{ci} [GPa].

SERIES		AGE				
		12 h	24 h	3 d	7 d	28 d
Cf30	Avg.	13.6	25.3	37.1	40.4	41.5
	CoV	17.86%	4.96%	4.31%	0.78%	2.31%
	$\left(\frac{E_{ci,t}}{E_{ci,28}}\right)$	0.328	0.609	0.895	0.973	1.000
Cf45	Avg.	18.8	22.4	31.4	31.9	34.5
	CoV	7.10%	5.83%	2.04%	2.14%	4.33%
	$\left(\frac{E_{ci,t}}{E_{ci,28}}\right)$	0.545	0.649	0.910	0.925	1.000

had an increment of only 3 GPa. These results point out that the stiffness of both SFRSCC is almost attained between the age of 3 to 7 days, due to the high matrix compacity of these concretes. In fact, at the age of 3 days, the stiffness of both series is approximately 90% of stifness observed at an age of 28 days. As an example, the $E_{ci,3}/E_{ci,28}$ computed from the equation suggested by the CEB-FIP (1993) for conventional concretes yields 0.814, i.e. at the age of 3 days the stiffness is nearby 81% of the one for 28 days.

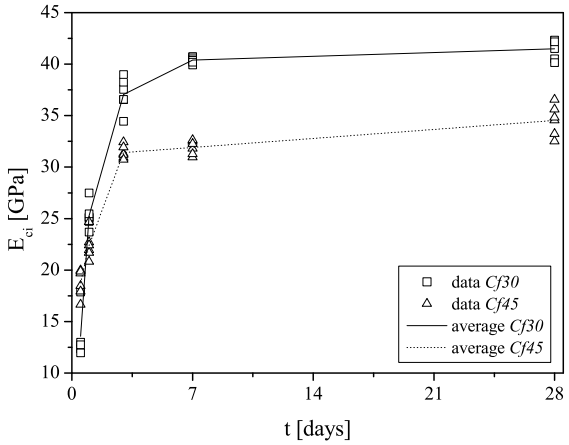

Figure 7.12: Influence of the age on the SFRSCC elasticity modulus, E_{ci}.

7.5.3 Strain at peak stress

The average values of the strain at peak stress, ε_{c1}, and the correspondent coefficients of variation, CoV, are included in Table 7.5. Due to the increase of the concrete stiffness, ε_{c1} decreased with age for both series. Since the increase of E_{ci} after 3 days is not significant, the variation of ε_{c1} is small after this age. Similar conclusions were also found by Yi et al. (2003) for the compressive behaviour of plain concrete at early ages.

Table 7.5: Average values of the strain at peak stress, ε_{c1} [mm/mm].

Series		Age				
		12 h	24 h	3 d	7 d	28 d
Cf30	Avg.	0.0067	0.0039	0.0030	0.0031	0.0031
	CoV	28.90%	7.84%	3.99%	5.14%	6.28%
	$\left(\frac{\varepsilon_{c1,t}}{\varepsilon_{c1,28}}\right)$	2.161	1.258	0.968	1.000	1.000
Cf45	Avg.	0.0047	0.0037	0.0030	0.0029	0.0028
	CoV	10.25%	5.27%	5.77%	9.55%	5.69%
	$\left(\frac{\varepsilon_{c1,t}}{\varepsilon_{c1,28}}\right)$	1.679	1.321	1.071	1.036	1.000

Figure 7.13 shows the variation of the ε_{c1} with age. The ε_{c1} decreased abruptly up to 3 days, however after this age the decrease is marginal. The ε_{c1} values at an age of 12 hours are rather large. At this stage, the stiffness of the concrete matrix is quite small (see values of the elasticity modulus in Table 7.4). Moreover, at this age the hydration processes are still growing, since calcium silicate hydrate and calcium hidroxide have not yet strongly interlaced together and there are more moisture and voids. As a result, it is observed a viscous behaviour of concrete, due to boundary sliding between group of hydration products (Jin and Li 2000).

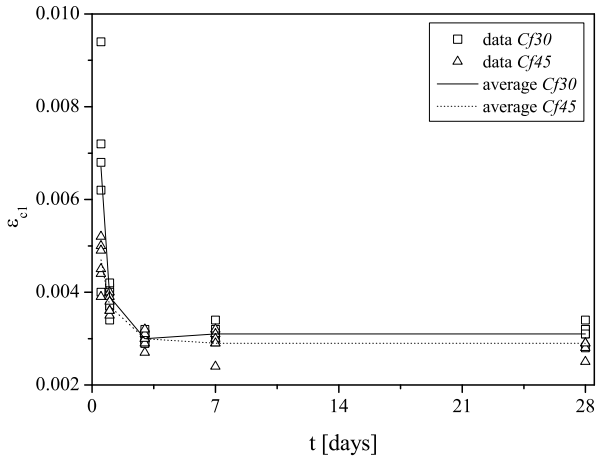

Figure 7.13: Influence of the age on the strain at peak stress, ε_{c1}.

On the other hand, the ε_{c1} values at the age of 28 days obtained for both series, are approximately about 0.003. Similar values of ε_{c1} were obtained for steel fibre reinforced concrete by L. S. Hsu and C. T. Hsu (1994), Barros (1995), Kooiman (2000) and Cunha (2004). This value is higher than the fixed value of 0.0022, proposed by the CEB-FIP (1993) for plain concrete. On the other hand, the EN 1992-1-1 (2004) suggests different values of ε_{c1} depending on the concrete strength classes. For the average compressive strength of the Cf30 series, the

value suggested by this standard is 0.0026, whereas for the average strength of Cf45 series the value proposed is 0.00245. This difference is due to the effect of the fibres bridging the cracks that are formed just before the peak load.

7.5.4 Energy dissipated under compression

The energy dissipated per unit volume under compression, G_c, was calculated as the area under the stress - strain curve, $\sigma_c - \varepsilon_c$. This value can be computed using Equation 7.2. The G_c value was always determined until an ultimate deformation, ε_u, of 0.05, where it was expected that the residual strength would be small.

$$G_c = \int_0^{\varepsilon_u} \sigma_c \, d\varepsilon \tag{7.2}$$

Table 7.6 includes the average values of G_c and the correspondent coefficients of variation, CoV. In general, the concrete energy absorption increased with age. The values of the coefficients of variation however, are quite high. The major part of the energy is released in the softening phase, which is too dependent on the fibre reinforcement mechanisms provided by fibres crossing the cracks. The efficiency of those mechanisms depend considerably on the fibre bond length and fibre orientation towards the cracks they bridge, whose homogeneity can not be assumed between two, apparently, equal batches. This justifies the high CoV values attained for the G_c.

Table 7.6: Average values of the energy dissipated under compression, G_c [N/mm^2].

SERIES		AGE				
		12 h	24 h	3 d	7 d	28 d
Cf30	Avg.	0.26	0.36	0.48	0.44	0.49
	CoV	18.03%	13.13%	12.70%	14.84%	10.31%
	$\left(\frac{G_{c,t}}{G_{c,28}}\right)$	0.530	0.735	0.980	0.898	1.000
Cf45	Avg.	0.33	0.38	0.46	0.47	0.39
	CoV	12.35%	12.01%	19.73%	34.37%	18.77%
	$\left(\frac{G_{c,t}}{G_{c,28}}\right)$	0.846	0.974	1.179	1.205	1.000

The influence of the age on the G_c values is represented in Figure 7.14. The G_c had an abrupt increase up to the 3 days, and kept almost constant after this age. The observed decrease on the G_c, for the series Cf30 with 7 days, and in the series Cf45 with 28 days is justified with the smaller number of fibres on the rupture surface, as referred in the section 7.3.

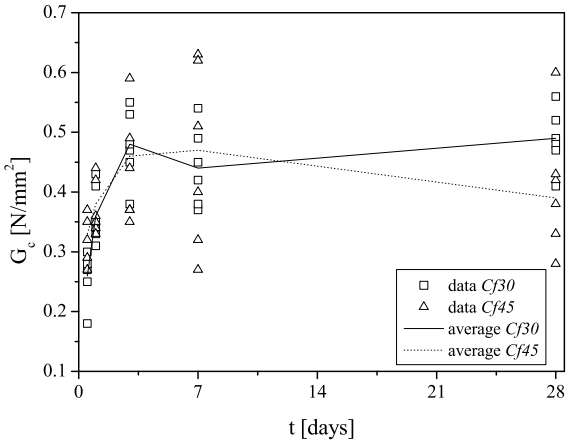

Figure 7.14: Energy dissipated under compression, G_c.

The variation of the energy dissipated under compression, G_c, with the strain is represented in Figure 7.15. In general, G_c increased with strain more swiftly for the older specimens 3, 7 and 28 days than for the specimens with 12 and 24 hours.

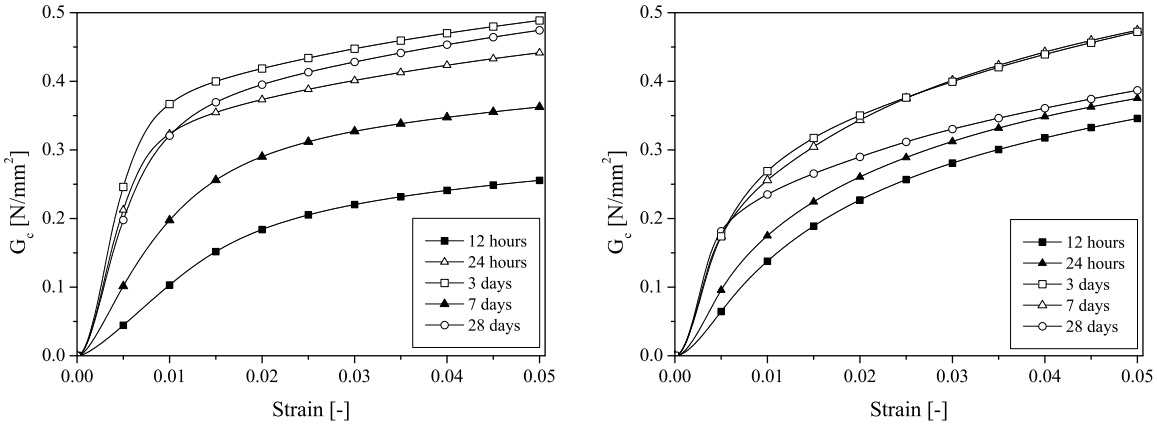

(a) (b)

Figure 7.15: Relationship between G_c and strain for: (a) Cf30 and (b) Cf45 series.

7.6 Compressive toughness index

The concrete toughness represents the material ability to absorb energy. A convenient way to quantify the increase of toughness provided by the fibre reinforcement is to define a toughness index, T.I., which is the ratio between the energy dissipated by the fibre reinforced concrete, up to a given strain limit, and the energy dissipated by its correspondent plain concrete (L. S.

Hsu and C. T. Hsu 1994). The toughness was computed using Equation 7.2, up to two levels of strain, 0.001 and 0.005. The stress - strain relationship for the plain concrete proposed by the CEB-FIP (1993) was used to determine the toughness of an equivalent strength class plain concrete. In order to define the stress - strain relationship, the values of f_{cm}, E_c must be known. For this purpose the average values from Tables 7.3 and 7.4 were used for each series of the steel fibre concrete. The ε_{c1} value for the correspondent plain concrete was always 0.0022.

In Figure 7.16 is represented the variation of the parameter T.I. with the reinforcement index, $R.I. = V_f \times l_f/d_f$, where V_f, l_f and d_f are, respectively, the fibre volume content, the fibre length and the fibre diameter. Notice that l_f/d_f is the fibre aspect ratio.

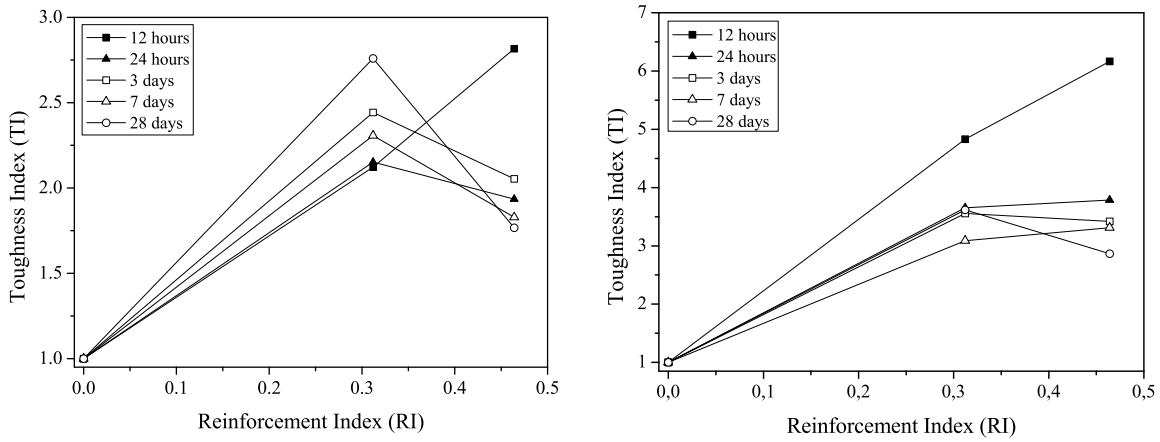

Figure 7.16: Variation of the toughness index with the reinforcement index up to a strain of: (a) 0.01 and (b) 0.05.

Figure 7.16(a) shows the T.I., calculated until a deformation of 0.01. The value of T.I. for the Cf30 series ($R.I = 0.33$), is in the range $[2, 2.75]$, meaning that the energy absorption of this concrete is 2 to 2.75 times higher that the one absorbed by the correspondent plain concrete, until a deformation of 0.01. On the other hand, for Cf45 series ($R.I. = 0.47$), apart from the 12 hours series, the values of T.I. have decreased comparatively to the ones of Cf30 series. This suggests that, for the designed SFRSCC, up to a deformation of 0.01, the increment of fibre content was not efficient in what concerns to its energy absorption capability. As already it was pointed out, this effect might be justified by the evolution of compressive strength and elasticity modulus of the SFRSCC of the Cf30 and Cf45 series.

In Figure 7.16(b) the T.I. was calculated until a deformation of 0.05. The values of T.I when compared to those obtained until a deformation of 0.01, increased substantially. The toughness index, for deformations up to 0.05, increased with the reinforcement index. The only exception

was the series with 28 days, that could be justified by the larger difference of the f_{cm} and E_{ci} between Cf30 and Cf45 series, for this age.

7.7 Analytical and numerical results

7.7.1 Statistic control

The experimental data presented in the previous chapter will be used to obtain expressions for evaluating the influence of age on the properties of the designed SFRSCC. In this section it will be presented the statistical treatment done to the experimental data. From the sample distribution, and adopting a confidence interval, $100(1-\alpha)$, of 95%, the lower and upper-confidence limits were determined. The confidence intervals were determined by the following expression (Montgomery and Runger 1994):

$$\bar{x} - z_{\alpha/2}\ \sigma/\sqrt{n} \leq \mu \leq \bar{x} + z_{\alpha/2}\ \sigma/\sqrt{n} \tag{7.3}$$

where n is the number of sample values, $\bar{x}$ and μ are, respectively, the mean of the sample and the mean of the population; σ^2 and $z_{\alpha/2}$ are, respectively, the variance and the upper $\alpha/2$ percentage point of the t-Student distribution. For small samples from non-normal populations the confidence level may not be exact. Thus, in all the samples was performed the Shapiro-Wilkin normality test (Montgomery and Runger 1994). The lower and upper-confidence limits obtained for the experimental data samples are presented on Annex IV.

7.7.2 Fitting method

To obtain expressions for the evaluation of the age influence on the concrete compressive strength, elasticity modulus, strain at peak-stress and energy absorption capacity, the non-linear square method was used (Ryan 1997). This method was also applied to obtain a time-dependent function defining a parameter used on the evaluation of the $\sigma(t) - \varepsilon(t)$ relationships for the defined SFRSCC. On any fitting procedure there are two main blocks:

1. The data obtained experimentally as a result of certain measurements, in which one or several independent variables $(x_{i1}, x_{i2}, \ldots)$, e.g. *strain*, are varied over a certain range, in a controllable manner, so as to produce the measured dependent variable(s) $(y_{i1}, y_{i2}, \ldots)$, e.g. *stress*.

2. The mathematical expression, $y_i = f_i(x_{i1}, x_{i2}, \ldots; p_{k1}, p_{k2}, \ldots)$, that represents the theoretical model used to reproduce the experimental data. The model usually depends on one or more parameters $(p_{k1}, p_{k2}, \ldots)$.

The aim of the fitting procedure is to find the values of the parameters which best describe the data. The best fitting was defined by choosing the parameters so that the sum of the squares of the deviations of the theoretical curve from the experimental points, for a range of independent variables, is minimum (equation 7.4).

$$\chi^2(p_{k1}, p_{k2}, \ldots) = \frac{1}{n^{eff} - p} \sum_i \sum_j w_{ij} \Big[y_{ji} - f_j(x_{i1}, x_{i2}, \ldots; p_{k1}, p_{k2}, \ldots) \Big]^2 \tag{7.4}$$

Where, y_{ji} are the measured values of the dependent variable, y_j, for the values of the independent variables, n^{eff} is the total number of experimental points used in the fitting, and p is the total number of adjustable parameters used in the fitting (the difference $d = n^{eff} - p$ is usually referred to as the number of degrees of freedom). The quantities w_{ij} represent the weights of each experimental point. In the present case there was no weighting therefore w_{ij}=1.

The minimization of $\chi^2(p_{j1}, p_{j2}, \ldots)$ is performed by a series of iterations on the parameter values and computing equation 7.4 at each stage. In order to accomplish that, the partial derivates $f_j^{'} = [\partial f_j/\partial p_{k1},\ \partial f_j/\partial p_{k2}, \ldots,\ \partial f_j/\partial p_{kp}]$ are determined for the parameters at each iteration.

7.7.3 Analytical expressions for the mechanical properties

In this section, the fitting method is applied for the establishment of analytical expressions to predict the most significant properties of the self-compacting steel fibre reinforced concrete, SFRSCC, at an age t: compressive strength, f_{cm}, the elasticity modulus, E_{ci}, strain at peak stress, ε_{c1} and the energy dissipated under compression, G_c.

Compressive strength, f_{cm}

To estimate the compressive strength of plain concrete at various ages, $f_{cm}(t)$, the CEB-FIP (1993) suggests an expression similar to the subsequent one:

$$f_{cm}(t) = f_{cm,28} \cdot \exp\left\{ a \left[1 - \left(\frac{28}{t} \right)^b \right] \right\} \tag{7.5}$$

where $f_{cm,28}$ is the mean compressive strength value at 28 days, a and b are two dimensionless

parameters. For plain concrete, CEB-FIP (1993) proposes $a = 0.2$, in case of using rapid hardening high strength cements, and a constant value of 0.5 for parameter b.

Using the $f_{cm,28}$ values obtained in the tested SFRSCC series, the $f_{cm}(t)/f_{cm,28}$ function, evaluated according to the CEB-FIP (1993) proposal, is depicted in Figure 7.17. In spite of the fact that the obtained correlation factors, R^2, were quite high, the compressive strength predicted by equation 7.5 at the ages of 3 and 7 days was underestimated, particularly, for the series with 45 kg/m^3 of steel fibres.

Using the fitting procedure described in the previous section, the values of parameters a and b of equation 7.5 were determined in order to improve its capability of simulating the age effect on the developed SFRSCC compressive strength. The degree of the simulation of the fitted curve increased considerably, specially at the ages of 3 and 7 days. The values of the fitted curve parameters, as well as, the values of R^2 are included in Figure 7.17.

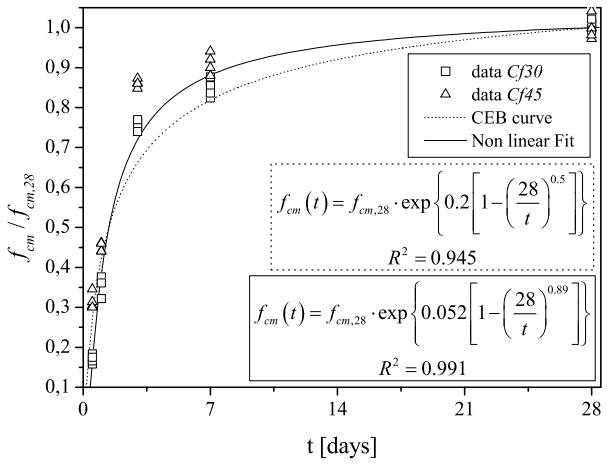

Figure 7.17: Simulation of the age influence on the concrete compressive strength.

Elasticity modulus, E_{ci}

In resemblance to the compressive strength, CEB-FIP (1993) proposes the following expression:

$$E_{ci}(t) = E_{ci,28} \cdot \left\{ \exp\left\{ a \left[1 - \left(\frac{28}{t} \right)^{b} \right] \right\} \right\}^{c} \tag{7.6}$$

to determine the elasticity modulus at an age of t days, $E_{ci}(t)$, where $E_{ci,28}$ is the elasticity modulus at an age of 28 days, a, b and c are dimensionless parameters. The CEB-FIP (1993) indicates for plain concrete $c = 0.5$, whereas the values of a and b are the same ones as those proposed for the equation 7.5.

Using the $E_{ci,28}$ values obtained in the tested SFRSCC series, the $E_{ci}(t)/E_{ci,28}$ function, evaluated according to the CEB-FIP (1993) recommendation, is depicted in Figure 7.18. The CEB-FIP (1993) approach, once again, underestimates the elastic modulus at the ages of 3 and 7 days, whereas overestimates it, at the age of 12 hours.

Fitting the parameters a, b and c of equation 7.6, the accuracy of the fitted curve also increased considerably. The fitted curve parameters, as well as the values of R^2 are indicated in Figure 7.18.

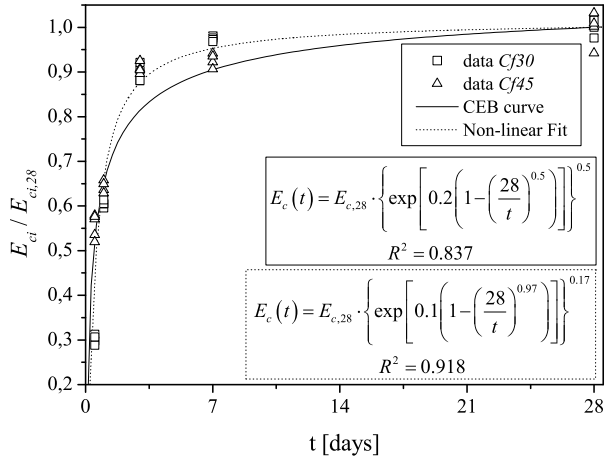

Figure 7.18: Simulation of the age influence on the concrete elasticity modulus.

The CEB-FIP (1993) also proposes equation 7.7 for determining the relationship between the elasticity modulus, E_{ci}, and the average compressive strength, f_{cm}, in which, for plain concrete, $E_{c0} = 21.5$ GPa, $f_{cm0} = 10$ MPa and $a = 1/3$.

$$E_{ci} = E_{c0} \cdot \left(\frac{f_{cm}}{f_{cm0}} \right)^{a} \tag{7.7}$$

The relationship between the elasticity modulus and the compressive strength is depicted in Figure 7.19. This figure also includes the analytical expression suggested by CEB-FIP (1993) and the one obtained by the non linear fitting procedure. Fitting parameters E_{c0} and a increased substantially the adjustment of equation 7.7 to the experimental data and consequently the correlation factor.

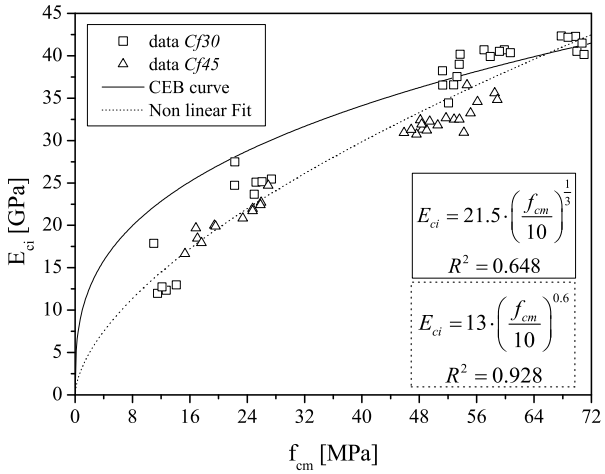

Figure 7.19: Analytical relationships between the elasticity modulus and the compressive strength.

Strain at peak stress, ε_{c1}

For predicting the influence of concrete age on the strain at peak stress, $\varepsilon_{c1}(t)$, it was used an hyperbolic function as indicated in equation 7.8, where $\varepsilon_{c1,28}$ is the strain at peak stress for the age 28 days. This expression was adjusted to the experimental data by fitting the dimensionless parameter a.

$$\varepsilon_{c1}(t) = \frac{\varepsilon_{c1,28} \cdot \dfrac{t}{28}}{a + \dfrac{t}{28}} \tag{7.8}$$

The analytical relationship obtained by applying the fitting procedure to equation 7.8 is represented in Figure 7.20.

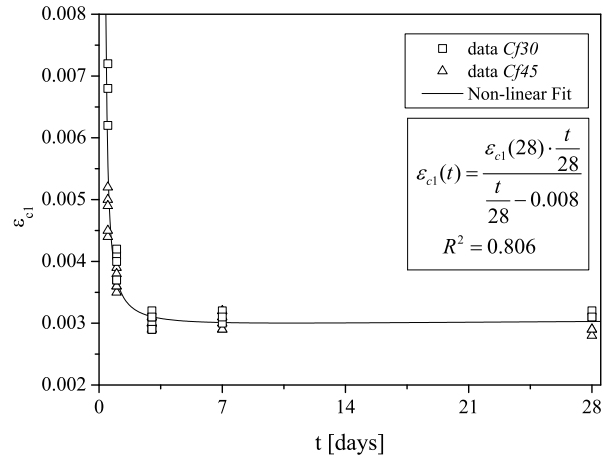

Figure 7.20: Simulation of the age influence on the strain at peak-stress, ε_{c1}.

The quality of the adjustment of the previous equation is quite good, however the obtained correlation factor is not too high. This is mainly due to the high scatter of the strain at peak stress observed for the age of 12 hours.

Energy dissipated under compression, G_c

The energy dissipated by a fibre reinforced composite is highly influenced by the fibre content, among several other factors. Nevertheless, the influence of the fibre addition to a cement matrix, on the composite toughness, is more preponderant when the material is in tension or tension under flexure. In fact, as previously seen in section 7.5.4, the differences on the dissipated energy under compression, between Cf30 and Cf45 series, were not so significant. For this reason, and also having in mind the high scatter observed for these series, especially for the Cf45 series, the analytical expression used for fitting the experimental data was applied to both series. To attain the relationship between the energy dissipated and age, $G_c(t)$, it was used equation 7.9.

$$G_c(t) = \frac{a \cdot \dfrac{t}{28}}{b + \dfrac{t}{28}} + \frac{c}{d + \dfrac{t}{28}} + e \cdot \frac{t}{28} \tag{7.9}$$

The variation of G_c with time, for both series, is depicted in Figure 7.21. The values of the parameters a, b, c, d and e obtained in the fitting procedure are indicated on Table 7.7. The correlation factor was small, $R^2 = 0.589$, due to the high scatter observed.

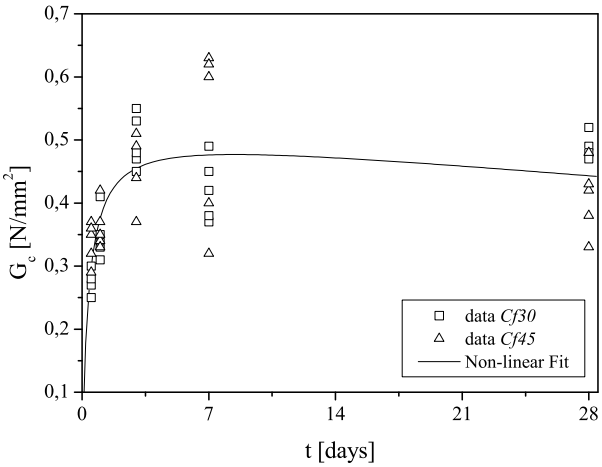

Figure 7.21: Simulation of the age influence on the energy dissipated under compression.

Table 7.7: Parameters obtained on the non-linear fitting of the $G_c(t)$ relationship.

a	b	c	d	e
0.52	0.013	1.1×10^{-4}	0.18	0.07

7.7.4 Analytical stress - strain relationships

The $\sigma_c - \varepsilon_c$ relationships available for modelling the compressive behaviour of plain (Carreira and Chu 1985, CEB-FIP 1993) and fibre reinforced concrete (Ezeldin and Balaguru 1992, L. S. Hsu and C. T. Hsu 1994) cannot be directly applied to the developed SFRSCC since the fitting degree they provide is not good enough. Therefore a new approach is proposed, in this section, to obtain a $\sigma_c - \varepsilon_c$ analytical expression that can predict the compression behaviour registered in the tested SFRSCC, at the distinct studied ages.

The expression adopted in the present work is similar to the one proposed by the CEB-FIP (1993) for plain concrete. The stress - strain diagram for loading under compression is represented schematically in Figure 7.22. In fact, the equation that corresponds to the branch represented by a straight line in Figure 7.22 is the same one proposed by the CEB-FIP (1993). For this branch, the stress - strain relationship is given by the following function:

$$\sigma(\varepsilon_c) = \frac{\dfrac{E_{ci}}{E_{c1}} \cdot \dfrac{\varepsilon_c}{\varepsilon_{c1}} - \left(\dfrac{\varepsilon_c}{\varepsilon_{c1}}\right)^2}{1 + \left(\dfrac{E_{ci}}{E_{c1}} - 2\right) \cdot \dfrac{\varepsilon_c}{\varepsilon_{c1}}} \cdot f_{cm} \qquad \text{for } \varepsilon_c \leq \varepsilon_{c,lim} \tag{7.10}$$

where E_{ci} and E_{c1} are, respectively, the tangent modulus and the secant modulus from the origin to the peak compressive stress ($E_{c1} = f_{cm}/\varepsilon_{c1}$); σ_c, ε_c and ε_{c1} are the compressive stress in (MPa), the compressive strain and the strain at the peak stress, respectively. The strain $\varepsilon_{c,lim}$ limits the applicability of equation 7.10 (see Figure 7.22).

For the descending part of the stress – strain diagram, equation 7.10 is valid only for strain values up to $\varepsilon_{c,lim}$. The strain $\varepsilon_{c,lim}$ at $\sigma_{c,lim}$ ($= \alpha \cdot f_{cm}$) may be computed from equation 7.11.

$$\varepsilon_{c,lim} = \left[\frac{1}{2}\left[(1-\alpha)\cdot\frac{E_{ci}}{E_{c1}} + 2\,\alpha\right] + \left[\frac{1}{4}\left[(1-\alpha)\cdot\frac{E_{ci}}{E_{c1}} + 2\,\alpha\right]^2 - \alpha\right]^{0.5}\right]\varepsilon_{c1} \tag{7.11}$$

For $\varepsilon_c > \varepsilon_{c,lim}$ the descending branch of the $\sigma_c - \varepsilon_c$ diagram (dashed line in Figure 7.22) is

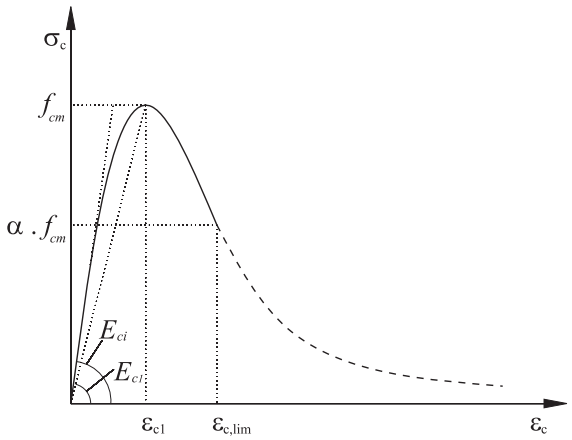

Figure 7.22: Stress strain diagram for uniaxial compression (CEB-FIP 1993).

described using an equation of the type:

$$\sigma(\varepsilon_c) = \left[a \left(\frac{\varepsilon_c}{\varepsilon_{c1}} \right)^2 + b \frac{\varepsilon_c}{\varepsilon_{c1}} \right]^{-1} \cdot f_{cm} \qquad \text{for } \varepsilon_c > \varepsilon_{c,lim} \tag{7.12}$$

where the values of parameters a and b are determined in order to assure the continuity of the function at the point $\varepsilon_{c,lim}$. Thus, the following conditions should be assured:

$$\begin{cases} \underbrace{\sigma_c(\varepsilon_{c,lim})}_{\text{equation 7.10}} = \underbrace{\sigma_c(\varepsilon_{c,lim})}_{\text{equation 7.12}} \\ \underbrace{\left.\dfrac{\partial \sigma_c}{\partial \varepsilon_c}\right|_{\varepsilon_{c,lim}}}_{\text{equation 7.10}} = \underbrace{\left.\dfrac{\partial \sigma_c}{\partial \varepsilon_c}\right|_{\varepsilon_{c,lim}}}_{\text{equation 7.12}} \end{cases} \tag{7.13}$$

Equation 7.12 is converted into the following one:

$$\sigma(\varepsilon_c) = \left[\left[\frac{1}{\dfrac{\varepsilon_{c,lim}}{\varepsilon_{c1}}} \xi \cdot \left(\frac{1}{2\,\alpha} \right)^2 - \frac{1}{\left(\dfrac{\varepsilon_c}{\varepsilon_{c1}} \right)^2} \cdot \frac{1}{\alpha} \right] \left(\frac{\varepsilon_c}{\varepsilon_{c1}} \right)^2 + \left[\frac{1}{\dfrac{\varepsilon_{c,lim}}{\varepsilon_{c1}}} \cdot \frac{2}{\alpha} - \xi \left(\frac{1}{2\,\alpha} \right)^2 \right] \frac{\varepsilon_c}{\varepsilon_{c1}} \right]^{-1} \cdot f_{cm} \tag{7.14}$$

with

$$\xi = \frac{4 \left[\left(\dfrac{\varepsilon_{c,lim}}{\varepsilon_{c1}} \right)^2 \left(\dfrac{E_{ci}}{E_{c1}} - 2 \right) + 2 \dfrac{\varepsilon_c}{\varepsilon_{c1}} - \dfrac{E_{ci}}{E_{c1}} \right]}{\left[\dfrac{\varepsilon_{c,lim}}{\varepsilon_{c1}} \left(\dfrac{E_{ci}}{E_{c1}} - 2 \right) + 1 \right]^2} \tag{7.15}$$

If $\alpha = 0.5$, equations 7.11 and 7.14 become those proposed by the CEB-FIP (1993).

In order to evaluate the applicability of the previous described relationship in the present experimental research, the following assumptions were done: the values of the elastic modulus, compressive strength and strain at peak stress, used in the simulation, were those obtained experimentally for each series; the parameter α was adjusted in order to obtain the best fit of the analytical expression to the average stress - strain curve recorded experimentally. The analytical stress - strain curves obtained from the best fit procedure and the experimental envelope are depicted in Figures 7.23 and 7.24. The accuracy of the proposed expression toward the experimental data is quite high.

The pre-peak phase was well simulated with the law suggested by CEB-FIP (1993), just by using the values of f_{cm}, E_{ci} and ε_{c1} obtained experimentally for the SFRSCC. For the Cf30 series, the post-peak behaviour was also modelled with exactness until high deformations. For this content of fibres, at the ages of 7 and 28 days, Figures 7.23(d) and 7.23(e), the residual strength was slightly underestimated after strains higher than 0.04. On the other hand, for the Cf45 series, at the age of 12 and 24 hours, the first part of the descending branch correspondent to the analytical curve is slightly less sharp than the experimental envelope. For the 28 day series, the post-peak behaviour is only correctly simulated up to a strain of 0.01. After this strain level the residual strength is underestimated, Figure 7.24(e).

The Table 7.8 includes the values of the parameter α obtained in the non-linear fitting procedure. The α parameter increased with age and tend to the limit value of 0.9.

Table 7.8: Values of parameter α obtained on the non linear fitting procedure.

Age	12 h	24 h	3 d	7 d	28 d
Cf30	0.423	0.657	0.839	0.871	0.889
Cf45	0.675	0.776	0.876	0.890	0.860

In Figure 7.25(a) is depicted the exponential function used to estimate the evolution of the parameter α with age. Additionally, the value suggested by CEB-FIP (1993) for plain concrete is represented. The values of α obtained on the fitting procedure for the developed SFRSCC are higher than the value proposed for plain concrete, excluding the series Cf30 at 12 hours. Equation 7.16 simulates the variation of parameter α with age. The correlation factor (R^2) obtained was 0.797.

$$\alpha(t) = 0.9 \cdot \exp\left\{0.005\left[1 - \left(\frac{28}{t}\right)^{1.16}\right]\right\} \tag{7.16}$$

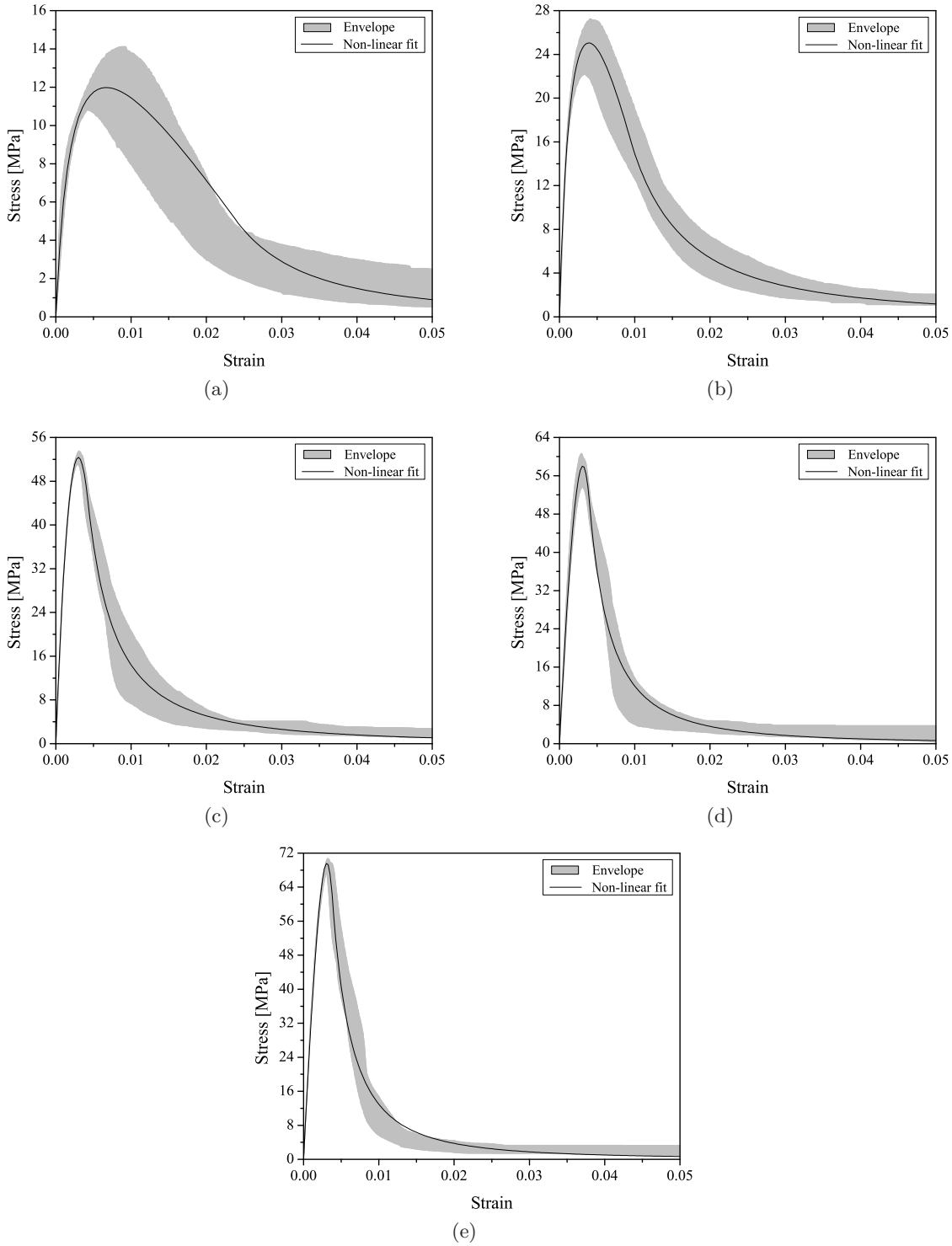

Figure 7.23: Experimental and analytical stress - strain relationships for the Cf30 series: (a) 12 hours, (b) 24 hours, (c) 3 days, (d) 7 days and (e) 28 days.

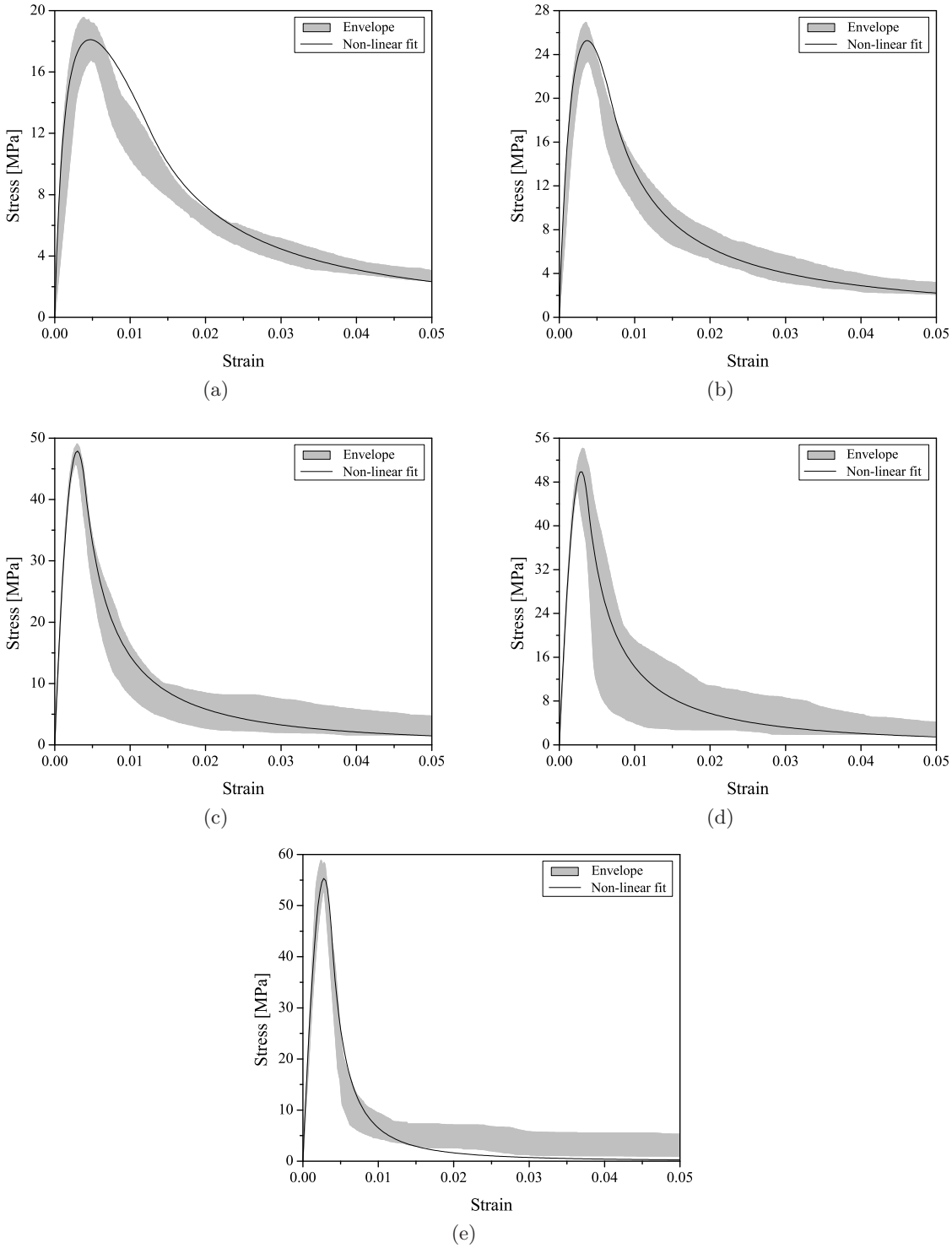

Figure 7.24: Experimental and analytical stress - strain relationships for the Cf45 series: (a) 12 hours, (b) 24 hours, (c) 3 days, (d) 7 days and (e) 28 days.

Due to the distinct compressive strengths for the Cf30 and Cf45 series at the same age, and considering that the compressive strength influences significantly the shape of stress - strain curve, better results are attained relating the parameter α with the compressive strength.

In Figure 7.25(b) is represented the exponential function (see equation 7.17) used to estimate the evolution of the parameter α with the compressive strength. The degree of accuracy increased significantly. The value of correlation factor was 0.938.

$$\alpha(f_{cm}(t)) = 0.87 \cdot \exp\left\{0.04\left[1 - \left(\frac{f_{cm,28}}{f_{cm}(t)}\right)^{1.8}\right]\right\} \tag{7.17}$$

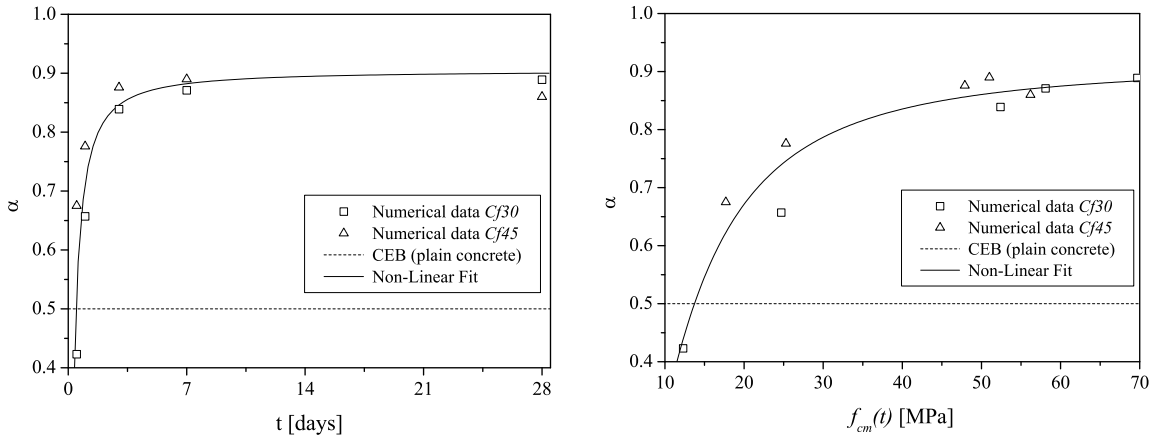

(a) (b)

Figure 7.25: Relationship between parameter α and the: (a) age, (b) compressive strength.

7.8 Conclusions

An experimental programme was carried out to evaluate the influence of the fibre content and concrete age on the compressive behaviour of steel fibre reinforced self-compacting concrete, SFRSCC.

The main mechanical properties of the SFRSCC, such as: the compressive strength, f_{cm}, the elasticity modulus, E_{ci}, strain at peak stress, $\varepsilon_{c,1}$ and the volumetric energy dissipated, G_c, were assessed for the ages of 12 hours, 24 hours, 3, 7 and 28 days. Two distinct contents of fibres were considered, 30 kg/m^3 and 45 kg/m^3.

The compressive strength, as well as the elasticity modulus increased with age, mainly in the recent ages, i.e. until the 3 days. Increasing the fibre content from 30 kg/m^3 to 45 kg/m^3, in general, a decrease of f_{cm} and E_{ci} values was observed. This might be justified by the increase

of the water/cement ratio and percentage of limestone filler, as well as the changes introduced in the solid skeleton from Cf30 to Cf45 series. More research in this field should be done to get more clear evidences of these aspects.

The strain at peak stress decreased with age for both series of distinct contents of fibres. The value obtained experimentally, for the 28 days, was slightly higher than the one of the corresponding plain concrete, and is similar to the values obtained by several authors for steel fibre reinforced concrete. In general, the energy dissipated under compression, G_c increased with age. However, it was not observed a significant change with the increment of the fibre content, from 30 kg/m^3 to 45 kg/m^3. Some series presented a lower value of G_c than it was expected. This can be justified with the number of fibres found on the rupture surface of these specimens. For the series of 3, 7 and 28 days the failure mode was exclusively by shear, whereas in the younger specimens two more types of failure modes were observed.

Analytical expressions to predict the most significant mechanical properties of the developed SFRSCC at an age t were presented. A stress - strain relationship was proposed to model the behaviour of the SFRSCC since the early ages. This relation was capable of modelling the complete compressive behaviour of SFRSCC with a high accuracy.

Chapter 8

Post-Cracking Behaviour (Experimental and Numerical Analysis)

8.1 Introduction

It is widely acknowledge that cracks may propagate under three basic fracture modes: tensile opening (Mode I), in-plane shear (Mode II) and out-of-plane shear (Mode III) (Shah et al. 1995, Van Mier 1997, Bazant and Planas 1998). Moreover, during the cracking process it is possible the combination of these three modes, also called of mixed modes. Modes II and III are out of the scope of the present work. Thus, in the present chapter, when referring to the post-cracking behaviour, it will always be meant the tensile crack opening mode.

The fracture mechanics of cement-based composites containing either notches and sharp cracks can be characterized by a cohesive zone, or also often called of fracture process zone (FPZ), which will be formed at their notch tips (Bentur and Mindess 1990, Shah et al. 1995, Van Mier 1997, Bazant and Planas 1998). Hence, the cohesive zone is the inelastic region around a crack tip, where due to complex phenomena the damage is accumulated and the fracture process is developed. Regarding plain concrete, the FPZ is a region of localized debonded and pulled out aggregates designated by aggregate interlock. In case of fibre reinforced composites, the FPZ is composed by a fibre-bridging zone, plus a fibre-bridging zone with aggregate interlock. Additionally, a small zone of diffuse microcracking develops ahead of the aggregate bridging zone. According to Li and Maalej (1996), the distinct FPZ's parts for a FRC are sketched in Figure 8.1.

As previously stated, an axiomatic aspect of the mechanical performance of fibre reinforced

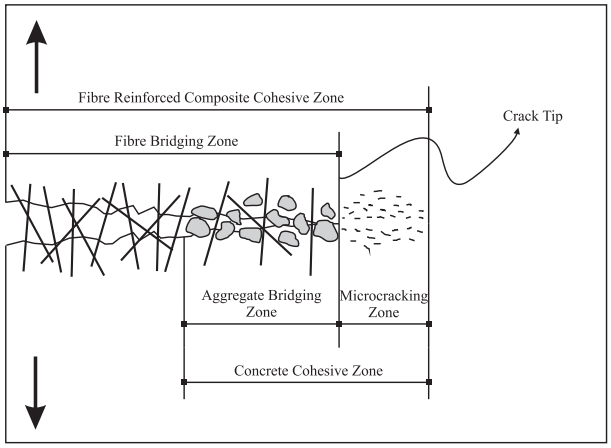

Figure 8.1: Definition of cohesive zones for either plain and fibre reinforced concrete (adapted from Li and Maalej 1996).

concrete, FRC, is the tensile post-cracking behaviour. Since this behaviour can mainly be related to multiple reinforcement mechanisms that arise at the fibre/matrix interface, such as debonding, frictional and mechanical mechanisms, which on its turn, depend from a multiplicity of factors, from which can be pointed out, geometry and material type of the fibre, and quality of the concrete matrix. Moreover, since fibres can bridge the crack surfaces for relatively large opening widths, the fibre bridging zone, when compared with the aggregate interlock zone, will be considerably larger. Consequently, the post-cracking behaviour of FRC is mainly governed by the fibre reinforcement mechanisms, as the aggregate interlock has a relatively smaller influence.

The post-cracking behaviour of a cement based material (either plain or fibre reinforced) can be predicted by the use of a stress - crack opening displacement relationship, $\sigma - w$. Regarding plain concrete, the post-cracking behaviour can be characterised by its tensile strength and fracture energy, since the $\sigma - w$ shape is not too dependent of the concrete strength class, see Petersson (1981), Gustafsson and Hillerborg (1985), Cornelissen et al. (1986), Rots (1988) and CEB-FIP (1993). Furthermore, in general, a bilinear $\sigma - w$ relationship renders a good estimation of the plain concrete's post-cracking behaviour. On the other hand, for FRC, the shape of $\sigma - w$ curves differs considerably depending on the fibre type, content and quality of the concrete matrix. Therefore, for each specific FRC composition it is necessary to determine the $\sigma - w$ law that best characterizes the mechanical behaviour of the composite in tension. Usually, "indirect" tensile tests are carried out and an inverse analysis procedure is used to determine the best fit parameters of the $\sigma - w$ curve throughout an optimization procedure, e.g. the least square approach (Roelfstra and Wittmann 1986). For FRC, and in comparison with plain concrete, it is more suitable to model the post-cracking behaviour with a trilinear diagram, as used by Hillerborg (1980), Barros et al. (2005) and Cominoli et al. (2007), although

good results have been achieved with a bilinear diagram (Kooiman 2000, Barragán 2002). The use of poly-linear functions is another approach for representing the $\sigma - w$ relationships, where the shape of the curve is also free to vary (Kitsutaka 1997, Kurihara et al. 2000, Löfgren et al. 2008). In the latter procedure a step-wise inverse analysis is carried out using segments of either the load - deflection or load - crack mouth opening width to acquire a piece-wise polylinear $\sigma - w$ law. According to Kurihara et al. (2000) and Löfgren et al. (2008) this approach will lead to an increase of the fitting quality. However, Uchida and Barr (1998) and Planas et al. (1999) state that this approach will render inconsistent results on the estimation of the first part of the $\sigma - w$ curve and, particularly, the tensile strength. The algorithm should be sensitive to variations in the fracture properties along the crack path. However, each one of the slopes of poly-linear softening curve depend on certain limited regions of the experimental load - displacement curve. In order to overcome these inconsistent results in the prediction of the initial part of the $\sigma - w$, the tensile strength should not be inferred from the inverse analysis, thus obtained experimentally (Kitsutaka 1997). Alternatively, the initial slope of the $\sigma - w$ may be pre-selected (Löfgren et al. 2008). Nevertheless, both approaches reduce the objectivity of the inverse analysis results. In order to investigate the possibility and reliability of extending the inverse analysis to more than bi-linear softening curves, Skocek and Stang (2008) performed a study of the optimal number of degrees of freedom in the softening curve. They concluded that up to a quad-linear softening curve, the widely used bilinear curve can be replaced with advantage. On the other hand, for softening curves with five or higher degrees of freedom occurred problems with local minima and the algorithm could not fulfil the convergence criteria defined.

Having in mind the aforementioned, the $\sigma - w$ relationship may be determined either directly, in a uniaxial tension test (UTT), or indirectly by performing an inverse analysis with test results of three point bending tests (3PBT), split cylinder tests (SCT) or wedge splitting tests (WST). Nevertheless, "indirect" tests methods for determining $\sigma - w$ relationship do not gather the consensus of the scientific community, since some held the believe that local minimums of the error function may restrict the inverse analysis from attaining a feasible solution, while others are concerned about the energy dissipated beyond the test end point. Therefore, research based upon indirect test methods should still be validated and calibrated using a "direct" uniaxial tension test.

Even though the gripping problems pointed to UTT have been highly reduced with the appearance of new strong epoxy resins, the UTT still is a sophisticated and time consuming test. Therefore, straightforward methods for material parameters determination, like tensile strength, fracture energy and the full $\sigma - w$ relationship are still an open research field. As aforementioned, three and four point bending tests, and splitting tensile tests have been pro-

posed as an alternative to the UTT. However, beside the drawbacks previously pointed out to the latter tests, there is also the disadvantage that all these tests superimpose a non-uniform state of stress over the local stress variation due to material heterogeneity, leading to considerable difficulties in the interpretation of the results (Van Mier 1997, Van Mier and Van Vliet 2002).

8.2 Test methods for assessing the post-cracking behaviour

An insight view of the most widely used tests for assessing the post-cracking behaviour of either plain or fibre reinforced concrete is given in this section. It is not intended to give a deep detail on test set-ups, specimens' geometry and dimensions, since an extensive review on this topic can be found elsewhere (e.g. Shah et al. 1995, Van Mier 1997, Bazant and Planas 1998, Rocco et al. 2001, Van Mier and Van Vliet 2002). A brief overview of some advantages/disadvantages of each test is presented. Furthermore, some considerations regarding the assessment of the post-cracking behaviour from each test will be discussed.

8.2.1 Estimation of the fracture energy

The more appropriate way for determining the fracture energy, G_f, is by performing an uniaxial tension test in notched specimens (Hordijk 1991, Barros 1995), under closed-loop displacement control. Thus, the fracture energy can be computed from the following equation:

$$G_f = \int_{w=0}^{w_{lim}} \sigma(w) \cdot dw \tag{8.1}$$

where w is the crack mouth opening (excluding deformation up to the peak load) and σ is the tensile stress, i.e. the load divided by the net cross section area of the specimen, whereas w_{lim} is the crack mouth opening for a null residual stress. Remark that the area used to compute the tensile stress is the projection of the fracture surface area in the orthogonal plane to the longitudinal specimen axis, at the notch. Therefore, the adopted area is a lower bound of the real fracture area, since the rugosity of the fracture surface is neglected (Bazant and Planas 1998).

In spite of the uniaxial tension being the most suitable test for determining the fracture energy of a cement composite, the testing rigs to perform this kind of tests are not available in all laboratories, due to its high cost. Therefore, a simpler test, such as the three point bending test of notched specimens, has been used for that purpose. In the early 80's, Petersson (1980) proposed a method to evaluate the fracture energy with the latter test. According to this researcher, in order to assume that the fracture energy is an actual material property it must

comply with the three following conditions. Firstly, the dissipated energy outside the fracture zone must be significantly smaller than at the fracture zone. To attain that purpose, the ratio between the notch depth and the beam height should be large enough. Another requirement is that the fracture energy should be independent from the specimen dimension and notch depth. Finally, the testing rig should be sufficiently stiff, enabling a stable fracture process.

To ensure a stable test in plain concrete, RILEM 50-FMC (1985) suggests that the dimensions of the specimens, as well the notch depth, should be specified according to the maximum aggregate dimension of the cement based material. Moreover, the ratio between the beam height and notch depth should be 0.5. An extensive research of the error sources on the determination of the fracture energy with a bending test was carried out by Planas and Elices (1989), Guinea et al. (1992) and Elices and Planas (1992). According to these authors, the major error sources are:

- The crushing of concrete at the supports, which may lead to an overestimation of the fracture energy;
- The bulk energy dissipated, i.e. the energy dissipated by the material parcel adjacent to the crack surface. Remark, that this parcel is relatively small in plain concrete, however in FRC with high fibre volumetric percentage this may be considerable due to the stresses redistribution;
- The contribution of the specimen self-weight and the residual energy which is not measured beyond the final end of the experimental test.

8.2.2 Uniaxial tension test

The uniaxial tension test is, probably, the only test that directly yields an unbiased stress-crack opening relationship throughout a simple interpretation of test results (Hordijk 1991, Van Mier and Van Vliet 2002). From these results all the relevant fracture parameters can be obtained. Nonetheless, care should be taken in order to reduce the effects of the specimen's structural behaviour on the obtained results. In spite of these effects can never be fully eliminated, setting-up some measures can mitigate them on the assessment of the concrete fracture behaviour.

Remark, however, that the acquirement of an unbiased stress-crack opening relationship only holds true if the test is conducted under very well controlled conditions. In experimental investigation, the key question that frequently arises is if the results obtained from the tests are a material property free from structural effects. Several researchers have carried out investigation of the specimen's geometry, size and boundary conditions influence on the results of uniaxial fracture tests of either plain concrete (Bazant and Pfeiffer 1987, Hordijk 1991, Rossi et al. 1994,

Vliet 2000, Carpinteri et al. 2002) or fibre reinforced concrete (Barragán 2002). Moreover, there is a multiplicity of technical problems that can lead to biased results. Among these can be pointed out the "perfect" manufacturing and alignment of the concrete specimen with the loading actuator, in order to avoid undesired secondary flexure; the adopted attachment between the specimen and loading platens; and the performance of the testing control system. It is known that the tensile strength decreases with the increasing of load eccentricity (Zhou 1988). However, when using a modern tensile rig with high rotational stiffness, the heterogeneity of the material will probably have more influence in the post-cracking behaviour than the load eccentricity from the machine (Van Mier and Van Vliet 2002).

An extensive overview of the aforementioned issues can be found elsewhere (Van Mier and Shi 2002, Van Mier and Van Vliet 2002). Nevertheless, in this section will be briefly addressed some of the more relevant issues regarding the uniaxial tension test set-up and its influence on the interpretation of the obtained $\sigma - w$ relationships.

A key issue of some controversy is the dependence of the crack propagation in specimens from the rotation at the specimen boundaries. Some researchers support that the specimen boundaries should be free to rotate (Van Mier et al. 1996, Van Mier 1997, Van Mier and Shi 2002), whereas others advocate that not only the specimen boundaries, but also, the material adjacent to the crack, i.e. crack planes, must be prevented from rotating (Hillerborg 1989, RILEM TC 162-TDF 2001, Ostergaard 2003). According to Van Mier et al. (1996), the use of loading platens with high rotational stiffness promotes the arisen of several crack planes and, consequently, the measured fracture toughness is artificially increased and, therefore, biased. However, rotating loading platens will increase the bending thus increasing the non-symmetric crack opening process in the specimen. Cattaneo and Rosati (1997), with the help of interferometry, have shown that high stiffness loading platens promotes a more even cracking, thus a more uniform strain field.

In spite of the concrete heterogeneity at a meso-level, if a representative volume element (RVE) is adopted, from a macroscopic point-of-view the material may be considered homogeneous. Thus a RVE can be regarded of an element containing a sufficiently number of micro-structural inhomogeneities in order for it to be considered macroscopically homogeneous (Dick-Nielsen et al. 2007). Therefore, if a sufficiently large RVE is adopted, it is feasible to assume that the stress variations are small and that the crack naturally starts to propagate at the weakest material point. However, remark that in notched specimens, the crack starts to propagate at the tip of the notch, due to stress concentrations in this zone (Shah et al. 1995, Van Mier 1997, Bazant and Planas 1998, Van Mier and Van Vliet 2002).

In Figure 8.2 is depicted the response for a RVE strip for distinct boundary conditions such as: free rotation, certain rotational stiffness and "infinite" rotational stiffness (clamped

boundary conditions). Regardless the boundary conditions, the concrete strip starts to crack at one of the notch tips (see point 1 in Figure 8.2). For the case where no rotational stiffness is adopted, the crack will propagate only from one side, since due to rotational freedom the crack plane rotation is not restrained, see points 2 to 4 in Figure 8.2(a). Consequently, the crack process is highly non-symmetric. According to several researchers (Zhou 1988, Hillerborg 1989, Ostergaard 2003) this justifies the recommendation for not obtaining the $\sigma - w$ relationship from load-deformation curve, since the displacement averaging may not be representative of the crack opening process. This was demonstrated by Ostergaard (2003) with a finite element analysis of a uniaxial tension test of a plain concrete specimen. Thus, for fibre reinforced concrete, which has significant residual stresses for crack width levels much higher than the ultimate crack width of the corresponding plain concrete, the displacement averaging process may even be more deviated from the reality. The anisotropic fibre distribution could also contribute for these phenomena. In terms of the necessary stiffness of the testing device, the more recent standard, e.g. RILEM TC 162-TDF (2001), requires that the flexural stiffness of both the machine and grips should be sufficient to prevent significant rotation. This is fulfilled by requiring that, at the end of the test, the maximum difference between the individual transducers signal and the average displacement will be smaller than 10%.

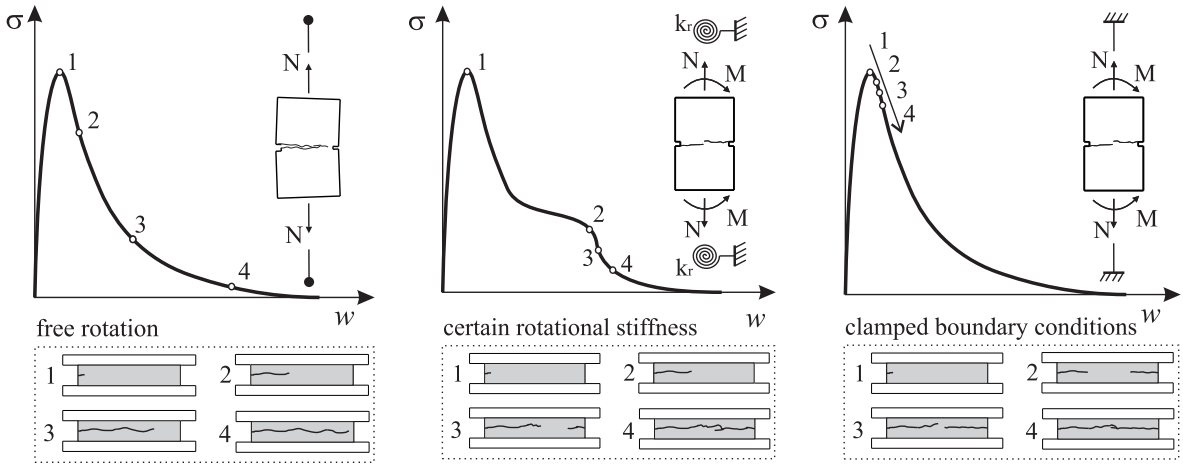

Figure 8.2: Effect of the boundary conditions in an uniaxial tension test for: (a) no rotational stiffness, (b) certain rotational stiffness and (c) infinite rotational stiffness of the boundary planes (adapted from Ostergaard 2003).

Having in mind the aforementioned, the rotation must somehow be eliminated. The complete inhibition of the rotation is difficult, resulting often in a partial restriction of the rotation. For the latter case, in a first stage the crack starts from one tip of the notch, see both points

1 and 2 in Figure 8.2(b). However, at some stage of the cracking process, since the rotation is limited, the equilibrium can no longer be maintained and the crack planes start to rotate back to the direction perpendicular to the load orientation. Hence, a second crack rapidly propagates from the other notch tip and coalesces into the first one (both points 3 and 4). According to (Zhou 1988, Hillerborg 1989, Ostergaard 2003) this originates the "hump" observed in the load - deflection curve, see Figure 8.2(b), since the crack planes will experience some rotation in order to attain equilibrium. Moreover, these two cracks will not coalesce perfectly into one crack due to the material heterogeneity (Van Mier 1997, Vliet 2000). These two authors have been advocating that this leads to an overestimation of the obtained fracture energy. Moreover, they point it out as a disadvantage of the non-rotating tests. Nevertheless, according to Ostergaard (2003) and the present's author opinion, this cannot be flashed as disadvantage of the non-rotation system, but as a disadvantage of the systems with certain rotational stiffness.

Finally, for the case where no rotational of the boundary planes is assumed, as in the previous cases, the crack starts from one of the notch tips, point 1 in Figure 8.2(c). However, since the crack boundary planes are restrained to rotate, the crack will rapidly propagate from both notch tips into a single crack, points 2 to 3 in Figure 8.2(c). This crack will experience similar opening throughout the strip width, hence enabling the correct derivation of a $\sigma - w$ relationship (Zhou 1988, Ostergaard 2003).

8.2.3 Three vs. four-point bending tests

Several international organizations have proposed distinct test configurations for ascertaining the tensile behaviour under flexure of fibre reinforced composites. Nevertheless, it should be stressed out two major groups of configurations, one with three loading points and the other with four loading points.

In the test set-ups with four loading points, two line loads are applied at the beam length thirds. Among the latter configuration, there are the JSCE – SF4 (1984), the ASTM C1018-89 (1991) and the ACI 544.1R-96 (1996) recommendations. In spite of the abovementioned organisms putting forward similar test configurations, the parameters determined to characterize the FRC behaviour in each recommendation are distinct. On the other hand, in the three point bending test, the line load is applied at half the beam's span (RILEM TC 162-TDF 2002b, EN 14651 2005, Fib TG-8.3 2007). Regardless the loading differences between the three and four point tests, there is one major aspect that differentiates them, since in the three point bending test the cross section has a notch at mid span, whereas in the four point bending test the beam is flush. Regarding the three-point bending tests, the notch promotes the localization of the crack initiation. On the other hand, in the four point bending tests, since the specimen

is not notched, for current fibre volume ratios and compressive strengths, several cracks can appear between the two applied loads.

According to Groth (2000), the three-point bending tests should not be used for determining the mechanical properties of FRC, since these tests are not able to show the capacity of FRC in favouring multiple cracking, and also due to preventing that the crack initiation arises at the weakest material point. However, this test configuration has widely been used, in detriment of the four-point loading configurations, for the assessment of the FRC post-cracking behaviour (e.g. Barros 1995, Kooiman 2000, Barragán 2002, Dupont 2003, Grünewald 2004, Barros et al. 2005, Löfgren et al. 2008).

On the following paragraphs some of the back points of two widely used standards for assessing the FRC properties in tension under four point bending test schemes will be presented and discussed.

The determination of the tenacity indexes, I_N, of ASTM C1018-89 (1991) is susceptible of errors. This is due to difficulty on ascertaining rigorously the deflection at the crack initiation. According to ASTM C1018-89 (1991) the deflection at crack initiation is: "*... the point at which the curvature first increases sharply and the slope of the curve exhibits a definite change ...*". From the previous transcription can be easily concluded that there is some subjectivity inherent to the determination of the crack initiation. Since I_N index depends of the beginning of cracking, these indexes are affected by a degree of uncertain. On the other hand, JSCE – SF4 (1984) suggests the determination of a unique tenacity index, F_T, which depends of the specimen geometry and from a limit deflection (span/150 [mm]). However, this deflection limit induces high levels of deformation and crack opening that are not complacent in current structures, i.e. the calculated F_T is not adequate for being used on the verifications for the serviceability limit states.

With the scope of enhancing some of the deficiencies previously pointed out to the ASTM C1018-89 (1991) and JSCE – SF4 (1984) standards, the RILEM TC 162-TDF (2002b) committee released a new recommendation to appraise the behaviour of FRC in tension under flexure. More recently, several standards (EN 14651 2005, Fib TG-8.3 2007) are being proposed based upon on the RILEM TC 162-TDF (2002b) recommendations. Comparatively to the ASTM C1018-89 (1991) standard, the proposal from the RILEM TC 162-TDF (2002b) suggests a more accurate method for excluding the parcel of the dissipated energy due to the cracking of matrix from the total energy dissipated by the FRC. Moreover, to characterize the flexural behaviour of FRC, some parameters are proposed, which are independent from a subjective determination of the crack initiation. Regarding the document from JSCE – SF4 (1984), the recommendation from the RILEM TC 162-TDF (2002b) has a novelty of defining parameters for being used on the verification for both the ultimate and serviceability limit states, as well as, excluding the

energy parcel due to concrete matrix during the cracking process. Beside the abovementioned improvements from RILEM TC 162-TDF (2002b), the typology of the three-point bending test, namely, with the notched specimen has the advantage of decreasing significantly the dispersion of the obtained results. This is due to the fact that the notch induces the crack at the notched cross section and, therefore, the results scatter can be attributed to the number, inclination, and degree of mobilization of the fibres at the fracture cross section.

Equivalent and residual stresses (RILEM TC 162-TDF 2002b)

The FRC post-peak behaviour is appraised by analysing the load - deflection or load - crack mouth opening curves obtained from three-point bending tests, namely, by assessing some parameters related to their shape and area. This standard presents two distinct concepts for characterizing the post-peak behaviour. The first one is supported on the concept of equivalent flexural tensile strength, f_{eq}, and is dependent of the energy dissipated up to certain deflection levels. The other one, designated by residual flexural tensile strength, $f_{R,i}$, conceptually different, is related to discrete load values obtained for distinct deflection or crack mouth opening levels.

Apart from the f_{eq} and $f_{R,i}$ parameters, the load at the limit of proportionality, F_L, is also calculated from this type of test. The latter concept can be regarded as the force at crack initiation, and corresponds to the highest load value up to a deflection of 0.05 mm, δ_L (Figure 8.3). Based on the F_L value, and assuming a linear stress distribution on the cross section at mid-span of the specimen, the stress at the limit of proportionality, $f_{fct,L}$, can be computed by:

$$f_{fct,L} = \frac{3F_L \cdot L}{2b \cdot h_{sp}^2} \tag{8.2}$$

where b and h_{sp} are, respectively, the width of the specimen and the distance between tip of the notch and the top of the cross section.

Using δ_L and F_L, and assuming an ultimate deflection of δ_L+0.3 mm (Figure 8.3), the energy absorption capacity due to the plain concrete contribution, D_{BZ}^c, and therefore the contribution of the fibres to the energy absorption capacity can be isolated. For the determination of the D_{BZ}^c area a bilinear diagram is assumed as representing the full flexural behaviour of a plain concrete specimen. In fact is assumed that the dividing line between the concrete and fibres contribution is defined by a straight line connecting the point on the curve corresponding to F_L and the point on the abscissa $\delta_L + 0.3$ mm (Figure 8.3).

Then, the influence of the steel fibres added to the cement matrix in terms of energy absorption capacity, D_{BZ}^f, can be evaluated by measuring the area under the load-deflection curve

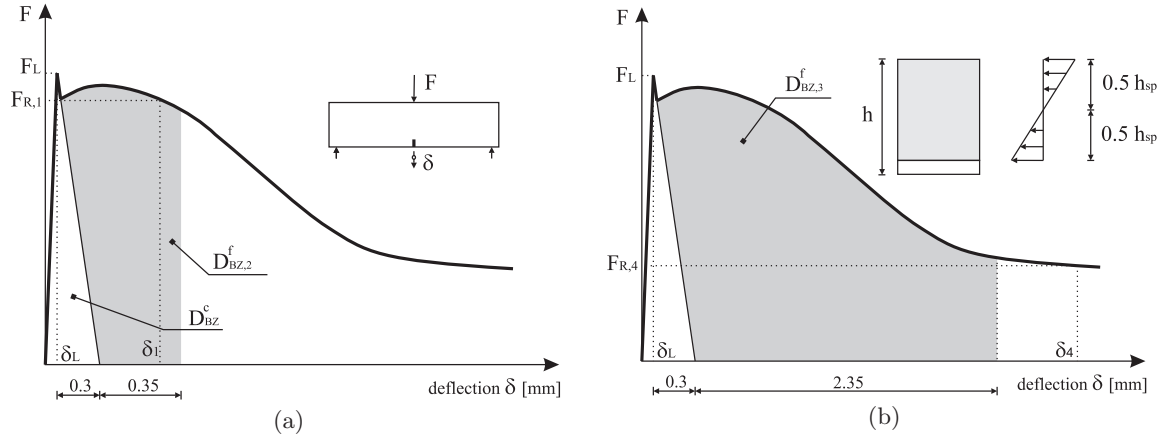

Figure 8.3: Load deflection diagrams for the determination of the equivalent and residual flexural tensile strengths (RILEM TC 162-TDF 2002b).

up to certain limit deflection and, then, by subtracting the parcel D^c_{BZ}. The contribution of fibres for the energy absorption capacity of the material is evaluated for two deflection limits, δ_2 ($= \delta_L + 0.65$ mm) and δ_3 ($= \delta_L + 2.65$ mm) determining $D^f_{BZ,2}$ and $D^f_{BZ,3}$ energy based concept parameters, the first one is used to calculate $f_{eq,2}$, while the $D^f_{BZ,3}$ is used to determine $f_{eq,3}$.

Based upon on the previous parameters, and once again assuming a linear stress distribution on the cross section at mid-span, the equivalent flexural tensile strength, $f_{eq,2}$ and $f_{eq,3}$ can be determined by:

$$f_{eq,2} = \frac{3}{2}\left(\frac{D^f_{BZ,2}}{0.50}\right)\frac{L}{b \cdot h^2_{sp}} \tag{8.3}$$

$$f_{eq,3} = \frac{3}{2}\left(\frac{D^f_{BZ,3}}{2.50}\right)\frac{L}{b \cdot h^2_{sp}} \tag{8.4}$$

On the other hand, the residual flexural tensile strength parameters, $f_{R,i}$, are related to discrete load values, $F_{R,i}$, obtained for distinct deflection levels, $\delta_{R,i}$, in the post-peak branch of the load-deflection curve. Assuming again a linear stress distribution, the residual flexural tensile strengths can be determined with the following equation:

$$f_{R,i} = \frac{3}{2}\frac{F_{R,i} \cdot L}{b \cdot h^2_{sp}} \tag{8.5}$$

The values of $f_{R,i}$ should be calculated for the force values corresponding to four distinct deflection levels: $\delta_{R,1} = 0.46$ mm, $\delta_{R,2} = 1.31$ mm, $\delta_{R,3} = 2.15$ mm and $\delta_{R,4} = 3.00$ mm.

Nevertheless, $f_{R,1}$ and $f_{R,4}$ are of more interest, since $f_{R,1}$ and $f_{eq,2}$ are used in the design at serviceability limit states, whereas $f_{R,4}$ and $f_{eq,3}$ in the design at ultimate limit states. More recently, the Fib TG-8.3 (2007) suggests for the design at the ultimate limit states the replacement of the residual stress $f_{R,4}$ by $f_{R,3}$ which is computed for a deflection of $\delta_{R,3} = 2.17$ mm or a correspondent crack opening of 2.5 mm.

8.2.4 Splitting tension test

The splitting tensile test, also worldwide known as the Brazilian test is widely accepted as a standard test method to indirectly assess the concrete's tensile strength. The main advantage of the splitting test is that only external compressive loading is required. Both cylindrical or prismatic specimen can be used. The diametrical loading scheme applied to the specimen induces an almost linear tensile stress field perpendicular to the loading plane in the central zone of the specimen's cross section (Timoshenko and Goodier 1991). This test is a standardized method comprised in several major international concrete standards such as: ISO 4108-1980 (1980), BS 1981:Part 117 (1983) and ASTM C496-90 (1991). Furthermore, it is also incorporated in reference design codes for concrete structures CEB-FIP (1993), ACI 318-R (1993) and EN 1992-1-1 (2004).

For a perfectly homogeneous material with linear elastic behaviour, the diametrically loading produces a nearly uniform tensile stress across the loading plane. Nevertheless, since concrete is a quasi-brittle material, and fibre reinforced concrete is a pseudo-ductile material, with the toughness level dependent on the fibre content, type of fibre and concrete matrix, this stress distribution will not be uniform. Moreover, it is well-known that the splitting tensile strength is higher than the uniaxial tensile strength. This is widely acknowledge in several standards and recommendations CEB-FIP (1993) and EN 1992-1-1 (2004).

More recently, another type of splitting test is being used for determining the concrete's fracture energy that is called the wedge splitting test, see Figure 8.4. This test consists into splitting a cube in two halves, by applying a wedge pressed between roller bearings placed on the top of the cube, while monitoring the load and crack mouth opening width. Although this test was firstly suggested for determining the fracture energy (Brühwiler and Wittman 1990, Abdalla and Karialloo 2003), several authors have successfully applied the wedge splitting test to determine, by inverse analysis, the stress - crack opening relationship, e.g Rossi et al. (1991), Que and Tin-Loi (2002), Ostergaard (2003) and Löfgren et al. (2008). The post-cracking relationship can be obtained by analytically closed-form equations supported on the fracture mechanics, namely, on the fictitious crack model (Hillerborg 1980).

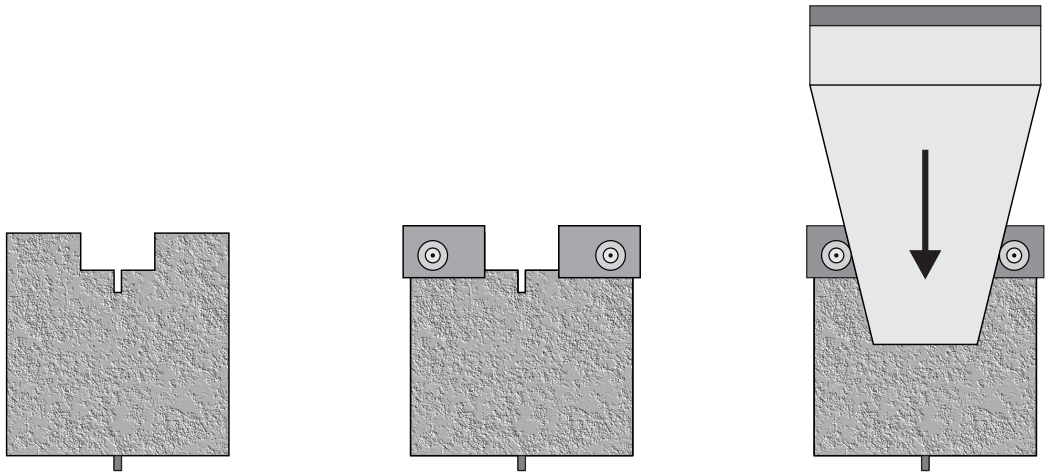

(a) (b) (c)

Figure 8.4: Wedge splitting test set-up: (a) specimen placed aligned with support, (b) mounting of the roller bearings and (c) wedge placed between roller bearings.

8.3 Experimental programme

8.3.1 Materials and specimens

The materials and mixture procedure used for the steel fibre reinforced self-compacting concrete, SFRSCC, were described in the previous chapter. To study the post-cracking behaviour of SFRSCC two batches with distinct contents of fibres (Cf) were used: 30 and 45 kg/m^3. Since the aggregates used for the SFRSCC composition with 45 kg/m^3 were from a different shipment, and in spite of being from the same supplier, the composition for the latter fibre content was slightly adjusted to take into account the differences on the aggregate granulometric curves. For that purpose, the solid skeleton of the composition was adjusted using the method described in the previous chapter.

Table 8.1 includes the composition that has best fitted self-compacting requirements for the two contents of fibres (Cf) adopted, 30 and 45 kg/m^3. Remark that, in Table 8.1, Ws is the water necessary to saturate the aggregates and W/C is the water/cement ratio. The Ws parcel was not used to compute the W/C ratio, on the other hand the water parcel from the superplasticizer was included. In Table 8.1, Lf and Sp are, respectively, the limestone filler and the superplasticizer; Fs, Cs and Ca are the fine sand, coarse sand and crushed aggregate, respectively.

For each batch eight cylinders with a diameter of 150 mm and 300 mm height were casted, as well as five beams with a cross section of 150 $\times$ 150 mm^2 and a 600 mm length. The compressive strength of each batch was assessed by means of three cylindrical specimens. At the date when

the tests were performed (approximately at 30 days), the series with 30 kg/m^3 of fibres had an average compressive strength of 71.1 MPa with a coefficient of variation, CoV, of 1.9%. On the other hand, for the series with 45 kg/m^3 of fibres an average value of 67.2 MPa for the compressive strength, with a CoV of 1.4%, was obtained.

Table 8.1: Compositions for 1 m^3 of SFRSCC.

C_F [kg]	Paste/Total volume [%]	Cement [kg]	L_F [kg]	Water [dm^3]	W_S [dm^3]	S_P [dm^3]	F_S [kg]	C_S [kg]	C_A [kg]	W/C [-]
30	0.34	359.4	312.2	96.9	64.7	6.9	108.2	709.4	665.2	0.29
45	0.38	401.7	344.3	117.3	65.4	7.6	178.3	668.1	600.0	0.31

8.3.2 Uniaxial tensile test

Test set-up and specimen preparation

The RILEM TC 162-TDF (2001) recommendation for the uniaxial tensile test of steel fibre reinforced concrete was adopted in this work, mainly due to the advantages pointed out in section 8.2.2.

In agreement to this standard, a notched cylinder of both diameter and height of 150 mm was used. The specimens were swan out from standard cylinders with 150 mm diameter and 300 mm height. Afterwards, a notch along the perimeter with a 15 mm depth and 5 mm thickness was swan at mid height of the final test specimen. All the operations related to sawing were performed on the mature specimen, hence eliminating any effects on the fibre spatial arrangement during casting at the notch region. A special care was taken in order to assume that the cuts were perpendicular to the specimens axis, particularly the notch, since in this work all specimens were ground.

Afterwards, the specimen was ground and carefully cleaned with both compressed air and solvent. The specimen was then directly glued, "*in-situ*", to the loading platens of the testing rig. The selected glue is a high strength epoxy resin, which achieves a tensile strength of nearby 30 MPa and a bond strength between 4 to 8 MPa (depending on the surface material and treatment). This procedure was adopted due to two reasons: i) to eliminate soft connections between specimen and testing rig, since this allows to take full advantage of the high rotational stiffness; ii) the *in-situ* curing of the adhesive mitigates the specimen misalignment and, consequently, conduces to a more uniform loading conditions.

A high stiff servo-hydraulic system of 2000 kN static load carrying capacity was the used testing equipment, Figure 8.5(a). The test was controlled in closed-loop displacement by the

average signal of three displacement transducers mounted on two steel rings disposed at equal distances along the perimeter of the specimen, see Figure 8.5(b). The adopted gauge length was 35 mm, smaller than the upper limit length of 40 mm suggested by RILEM TC 162-TDF (2001). The adopted displacement rates are: 5 μm/min up to a displacement of 0.1 mm, and 100 μm/min until the completion of the test, i.e. a 2 mm displacement.

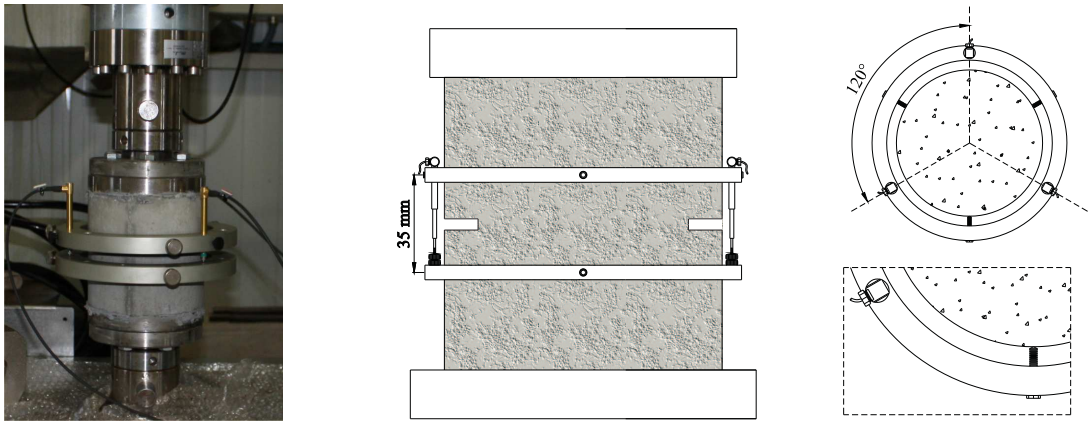

(a) (b)

Figure 8.5: Uniaxial tension test set-up: (a) general view and (b) positioning of displacement transducers (not scaled).

Stress - crack opening curves

In all the performed uniaxial tension tests, the cracking occurred at the notch plane, hence a desired failure mode was attained. Moreover, due to the careful measures taken in the specimen's gluing process, it was not observed failure at the boundaries of the specimen, even though the relatively high concrete's strength. Nevertheless, from the ten specimens tested, only eight of them were successfully tested for each series.

The average curve and the envelope of the experimental uniaxial tension stress - average displacement relationships, $\sigma - \delta_{avg}$, are depicted in Figures 8.6 and 8.7, respectively, for a fibre content of 30 and 45 kg/m^3. Hereinafter, these series will be designated of Cf30 and Cf45, respectively. A detailed view of the initial part of the experimental response is depicted on the right side of the figure. In Annex V is enclosed the experimental response of each specimen.

For both tested series, the $\sigma - \delta_{avg}$ response is linear almost up to peak. Only just before the peak load is observed some non-linearity. However, it can be ascertained that the pre-peak branch stiffness is slightly higher for the Cf30 series (see Figures 8.6 and 8.7). The values of the tangent stiffness, computed from the tensile load stress - displacement curves, are 22.5

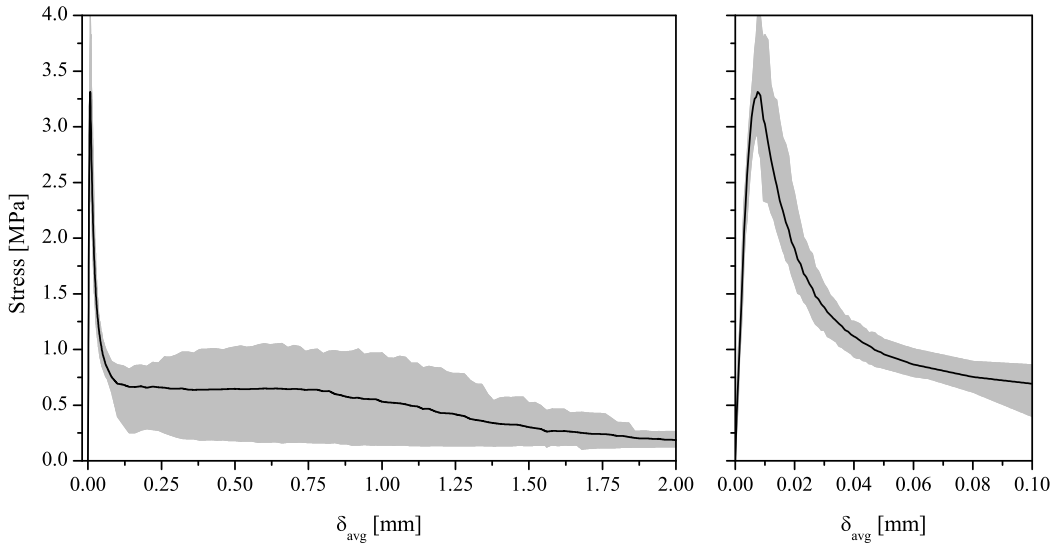

Figure 8.6: Experimental uniaxial tension stress - displacement relationship with 30 kg/m^3.

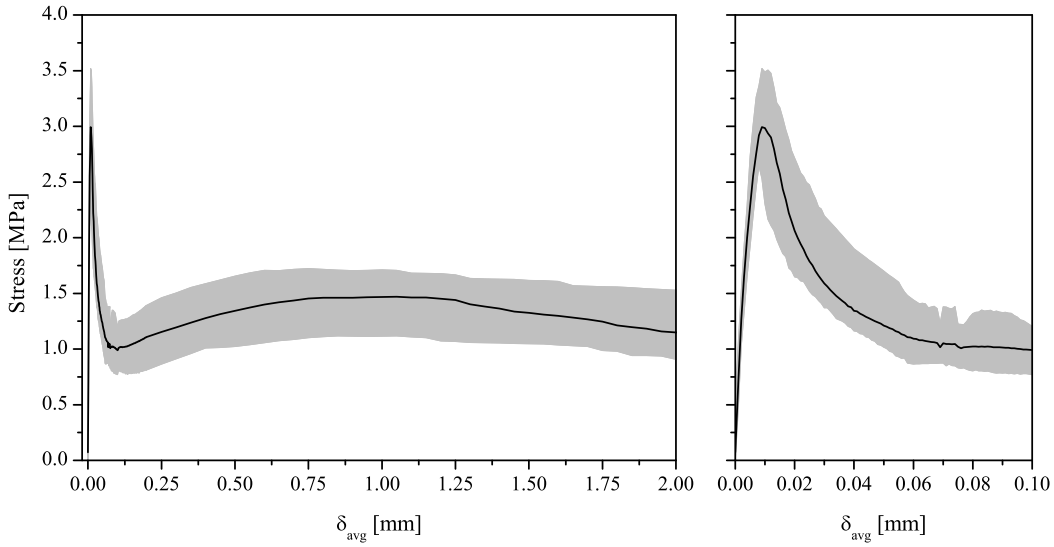

Figure 8.7: Experimental uniaxial tension stress - displacement relationship with 45 kg/m^3.

and 19.2 GPa, respectively, for the Cf30 and Cf45 series. Remark that the same gauge length was used for the displacements transducers in all the tested specimens. Only for that reason, can undoubtedly be stated that the stiffnesses are different, otherwise it could be related to distinct gauge lengths. Moreover, since the elasticity modulus for the amount and type of fibres used could be assumed to be similar in compression and tension, the difference between the stiffness in tension of the Cf30 and Cf45 series is in accordance with the trends obtained in the compressive results in Chapter 7. Once the peak load is attained, the load smoothly decreases up to a minimum post-peak stress nearby a displacement of 0.10 mm (see right side of both

Figures 8.6 and 8.7). Beyond this displacement, it is observed either a plateau or a hardening-plastic response, depending on the fibre content. In general, the post-peak hardening is observed in the series with a higher content of fibres (Cf45). Nevertheless, a hardening behaviour was also observed in some specimens of the Cf30 series (see Annex V).

After the plateau on the Cf30 series, i.e. beyond a displacement of nearby 0.8 mm, the residual stress starts to decrease with sudden stress losses corresponding to the fibre fracture. In fact during the tests it was audible by the peculiar sound of a fibre fracturing. Due to the averaging process of the specimens response, this is not perceptible in Figure 8.6, however this can be observed in the responses of the individual specimens (see Annex V). The displacement value of 0.8 mm is in the range of the pullout peak slip values interval obtained for the hooked fibres with an inclination angle of 30º (see Chapter 4). Have in mind that the fracture process during the uniaxial tension response of a FRC can be regarded as the sum of all single fibres contribution, as well as that the fibre orientation angle enclosed with the load direction influences significantly the individual fibre pullout response. Moreover, according to Stroeven and Hu (2006) the average orientation angle value of the active fibres crossing a leading crack is 35º (value analytically derived), which is quite similar to the value of 34º experimentally registered by Soroushian and Lee (1990). In the uniaxial tension response the sudden stress drops start to be more visible after the displacement of 0.8 mm, which corresponds to the fracture of the fibres with an angle of approximately 30º.

Remark that, from a theoretically point of view, the previous analysis should be made with the $\sigma - w$ relationship, and not with the $\sigma - \delta_{avg}$. However, for the latter gauge displacement's amplitudes the difference between crack opening width and correspondent displacement can be neglected.

Regarding the Cf45 series, the observed post-peak pseudo-hardening can be ascribed to two reasons. Firstly, there is a higher number of active fibres crossing the crack. The other reason, and probably the most important, is that both the compressive strength and stiffness of the Cf45 series matrix is lower than the Cf30. In the softening phase after peak stress, the stress decreased until a minimum stress is attained, roughly at about a deflection of 0.1 mm. For larger displacements the reinforcement mechanisms provided by the fibre hooked end start to be further mobilized contributing to the observed pseudo-hardening phase. Since there are more fibres intersecting the crack and concrete is of lower tensile strength, the accumulated bulk energy dissipated during cracking for the Cf45 series is smaller when compared with correspondent released energy in the Cf30 series. Moreover, due to the lower tensile strength and stiffness of the matrix, fibres did not fracture so often as in the Cf30 series. Consequently, the residual stress for the Cf45 series is increased due to the full mobilization of the hooked-end. In spite of the observation of the fibres at specimen's crack surfaces after the finalization of the

uniaxial tension test, fibre pullout tests from a matrix with the series Cf45 composition should be conducted in order to assess the real contribution of a single fibre in the latter matrix.

In general, the responses exhibit very low scatter in the pre-peak branch. On the other hand, in the post-peak branch the scatter was considerably higher, particularly in Cf30 series, and for a displacement higher than 0.1 mm. Up to this displacement the commanding pullout reinforcement mechanisms are the chemical bond and debonding due to the micro-cracking of the ITZ, hence the influence of the fibre dispersion (implicitly orientation) is not so important. As the crack width increases, the reinforcement mechanisms of the fibres hooked end start to be mobilized, hence the scatter of the post-peak behaviour increases due to the variation of the fibre dispersion between different specimens, namely, the fibre orientation. In addition to the aforementioned, for the Cf30 series, in general, fibre rupture was observed, as it was expected from the pullout tests' results presented described in Chapter 4.

In Figures 8.8 and 8.9 are depicted the experimental average and characteristic uniaxial tension stress - crack width relationships, respectively, for the Cf30 and Cf45 series obtained from the previous $\sigma - \delta_{avg}$ curves accordingly to the recommendation from RILEM TC 162-TDF (2001). The characteristic stress-crack opening curve for the lower bound (L.B.) and upper bound (U.B.) with a confidence level of $k = 95\%$ was obtained from the average curve computed from all tests, $\overline{\sigma}_w(w)$, according to (RILEM TC 162-TDF 2001):

$$\sigma_{w,k}(w) = \overline{\sigma}_w(w)\frac{G_{F2mm,k}}{\overline{G}_{F2mm}} \tag{8.6}$$

where $\overline{G}_{F2mm}$ is the average energy dissipated up to a crack opening of 2 mm and $G_{F2mm,k}$ is the characteristic energy dissipated for the same crack opening value. For computing the latter parameter a t-Student distribution was assumed.

Stress and toughness parameters

In Table 8.2 are included the average and characteristic stresses and toughness parameters, as well as the respective coefficient of variation obtained from the performed uniaxial tests. In this table σ_{peak} is the maximum stress, and $\sigma_{0.3mm}$, σ_{1mm} and σ_{2mm} are the stresses at a crack opening width of, respectively, 0.3, 1 and 2 mm. On the other hand, G_{F1mm} and G_{F2mm} are the dissipated energy up to a crack opening width of, respectively, 1 and 2 mm. The characteristic values were obtained for a $k = 95\%$ confidence level assuming a t-Student distribution. The normality of the sample was ascertained by the Shapiro-Wilk test (Montgomery and Runger 1994).

In Table 8.2 are also included the total number of fibres, N_f, and effective fibres, N_f^{eff}, counted at the fracture surface. As effective fibres were considered all the fibres that had the

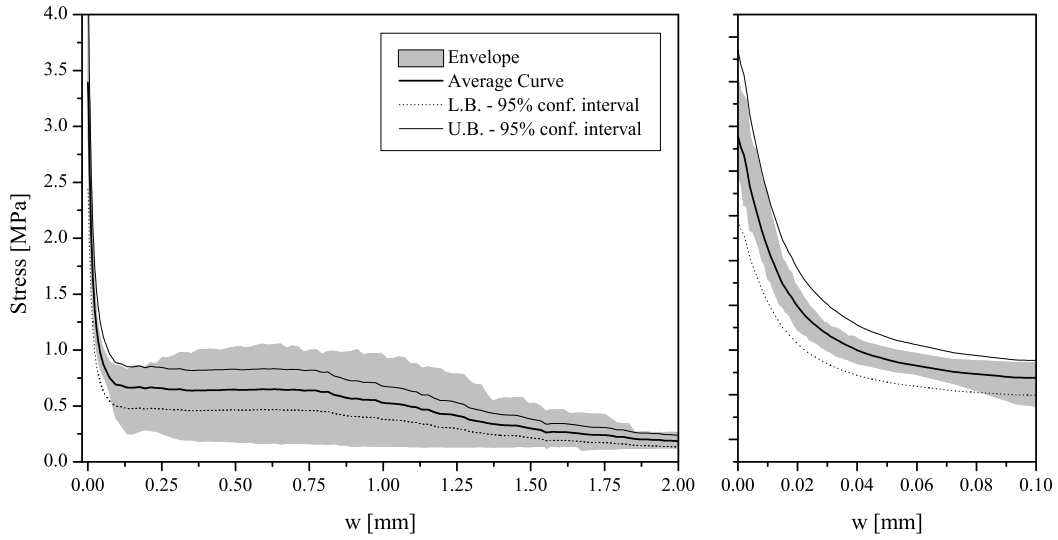

Figure 8.8: Experimental uniaxial tension $\sigma - w$ relationship for SFRSCC with 30 kg/m^3.

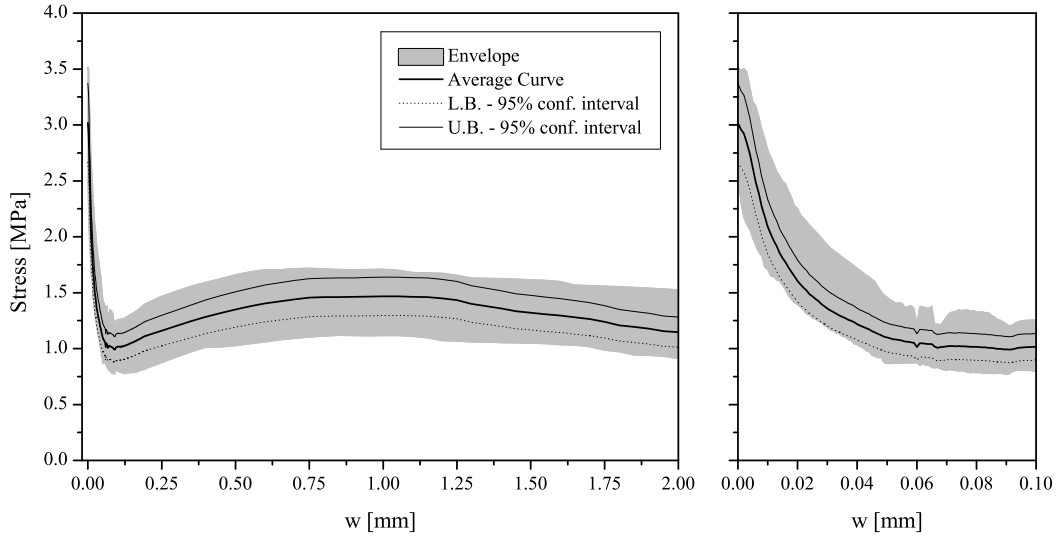

Figure 8.9: Experimental uniaxial tension $\sigma - w$ relationship for SFRSCC with 45 kg/m^3.

hooked end deformed (by a visual inspection), as well as the fibres that have fractured. In spite of some researchers do not consider the fractured fibres as "effective", in the author opinion they should be considered, since they offered resistance to crack opening up to their failure. Their full effectiveness can be questionable, but it is feasible to admit that they were "partially effective". For the simplicity sake, lets assume that the fibre slip when its being pulled out is approximately equal to the crack opening width. Then, as it was observed in Chapter 4, in the pullout behaviour of inclined fibres, depending on the inclination angle and embedded length, a fractured fibre can sustain forces up to a slip, i.e. crack opening width, that varies

approximately from 0.7 mm to 4 mm.

In general, the stresses and toughness parameters increased with the increase of the fibre content, as it would be expected. The only exception was the peak stress which was nearby 10% lower for the series with a content of fibres of 45 kg/m^3. Remark, that this decrease is not due to the content of fibre, even though it could be indirectly appointed to it, since the aggregates, cement and additions contents for each series are distinct in order to attain self-compatibility requirements. Moreover, the peak stress cannot be regarded as the tensile strength, but as an estimation, since due to the notch on specimen used, cracking does not starts at the weakest material point, and also because there is a stress concentration at the notch tip (Van Mier and Van Vliet 2002).

Table 8.2: Stress and toughness parameters obtained from the uniaxial tension test.

CF [kg/m^3]		N_f [-]	N_f^{eff} [-]	σ_{peak} [MPa]	$\sigma_{0.3mm}$ [MPa]	σ_{1mm} [MPa]	σ_{2mm} [MPa]	G_{F1mm} [N/mm]	G_{F2mm} [N/mm]
30	Avg.	27	19	3.392	0.649	0.520	0.186	0.685	1.007
	CoV	30.8%	28.8%	13.0%	36.6%	45.1%	22.8%	32.3%	33.7%
	$k_{95\%}$	20	14	3.024	0.450	0.324	0.250	0.500	0.724
45	Avg.	67	39	3.019	1.219	1.466	1.342	1.342	2.645
	CoV	16.1%	16.5%	9.9%	18.0%	12.7%	18.0%	13.6%	13.1%
	$k_{95\%}$	58	34	2.768	1.036	1.310	0.972	1.189	2.356

Regarding the post-cracking stresses, a significant increase with the fibre content was observed. An increase of the fibre content in 15 kg/m^3 provided high increments on the values of the residual stresses, which vary from 2 to 7 times depending on the crack width. Such increase on the residual stresses is not simply justified by the higher number of fibres crossing the crack surface for the Cf45 series. Other factors may also have contributed to this. During the uniaxial tension tests of the Cf30 series, the main fibre failure mode was fibre rupture. The results of the pullout tests in Chapter 4, performed with specimens of the same SFRSCC composition of the Cf30, support this type of the fibre rupture. In comparison to Cf30 series, a significant increase of the dissipated energy was observed up to both deflections of 1 and 2 mm. The increment ranged between 2 to 2.6 times.

In general, the CoV values obtained for the toughness parameters were considerably smaller for the Cf45 series. At a first glance, these values may seem relatively high. However, the magnitude of such values is within the expected for this type of material. In fact, generally, the CoV values were smaller than the ones obtained by other authors with the same test procedure and specimen's dimensions for conventional fibre reinforced concrete, CFRC, (Barragán 2002, Löfgren et al. 2008), which indicates a better fibre distribution in SFRSCC than in CFRC.

In Figure 8.10 is depicted the relation between the total number of fibres and effective fibres at the fracture surface, both registered experimentally in all the tested specimens of Cf30 and Cf45 series.

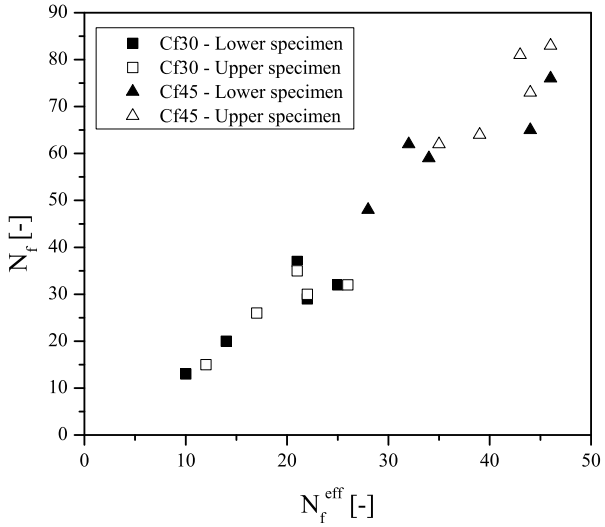

Figure 8.10: Relationship between the total number of fibres and number of effective fibres at the crack surface.

Since the uniaxial tension test specimens (with 150 mm height) were obtained from distinct parts of a standard cylinder with 300 mm height, additionally, in the aforementioned figure are distinguished the specimens obtained from the bottom and upper part of the standard cylinder. This strategy enables to assess "indirectly", if there is any influence of the gravity on the fibre distribution. It was observed a linear relationship between the N_f and N_f^{eff}. Moreover, it was not found a significant correlation between the number of fibres at the crack surface and the gravity influence in the production, i.e. type of casting, of these specimens. Dupont (2003) has also found a linear relationship between the total number of fibres and the number of effective fibres for small fibre contents. However, for higher contents, this relationship becomes non-linear. Remark, that the previous comparison is only qualitative, since the fibre mobilization depends on various factors, such as the type of fibre, the matrix quality, and at last, but not less important, the group effect, which for higher fibre contents is quite important, since fibre spacing influences the efficiency of a group of fibres. Thus the number of effective fibres may decrease as the fibre spacing decreases, due to the higher probability of mutual influence of adjacent fibres (Naaman and Shah 1976).

Influence of the number of effective fibers on the post-cracking parameters

Throughout Figures 8.11(a) to 8.11(f) are depicted the relationships between the effective number of fibres at the specimen's fracture surface, N_f^{eff}, and the aforementioned post-cracking parameters obtained from the uniaxial tension test.

Regarding the peak stress, σ_{peak}, no significant relation was observed with the N_f^{eff} increase, see Figure 8.11(a). Since σ_{peak} is mainly governed by the strength of the matrix a smaller σ_{peak} for Cf45 was expected, which was confirmed by the obtained results. There was also no significant relation between σ_{peak} and the provenience of specimen, i.e. from lower or upper part of a standard cylinder. This suggests that there is no significant segregation of the matrix skeleton and paste in the casted cylinders. On the other hand, for the residual stresses at a crack opening width of 0.3 and 1 mm, respectively, $\sigma_{0.3mm}$ and σ_{1mm}, it is clearly visible for both, a linear relationship between these stresses and the N_f^{eff}, see Figures 8.11(b) and 8.11(c). This was expected, since the residual stress sustained by the crack is intimately related to number of mobilized fibres. Concerning the Cf45 series, the residual stresses for the "upper specimen" exhibited a lower scatter when compared to the "lower specimens" results. Since due to technical problems during testing, the number of tested specimens from the lower part (5) was different of the specimens from the upper part of the standard cylinder (3), no conclusive elations could be withdraw.

In Figure 8.11(d) is represented the relation between the residual stress at a crack opening of 2 mm, σ_{2mm}, and the N_f^{eff}. When compared to the $\sigma_{0.3mm}$ and σ_{1mm} relationships, the overall trend is distinct. First of all, there are two clear distinct trends for σ_{2mm}. For the Cf30 series, the increase of σ_{2mm} with N_f^{eff} is marginal and can be assumed null. On the other hand, for the Cf45 series it is visible a linear increase of σ_{2mm} with N_f^{eff}, in spite of a higher scatter. Moreover, it is visible a clear jump on the σ_{2mm} value from the series Cf30 to Cf45, even though the small difference between the Cf30 series' specimen with the highest number of fibres and the lowest of the Cf45 series. This considerable jump on σ_{2mm} value from the Cf30 to Cf45 specimens is not ascribed to the increase of effective fibres, hence this jump comprises the differences on the fibre micro-mechanical behaviour between the two series with distinct fibre content, as previously stated. In fact for the series Cf30, in general, the fibres fractured before a 2 mm crack width, while for the Cf45 series, in general, the fibres were fully pulled-out, which enabled a higher crack bridging stress at these crack openings.

Finally, in the overall, the dissipated energy has shown a linear increase with the N_f^{eff}, for both limits of the crack opening studied. Nevertheless, there are two aspects that should be enlighten. For the dissipated energy up to a 2 mm crack opening, G_{F2mm}, there is also a jump on the G_{F2mm} value from the series Cf30 to Cf45 for the same reasons pointed for the

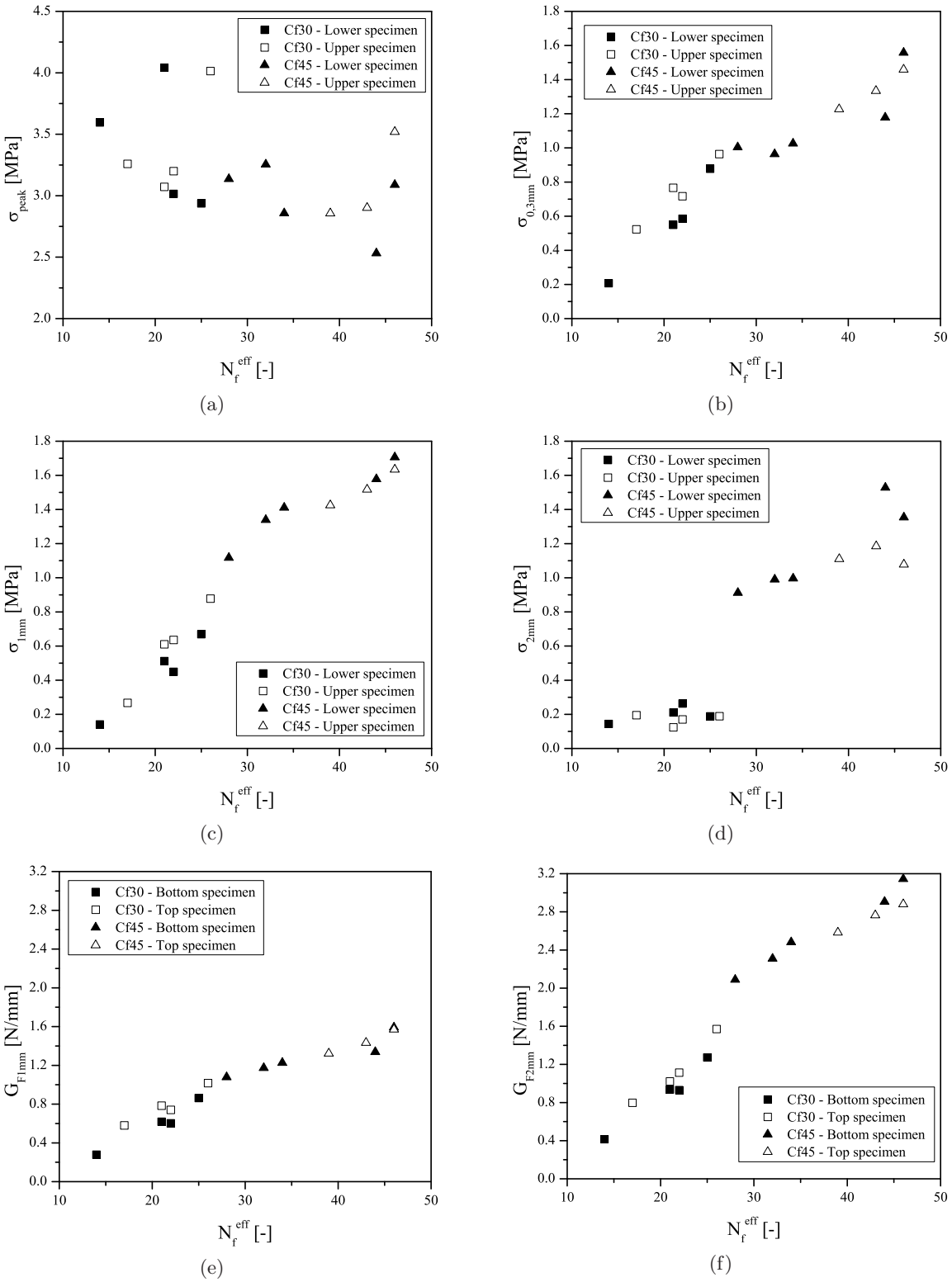

Figure 8.11: Relationships between the number of effective fibres and the post-cracking parameters: (a) peak stress, (b), (c) and (d) stress at a 0.3, 1 and 2 mm crack width, respectively; (e) and (f) dissipated energy up to 1 and 2 mm crack width, respectively.

σ_{2mm}. However, this jump has a much smaller amplitude than the one observed for σ_{2mm}, since G_{F2mm} represents the accumulated energy dissipated up to 2 mm of crack width, while σ_{2mm} represents the residual strength at this crack width, therefore much more susceptible to the failure modes of the fibres. Another interesting aspect is that the increment rate of both G_{F1mm} and G_{F2mm} with N_f^{eff} for the Cf45 series was slightly smaller than for Cf30 series, due to the detrimental fibre group effect already pointed out.

8.3.3 Three-point bending tests

Test set-up

The tensile behaviour under flexure of the SFRSCC was assessed accordingly to the RILEM TC 162-TDF (2002b) recommendation (Figure 8.12). In general, in the specimens' preparation all the requirements of this recommendation were fulfilled. However, the recommended procedure by RILEM TC 162-TDF (2002b) for filling the moulds was not applicable to the present case, since the high fluidity of the prepared mixtures would not allowed it.

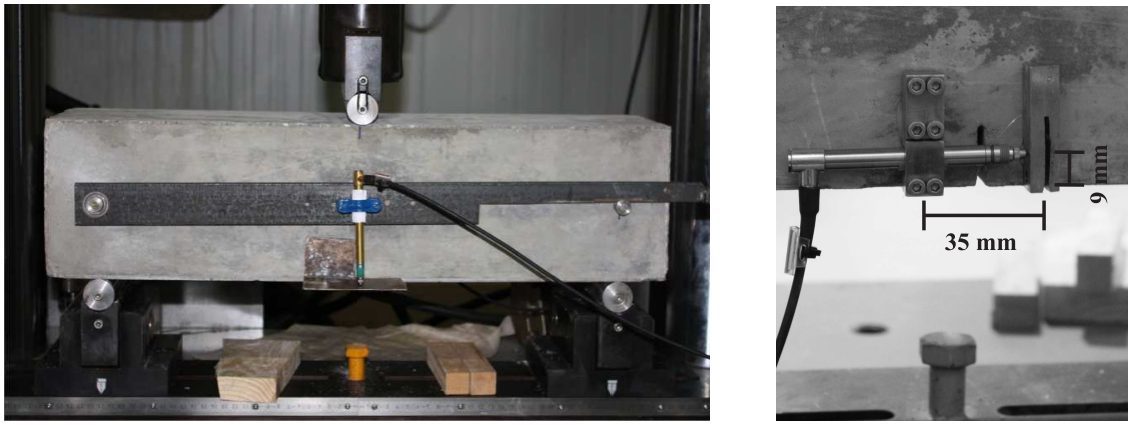

(a) (b)

Figure 8.12: Three-point bending test set-up: (a) general view and (b) positioning of CMOD transducer.

Prismatic specimens of 150×150 mm^2 cross section and a length of 600 mm were used. The beams were notched on one of the faces perpendicular to the casting surface, using wet sawing, through the width of the beam at its midspan. The width and depth of the notch was 5 mm and 25 mm, respectively. The specimens were placed on roller supports, giving to the beam a free span of 500 mm. Special care was taken to ensure the correct positioning of the beam and the loading roller.

The tests were performed using a closed loop system based on deformation-control, using

the deflection measured at midspan as control variable, Figure 8.12(a). A constant rate of 0.2 mm/s was adopted. The crack mouth opening displacement, CMOD, was not measured as suggested by RILEM TC 162-TDF (2002b), i.e. along the longitudinal axis at the mid-width of the specimen's bottom face, but on the lateral face of the beam,Figure 8.12(b). Nevertheless, it was adopted a 35 mm distance between the reference points for measuring the CMOD, which is a smaller value than the one suggested by RILEM TC 162-TDF (2002b).

Load - deflection curves

In Figures 8.13 and 8.14 are depicted the load - deflection at mid-span relationships, respectively, for the series Cf30 and Cf45. A detailed view of the initial part of the experimental response, i.e. up to a 3 mm deflection, is comprised on the right side of these figures. Additionally, from the average curve computed from all tests, the characteristic load - deflection curves obtained for the lower bound (L.B.) and upper bound (U.B.) are also included, where a confidence level of $k = 95\%$ was assumed.

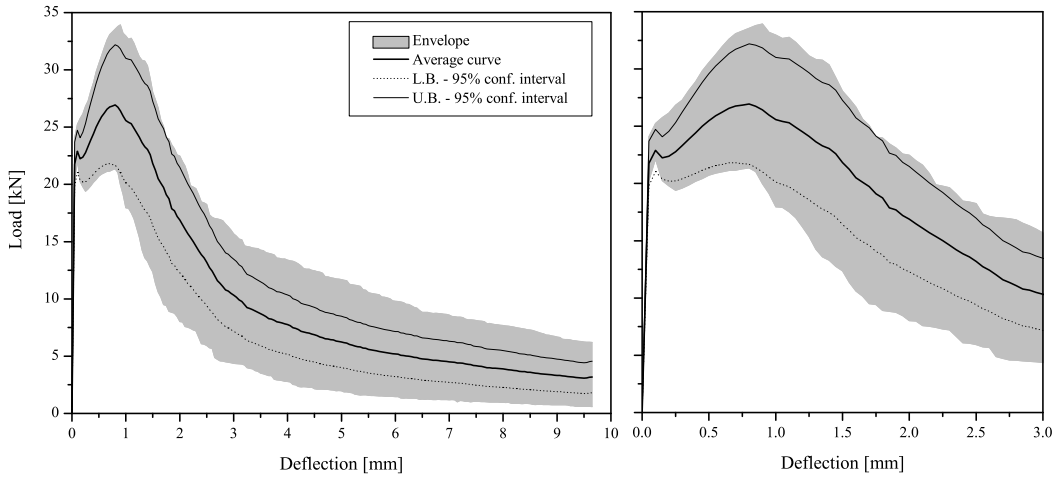

Figure 8.13: Experimental load - deflection relationship for the Cf30 series (30 kg/m^3 of fibres).

Regarding the pre-peak behaviour, the series Cf30 after attaining the load at the limit of proportionality revealed a very small load decrease followed by deflection-hardening phase up to a deflection of approximately 1 mm due to the mobilization of the fibre reinforcement mechanisms. On the other hand, this load decay just after reaching the load at the limit of proportionality was not observed in the Cf45 series. Due to the higher fibre content, a markedly non-linear behaviour is visible up to the peak load.

When the peak load is attained two distinct behaviours are observed for the studied series.

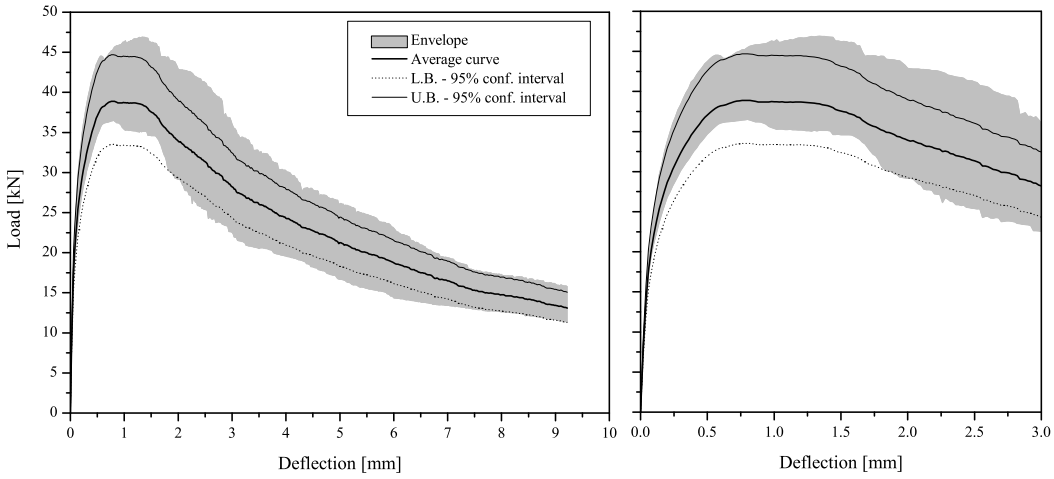

Figure 8.14: Experimental load - deflection relationship for the Cf45 series (45 kg/m^3 of fibres).

In the Cf30 series the load decreases considerably, whereas in the Cf45 series is observed a plateau up to a deflection of nearby 1.5 mm.

In what concerns to the Cf30 series, this can be ascribed to the fibre fracture, which was also observed on the uniaxial tension tests, and previously ascertained on the micro-mechanical pullout tests. In the bending tests, in opposite to the uniaxial tests, the crack opening width varies along the crack surface plane, therefore the fibres disposed along the specimen's height are mobilized at different stages regarding their location towards the neutral axis. The fibres disposed more distant to the neutral axis have higher probability of fracture first. As it will be presented in next section, to a deflection of 1 mm corresponds a CMOD just slightly higher. Having in mind that fibre rupture was observed for a slip value smaller than 1 mm, the fibres nearest to the bottom face of the beam start to fracture. For simplicity it is admitted that the slip is equal to the crack width. When the first fibres start to fracture (the ones near the bottom face), the residual load decay starts to accentuate, since the part of the energy released during the fibre fracture is sustained by the other fibres, thus rapidly accelerating the pullout process of these fibres positioned above. However, remark that the bending and uniaxial specimens have considerably different fibre distributions, as observed in Chapter 6. Due to the geometry and dimensions of the bending specimen's and high flowability of the concrete mixture, the fibres tend to be oriented with the longitudinal axis of the beam and, consequently, the average angle of the fibre towards the crack plane decreases. Since the average fibre angle is smaller, then the probability of fibre rupture decreases, when compared to the conditions found in the uniaxial tests.

In comparison, a smaller load decay is observed in the Cf45 series, which is justified by both the higher fibre content and smaller amount of fibres that have fracture. These reasons also

contributed to the lower scatter observed in the flexure responses.

Table 8.3 includes the average and characteristic values of the post-peak parameters obtained from the three-point bending tests. Moreover, the number of total and effective fibres at the crack surfaces are also included. The procedure for fibre counting was the same as used for the uniaxial tension specimens. The meaning and computation procedure of the post-cracking parameters was already described in section 8.2.3.

Regarding the limit of proportionality, $f_{ct,L}$, which corresponds to the end of the linear elastic phase, i.e crack initiation, a decrease of nearby 19% was observed with the fibre increase. This decrease of $f_{ct,L}$ was expected, since during uniaxial tests was observed a decrease on the tensile strength due to distinct concrete compositions. However, the decrease on $f_{ct,L}$ was relatively higher than the reduction observed for tensile strength in the uniaxial tests ($\approx 10\%$). The higher decrease on $f_{ct,L}$, when compared with the observed in the tensile strength, can be ascribed to a less stiffer matrix of the Cf45 series. The deflection limit adopted to evaluate $f_{ct,L}$ (0.05 mm) can also contribute for this result, since the deviation from linearity of the force - deflection curve can occur for deflection values larger than this limit, depending on the content of fibres of the tested FRC and the properties of the cement matrix. Furthermore, the flexural strength is a composed effect of a concrete volume in compression and another part in tension.

Table 8.3: Average and characteristic results of the three point bending tests.

Cf [kg/m^3]		N_f [-]	N_{eff} [-]	F_L [kN]	δ_L [mm]	$f_{ct,L}$ [MPa]	$f_{eq,2}$ [MPa]	$f_{eq,3}$ [MPa]	$f_{R,1}$ [MPa]	$f_{R,4}$ [MPa]
30	Avg.	116	107	21.758	0.050	6.963	8.002	6.661	7.999	3.322
	CoV	15.8%	14.6%	7.2%	0%	7.2%	18.7%	25.2%	17.6%	47.3%
	$k_{95\%}$	93	88	19.802	0.050	6.337	6.145	4.578	6.248	1.371
45	Avg.	171	141	17.663	0.050	5.652	10.844	11.332	11.639	9.033
	CoV	5.7%	5.8%	3.8%	0%	3.8%	10.7%	13.1%	10.4%	19.0%
	$k_{95\%}$	155	131	16.841	0.050	5.389	9.399	9.491	10.141	6.899

Both the equivalent and residual strengths have shown a considerable increase with the fibre increment. In what concerns to $f_{eq,2}$ and $f_{R,1}$, which are used in the design verifications for the serviceability limit states, it was observed an increase of, respectively, 35% and 45%. On the other hand, $f_{eq,3}$ and $f_{R,4}$, corresponding to the ultimate limit state design, have revealed a higher increase with the fibre increment, respectively, 70% and 172%. For $f_{eq,2}$ and $f_{R,1}$ the increment observed with the fibre content is just ascribed to the higher number of fibres intersecting the crack plane, since for the Cf45 series there is 47% more fibres crossing the crack plane than for the Cf30 series. Moreover, the number of fibres at the cross section increment

ratio is nearby to the increment range observed for $f_{eq,2}$ and $f_{R,1}$.

On the other hand, the increase observed for $f_{eq,3}$ and $f_{R,4}$ in Cf45 series, when compared to $f_{eq,3}$ and $f_{R,4}$ values for the Cf30 series, cannot be only justified with the increase of the number of fibres at the crack plane. Once again, the reason lies on the distinct fibre micro-mechanical behaviour for each series, i.e. fibre rupture was observed for the Cf30 series, while the governing fibre failure mode in the Cf45 series was pullout. Since $f_{eq,3}$ and $f_{R,4}$ are evaluated for higher deflections and, consequently, higher crack widths, the position of the neutral axis will be very near the top beam's face. Even though, the crack width varies from a null value at a small distance of the the neutral axis up to the maximum width at the the bottom beam's surface, there will be a considerable parcel of the cross section in which the crack width is larger than 1 mm. In fact, from a finite element analysis of a beam with feasible values of the material properties' parameters, for a deflection at mid span of 2.85 mm (average of the deflections for which $f_{eq,3}$ and $f_{R,4}$ are computed), 60% of the net cross section has a crack opening width higher than 1 mm. Hence, there is a high probability of fibres to fracture for the Cf30 series in a great parcel of the net cross section. Nevertheless, one should be aware that the ratio of fibres that fracture is intimately linked to their angle towards the active crack plane, as well as the strength of the surrounding matrix. In addition for the prismatic beams used in the three-point bending tests a higher fibre orientation factor was observed than for the uniaxial tension test specimens, i.e. lower fibre inclination towards the crack's plane.

Crack opening mouth displacement versus deflection relationship

In Figures 8.15(a) and 8.15(b) are represented the experimental relationships between the deflection at mid-span and the crack mouth opening displacement, CMOD, respectively, for the Cf30 and Cf45 series. Additionally, it is included the relationship proposed by RILEM TC 162-TDF (2002b).

For the Cf30 series, the RILEM TC 162-TDF (2002b) relationship is within the experimental envelope and quite close to the average curve. On the other hand for the Cf45 the agreement was not so good. Comparing the relationships for the two series, for the same deflection a smaller crack opening was observed for the Cf45 series. This was expected since the crack opening will be as smaller as more fibres bridge the crack. Nevertheless, the placement of the transducer for measuring the CMOD could somewhat have influenced the results. Since the CMOD was measured from one of the beams' sides, if the crack opening width is not symmetric for both lateral sides, due to an asymmetric fibre distribution, the CMOD can be incorrectly acquired.

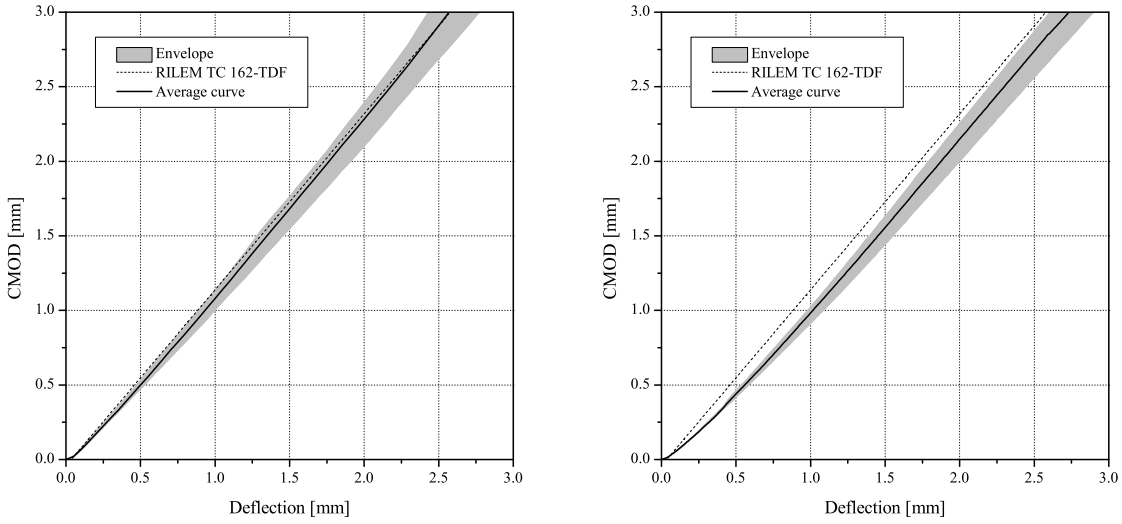

Figure 8.15: CMOD *vs.* deflection relationship for: (a) Cf30 and (b) Cf45 series.

Influence of the number of effective fibres on the post-cracking parameters

In Figure 8.16(a) is included the relationship between the number of effective fibres and total fibres at the crack surfaces, whereas throughout Figures 8.16(b) to 8.16(f) are depicted the relationships between the number of effective fibres and the computed post-cracking parameters from the flexural responses.

As it was previously ascertained in the uniaxial tension specimens, a linear relationship between the number of effective fibres and total fibres was observed. Regarding the limit of proportionality, $f_{ct,L}$, no trend was observed with the increment of fibres within the same series. However, as it would be expected, the specimens from the Cf45 series presented lower values of $f_{ct,L}$ due to the lower matrix tensile strength of this series, as consequence of different concrete compositions in the Cf30 and Cf45 series.

Concerning both the residual and equivalent strengths, in general, a linear trend was observed with the increase of effective fibres. For $f_{eq,2}$ and $f_{R,1}$, and in spite of the observed scatter, the transition from the series Cf30 to Cf45 is relatively "smooth", i.e. continuous, as the specimen from Cf30 series with the highest number of effective fibres has very similar strengths to the specimen from the series Cf45 with the lowest number of effective fibres. On the other hand, for the $f_{eq,3}$ and $f_{R,4}$ it is clearly visible a discontinuity from the series Cf30 and Cf45. As previously explained, for the relatively high levels of deformation at which these parameters are evaluated and, consequently, relatively high crack openings, the occurrence of fibre rupture in the series Cf30 justifies this discontinuity. Therefore, the strengths values between the two series are quite different, even for similar number of effective fibres. Additionally,

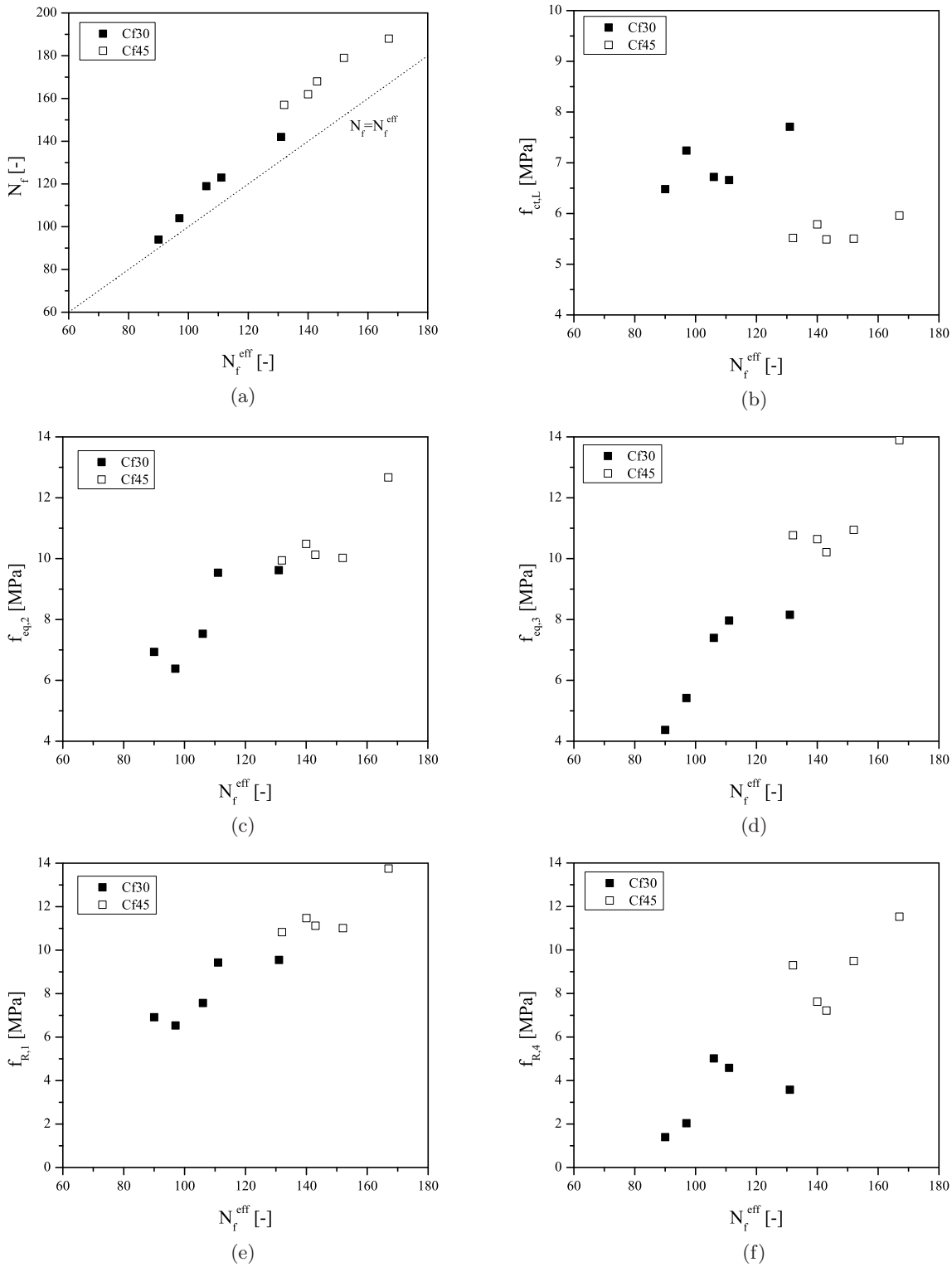

Figure 8.16: Relationship between the number of effective fibres and the: (a) total number of fibres, (b) limit of proportionality, equivalent flexure tensile strengths (c) $f_{eq,2}$ and (d) $f_{eq,3}$; and residual flexural tensile strengths (e) $f_{R,1}$ and (f) $f_{R,4}$.

the steeper "jump" observed for the $f_{R,4}$ when comparing to $f_{eq,3}$ is due to the procedure for computing each of the flexural tensile strengths, since $f_{eq,3}$ is determined based upon an energy criterion, thus the energy dissipated by the fibre prior its fracture helps mitigate these differences between these series. Remark, that when referring to fibre rupture exclusively during the Cf30 series tests, it is not intended to rule out the possibility of fibre rupture in the Cf45 series tests. Hence, what is intended is to state that for the series Cf30 there is a higher probability of fibre rupture. Both the uniaxial and bending test results stress out the aforementioned.

8.3.4 Splitting tests

Test set-up

The specimens used on the splitting tests were obtained from the extremities of the tested bending specimens. For that purpose, for each series, five cubic specimens with a 150 mm edge length were swan out from the prismatic bending specimens. The geometry and dimensions were the suggested by the BS 1981:Part 117 (1983). Afterwards, and in order to induce the crack plane, two notches were swan upon opposite faces. The notch width and depth was of 5 mm and 15 mm, respectively. A sketch of the specimen geometry is depicted in Figure 8.17.

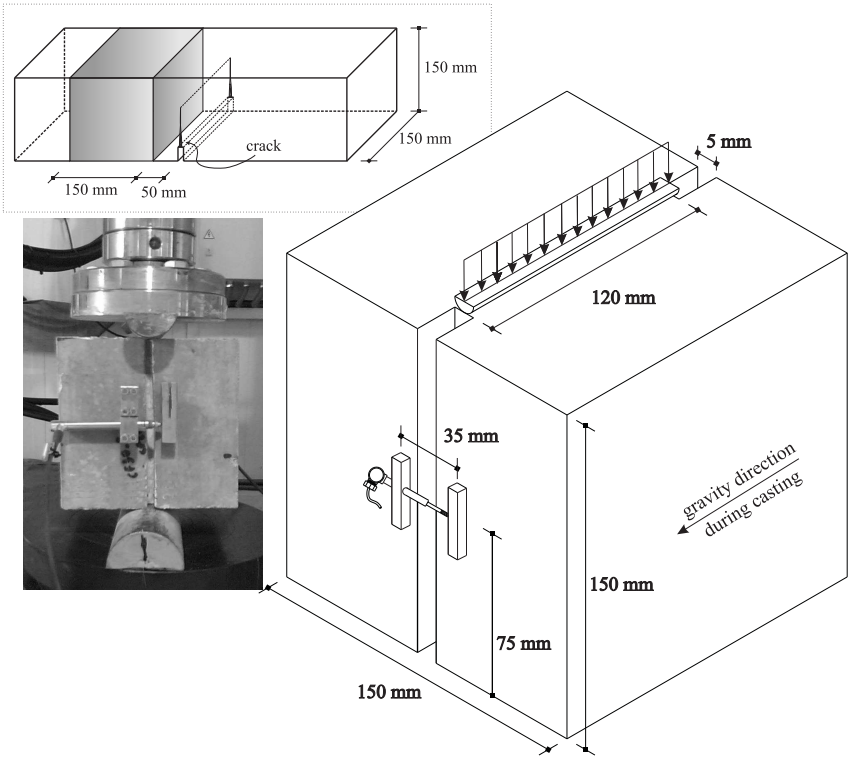

Figure 8.17: Splitting test set-up and specimen's geometry.

Additionally, the localization from which the splitting test specimens were sawn out on the three point bending specimens is represented.

The tests were conducted on a servo-hydraulic system with a 2000 kN static load carrying capacity with a high stiff frame. This type of test was performed under closed-loop displacement control by the average signal of two displacement transducers disposed over the two notches at the specimen's mid-height (see Figure 8.17). A displacement rate of 0.01 mm/min was used up to a displacement of 0.2 mm, and 0.1 mm/min until the completion of the test.

Load vs. crack opening mouth displacement curves

In Figures 8.18(a) and 8.18(b) are depicted the experimental load versus crack opening mouth displacement envelope and corresponding average curve for the Cf30 and Cf45 series, respectively. The individual responses of each specimen can be found in Annex V.

In general, the splitting test responses had a similar behaviour to the one observed for the bending tests. For the series Cf30, after the crack initiation, it was visualized a small load decay followed by a slight deflection-hardening branch, whereas in the Cf45 series, after the crack initiation, a hardening branch up to the peak load was observed. Afterwards, the peak load was attained at a CMOD of 0.4 mm, followed by a load decay in both series. The Cf30 series post-peak behaviour, in comparison to the corresponding bending responses, presented a smaller load decay rate.

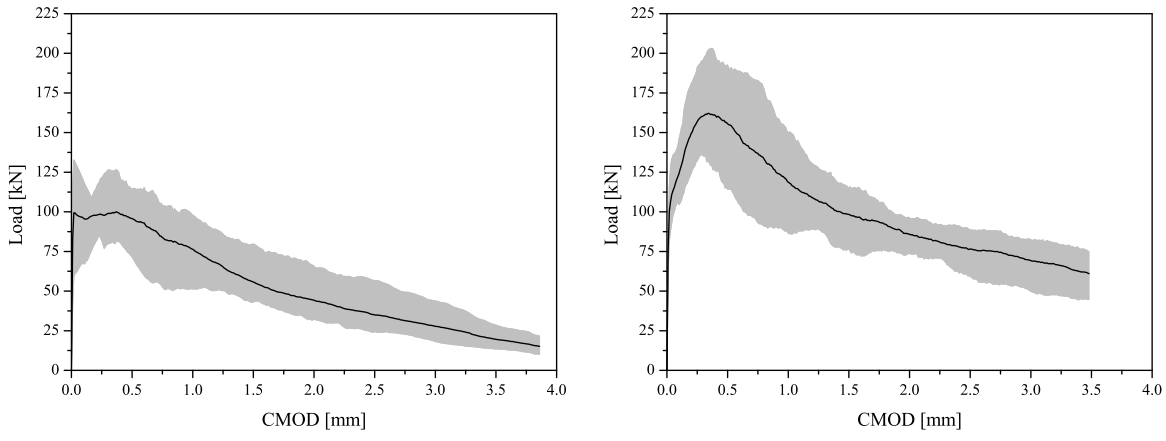

Figure 8.18: Experimental load versus crack opening mouth displacement relationships with: (a) 30 kg/m^3 and (b) 45 kg/m^3.

A nominal tensile strength, σ_{nom}, can be obtained from the load value of the splitting-tension tests using the following equation (Timoshenko and Goodier 1991):

$$\sigma_{nom} = \frac{2 \cdot P}{\pi \cdot d \cdot t} \tag{8.7}$$

where P, d and t are, respectively, the load, height and thickness of the prism. Remark, that equation 8.7 is derived for a disc with a diameter d and thickness t. However due to the distribution of the compressive load trough the cube, the corners of the cube do not have significant stresses. Therefore, the behaviour of a cubic and cylindric specimens is similar. The relationship between the nominal stress and crack mouth opening is represented in Figure 8.19.

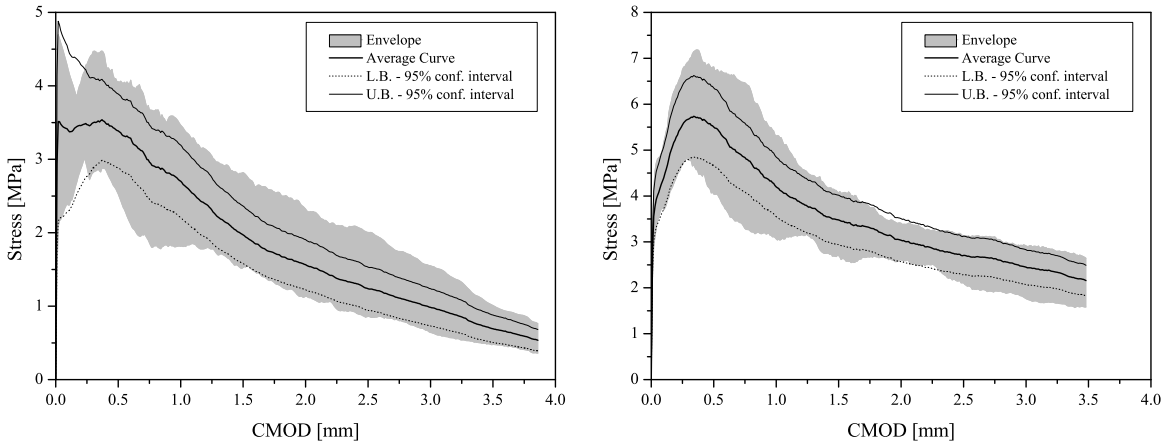

Figure 8.19: Nominal tensile stress - crack opening mouth displacement relationships with: (a) 30 kg/m^3 and (b) 45 kg/m^3.

The average tensile strength obtained from the splitting tests, for both series, is similar to the one obtained from the uniaxial tension tests, 3.5 MPa and 3.3 MPa, respectively, for the Cf30 and Cf45 series. However the scatter observed in tensile strengths obtained from the splitting tests was quite higher, particularly in the series Cf30, ranging approximately between 2 and 4.5 MPa.

8.4 Determination of the $\sigma - w$ law by inverse analysis

In this section, the post-cracking behaviour of SFRSCC is assessed by inverse analysis taking the results from the three-point bending tests. For this purpose, the experimental load-deflection curves are simulated using the FEMIX finite element program (Azevedo et al. 2003). The implemented algorithm of the inverse analysis procedure is schematically represented in Figure 8.20, which according to Roelfstra and Wittmann (1986) can be subdivided into three levels.

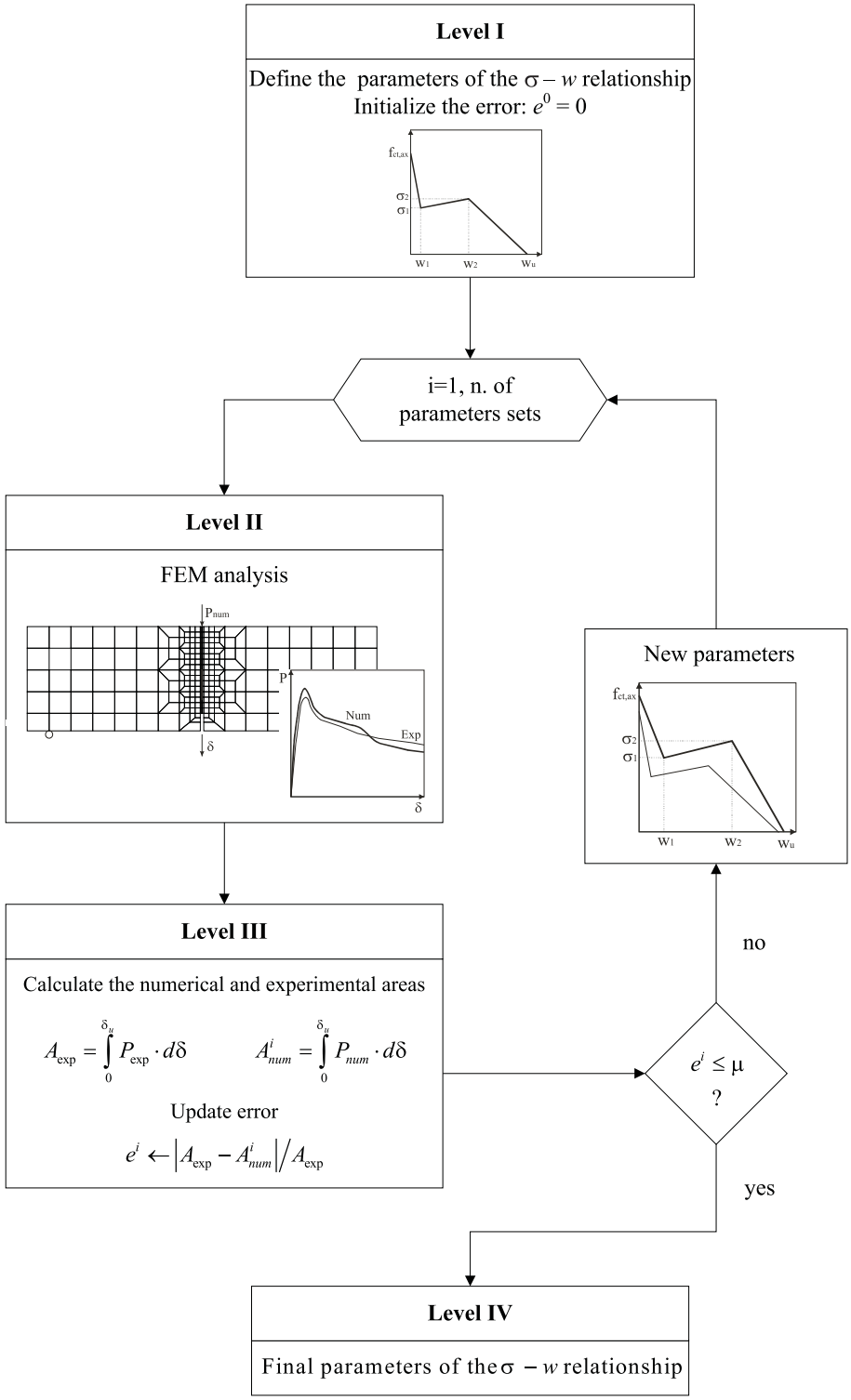

Figure 8.20: Inverse analysis procedure (adapted from Roelfstra and Wittmann 1986).

The first level is designated as input level, where the geometrical boundary conditions of the specimen are introduced and the parameters defining the post-cracking tensile behaviour ($\sigma - w$) of the material are initialized. The second level is the numerical simulation of the experimental test where the discretized specimen is subjected to a non-linear finite element analysis in order to acquire the numerical load - deflection response. In the third level, the accuracy of the computed numerical response is assessed. Finally, the fourth level is the output level, in which the values of the parameters that lead to the smaller error and comply with the imposed restrictions for the maximum load value and correspondent deflection are obtained.

In the input level of the inverse analysis approach, the geometrical boundary conditions and the material behaviour laws are defined under the framework of a FEM-based numerical simulation. From preliminary numerical FEM-simulations carried out in the scope of the present research project, it was observed that the maximum compressive stress values were just attained nearby the load application's place, and rapidly decreased to relatively low values, in addition they were significantly lower than the compressive strengths values of the studied self-compacting matrices. Moreover, two numerical simulations were previously carried out, one of them using a plasticity model for the compressive behaviour, and another assuming a linear elastic behaviour, and no significant differences were found in the load - deflection responses. Thus, in the inverse analysis was assumed a linear elastic behaviour in compression in order to make the numerical iterative process more straightforward. To simulate the post-cracking tensile behaviour, a tri-linear stress crack width relationship was adopted. Since in the present work an exhaustive search method was used, the intervals and step increment of each parameter were also defined.

In level II, the numerical simulation is carried out based on the finite element method. All the aspects regarding the mesh discretization, type of finite element, integration type and scheme, and ascribed material properties are discussed later on. In last stage (III), the numerical load - deflection curve is compared to the correspondent experimental one. The areas beneath the load - deflection curves are computed and the normalized error, e^i, between them is determined. If the e^i is smaller than the predefined value of 1% (assumed tolerance, μ) the iterative procedure stops, otherwise a new set of $\sigma - w$ parameters is updated and checked out. Additionally, a restriction was imposed regarding the fitting accuracy of the peak load and its correspondent deflection, which cannot differ from the experimental ones in 2%, otherwise the current numerical simulation is discarded.

8.4.1 Three-point bending tests

Due to the geometry, support and loading conditions used in the test setup proposed by RILEM TC 162-TDF (2002b) in the three point bending test for the characterization of the tensile

behaviour under flexure of SFRSCC, a plane stress state installed in the beam was assumed. By definition, a prismatic structural element is under a plane stress behaviour if one of the dimensions (thickness) is significantly smaller than the other two, the stress component normal to the simulated plane is null (Onãte 1992). Regarding the present example, in spite of the width and height of the beam's cross section are equal, it is feasible to suppose installed in the beam a plane stress state, since apart the loaded zones of reduced volumetric amplitude, the stress component orthogonal to the loading plane and the two out-plane shear component are of marginal significance when compared to the three stress components that characterize a plane stress-state.

For the numerical simulation of the crack initiation and propagation, 2D line interface elements located at the specimen´s symmetry axis were used. The remaining part of the specimen was modelled with eight-node Serendipity plane-stress elements, assuming a linear elastic behaviour for the material they represent.

In Figure 8.21 is depicted the mesh used in the simulations. In the present mesh were used two integration schemes. For the 2D line interface elements was used a Gauss-Lobatto integration scheme with three integration points (IP), whereas for the eight-node elements was adopted a Gauss-Legendre integration scheme with 2×2 IP. To avoid undesired spurious oscillations of the stress field a value of 1×10^6 N/mm^3 was used for the Mode I initial stiffness modulus (Schellekens 1990, Sena-Cruz et al. 2004). Since for the current problem sliding does not occur in the interface elements, the analysis' results are independent of the values assigned to the Mode II initial stiffness modulus. The values of the material properties used in the inverse analysis are comprised in Table 8.4.

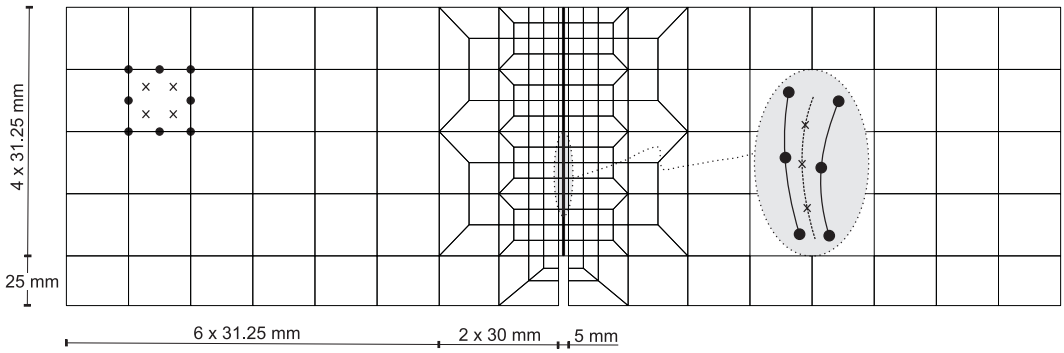

Figure 8.21: Finite element mesh used in the simulation of the three point bending tests.

The inverse analysis simulations were performed by "brute force" analysis, i.e. exhaustive search method, using for comparison purposes the experimental average curves of each series. The simulations were carried out for two levels of deformation, one using the full load - deflection

Table 8.4: Concrete properties used in the simulation of the three point bending tests.

Property	Series	
	Cf30	Cf45
Density	$\rho = 2.4 \times 10^{-5}$ N/mm^3	
Poisson's ratio	$\nu_c = 0.20$	
Young's modulus	41300 N/mm^2	40600 N/mm^2
Tensile strength	Inverse analysis	
Tri-linear softening parameters	Inverse analysis	

response (i.e. up to deflection of nearby 9 mm), and another using the response only up to a deflection of 4 mm.

In Figures 8.22 and 8.23 are depicted both the experimental and numerical load - deflection curves for the two distinct levels of deformation, respectively, for approximately 9 mm and 4 mm. The agreement between the numerical and the experimental curves is considerably good for both series and both deflection levels, which indicates that the trilinear $\sigma - w$ relationship is capable of simulating accurately the post-cracking behaviour of SFRSCC. When comparing the performed simulations, the numerical curve regarding the Cf30 series response up to a deflection of 9 mm has shown a slightly worse agreement in the pre-peak branch, Figure 8.22(a). This is ascribed to both the number of branches of the post-cracking law (limited to 3) and to the reason that all stages of the response have the same weight on the fitting procedure. Therefore, in order to attain a good approximation of the full bending response, the initial part of the experimental curve is not so well modelled. On the other hand, the numerical simulation of the Cf30 series response up to a deflection of 4 mm has shown a better agreement with the experimental data for this initial stage of the bending response. This is related with the $\sigma - w$ law parameters found in the IA that will be discussed in more detail later on.

The obtained $\sigma - w$ relationship parameters, and equivalent fitting error (e), are indicated in Table 8.5. At a first glance, it is clear that the $\sigma - w$ parameters obtained for the Cf30 series are quite different for the distinct deformation levels analysed. In the Cf45 series the values of the parameters are not so distinct for both the studied deflection levels, with the exception of the ultimate crack opening w_u.

Table 8.5: Parameters of the $\sigma - w$ relationship obtained by inverse analysis.

Cf [kg/m^3]		f_{ct} [MPa]	σ_1 [MPa]	σ_2 [MPa]	w_1 [mm]	w_2 [mm]	w_u [mm]	G_f [N/mm]	e [%]
30	(9 mm)	2.80	2.86	0.56	0.50	2.10	9.0	6.08	2.9
	(4 mm)	3.60	2.45	1.87	0.06	0.89	3.1	4.04	1.8
45	(9 mm)	3.90	4.56	1.99	0.43	2.90	12.0	14.80	1.3
	(4 mm)	3.70	4.66	3.18	0.31	1.72	5.6	11.70	0.9

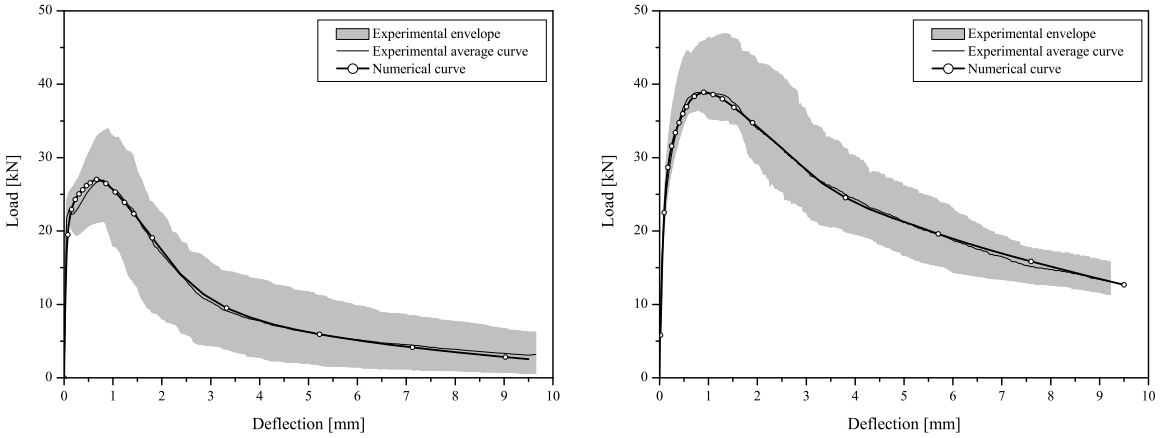

Figure 8.22: Numerical simulation of the three point bending tests with: (a) 30 kg/m^3 and (b) 45 kg/m^3.

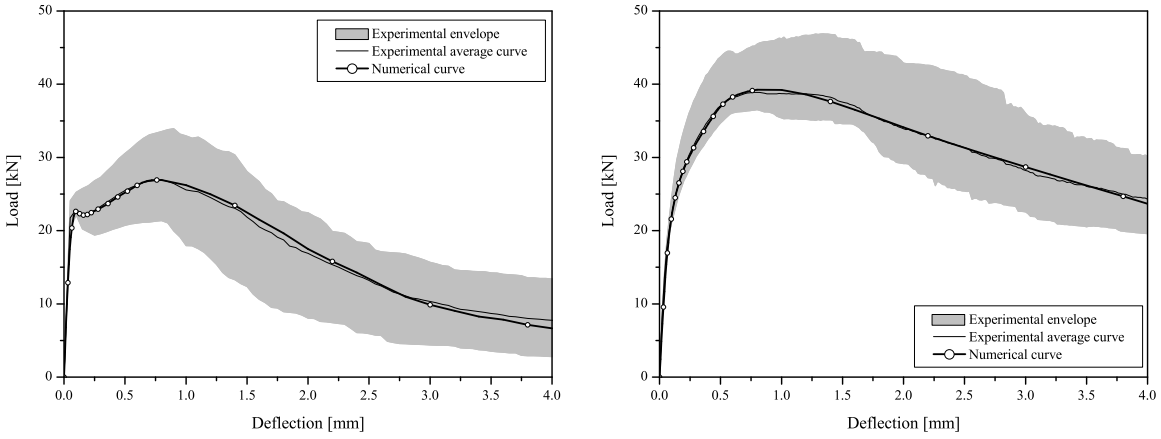

Figure 8.23: Numerical simulation up to a deflection of 4 mm of the three point bending tests with: (a) 30 kg/m^3 and (b) 45 kg/m^3.

Regarding the values found for f_{ct} in the Cf45 series, they are higher than the tensile strength found in the uniaxial tension tests ($\approx$ 20 to 30%). A similar difference between the tensile strength obtained from the uniaxial and bending tests (11 to 35%) was observed by Löfgren et al. (2008) for conventional fibre reinforced concrete with fibre contents of 39 and 78 kg/m^3. For the Cf30 series, the numerical simulation up to a deflection of 4 mm provided a f_{ct} value in good compliance with the uniaxial tensile strength. Remark, however that the uniaxial tension test set-up used is not suitable for determining the material tensile strength. In fact, when comparing the obtained values with the ones suggested from CEB-FIP (1993) (based on empirical relationship with the compressive strength), they are approximately 25 to 35% smaller than the "real" tensile strength (3.6 and 4.5 MPa, respectively, for Cf30 and Cf45 series). Rossi

et al. (1991) using the wedge splitting tests to obtain stress-crack opening relationships for concrete by an inverse analysis procedure, point out the need for the determination of the tensile strength apart from the inverse analysis. These author used a split cylinder test, since their estimations of the tensile strength obtained by IA method were biased.

The graphical representation of the $\sigma - w$ law is depicted in Figure 8.24. Regarding the laws obtained by IA for the Cf30 series, the shape of the initial part of the $\sigma - w$ law is quite different in case that the IA is performed either up to a 4 mm or 9 mm deflection. In the simulation up to a 4 mm, a sharp load decay is observed on the $\sigma - w$ law, while for the simulation up to 9 mm, the lower tensile strength obtained in the IA is compensated with a strain hardening in the first post-cracking branch. The higher fracture energy on the $\sigma - w$ law (until crack widths of 1 mm) for a 9 mm deflection simulation is clearly related in the overestimation on the corresponding experimental load - deflection response, see Figure 8.22(a). In what concerns to the numerical $\sigma - w$ relationships obtained for the Cf45 series, up to a crack width of 3 mm the ascertained laws are almost identical, see Figure 8.24. This is reflected in the numerical simulation of the load - deflection responses carried out for the Cf45 series, compare Figures 8.22(b) and 8.23(b).

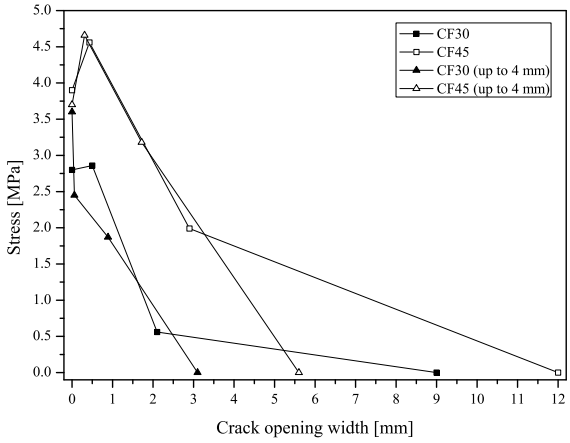

Figure 8.24: $\sigma - w$ relationships obtained by inverse analysis.

The interest of determining the ultimate crack opening, w_u, for fibre reinforced composites can be questionable, since for practical structural applications the load bearing capacity of these materials will correspond to considerably higher crack opening widths than the usual allowed at the serviceability limit states for the design of a concrete structure. In opposition can be asserted that only with a full knowledge of the material behaviour, hence the knowledge of the ultimate crack width value, there is the possibility of a correct fracture energy estimation and, consequently, the real limit capacity of the structure can be determined.

For the determination of the ultimate crack width by IA, it is important the level of deformation for which the numerical analysis is conducted. Even though the present experimental results were obtained for considerable high deformations (over 9 mm), the residual load at these deformations is still considerable, therefore the rest of the bending response, particularly for the Cf45 series, should not be neglected. The physical meaning of the w_u values obtained by IA will be now analysed. According to Kooiman (2000), the ultimate crack width can be supposed equal to the average projected embedded length of the fibres, $L_{b,proj}$, defined as:

$$L_{b,proj} = \eta_\theta \frac{L_f}{2} \tag{8.8}$$

where L_f is the fibre length and η_θ is the fibre effectiveness factor. Remember that the statistical average fibre embedded length, L_b, crossing an active crack is one fourth of the total fibre length (Stroeven 1986a), thus for the particular used fibres, $L_b = L_f/4 = 15$ mm. Therefore, if an averaging approach is taken, and assuming for the fibre effectiveness factor a value of 0.5 (3D IURD), equation 8.8 will render a value of the ultimate crack opening width, which in practical sense can be regarded as a lower limit for the ultimate crack width ($L_{b,proj} = 0.5 \cdot 60/2 = 15$ mm).

The fibre effectiveness factor can be computed from equation 8.9, where N_f is the counted number of fibres at crack section (see Table 8.3), and A_c, A_f and V_f are, respectively, the beam's net cross section area, the fibre cross section area and the fibre content in volume. Thus, the fibre effectiveness factors yields for the Cf30 and Cf45 series, respectively, 0.711 and 0.694. These values are within the range of the theoretical values, assuming a uniform isotropic fibre distribution, for the 1D and 2D cases, respectively, 1 and $2/\pi$ (Stroeven and Hu 2006). Consequently, by inserting the computed effectiveness factors in equation 8.8, the ultimate crack width opening will render approximately 21 and 18 mm, respectively, for the series Cf30 and Cf45. These theoretical values are far from the ones obtained from the IA. Hence, this strengthens the idea that the deformation level of 9 mm is not suffice to render an accurate estimation of the fracture parameters, in particular the fracture energy.

$$N_f = \eta_\theta \frac{V_f \cdot A_c}{A_f} \tag{8.9}$$

8.4.2 Analysis of the parameters obtained from the distinct tests

The post-cracking behaviour of the studied steel fibre reinforced self-compacting concrete was assessed from distinct tests. In Figure 8.25 are included the stress - crack opening width relationships obtained from the uniaxial tensile tests (UTT), by the inverse analysis of the

three-point bending tests (3PBT) and the splitting tests (SPLT). The stress - crack opening obtained from the inverse analysis of the three-point bending tests and from the splitting experimental tests clearly overestimates considerably the $\sigma - w$ relation obtained from the uniaxial experimental tests for both tested series. This was also observed by other researchers for conventional fibre reinforced concrete (Barragán 2002, Löfgren et al. 2008, Strack 2008). This is due to different fibre structures for each type of specimen, in consequence of distinct concrete casting, different mould dimensions and geometry that induce distinct fibre orientations. As observed in Chapter 6, in the prismatic specimens, the fibres are predominantly oriented along the specimen's longitudinal axis, i.e. with a lower inclination towards the crack plane. On the other hand, in the cylinders (specimens for the UTT), the fibres are positioned with a smaller angle towards the horizontal plane, and therefore to the cracking plane, thus a fibre orientation distribution nearer to a 3D uniform isotropic distribution was observed. It should also be noticed, that the $\sigma - w$ relationship determined for the splitting tests is not accurate, since it was computed by equation 8.7 assuming a linear elastic stress distribution, therefore as the crack opening increases, the $\sigma - w$ curve determined is more imprecise.

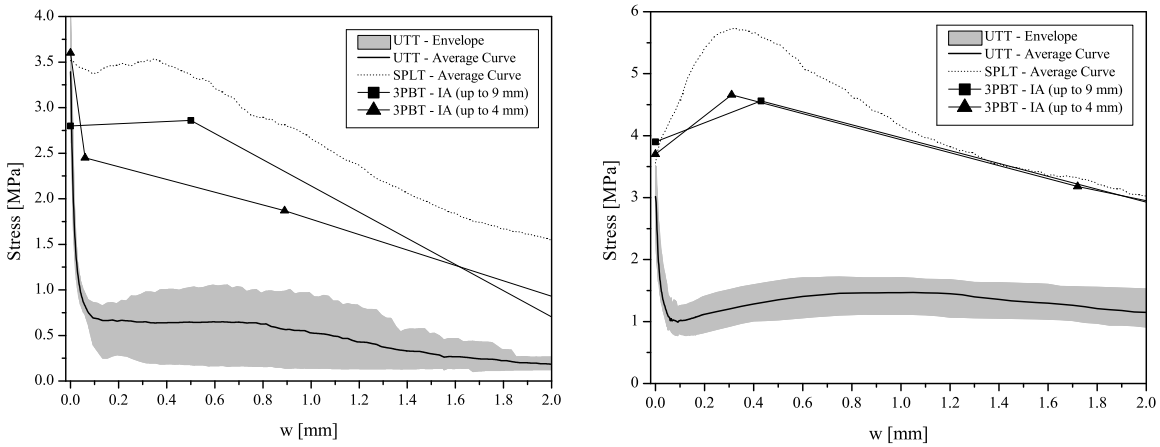

Figure 8.25: Stress - crack opening laws for the series with: (a) 30 kg/m^3 and (b) 45 kg/m^3.

As previously visualized, the responses from the indirect tests overestimated considerably the uniaxial tensile behaviour. Hence, in order to account the distinct fibre distributions, the $\sigma - w$ laws obtained from the indirect tests can be corrected using a ratio between the fibre effectiveness factor for the UTT specimens and the fibre effectiveness factor for the indirect tensile tests ($\eta_{\theta,UTT}/\eta_{\theta,3PBT}$ for the bending and $\eta_{\theta,UTT}/\eta_{\theta,SPLT}$ for splitting specimens). This methodology was used by Strack (2008) for correcting the $\sigma - w$ laws obtained by inverse

analysis from 3PBT. Each effectiveness factor is computed from equation 8.9 using the number of fibres experimentally counted at the crack surface (since for the SPLT tests it was not evaluated the number of fibre at the crack surfaces, it was used the fibre density obtained from the image analysis study). The effectiveness factors obtained are indicated in Table 8.6. In the present work the latter factors were computed using either the total number of fibres and the effective number of fibres at the crack surfaces. Remember that in the present work the fibres were considered effective as long their hooked end is deformed or if they have fractured. The differences between using either the total or the effective number of fibres will be discussed later on.

Table 8.6: Average fibre effectiveness factors for the distinct tests.

SERIES	Num. fibres	$\eta_{\theta,UTT}$	$\eta_{\theta,3PBT}$	$\eta_{\theta,SPLT}$	$\frac{\eta_{\theta,UTT}}{\eta_{\theta,3PBT}}$	$\frac{\eta_{\theta,UTT}}{\eta_{\theta,SPLT}}$
Cf30	total	0.274	0.711	0.743	0.385	0.369
Cf45		0.454	0.698	0.768	0.650	0.591
Cf30	effective	0.193	0.656	–	0.294	–
Cf45		0.264	0.576		0.458	

The $\sigma - w$ laws corrected with the effectiveness ratio computed from the total number of fibres (e.g. $\sigma_i \cdot \eta_{\theta,UTT}/\eta_{\theta,3PBT}$ for the bending tests) are depicted in Figure 8.26. Regarding the Cf30 series a good agreement with the uniaxial tension behaviour is observed, for both the $\sigma - w$ relationships from the splitting and bending responses. On the other hand, for the Cf45 series, the uniaxial tension response is still overestimated, in spite of the approximation of the curves due to adopted strategy. The effectiveness factor computed by equation 8.9 gives an idea of the orientation degree of a certain fibre structure and is related to the number of fibres that intersect a certain plane, since the fibre orientation influences the probability of a fibre crossing a particular surface. Nevertheless, in spite of the effectiveness factor being computed with the total number of fibres, that intersect an active crack, not all the fibres that bridge the crack surfaces may be mobilized and, consequently, contribute for the composite response. For instance, both the fibre inclination angle towards the crack surface plane and the fibre embedded length play an important role on the probability of a fibre being mobilised. If the embedded fibre length is smaller than the end-hook, the mechanical deformation of the hook will not be mobilised (Robins et al. 2002). On the other hand, as the fibre inclination angle increases the fibre's surrounding matrix will be more prone to spalling and, in a limit case. a concrete volume containing the hooked end can spall before the mobilization, i.e. plastic deformation of the hook. Therefore, having in mind the abovementioned, a more realistic corrective procedure

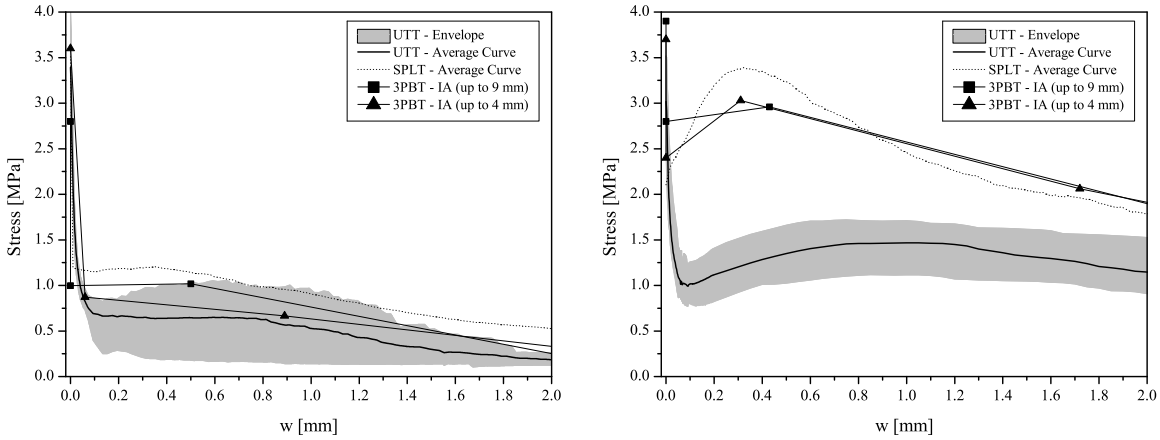

Figure 8.26: Stress - crack opening laws corrected with the effectiveness factors for the series with: (a) 30 kg/m^3 and (b) 45 kg/m^3 (adopting the total number of fibres).

for the $\sigma - w$ laws might be assured using the effectiveness ratio computed with the effective number of fibres. In Figure 8.27 are depicted the $\sigma - w$ laws obtained by inverse analysis after being corrected according to this methodology. This approach was not performed for the splitting tests, since there is not available data regarding the number of effective fibres for these specimens.

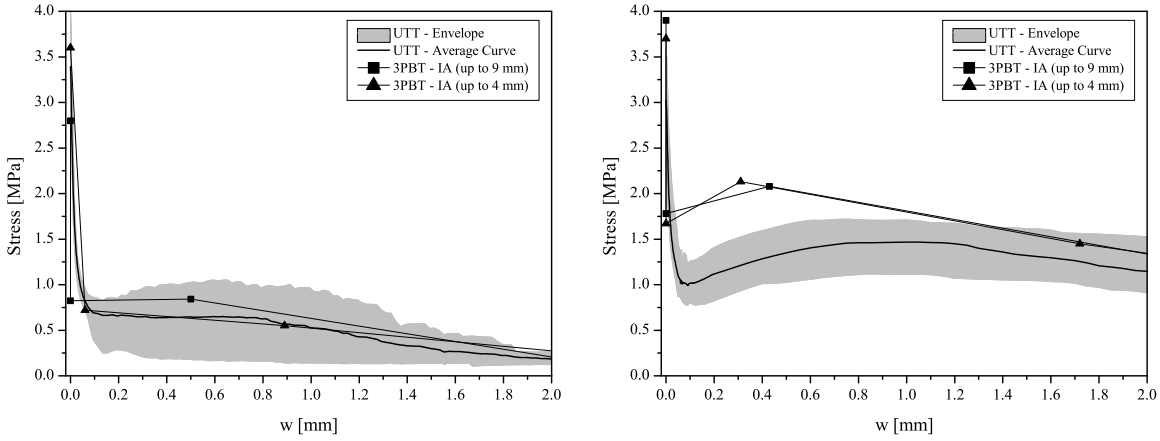

Figure 8.27: Stress - crack opening laws corrected with distinct effectiveness factors for the series with: (a) 30 kg/m^3 and (b) 45 kg/m^3 (adopting the number of effective fibres).

The agreement between the $\sigma - w$ laws obtained by inverse analysis and the uniaxial tensile response increased significantly for both studied series. However, even using the latter methodology the results for the Cf45 series are still predicting a residual strength higher than the one

registered in the UTT. Since the fibre content increased, and, consequently, there are more fibres bridging the crack surfaces, this will favour the concrete's stress redistribution, in spite of the crack progression being forced. Therefore, in the bending tests of the Cf45 series the fracture process zone probably is wider, i.e. diffuse cracking surrounding the main crack. Thus, energy could be dissipated outside the primary crack surface, hence leading to an overestimation of uniaxial tension behaviour by the inverse analysis.

8.5 Conclusions

In this chapter the post-cracking behaviour of steel fibre reinforced self-compacting concrete was assessed by three distinct tests (uniaxial tension, three point bending and splitting) for two compositions with distinct fibre contents, either 30 and 45 kg/m^3.

The increase of the fibre content enhanced considerably the concrete's post-cracking residual strength. Nevertheless, this was not ascribed just to the fibre content increase, since, for the series with 30 kg/m^3, fibre rupture during the post-cracking behaviour has occurred more often, due to a relatively resistant matrix and smaller number of fibres. Hence, the post-cracking behaviour of the Cf30 series can be considerably improved by changing the type of fibre used. Therefore, a fibre of higher tensile strength would be more suitable to these relatively high strength matrices, since fibre rupture will be prevented. Selecting a fibre of higher aspect ratio is another possibility, since higher number of fibres will be available per concrete volume. However, the use of a fibre of distinct geometrical characteristics demands the development of a new composition, since SFRSCC mix design optimization takes into account the characteristics of the fibre.

The tri-linear post-cracking relationships applied in the simulation of the three point bending tests has shown to be capable of describing the load - deflection curves rather well, even for large deflection levels. In addition, the peak load was also predicted with accuracy. The inverse analysis was conducted for distinct deformation levels, up to 4 and 9 mm, and revealed that, even for a large deflection at mid span (9 mm) the ultimate crack opening value estimated is probably incorrect, hence leading to incorrect estimation of the fracture energy.

When comparing the $\sigma - w$ relationships acquired from the indirect tests (3PBT and SPLT) with the uniaxial tension $\sigma - w$ response a huge discrepancy was observed. This difference was ascribed to the distinct fibre distributions within the specimens used for the different tests. Using a ratio computed based on the fibre effectiveness factor for each type of specimen, a good agreement was observed in both series. Nevertheless, for the Cf45 series this corrective factor lead to a relatively worse approximation and could be related to the energy dissipation outside the primary crack, hence overestimating the real post-cracking behaviour.

Chapter 9

Finite Element Model with Short Discrete Embedded Fibres for FRC

9.1 Introduction

Within steel fibre reinforced concrete, SFRC, steel fibres and matrix are bonded together through a weak interface, which behaviour is important to understand and accurately model the mechanical behaviour of SFRC, since the properties of this composite are greatly influenced by the interface zone between fibre/matrix and, consequently, by the micro-mechanical fibre reinforcement mechanisms that are mobilised. For these composites, when reinforced with low fibre volume ratios, the fibre contribution benefits arise, mainly, not to say almost exclusively, after the crack initiation. As previously ascertained in the first part of this work regarding the fibre pullout behaviour, this fact is related to the main reinforcement mechanism of hooked-end fibres, i.e. mechanical contribution by the deformation of the hook, being considerable higher than the chemical bond contribution that is mobilized for small crack widths (e.g. < 0.05 mm). Moreover, the mechanical mechanism is mobilized up to relatively high slips, consequently to high crack opening widths. Nevertheless, even for low fibre volume ratios, the contribution for the post-cracking behaviour of the fibres intersecting an active crack tenfold the contribution of the unreinforced concrete matrix.

The post-cracking behaviour of random discontinuous fibre reinforced brittle-matrix composites can be predicted by the use of a stress - crack opening displacement relationship, $\sigma - w$. Several authors developed micro-mechanical models for obtaining the $\sigma - w$ relationship, since for quasi-brittle materials, the stress-crack opening relationship that simulates the stress trans-

fer between the faces of the crack has a significant impact on the behaviour of a structure after its cracking initiation. In case of FRC, the $\sigma - w$ relationship can be approximated by averaging the contributions of the individual fibres bridging the matrix crack plane, defining for this purpose probability-density functions of the centroidal distance of fibres from the matrix crack plane, and of the orientation angle (Li et al. 1991). Visalvanich and Naaman (1983) derived a semi-empirical model to simulate the tension - softening behaviour of a cement based material reinforced with discontinuous randomly distributed steel fibre. In this work they assumed a purely frictional fibre/matrix interface and the possibility of fibre fracture was not contemplated. Based on the assumptions of the latter model, Li (1992) developed an analytical model which take into account an additional frictional effect called snubbing effect (factor which considers the angle effect of non-aligned fibres on the pullout load). Maalej et al. (1995) extended the latter fibre pullout model by explicitly accounting for potential fibre tensile rupture.

The latter models, which are based on an averaging process of all the forces that are carried out by the fibres over a crack plane, can provide the general material composite behaviour with reasonable accuracy by modelling the main mechanisms on a single fibre pullout. However, they do not account for some aspects, such as, fibre bending rupture, and matrix spalling at the exit points of inclined fibres. Moreover, the possible interaction between neighbouring fibres, as well as the modification of the matrix modulus and packing density by the addition of fibres are neglected in the above-mentioned models.

Another difficulty on the prediction of the post-cracking behaviour of a FRC in a real structure is that the material behaviour in a test specimen may differ from the behaviour of a real structural element. It is well described in literature that various casting procedures and structural shapes may result in predominant fibre orientation into parallel planes (Stroeven 1986a, RILEM TC 162-TDF 2002a). In the case of steel fibre reinforced self-compacting concrete, SFRSCC, the predominant fibre orientation can be along the flow itself (in the fresh state) and along the boundary surfaces due to the wall-effect (Grünewald and Walraven 2003, Stähli et al. 2008, Vandewalle et al. 2008). The fibre orientation nearby the walls of a structural element is not representative of the material, but of a structure (Stroeven 1986a). A predefined orientation of the steel fibres parallel to the tension direction in a test specimen may result in overestimating the post-cracking mechanical properties of the steel fibre reinforced concrete, when compared with specimens with equal amount of fibres, however with a random fibre orientation. Moreover, in laminar structures (i.e. with reduced thickness), the material properties are better determined by performing "structural tests", as suggested by the work group TG 8.3 ("Fibre Reinforced Concrete") who is preparing some sections on FRC to be appended into the new *fib* Model Code.

Having in mind this brief introduction of the principal aspects and factors that influence

and contribute to the post-cracking behaviour of a FRC, approaching the FRC as a continuum material may lead to a rough estimation, and difficult one, of the mechanical behaviour of a certain FRC structural element. Even though, material behaviour laws for FRC can be obtained with great accuracy by inverse analysis procedures of test specimens, these laws may not translate the accurate material behaviour within a specific structural element, due to the aforementioned factors that influences this material behaviour. This composite can be assumed as a two-phase material, namely, an unreinforced concrete matrix phase and a fibre phase, with the latter one comprising information about fibre density and orientation depending on where and how the material is applied. Hence, this approach can somehow enhance the numerical simulation of FRC structures, thus excluding the use of biased material behaviour laws, i.e. from a macro-mechanical behaviour point of view, obtained from the inverse analysis of experimental tests.

Therefore, based on the prior reasoning, in the present chapter is detailed a numerical approach where SFRC is treated as a heterogeneous medium comprised by one homogeneous phase (aggregates and paste), and another one composed by the steel fibres. The fracture process of the cementicious matrix (unreinforced) is modelled with a multi-fixed smeared cracking model. This unreinforced concrete phase is discretized by solid finite elements. On the other hand, the stress transfer between crack planes due to the fibres bridging active cracks is modelled with 3D truss elements. A non-linear behaviour law is assigned to these last elements in order to account the fibre-matrix interface properties. These laws are based upon the micro-mechanical behaviour of the fibres. The random fibre distribution, over the matrix, is simulated with an algorithm supported on the Monte Carlo method, providing a realistic distribution of the fibres over a bulk element. The developed algorithm enables to have into account factors that influence the fibre structure, such as: the so-called wall-effect and the high flowability of SFRSCC. The geometry, positioning and orientation of the fibres are subsequently inserted in a three dimensional finite element mesh. The truss elements representing the fibres are considered as embedded elements. Since the stiffness of the truss elements may not be homogeneously and isotropically distributed over the intersected "parent" elements (solid elements discretizing the concrete phase), an inverse mapping algorithm was developed and implemented for enabling the accurate assessment of the fibre stiffness contribution to the stiffness of the correspondent "parent" elements.

The elements from the fibre mesh were modelled as embedded elements. In the past decades, several models for embedded elements have arisen either for two-dimensional (Chang et al. 1987, Elwi and Hurdey 1989) and three-dimensional cases (Bhatt et al. 1989, Ranjbaran 1996) diferring in their complexity. The present formulation of the embedded fibre model does not take into account fibre bond - slip capability in a direct fashion. In order to accomplish this,

another compatibility condition is needed beside the conventional FEM relation between the strain, $\underline{\varepsilon}$, and displacements, $\underline{u}$, fields ($\underline{\varepsilon} = \underline{B}\,\underline{u}$ where $\underline{B}$ is the well-known strain - displacement matrix). The additional compatibility relation would relate the slip, i.e relative displacement at the fibre/matrix interface, with the nodal displacements ($s = \partial_s\,\underline{u}$ where ∂_s is a differential operator). However, this would not be enough. Hence, it also would be necessary to insert a differential equation of equilibrium to have into account the bond - slip behaviour. This approach would lead to an increase of model's complexity and, consequently, on the computation time.

In the present work, within a first stage of the research, as a simplification, the embedded element is modelled with a perfectly bonded formulation. Hence, the bond - slip behaviour is simulated in an indirect fashion from the transformation of a load - slip relationship to a tension stress - strain relation. Moreover, in the author's knowledge this kind of approach is quite novel, and within numerical models for FRC with the same philosophy only mesolevel models using lattice structures are known, e.g. Van Hauwaert and Van Mier (1998), Leite et al. (2004) and Bolander (2004).

9.2 Random fibre distribution generation

In order to model the fibre distribution in a self-compacting concrete medium a numerical code was implemented in C^{++} language, designated by "`RFD3D - Random fibre distribution 3D`". This programme, based on the fibre content and geometrical properties of both the fibre and concrete mould, enables to randomly generate a fibre distribution over a specific volume representing a test specimen. The fibre structure, whose random configuration is to be generated, may be distributed over a prismatic, cylindric or even arbitrary volume depending on the type of concrete specimen to be studied. In this work, the generation of the random fibre structure configuration is restricted to specimens of prismatic and cylindric form. Moreover, in the current algorithm, it is possible to either generate an isotropic uniform random distribution or according to a determinate probabilistic distribution. In addition, the wall-effect of the mould is also taken into account during the fibre structure generation.

In this section it is briefly addressed the implemented algorithm. Additionally, the numerical data from the fibres structures generated with the developed algorithm were compared with the experimental results obtained in Chapter 6, namely, its density and orientation factors. The fibre segregation was not modelled, since for the cylindric specimens was not significant. On the other hand, for the prismatic specimens this was also not taken into account, since the loading direction is orthogonal to the casting direction in order to mitigate the gravity influence on the fibre segregation. Even though the fibre segregation influence is not very

significant for obtaining the response of this specific type of specimens, modelling this effect would be into some extent interesting. In fact, this would enable to model the uneven crack opening propagation commonly observed in this type of test when fibre segregation is rather large.

9.2.1 Adopted probabilistic distributions

In the present section, it will be briefly addressed some mathematical aspects regarding probabilistic distributions. Within the implemented numerical code, which will be further ahead detailed and discussed, were used three kinds of probabilistic distributions for obtaining the fibre distribution, namely, uniform, normal or Gaussian and Weibull distributions. In Figure 9.1 are depicted both the probability density and cumulative probability functions, respectively, for the three types of adopted distributions.

The uniform density function was used for the generation of both the fibres' geometrical gravity centres and the versor corresponding to the fibre's orientation. A probability density function of a continuous random variable, $f_{\mathrm{X}}(x)$, is a function that defines the relative likelihood for this random variable, X, to occur at a certain point in the observation interval $[x_1, x_2]$. For the particular case of a uniform density function, X is equally probable of occurring within the observation interval $[x_1, x_2]$ (see Figure 9.1). This distribution is often abbreviated $G(x_1, x_2)$.

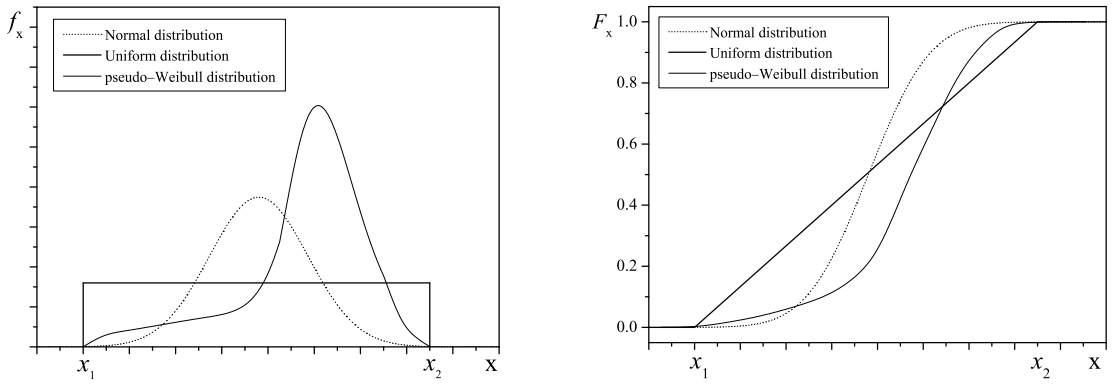

(a) (b)

Figure 9.1: Adopted probability distributions: (a) density and (b) cumulative.

The Weibull distribution provides a great deal of flexibility and, for this reason, is commonly used in engineering for modelling several and distinct problems. In the present work, a pseudo-Weibull distribution was also used for modelling the fibre orientation whenever a partially oriented fibre structure was desired. The implications of using either uniform or Weibull density functions to generate the fibre orientation will be discussed later on.

Finally, the normal or Gaussian density function was not used directly in the fibre generation algorithm. However, it was applied for comparing the experimental data regarding the fibre structure with the numerical data obtained from the Monte-Carlo procedure used on the generation of the fibre structures.

Both the uniform and Gaussian density functions are widely used since a long time ago and, therefore an extensive description of their definition and characterization is available in literature, consequently, they are not addressed in full detail in the present work. In spite of the relatively recent use of the Weibull distribution in engineering problems, its application in scientific phenomena is quite considerable. The pseudo-Weibull distribution used in the present work was adapted from the classical definition of a Weibull density function. Therefore, only the analytical expressions of frequency and cumulative probability functions of the adopted pseudo-Weibull distribution will be presented.

Frequency probability function

The pseudo-Weibull distribution function used for modelling the relative frequency of the fibre orientation towards a selected plane's orientation is given by:

$$f\left(x;\beta,\delta,\lambda,\varpi\right)=\frac{1}{\varpi}\cdot\left[x^{\lambda-1}\cdot\exp^{-x^{\lambda}}+\frac{\beta}{\delta}\cdot\left(\frac{1-x}{\delta}\right)^{\beta-1}\cdot\exp^{-\left(\frac{1-x}{\delta}\right)^{\beta}}\right] \tag{9.1}$$

where $\delta>0$ and $\varpi>0$ are both scale parameters, whereas $\beta>0$ and $\lambda>0$ are both shape parameters. Additionally, equation 9.1 is only valid for $0\leq x\leq 1$, and outside this domain a constant null value was adopted for the distribution. These parameters, which define the pseudo-Weibull distribution, are determined by a non-linear fitting procedure, based upon the experimental data of the fibre orientation accessed and already discussed in Chapter 6.

According to Montgomery and Runger (1994), the function $f_{\mathrm{X}}(x)$ is a probability density function of the continuous random variable X, if for any interval of real numbers $[x_1,x_2]$ complies with the following conditions:

$$\begin{aligned}
&(A) \qquad f_{\mathrm{X}}(x)\geq 0\\
&(B) \qquad \int_{-\infty}^{+\infty} f_{\mathrm{X}}(x)\,dx=1\\
&(C) \qquad P(x_1\leq \mathrm{X}\leq x_2)=\int_{x_1}^{x_2} f_{\mathrm{X}}(x)\,dx
\end{aligned} \tag{9.2}$$

Equation 9.1 fulfils condition A of equation 9.2, however, both conditions B and C are not fulfilled since the probability that x assumes in its range is different than one. Therefore, to obtain the probability density function, equation 9.1 must be normalized in order that the probability in its domain is equal to one and yields:

$$f_{\mathrm{X}}(x;\beta,\delta,\lambda,\varpi) = \frac{f(x;\ldots)}{\displaystyle\int_0^1 f(x;\ldots)\,dx} \tag{9.3}$$

with,

$$\int_0^1 f(x;\ldots)\,dx = \frac{1}{\varpi}\cdot\left[\frac{1}{\lambda}\left(\lambda+1-\exp^{-1}\right)-\exp^{-\left(\frac{1}{\delta}\right)^{\beta}}\right] \tag{9.4}$$

Notice that for the current practical application, x can be assigned as the orientation angle of a single fibre. For simplicity, in the present work, the variable transformation $x = \cos\theta$ was applied, thus x is defined in $[0,1]$ interval. On the other hand, $f_{\mathrm{X}}(x)$ can be regarded as the probability of a fibre having an orientation angle x towards a specific plane orientation.

Cumulative probability function

As it will be seen in the next section, the generation of the non-uniform random variable, e.g. from a Weibull distribution, was accomplished from the inverse cumulative distribution function method. As its name suggests, it requires the definition of the cumulative function. Hence, the cumulative probability function of a continuous random variable x with a pseudo-Weibull probability density function $f_{\mathrm{X}}(x)$ is given by:

$$\begin{aligned} F_{\mathrm{X}}(x;\beta,\delta,\lambda,\varpi) &= \int_{-\infty}^{x} f_{\mathrm{X}}(u)\,du \\ &= \frac{1}{\varpi}\cdot\frac{-\frac{1}{\lambda}\cdot\exp^{-x^{\lambda}}+\exp^{-\left(\frac{1-x}{\delta}\right)^{\beta}}-\exp^{-\left(\frac{1}{\delta}\right)^{\beta}}+\frac{1}{\lambda}}{\displaystyle\int_0^1 f(x;\ldots)dx} \end{aligned} \tag{9.5}$$

Remark that equation 9.3 is only valid for the interval $]0,1]$ and, consequently, equation 9.5 is just valid for the same domain.

9.2.2 Inverse distribution function method

In this section, the meaning of the terms "random numbers" and "random variates" is not distinguished, thus they are used interchangeably and applied to any pseudo-random numbers that arise from a distribution, being it uniform or other kind. Generating random variates from a non-uniform distribution, such as Weibull, usually is achieved by applying a transformation to uniform variates. Each generation of the non-uniform random variable can be achieved by a single uniform variate or from a sequence of uniforms (Gentle 1998).

In the present work, a straightforward transformation, namely, the inverse cumulative distribution function method, was used to convert a uniform random number to a number from a non-uniform distribution (Gentle 1998). If X is a scalar random variable and F_{X} is the pseudo-Weibull non-uniform cumulative distribution function, then the random variable:

$$G = F_{\mathrm{X}}(\mathrm{X}) \tag{9.6}$$

has a $G(0,1)$ distribution, i.e it is an uniform distribution over the unit interval $(0,1)$. Therefore, the simple relationship between a uniform random variable G and a random variable X with a cumulative distribution function F_{X} is easily achieved by:

$$X = F_{\mathrm{X}}^{-1}(G) \tag{9.7}$$

A graphical explanation of this method is depicted in Figure 9.2. Since the inverse of the adopted pseudo-Weibull function does not have an analytical closed-form solution, the generation of random variables X is obtained by solving with an iterative procedure the equation $F_{\mathrm{X}}(x) - G = 0$.

9.2.3 Algorithm

For the implementation of the fibre distribution algorithm some considerations and simplifications were made. The fibre thickness was assumed to be null, i.e. the fibre was considered as one-dimensional element and the shape of the end-hooks was also disregarded. Additionally, overlapping between fibres is not checked and therefore allowed. According to some researchers (Wittmann et al. 1984, Schlangen and Van Mier 1992, Wang et al. 1999), there is a minimum gap between adjacent particles (i.e. aggregates), since they must be coated with a minimum thickness of mortar. Thus, a minimum distance exists either between two adjacent fibres or between a fibre and specimen's boundary. However, this distance was not taken into account in the developed algorithm. According to Stroeven and Hu (2006), the actual fibre distribution in a certain specimen can be simulated with one of the following modelling strategies:

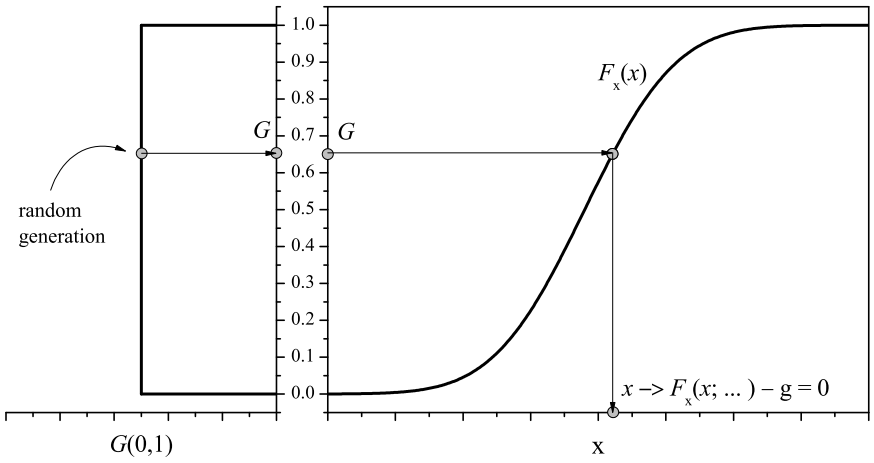

Figure 9.2: The inverse cumulative function method to convert an uniform random number to number from a continuous distribution.

a) The conventional random sequential addition algorithm. In this approach, fibres violating the boundary conditions are rejected. A logic consequence of this approach is that the fibre density decreases when approaching the external surface.

b) In the other approach, for the rejected fibres only new orientations are generated, until they fit in the physical system without violating the boundary conditions. This results in a uniform distribution of the fibre density over the specimen's full cross section, but with adjusted orientations in the boundary zone.

Stroeven and Hu (2006) plead that, the conventional random sequential addition algorithm should be used. According to these authors, this argument is supported in experimental research carried out for steel fibre reinforced concretes (Stroeven 1986b). However, other researchers (Hoy 1998, Kooiman 2000, Gettu et al. 2005) have found evidence of the fibre density close to boundaries being higher than in the bulk material. It should be realized that in concretes with high flowability, e.g. SCC, the fibres tend to be preferentially aligned along the flow direction, due to distinct velocities in the flow velocity profile (Stähli et al. 2008). Therefore, in the prismatic specimens used where the main concrete flow is along its longitudinal length, this will probably influence the fibre density due a fibre alignment. Moreover, according to the justification presented by Stähli et al. (2008), the fibre re-orientation ascribed to the flow profile will be more predominant in the zones nearer the boundary surfaces (see Figure 6.2). Since some researchers have found that there is an under reinforcement in the zones near to the boundaries, while others have found the opposite, in the present work the fibres' location assumes, within the specimen, an equal probability. Thus for the fibres violating the boundary conditions a new orientation is assumed.

In the author opinion, all the assumptions and simplification previously made seem feasible, taking into account that in the present work only low fibre contents are used, thus resulting in a significantly low spatial density of fibres when comparing, for instance, with the spatial density distribution of aggregates in a concrete volume. Moreover, the mechanical behaviour of SFRSCC is quite complex, due to the multiplicity of the reinforcement mechanisms involved. Since, when modelling the composite behaviour with the developed finite element model, there will be made many simplifications, in the present stage of the research it is not so important to have an extremely accurate fibre distribution algorithm.

The developed algorithm for generating the fibre structure is depicted in Figure 9.3 and can be summarised in the following steps:

1. The problem variables are defined. The specimen's geometry is selected and its dimensions are imputed. The content and geometrical data regarding the fibres is also defined. Moreover, the type and parameters of the adopted probability distribution for the generation of the fibre structure is selected, as isotropic uniform randomly distributed or following a pseudo-Weibull distribution. The variables are initialized as:

   `Geometrical data of the fibres`

   l_f, A_f: fibre length and cross sectional area

   m_f, C_f: mass weight of a single fibre and fibre content (weight per volume)

   `Geometrical data of the specimen mould`

   h_{rct}, b_{rct}, l_{rct}: height, width and length of the prismatic specimen

   h_{cyl}, r_{cyl}: height and radius length of the cylindric specimen

   `Pseudo-Weibull distribution parameters`

   δ, ϖ: scale parameters

   β, λ: shape parameters

2. Initialize the random number generation engine. In the present work was used the Mersenne-Twister (MT) engine. According to the developers, Matsumoto and Nishimura (1998), the uniform pseudo-random generator has the astronomical period of $2^{19937} - 1$ and 623-dimensional equidistribution property. Two functions are used for generating uniform random numbers, one named by `unif.pos(...)` that generates real numbers with `double` precision between [0, 1], the other designated by `unif.neg.pos(...)` that also generates uniform random numbers with `double` precision, however, between a $[-1, 1]$ interval.

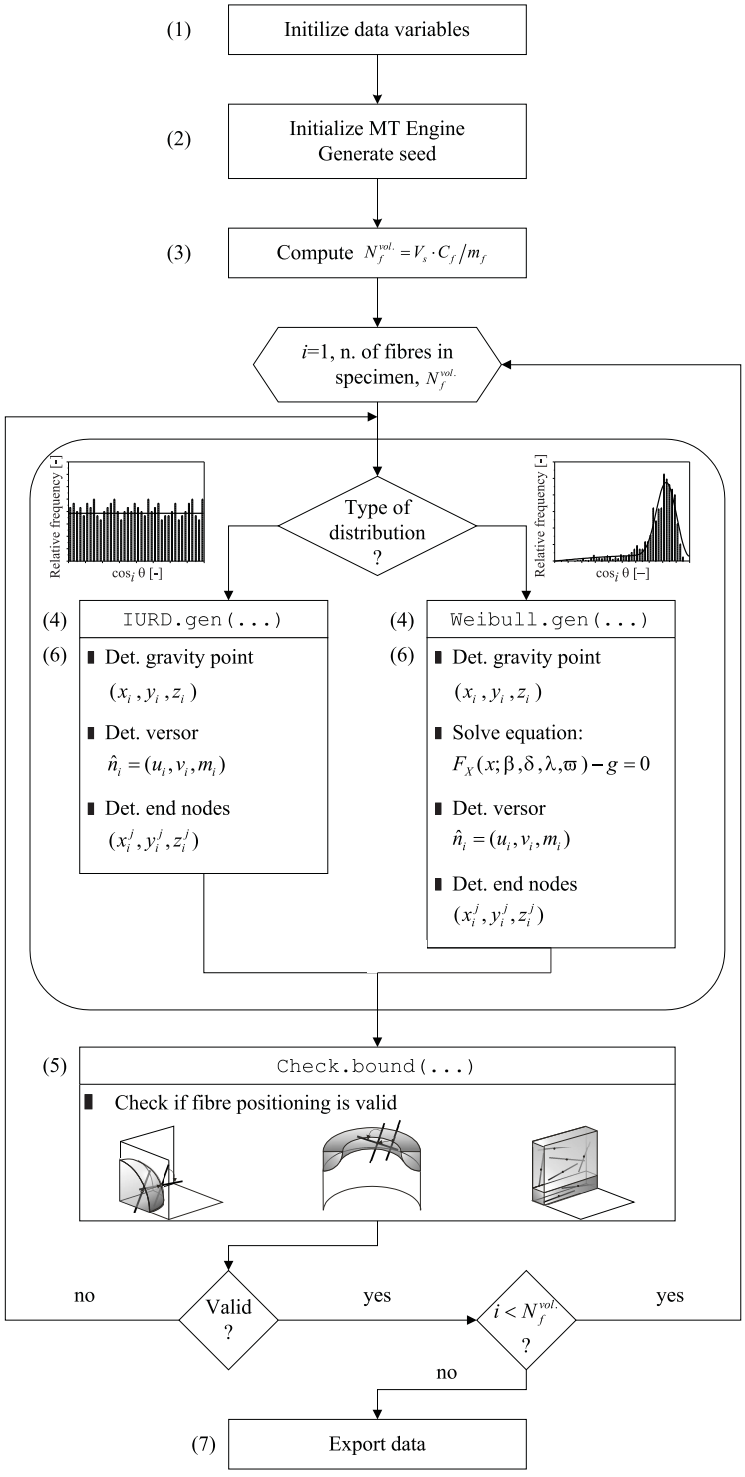

Figure 9.3: Implemented algorithm for the fibre's mesh generation.

The seed for the MT engine is randomly generated. In a first stage two `integer` values are randomly generated with C^{++} `rand(...)` function. In order to generate random-like

numbers, the seed for the previous function is generated with C^{++} `srand(...)` being initialized with a distinct value related to the program's execution time/date. Afterwards, the seed for the MT is a `long integer` obtained from the product of the two `integers` previously generated with the `rand(...)` function. There are other fancier procedures for generating the seed (Marsaglia 2003), however, for the practical applications of the present numerical code, the adopted approach guarantees more than a sufficient large number of starting points for the MT engine.

3. The specimen's volume, V_s, is computed, afterwards the number of fibres contained in the specimen is determined by:

$$N_f^{vol.} = V_s \frac{C_f}{m_f} \tag{9.8}$$

Hereinafter, with the exception of the last step, the algorithm steps will be repeated until $N_f^{vol.}$ is attained.

4. Random generation of the fibre localization coordinates and orientation. Depending on the geometry of the specimen, prismatic or cylindric, the coordinates are generated, respectively, in a Cartesian or spherical coordinate system. Moreover, based on the type of the selected fibre orientation distribution, the two following approaches are considered:

   (a) For an uniform isotropic random distribution the `IURD.gen(...)` routine is called:

      i. A set of three uniform random numbers, (ξ_x, ξ_y, ξ_z), are generated from the `unif.pos(...)` function. The i^{th} fibre's centre of gravity coordinates are computed, (x_i, y_i, z_i), as:

$$\begin{aligned} x_i &= \xi_x \, b_{rct} \\ y_i &= \xi_y \, l_{rct} \\ z_i &= \xi_z \, h_{rct} \end{aligned} \tag{9.9}$$

      ii. The numbers (η_x, η_y, η_z) are randomly generated from the `unif.neg.pos(...)` function. The i^{th} fibre orientation versor $\hat{n}_i = (u_i, v_i, m_i)$ is determined from:

$$\begin{aligned} u_i &= \eta_x \, / \, \|n_i\| \\ v_i &= \eta_y \, / \, \|n_i\| \\ m_i &= \eta_z \, / \, \|n_i\| \end{aligned} \tag{9.10}$$

      where $\|n_i\|$ is the norm of the vector $n_i = (\eta_x, \, \eta_y, \, \eta_z)$.

iii. The coordinates of the i^{th} fibre end-nodes ($j = 1, 2$) are computed as:

$$\begin{aligned} x_i^j &= x_i \pm l_f\, u_i/2 \\ y_i^j &= y_i \pm l_f\, v_i/2 \\ z_i^j &= z_i \pm l_f\, m_i/2 \end{aligned} \tag{9.11}$$

In case of using spherical coordinates a similar procedure is adopted.

(b) On the other hand, for a pseudo-Weibull distribution, the `WBull.gen(...)` routine is called:

i. The i^{th} fibre centre of gravity coordinates are randomly generated, (x_i, y_i, z_i), according to equation 9.9 as described in the procedure step *(a)i.*

ii. It is randomly generated a value, G, from the `unif.pos(...)` function, thus laying between [0, 1]. This value is assigned to the dependent variable of the cumulative frequency pseudo-Weibull function, $F_{\mathrm{X}}(x; \beta, \delta, \lambda, \varpi) = G$. The derivation of this function, adopted parameters and justification for using a cumulative instead of a frequency probability function will be addressed in a posterior section.

iii. The fibre orientation is set as the independent variable, $x = \cos\theta_i$, therefore $F_{\mathrm{X}}(x; \beta, \delta, \lambda, \varpi) - G = 0$ is solved by the `solve.eq(...)` routine. In this routine the Newton-Raphson method is used, whenever this method failed to converge, the bisection method is used.

iv. The i^{th} fibre orientation versor $\hat{n}_i$ is determined. Firstly, two aleatory components of the fibre orientation versor, $\hat{n}_i$, are randomly generated as described in step *(a)ii.* The other component is determined from solving:

$$\cos(\theta_i) = \hat{u} \otimes \hat{v} \tag{9.12}$$

where $\cos(\theta_i)$ is the fibre orientation towards the selected studied plane according to the cumulative pseudo-Weibull function determined in the prior step, and $\hat{v}$ is the aforementioned plane's normal versor. Equation 9.12 is solved with the routine `solve.eq(...)`.

v. The coordinates of the i^{th} fibre end-nodes are computed as in equation 9.11.

5. The routine `check.bound(...)` is called to check if the positioning of the i^{th} fibre's gravity centre (x_i, y_i, z_i) allows a valid physical placement of the fibre within the specimen mould. Moreover the i^{th} fibre end-nodes coordinates (x_i^j, y_i^j, z_i^j) must satisfy also the specimen

boundary conditions:

$$\begin{cases} 0 \leq x_i^j \leq b_{rct} \\ 0 \leq y_i^j \leq l_{rct} \\ 0 \leq z_i^j \leq h_{rct}, \quad j = 1, 2 \end{cases} \tag{9.13}$$

Regarding the first condition respecting the fibre's gravity centre positioning, in the case of a prismatic specimen, if the fibre's gravity centre distance to a corner is less than half the fibre length, $l_f/2$, then the fibre cannot be physically contained in the specimen without being bent, see Figure 9.4(a). For the simplicity sake, it is assumed that fibres cannot be bent and remain always straight, thus the following condition must be satisfied:

$$\left(x_i - x_0^k\right)^2 + \left(y_i - y_0^k\right)^2 + \left(z_i - z_0^k\right)^2 \geq \left(\frac{l_f}{2}\right)^2, \quad k = 1, \ldots, 8 \tag{9.14}$$

where the coordinates (x_0^k, y_0^k, z_0^k) are the centre coordinates of a sphere positioned in k^{th} corner node of the prismatic specimen. A similar reasoning can be made for the cylindric specimens using spherical coordinates, hence the inequation used it is the correspondent for a torus volume with a cross section of a quarter's circle. The centre of the torus is placed at the cylinder top and bottom circular surface centres, see Figure 9.4(b).

6. If checking these conditions with `check.bound(...)` routine reveals that one of them is violated, the fibre is not placed into the specimen.

   When the violation is due to the first condition, the gravity centre of the fibre is shifted to the nearest sphere surface point, which enables the fibre being contained in the specimen without being bent, see Figure 9.4(a). Therefore, the following non-linear equation system is solved with the `solve.eq(...)` routine:

$$\begin{cases} \left(x - x_0^k\right)^2 + \left(y - y_0^k\right)^2 + \left(z - z_0^k\right)^2 = \left(\frac{l_f}{2}\right)^2 \\ \\ \min \ \|t\| = \sqrt{(x - x_i)^2 + (y - y_i)^2 + (z - z_i)^2} \end{cases} \tag{9.15}$$

   where $\|t\|$ is the norm of the vector comprising the invalid fibre gravity centre and a certain point from the sphere surface. Afterwards, steps *(a)ii* and *(a)iii* from `IURD.gen(...)` routine, or steps *(b)ii* to *(b)v* from the `WBull.gen(...)` are repeated until valid solution is attained with the `check.bound(...)` routine.

   In the other case, in which the second condition is not satisfied, then only the fibre orientation versor is randomly generated until both the end-nodes coordinates do not violate

the boundary restrictions. Thus steps *(a)ii* and *(a)iii* from `IURD.gen(...)` routine, or steps *(b)ii* to *(b)v* from the `WBull.gen(...)` are repeated until valid solution is attained. This procedure allows in an indirect fashion to take into account the wall-effect of the mould. Fibres with a gravity centre nearby the specimen walls, i.e. within a distance smaller than half the fibre length will be preferentially aligned within a direction parallel to the wall surface, see Figure 9.4(c).

7. The fibres end-nodes coordinates are saved into an output file. The number of fibres intersecting a specific plane and its correspondent orientation towards the plane are also saved into a result file.

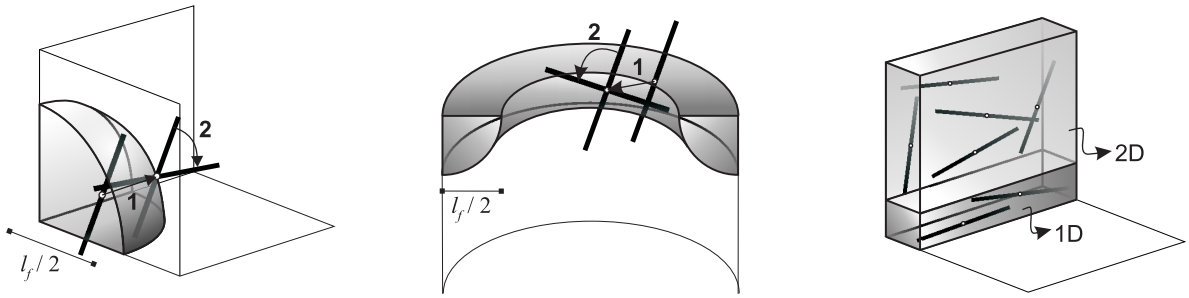

(a) (b) (c)

Figure 9.4: Restrictions to fibre positioning: (a) corner of prismatic specimen, (b) base of cylindric specimen and (c) prismatic mould surfaces.

9.2.4 Numerical simulation of the prismatic specimens

As previously ascertained in Chapter 6, there is a significant difference between the orientation factors and fibre densities obtained from planes with distinct directions. Thus, it is feasible to assume the hypothesis that there is an effect of the variable direction on those parameters. Since the observed differences on both fibre density and orientation between distinct plane directions are considerable, the fibre orientation factors and densities for distinct orientations must be analysed separately. This was corroborated by statistical T-tests (Montgomery and Runger 1994) for a significance level of 0.05, in which the means of the samples from planes with distinct orientations are statistically different from each other.

Having in mind the abovementioned, and that the orientation of the planes designated as parallel when assessing the fibre structure parameters, in the image analysis procedure (see Chapter 6), is the same as the expected orientation of the crack planes, then the parameters of the fibre structure numerically generated were only compared with the correspondent

experimental parameters for the referred parallel planes. Since, in the present work, is only comprehended the modelling of fracture problems, in which the orientation of the crack planes is well known, this is a reasonable simplification. However, if the fracture plane direction is another one than the direction of the studied planes, the fibre distribution parameters in more than one direction needs to be assessed, in order to assure a better approximation of the real fibre structure.

Isotropic uniform random distribution

In Figures 9.5(a) and 9.5(b) are depicted, for the Cf30 series, the relative and cumulative frequency, respectively, for both the experimental and numerical fibre orientation factors. The values of the orientation factors obtained by the image analysis procedure, presented in Table 6.4, are used for computing the normal distribution curves related to the experimental image analysis. For this purpose, it was used the information of the four planes studied per specimen, i.e. with a grand total of twenty planes. On the other hand, concerning the numerical data, both relative and cumulative frequencies, and normal distribution curves were obtained from the statistical analysis of the five fibre meshes numerically generated assuming an IURD for the orientation. Within each fibre mesh, the fibre orientation factor was assessed in four distinct planes (placed at 50, 100, 200 and 300 mm along the specimen's longitudinal axis).

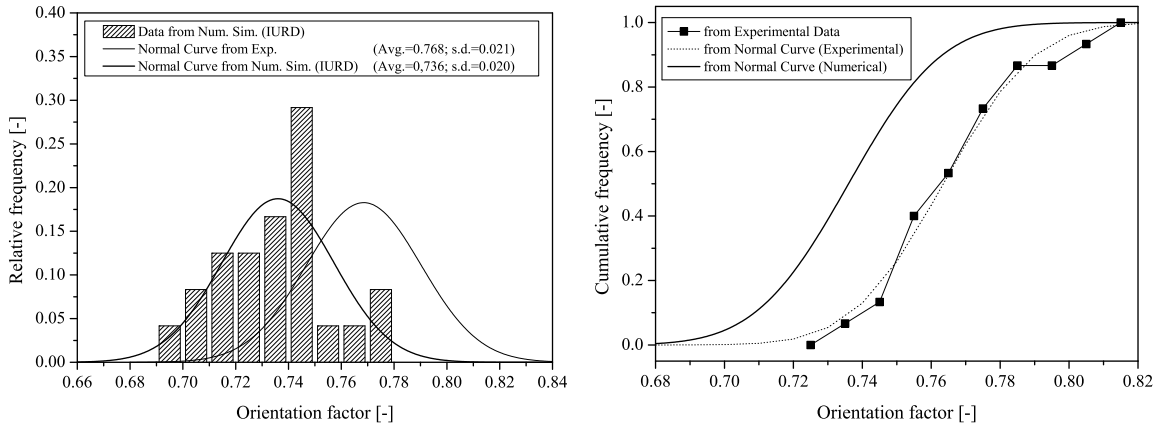

(a) (b)

Figure 9.5: Orientation factors frequency for the Cf30 series: (a) relative frequency and (b) cumulative frequency.

The normal distribution functions obtained for the orientation factor, respectively, from the experimental data and numerical simulations have a similar shape. This is due to the fact that the normal distribution shape is characterised by the value of the sample's standard deviation,

since the experimental and numerical samples have almost identical values of standard deviation, the shape is similar for both distributions. However, the mean value of the orientation factor from the numerical analysis is lower than the obtained from the specimen's cross section image analysis. This was expectable, since as already discussed, the orientation factor observed for the prismatic specimens was considerable higher than the theoretical value for a three-dimensional IURD (see sections 6.6.2 and 6.6.2). The same reasoning can be applied to the cumulative frequency distributions.

In Figures 9.6(a) and 9.6(b) are depicted the relative and cumulative frequency, respectively, for both the experimental and numerical fibre orientation factor assuming an isotropic uniform random fibre orientation for Cf45 series' specimens. The procedure for obtaining the experimental and numerical normal distribution functions was identical to the one described for the Cf30 series. For the Cf45 series, the shape of the normal distributions regarding the experimental and numerical results is now slightly different, particularly, the one obtained from the numerical analysis, which is slightly more skewed, i.e. with a lower standard variation of fibre orientation. Nevertheless, the mean value of the numerical orientation factors is still lower than the corresponding experimental ones, in similarity to the observed for the series Cf30.

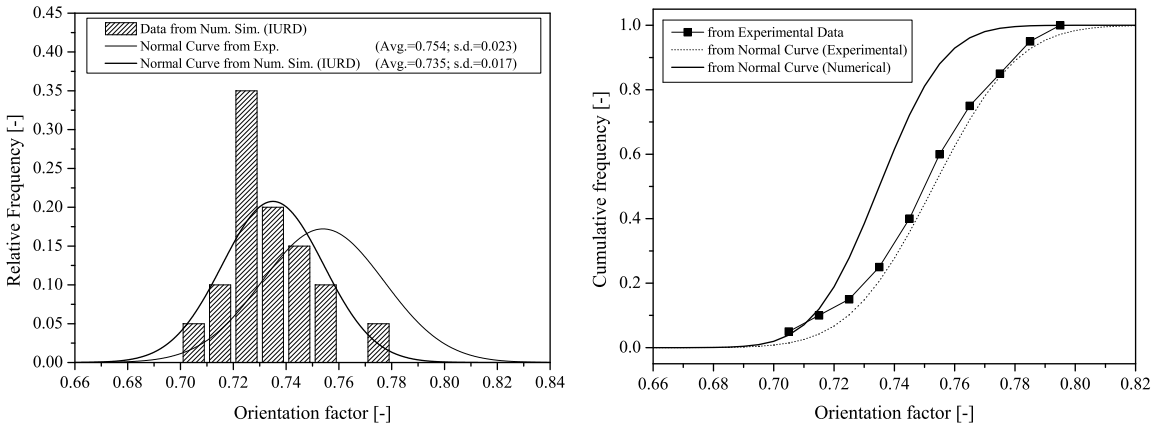

(a) (b)

Figure 9.6: Experimental and numerical orientation factor for specimens with 45 kg/m^3: (a) relative frequency and (b) cumulative frequency.

The average experimental and numerical fibre densities along the longitudinal axis of the prismatic specimens of both Cf30 and Cf45 series are included in Figure 9.7. The standard deviation, s.d., correspondent to the average density values is also included in this figure. The data concerning the numerical analysis was withdraw from the five meshes previously generated with the fibre orientation factors presented in Figures 9.5(a) and 9.6(a).

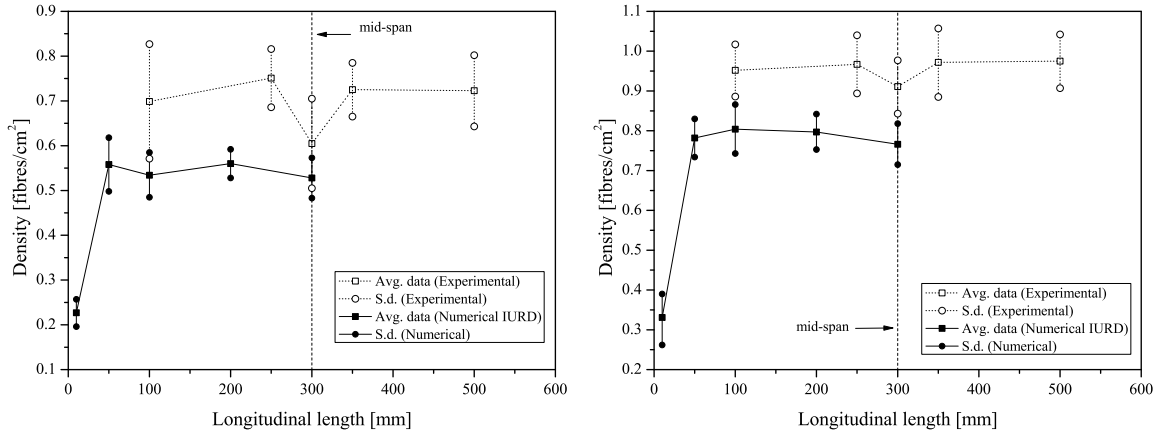

Figure 9.7: Fibre density in the RILEM beams assuming an IUR distribution for specimens with: (a) 30 kg/m^3 (b) 45 kg/m^3.

The predicted fibre density with the developed algorithm, in general, underestimated the fibre density along the studied planes measured from the experimental specimens. Moreover, this difference was slightly higher for the Cf30 series. This is quite reasonable, since for the Cf30 series, the average fibre orientation factor obtained numerically was farther from the correspondent experimental one when comparing with the Cf45 series. However, curiously, the average fibre density of the numerical meshes of the Cf30 series (0.528) is within the interval range of the fibre density at the prismatic beam's mid-span, [0.505, 0.705]. Remark again, as discussed in Chapter 6, this results could be biased, due to the beam's notch, which was executed in a zone where it is present the wall-effect, i.e. probably with a higher fibre density.

Pseudo-Weibull random distribution

As seen in the previous section, the fibre orientation factors and fibre densities of the numerically generated meshes, assuming an IURD for the fibre orientation, are quite different from the fibre distribution assessed by the image analysis procedure. Therefore, the adopted strategy comprises the generation of five new fibre meshes adopting a pseudo-Weibull distribution for the fibres' orientation, with the scope of obtaining "virtual" fibre meshes that better reproduce the experimentally observed.

The fibre orientation frequencies were assessed regarding each single fibre inclination in all the parallel cross sections from the prismatic specimens analysed with the image software. The frequency distributions were assessed separately for each studied series. The frequency distribution for the Cf30 and Cf45 series are depicted in Figures 9.8(a) and 9.8(b), respectively. Afterwards, the parameters of the proposed pseudo-Weibull frequency function, see

equation 9.1, were obtained by a non-linear fitting procedure for each series.

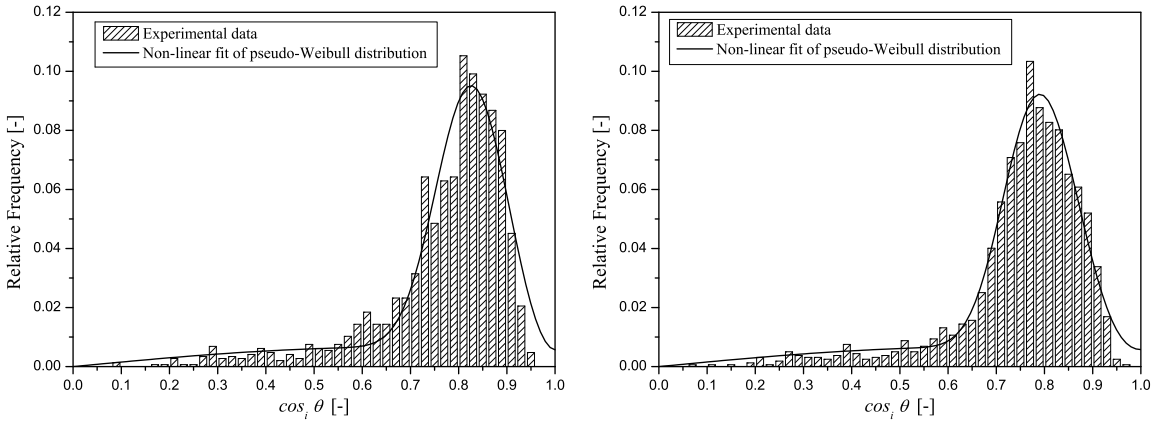

(a) (b)

Figure 9.8: Fitted curves of the pseudo-Weibull distribution function for: (a) Cf30 and (b) Cf45 series.

In Table 9.1 are presented the parameters of the pseudo-Weibull frequency function, as well as the regression coefficient value (R^2) obtained by non-linear fitting of the experimental data from the image cross section analysis of the prismatic beams. The numerical distribution curve has fitted the experimental data with a good agreement, see Figures 9.8(a) and 9.8(b).

Table 9.1: Parameters obtained by non-linear fit of the pseudo-Weibull distribution function.

Series	Parameters				R^2
	ϖ	λ	β	δ	
Cf30	64.51	2	2.923	0.200	0.94
Cf45	63.85	2	3.230	0.234	0.98

In Figures 9.9(a) and 9.9(b) is included, respectively, the relative and cumulative frequency functions for the fibre orientation factor assuming the abovementioned pseudo-Weibull function, namely, for the Cf30 series. Remark that the frequency function of the fibre orientation fitted in Figures 9.8(a) and 9.8(b) regards the inclination of a single fibre, i.e. is the relative frequency of all the fibres' inclination angle in all the studied cross sections, whereas the normal distribution function presented in Figures 9.9(a) and 9.9(b) concerns to the fibre orientation factor, which is the computed mean value of the fibres' orientation in a single plane. The average fibre orientation factor of the numerical meshes generated with a pseudo-Weibull function is closer to the average fibre orientation factor assessed experimentally, when comparing with numerical simulations assuming an IURD. Nevertheless, the numerical average orientation factor is now

slightly higher than the orientation factor assessed experimentally.

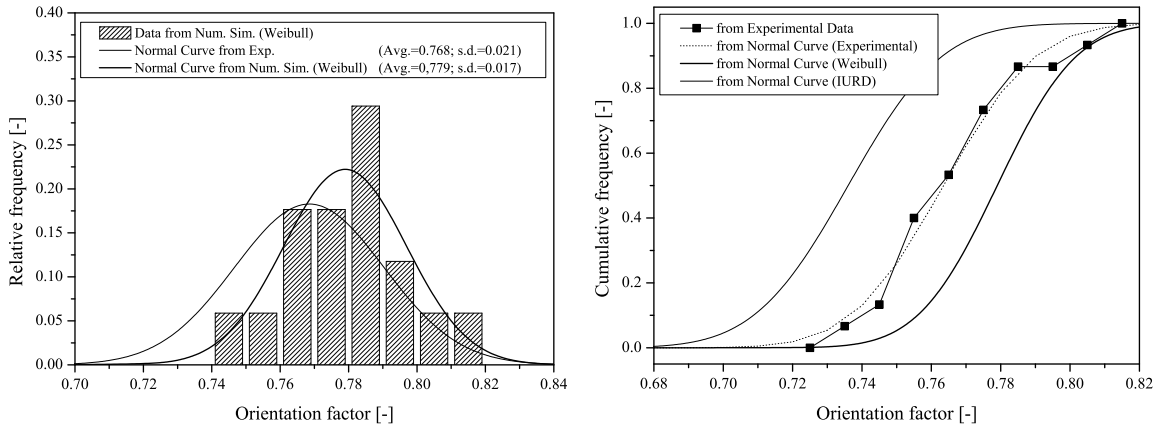

(a) (b)

Figure 9.9: Experimental and numerical orientation factor for specimens with 30 kg/m^3: (a) relative frequency and (b) cumulative frequency.

The relative and cumulative frequency function for the fibre orientation factor, in series Cf45, assuming the abovementioned pseudo-Weibull function for the fibre orientation is comprised, respectively, in Figures 9.10(a) and 9.10(b). The average orientation factor obtained numerically, for the referred series, is also closer and slightly higher to the corresponding experimental, when comparing to the simulations assuming an IURD fibre orientation, for the Cf45 series. However, the shape of the numerical normal distribution is more skewed than the experimental one, thus a worse simulation of the fibre orientation factor's scatter is obtained with a pseudo-Weibull function.

Finally, in Figures 9.11(a) and 9.11(b) is depicted, respectively, for the Cf30 and Cf45 series, the experimental and numerical fibre density along the longitudinal axis of the prismatic beams adopting a pseudo-Weibull distribution for the fibre orientation. The agreement between the experimental results and numerical ones was very good, and increased considerably when compared with the simulation assuming an IUR distribution, see Figures 9.7(a) and 9.7(b). In general, the predicted fibre density from the virtual fibre meshes was slightly higher than the fibre density observed on the specimens. This was already expectable, since this is a direct consequence of the higher numerical orientation factor when comparing to the one observed experimentally. Curiously, for the Cf30 series, the fibre density numerically computed at the specimen's mid-span differed 12 % from the observations made on the beams at this location, while it differed considerably less, nearby 6 %, from the average fibre density observed at the other plane sections.

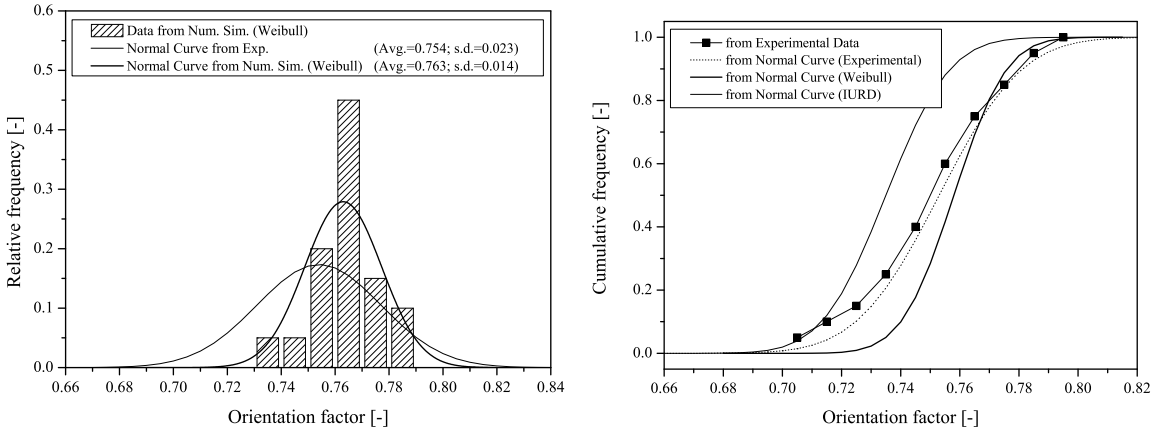

(a) (b)

Figure 9.10: Experimental and numerical orientation factor for specimens with 45 kg/m^3: (a) relative frequency and (b) cumulative frequency.

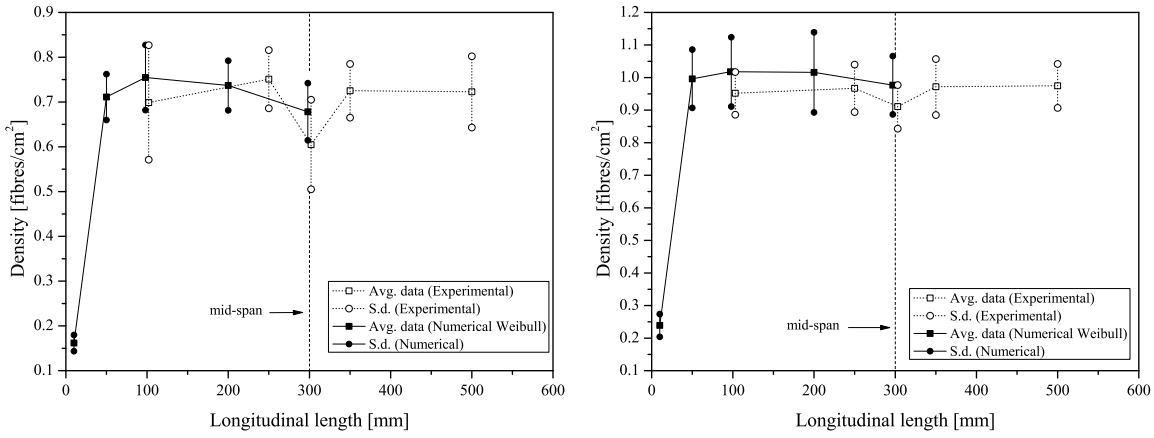

(a) (b)

Figure 9.11: Fibre density along the longitudinal axis of the RILEM beams assuming a pseudo-Weibull distribution for: (a) Cf30 and (b) Cf45 series.

9.2.5 Numerical simulation of the cylinders

In Figures 9.12(a) and 9.12(b) are included the fibre density along the cylindric specimen longitudinal length observed experimentally and the correspondent numerical simulation, respectively, for the Cf30 and Cf45 series. The numerical data arises from five fibre meshes generated assuming an isotropic uniform random distribution, IURD. The agreement between the numerical fibre meshes' density with the one observed experimentally is quite different for the Cf30 or Cf45 series.

For the Cf30 series the average number of fibres, i.e. average fibre density, of the numerical fibres that intersect the studied planes is significantly higher than the one observed experimen-

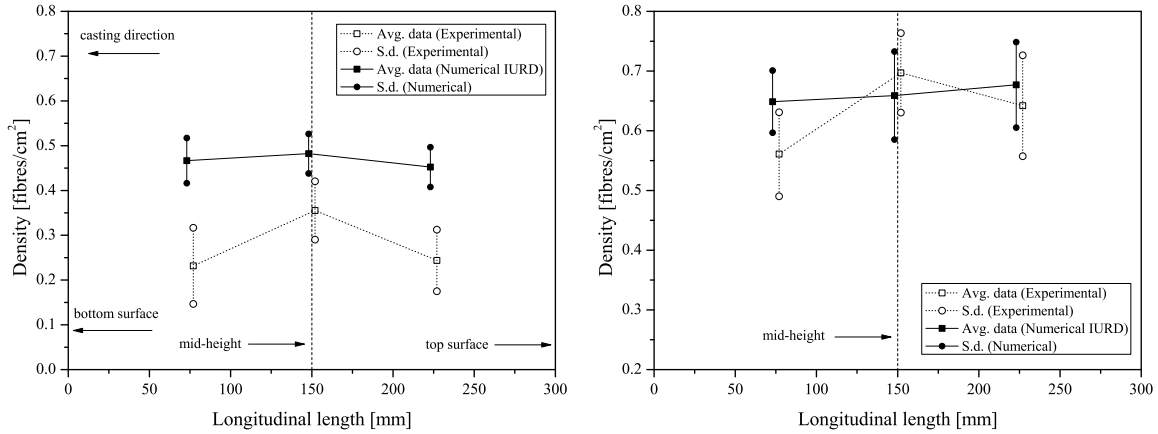

Figure 9.12: Fibre density along the longitudinal axis of the cylindric specimens assuming a IUR distribution for: (a) Cf30 and (b) Cf45 series.

tally. On the other hand, for the Cf45 series the agreement is quite good. Remember that for the Cf30 series the theoretical density value assuming a three-dimensional IURD is 0.435, see Chapter 6. As can be observed in Figure 9.12(a), the average fibre density of the numerical simulations is higher than the theoretical value, in opposition the experimental one is considerably smaller than the referred theoretical value. Thus, if having in mind that the cylindric specimen is relatively slender, which favours the fibre orientation along the lengthier dimension due to the wall effect, it is quite feasible that the expected fibre density will be higher than the theoretical one assuming a three-dimensional IURD. Moreover, the average orientation factor obtained from the image analysis procedure, 0.586, is higher than the theoretical orientation factor for a three-dimensional IURD, 0.5. The use of this last value in equation 6.20 yields the referred theoretical fibre density value of 0.435 for a three-dimensional IURD.

These facts and the good agreement obtained with the Cf45 series could suggest that the observed experimental fibre density in the cylindric specimens may not correspond to a fibre content of 30 kg/m^3. That is to say, the "real" fibre content comprised in each cylinder volume may not correspond to the 30 kg/m^3, this could be ascribed to a improper filling of the moulds during the casting procedure or a deficient dispersion of the fibres in the mixer.

Due to the aforementioned arguments, and taking into account the relatively small experimental data obtained from the image analysis procedure for the cylindric specimens, which does not allow to have a statistical significant sample, a different approach than the one used for the prismatic specimens was adopted, in order to obtain a better simulation of the fibre density in the cylindric specimens. Therefore, the fibre structure of the Cf30 series' specimens was obtained assuming a reduction of the fibre content. In spite of this approach being question-

able, the analysis of the experimental data point out that it is quite feasible that the cylindric specimens in reality have a reduced fibre volume ratio than the expected one. Moreover, from the academic point of view, this will enable to model the uniaxial tensile behaviour of this series with the developed strategy. In Figure 9.13 is depicted the fibre density along the cylindric specimen obtained from the numerical simulation assuming a fibre content reduction. The numerical simulations were carried out adopting a fibre content of 20 kg/m^3, i.e a 33% reduction on the fibre volume ratio. This reduction was selected by trial and error, until a resonable agreement with experimental data was achieved.

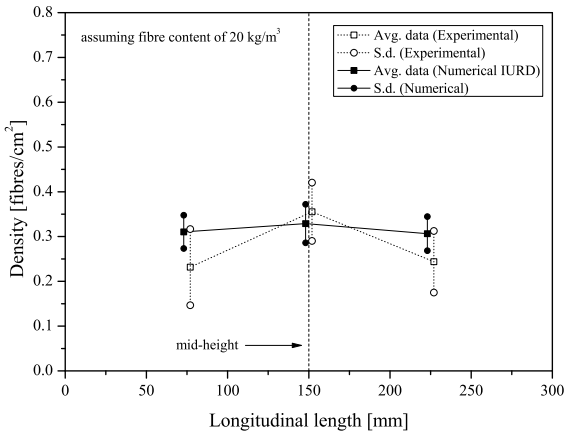

Figure 9.13: Fibre density on the cylindric specimens assuming a reduction on the fibre volume ratio for the Cf30 series.

9.3 Finite element model with short discrete embedded reinforcements

9.3.1 Concrete material modelling

The nonlinear behaviour of the concrete matrix was modelled with a multi-fixed smeared crack model. This model was firstly implemented by Barros (1995) on the FEMIX software and later was reimplemented in the FEMIX 4.0 version for the two-dimensional case by Sena-Cruz (2005), and extended by Ventura-Gouveia et al. (2008) for the three-dimensional case. In the present work, the modelled specimens have a notch to force the occurrence of a single macro-crack in the notched plane, consequently, only one crack is admitted per integration point of the finite element. Thus the described formulation included in this section only envisages one crack per integration point and is a particular case of the multi-fixed smeared crack model formulation.

The extension of this formulation for the multi-cracks' case can be found elsewhere (Sena-Cruz 2005, Ventura-Gouveia et al. 2008).

Since it was adopted a nonlinear material model to simulate the crack propagation into concrete, an incremental-iterative procedure is used to solve the resulting system of nonlinear equations. The relationship between the incremental strain and stress is given by the well-known equation:

$$\Delta\underline{\sigma} = \underline{D}\ \Delta\underline{\varepsilon} \tag{9.16}$$

where $\Delta\underline{\sigma}$ and $\Delta\underline{\varepsilon}$ are, respectively, the stress and strain increment vectors and $\underline{D}$ is tangent constitutive matrix.

In smeared crack models, the incremental strain vector is decomposed into an incremental crack strain vector, $\Delta\underline{\varepsilon}^{cr}$, and an incremental strain vector regarding the contribution of the uncracked concrete, i.e. concrete between cracks, $\Delta\underline{\varepsilon}^{co}$:

$$\Delta\underline{\varepsilon} = \Delta\underline{\varepsilon}^{cr} + \Delta\underline{\varepsilon}^{co} \tag{9.17}$$

The strain decomposition in equation 9.17 is the main basic assumption of the smeared crack models and has been widely adopted by several researchers (Bazant and Gambarova 1980, de Borst and Nauta 1985, Rots 1988, Barros 1995, Sena-Cruz 2005, Ventura-Gouveia et al. 2008).

Crack strain and stress vectors

In Figure 9.14(a) is comprised a sketch of the crack plane within a solid finite element, for the three-dimensional case. According to the classical fracture mechanics three distinct types of crack modes can be considered. The crack opening mode, Mode I, the in-plane shear mode, Mode II, and the out-of-plane shear mode, Mode III, (Shah et al. 1995, Bazant and Planas 1998). Remark that, for the three-dimensional case the distinction between the Mode II and III can be disregarded, see Figure 9.14(b). The referred fracture modes are correlated to the relative displacements between the crack surfaces: Mode I with the crack opening displacement, w, and Modes II and III with the crack sliding displacements, respectively, s_1 and s_2. The local axes of the crack's coordinate system are defined by the crack normal direction, $\hat{n}$, and both crack tangential directions, $\hat{t}_1$ and $\hat{t}_2$, see Figure 9.14(a).

Hereinafter, it is adopted the *contracted notation* for stresses and strains. Therefore, the directions of both normal stresses and strain are indicated with subscripts corresponding the direction of the stress or strain (e.g. σ_1 ε_1). On the other hand, the shear stresses and strains are indicated by two subscripts regarding the plane where the stresses and strains act (e.g. τ_{12} and γ_{12}). In the local coordinate system, the directions of all the stresses and strain components

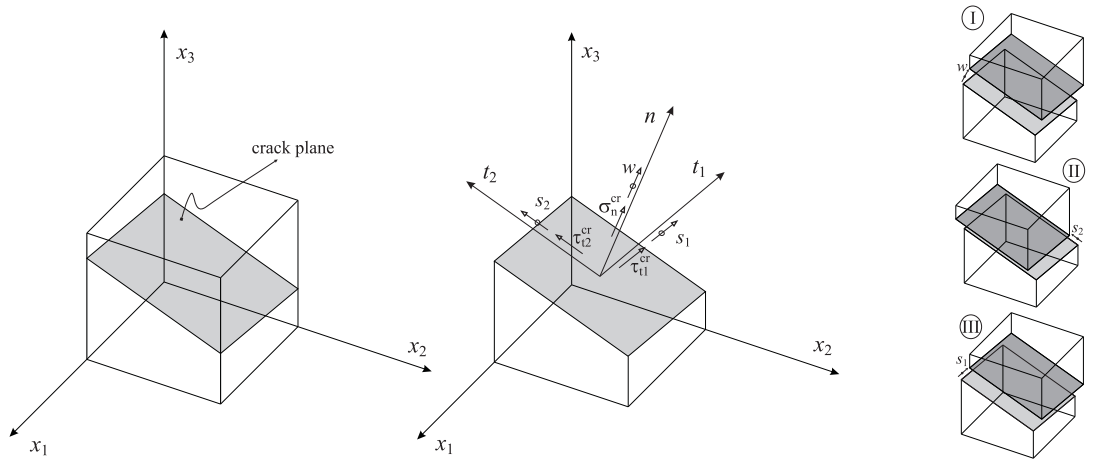

(a) (b)

Figure 9.14: Three-dimensional scheme of the crack plane: (a) stress components, displacements and coordinate systems (after Ventura-Gouveia et al. 2008), (b) fracture modes.

are indicated with subscripts corresponding the direction of the stress or strain (e.g. σ_n^{cr} and τ_{t1}^{cr}).

In the smeared crack approach, w is replaced with a crack normal strain, ε_n^{cr}, and both s_1 and s_2 are replaced, respectively, with the crack shear strain γ_{t1}^{cr} and γ_{t2}^{cr}. Thus, the incremental local crack strain vector, $\Delta\underline{\varepsilon}_l^{cr}$, has the following components:

$$\Delta\underline{\varepsilon}_l^{cr} = [\Delta\varepsilon_n^{cr},\ \Delta\gamma_{t1}^{cr},\ \Delta\gamma_{t1}^{cr}]^T \tag{9.18}$$

whereas the incremental crack strain in the global coordinate system is defined by:

$$\Delta\underline{\varepsilon}^{cr} = [\Delta\varepsilon_1^{cr},\ \Delta\varepsilon_2^{cr},\ \Delta\varepsilon_3^{cr},\ \Delta\gamma_{23}^{cr},\ \Delta\gamma_{31}^{cr},\ \Delta\gamma_{12}^{cr}]^T \tag{9.19}$$

The transformation of the incremental crack strain vector between the local and global coordinate system is represented by:

$$\Delta\underline{\varepsilon}^{cr} = [\underline{T}^{cr}]^T\ \Delta\underline{\varepsilon}_l^{cr} \tag{9.20}$$

in which $\underline{T}^{cr}$ is the transformation matrix:

$$\underline{T}^{cr} = \begin{bmatrix} a_{11}^2 & a_{12}^2 & a_{13}^2 & 2\,a_{12}\,a_{13} & 2\,a_{11}\,a_{13} & 2\,a_{11}\,a_{12} \\ a_{11}\,a_{21} & a_{12}\,a_{22} & a_{13}\,a_{23} & a_{12}\,a_{23}+a_{13}\,a_{22} & a_{11}\,a_{23}+a_{13}\,a_{21} & a_{11}\,a_{22}+a_{12}\,a_{21} \\ a_{11}\,a_{31} & a_{12}\,a_{32} & a_{13}\,a_{33} & a_{13}\,a_{32}+a_{12}\,a_{33} & a_{13}\,a_{31}+a_{11}\,a_{33} & a_{12}\,a_{31}+a_{11}\,a_{32} \end{bmatrix} \tag{9.21}$$

where a_{ij} are the components of the matrix $\underline{a}$ comprising the direction cosines:

$$\underline{a} = \begin{bmatrix} a_{11} & a_{12} & a_{13} \\ a_{21} & a_{22} & a_{23} \\ a_{31} & a_{32} & a_{33} \end{bmatrix} = \begin{bmatrix} \cos(n,\, x_1) & \cos(n,\, x_2) & \cos(n,\, x_3) \\ \cos(t_1,\, x_1) & \cos(t_1,\, x_2) & \cos(t_1,\, x_3) \\ \cos(t_2,\, x_3) & \cos(t_2,\, x_2) & \cos(t_2,\, x_3) \end{bmatrix} \tag{9.22}$$

The incremental stress vector in the local coordinate system, $\Delta\underline{\sigma}_l^{cr}$, has the following components:

$$\Delta\underline{\sigma}_l^{cr} = [\Delta\sigma_n^{cr},\ \Delta\tau_{t1}^{cr},\ \Delta\tau_{t1}^{cr}]^T \tag{9.23}$$

where $\Delta\sigma_n^{cr}$ is the incremental crack normal stress, and $\Delta\tau_{t1}^{cr}$ and $\Delta\tau_{t2}^{cr}$ are the incremental crack shear stresses, respectively, in $\hat{t}_1$ and $\hat{t}_2$ directions.

Concrete constitutive law

An isotropic linear elastic behaviour was assumed for concrete between cracks, i.e. uncracked or undamaged concrete. Thus, the constitutive relation between $\Delta\underline{\varepsilon}^{co}$ and $\Delta\underline{\sigma}$ stands:

$$\Delta\underline{\sigma} = \underline{D}^{co}\ \Delta\underline{\varepsilon}^{co} \tag{9.24}$$

with,

$$\underline{D}^{co} = \frac{E_c}{(1+\nu_c)\,(1-2\nu_c)} \begin{bmatrix} (1-\nu_c) & \nu_c & \nu_c & 0 & 0 & 0 \\ \nu_c & (1-\nu_c) & \nu_c & 0 & 0 & 0 \\ \nu_c & \nu_c & (1-\nu_c) & 0 & 0 & 0 \\ 0 & 0 & 0 & \dfrac{1-2\nu_c}{2} & 0 & 0 \\ 0 & 0 & 0 & 0 & \dfrac{1-2\nu_c}{2} & 0 \\ 0 & 0 & 0 & 0 & 0 & \dfrac{1-2\nu_c}{2} \end{bmatrix} \tag{9.25}$$

where, E_c and ν_c are, respectively, the Young's modulus and Poisson's ratio of the concrete.

In similarity to equation 9.24, the crack opening and shear sliding behaviour can be established in terms of a relationship between $\Delta\underline{\sigma}_l^{cr}$ and $\Delta\underline{\varepsilon}_l^{cr}$:

$$\Delta\underline{\sigma}_l^{cr} = \underline{D}^{cr}\ \Delta\underline{\varepsilon}_l^{cr} \tag{9.26}$$

where $\underline{D}^{cr}$ is the crack's constitutive matrix comprising Modes I, II and III crack fracture parameters. Combining equations 9.16 to 9.26, can be obtained the constitutive law of the cracked concrete, which yields:

$$\Delta\underline{\sigma} = \underline{D}^{crco}\ \Delta\underline{\varepsilon} \tag{9.27}$$

with,

$$\underline{D}^{crco} = \underline{D}^{co} - \underline{D}^{co}\ \left[\underline{T}^{cr}\right]^{T}\ \left(\underline{D}^{cr} + \underline{T}^{cr}\ \underline{D}^{co}\ \left[\underline{T}^{cr}\right]^{T}\right)^{-1}\ \underline{T}^{cr}\ \underline{D}^{co} \tag{9.28}$$

where $\underline{D}^{crco}$ is the constitutive matrix of the cracked concrete. The deduction of this matrix can be found elsewhere (Barros 1995, Sena-Cruz 2005).

The $\underline{D}^{cr}$ matrix of the present model does not account with the shear-normal stress coupling, therefore this matrix is diagonal with the non-null terms being the crack's stiffness modulus associated to each fracture mode (Mode I, II and III). The crack opening mode was simulated by an exponential tensile-softening diagram proposed by Cornelissen et al. (1986) defined by:

$$\frac{\sigma_n^{cr}(\varepsilon_n^{cr})}{f_{ct}} = \begin{cases} \left(1 + \left(c_1 \dfrac{\varepsilon_n^{cr}}{\varepsilon_{n,ult}^{cr}}\right)^3\right) \exp\left(-c_2 \dfrac{\varepsilon_n^{cr}}{\varepsilon_{n,ult}^{cr}}\right) - \dfrac{\varepsilon_n^{cr}}{\varepsilon_{n,ult}^{cr}} \left(1 + c_1^3\right) \exp\left(-c_2\right) & \text{if} \quad 0 < \varepsilon_n^{cr} < \varepsilon_{n,ult}^{cr} \\ 0 & \text{if} \quad \varepsilon_n^{cr} \geq \varepsilon_{n,ult}^{cr} \end{cases} \tag{9.29}$$

where $c_1 = 3.0$ and $c_2 = 6.93$, for plain concrete. The ultimate crack normal strain, $\varepsilon_{n,ult}^{cr}$, is computed from:

$$\varepsilon_{n,ult}^{cr} = \frac{1}{k} \cdot \frac{G_f}{f_{ct}\, l_b} \tag{9.30}$$

where f_{ct}, G_f and l_b are the tensile strength, fracture energy and crack band-width, respectively, whereas k is a constant computed from:

$$k = \left[\frac{1}{c_2}\left[1 + 6\left(\frac{c_1}{c_2}\right)^3\right] - \left[\frac{1}{c_2} + c_1^3\left(\frac{1}{c_2} + \frac{3}{c_2^2} + \frac{6}{c_2^3} + \frac{6}{c_2^4}\right) + \frac{1}{2}\left(1 + c_1^3\right)\right]\right] \exp(-c_2) \tag{9.31}$$

The Mode I stiffness modulus, D_n^{cr}, comprised in the $\underline{D}^{cr}$ matrix is determined with:

$$\begin{aligned} D_n^{cr} = f_{ct} \Bigg[& 3\left(c_1 \frac{\varepsilon_n^{cr}}{\varepsilon_{n,ult}^{cr}}\right)^2 \frac{c_1}{\varepsilon_{n,ult}^{cr}} \exp\left(-c_2 \frac{\varepsilon_n^{cr}}{\varepsilon_{n,ult}^{cr}}\right) + \\ & \exp\left(-c_2 \frac{\varepsilon_n^{cr}}{\varepsilon_{n,ult}^{cr}}\right)\left(-c_2 \frac{\varepsilon_n^{cr}}{\varepsilon_{n,ult}^{cr}}\right)\left[1 + \left(c_1 \frac{\varepsilon_n^{cr}}{\varepsilon_{n,ult}^{cr}}\right)^3\right] - \frac{1 + c_1^3}{\varepsilon_{n,ult}^{cr}} \exp\left(-c_2\right) \Bigg] \end{aligned} \tag{9.32}$$

The shear fracture modes II and III stiffness modulus, respectively, D_{t1}^{cr} and D_{t2}^{cr} are computed from:

$$D_{t1}^{cr} = D_{t2}^{cr} = \frac{\beta}{1-\beta} G_c \tag{9.33}$$

where G_c and β are, respectively, the elastic shear modulus and the shear retention factor. A linear softening constitutive law is used to model the shear degradation of the concrete.

9.3.2 Fibre structure model

In section 9.2 was presented the methodology to randomly generate a fibre structure that represented, with a certain level of accuracy, the distribution of fibres in a hardened matrix. After the generation of the elements' mesh representing the fibres, there is the need to insert it in the solid three-dimensional mesh for modelling the plain concrete.

In the present work, since it is assumed that the embedded cables (representing the fibres) are always straight, it is enough to represent the fibre by two end-nodes defined in the global coordinate system. Remark, however, that a fibre can intersect one or even several solid elements, thus there is the need to account with several additional points for the distinct intersection points. A fibre is represented by several embedded cables segments, in which each segment contribute exclusively to the reinforcement of a single solid brick. The determination of these intersecting points was performed by an inverse mapping technique. Therefore, the search of the intersecting points was carried out at the element natural axis, within the computational domain.

Inverse mapping technique

The global coordinates of a point contained in an embedded cable either curved or straight can be evaluated in a general manner as:

$$\begin{bmatrix} x^f \\ y^f \\ z^f \end{bmatrix} = \begin{bmatrix} \sum_{i=1}^{n_f} N_i^f(\zeta)\, x_i^f \\ \sum_{i=1}^{n_f} N_i^f(\zeta)\, y_i^f \\ \sum_{i=1}^{n_f} N_i^f(\zeta)\, z_i^f \end{bmatrix} \tag{9.34}$$

where $N_i^f(\zeta)$ is the embedded cable Lagrangian interpolation functions, ζ is the parametric coordinate in the interval $[-1, 1]$; x_i^f, y_i^f and z_i^f are the global coordinates of the embedded

cable nodes with $n_f = 2$ in the present work. On the other hand, the point belonging to an embedded cable that intersects an element face must satisfy one of the following conditions:

$$\begin{aligned} \left\|\xi^f\right\| = 1 \ \wedge \ \left\|\eta^f\right\| \leq 1 \ \wedge \ \left\|\varsigma^f\right\| \leq 1 \\ \left\|\xi^f\right\| \leq 1 \ \wedge \ \left\|\eta^f\right\| = 1 \ \wedge \ \left\|\varsigma^f\right\| \leq 1 \\ \left\|\xi^f\right\| \leq 1 \ \wedge \ \left\|\eta^f\right\| \leq 1 \ \wedge \ \left\|\varsigma^f\right\| = 1 \end{aligned} \tag{9.35}$$

where ξ^f, η^f and ς^f are the natural embedded cable coordinates in the solid element natural coordinate system. Thus, the natural coordinates of the embedded cable may be evaluated as:

$$\begin{bmatrix} \xi^f \\ \eta^f \\ \varsigma^f \end{bmatrix} = \text{Inverse mapping of} \begin{bmatrix} \sum_{i=1}^{n_f} N_i^f(\zeta)\, x_i^f \\ \sum_{i=1}^{n_f} N_i^f(\zeta)\, y_i^f \\ \sum_{i=1}^{n_f} N_i^f(\zeta)\, z_i^f \end{bmatrix} \tag{9.36}$$

The inverse mapping technique, basically, consists on looking within the solid element's natural coordinates domain, correspondent to the solid global coordinates, which match the embedded cable global coordinates. Therefore, equating the element global coordinates to the embedded cable global coordinates, yields:

$$\begin{bmatrix} x^f \\ y^f \\ z^f \end{bmatrix} - \begin{bmatrix} \sum_{i=1}^{n_c} N_i^c(\xi, \eta, \varsigma)\, x_i^c \\ \sum_{i=1}^{n_c} N_i^c(\xi, \eta, \varsigma)\, y_i^c \\ \sum_{i=1}^{n_c} N_i^c(\xi, \eta, \varsigma)\, z_i^c \end{bmatrix} = 0 \tag{9.37}$$

where $N_i^c(\xi, \eta, \varsigma)$ are the solid element shape functions; x_i^c, y_i^c and z_i^c are the solid element nodal coordinates and nc is the number of nodes of the solid element. Equation 9.37 is solved by the Newton-Raphson method, whenever this method fails to converge the bisection method is used. For each embedded cable, a search is performed in natural coordinate system looking upon the ζ belonging to any embedded cable that intercepts, skirts or touches one of solid element's face.

Afterwards the completion of the point intersection determination, the embedded cable mesh data is rewritten in order to take into account the compatibility between the embedded cables and the solid mesh elements. Coincident nodes from different solid element faces belonging to the same embedded cable are eliminated, finally, the embedded cables nodes are renumbered.

Constitutive model for the embedded fibres

The present formulation of the embedded fibre model does not take into account fibre bond-slip capability in a direct fashion. Therefore, the embedded cable is modelled with a perfectly bonded assumption. Hence, the bond - slip behaviour is simulated in an indirect fashion from the transformation of a load - slip relationship to a tension stress - strain relation.

The constitutive laws for the embedded cables were determined from the fibre pullout tests. Three distinct $\sigma_f - \varepsilon_f$ laws corresponding, respectively, to the studied fibres pullout inclination angles, α, (0^o, 30^o and 60^o) were ascertained. In Figure 9.15 is depicted the procedure adopted to obtain the $\sigma_f - \varepsilon_f$ relationship, where ε_f, l_b and s are, respectively, the embedded cable strain, the crack band-width and the steel fibre's slip; σ_f is the stress computed from the pullout force, P, divided by the fibre's cross sectional area, A_f.

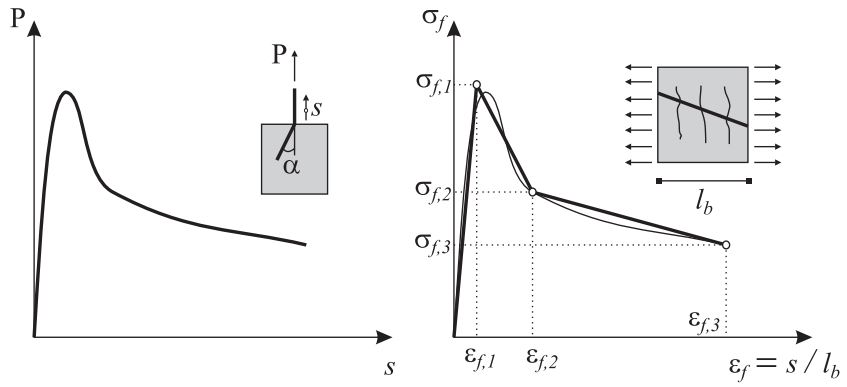

Figure 9.15: Determination of the embedded cable's stress - strain diagram based on the experimental pullout force - slip relationship.

The tri-linear stress-strain $\sigma_f - \varepsilon_f$ diagram used for modelling the fibres including the bond-slip effect was obtained from fitting the experimental pullout load-slip curves. For each fibre's inclination angle, α, an average pullout load-slip curve was computed from the experimental envelope of the series with a 10 mm and 20 mm embedded length, thus corresponding, approximately, to the expected pullout load-slip behaviour of a fibre with an embedded length of 15 mm. This averaging procedure was adopted due to two reasons. The influence of the fibre embedded length on the pullout behaviour is not so significant as the angle effect, moreover its

influence is practically linear (see Chapter 4). In addition, the theoretical average value of the embedded length of a fibre crossing an active crack is $l_f/4 = 15$ mm (Stroeven and Hu 2006). This simplification has rational and scientific fundaments and accomplishes the purpose of developing a model that takes into account the most relevant data obtained from fibre pullout tests, and it does not require too computing time in the numerical simulations.

The tensile - strain law assigned to an embedded cable depends on the inclination angle, θ, between the cable and the normal vector of the active crack surface, (see Figure 9.16). Moreover, also depends on the crack band-width, l_b, of the intersected solid element (see Figure 9.15). Due to the impossibility of having a $\sigma_f - \varepsilon_f$ law for every possible inclination angle and embedded length, the $\sigma_f - \varepsilon_f$ laws obtained from the pullout tests with an angle α of 0º, 30º and 60º were assigned to the embedded cables with an orientation towards the active crack surface θ ranging from, respectively, [0º, 15º], [15º, 45º] and [45º, 75º]. The contribution of the fibres with θ in the interval [75º, 90º] was neglected.

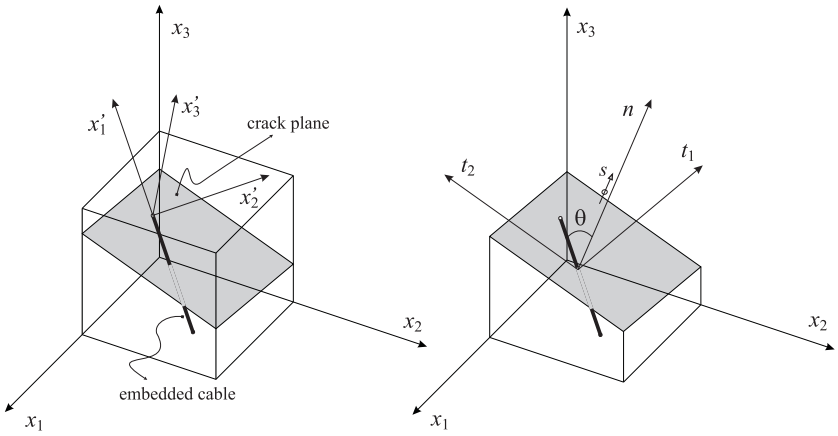

Figure 9.16: Three-dimensional scheme of the embedded cable intersecting an active crack (n is the vector normal to the crack plane).

9.3.3 Evaluation of the concrete and embedded fibre structure stiffness matrix

In order to model both the concrete and fibre reinforcement contribution, it was adopted an embedded formulation. The element stiffness matrix representing a concrete bulk reinforced with fibres can be expressed as:

$$\underline{K}^{rc} = \underline{K}^{crco} + \sum_{i=1}^{n_f} \underline{K}_i^f \tag{9.38}$$

where $\underline{K}^{crco}$, $\underline{K}_i^f$ and n_f are, respectively, the concrete element stiffness matrix, the stiffness matrix of the i^{th} fibre that is embodied in the concrete mother-element, and the total number of embodied fibres in the concrete element. The concrete element stiffness matrix is given by:

$$\underline{K}^{crco} = \int_V \underline{B}_c^T \, \underline{D}^{crco} \, \underline{B} \, dV \tag{9.39}$$

where $\underline{D}^{crco}$ is the cracked concrete's constitutive matrix (determined from equation 9.28) and $\underline{B}$ is the well-known strain – displacement matrix of a solid element (see Zienkiewicz and Taylor 2000).

The axial contribution of the fibre reinforcement to the stiffness matrix can be computed by the internal work regarding the axial component as follow:

$$\begin{aligned} W_a &= \int_V \varepsilon_f^T \, \sigma_f \, dV \\ &= \int_L \varepsilon_f^T \, \varepsilon_f \, E_f \, A_f \, dL \end{aligned} \tag{9.40}$$

with,

$$dL = \sqrt{\left(\frac{dx_1}{ds}\right)^2 + \left(\frac{dx_2}{ds}\right)^2 + \left(\frac{dx_3}{ds}\right)^2} \cdot ds = J \, ds \tag{9.41}$$

where σ_f, ε_f and A_f are the stress, strain and cross-sectional area of the fibre, whereas J is the Jacobian at a generic point of the fibre. Thus, substituting equation 9.41 in equation 9.40, the internal work can be computed in natural coordinates by:

$$W_a = \int_{-1}^{+1} \varepsilon_f^T \, \varepsilon_f \, E_f \, A_f \, J \, ds \tag{9.42}$$

The stiffness matrix is obtained by substituting $\varepsilon_f = \underline{T}_1^f \, \underline{B} \, \underline{a}$ in equation 9.42, where $\underline{a}$ is the vector with the solid element nodal displacements and $\underline{T}_1^f$ is the vector corresponding to the first line of the transformation matrix from the fibre's local coordinate system to the global coordinate system, $\underline{T}^f$ given by:

$$\underline{T}^f = \begin{bmatrix} a_{11}^2 & a_{12}^2 & a_{13}^2 & a_{12}\,a_{13} & a_{11}\,a_{13} & a_{11}\,a_{12} \\ a_{21}a_{31} & a_{22}a_{32} & a_{23}a_{33} & 0.5(a_{22}a_{33}+a_{23}a_{32}) & 0.5(a_{23}a_{31}+a_{21}a_{33}) & 0.5(a_{21}a_{32}+a_{12}a_{31}) \\ a_{11}a_{31} & a_{12}a_{32} & a_{13}a_{33} & 0.5(a_{13}a_{32}+a_{12}a_{33}) & 0.5(a_{13}a_{31}+a_{11}a_{33}) & 0.5(a_{12}a_{31}+a_{11}a_{32}) \end{bmatrix} \tag{9.43}$$

where a_{ij} are the components of the matrix $\underline{a}$ comprising the direction cosines:

$$\underline{a}^f = \begin{bmatrix} a_{11} & a_{12} & a_{13} \\ a_{21} & a_{22} & a_{23} \\ a_{31} & a_{32} & a_{33} \end{bmatrix} = \begin{bmatrix} cos(x'_1, x_1) & cos(x'_1, x_2) & cos(x'_1, x_3) \\ cos(x'_2, x_1) & cos(x'_2, x_2) & cos(x'_2, x_3) \\ cos(x'_3, x_3) & cos(x'_3, x_2) & cos(x'_3, x_3) \end{bmatrix} \tag{9.44}$$

Hence, the component of the stiffness matrix with the fibre's axial contribution is given by:

$$\underline{K}_a^f = \int_{-1}^{1} \underline{B}^T \, \underline{T}_1^{f\,T} \, \underline{T}_1^f \, \underline{B} \, E_f \, A_f \, J \, ds \tag{9.45}$$

In a similar way the components of the fibre stiffness matrix with the shear contribution is given by:

$$\begin{aligned} \underline{K}_{s,1}^f &= \int_{-1}^{1} \underline{B}^T \, \underline{T}_2^{f\,T} \, \underline{T}_2^f \, \underline{B} \, G_f \, \bar{A}_f \, J \, ds \\ \underline{K}_{s,2}^f &= \int_{-1}^{1} \underline{B}^T \, \underline{T}_3^{f\,T} \, \underline{T}_3^f \, \underline{B} \, G_f \, \bar{A}_f \, J \, ds \end{aligned} \tag{9.46}$$

where G_f is the fibre's elastic shear modulus, $\underline{T}_2^f$ and $\underline{T}_3^f$ are, respectively, the vector corresponding to the second and third lines of the transformation matrix, see equation 9.43. For the shear components, the value adopted for $\bar{A}_f$ is the reduced shear area for circular sections (Timoshenko and Goodier 1991).

The equivalent nodal forces vector, $\underline{q}^e$ is computed from:

$$\underline{q}^e = \underbrace{\int_V \underline{B}^T \, \underline{\sigma} \, dV}_{\text{concrete}} + \underbrace{\underbrace{\int_{-1}^{1} \underline{B}^T \, \underline{T}^T \, \sigma_f \, A_f \, J \, ds}_{\text{axial component}} + \underbrace{\int_{-1}^{1} \underline{B}^T \, \underline{T}^T \, \underline{\tau}_f \, \bar{A}_f \, J \, ds}_{\text{shear component}}}_{\text{fibre contribution}} \tag{9.47}$$

where σ_f is the fibre's stress with axial component obtained from the adopted tension stress - strain diagram for modelling the fibre pullout behaviour. On the other hand, $\underline{\tau}_f$ is the fibre's stress vector with the two shear components. For the fibre shear behaviour was adopted an elasto-plastic behaviour. A shear stress cut-off was introduced for shear strains higher than 0.01. Moreover, the fibre's shear contribution was just take into account for crack opening width smaller than 0.5 mm. The shear stress yield criterion used in the present work is uncoupled.

9.4 Appraisal of the numerical model

The model performance is appraised by simulating the uniaxial tension tests and the three-point bending tests already presented in this work. The numerical simulations of the uniaxial and

bending tests were performed on only one mesh per each studied series, i.e. only one generated fibre structure was run under the FEM basis. Note that, due to randomness of the developed approach there is the possibility of obtaining an envelope of numerical responses with a certain scatter associated to distinct fibre structures, i.e. different number of fibres crossing an active fibre and with distinct inclination angles. This is one of the research topics for future works to be suggested in next chapters.

9.4.1 Numerical simulation of the uniaxial tension tests

In Figure 9.17(a) is represented the mesh used exclusively for the concrete matrix phase, whereas in Figures 9.17(b) and 9.17(c) are depicted the three-dimensional meshes used for modelling the steel fibre contribution, respectively, for the Cf30 and Cf45 series. Remark, that the fibres intersected by the notch were not included on the finite element mesh. Moreover, since the numerical fibre mesh was obtained for a cylinder with 300 mm of height, and on another hand the tested cylinder had only a height of 150 mm, the fibres which are not fully comprised in only one half of the specimen were also removed. These simplifications have an almost null influence on the numerical simulations, since the fibre contribution outside the fracture zone is very reduced for this kind of material and test setup.

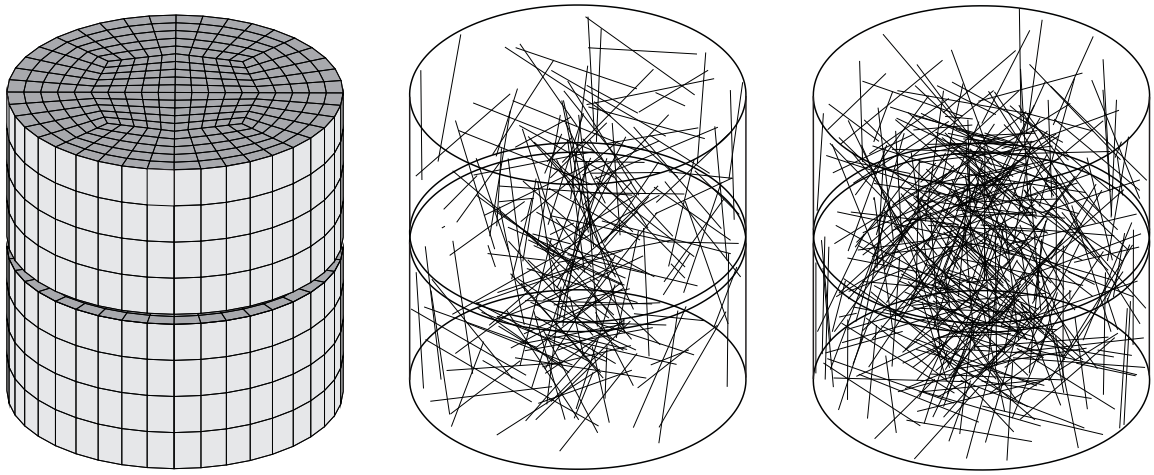

(a) (b) (c)

Figure 9.17: Three-dimensional finite element mesh of the cylindric specimens: (a) concrete phase, (b) fibre phase for the Cf30 series and (c) fibre phase for the Cf45 series.

In the present mesh are used Lagrangian 8-node solid elements for modelling the plain concrete contribution. Since the specimen had a notch at its mid-height, all the non-linear behaviour was localized at the notch region, thus a $2 \times 2 \times 1$ Gauss-Legendre integration scheme

is used (1 integration point in the loading direction). The remaining solid elements are modelled with linear elastic behaviour, and a $2 \times 2 \times 2$ Gauss-Legendre integration scheme is adopted. The Cornelissen et al. (1986) softening law was used for modelling the nonlinear behaviour of SCC. The material properties of the concrete matrix used in the simulations are included in Table 9.2. These values were obtained taking into account the strength class (CEB-FIP 1993) registered for the Cf30 and Cf45 series. On the other hand, the steel fibres are modelled with 3D embedded elements with two integration points (Gauss-Legendre). For all the embedded elements is assumed a nonlinear behaviour.

Table 9.2: Concrete properties used in the simulation.

Property	Series	
	Cf30	Cf45
Density	$\rho = 2.4 \times 10^{-5}$ N/mm^3	
Poisson's ratio	$\nu_c = 0.20$	
Young's modulus	41300 N/mm^2	40600 N/mm^2
Compressive strength	71.1 N/mm^2	67.2 N/mm^2
Tensile strength	4.6 N/mm^2	4.5 N/mm^2
Fracture energy	0.117 N/mm	0.114 N/mm
Crack band-width	$l_b = 5$ mm (equal to element height at the notch)	

In Figures 9.18 and 9.19 are depicted the numerical simulations of the uniaxial tension tests of the Cf30 and Cf45 series, respectively. Regarding the Cf30 series a good agreement with the experimental response was obtained. The predicted numerical tensile strength is nearby the upper bound limit of the experimental envelope. This is feasible, since during testing is almost impossible to completely exclude eccentricities, thus the experimental post-cracking average strength is smaller than the correspondent numerical one. Moreover, the maximum tensile stress obtained in the numerical simulations is smaller than the value of the adopted tensile strength for concrete. This is due to the stress concentrations that arise at the notch tip. Thus, when the concrete's tensile strength is attained near the notch tip, for the maximum load capacity of the specimen, the overall tensile stress computed from averaging the tensile load with the net cross section at the notch will be smaller than the concrete's tensile strength defined as a material property.

On the other hand, for the Cf45 series two numerical simulations were carried out. The first one adopting the $\sigma - \varepsilon_f$ cable laws obtained from the fibre pullout tests (in which fibre rupture was observed for an $\alpha = 30^o$ and 60^o). Up to a crack width of approximately 1.0 mm a relatively good agreement with the experimental response is observed. However, a significant stress decay is observed after this crack width limit (1 mm) due, mainly, to the rupture of the

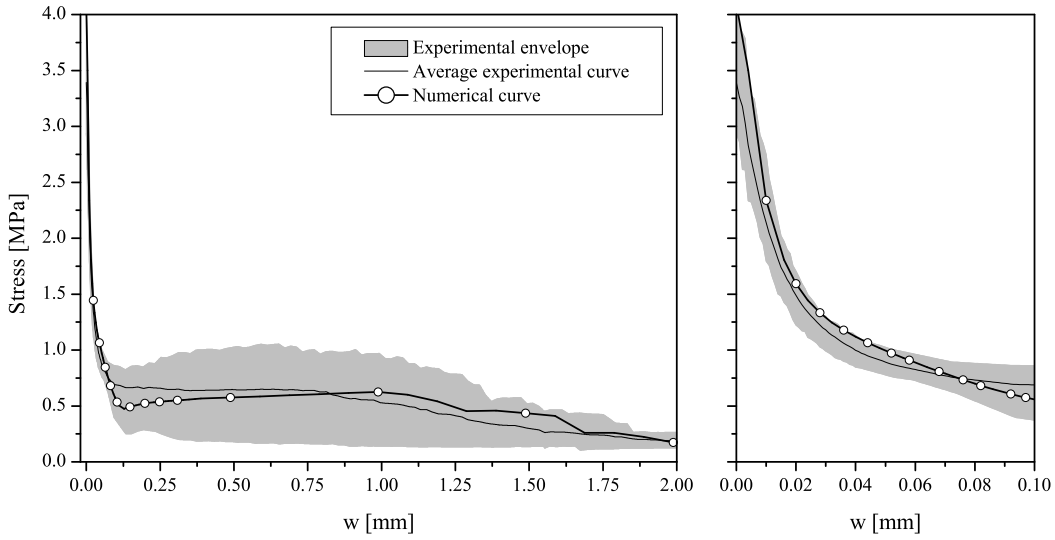

Figure 9.18: Numerical simulation of the uniaxial tension tests for the Cf30 series.

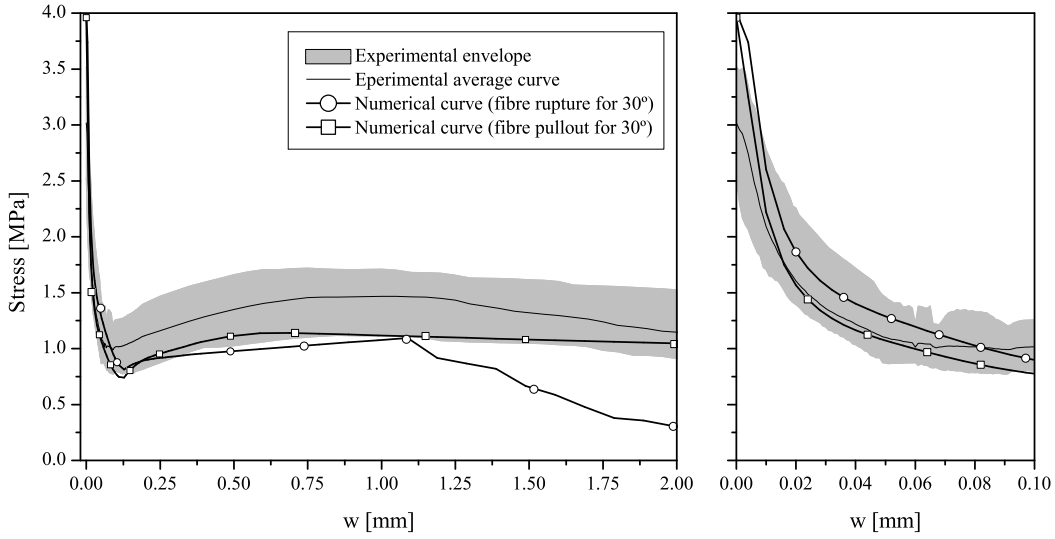

Figure 9.19: Numerical simulation of the uniaxial tension tests for the Cf45 series.

embedded cables with an inclination between 15º and 45º. Remark that, the embedded cables with an inclination between 45º and 75º have also rupture, but only for crack widths higher than 2 mm. Since for the uniaxial tension tests of Cf45 series, fibre rupture did not occur so often, due to both a less resistant matrix and a higher number of fibres crossing the crack's fracture surface, another simulation was carried out assuming that the embedded cables with an inclination angle θ between 15º and 45º did not rupture. For this purpose it were used the pullout load - slip test results with an inclination of 30º in which fibre rupture did not occur (see Chapter 4). With this approach the quality of the simulation was improved (see Figure 9.19).

9.4.2 Numerical simulation of the three-point bending tests

The sketch of the finite element mesh used for modelling the concrete matrix phase in the prismatic specimens, for both Cf30 and Cf45 series, is included in Figure 9.20(a). On another hand, in Figure 9.20(b) is included a three-dimensional view of the mesh used for modelling the steel fibre phase contribution for the Cf30 series. The steel fibre mesh for the Cf45 series is not here represented since its graphical rendering would not enable a clear visualization. The fibres that intersected the notch were removed, in similarity to the performed for the tensile test simulations.

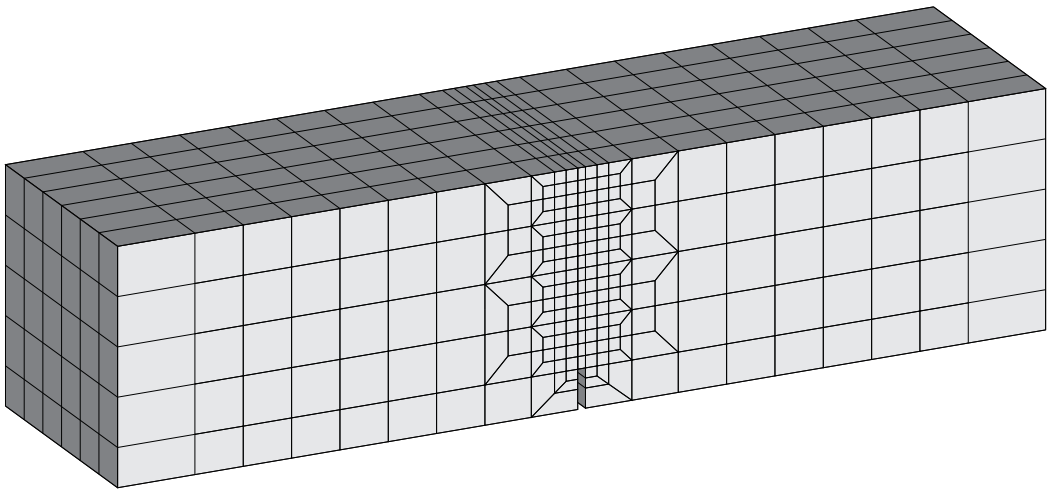

(a)

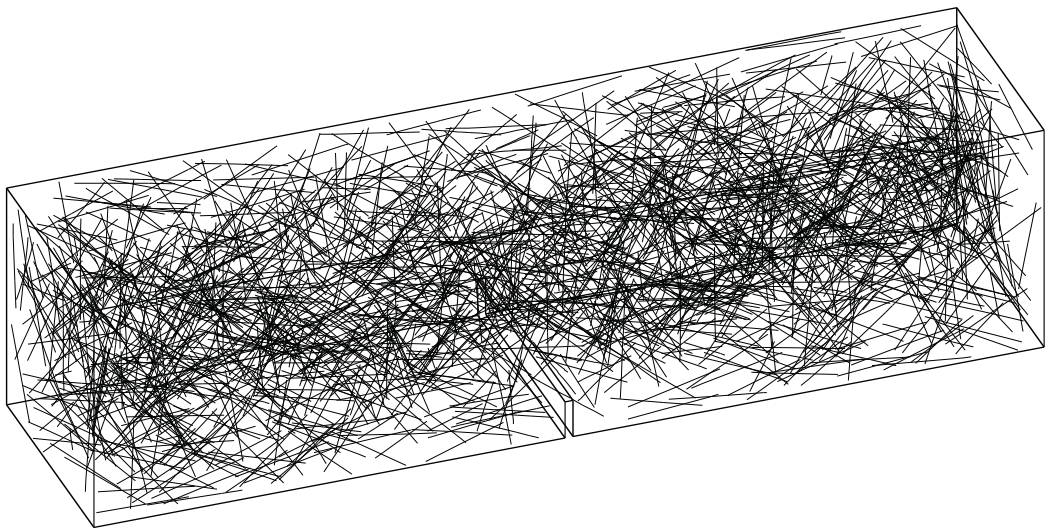

(b)

Figure 9.20: Three-dimensional finite element mesh of the prismatic specimens: (a) concrete phase and (b) fibres phase (Cf30 series).

In the prismatic specimen's finite element mesh are also used Lagrangian 8-node solid elements for modelling the concrete behaviour. In similarity to what was carried out for modelling the tension tests, all the non-linear behaviour was localized at the notch region, in this specific case at mid-span of the beam. Thus, a $2 \times 1 \times 2$ Gauss-Legendre integration scheme is used (1 integration point in the normal direction to the crack surface, i.e. accordingly to the longitudinal axis of the prism. The remaining solid elements are assumed as having a linear elastic behaviour, and a $2 \times 2 \times 2$ Gauss-Legendre integration scheme is adopted. The Cornelissen et al. (1986) softening law was used to simulate the SCC fracture mode I propagation. The values of the material properties of the concrete used in the current simulations are the same already adopted in the simulations of the uniaxial tension tests, see Table 9.2. The steel fibres are modelled with 3D embedded elements with two Gauss-Legendre integration points. For all the embedded elements is assumed a nonlinear behaviour.

The numerical simulations of the three-point bending tests are included in Figures 9.21(a) and 9.21(b), respectively, for the Cf30 and Cf45 series. The agreement between the numerical curve and the experimental results was quite good for both series.

Regarding the Cf30 series, the numerical load correspondent to the crack initiation was modelled with accuracy, however, afterwards is observed a significant load decay of the numerical curve down to the lower bound, L.B., of the experimental results envelope. This sudden decrease on the numerical response was also observed on the numerical simulations of uniaxial tension tests, however, not with such intensity. Up to a deflection of nearby 0.75 mm the numerical curves arises just below the L.B. of the experimental envelope. After the later deflection, the curve is within the experimental envelope.

Concerning the sudden load decay, in the author opinion, this is ascribed to some limitations of the developed model, beside the adopted simplifications on the procedure for transforming the fibres' load-slip relationship into the fibres' constitutive laws, there is one aspect that was not take into account. In particular, the fact that the fibre slip was assumed equal to the crack width. In the first stage of the fibre pullout, while the fibre's embedded halves are in the debonding phase, the process of fibre debonding starts from both crack surfaces throughout the two embedded halves of the fibre. This stage finishes when the end of the shortest embedded half is reached, afterwards one of the fibre's hooked end is mobilised. Thus, during this debonding stage the slip cannot be assumed equal to the crack width.

On the other hand, the agreement between the numerical curve of the Cf45 series and the experimental results was considerably higher than the observed for the CF30 series. Moreover, the abovementioned load decay was not observed for the numerical simulation of the Cf45 series. Since this series was modelled posteriorly to the Cf30 series and knowing of the model's limitation, it was chosen from the five meshes generated in section 9.2.4 the one with the

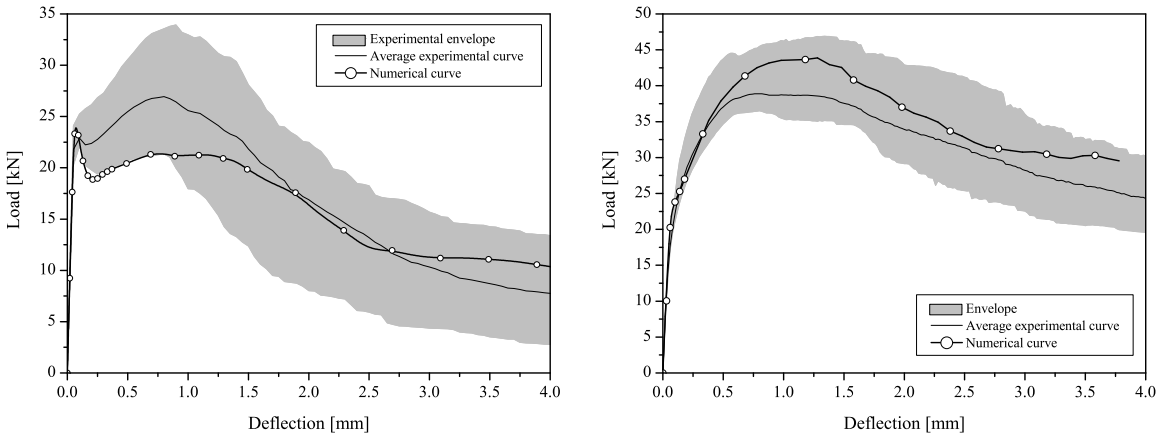

(a) (b)

Figure 9.21: Numerical simulation of the three-point bending tests for: (a) Cf30 and (b) Cf45 series.

highest number of fibres intersecting the mid-span section. Thus, the numerical curve shown in Figure 9.21(b) can be regarded as the upper bound of the numerical envelope if all the fibre meshes generated would been simulated.

9.5 Conclusions

In this chapter was presented a numerical approach for modelling the behaviour of FRC, based upon the micro-mechanical behaviour of the steel fibres. The adopted strategy comprises three main steps: i) assessing the fibre pullout behaviour (micro-level); ii) generation of "virtual" fibre structures (meso-level); and iii) modelling the SFRSCC as a two phase material, in which the concrete phase is modelled with a smeared-crack model, while the fibre phase are ascribed the fibre's positioning and orientation obtained from step ii, whereas the fibre reinforcement mechanisms are modelled with the micro-mechanical behaviour laws obtained in step i.

In what concerns to the fibre meshes generation, the implemented algorithm enabled to model the fibre structure parameters assessed experimentally with good accuracy. When assuming an isotropic uniform random distribution, IURD, for the fibre orientation, the generated meshes underestimated both fibre densities and orientation factors observed experimentally for the prismatic specimens. This may be ascribed to the high flowability of SFRSCC which favours the alignment of fibres according the lengthier dimension of the mould. To overcome this, it was used a non-uniform distribution function for the fibre orientation. The parameters of the latter distribution were fitted using experimental data from the image analysis procedure. The agreement of the numerical results with experimental data increased considerably by using this approach, in particular, the fibre density and orientation factor parameters. Regarding the

cylindric specimens, only IURD was adopted. The numerical fibre density obtained on the "virtual" generated fibre meshes for the Cf45 series was quite proximate of the experimental data. On the other hand, for the Cf30 series, it were not obtained so satisfying results. However, this probably is not related to the fibre generating algorithm, but with an effective smaller fibre content on the cylindric specimens of this series, as the information from the image analysis procedure suggests.

Finally, the numerical finite element simulations of both the uniaxial tension tests and three-point bending tests revealed a very good agreement with the experimental test results. In spite of the model's good performance, the developed model has some limitations, mainly, due to some simplifications adopted during its implementation. Amongst these simplifications, can be extolled the fact of not have been considered a "pure" fibre bond-slip formulation. Instead, it was adopted an indirect procedure for modelling the micro-mechanical behaviour of the fibres. In a general manner, the numerical response after the crack initiation slightly underestimates the experimental responses. This can be ascribed to the adopted procedure for transforming the fibres' load-slip relationship into the fibres' constitutive laws. In addition, the crack width is assumed equal to the fibre slip, which for small crack widths, thus just after the crack initiation stage, may be a rough estimate.

Chapter 10

Conclusions

10.1 General conclusions

The present work has been carried out involving both experimental and analytical/numerical research regarding the behaviour of steel fibre reinforced self-compacting concrete, SFRSCC. The main purpose was to achieve, as much as possible, a consistent comprehension of the behaviour of this composite material, and to collect data for the calibration of the analytical formulations and FEM-based numerical models.

The experimental research covers aspects from distinct scale levels, in which during this work were approached from an increasing scale level point of view. At a micro-level, micro-mechanics aspects were ascertained, i.e. fibre reinforcement mechanisms embraced on the fibre pullout. At second stage, passing through a meso-level, where the fibre distribution structure on the hardened concrete was assessed. The research carried out at a micro/meso-level enables to have a deeper understanding of the multiple reinforcement mechanisms and factors that influences the overall composite behaviour at a macro-level. Finally, at macro-level, the composite mechanical behaviour, namely, compressive, flexural and uniaxial tensile behaviour is assessed. The assessment of the mechanical behaviour of SFRSCC, under different loading conditions, has been limited to the short-term response, i.e. no creep and shrinkage was accounted for.

With the gathered experimental information at the distinct studied scale levels, analytical and numerical tools were developed and their predictive performance was appraised. One of the objectives is to acquire a deeper knowledge of the multiple reinforcement mechanisms involved. In terms of the numerical research, the main goal was the development of an integrated numerical approach that, from a rational and sustainable point of view, was capable of predicting the mechanical properties of fibre reinforced composites, based on the main fibres'

micro-mechanical properties.

10.1.1 Micro-mechanical behaviour

Fibre pullout in CFRC

A preliminary study of the micro-mechanical behaviour of three types of hooked fibres (TYPE A, TYPE B and TYPE C) was carried out in a conventional vibrated fibre reinforced concrete. The results from this study were used to select the fibre type to be used in SFRSCC and to serve as reference when studying the fibre's micro-mechanical behaviour in a SFRSCC medium.

Regarding the pullout performance, the TYPE A and TYPE C fibres, for a 0^o orientation angle, revealed a similar performance, as it was expected, since they are both very similar from the geometrical point of view. When comparing the pullout performance of those two types of fibres, for an orientation angle of 30^o, the dissipated energy of the TYPE A fibres was considerable higher than of the TYPE C, in spite of the maximum pullout load has been quite similar. This difference is ascribed to the distinct failure modes observed for each brand, i.e. fibre pullout for TYPE A and fibre rupture for TYPE C. Hence, the slight difference observed between the tensile strength of TYPE A and TYPE C fibres (nearby 10% higher in TYPE A) influenced considerably the dissipated energy during the pullout process. The pullout response of the fibres with a higher diameter and hook length (TYPE B) has shown, in general, a significantly higher pullout load and dissipated energy, when comparing with the other two brands of smaller diameter. However, in the context of the post-cracking behaviour of a steel fibre reinforced concrete element, it should be noticed that as larger is the number of fibres effectively oriented in terms of a potential crack planes, as higher is the effectiveness of the fibre reinforcement. Therefore the fibre pullout performance is only one of the aspects on the fibre strengthening efficiency.

The fibre to be used in steel fibre reinforced self-compacting concrete was selected based on the pullout performance of each fibre brand. The two types of fibres with similar geometry, in general, exhibited a very similar behaviour. However, the pullout response of the TYPE A fibres was considerably better for an orientation angle of 30^o. Thus, and apart economical aspects, intuitively this fibre was chosen in detriment of the TYPE C fibres.

On the other hand, opting from the TYPE A and TYPE B fibres was not a so straightforward task, since these fibres have distinct geometry dimensions. Hence, assuming a 3D isotropic uniform random distribution of the fibres, it was computed that for the TYPE A fibre there will be approximately 78% more fibres intersecting a certain plane. Therefore, the benefits that the better micro-mechanical behaviour of TYPE B fibre seem to provide can be of smaller significance when compared to the reinforcement benefits derived from the fact that a higher number

of fibres is available when TYPE A fibre is selected. Thus, probably, the overall mechanical behaviour of a composite reinforced with TYPE A fibres will be better than other composite reinforced with TYPE B fibres. For these reasons, the TYPE A fibre was used in the composition of the steel fibre reinforced self-compacting concrete.

Fibre pullout in SFRSCC

In general, two main pullout failures modes were observed during the pullout tests. The complete fibre pullout was observed for aligned hooked fibres and smooth fibres (either aligned or inclined), whereas for inclined hooked fibres the principal failure mode observed was fibre rupture. The relatively high strength and compact concrete matrix would have contributed for the occurrence of the type of failure mode observed in the hooked inclined.

Generally, the maximum pullout load increased linearly with the embedded length for both hooked and smooth fibres. However, this increase was more significant on the smooth fibres, since the pullout response of hooked fibres at a given embedment length is predominantly influenced by the mobilisation and straightening of the hook. Regarding the effect of the orientation angle, the maximum pullout load increased up to a inclination angle of 30°, i.e. from 0° to 30°, and then decreased from 30° to 60° inclination angle. For both hooked and smooth fibres the highest maximum pullout load was observed for an inclination angle of 30°. However, the increase of the maximum pullout load with the inclination angle was more significant on the smooth fibre series. The pullout toughness was computed by integrating the load - slip curve up to slips of 1 and 3 mm, respectively, G_{1mm} and G_{3mm}. In general, as the fibre embedded length increased, the toughness to a given slip also increased. Looking upon the influence of the inclination angle on the toughness, in general, an increase of G_{1mm} was observed up to an inclination angle of 30° followed by a decrease for a 60° angle. On the other hand for the G_{3mm}, two distinct trends were perceived for each the smooth and hooked series. Concerning the smooth series, an increase of G_{3mm} was observed with the orientation angle, while for the hooked series the opposite was observed. The overall toughness was markedly influenced by the type of failure, since fibre fracture significantly reduced the toughness when comparing to fibres that underwent a complete pullout.

Regarding the influence of the matrix type, the inclusion of large amounts of limestone filler in the SFRSCC, in order to attain self-compactability requirements, has an important influence in the fibre/matrix interface properties, namely, bond strength and mobilization of the mechanical anchorage. The principal differences between the pullout responses from SFRSCC and CFRC are during the post-peak stage. These differences arise from distinct grades of the hooked end mobilization and the frictional resistance. The higher strength and compactness of

the SFRSCC matrix enables a better mobilization of the hook, however both the smoothness of the matrix and limestone filler favour the fibre pullout under frictional resistance. The post-peak response of the aligned hooked fibres pulled-out from CFRC specimens had an higher residual pullout strength and toughness than the for SFRSCC. However, for the series with an inclination of 30º, it was not possible to withdraw conclusive remarks, due to the unexpected distinct tensile strengths of the fibres used in each CFCR and SFRSCC compositions.

Analytical model for fibre pullout

The analytical model developed was able to simulate with extreme accuracy the experimental pullout load - slip curves, even for high slips, for both hooked and smooth fibres (aligned or inclined). In the simulation of inclined fibres, the present model neglected the following aspects: bending and plastification of the fibre, spalling of the concrete matrix at the fibre exit point and, finally, the change on the embedded length due to matrix spalling. In spite of the accurateness of the numerical simulation, the coefficients of variation of the bond law parameters were extremely high. This fact can be related to the method used in back-analysis (exhaustive search), since the parameters search is based on a previously defined range and step, i.e. the parameter variables are discrete. Moreover, it was used only one objective function, i.e. difference between the area under the experimental and numerical curves to determine the best fit for each series. A possible way to solve this problem could be the utilisation of a multi-objective function, hence additional study should be performed in order to ascertain the local bond law parameters with a lower coefficient of variation.

10.1.2 Fibre structure at a meso-scale

Within the analysis of the fibre distribution in a self-compacting concrete matrix, it were ascertained some parameters that give an idea of the fibre structure, such as: fibre density, orientation and segregation. The obtained experimental results were compared with results from literature for conventional vibrated fibre reinforced concrete, CFRC, and other concretes with self-compacting ability. The fibre structure analysis was performed in cylindric and prismatic specimens, by means of fibre counting at the fractured surfaces of the specimens, and using an image analysis procedure on sawn sections from the specimens.

Regarding the prismatic specimens, the fibre density and orientation factor were assessed in two orthogonal planes' directions. One plane is parallel (||) to the notched plane (crack surface) of the tested specimens, and the other is perpendicular ($\perp$) to this surface. The fibre density measured for SFRSCC at the parallel planes, $N_f^{||}$, was considerably higher than the expected theoretical fibre density assuming a 3D isotropic uniform random distribution, N_f^{3D}.

In fact, $N_f^{||}$ was between 47% and 66% higher than N_f^{3D}. This effective increase on the fibre density can be ascribed to both the wall-effect and high flowability of the SFRSCC in the fresh state. This effective increase on the fibre density for SFRSCC was higher than for conventional SFRC. This was to some extent expected, if having in mind that an eventual effective increase for conventional SFRC can only be justified by the wall-effect, abnormal high vibration or a poor fibre dispersion, i.e. fibre bundles at the measured sections. In what concerns to the fibre orientation factor similar findings can be pointed out. In fact, the difference between the measured fibre density and the correspondent expected one for SFRSCC is due to an increase of the average orientation factor, consequence of a fibre alignment along the concrete's flow direction. The degree of fibre segregation due to gravity effect on the SFRSCC was slightly smaller than the fibre segregation of CFRC.

For the cylindric specimens, both the fibre density and orientation factor were much closer to the expected theoretical values assuming a 3D isotropic random distribution, when comparing with the results obtained in the prismatic specimens. However, in general, the experimental fibre density was smaller than the theoretical one for a 3D random distribution.

At last, epitomizing, the fibre structure parameters assessed for the prismatic and cylindric specimens shown that there are considerable differences on their fibre structure. The differences on the fibre effectiveness found for each type of specimen, due to distinct geometries of the mould and casting procedures, will lead to distinct mechanical performance of the composite. The knowledge of how the fibre orientates within certain test specimens (e.g. cylindric - uniaxial tension tests; prismatic - three-point bending tests) enables a better understanding of the post-cracking behaviour derived from each experimental test.

10.1.3 Mechanical behaviour of SFRSCC

Compressive behaviour

An experimental programme was carried out to evaluate the influence of the fibre content and concrete age on the compressive behaviour of steel fibre reinforced self-compacting concrete, SFRSCC. The main mechanical properties of the SFRSCC, such as: the compressive strength, f_{cm}, the elasticity modulus, E_{ci}, strain at peak stress, ε_{c1} and the volumetric dissipated energy, G_c, were assessed for the ages of 12 hours, 24 hours, 3, 7 and 28 days. Two distinct contents of fibres were considered, 30 kg/m^3 and 45 kg/m^3.

The increase of the compressive strength and the elasticity modulus was quite pronounced up to 3 days. Increasing the fibre content from 30 kg/m^3 to 45 kg/m^3, in general, conducted to a decrease of f_{cm} and E_{ci}. This might be justified by the increase of the water/cement ratio and percentage of limestone filler, as well as the changes introduced in the solid skeleton from

Cf30 to Cf45 series, in order to assure self-compacting requirements with the increase of the fibre content. More research in this field should be done to get more clear evidences of these aspects.

In general, the energy dissipated under compression, G_c, increased with age. However, it was not observed a significant change with the increment of the fibre content, from 30 kg/m^3 to 45 kg/m^3. Some series presented a lower value of G_c than it was expected. This can be justified with the number of fibres found on the rupture surface of these specimens. For the series of 3, 7 and 28 days the failure mode was exclusively by shear.

Analytical expressions to predict the most significant mechanical properties of the developed SFRSCC at an age t were presented. A stress-strain relationship was proposed to model the behaviour of the SFRSCC since the early ages. This relation was capable of modelling the complete compressive behaviour of SFRSCC with a high accuracy.

Post-cracking behaviour

The post-cracking behaviour of steel fibre reinforced self-compacting concrete was assessed by three distinct tests (uniaxial tension, UTT, three-point bending, 3PBT, and splitting, SPLT) for two compositions with distinct fibre contents, either 30 and 45 kg/m^3, Cf30 and Cf45, respectively.

The increase of the fibre content enhanced considerably the concrete's post-cracking residual strength. Nevertheless, this was not ascribed just to the fibre content increase, since, for the series with 30 kg/m^3, fibre rupture during the post-cracking behaviour has occurred more often, due to a relatively higher resistant matrix and smaller number of fibres. Hence, the post-cracking behaviour of the Cf30 series can be considerably improved by changing the type of fibre used. Therefore, a fibre of higher tensile strength would be more suitable to these stiffer matrices since fibre rupture will be prevented. Selecting a fibre of higher aspect ratio is another possibility, since higher number of fibres will be available per concrete volume. However, the use of a fibre of distinct geometrical characteristics demands the development of a new composition, since SFRSCC mix design optimization should take into account the characteristics of the fibre.

The tri-linear post-cracking relationships applied in the simulation of the three point bending tests have shown to be capable of describing the load - deflection curves rather well, even for large deflection levels. In addition, the peak load was also predicted with accuracy. The inverse analysis was conducted for distinct deformation levels, namely up to 4 and 9 mm, and revealed that, for a large deflection at mid span (9 mm), the ultimate crack opening value estimated is probably incorrect, hence leading to incorrect estimation of the fracture energy.

When comparing the $\sigma - w$ relationships acquired from the indirect tests (3PBT and SPLT)

with the uniaxial tension $\sigma - w$ response a huge discrepancy was observed. This difference was ascribed to the distinct fibre distributions within the specimens used for the different tests. Using a ratio computed based on the fibre effectiveness factor for each type of specimen, a good agreement was observed in both series. Nevertheless, for the Cf45 series this corrective factor still was not enough to assure a good approximation, which could be related to the energy dissipation outside the primary crack, hence overestimating the real post-cracking behaviour.

10.1.4 FEM model with short discrete embedded fibres for FRC

A rather innovative numerical approach was used for modelling the mechanical behaviour of FRC. This model was based upon the micro-mechanical behaviour of the steel fibres. The adopted strategy comprises three main steps: i) assessing the fibre pullout behaviour (micro-level); ii) generation of "virtual" fibre structures (meso-level); and iii) modelling the SFRSCC as a two phase material, in which the concrete phase is modelled with a smeared crack model and the fibre phase deals with the fibre's positioning and orientation obtained from step ii. The fibre reinforcement mechanisms are modelled with the micro-mechanical behaviour laws obtained in step i.

In what concerns to the fibre meshes generation, the implemented algorithm enabled to model the fibre structure parameters assessed experimentally with good accuracy. When assuming an isotropic uniform random distribution, IURD, for the fibre orientation, the generated meshes underestimated both fibre densities and orientation factors observed experimentally for the prismatic specimens. This may be ascribed to the high flowability of SFRSCC, which favours the alignment of fibres according the lengthier dimension of the mould. To overcome this, a non-uniform distribution function was used for the fibre orientation. The parameters of this distribution were fitted using experimental data from the image analysis procedure. The agreement of the numerical results with experimental data increased considerably by using this approach, in particular, when adopted the fibre density and orientation factor parameters. Regarding the cylindric specimens, only an IURD was adopted. The numerical fibre density obtained on the "virtual" generated fibre meshes for the Cf45 series was quite proximate from the experimental data. On the other hand, for the Cf30 series it was not obtained so satisfying results. However, probably, this is not related to the fibre generating algorithm, but with an effective fibre content reduction in the cylindric specimens of this series, as the information from the image analysis procedure suggests.

Finally, the numerical finite element simulations of both the uniaxial tension tests and three-point bending tests revealed a very good agreement with the experimental test results. In spite of the model's good performance, the developed model has some limitations, mainly, due to

some simplifications assumed during the implementation. Amongst these simplifications, it can be extolled the fact that instead of having considered a "pure" fibre bond - slip formulation it was adopted an indirect procedure for modelling the micro-mechanical behaviour of the fibres. In a general manner, the numerical response after the crack initiation slightly underestimates the experimental responses, which can be ascribed to the adopted procedure to transform the fibres' load - slip relationship into the fibres' constitutive laws. In addition, the crack width is assumed equal to the fibre slip, which for small crack widths, thus just after the crack initiation stage, may be a rough estimate.

10.2 Recommendations for future research

Research is a torturous and long-term process, since rarely from the obtained results can be unfold or perceived definitively conclusions and often lead to further stages of experimental/numerical investigation. This work is not an exception, even though it provides some answers and a rather innovative modelling approach for fibre reinforced concretes, also yields a number of new questions that should be assessed with further investigation. The main goal when developing/studying rather new materials is to promote their utilization into new applications, whereas establishing them in the building industry. Moreover, it is also intended to push through the available knowledge, so that new materials could be covered within the scope of design guidelines and recommendations. Regarding these aspects, the studied steel fibre reinforced self-compacting concrete was successfully employed in pre-casting industry, in particular, in the fabrication of light-weighted façade panels.

In the present work, the assessment of the mechanical behaviour of SFRSCC, under different loading conditions, has been limited to the short-term response. So in a more abroad sense, this study should be extended to cyclic behaviour, since few research is available for this kind of fibre reinforced composites. Moreover, the knowledge of the behaviour of SFRSCC structures during their service life is also scarce, and therefore is an interesting area that should be investigated. Hence, more research on durability, shrinkage, fire resistance and fatigue of SFRSCC is recommended.

Regarding the further developments, that directly have arisen from the investigation carried in this work, the following points are recommended for future research:

- **Micro-mechanical behaviour of fibres**

  i) Assessment of the pullout behaviour under cyclic and fatigue loading conditions;

  ii) Assessment of the pullout behaviour for distinct confinement conditions, since in a structural element, very rarely it's subjected to a pure uniaxial tensile loading state;

iii) A further optimization of the hooked end fibre to be used in SFRSCC should be conducted, in particular, the use of fibres with high strength, i.e. with high carbon content;

iv) Depending on the grade of the fibre pullout mobilization of hooked fibres, it should also be assessed the employment of other mechanical deformed fibres, e.g. crimped, in order to take advantage of both the high strength and compactness of the SFRSCC matrices;

v) Regarding the analytical modelling of fibre's pullout behaviour, the presented model should be enhanced, in particular, for inclined fibres. Thus, it should be comprised the variation of the embedded length due to matrix spalling.

- **Fibre structure**

i) Development of empirical/analytical relations between the rheology of the fresh SFRSCC mixtures and properties of fibre structure within structural elements made by this material. If this is achieved, then the rheology of the fresh SFRSCC mixture can be correlated with the mechanical properties of a structural element;

ii) More investigation on the orientation of fibres in different types of structural elements is required (beams, plates, shells, columns), and for different casting procedures;

iii) Development and implementation of computational models able to predict the fibre dispersion and orientation, based upon rheological parameters, concrete's flow direction and mould geometry.

- **Stress - crack relationship ($\sigma - w$)**

i) Further investigation should be conducted on the assessment of the $\sigma - w$ law, especially, within the indirect test methods. The $\sigma - w$ is not a pure material property but more a structural material property, since it depends on specimens' boundary conditions (size, shape), way of manufacturing (mixture composition, wall effects, casting direction) and loading conditions;

ii) Development of a more reliable inverse analysis method for obtaining the $\sigma - w$ law from indirect tests. Other optimization methods, such as genetic or evolutive algorithms, should be checked. Moreover, multi-objective error functions should be used.

- **Mechanical behaviour**

i) The mechanical behaviour for the SFRSCC should be further assessed, now, for new compositions using an enhanced fibre material/geometry optimization;

ii) Study of the SFRSCC mechanical behaviour under shear. For that is important a rational assessment of the shear fracture mode (Mode II). This fracture mode should be assessed for distinct crack-openings, since the referred mode cannot be dissociated from a pure tensile fracture mode (Mode I);

iii) Assessment of the SFRSCC behaviour performance on large scale elements.

- **FEM model with short discrete embedded fibres for FRC**

i) Further appraisal of the developed model performance, in particular, within the behaviour's numerical simulation of either large scale specimens and with distinct geometries;

ii) Development of a "pure" fibre bond - slip formulation instead of the adopted indirect procedure for modelling the micro-mechanical behaviour of the fibres;

iii) Incorporation of the model within the scope of other non-classical finite element method formulations, such as: strong embedded discontinues or extended finite elements. Probably, this will be mandatory for an accurate simulation of the behaviour of specimens under mixed fracture modes.

Chapter 11

References

Abdalla H. and Karialloo B. (2003). Determination of size independent specific fracture energy of concrete from three-point bending tests and wedge splitting tests. *Magazine of Concrete Research*, 55(2), 133–141.

ACI Committee 544 (1988). Measurement of properties of fiber reinforced concrete. *ACI Materials Journal*, pages 583–593.

ACI 318-R (1993). *ACI Manual of concrete practice*. American Concrete Institute.

ACI 544.1R-96 (1996). State-of-the-art report on fiber reinforced concrete. Technical report, American Concrete Institute.

Alwan J.M., Naaman A.E., and Guerrero P. (1999). Effect of mechanical clamping on the pull-out response of hooked steel fibers embedded in cementicious matrices. *Concrete Science and Engineering RILEM*, 1(1), 15–25.

ASTM C469 (1994). Standard test method for static modulus of elasticity and poisson's ratio of concrete in compression. *Annual Book of ASTM Standards, American Society of Testing Materials*, 4(2), 241–244.

ASTM A820-90 (1990). Standard specification for steel fibres for fibre reinforced concrete. Technical report, American Concrete Institute, Detroit, USA.

ASTM C1018-89 (1991). Standard test method for flexural toughness and first-crack strength of fiber-reinforced concrete (using beam with third-point loading). Book of ASTM standards: Part 04.02, American Society for Testing and Materials, Philadelphia.

ASTM C496-90 (1991). Standard test method for splitting tensile strength of cylindrical concrete specimens. In *Annual Book ASTM Standards 4 (04.02)*, pages 266–269.

Azevedo A.F.M., Barros J.A.O., Sena-Cruz J.M., and Gouveia A.V. (2003). Software in structural engineering education and design. In *III Portuguese-Mozambican Conference of Engineering*, pages 81–92.

Babut R. (1986). Structural investigation of steel fibre reinforced concrete. In *Heron - Fracture mechanics and structural aspects of concrete*, volume 31, pages 29–44. Delft, Netherlands.

Balaguru P.N. and Shah S.P. (1992). *Fiber Reinforced Cement Composites*. McGraw-Hill Inc, New York.

Banholzer B., Brameshuber W., and Jung W. (2005). Analytical simulation of pull-out tests - the direct problem. *Cement & Concrete Composites*, 27, 93–101.

Banthia N. and Trottier J. (1991). Deformed steel fiber cementicious matrix bond under impact. *Cement and Concrete Research*, 21(1), 158–168.

Banthia N. and Trottier J. (1992). Micromechanics of steel pull-out, rate sensitivity al very low temperatures. *Cement and Concrete Composites*, 14, 119–130.

Banthia N. and Trottier J. (1994). Concrete reinforced with deformed steel fibers, Part I: Bond – slip mechanisms. *ACI Materials Journal*, 91(5), 435–446.

Barr B.I.G., Lee M.K., Hansen E., Dupont D., Schaerlaekens E.E.S., Schnütgen B., Stang H., and Vandewalle L. (2003). Round-robin analysis of the RILEM TC 162-TDF beam bending test: Part 3 – fibre distribution. *Materials and Structures*, 36(263), 631–635.

Barragán B.E. (2002). *Failure and Toughness of Steel Fiber Reinforced Concrete under Tension and Shear*. Ph.D. thesis, Universitat Politecnica de Catalunya, Barcelona, Spain.

Barros J. and Antunes J. (2003). Experimental characterization of the flexural behaviour of steel fibre reinforced concrete according to RILEM TC 162-TDF recommendations. In B. Schnütgen and L. Vandewalle, editors, *Test and design methods for steel fibre reinforced concrete – background and experiences*, pages 77–89. Bochum, Germany.

Barros J.A.O. (1995). *Comportamento do betão reforçado com fibras, análise experimental e simulação numérica*. Ph.D. thesis, Faculdade de Engenharia da Universidade do Porto, Portugal (in Portuguese).

Barros J.A.O., Antunes J.A.B., and Amorim J.A.S.B.A. (2002). Influência da quantidade de fibras, percentagem de cinzas volantes e idade no comportamento à flexão de betão reforçado com fibras de aço Dramix RC-80/60-BN (in portuguese). Technical report, 02-DEC/E-11, University of Minho, Portugal.

Barros J.A.O., Cunha V.M.C.F., Ribeiro A.F., and Antunes J.A.B. (2005). Post-cracking behaviour of steel fibre reinforced concrete. *Materials and Structures*, 38(1), 47–56.

Bartos P.J.M. (1981). Bond in fibre reinforced cement and concretes. *The International Journal of Cement Composites*, 3(3), 159–177.

Bartos P.J.M. and Duris M. (1994). Inclined tensile strength of steel fibres in a cement-based composite. *Composites*, 25(10), 945–952.

Bazant P.Z. and Planas J. (1998). *Fracture and size effect in concrete and other quasibrittle materials*. New directions in Civil Engeneering, CRC Press, Boca Raton, Florida.

Bazant Z. and Gambarova P. (1980). Rough cracks in reinforced concrete. *ASCE Journal of Structural Division*, 106(4), 819–842.

Bazant Z.P. and Pfeiffer P.A. (1987). Determination of fracture energy from size effect and brittleness number. *Cement Concrete Composites*, 84(6), 463–480.

Beaumont P.W.R. and Aleska J.C. (1978). Cracking and toughning of concrete and polymer concrete dispersed with short steel wires. *Journal of Materials Science*, 13(8), 1749–1760.

Bentur A. and Mindess S. (1990). *Fibre reinforced cementitious composites*. Elsevier Applied Science, London.

Bhatt P., Barj M.S., Elnounu G.F., and Memon M. (1989). Non-linear finite element analysis of shearwall-floor slab junction. In D.R. Owen and E. Hinton, editors, *Second International Conference on Computational Plasticity*, pages 1319–1330. Swansea, Wales.

Bindiganavile V. and Banthia N. (2001). Polymer and steel fiber-reinforced cementicious composites under impact loading - Part 1: Bond slip response. *ACI Materials Journal*, 98(1), 10–16.

Bolander J.E. (2004). Numerical modelling of fibre reinforced cement composites: linking material scales. In M. Prisco, R. Felicetti, and G. Plizzari, editors, 6^{th} *RILEM Symposium on Fibre Reinforced Concretes*, pages 45–60. Varenna, Italy.

Brandt A.M. (1985). On the optimal direction of short metal fibres in britle matrix composites. *Journal of Materials Science*, 20, 3835–3841.

Brühwiler E. and Wittman F. (1990). The wedge splitting test, a new method of performing stable fracture mechanics tests. *Engineering Fracture Mechanics*, 35, 117–125.

BS 1981:Part 117 (1983). *Testing concrete method for determination of tensile splitting strength.* British Standard Institute.

Camões A.F.F. (2002). *Betões de elevado desempenho com incorporação de cinzas.* Ph.D. thesis, Escola de Engenharia da Universidade do Minho (in Portuguese).

Campbell D. and Folk R. (1991). The ancient pyramids - concrete or rock? *ACI Concrete International*, 13(8), 28–39.

Carpinteri A., Chiaia B., and Cornetti P. (2002). A scale-invariant cohesive crack model for quasi-brittle materials. *Engineering Fracture Mechanics*, 69(2), 207–217.

Carreira D.J. and Chu K.H. (1985). Stress-strain relationship for plain concrete in compression. *ACI journal*, 82(6), 797–804.

Casanova P. (1996). *Bétons renforcés de fibres métalliques du materiau à la structure.* Ph.D. thesis, Ecole nationale dês Ponts et Chaussées (in French).

Cattaneo S. and Rosati G. (1997). Effect of different boundary conditions in direct tensile tests: Experimental results. *Magazine of Concrete Research*, 51(5), 365–374.

CEB-FIP (1993). CEB-FIP Model Code 1990: Design code. Ceb bulletin d'information no. 190, CEB-FIP Comité Euro-International du Béton, Paris, France.

Chandra S. (2002). *Properties of concrete with mineral and chemical admixtures.* Spon Press, London.

Chang T.Y., Taniguchi H., and Chen W.F. (1987). Non-linear finite element analysis of reinforced concrete beams. *Journal Structural Engineering ASCE*, 113(1), 122–140.

Chanvillard G. (1993). *Analyse expérimentale et modelisation micromécanique du comportament des fibres d'acier tréfilées, ancrées dans une matrice cimentaire.* Ph.D. thesis, Laboratoire Central de Ponts et Chaussées.

Chanvillard G. and Aïtcin P.C. (1996). Pull-out behavior of corrugated steel fibers (qualitative and statical analysis). *Advanced Cement Based Materials*, 4, 28–41.

Cominoli L., Medal A., and Plizarri A. (2007). Fracture properties of high-strength hybrid fiber-reinforced concrete. In C.U. Grosse and S. Hans-Wolf Reinhardt, editors, *Advances in Construction Materials*, pages 323–332.

Cornelissen H.A.W., Hordijk D.A., and Reinhardt H.W. (1986). Experimental determination of crack softening characteristics of normal and lightweight concrete. *HERON, Fracture Mechanics and Structural Aspects of Concrete*, 31(2), 45–56.

Cunha V.M.C.F. (2004). *Experimental and Numerical Analysis of Steel Fibre Reinforced Concrete under tension, "Análise experimental e numérica do comportamento à tracção de betão reforçado com fibras de aço"*. Master's thesis, Universidade do Minho, Guimarães, Portugal (in Portuguese).

D'Aloia G.C.L. (1997). Concrete strength estimation at early ages: Modification of the method of equivalent age. *ACI Materials Journal*, 94(6), 520–530.

de Borst R. and Nauta P. (1985). Non-orthogonal cracks in smeared finite element model. *Engineering Computations Journal*, 2, 35–46.

Diamond S. and Huang J. (2001). The itz in concrete - a different view based on image analysis and sem observations. *Cement and Concrete Composites*, 23(2-3), 179–188.

Dick-Nielsen L., Stang H., and Poulsen P.N. (2007). Micro-mechanical analysis of fibre reinforced cementicious composites. *Journal of Advance Concrete Technology*, 5(3), 373–382.

Dupont D. (2003). *Modeling and experimental validation of the constitutive law ($\sigma - \epsilon$) and cracking behaviour of steel fibre reinforced concrete*. Ph.D. thesis, Department of Civil Engineering, Catholic University of Leuven, Belgium.

Eberhardt C. and Clarke A. (2001). Fibre-orientation measurements in short-glass-fibre composites. part i: automated, high-angular-resolution measurement by confocal microscopy. *Composites Science and Technology*, 61, 1389–1400.

Elices M. and Planas J. (1992). Size efect in concrete structures: in r-curve aproach. In Chapman and Hall, editors, *Analisys of Concrete Structures by fracture Mechanics*, pages 99–127. London.

Eligehausen R., Popov E.P., and Bertero V. (1983). Local bond stress-slip relationships of deformed bars under generalized excitations. Technical report, Report No. UCB/EERC-83/23, Earthquake Engineering Research Center, College of Engineering, University of California, Berkeley, California, US, 162 pp.

Elwi A. and Hurdey M. (1989). Finite element model for curved embedding reinforcement. *Journal Engineering Mechanics ASCE*, 115(4), 740–757.

EN 14651 (2005). *Test method for metallic fibered concrete - Measuring the flexural tensile strength (limit of proportionality (LOP), residual)*. European Committee for Standardization, Brussels.

EN 1992-1-1 (2004). *Eurocode 2: Design of concrete structures – Part 1 – 1: General rules and rules for buildings*. European Committee for Standardization, Brussels.

Ezeldin A.S. and Balaguru P.N. (1992). Normal and high strength fiber reinforced concrete under compression. *Journal of Materials in Civil Engineering*, 4(4), 415–427.

Fanella D. and Naaman A. (1985). Stress-strain properties of fiber reinforced mortar in compression. *ACI Journal*, 82(4), 475–483.

Farhat F.A., Nicolaides D., Kanellopoulos A., and Karihaloo B.L. (2007). High performance fibre-reinforced cementitious composite (CARDIFRC) performance and application to retrofitting. *Engineering Fracture Mechanics*, 74, 151–167.

Ferrara L. and Meda A. (2006). Relationships between fibre distribution, workability and the mechanical properties of sfrc applied to precast roof elements. *Materials and Structures*, 39(5), 411–420.

Ferrara L., Dozio D., and di Prisco M. (2007). On the connections between fresh state behavior, fiber dispersion and toughness properties of steel fiber reinforced concrete. In A. Naaman and H. Reinhardt, editors, 5^{th} *International RILEM workshop on high performance fiber reinforced cement composites*, pages 249–258. Mainz, Germany.

Ferrara L., di Prisco M., and Khurana R. (2008). Tailoring optimum performance for the structural use of self consolidating sfrc. In R. Gettu, editor, *Sevnth. Intnl. RILEM Symposium on Fibre Reinforced Concrete: Design and Applications*, pages 739–750. Chennai, India.

Fib TG-8.3 (2007). *Fib Model Code 2007: Fibre reinforced concrete*. (draft version), Lausanne, Swiss.

Focacci F., Nanni A., and Bakis C. (2000). Local bond-slip relationship for FRP reinforcement in concrete. *Journal of Composites for Construction ASCE*, 4(1), 24–31.

Franchois A., Taerwe L., and van Damme S. (2004). A microwave probe for non-destructive determination of steel fiber content in concrete slabs. In M. di Prisco, editor, *Fourth Intnl. RILEM Symposium on Fiber Reinforced Concrete*, pages 249–256. Varenna, Italy.

Gentle J.E. (1998). *Statistics and Computing: Random Number Generation and Monte Carlo Methods*. Springer, New York, USA.

Gettu R., Gardner D.R., Saldívar H., and Barragán B.E. (2005). Study of the distribution and orientation of fibers in sfrc specimens. *Materials and Structures*, 38(1), 31–37.

Gokoz U.N. and Naaman A.E. (1981). Effect of strain rate on the pullout behaviour of fibres in mortar. *International Journal of Cement Composites and Lighweight Concrete*, 3(3), 187–202.

Gopalaratnam V. and Shah S.P. (1987). Failure mechanisms and fracture of fiber reinforced concret. In A. SP-105, editor, *Fiber Reinforced Concrete Properties and Applications*, pages 1–25. Oslo, Norway.

Gray R.J. (1984). Analysis of the embedded fibre length on fibre debonding and pull-out from an elastic matrix - Part 1: Review theories. *Journal of Materials Science*, 10(3), 861–870.

Grünewald S. (2004). *Performance-based design of self-compacting fibre reinforced concrete*. Ph.D. thesis, Delft University, Netherlands.

Grünewald S. and Walraven J.C. (2003). Self-compacting fibre reinforced concrete - orientation effect of steel fibres in large beams. In *Workshop - Design rules for steel fibre reinforced concrete structures*, pages 107–113. Oslo, Norway.

Groth P. (2000). *Fibre reinforced concrete - Fracture mechanics methods applied on self-compacting concrete and energetically modified binders*. Ph.D. thesis, Department of Civil and Mining Engineering, Lulea University of Technology, Sweden.

Guererro P. and Naaman A.E. (2000). Effect of mortar fineness and adhesive agents on pullout response of steel fibres. *ACI Materials Journal*, 97(1), 12–20.

Guinea G.V., Planas J., and Elices M. (1992). Measurement of the fracture energy using three-point bend tests: 1. influence of experimental procedures. *Materials and Structures*, 25, 212–218.

Gustafsson P.J. and Hillerborg A. (1985). Improvements in concrete design achieved through application of fracture mechanics. In *Application of fracture mechanics to cementitious composites. NATO Advanced Research Workshop*, pages 639–680. Evanston, USA.

Gysel A.V. (1999). A pullout model for hooked end steel fibres. In RILEM, editor, *HPFRCC3 - High performance fiber reinforced cement composites*, pages 351–359. Mainz, Germany.

Hackman L., Farrell M., and Dunham O. (1992). Slurry infiltrated mat concrete - SIMCON. *ACI Concrete International*, 14(10), 53–56.

Hannant D.J. (1987). *Fibre cements and fibre concretes*. John Wiley & Sons, Chischester.

Hauser S. and Worner J. (1999). Ducon, a durable overlay. In H. Reinhardt and A. Naaman, editors, *High Performance Cementitious Composites - HPFRCC 3*, pages 603–615. RILEM Publications S.A.R.L.

Hegger J., Rauscher S., Lange J., and Zell M. (2008). Fibre orientation in ultra-high performance concrete. In *Seventh International. RILEM Symposium on Fibre Reinforced Concrete: Design and Applications*, pages 191–199. Chennay, India.

Helfet J. and Harris B. (1972). Fracture toughness of composites reinforced with discontinous fibres. *Journal of Materials Science*, 7(5), 494–498.

Hillerborg A. (1980). Analysis of fracture by means of the fictitious crack model, particularly for fibre reinforced concrete. *International Journal Composites Cements*, 2(4), 177–184.

Hillerborg A. (1989). Stability problems in fracture mechanics testing. In *Fracture of Concrete and Rock: Recent Developments, Elsevier Applied Science*, pages 369–378.

Hing P. and Groves G. (1972). The strength and fracture toughness of polycristalline magnesium oxide containing metallic particles and fibers. *Journal of Materials Science*, 7(4), 427–434.

Homrich J. and Naaman A. (1987). Stress-strain properties of sifcon in compression. In u. SP 105, editor, *Fiber Reinforced Concrete Properties and Applications*, pages 283–304. Oslo, Norway.

Hordijk D. (1991). *Local Approach to Fatigue of Concrete*. Ph.D. thesis, Delft University of Technology, Netherlands.

Hoy C.W. (1998). *Mixing and mix proportioning of fibre reinforced concrete*. Ph.D. thesis, Department of Civil , Structural and Environmental Engineering, University of Paisly, Scotland.

Hughes B.P. and Fattuhi N.I. (1975). Fiber bond strengths in cement and concrete. *Magazine of Concrete Research*, 27(92), 161–166.

ISO 4108-1980 (1980). *Concrete determination of tensile splitting strength of test specimen*. International Standards.

Jin X. and Li Z. (2000). Investigation on mechanical properties of young concrete. *Materials and Structures*, 33(10), 627–633.

JSCE – SF4 (1984). Part III - 2 method of tests for steel fiber reinforced concrete. *Concrete Library of Japanese Society of Civil Engineers*, 3, 74.

Kabele P. (2000). Assessment of structural performance of engineered cementitious composites by computer simulation. Technical report, Proofs for the appointment as an Associate Professor, Czech Technical University, Prague.

Kamerwara Rao C.V.S. (1979). Effectiveness of random fibres in composites. *Cement and Concrete Research*, 9, 685–693.

Kanda T. and Li V.C. (2006). Practical design criteria for saturated pseudo strain hardening behavior in ecc. *Journal of Advanced Concrete Technology*, 4(1), 59–72.

Kasperkiewicz J., Malmberg B., and Skarendahl A. (1978). Determination of fibre content, distribution and orientation in steel fibre concrete by x-ray technique. In *Proceedings RILEM Syposium. Testing and test methods of fibre cement composites*, pages 297–314. Sheffield.

Kelly A. and Sweben C. (1976). Poison effects in aligned fibre composites showing pull-out. *Journal of Materials Science Letter*, 11(3), 583–586.

Kim J.K., Han S.H., and Lee K.M. (2000). Estimation of compressive strength by new apparent activation energy function. *Cement and Concrete Research*, 31, 217–225.

Kitsutaka Y. (1997). Fracture parameters by polylinear tension-softening analysis. *Journal of Engineering Mechanics*, 123(5), 444–450.

Kjellsen K. and Detwiler R. (1992). Reaction kinetics of portland cement mortars hydrated at different temperatures. *Cement and Concrete Research*, 22(11), 112–120.

Kodur V.K.R. and Bisby L.A. (2005). Evaluation of fire endurance of concrete slabs reinforced with fiber-reinforced polymer bars. *Journal of Structural Engineering*, 131(1), 34–43.

Kooiman A.G. (2000). *Modelling Steel Fibre Reinforced Concrete for Structural Design*. Ph.D. thesis, TU Delft, Netherlands.

Krenchel H. (1975). Fibre spacing and specific fibre surface. In *RILEM Symposium: Fibre Reinforced Cement and Concrete*, volume 1, pages 69–79. Horneby, Lencaster.

Kreyszig E. (1993). *Advanced Engineering mathematics*. John Wiley & Sons, Inc.

Kurihara N., Kunieda M., Kamada T., Uchida Y., and Rokugo K. (2000). Tension softening diagrams and evaluation of properties of steel fiber reinforced concrete. *Engineering Fracture Mechanics*, 65(2-3), 235–245.

L. S. Hsu and C. T. Hsu (1994). Stress – strain behavior of steel-fiber high strength concrete. *ACI Structural Journal*, 91(4), 448 – 457.

Lancaster L.C. (2005). *Concrete Vaulted Construction in Imperial Rome - Innovations in Context*. Cambridge University Press, New York, USA. ISBN 978-0-521-84202-0.

Lappa E.S. (2007). *High strength fibre reinforced concrete - static and fatigue behaviour in bending*. Ph.D. thesis, Delft University of Technology, Netherlands.

Lawrence P. (1972). Some theoretical considerations of fibre pull-out from an elastic matrix. *Journal of Materials Science*, 7(1), 1–7.

Laws V., Lawrence P., and Nurse R. (1972). Reinforcement of britle matrices by glass fibers. *Journal of Physics: D Applied Physics*, 6, 523–537.

Leite J.P.B., Slowik V., and Mihashi H. (2004). Computer simulation of fracture processes of concrete using mesolevel models of lattice structures. *Cement and Concrete Research*, 34(6), 1025–1033.

Leung C. (1996). Design criteria for pseudo ductile fiber-reinforced composites. *Journal of Engineering Mechanics*, 122(1), 10–18.

Leung C.K.Y. and Geng Y. (1995). Effect of lateral stresses on fiber debonding pull-out. *J. Compos. Eng.*, 5(10-11), 1331–1348.

Leung C.K.Y. and Geng Y.P. (1998). Micromechanical modeling of softening behaviour in steel fibre reinforced cementicious composites. *Int. Journal Solids Strucutres*, 35(32), 4205–4222.

Leung C.K.Y. and Li V. (1992). Effect of fiber inclination on crack bridging stress in brittle fiber reinforced brittle matrix composites. *Journal of Mechanics and Physics of Solids*, 40(6), 1333–1362.

Löfgren I., Stang H., and Olesen J.F. (2008). The WST method, a fracture mechanics test method for frc. *Materials and Structures*, 41, 197–211.

Li V. and Leung C. (1992). Steady state and multiple cracking of short random fiber composites. *ASCE Journal of Engineering Mechanics*, 188(11), 2246–2264.

Li V. and Wu H. (1992). Conditions for pseudo strain-hardening in fiber reinforced brittle matrix composites. *Journal of Applied Mechanics Review*, 45(8), 390–398.

Li V.C. (1992). Postcrack scaling relations for fiber reinforced cementicious composites. *ASCE Journal of Materials in Civil Engineering*, 4(1), 41–57.

Li V.C. and Chan Y.W. (1994). Determination of interfacial debond mode for fiber-reinforced cementitious composites. *ASCE Journal of Engineering Mechanics*, 120(4), 707–719.

Li V.C. and Maalej M. (1996). Toughening in cement based composites. part i: cement, mortar and concrete. *Cement Concrete Composites*, 18, 223–237.

Li V.C. and Stang H. (1997). Interface pproperty characterisation and strengthening mechanisms in fibre reinforced cement based composites. *Advanced Cement Based Composites*, 6, 1–20.

Li V.C., Wang Y., and Backer S. (1990). Effect of inclining angle, bundling, and surface treatment on surface treatment on synthetic fiber pull-out from a cement matrix. *Composites*, 21(2), 132–140.

Li V.C., Wang Y., and Baker S. (1991). A micromechanical model of tension softening and bridging toughning of short random fiber reinforced britle matrix composites. *J. Mech. Phys. Solids*, 39(5), 607–625.

Lim T., Paramasivam P., and Lee S. (1987). Analytical model for tensile behavior of steel-fibre concrete. *ACI Materials Journal*, 84(4), 286–298.

LNEC E397 (1993). Betões – determinação do módulo de elasticidade em compressão. Technical report, Laboratório Nacional de Engenharia Civil, Lisboa (in Portuguese).

Lorenzis L.D., Rizzo A., and Tegola A.L. (2002). A modified pull-out test for bond of near-surface mounted frp rods in concrete. *Journal of Composites Part B: Engineering*, 33(8), 589–603.

Maage M. (1977). Interaction between steel fibres and cement-based matrices. *Materials and Structures, Research and Testing* (RILEM), 10(59), 297–301.

Maalej M., Li V.C., and Hashida T. (1995). Effect of fiber rupture on tensile properties of short fiber composites. *ASCE Journal of Engineering Mechanics*, 121(8), 903–913.

Markovic I. (2006). *High-Performance Hybrid-Fibre Concrete - Development and utilization.* Ph.D. thesis, Delft University, Netherlands.

Marsaglia G. (2003). Random number generators. *Journal of Modern Applied Statistical Methods*, 2(1), 2–13.

Matsumoto M. and Nishimura T. (1998). Mersenne twister: A 623-dimensionally equidistributed uniform pseudorandom number generator. *ACM Transactions on Modelling and Computer Simulations*, 8(11), 3–30.

Mier J.V. (1984). *Strain-softening of concrete under multiaxial loading conditions.* Ph.D. thesis, University of Delft, Neatherland.

Mindess S., Young J.F., and Darwin D. (2003). *Concrete.* Pearson Education, Inc., NJ, USA. ISBN 0-13-064632-6.

Montgomery D.C. and Runger G.C. (1994). *Applied statistics and probability for engineers.* John Wiley & Sons, Inc., Ney York, USA.

Morton J. and Groves G.W. (1974). The cracking of composites consisting of discontinous ductile fibres in a britle matrix - effect of fibre orientation. *Journal of Materials Science*, 9, 1439–1445.

Naaman A. (1992). SIFCON: Tailored properties for structural performance. In H. Reinhardt and A. Naaman, editors, *Performance Fiber Reinforced Cementitious Composites*, pages 18–38. E & FN Spon, London.

Naaman A. (2003). Engineered steel fibers with optimal properties for reinforcement of cement composites. *Journal of Advanced Concrete Technology*, 1(3), 241–252.

Naaman A. and Shah S. (1976). Pullout mechanism in steel fibre reinforced concrete. *ASCE Journal Struct. Div.*, 102, 1537–1548.

Naaman A.E. and Najm H. (1991). Bond-slip mechanisms of steel fibers in concrete. *ACI Materials Journal*, 88(2), 135–145.

Naaman A.E., Namur G.G., Alwan J.M., and Najm H.S. (1991b). Fiber pullout and bond slip I: Analytical study. *Journal of Structural Engineering ASCE*, 117(9), 2769–2790.

Nataraja M., Dhang N., and Gupta A. (1999). Stress-strain curves for steel-fiber reinforced concrete under compression. *Cement and Concrete Composites*, 21, 383–390.

Okamura H. (1997). Ferguson lecture for 1996: Self-compacting high-performance concrete. *Concrete International*, 19(7), 50–54.

Okamura H. and Ozawa K. (1996). Self-compactable high performance concrete in japan. *ACI Special Publication*, 159, 31–44.

Oñate E. (1992). *Cálculo de estructuras por el método de elementos finitos - Structural calculus by the finite element method (in spanish).* Centro International de Métodos Numéricos en Ingniería, Barcelona.

Ostergaard L. (2003). *Early-age fracture mechanics and cracking of concrete*. Ph.D. thesis, Department of Civil Engineering, Technical University of Denmark.

Ouyang C., Palacios A., and Shah S.P. (1994). Pullout of inclined fibers from cementicious matrix. *ASCE Journal of Engineering Mechanics*, 120(12), 2641–2659.

Ozyurt N., Mason T.O., and Shah S.P. (2006a). Non-destructive monitoring of fiber orientation using AC-IS: An industrial-scale application. *Cement and Concrete Research*, 36(9), 1653–1660. ISSN 0008-8846.

Ozyurt N., Woo L., Manson T., and Shah S. (2006b). Monitoring fiber dispersion in fiber reinforced cementicious materials: comparison of AC-impedance spectroscopy and image analysis. *ACI Materials Journal*, 103(5), 340–347.

Ozyurt N., Mason T.O., and Shah S.P. (2007). Correlation of fiber dispersion, rheology and mechanical performance of frcs. *Cement and Concrete Composites*, 29(2), 70–79.

Pereira E. (2006). *Steel Fibre Reinforced Self-compacting Concrete: from material to mechanical behaviour*. Master's thesis, Universidade do Minho, Guimarães, Portugal.

Pereira E.B., Barros J.A.O., Ribeiro A., Cunha V.M.C.F., and Antunes J.A.B. (2004). Self compacting steel fibre reinforced concrete for precasted sandwich panels - experimental and numerical research. In *Proocedings BeFib 2004*, pages 15–17. Ancona, Italy.

Pereira E.B., Barros J.A.O., Cunha V.M.C.F., and Antunes J.A.B. (2005). Steel fiber reinforced self-compacting concrete for precasted sandwich panels. In *Third International Conference Construction Materials: Performance, Innovations and Structural Implications*. Vancouver, Canada.

Petersson P.E. (1980). Fracture energy of concrete. method of determination. *Cement and Concrete Research*, 10(1), 91–101.

Petersson P.E. (1981). Crack growth and development of fracture zone in plane concrete and similar materials. Report no. tvbm-1006, division of building materials, Lund Institute of Technology, Lund, Sweden.

Planas J. and Elices M. (1989). Conceptual and experimental problems in the determination of the fracture energy of concrete. In Balkema, editor, *Fracture Toughness and Fracture Energy: Test methods for Concrete and Rock*, pages 165–181. Rotterdam.

Planas J., Guinea G.V., , and Elices M. (1999). Size effect and inverse analysis in concrete fracture. *International Journal of Fracture*, 95(5), 367–378.

Poppe A.M. and Schutter G. (2005). Cement hydration in the presence of high filler contents. *Cement and Concrete Research*, 35, 2290–2299.

Que N.S. and Tin-Loi F. (2002). Numerical evaluation of cohesive fracture parameters from a wedge splitting test. *Engineering Fracture Mechanics*, 69, 1269–1286.

Ranjbaran A. (1996). Mathematical formulation of embedded reinforcements in 3d bricks elements. *Communications in Numerical Methods in Engineering*, 12, 897–903.

RILEM TC 14-CPC (1975). Modulus of elasticity of concrete in compression (CPC8). *Materials and Structures*, 6(30), 25–27.

RILEM TC 148-SSC (2000). Strain softening of concrete- test methods for compressive softening, test method for measurement of the strain-softening behaviour of concrete under uniaxial compression. *Materials and Structures*, 33(230), 347–351.

RILEM 50-FMC (1985). Determination of the fracture energy of mortar rand concrete by means of three-point bending tests on notched beams. *Materials and Structures*, 85, 285–290.

RILEM TC 162-TDF (2001). Test and design methods for steel fibre reinforced concretes: Uni-axial tension test for steel fibre reinforced concrete. *Journal of Materials and Structures*, 34(1), 3–6.

RILEM TC 162-TDF (2002a). Test and design methods for steel fibre reinforced concrete – design of steel fibre reinforced concrete using the σ-w method: principles and application. *Journal Materials and Structures*, 35(249), 262–276.

RILEM TC 162-TDF (2002b). Test and design methods for steel fibre reinforced concrete - bending test (final recommendation). *Journal of Materials and Structures*, 35(253), 579–582.

Robins P., Austin S., and Jones P. (2002). Pull-out behaviour of hooked steel fibres. *RILEM Journal of Engineering Mechanics*, 35(251), 434–442.

Rocco C., Guinea G.V., Planas J., and Elices M. (2001). Review of the splitting-test standards from a fracture mechanics point of view. *Cement and Concrete Research*, 31(1), 73–82.

Roelfstra P.E. and Wittmann F.H. (1986). Numerical method to link strain softening with failure of concrete. In F.H. Wittmann, editor, *Fracture Toughness and Fracture Energy*, pages 163–175. Elsevier, London.

Rosenbusch J. and Teutsch M. (2003). Shear design with method, test and design methods for steel fibre reinforced concrete - background and experiences. In Schnutgen and Vandewalle, editors, *RILEM publication PRO 31*, pages 105–118.

Rossi P. and Chanvillard G. (1996). New geometry of steel fibre for fibre reinforced concrete. In H.W. Reinhardt and A.E. Naaman, editors, *High Performance Fiber Reinforced Cement Composites*, pages 129–139. E. & F. N. Spon, London.

Rossi P., Bräuhwiler E., Chuy S., Jenq S., and Shah S. (1991). Fracture properties of concrete as determined by means of wedge splitting tests and tapered double cantilever beam tests. In S. Shah and A. Carpintieri, editors, *Fracture Mechanics Test methods for Concrete*, pages 87–128. Chapmann & Hall.

Rossi P., Wu X., Maou F.L., and Belloc A. (1994). Scale effect on concrete in tension. *Materials and Structures*, 27(8), 437–444.

Rots J.G. (1988). *Computational modelling of concrete fracture*. Ph.D. thesis, Delft University of Technology, Netherlands.

Russo G., Zingone G., and Romano F. (1990). Analytical solution for bond-slip of reinforcing bars in R.C. joints. *Journal of Structural Engineering ASCE*, 116(2), 336–355.

Ryan T.P. (1997). *Modern regression methods*. John Wiley & Sons, Inc., Ney York, USA.

Schellekens J.C.J. (1990). Interface elements in finite element analysis. Technical report, TU-Delft report 25.2-90-5-17/ TNO-IBBC report BI-90-165.

Schindler A.K. (2004). Effect of temperature on hydration of cementicious materials. *ACI Materials Journal*, 101(1), 72–81.

Schlangen E. and Van Mier J.G.M. (1992). Simple lattice model for numerical simulation of fracture of concrete materials and structures. *Materials and Structures*, 25, 534–542.

Schumacher P. (2006). *Rotation Capacity of Self-Compacting Steel Fiber Reinforced Concrete*. Ph.D. thesis, Delft University of Technology, Netherlands.

Sena-Cruz J.M. (2005). *Strenghning of concrete structures with near surface mounted CFRP laminate strips*. Ph.D. thesis, Dep. Civil Engineering, Universidade do Minho, Portugal.

Sena-Cruz J.M., Barros J.A.O., Ribeiro A.R., Azevedo A.F.M., and Camões A. (2004). Stress-crack opening relationship enhanced performance concrete. In 9^{th} *Portuguese Conference on Fracture*, pages 1–9.

Shah S.P. and Ferrara L. (2008). Self consolidating fiber reinforced concrete. In R. Gettu, editor, *Sevnth. Intnl. RILEM Symposium on Fibre Reinforced Concrete: Design and Applications*, pages 641–659. Chennai, India.

Shah S.P., Swartz S.E., and Ouyang C. (1995). *Fracture machanics of concrete (application of fracture mechanics to concete, rock and other quasi-britle materials).* John Wiley & Sons, Inc.

Skocek J. and Stang H. (2008). Inverse analysis of the wedge-splitting test. *Engineering Fracture Mechanics*, 75(10), 3173–3188.

Soroushian P. and Bayasi Z. (1991). Fiber-type effects on the performance of steel fiber reinforced concrete. *ACI Materials Journal*, 88(2), 129–134.

Soroushian P. and Lee C.D. (1990). Distribution and orientation of fibers in steel fiber reinforced concrete. *ACI Materials Journal*, 87(5), 433–439.

Stang H. and Aarre T. (1992). Evaluation of crack width in FRC with conventional reinforcement. *Cement & Concrete Composites*, 14(1), 143–154.

Stang H., Li Z., and Shah S.P. (1990). Pullout problem: Stress versus fracture mechanical approach. *Journal of Engineering Mechanics*, 116(10), 2136–2150.

Stähli P., Custer R., and van Mier J. (2008). On flow properties, fibre distribution, fibre orientation and flexural behaviour of frc. *Materials and Structures*, 41(1), 189–196.

Strack M. (2008). Modelling of crack opening in steel fibre reinforced under tension and bending. In R. Gettu, editor, *Seventh International RILEM Symposium on Fibre Reinforced Concrete: Design and Aplications*, pages 323–332. Chennai, India.

Stroeven P. (1978). Morphometry of fibre reinforced cementitious materials – part 1: Efficiency and spacing in idealized structures. *Materials and Structures*, 11(1), 31–37.

Stroeven P. (1979). Morphometry of fibre reinforced cementicious materials. part II: Inhomogeneity, segregation and anisometry of partially oriented fibre structure. *Materiaux et Construcion*, 12(67), 9–20.

Stroeven P. (1986a). Stereology of concrete reinforced with short steel fibres. *Fract. Mech. Struct. Aspects Concr.*, 31, 15–28.

Stroeven P. (1986b). Stereology of concrete reinforced with short steel fibres. In *Heron - Fracture mechanics and structural aspects of concrete*, volume 31, pages 15–28. Delft, Netherlands.

Stroeven P. (1994). Steel wire efficiency in mechanical testing of concrete. *Acta Stereologica*, 13(2), 363–368.

Stroeven P. (2008). Reliability and economy of pull-out testing for predicting engineering behaviour of sfrc. In R. Gettu, editor, *Sevnth. Intnl. RILEM Symposium on Fibre Reinforced Concrete: Design and Applications*, pages 75–82. Chennai, India.

Stroeven P. and Guo Z. (2008). Distribution and orientation of fibres in the perspective of the mechanical properties of concrete. In R. Gettu, editor, *Sevnth. Intnl. RILEM Symposium on Fibre Reinforced Concrete: Design and Applications*, pages 145–153. Chennai, India.

Stroeven P. and Hu J. (2006). Effectivness near boundaries of fibre reinforcement in concrete. *Materials and Structures*, 39, 1001–1013.

Stroeven P. and Shah S.P. (1978). Use of radiography-image analysis for steel fibre reinforced concrete. In *Proceedings RILEM Syposium. Testing and test methods of fibre cement composites*, pages 345–353. Sheffield.

Sujivorakul C., Waas A.M., and Naaman A. (2000). Pullout response of a smooth fiber with an end anchorage. *Journal of Engineering Mechanics*, 126(9), 986–993.

Swamy R.N., Mangat P.S., and Rao C.V.S.K. (1974). The mechanisms of fibre reinforcement of cement matrices. *ACI Special Publication*, SP-44, 1–28.

Timoshenko S.P. and Goodier J.N. (1991). *Theory of Elasticity*. McGraw-Hill, New York.

Torrijos M.C., Tobes J.M., Barragán B., and Zerbino R. (2008). Orientation and distribution of steel fibres in self-compacting concrete. In R. Gettu, editor, *Sevnth. Intnl. RILEM Symposium on Fibre Reinforced Concrete: Design and Applications*, pages 729–738. Chennai, India.

Toutanji H. and Bayasi Z. (1998). Effect of manufacturing techniques on the flexural behaviour of steel fiber–reinforced concrete. *Cement and Concrete Research*, 28(1), 115–124.

Uchida Y. and Barr B. (1998). Tension softening curves of concrete determined from different test specimen geometries. In H. Mihashi and K. Rokugo, editors, *Fracture Mechanics of Concrete Structures*, pages 387–398. Freiburg, Germany.

Van Hauwaert A. and Van Mier J.G.M. (1998). Computational modelling of the fibre-matrix bond in steel fibre reinforced concrete. In H. Mihashi and K. Rokugo, editors, *Fracture Mechanics of Concrete Structures*, pages 561–571. Freiburg, Germany.

Van Mier J.G.M. (1997). *Fracture processes of concrete (Assessment of Material Parameters for Fracture Models)*. CRC Press, Boca Raton(FL).

Van Mier J.G.M. and Shi C. (2002). Stability issues in uniaxial tensile tests on brittle disordered materials. *International Journal of Solids and Structures*, 39, 3359–3372.

Van Mier J.G.M. and Van Vliet M.R.A. (2002). Uniaxial tension test for the determination of fracture parameters: state of the art. *Journal of Engineering Fracture Mechanics*, 69, 235–247.

Van Mier J.G.M., Schlangen E., and Vervuurt A. (1996). Tensile cracking in concrete and sandstone: Part 2 - effect of boundary rotations. *Materials and Structures*, 29(186), 87–96.

Vandewalle L., Heirman G., and Van Rickstal F. (2008). Fibre orientation in self-comapcting fibre reinforced concrete. In R. Gettu, editor, *Sevnth. Intnl. RILEM Symposium on Fibre Reinforced Concrete: Design and Applications*, pages 719–728. Chennai, India.

Ventura-Gouveia A., Barros J.A.O., Álvaro Azevedo, and Sena-Cruz J. (2008). Multi-fixed smeared 3d crack model to simulate the behaviour of fibre reinforced concrete structures. In T.M. et al., editor, *CCC 2008 – Challenges for Civil Construction*, pages Paper T2–3, 11 pp. FEUP, Porto.

Visalvanich K. and Naaman A.E. (1983). Fracture model for fiber reinforced concrete. *ACI Journal*, 80(2), 128–138.

Vliet M.R.A. (2000). *Size Effect in Tensile Fracture of Concrete and Rock*. Ph.D. thesis, Delft University of Technology, Netherlands.

Wang P.T., Shah S.P., and Naaman A. (1978). Stress-strain curves of normal and light-weight concrete in compression. *ACI Journal*, 75(11), 603–611.

Wang Y., Li V., and Backer S. (1988). Modelling fiber pullout from a cement matrix. *International Journal of Cement Composites and Lightweight Concrete*, 10(3), 143–149.

Wang Z.M., Kwan A.K.H., and Chan H.C. (1999). Mesoscopic study of concrete i: generation of random aggregate structure and finite element mesh. *Computation of Strucures*, 70(5), 533–544.

Wei S., Mandel J., and Said S. (1986). Study of the interface strength of steel fibre reinforced cement based composites. *ACI Journal*, 83, 597–605.

Wittmann F.H., Roelfstra P.E., and Sadouki H. (1984). Simulation and analysis of composite structures. *Materials Science Engineering*, 68(2), 239–248.

Woo L.Y., Wansom S., Ozyurt N., Hu B., Shah S., and Manson T. (2005). Characterizing fiber dispersion in cement composites using AC-impedance spectroscopy. *Cement and Concrete Composites*, 27, 627–636.

Yi S.T., Kim J.K., and Oh T.K. (2003). Effect of strength and age on the stress-strain curves of concrete specimens. *Cement and Concrete Research*, 33, 1235–1244.

Zhou F.P. (1988). Some aspects of tensile fracture behaviour and structural response of cementicious materials. Report no. tvbm-1008, division of building materials, Lund Institute of Technology, Lund, Sweden.

Zienkiewicz O. and Taylor R. (2000). *Finite element method – Vol. 1: The basis*. Butterworth-Heinemann, Oxford, England.

Annex I

Experimental Pullout Results – SFRC

In Tables I.1, I.2 are indicated, respectively the average maximum pullout load and the average slip at peak load.

Table I.1: Average values of the maximum pullout load, N_{max}.

Fibre type		Orientation angle 0°		30°		60°	
		N_{max} [N]	CoV [%]	N_{max} [N]	CoV [%]	N_{max} [N]	CoV [%]
Smooth	A	194.4	23.3	244.9	9.1	211.0	15.1
	B	398.8	17.6	328.4	16.9	319.0	34.4
	C	182.3	17.8	237.6	14.0	239.2	13.6
Hooked	A	373.1	15.7	412.1	5.6	360.1	5.7
	B	639.3	12.6	696.6	14.4	560.7	33.3
	C	387.6	9.4	420.4	4.9	343.1	7.0

Tables I.3 and I.4 comprise the average values of the energy dissipated up to a 1 mm and 3 mm slip, respectively.

In Figures I.1, I.2 and I.3 are depicted, respectively, for a fibre inclination angle of 0°, 30° and 60°, the pullout load-slip curves for each specimen tested.

Table I.2: Average values of the slip at maximum pullout load, s_{peak}.

Fibre type		Orientation angle 0°		30°		60°	
		s_{peak} [mm]	CoV [%]	s_{peak} [mm]	CoV [%]	s_{peak} [mm]	CoV [%]
Smooth	A	1.525	23.3	1.697	171.7	4.367	44.8
	B	2.223	17.6	0.307	47.7	3.435	74.1
	C	4.095	17.8	2.804	64.8	4.603	69.4
Hooked	A	0.878	15.7	3.348	40.3	4.106	22.4
	B	2.278	12.6	2.842	52.7	3.746	62.8
	C	2.114	9.4	1.682	26.1	3.354	31.4

Table I.3: Average values of the energy dissipated up to a 1 mm slip, G_{1mm}.

Fibre type		Orientation angle 0°		30°		60°	
		G_{1mm} [kN.mm]	CoV [%]	G_{1mm} [kN.mm]	CoV [%]	G_{1mm} [kN.mm]	CoV [%]
Smooth	A	0.149	34.9	0.167	22.5	0.112	11.4
	B	0.231	13.5	0.199	31.0	0.178	38.1
	C	0.132	30.2	0.144	30.2	0.096	24.3
Hooked	A	0.312	16.6	0.253	8.0	0.119	13.2
	B	0.489	11.9	0.392	13.9	0.267	14.3
	C	0.304	16.7	0.235	15.1	0.162	18.6

Table I.4: Average values of the energy dissipated up to a 3 mm slip, G_{3mm}.

Fibre type		Orientation angle 0°		30°		60°	
		G_{3mm} [kN.mm]	CoV [%]	G_{3mm} [kN.mm]	CoV [%]	G_{3mm} [kN.mm]	CoV [%]
Smooth	A	0.438	33.7	0.462	29.6	0.429	17.3
	B	0.627	41.5	0.424	44.2	0.540	19.4
	C	0.387	29.7	0.553	28.6	0.368	12.1
Hooked	A	0.964	12.1	1.000	6.9	0.524	22.2
	B	1.665	10.2	1.505	21.1	1.020	31.6
	C	0.964	7.8	0.569	28.5	0.612	14.9

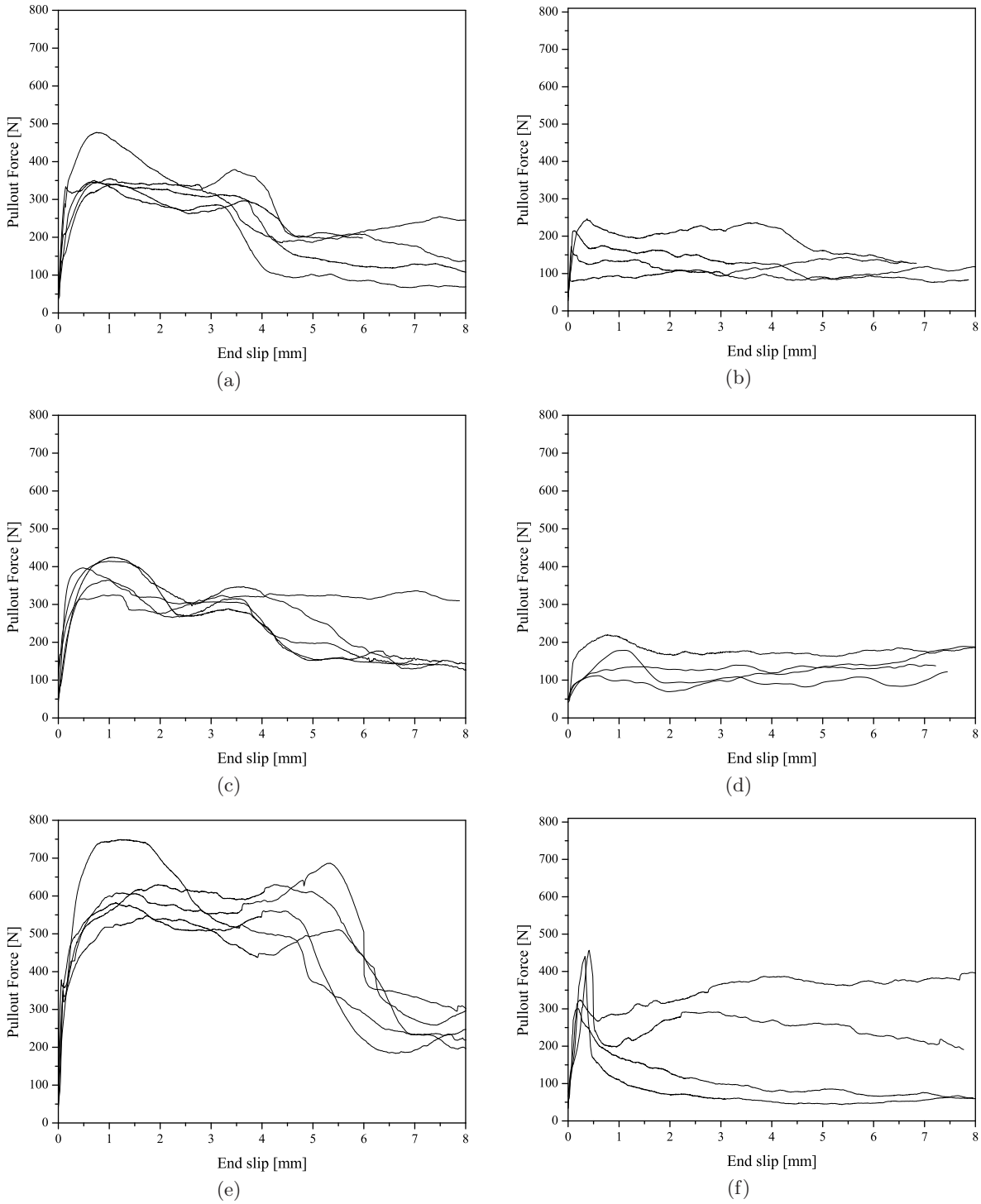

Figure I.1: Pullout load - slip curves for a 0° fibre inclination angle: (a), (c) and (e) hooked end fibres from TYPE A, TYPE C and TYPE B, respectively; (b), (d) and (f) smooth fibres from TYPE A, TYPE C and TYPE B, respectively.

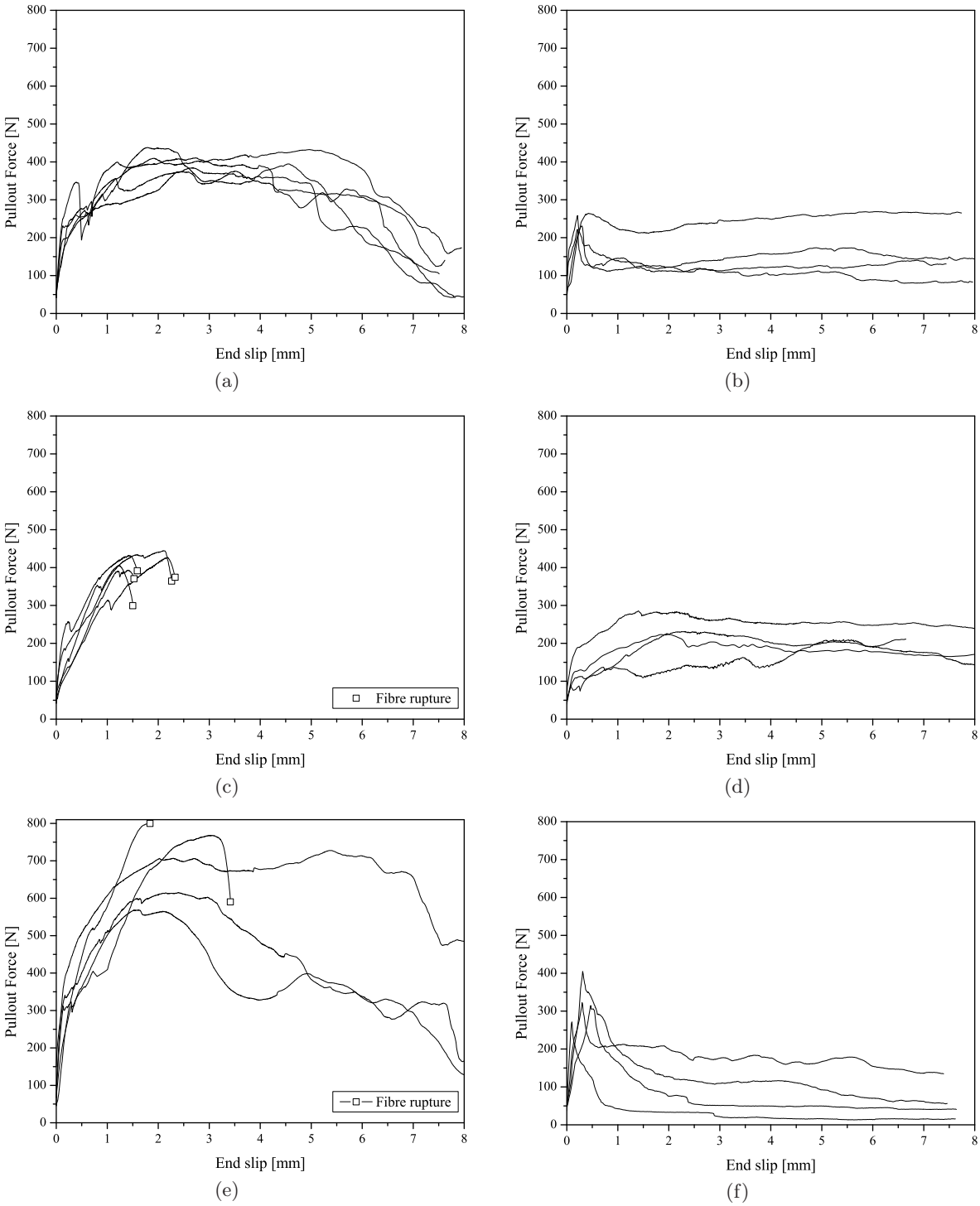

Figure I.2: Pullout load - slip curves for a 30° fibre inclination angle: (a), (c) and (e) hooked end fibres from TYPE A, TYPE C and TYPE B, respectively; (b), (d) and (f) smooth fibres from TYPE A, TYPE C and TYPE B, respectively.

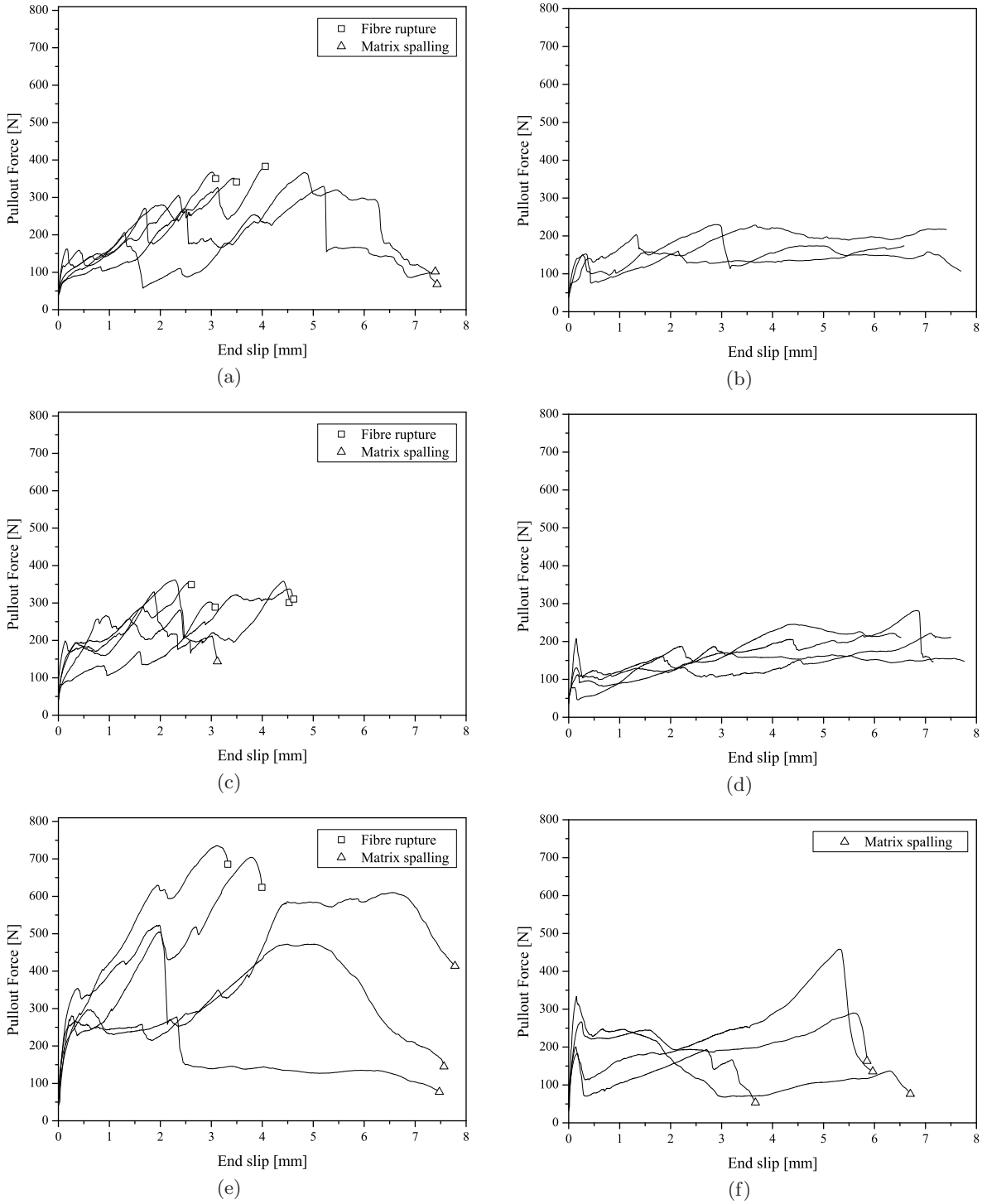

Figure I.3: Pullout load - slip curves for a 60° fibre inclination angle: (a), (c) and (e) hooked end fibres from TYPE A, TYPE C and TYPE B, respectively; (b), (d) and (f) smooth fibres from TYPE A, TYPE C and TYPE B, respectively.

Annex II

Experimental Pullout Results – SFRSCC

In Tables II.1 and II.2 are indicated, respectively, the average maximum pullout load and the average slip at peak load.

Table II.1: Average values of the maximum pullout load, N_{max}.

	L_b [mm]	Orientation angle 0°		30°		60°	
		N_{max} [N]	CoV [%]	N_{max} [N]	CoV [%]	N_{max} [N]	CoV [%]
Smooth	10	-	-	-	-	154.2	43.8
	20	77.4	2.0	173.5	18.2	172.8	8.7
	30	155.2	9.7	203.7	13.8	189.4	15.0
Hooked	10	321.8	5.6	360.9	13.9	342.0	2.3
	20	347.8	2.8	400.1	4.9	335.2	3.0
	30	388.2	1.6	416.0	3.4	365.1	2.5

Tables II.3 and II.4 comprise the average values of the energy dissipated up to a 1 mm and 3 mm slip, respectively.

In Figures II.1, II.2 and II.3 are depicted for a fibre inclination angle of 0°, 30° and 60°, respectively, the pullout load-slip curves for each specimen tested.

Table II.2: Average values of the slip at maximum pullout load, s_{peak}.

	L_b [mm]	Orientation angle					
		0°		30°		60°	
		s_{peak} [mm]	CoV [%]	s_{peak} [mm]	CoV [%]	s_{peak} [mm]	CoV [%]
Smooth	10	-	-	-	-	3.34	45.6
	20	0.12	11.8	0.19	7.4	2.02	2.0
	30	0.25	14.4	0.38	32.3	2.17	11.8
Hooked	10	0.59	8.7	0.94	11.4	2.40	20.81
	20	0.65	9.4	1.00	9.7	2.33	15.1
	30	0.69	11.0	0.80	19.3	2.64	23.2

Table II.3: Average values of the energy dissipated up to a 1 mm slip, G_{1mm}.

	L_b [mm]	Orientation angle					
		0°		30°		60°	
		G_{1mm} [kN.mm]	CoV [%]	G_{1mm} [kN.mm]	CoV [%]	G_{1mm} [kN.mm]	CoV [%]
Smooth	10	-	-	-	-	0.074	19.1
	20	0.046	3.1	0.114	6.9	0.105	2.0
	30	0.095	5.9	0.141	7.4	0.100	4.4
Hooked	10	0.273	5.6	0.290	11.7	0.125	19.4
	20	0.283	3.6	0.314	5.6	0.129	15.4
	30	0.322	2.5	0.286	11.8	0.126	37.8

Table II.4: Average values of the energy dissipated up to a 3 mm slip, G_{3mm}.

	L_b [mm]	Orientation angle					
		0°		30°		60°	
		G_{3mm} [kN.mm]	CoV [%]	G_{3mm} [kN.mm]	CoV [%]	G_{3mm} [kN.mm]	CoV [%]
Smooth	10	-	-	-	-	0.263	13.4
	20	0.117	8.5	0.282	4.0	0.420	6.4
	30	0.251	9.3	0.356	9.7	0.418	5.8
Hooked	10	0.689	5.1	0.465	41.9	0.482	21.3
	20	0.756	5.5	0.558	53.6	0.490	15.3
	30	0.886	1.3	0.317	23.7	0.523	15.2

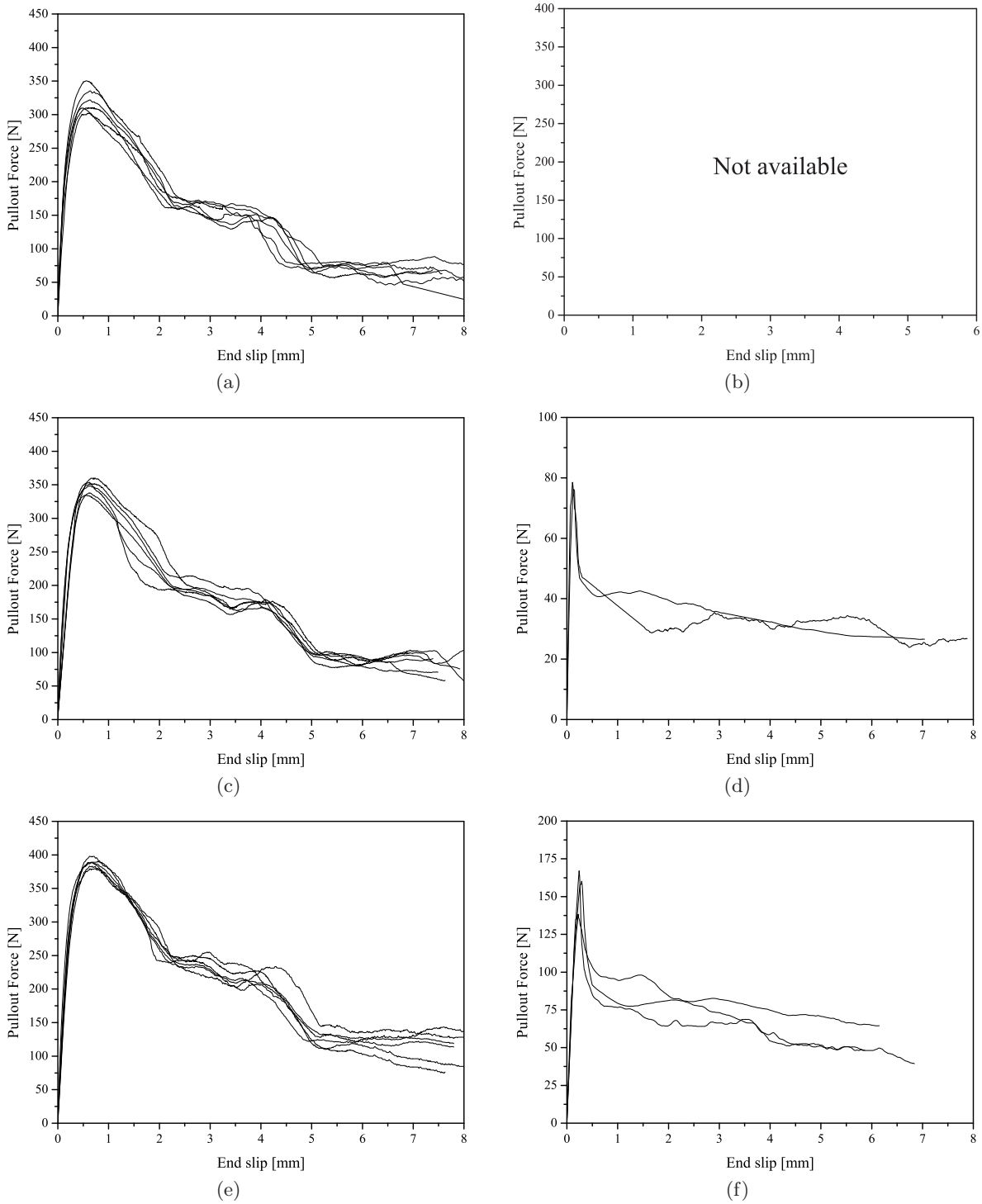

Figure II.1: Pullout load - slip curves for a 0° fibre inclination angle: (a), (c) and (e) hooked end fibres with an embedded length of 10, 20 and 30 mm, respectively. (b), (d) and (f) smooth fibres with an embedded length of 10, 20 and 30 mm, respectively.

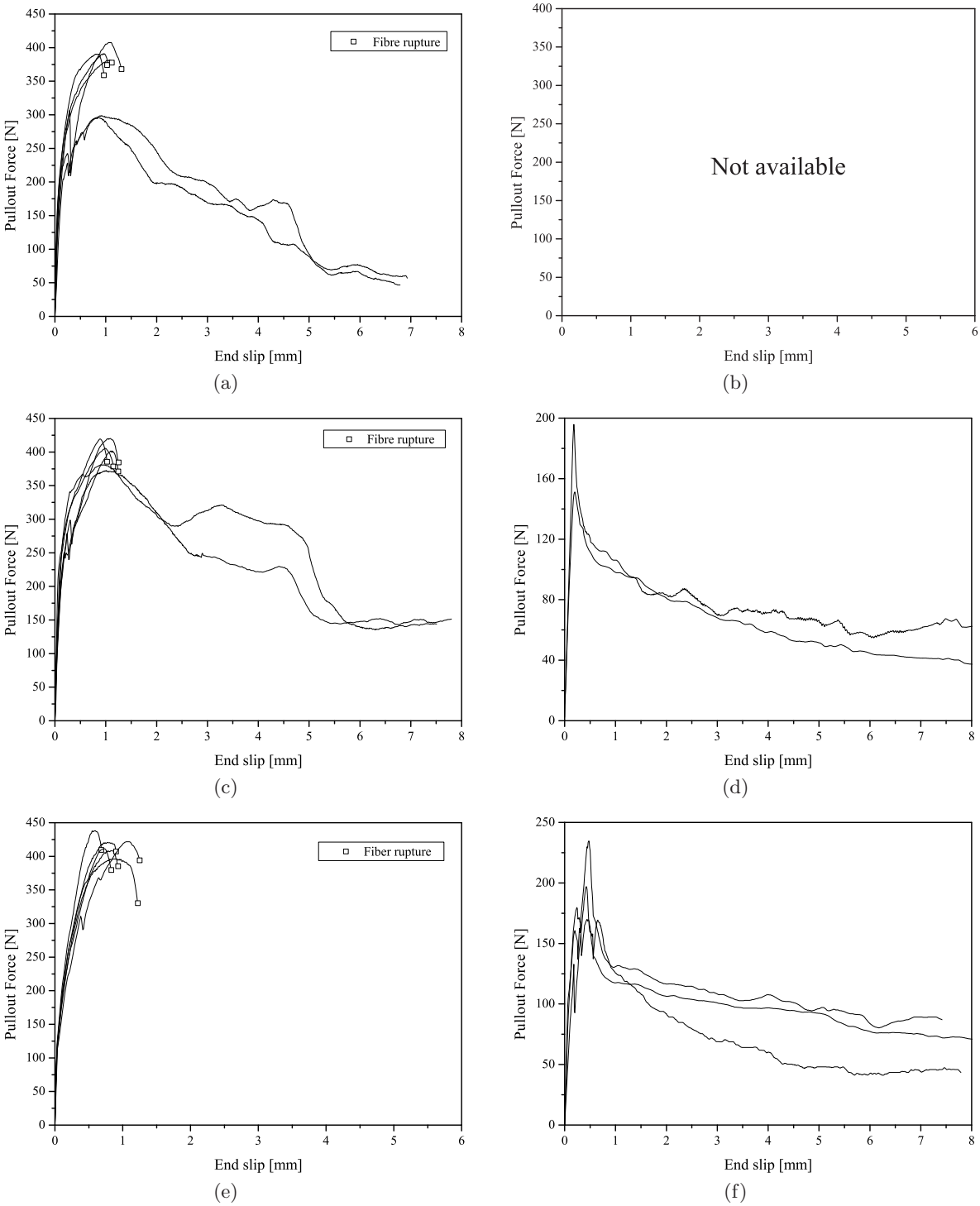

Figure II.2: Pullout load - slip curves for a 30° fibre inclination angle: (a), (c) and (e) hooked end fibres with an embedded length of 10, 20 and 30 mm, respectively. (b), (d) and (f) smooth fibres with an embedded length of 10, 20 and 30 mm, respectively.

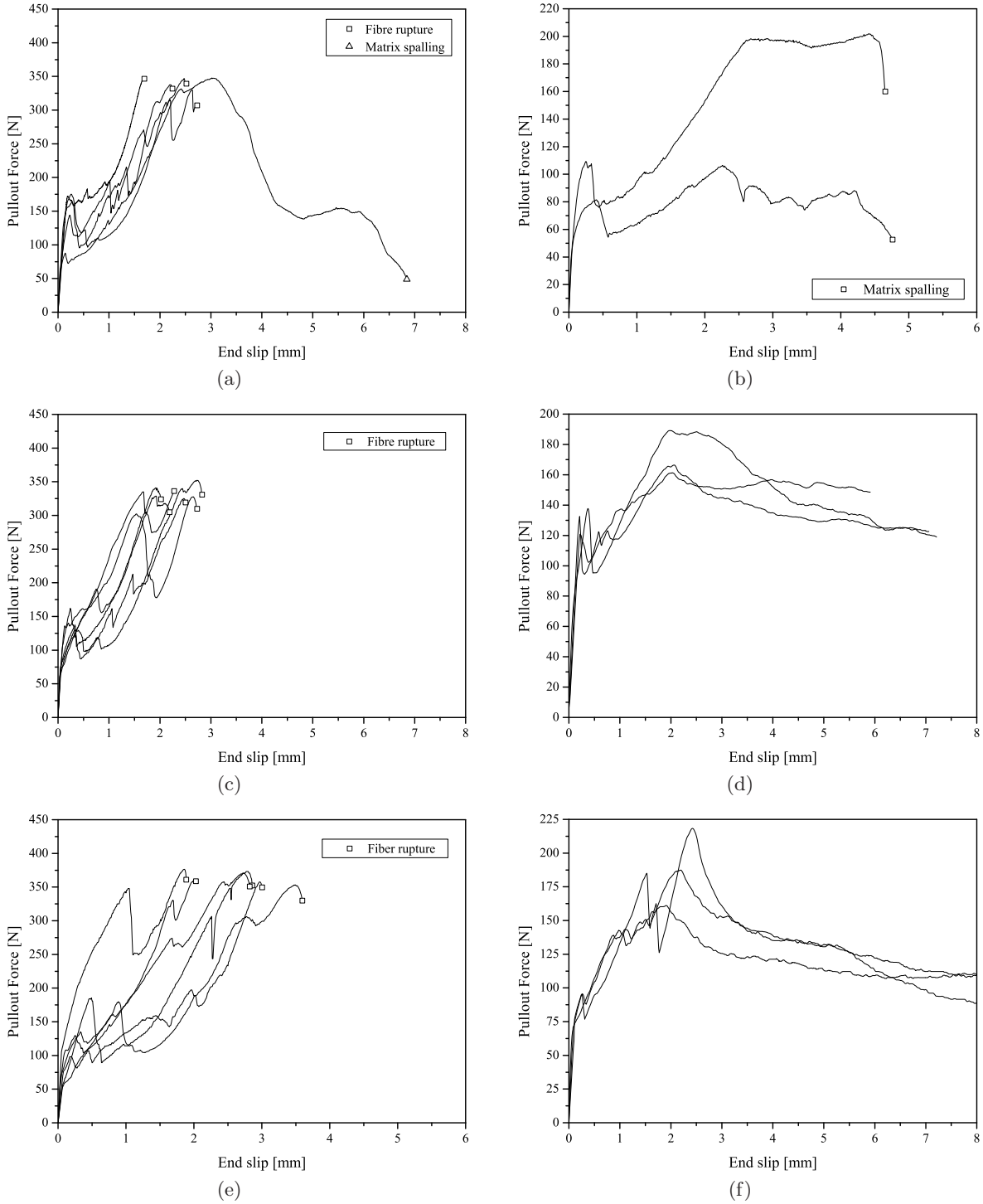

Figure II.3: Pullout load - slip curves for a 60° fibre inclination angle: (a), (c) and (e) hooked end fibres with an embedded length of 10, 20 and 30 mm, respectively. (b), (d) and (f) smooth fibres with an embedded length of 10, 20 and 30 mm, respectively.

Annex III

Runge-Kutta-Nyström Methods

The Runge-Kutta-Nyström (RKN) method (Kreyszig 1993) computes the solution of $y'' = f(x, y, y')$ using the initial values $y(x_0) = y_0$, $y'(x_0) = y'_0$ at equidistant points $x_1 = x_0 + h$, $x_2 = x_0 + 2h$, ..., $x_N = x_0 + Nh$, h the step length and N the number of steps. Figure II.1 shows the corresponding algorithm.

The following functions are used in the present study:

$$y'' = \frac{d^2 s}{dx^2}$$

$$f(x, y, y') = \frac{P_f}{(E_f A_f)} \cdot \tau(s) \tag{3.1}$$

The first point of the effective bond length, L_{ef}, is $x_0 = 0$ and the last one is $x_N = L_{ef}$. The effective bond length was divided in 100 segments of equal width ($N = 100$).

The initial values are the free end slip, $y(x_0) = s_f$, and the fibre strain at the free end, $y'(x_0) = (ds/dx)_0 = \varepsilon(x = 0) = 0$. According to the algorithm represented in Figure II.1, the loaded end slip, $y(x_N) = s_l$, and the laminate strain at the loaded end, $y'(x_N) = \varepsilon(x_N)$, are calculated.

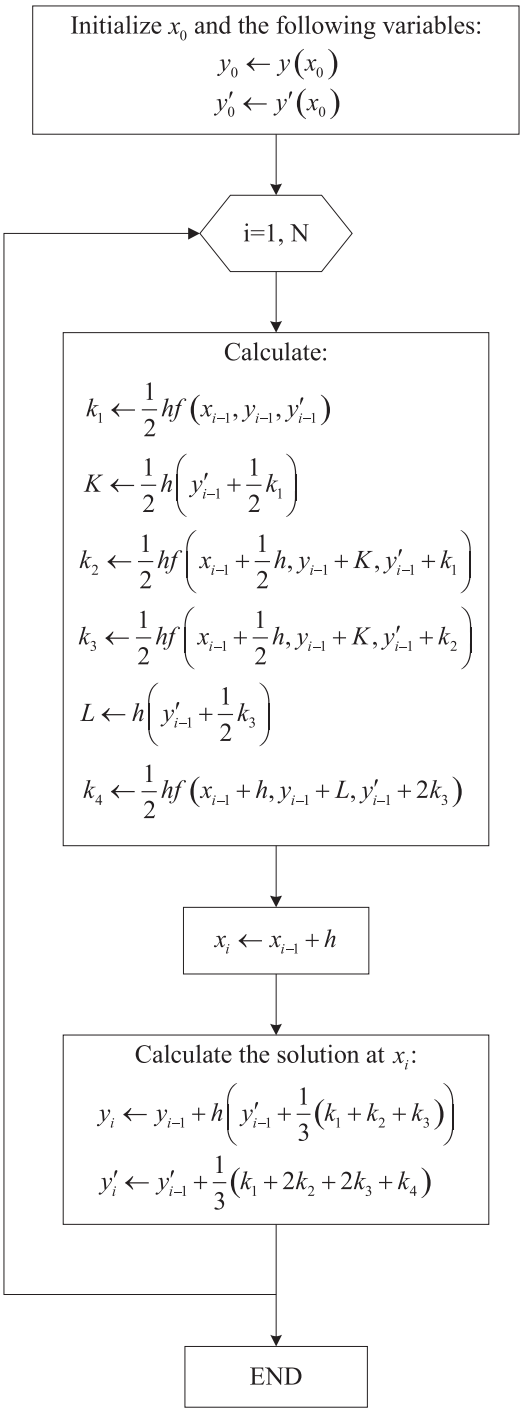

Figure III.1: Runge-Kutta-Nyström algorithm.

Annex IV

Uniaxial Compressive Behaviour

I Experimental results

Tables IV.1 and IV.2 indicate the values of the compressive strength obtained for all the tested specimens for the Cf30 and Cf45 series, respectively.

Table IV.1: Compressive strength values obtained in the Cf30 series [MPa].

Age	Specimen						Average
	1	2	3	4	5	6	
12 h	14.12	10.95	12.71	11.50	12.12	-	**12.3**
24 h	22.22	22.96	25.23	26.06	27.36	24.99	**24.7**
3 d	51.27	52.78	52.07	53.26	51.22	53.55	**52.4**
7 d	57.02	59.87	59.18	60.68	57.90	53.70	**58.1**
28 d	69.80	69.97	70.97	67.79	70.69	68.74	**69.7**

Table IV.2: Compressive strength values obtained in the Cf45 series [MPa].

Age	Specimen						Average
	1	2	3	4	5	6	
12 h	15.32	17.08	17.62	19.43	16.85	19.60	**17.7**
24 h	24.77	23.39	24.75	26.94	25.94	25.85	**25.3**
3 d	48.40	45.86	48.16	49.05	47.63	48.33	**47.9**
7 d	52.86	51.73	54.22	50.56	46.87	49.45	**51.0**
28 d	56.12	54.64	53.58	58.52	55.14	58.90	**56.2**

In Tables IV.3 and IV.4 are comprised the values of the elasticity modulus obtained for each specimen tested.

Table IV.3: Elasticity modulus values obtained in the Cf30 series [GPa].

AGE	SPECIMEN						AVERAGE
	1	2	3	4	5	6	
12 h	12.99	17.87	12.35	11.97	12.74	-	**13.6**
24 h	24.72	27.50	25.10	25.14	25.47	23.68	**25.3**
3 d	36.55	36.57	34.44	37.54	38.24	39.00	**37.1**
7 d	40.72	40.71	40.52	40.37	39.92	40.18	**40.4**
28 d	42.30	40.52	40.15	42.32	41.51	42.17	**41.5**

Table IV.4: Elasticity modulus values obtained in the Cf45 series [GPa].

AGE	SPECIMEN						AVERAGE
	1	2	3	4	5	6	
12 h	16.64	18.47	17.92	19.98	19.68	19.88	**18.8**
24 h	21.96	20.82	21.69	24.69	22.69	22.40	**22.4**
3 d	31.30	30.91	32.42	31.20	30.73	31.92	**31.4**
7 d	32.48	32.64	30.95	31.81	31.27	32.26	**31.9**
28 d	34.56	36.55	32.50	35.61	33.22	34.81	**34.5**

Tables IV.5 and IV.6 include the values of the elasticity modulus obtained for each specimen tested.

Table IV.5: Strain at peak stress values obtained in the Cf30 series.

AGE	SPECIMEN						AVERAGE
	1	2	3	4	5	6	
12 h	0.0094	0.0040	0.0072	0.0068	0.0062	-	**0.0067**
24 h	0.0034	0.0041	0.0037	0.0040	0.0042	0.0037	**0.0039**
3 d	0.0030	0.0031	0.0029	0.0032	0.0029	0.0031	**0.0030**
7 d	0.0034	0.0032	0.0030	0.0030	0.0030	0.0031	**0.0031**
28 d	0.0031	0.0034	0.0032	0.0028	0.0032	0.0031	**0.0031**

In Tables IV.7 and IV.8 are indicated the values of the energy dissipated under compression obtained for each specimen tested.

In Figures IV.1 and IV.2 is represented the relationship between the dissipated energy under compression and the strain.

Table IV.6: Strain at peak stress values obtained in the Cf45 series.

Age	Specimen						Average
	1	2	3	4	5	6	
12 h	0.0050	0.0052	0.0044	0.0045	0.0049	0.0039	**0.0047**
24 h	0.0040	0.0039	0.0035	0.0036	0.0038	0.0036	**0.0037**
3 d	0.0031	0.0027	0.0029	0.0030	0.0031	0.0032	**0.0030**
7 d	0.0032	0.0029	0.0031	0.0030	0.0024	0.0029	**0.0029**
28 d	0.0029	0.0029	0.0029	0.0028	0.0029	0.0025	**0.0028**

Table IV.7: Energy dissipated under compression values obtained in the Cf30 series [N/mm^2].

Age	Specimen						Average
	1	2	3	4	5	6	
12 h	0.30	0.18	0.27	0.28	0.25	-	**0.26**
24 h	0.41	0.33	0.34	0.35	0.43	0.31	**0.36**
3 d	0.55	0.53	0.38	0.47	0.48	0.45	**0.48**
7 d	0.45	0.49	0.54	0.37	0.42	0.38	**0.44**
28 d	0.52	0.56	0.49	0.48	0.41	0.47	**0.49**

Table IV.8: Energy dissipated under compression obtained in the Cf45 series [N/mm^2].

Age	Specimen						Average
	1	2	3	4	5	6	
12 h	0.29	0.35	0.32	0.27	0.37	0.36	**0.33**
24 h	0.44	0.34	0.33	0.42	0.35	0.37	**0.38**
3 d	0.59	0.49	0.44	0.35	0.37	0.51	**0.46**
7 d	0.63	0.32	0.62	0.40	0.27	0.60	**0.47**
28 d	0.38	0.42	0.28	0.43	0.33	0.48	**0.39**

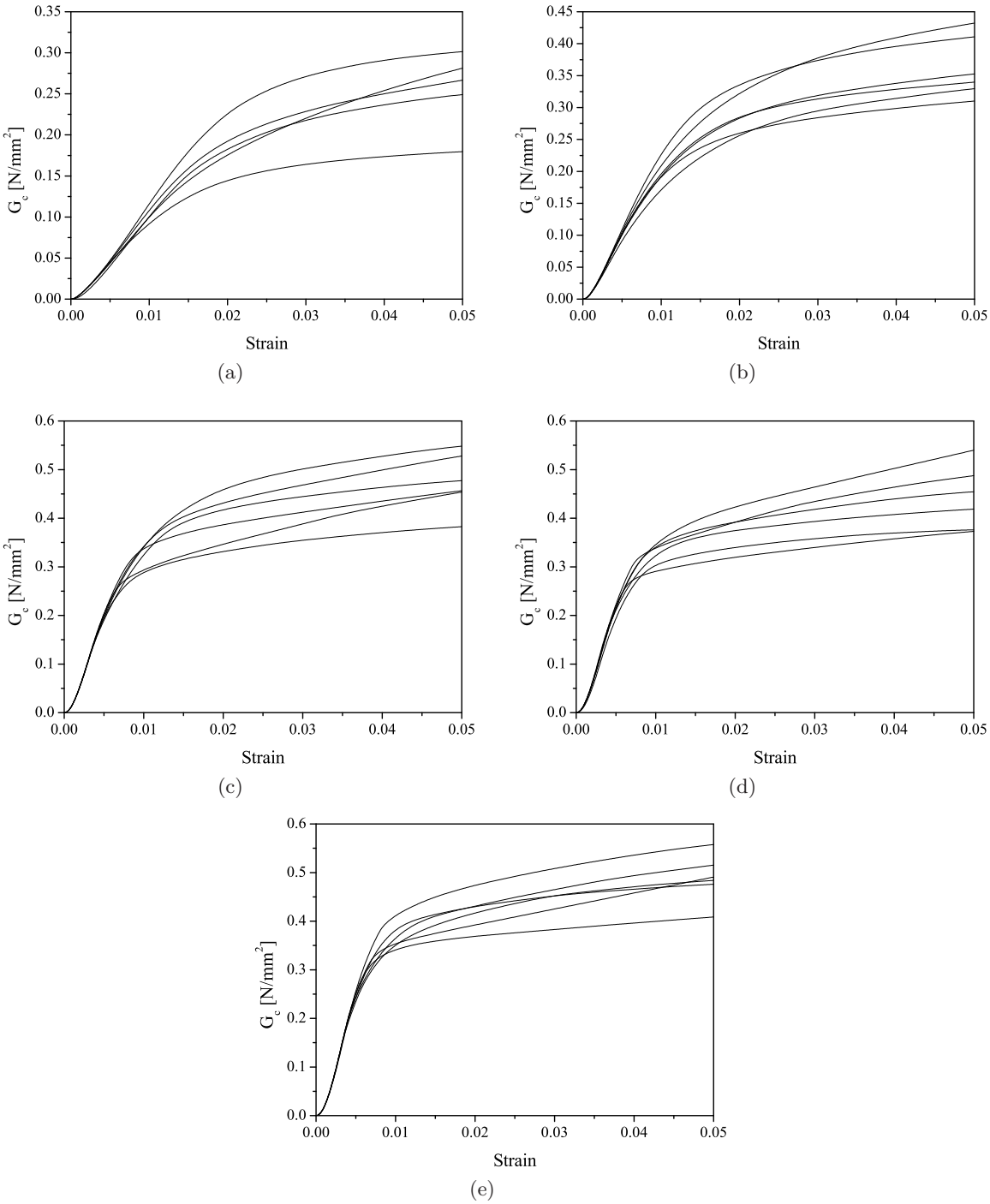

Figure IV.1: Relationship between the energy dissipated under compression and the strain for the series Cf30: (a) 12 hours, (b) 24 hours, (c) 3 days, (d) 7 days and (e) 28 days.

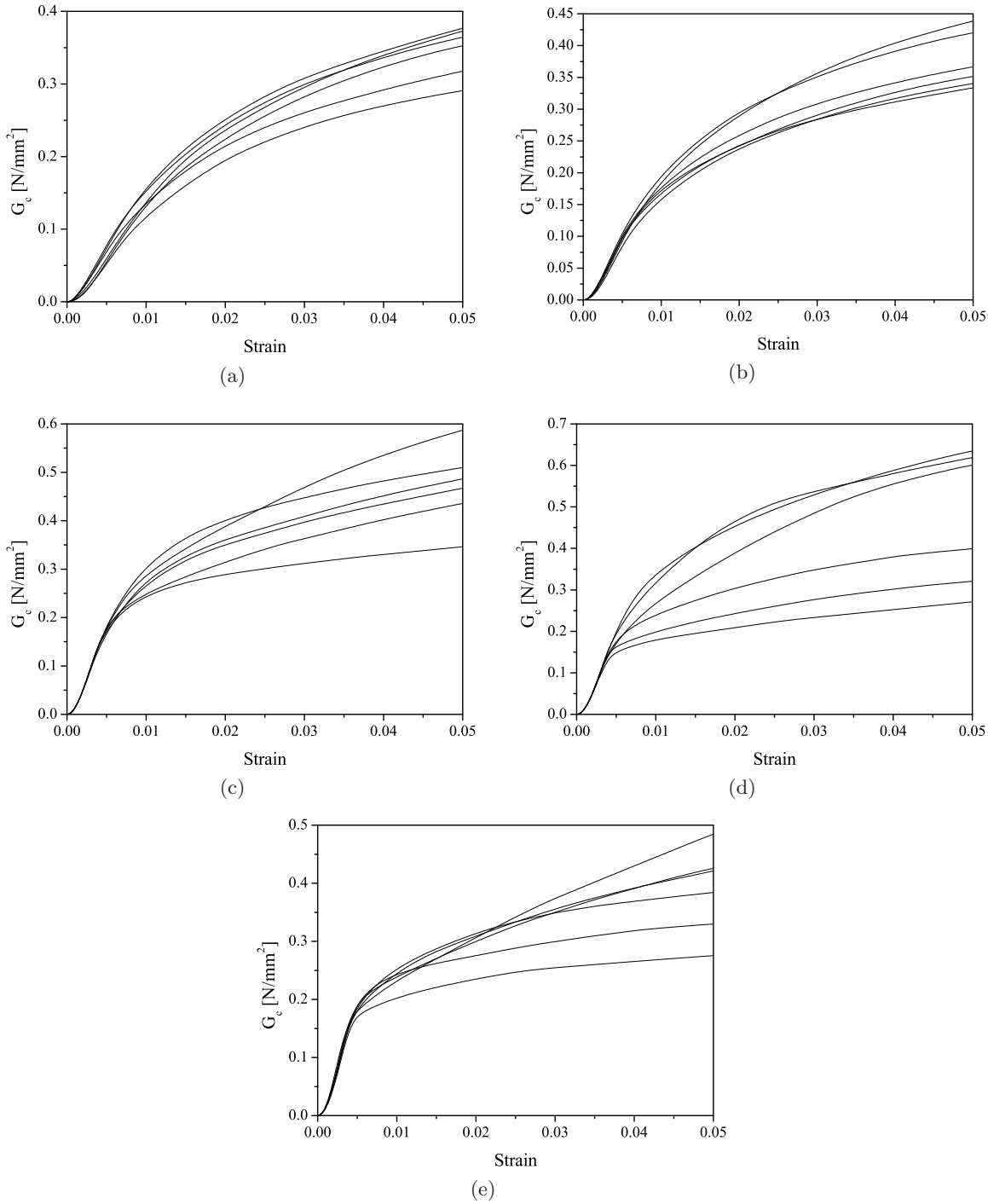

Figure IV.2: Relationship between the energy dissipated under compression and the strain for the series Cf45: (a) 12 hours, (b) 24 hours, (c) 3 days, (d) 7 days and (e) 28 days.

II Analytical and numerical results

In Table IV.9 are indicated the lower-confidence limit (lc) and the upper-confidence limit (uc) values, for the sample with the compressive strength values, whereas in Tables IV.10, IV.11 and IV.12 are indicated, respectively, the (lc) and (uc) values for the samples of the elasticity modulus, strain at peak-stress and energy dissipated under compression.

Table IV.9: Confidence limits for the compressive strength.

AGE	Cf30		Cf45	
	lc [MPa]	lc [MPa]	lc [MPa]	lc [MPa]
12 h	10.76	13.80	15.93	19.36
24 h	22.52	26.86	23.98	26.57
3 d	51.31	53.40	46.75	49.06
7 d	55.42	60.69	48.21	53.68
28 d	68.40	70.92	53.89	58.40

Table IV.10: Confidence limits for the elasticity modulus.

AGE	Cf30		Cf45	
	lc [MPa]	uc [MPa]	lc [MPa]	uc [MPa]
12 h	10.57	16.60	17.36	20.16
24 h	23.95	26.59	21.00	23.74
3 d	35.38	38.73	30.74	32.08
7 d	40.07	40.73	31.19	32.61
28 d	40.49	42.50	32.97	36.11

Table IV.11: Confidence limits for the strain at peak-stress.

AGE	Cf30		Cf45	
	lc [-]	uc [-]	lc [-]	uc [-]
12 h	0.0043	0.0091	0.0041	0.0051
24 h	0.0035	0.0042	0.0035	0.0039
3 d	0.0029	0.0032	0.0028	0.0031
7 d	0.0029	0.0032	0.0026	0.0032
28 d	0.0029	0.0033	0.0026	0.0030

Table IV.12: Confidence limits for the energy dissipated under compression.

Age	Cf30		Cf45	
	lc [N/mm^2]	*uc* [N/mm^2]	*lc* [N/mm^2]	*uc* [N/mm^2]
12 h	0.20	0.31	0.28	0.37
24 h	0.31	0.41	0.33	0.42
3 d	0.41	0.54	0.36	0.55
7 d	0.37	0.51	0.30	0.64
28 d	0.43	0.54	0.31	0.46

Annex V

Post-Cracking Behaviour

I Uniaxial tension test results

In Figures V.1 and V.2 are depicted the experimental uniaxial tension stress - displacement curves, respectively, with 30 kg/m^3 and 45 kg/m^3 of fibres for all tested specimens. Where as, in Figures V.3 and V.4 are depicted the experimental uniaxial tension tension $\sigma - w$ curves, respectively, with 30 kg/m^3 and 45 kg/m^3 of fibres for all tested specimens.

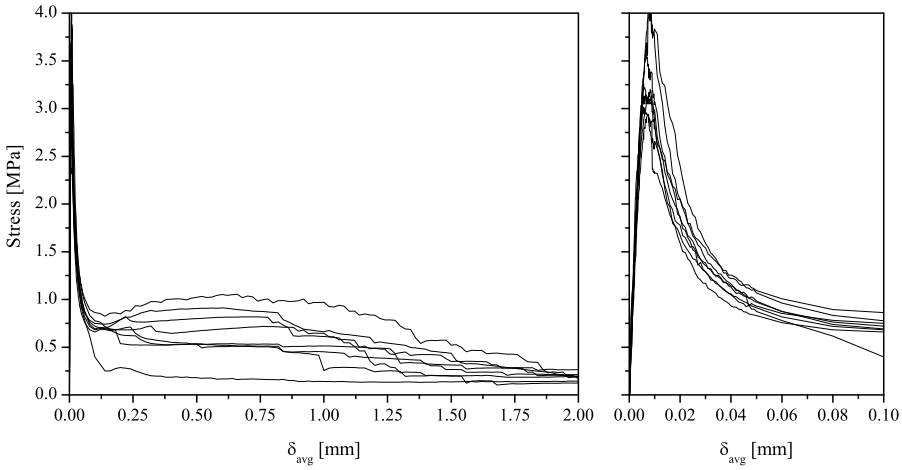

Figure V.1: Experimental uniaxial tension stress - displacement relationship with 30 kg/m^3.

In Table V.1 are included the values of the stress and toughness parameters obtained in all the uniaxial tension tests performed. Additionally are included the average values for each

batch, Avg., as well as the correspondent coefficients of variation, CoV. In the latter table, N_f and N_{eff} are, respectively, the total and effective number of fibres; σ_{peak} is the tensile strength, $\sigma_{0.3mm}$, σ_{1mm} and σ_{2mm} are the post-cracking stress for a crack opening of 0.3, 1 and 2 mm, respectively; G_{F1mm} and G_{F2mm} is the fracture energy dissipated up to a crack opening width of 1 and 2 mm, respectively.

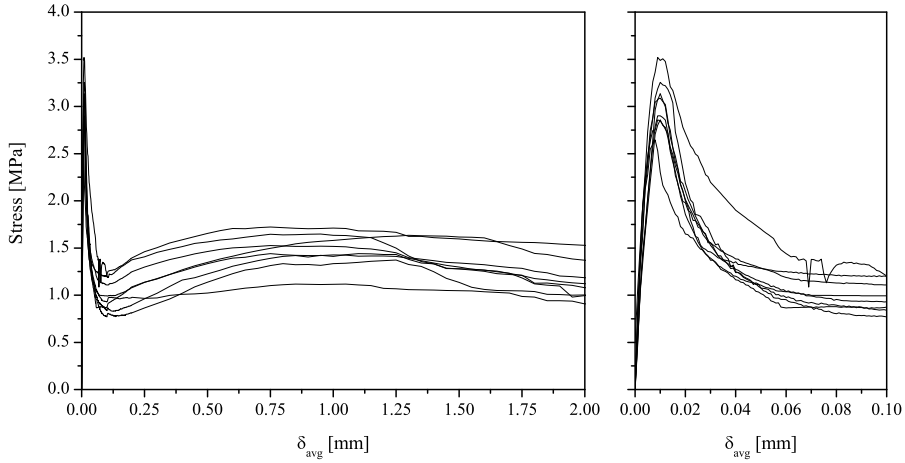

Figure V.2: Experimental uniaxial tension stress - displacement relationship with 45 kg/m^3 of fibres.

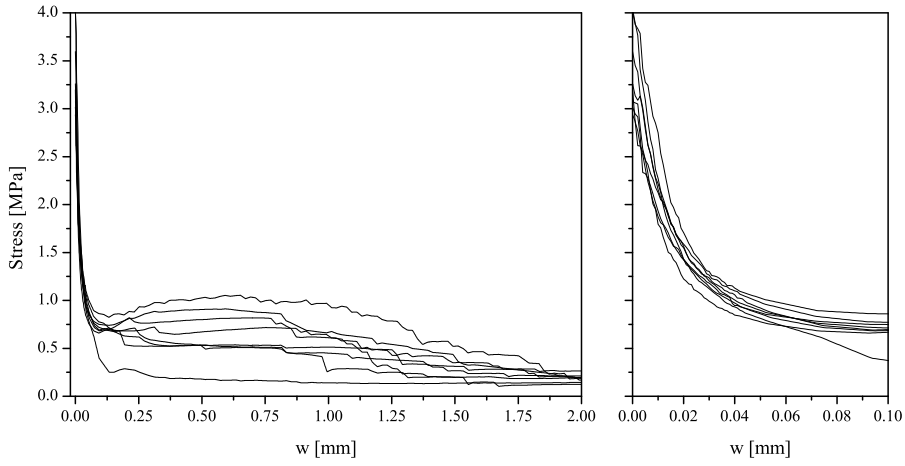

Figure V.3: Experimental uniaxial tension $\sigma - w$ relationship with 30 kg/m^3 of fibres.

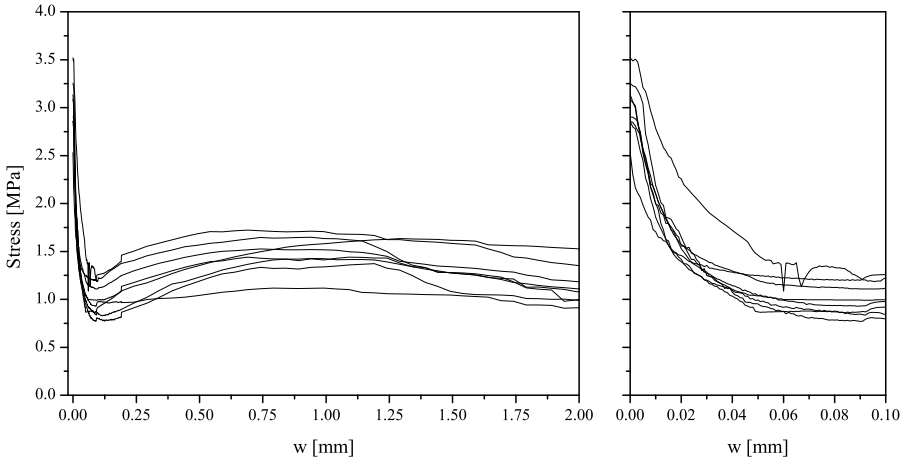

Figure V.4: Experimental uniaxial tension $\sigma - w$ relationship with 45 kg/m^3 of fibres.

Table V.1: Stress and toughness parameters from the uniaxial tension test.

Specimen		N_f [-]	N_{eff} [-]	σ_{peak} [MPa]	$\sigma_{0.3mm}$ [MPa]	σ_{1mm} [MPa]	σ_{2mm} [MPa]	G_{F1mm} [N/mm]	G_{F2mm} [N/mm]
Cf30	1	29	22	3.015	0.585	0.449	0.263	0.602	0.930
	2	32	25	2.937	0.878	0.669	0.188	0.863	1.273
	3	32	26	4.014	0.964	0.878	0.189	1.016	1.571
	4	37	21	4.042	0.549	0.512	0.211	0.618	0.937
	5	26	17	3.259	0.523	0.267	0.195	0.580	0.797
	6	20	14	3.596	0.207	0.141	0.144	0.278	0.415
	7	30	22	3.207	0.717	0.636	0.170	0.740	1.114
	8	35	21	3.072	0.766	0.610	0.124	0.784	1.022
	Avg.	27	19	3.392	0.649	0.520	0.186	0.685	1.007
	CoV	30.8%	28.8%	13.0%	36.6%	45.1%	22.8%	32.3%	33.7%
Cf45	1	83	46	3.520	1.459	1.634	1.078	1.571	2.880
	2	65	44	2.532	1.178	1.578	1.528	1.338	2.906
	3	59	34	2.858	1.026	1.411	0.996	1.227	2.482
	4	81	43	2.902	1.334	1.517	1.185	1.434	2.765
	5	76	46	3.089	1.558	1.706	1.354	1.591	3.145
	6	64	39	2.857	1.227	1.425	1.110	1.323	2.584
	7	62	32	3.255	0.964	1.339	0.990	1.173	2.310
	8	48	28	3.136	1.004	1.117	0.912	1.087	2.089
	Avg.	67	39	3.019	1.219	1.466	1.342	1.342	2.645
	CoV	16.1%	16.5%	9.9%	18.0%	12.7%	18.0%	13.6%	13.1%

II Three-point bending test results

In Figures V.5 and V.6 are depicted the experimental three point bending load - deflection curves, respectively, with 30 kg/m^3 and 45 kg/m^3 of fibres for all tested specimens. On the other hand, in Table V.2 are included the main flexure properties obtained from load - deflection relationships. In the latter table, F_L, $f_{ct,L}$ and δ_L are, respectively, the load, stress and deflection at the limit of proportionality; $f_{eq,i}$ and $f_{R,i}$ are the equivalent and residual flexural tensile strengths, respectively.

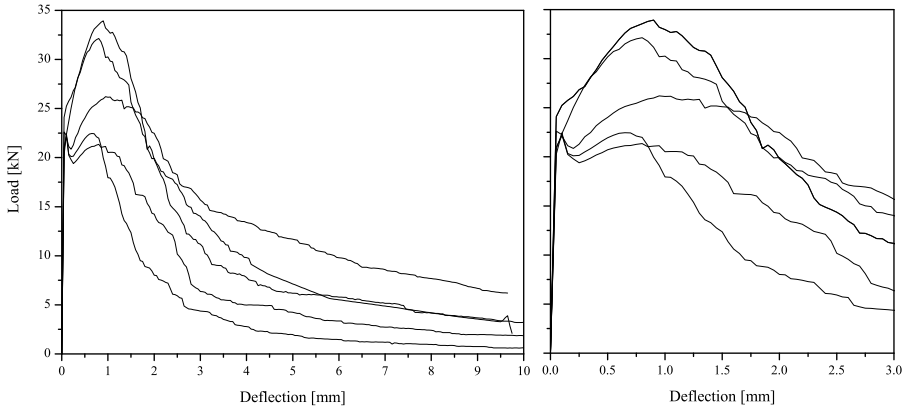

Figure V.5: Three point bending experimental load - deflection curves with 30 kg/m^3 of fibres.

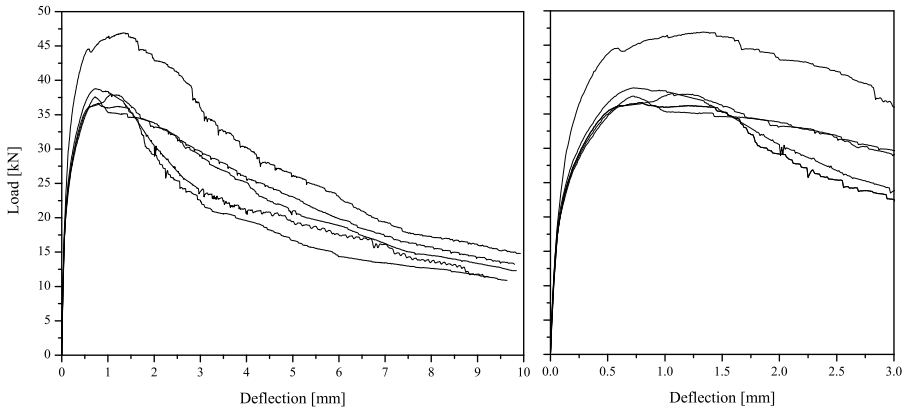

Figure V.6: Three point bending experimental load - deflection curves with 45 kg/m^3 of fibres.

Table V.2: Average and characteristic results of the three point bending tests.

Specimen		N_f [-]	N_{eff} [-]	F_L [kN]	δ_L [mm]	$f_{ct,L}$ [MPa]	$f_{eq,2}$ [MPa]	$f_{eq,3}$ [MPa]	$f_{R,1}$ [MPa]	$f_{R,4}$ [MPa]
Cf30	1	142	131	24.084	0.050	7.710	9.620	8.154	9.551	3.578
	2	104	97	22.625	0.050	7.240	6.385	5.419	6.535	2.036
	3	94	90	20.255	0.050	6.482	6.937	4.371	6.913	1.399
	4	123	111	20.813	0.050	6.660	9.538	7.966	9.430	4.580
	5	119	106	21.004	0.050	6.721	7.531	7.396	7.568	5.018
	Avg.	116	107	21.758	0.050	6.963	8.002	6.661	7.999	3.322
	CoV	15.8%	14.6%	7.2%	0.0%	7.2%	18.7%	25.2%	17.6%	47.3%
Cf40	1	168	143	17.124	0.050	5.490	10.327	10.255	11.122	7.214
	2	157	132	17.246	0.050	5.519	10.102	10.802	10.831	9.304
	3	179	152	17.201	0.050	5.504	10.212	10.984	11.013	9.496
	4	188	167	18.628	0.050	5.961	12.892	13.940	13.755	11.531
	5	162	140	18.083	0.050	5.787	10.668	10.678	11.472	7.623
	Avg.	171	141	17.663	0.050	5.652	10.844	11.332	11.639	9.033
	CoV	5.7%	5.8%	3.8%	0%	3.8%	10.7%	13.1%	10.4%	19.0%

III Splitting test results

In Figures V.7(a) and V.7(b) are depicted the experimental splitting load - crack mouth opening displacement curves, respectively, with 30 kg/m^3 and 45 kg/m^3 of fibres for all tested specimens.

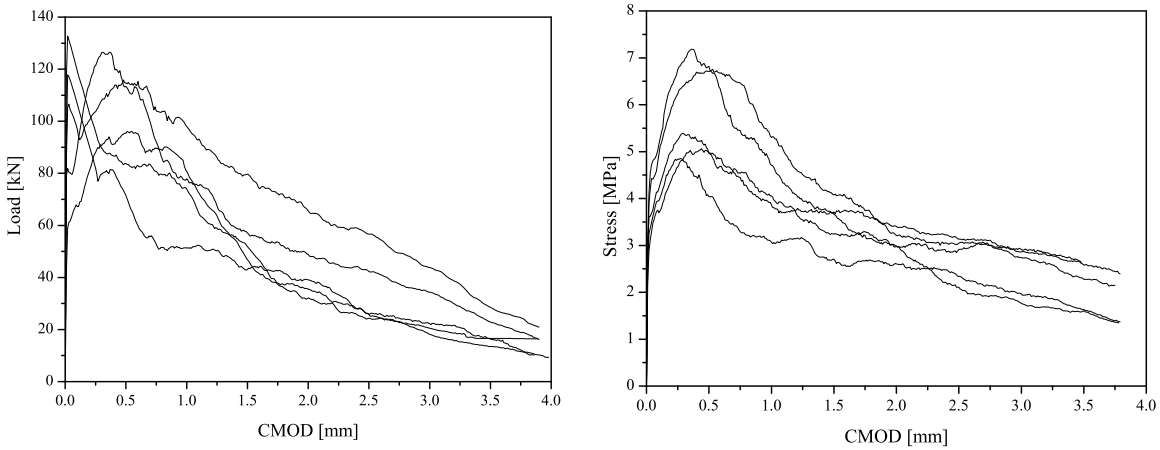

(a) (b)

Figure V.7: Experimental load - crack opening mouth displacement relationships with: (a) 30 kg/m^3 and (b) 45 kg/m^3 of fibres.